

Lecture Notes in Electrical Engineering 575

Koushik Maharatna  
Maitreyi Ray Kanjilal  
Sukumar Chandra Konar  
Sumit Nandi  
Kunal Das *Editors*

# Computational Advancement in Communication Circuits and Systems

Proceedings of ICCACCS 2018

 Springer

# Lecture Notes in Electrical Engineering

## Volume 575

### Series Editors

Leopoldo Angrisani, Department of Electrical and Information Technologies Engineering, University of Napoli Federico II, Naples, Italy

Marco Arteaga, Departament de Control y Robótica, Universidad Nacional Autónoma de México, Coyoacán, Mexico

Bijaya Ketan Panigrahi, Electrical Engineering, Indian Institute of Technology Delhi, New Delhi, Delhi, India

Samarjit Chakraborty, Fakultät für Elektrotechnik und Informationstechnik, TU München, Munich, Germany

Jiming Chen, Zhejiang University, Hangzhou, Zhejiang, China

Shanben Chen, Materials Science and Engineering, Shanghai Jiao Tong University, Shanghai, China

Tan Kay Chen, Department of Electrical and Computer Engineering, National University of Singapore, Singapore, Singapore

Rüdiger Dillmann, Humanoids and Intelligent Systems Lab, Karlsruhe Institute for Technology, Karlsruhe, Baden-Württemberg, Germany

Haibin Duan, Beijing University of Aeronautics and Astronautics, Beijing, China

Gianluigi Ferrari, Università di Parma, Parma, Italy

Manuel Ferre, Centre for Automation and Robotics CAR (UPM-CSIC), Universidad Politécnica de Madrid, Madrid, Spain

Sandra Hirche, Department of Electrical Engineering and Information Science, Technische Universität München, Munich, Germany

Faryar Jabbari, Department of Mechanical and Aerospace Engineering, University of California, Irvine, CA, USA

Limin Jia, State Key Laboratory of Rail Traffic Control and Safety, Beijing Jiaotong University, Beijing, China

Janusz Kacprzyk, Systems Research Institute, Polish Academy of Sciences, Warsaw, Poland

Alaa Khamis, German University in Egypt El Tagamoa El Khames, New Cairo City, Egypt

Torsten Kroeger, Stanford University, Stanford, CA, USA

Qilian Liang, Department of Electrical Engineering, University of Texas at Arlington, Arlington, TX, USA

Ferran Martin, Departament d'Enginyeria Electrònica, Universitat Autònoma de Barcelona, Bellaterra, Barcelona, Spain

Tan Cher Ming, College of Engineering, Nanyang Technological University, Singapore, Singapore

Wolfgang Minker, Institute of Information Technology, University of Ulm, Ulm, Germany

Pradeep Misra, Department of Electrical Engineering, Wright State University, Dayton, OH, USA

Sebastian Möller, Quality and Usability Lab, TU Berlin, Berlin, Germany

Subhas Mukhopadhyay, School of Engineering & Advanced Technology, Massey University, Palmerston North, Manawatu-Wanganui, New Zealand

Cun-Zheng Ning, Electrical Engineering, Arizona State University, Tempe, AZ, USA

Toyoaki Nishida, Graduate School of Informatics, Kyoto University, Kyoto, Japan

Federica Pascucci, Dipartimento di Ingegneria, Università degli Studi "Roma Tre", Rome, Italy

Yong Qin, State Key Laboratory of Rail Traffic Control and Safety, Beijing Jiaotong University, Beijing, China

Gan Woon Seng, School of Electrical & Electronic Engineering, Nanyang Technological University, Singapore, Singapore

Joachim Speidel, Institute of Telecommunications, Universität Stuttgart, Stuttgart, Baden-Württemberg, Germany

Germano Veiga, Campus da FEUP, INESC Porto, Porto, Portugal

Haitao Wu, Academy of Opto-electronics, Chinese Academy of Sciences, Beijing, China

Junjie James Zhang, Charlotte, NC, USA

The book series *Lecture Notes in Electrical Engineering* (LNEE) publishes the latest developments in Electrical Engineering - quickly, informally and in high quality. While original research reported in proceedings and monographs has traditionally formed the core of LNEE, we also encourage authors to submit books devoted to supporting student education and professional training in the various fields and applications areas of electrical engineering. The series cover classical and emerging topics concerning:

- Communication Engineering, Information Theory and Networks
- Electronics Engineering and Microelectronics
- Signal, Image and Speech Processing
- Wireless and Mobile Communication
- Circuits and Systems
- Energy Systems, Power Electronics and Electrical Machines
- Electro-optical Engineering
- Instrumentation Engineering
- Avionics Engineering
- Control Systems
- Internet-of-Things and Cybersecurity
- Biomedical Devices, MEMS and NEMS

For general information about this book series, comments or suggestions, please contact [leontina.dicecco@springer.com](mailto:leontina.dicecco@springer.com).

To submit a proposal or request further information, please contact the Publishing Editor in your country:

#### **China**

Jasmine Dou, Associate Editor ([jasmine.dou@springer.com](mailto:jasmine.dou@springer.com))

#### **India**

Swati Meherishi, Executive Editor ([swati.meherishi@springer.com](mailto:swati.meherishi@springer.com))

Aninda Bose, Senior Editor ([aninda.bose@springer.com](mailto:aninda.bose@springer.com))

#### **Japan**

Takeyuki Yonezawa, Editorial Director ([takeyuki.yonezawa@springer.com](mailto:takeyuki.yonezawa@springer.com))

#### **South Korea**

Smith (Ahram) Chae, Editor ([smith.chae@springer.com](mailto:smith.chae@springer.com))

#### **Southeast Asia**

Ramesh Nath Premnath, Editor ([ramesh.premnath@springer.com](mailto:ramesh.premnath@springer.com))

#### **USA, Canada:**

Michael Luby, Senior Editor ([michael.luby@springer.com](mailto:michael.luby@springer.com))

#### **All other Countries:**

Leontina Di Cecco, Senior Editor ([leontina.dicecco@springer.com](mailto:leontina.dicecco@springer.com))

Christoph Baumann, Executive Editor ([christoph.baumann@springer.com](mailto:christoph.baumann@springer.com))

**\*\* Indexing: The books of this series are submitted to ISI Proceedings, EI-Compindex, SCOPUS, MetaPress, Web of Science and Springerlink \*\***

More information about this series at <http://www.springer.com/series/7818>

Koushik Maharatna · Maitreyi Ray Kanjilal ·  
Sukumar Chandra Konar ·  
Sumit Nandi · Kunal Das  
Editors

# Computational Advancement in Communication Circuits and Systems

Proceedings of ICCACCS 2018

 Springer

*Editors*

Koushik Maharatna  
School of Electronics and Computer Science  
University of Southampton  
Southampton, UK

Maitreyi Ray Kanjilal  
Narula Institute of Technology  
Kolkata, West Bengal, India

Sukumar Chandra Konar  
Narula Institute of Technology  
Kolkata, West Bengal, India

Sumit Nandi  
Narula Institute of Technology  
Kolkata, West Bengal, India

Kunal Das  
Narula Institute of Technology  
Kolkata, West Bengal, India

ISSN 1876-1100

ISSN 1876-1119 (electronic)

Lecture Notes in Electrical Engineering

ISBN 978-981-13-8686-2

ISBN 978-981-13-8687-9 (eBook)

<https://doi.org/10.1007/978-981-13-8687-9>

© Springer Nature Singapore Pte Ltd. 2020

This work is subject to copyright. All rights are reserved by the Publisher, whether the whole or part of the material is concerned, specifically the rights of translation, reprinting, reuse of illustrations, recitation, broadcasting, reproduction on microfilms or in any other physical way, and transmission or information storage and retrieval, electronic adaptation, computer software, or by similar or dissimilar methodology now known or hereafter developed.

The use of general descriptive names, registered names, trademarks, service marks, etc. in this publication does not imply, even in the absence of a specific statement, that such names are exempt from the relevant protective laws and regulations and therefore free for general use.

The publisher, the authors and the editors are safe to assume that the advice and information in this book are believed to be true and accurate at the date of publication. Neither the publisher nor the authors or the editors give a warranty, expressed or implied, with respect to the material contained herein or for any errors or omissions that may have been made. The publisher remains neutral with regard to jurisdictional claims in published maps and institutional affiliations.

This Springer imprint is published by the registered company Springer Nature Singapore Pte Ltd. The registered company address is: 152 Beach Road, #21-01/04 Gateway East, Singapore 189721, Singapore

# Preface

It is an immense pleasure to release the Proceedings of 2nd International Conference on Computational Advancement in Communication Circuit and System (ICCACCS 2018) which was organized by Narula Institute of Technology, Agarpara, Kolkata, India, on November 23–24, 2018. In this conference, we received 84 papers for consideration. Finally, after reviewing all the papers by an expert reviewer, we accepted only 42 papers for publishing in Springer Lecture Note on Electrical Engineering.

The aim of the conference was to bring together national and international researchers, industrial experts and academicians to present papers and generate discussions on current research and development in the state-of-the-art technologies in computing and communication, environment-friendly computing, reconfigurable computing and low-power nanotechnology and VLSI design, and it provided a forum for sharing insights, experiences and interaction on various facets of evolving technologies and patterns related to computer science, information technology, electrical and electronics, etc. The investigation, simulation, analysis and solving complex issues and phenomena in the areas of computation, communication circuit and system design in engineering also represented the current state-of-the-art technology and the outcome of the ongoing research in the area of advanced applied science and engineering.

We would like to take this opportunity to thank all esteemed authors for contributing their research work to this conference. We were able to obtain the quality of research article only because of esteemed reviewers which will be published in this Springer Lecture Note. We are extremely thankful to them for their effort and time in reviewing the papers critically. We express our gratitude to Prof. Bhargav B. Bhattacharya, ISI, Kolkata, for reviewing the papers even during the travel around the USA. We respect the dedication and efforts that were made by our reviewers to make this Lecture Note qualitative. We are thankful to the management of Narula Institute of Technology, Mr. Taranjit Singh and Mr. Simarpreet Singh, for their

continuous support and trust. Our sincere thanks to Mr. Aninda Bose, Editor, Springer Lecture Note, Springer India Pvt. Ltd., for his cooperation and support. Special thanks to all faculty members, advisory committee, organizing committee, student and staff members of Narula Institute of Technology for their hard work.

Southampton, UK  
Kolkata, India  
Kolkata, India  
Kolkata, India  
Kolkata, India

Koushik Maharatna  
Maitreyi Ray Kanjilal  
Sukumar Chandra Konar  
Sumit Nandi  
Kunal Das

# **Organizing Committee**

## **Chief Patron**

Sardar Taranjit Singh, Managing Director, JIS Group

## **Patron**

Prof. S. M. Chatterjee, Chairman—BOG, JIS Group

Mr. Harenjeet Singh, Trustee Member, JIS Group

Mr. Amrk Singh, Trustee Member, JIS Group

Mr. S. S. Datta Gupta, Director, JIS Group

Prof. Asit Guha, Advisor, JIS Group

Mr. U. S. Mukherjee, Deputy Director, JIS Group

Mr. Simarpreet Singh, Director, JIS Group

Manpreet Kaur, CEO, JIS Group

Jaspreet Kaur, Trustee Member, JIS Group

Mr. Harjot Singh, Director, JIS Group

Mr. Amanjot Singh, Director, JIS Group

## **General Chair**

Prof. Amlan Chakraborty, Dean, CU

Prof. Koushik Maharatna, University of Southampton, London



## **Program Chair**

Prof. (Dr.) Sumana Chowdhuri, Applied Physics, CU

Prof. (Dr.) Debashis De, MAKAUT

## **Advisory Committee**

Dr. Manpreet Singh Manna, Director, AICTE

Prof. Goutam Kumar Dalapati, IMRE, Singapore

Prof. (Dr.) Bhargav B. Bhattacharya, ISI, Kolkata

Prof. (Dr.) Dulal Acharya, Director, ACT, Kolkata

Prof. (Dr.) B. P. Sinha, Ex-Prof., ISI, Kolkata

Prof. S. K. Sanyal, Jadavpur University, Kolkata

Prof. Sanatan Chattopadhyay, Calcutta University

Prof. Soma Das, Guru Ghasidas Central University, Bilaspur

Prof. Swapna S. Nair, Central University, Kerala

Prof. P. K. Banerjee, Ex-Prof., Jadavpur University, Kolkata

Prof. J. K. Das, Advisor, R&D, Narula Institute of Technology

Prof. A. K. Mallick, Ex-Prof., IIT Kharagpur

Prof. D. Ghosh Dastidar, Ex-Prof., Jadavpur University, Kolkata

Prof. (Dr.) K. K. Aggarwal, Chancellor, K. R. Mangalam University

Mr. Sanjiv Goswami, Managing Director, Springer Nature

## **Program Committee**

Prof. Nabanita Das, ISI, Kolkata

Prof. Hafizur Rahaman, IEST, Shibpur

Prof. (Dr.) Chandan Kr. Sarkar, Ex-Prof., Jadavpur University, Kolkata

Prof. (Dr.) Paramartha Dutta, Visva-Bharati University

Prof. Nabendu Chaki, University of Calcutta

Prof. J. P. Singh, NIT Patna

Prof. (Dr.) Debnath Bhattacharyya, VIIT, Vizag

Prof. (Dr.) J. K. Mandal, University of Kalyani

Dr. Ram Sarkar, Jadavpur University

Dr. Abhishek Das, Aliah University, Kolkata

Dr. Siddartha Bhattacharya, Principal, RCC Institute of Information Technology

Mr. Lokesh Mehra, Director, Millionlights, and Former Director, Microsoft and Oracle

Mr. Roger Raphael, Senior Technical Staff, IBM, San Francisco Bay Area

Dr. Moumita Mukherjee, Assoc. Dean, Adamas University

## **Organizing Chair**

Prof. (Dr.). M. R. Kanjilal, Principal, Narula Institute of Technology

## **Convener**

Prof. Sukumar Chandra Konar, Dean, R&D, Narula Institute of Technology

## **Jt. Convener**

Dr. Sumit Nandi, HOD—BS & HU, Narula Institute of Technology

Dr. Kunal Das, Associate Professor, CSE, Narula Institute of Technology

## **Secretary**

Sandhya Pattanyak, Assistant Professor (ECE), Narula Institute of Technology

Mr. Arkendu Mitra, Assistant Professor, Narula Institute of Technology

## **Treasurer**

Prof. Surajit Bari, ECE

Mr. Nilanjan Mitra, Accounts

## **Organizing Committee**

Prof. B. K. Medya, HOD, IT

Prof. Biman Mukherjee, HOD, CE

Dr. Sandip Chanda, HOD, EE

Prof. Jayanta Pal, HOD, CSE

Prof. Saradindu Panda, HOD, ECE

Prof. J. C. Guha, CE

Prof. Bansari Deb Majumder, TIC, EIE

Dr. Sumit Chabri, HOD, ME

Dr. Sanjay Goswami, HOD, MCA

## **Technical Program Committee**

Sandhya Pattanyak, ECE (Coordinator)  
Dr. Rupa Bhattacharyya, BS & HU  
Sagarika Chowdhury, CSE  
Dr. Arup Sarkar, CSE  
Kousik Sarkar, ECE

## **Web Design, Publication, Print Media and Publicity Committee**

Subhendu Banerjee, CSE (Coordinator)  
Soumya Bhattacharyya, IT  
Rimpi data, ECE

## **Accommodation & Transport Committee**

Sudhangshu Sarkar, EE (Coordinator)  
Dr. Dhananjoy Tripathi, BS & HU  
Abhijit Ghosh, ECE

## **Refreshment Committee**

Soumen Pal, ECE (Coordinator)  
Dr. Nikhilesh Sil, BS & HU  
Rahul Biswas Deb, CE

## **Registration Committee**

Dr. Susmita Karan, BS & HU (Coordinator)  
Sangita Roy, ECE  
Sujata Kundu, IT  
Kamalika Banerjee, EE

# About the Institute

Narula Institute of Technology is a leading autonomous engineering and management college, located at Agarpara near Kolkata under the aegis of JIS Group Educational Initiatives since 2001.

## **Affiliations/Accreditations**

It is approved by AICTE and affiliated to MAKAUT, West Bengal—formerly known as West Bengal University of Technology—which has NBA-accredited degree programs in engineering. It boasts of the prestigious NIRF ranking among 150 selected institutes of India. It is also accredited by the National Assessment and Accreditation Council (NAAC). The college has also received the notable World Bank-assisted and MHRD-approved TEQIP (Phase II) grants for the advancement of technical education. It is eligible for receiving Central assistance under the recognition of 2(f) and 12(B) under the UGC Act.

## **Courses**

The four-year B.Tech. course is imparted in the streams of CSE, ECE, EE, CE, IT, EIE and ME. The institute provides a brilliant platform for pursuing higher studies through PG courses like M.Tech. (CSE, ECE, EE—power system, CE—structural engineering), MBA and MCA. It has expanded to include diploma programs in EE, CE and ECTC under the affiliation of West Bengal State Council of Technical Education.

## **Research and Development**

The institute boasts of a powerful R&D cell with immense contribution from the scholarly faculty members. There is an enormous repository of national and international journal publications, e-books, online lectures which have drawn nationwide attention. With the encouragement and support from the college, around ten projects funded by organizations like UGC, BRNS and AICTE are running successfully by the faculty members till date. Very recently, the ECE, CSE

Department have secured the MODROBS, SERB, AICTE-RPS Projects and Institute level DST-FIST grant is received for upgrading their Cloud Computing, Wireless Sensor Network Lab, Embedded System and Electronic Design Automation Lab, etc.

**Collaborations**

The college is in collaboration with Tech Mahindra, Reliance Jio Infocomm Limited, CII, NASSCOM, Aspire Disruptive Skill Foundation, Oracle, Infosys, TCS, NIT Sikkim, IIT KGP, AIT, Bangkok, and other organizations of repute. The students get an opportunity to interact in an international platform through seminars, conferences and special teaching-learning sessions. The student chapter plays a crucial role in organizing informative technical events within the campus. At present, there are five student chapters in our college: IETE student forum of Electronics and Communication Engineering Department, ICE and ASCE of Civil Engineering Department, CSI of Computer Science Engineering, Information Technology and MCA Department and Institute of Engineers India (IEI) of Electrical Engineering Department.

# About the Conference

The 2nd International Conference on Computational Advancement in Communication Circuit and System (ICCACCS 2018) was held during November 23–24, 2018, at Narula Institute of Technology, Agarpara, Kolkata, India. The aim of the conference was to bring together national and international researchers, industrial experts and academicians to present papers and generate discussions on current research and development in the state-of-the-art technologies in computing and communication, environment-friendly computing, reconfigurable computing and low-power nanotechnology and VLSI design, and it provided a forum for sharing insights, experiences and interaction on various facets of evolving technologies and patterns related to computer science, information technology, electrical and electronics, etc. The investigation, simulation, analysis and solving complex issues and phenomena in the areas of computation, communication circuit and system design in engineering also represented the current state-of-the-art technology and the outcome of the ongoing research in the area of advanced applied science and engineering. Conference technical program consisted of plenary and keynote lectures, tutorial/workshop, oral presentation session, in which the leading expert from all around the world presented the state-of-the-art reviews of rapidly developing and exciting areas and reported the latest significant findings and development in all major fields of applied science and engineering. We cordially invited all to participate in this exciting conference as a presenter.

We organized the 1st International Conference on Computational Advancement in Communication Circuit and System (ICCACCS 2014) during October 30–November 1, 2014. The conference was supported by Technical Education Quality Improvement Program (TEQIP), New Delhi, India, and we had technical collaboration with IEEE Kolkata Section, along with publication partner Springer. The Proceedings of the International Conference was published by Springer Lecture Note on Electrical Engineering. <https://www.springer.com/in/book/9788132222736>.

In the 2nd International Conference on Computational Advancement in Communication Circuit and System (ICCACCS 2018), we encouraged all to share

their research work describing original work on theories, methodologies, abstraction, algorithms, industry applications and case studies with others by submitting original paper(s). We greatly appreciated the interest of all in the ICCACCS 2018 and for their presence at Narula Institute of Technology, Kolkata, India, in November 2018.

# Contents

## Part I Modeling of Energy Systems

<b>Congested Power Transmission System in a Deregulated Power Market</b> .....	3
Bishaljit Paul, Chandan Kumar Chanda, Jagadish Pal and Manish Kumar Pathak	
<b>Integration of DSTATCOM and Distributed Generation with Nonlinear Loads</b> .....	15
Mukul Anand, Amit Kumar, Rahul Dev and Pradeep Kumar	
<b>Comparison of Improvement in Technical, Commercial and Environmental Benefits by Optimal Single-Point, Twin-Point and Triple-Point Deterministic PV-Based DG Injection by Jaya Algorithm</b> .....	25
Anirban Chowdhury, Ranjit Roy, Kamal Krishna Mandal, Soumyajit Bhattacharya, Priyankar Biswas and Sayani Nandy	
<b>Optimal Reactive Power Dispatch Incorporating Solar Power Using Jaya Algorithm</b> .....	37
Tanmay Das, Ranjit Roy, Kamal Krishna Mandal, Souren Mondal, Soumaymoy Mondal, Pares Hait and Moloy Kumar Das	
<b>Bat-Algorithm-Based Transmission Expansion Planning</b> .....	49
P. Das, P. S. Bera and P. Biswaas	
<b>Emergency Restoration Based on Priority of Load Importance Using Floyd–Warshall Shortest Path Algorithm</b> .....	59
Dipu Sarkar, Maitrayee Chakrabarty, Abhinandan De and Sanjay Goswami	
<b>Fault Detection During Power Swing Using Fast Discrete S-transform</b> .....	73
Arkadeep Mondal, Sayan Das and Bikash Patel	



<b>Detection and Classification of Faults on the Transmission Line Using Lissajous Figure</b> .....	81
Sayan Das, Arkadeep Mondal and Bikash Patel	
<b>Design and Fabrication of Solar-Powered Water Pumping Unit for Irrigation System</b> .....	89
Pronami Mukherjee and Tapas Kumar Sengupta	
<b>Power Grid Generation with Tectonic Mechanism Wind Energy Resources</b> .....	103
Pratyusha Biswas Deb, Susmita Das, Arnima Das, Ronojit Bose, Aritra Das and Maitreyi Ray Kanjilal	
<b>Part II Cloud Computing, Internet on Things, Machine Learning and Big Data Analytics</b>	
<b>Mining Social Network Data for Predictive Personality Modelling by Employing Machine Learning Techniques</b> .....	113
Arjun Sengupta and Anupam Ghosh	
<b>An Ensemble Learning-Based Language Identification System</b> .....	129
Himadri Mukherjee, Sahana Das, Ankita Dhar, Sk. Md. Obaidullah, K. C. Santosh, Santanu Phadikar and Kaushik Roy	
<b>Kinect Sensor Based Single Person Hand Gesture Recognition for Man–Machine Interaction</b> .....	139
Biswarup Ganguly, Priyanka Vishwakarma, Shreya Biswas and Rahul	
<b>Artificial Intelligence-Based Economic Control of Micro-grids: A Review of Application of IoT</b> .....	145
Promila Das, Sandip Chanda and A. De	
<b>Analysis of Heart Rate Variability to Understand the Immediate Effect of Smoking on the Autonomic Nervous System Activity</b> .....	157
Prerana Talukdar, Suraj Kumar Nayak, Dibyajyoti Biswal, Anilesh Dey and Kunal Pal	
<b>Recurrence Quantification Analysis of Electrocardiogram Signals to Recognize the Effect of a Motivational Song on the Cardiac Electrophysiology</b> .....	165
Swatilekha Paul, Gitika Yadu, Suraj Kumar Nayak, Anilesh Dey and Kunal Pal	
<b>Part III Communication</b>	
<b>Meteorological Parameter Studies During 6 December 2016 Indonesia Earthquake (<math>M_w</math> 6.5)</b> .....	175
Pranab Hazra, Suman Paul, Shreya Chatterjee and Anindita Chandra	

**WARP Test Bed Implementation of Lag Order and Data Length-optimized AR Spectrum Estimation Algorithm** ..... 191  
 Debashis Chakraborty and Salil Kumar Sanyal

**Detection of Black Hole Attack in Delay-Tolerant Network** ..... 205  
 Chandrima Chakrabarti, Ananya Banerjee, Anirban Das, Souradip Ganguly, Somraj Mukherjee, Rohan Dutta and Jagriti Chourasia

**Unvoiced Speech Recognition Using Dynamic Analysis of EMG Signal** ..... 217  
 Paromita Das, Biswarup Neogi, Aniruddha Chandra and Anilesh Dey

**Study the Effect of Cognitive Stress on HRV Signal Using 3D Phase Space Plot in Spherical Coordinate System** ..... 227  
 Sudhangshu Sarkar, Pallav Dutta, Aniruddha Chandra and Anilesh Dey

**Part IV Network Security & Cryptography**

**MVTRNG: Majority Voter-Based Crossed Loop Quantum True Random Number Generator in QCA Nanotechnology** ..... 241  
 Arindam Sadhu, Kunal Das, Debashis De and Maitreyi Ray Kanjilal

**Applying Encryption Algorithm on Text Steganography Based on Number System** ..... 255  
 Kunal Kumar Mandal, Siddhartha Chatterjee, Avishek Chakraborty, Saptarshi Mondal and Saikat Samanta

**Part V VLSI and Image Processing**

**Four-Directional Detection-Based Gaussian Noise Removal** ..... 269  
 Shubhendu Banerjee, Aritra Bandyopadhyay, Rajib Bag and Atanu Das

**Comparative Analysis of 6-T SRAM Cell in Terms of Power Using CMOS and DGMOS** ..... 279  
 Srabani Das (Roy), Saradindu Panda and Gourav Chakraborty

**Low-Power FPGA-Based Hardware Implementation of Reversible Watermarking Scheme for Medical Image** ..... 287  
 Poulami Jana and Amit Phadikar

**A New Approach Toward Invariant Shape Descriptor Tools for Shape Classification Through Morphological Analysis of Image** ..... 297  
 Soumen Santra and Surajit Mandal

**A Variable Delay Circuit to Develop Identical Rise/Fall Time in the Output** ..... 305  
 Pritam Bhattacharjee and Alak Majumder

<b>Algorithms for Minimizing Bottleneck Crosstalk in Two-Layer Channel Routing</b> .....	313
Tarak Nath Mandal, Ankita Dutta Banik, Kaushik Dey, Ranjan Mehera and Rajat Kumar Pal	
<b>Design and Comparative Analysis of Low-Power, High-Speed, 3-Bit Flash ADC for Biomedical Signal Processing Using 45-nm CMOS Technology</b> .....	331
Sk. Firojuddin, Soumen Pal and Puspak Pain	
<b>Part VI Nano Technology</b>	
<b>Influence of Gate and Channel Engineering on Multigate Tunnel FETs: A Review</b> .....	345
Ritam Dutta, Sukumar Chandra Konar and Nitai Paitya	
<b>Quantitative Structure–Activity Relationship (QSAR) Study of Some DNA-Intercalating Anticancer Drugs</b> .....	357
Indrani Sarkar, Sanjay Goswami and Paushali Majumder	
<b>To Explore Compounds as Tuberculosis Inhibitors—A Combination of Pharmacophore Modelling, Virtual Screening and Molecular Docking Studies</b> .....	367
Indrani Sarkar, Sanjay Goswami and Paushali Majumder	
<b>Physical Proof and Simulation of Ternary Logic Gate in Ternary Quantum Dot Cellular Automata</b> .....	375
Puspak Pain, Arindam Sadhu, Kunal Das and Maitreyi Ray Kanjilal	
<b>Optical Properties of Fe-Doped ZnO Thin Film on p-Si by Spin Coating</b> .....	387
Amalendu Bera and Sourav Chattopadhyay	
<b>Part VII Reconfigurable Computing</b>	
<b>AVR Microcontroller-Based Error-Free Public Addressing System</b> . . . .	399
Suvamoy Bhattacharyya, Partha Sarkar, Arijit Sen, Ashesh Sinha and Sandip Chanda	
<b>Prototype Model for Controlling of Soil Moisture and pH in Smart Farming System</b> .....	405
Suvamoy Bhattacharyya, Partha Sarkar, Sharthak Sarkar, Ashesh Sinha and Sandip Chanda	
<b>Author Index</b> .....	413

## About the Editors



**Prof. Koushik Maharatna** received his B.Sc. in Physics and M.Sc. in Electronic Science from Calcutta University, Calcutta, India in 1993 and 1995 respectively. He received his Ph.D. degree from Jadavpur University, Calcutta, India, in 2002. At present he is a Chair in Signal Processing Systems Design in the School of Electronics and Computer Science (ECS) at the University of Southampton, UK and is part of the Biomedical Electronics research group. He has served as Technical Programmes Committee member in a number of prestigious IEEE Conferences and is a member of IEEE VLSI Systems Application Technical Committee. Prof. Maharatna has over 110 scientific publications in high-impact conferences and journals to his credit.



**Dr. Maitreyi Ray Kanjilal** is Principal at Narula Institute of Technology. She has also worked in Techno India College of Technology and Asansol Engineering College. She completed her Ph.D. in Electronic sciences. Her areas of interests include Wide-band gap semiconductor devices, nanoscale devices, heterostructures and heterojunction semiconductor devices, microelectronics fabrication, low power devices and VLSI circuits, and spintronics. She has published many papers in international journals and conferences. She has also filed a patent in 2016 titled ‘A system for generation of electricity and method there off’.



**Dr. Sukumar Chandra Konar** is Ex-Professor & Head of Department of Electrical Engineering, Indian Institute of Engineering Science and Technology. Presently, he is Professor and Dean of Electrical Engineering Department of Narula Institute of Technology. He has +35 years of teaching and research experience. He has published around 30 papers in international journals and conferences. Dr. Konar has also published a book titled ‘Robust Stability and Performance of Analysis of Power Systems’ with Lap Lambert Academic Publishing GmbH & Co. He also acts as a reviewer of many journals and conferences—Institution of Engineers (India) Journal; Taylor and Francis Journal & AMSE (France) Journal; Electric Power Components and Systems; International Journal of Sustainable Energy.



**Dr. Sumit Nandi** received his B.Tech., M.Tech. and Ph.D. degree from Calcutta University in Chemical Technology, Oil Technology and Processing of refinery by-products respectively. He has also completed his M.B.A. from Sikkim Manipal University in Finance and Marketing. Currently he is Head and Associate Professor in Department of Basic Sciences and Humanities, Narula Institute of Technology. His areas of research interests include preparation of biodiesel from natural resources, mathematical modelling on enzyme kinetics, enzyme-catalyzed production of different value-added products. He has published more than 50 papers in international journals and conferences in these areas.

He has also filed two patents—‘A process for preparing biodiesel from *Jatropha Curcas* oil’ and ‘Interpenetrating polymer network structure and preparation method thereof’. He has published one book ‘Engineering Chemistry Simplified’ with Chhaya Prakashani Private Limited.



**Dr. Kunal Das** received his B.Sc.(H) in Electronics Science, B.Tech. (Information Technology) and M.Tech. (Information Technology) degrees from Calcutta University, Kolkata, India. He was awarded the Ph.D. degree from the University of Kalyani. He is working as an associate professor in the Department of Computer Science & Engineering, Narula Institute of Technology, Kolkata, and was the former assistant professor in the Department of Computer Science & Engineering, National Institute of Technology, Arunachal Pradesh, India. He has authored several international journal papers and several conference papers, and many SCI journals like Elsevier Microelectronics Journal, Springer JETTA, IEEE Transactions, and worked as editor in many international books. He is the recipient of Early Career Research Award Grant from SCIENCE & ENGINEERING RESEARCH BOARD (SERB), DST, Govt. of India as Principal Investigator.

**Part I**  
**Modeling of Energy Systems**

# Congested Power Transmission System in a Deregulated Power Market



Bishaljit Paul, Chandan Kumar Chanda, Jagadish Pal  
and Manish Kumar Pathak

**Abstract** The optimum and marginal generator dispatch in the deregulated power industry is one of the managerial tasks to eradicate congestion in the transmission lines which is necessary for the online control action in the power system. So optimum power flow has been chosen as the most versatile technique for system security through economic generated dispatch under all parameter constraints. The significance of this work is to give enough logic that in some real time systems is to manage the generator scheduling during overloading of the lines or during outage of the elements, also to know the performance index of the lines based on their contingency studies, to correct overloading by both scheduling and even by load shedding and in the event of bilateral transactions by the market participants through the concept of nodal pricing or locational marginal prices, the owners for the transactions are owned with Financial Transmission Rights which act as perfect hedge for the congestion surplus, all can relief congestion, are explained through a five-bus network.

**Keywords** Congestion · Congestion surplus · Contingency · Deregulation · Financial transmission rights · Locational marginal prices · Optimal power flow · Performance index

---

B. Paul (✉) · M. K. Pathak  
Department of Electrical Engineering, Silli Polytechnic, Ranchi 835102, Jharkhand, India  
e-mail: [paul1bishaljit@gmail.com](mailto:paul1bishaljit@gmail.com)

M. K. Pathak  
e-mail: [manishpathak5ster@gmail.com](mailto:manishpathak5ster@gmail.com)

C. K. Chanda · J. Pal  
Department of Electrical Engineering, IEST, Shibpur, Howrah 711103, India  
e-mail: [ckc\\_math@yahoo.com](mailto:ckc_math@yahoo.com)

J. Pal  
e-mail: [jagadish\\_pal@hotmail.com](mailto:jagadish_pal@hotmail.com)

© Springer Nature Singapore Pte Ltd. 2020  
K. Maharatna et al. (eds.), *Computational Advancement in Communication Circuits and Systems*, Lecture Notes in Electrical Engineering 575,  
[https://doi.org/10.1007/978-981-13-8687-9\\_1](https://doi.org/10.1007/978-981-13-8687-9_1)



# 1 Introduction

Due to deregulation and privatization of the electricity markets, there is a large impact on power transmission around the whole world. There is an obstacle among the market participants in the competitive market scenario due to the bottlenecks of transmission capability in the transmission lines [1]. So planning in the transmission lines should be meticulously done. Buyers and sellers make the electricity market very complex and competitive. Due to the limitations of the available transmission capability, the sole reason behind the complexity is the balancing of the supply and demand at all real times. A congested system arises when producers and consumers of electrical energy make the transmission lines beyond their transfer capabilities. Spots of congestion are indicated by the locational marginal prices (LMPs) [2] in the systems.

Congestion management [3] provides a market-based solution with economic efficiency for a multi-buyer and multi-seller system. For a vertically integrated utility structure, generation, transmission and distribution are within a control of a central agency. Generation is dispatched at least cost accordingly. Security-constrained economic dispatch (SCED) [4] provides an optimal solution and eliminates congestion. So the power flow limits are not exceeded in the transmission lines and the generators are dispatched accordingly. Congestion management states that the transactions are to be prioritized and committed to work in such a schedule by the system operator that does not overload the network. A set of definite rules are to be ensured and enforced by the congestion management such that it takes control over generation and loads to maintain security and reliability in the system. Under open market structure, the rules ensure market efficiency maximization and a set of market players will always look for loopholes to exploit it. Modelling of the market structure [5] in the deregulated environment will be such that the participants can engage freely for their transactions so that the security is not threatened or alarmed. Market efficiency stands [6] with respect to cost-effective generation when they are used to serve the load. The efficiency of a real market is the difference of social welfare between real market and perfect market. In a competitive electricity market, due to competitiveness [7] among the market participants, overloading of the transmission lines occurs while settling the market, and so congestion prevails. In the deregulated scenario, the chances of congestion are quite high as all the customers would like to purchase electricity from the cheapest source of energy. For the secured operation of the system, the congestion should be alleviated. Optimal power flow techniques use congestion management strategies [8] like rescheduling of generators, use of compensating devices and even load curtailments to release congestion. If congestion persists for a long time, the transmission lines operate beyond the transfer limits, and there is a sudden rise in price of electricity which threatens security and reliability of the system. So congestion management is one of the challenging tasks for the system operator in the deregulated environment [9]. Optimal power flow-based congestion management minimizes the generator's operating cost subject to set of constraints based on transmission system. Though there are different levels of economic signals

for different methods of congestion management, locational marginal price is the most sensitive mechanism [10] as it provides the strongest price signal to the players in the power market. They are the incremental increase or decrease of prices of energy at every bus in the congested power system. When a transmission line is constrained, another unit becomes marginal in the sense that it is neither at its maximum nor at its minimum. If there are ' $p$ ' transmission constraints in the system, there will be ' $p + 1$ ' marginal generators [11, 12]. LMP at any bus is defined as the marginal cost of the marginal generators of supplying the next increment of electrical energy at that bus while maintaining the physical aspects of transmission system. Shadow prices are the maximum dispatch cost saved due to an increment increase of flow capacity in the line without violating transmission constraints. Shadow prices are the Lagrange multipliers for the inequality constraints. Though LMPs vary significantly from one bus to another and they are decomposed into three components; marginal energy price (MEP), marginal congestion price (MCP) and marginal loss price (MLP) are not unique due to transmission open access and large transactions [13, 14]. For an ' $n$ ' component power network, if one component is under outage, it is called ' $n - 1$ ' contingency. Similarly, for two-component outages, it is called ' $n - 2$ ' contingency. Security-constrained economic dispatch optimal power flow programs are analysed for the system security. If energy is bought and sold at nodal marginal prices, the payments made by the generator companies to the ISO and the revenues collected by the generator companies from the consumers do not match. More money is collected from the consumers than it is paid to the generators. The difference is called the congestion surplus or merchandising surplus, and it is caused due to the congestion in the network. In an unconstrained economic dispatch, as the marginal prices are identical at all nodes, the total amount collected by the generator companies is equal to the amount paid by the consumers. So the congestion surplus is zero.

Financial Transmission Rights (FTRs) [15–19] are defined that provide the market player holder to collect a revenue equal to the amount of flow of power of ' $F$ ' MW between two nodes and the price differential between that two nodes or buses. FTRs completely debar the risks of congestion from the network by paying the amount to the market players.

## 2 Mathematical Formulation

Let us consider that the line connecting the nodes ' $i$ ' and ' $j$ ' is constrained and the power flow is at its limit. So this has violated the security of the system. This causes two marginal generators to operate. Let the marginal generators be  $P_A$  and  $P_B$ . To determine the LMP and by implementing congestion management strategies [20] which are flow tariffs, costs of loads and generator bids at different buses, zero congestion surplus and by changing the reference buses [21, 22]. At any node ' $k$ ', it is required to calculate incremental inputs  $\Delta P_A$  and  $\Delta P_B$  of the marginal units at nodes ' $l$ ' and ' $m$ ' so as to deliver 1 MW to node ' $k$ ', without increasing the flow between the nodes ' $i$ ' and ' $j$ ' of the congested line.

From the power transfer distribution matrix (PTDF), if 1 MW of power is injected at node ' $l$ ' where there is a marginal generator and withdrawn at node ' $k$ ' where LMP is to be found, there may be an increase or decrease of flow in line connecting between the nodes ' $i$ ' and ' $j$ '.

$$\Delta Flow_{(i-j)l} = PTDF_{(i-j)l} - PTDF_{(i-j)k} \quad (1)$$

$$\begin{bmatrix} \Delta Flow_{(i-j)l} & \Delta Flow_{(i-j)m} \\ \mathbf{1} & \mathbf{1} \end{bmatrix} * \begin{bmatrix} \Delta P_A \\ \Delta P_B \end{bmatrix} = \begin{bmatrix} \mathbf{0} \\ \mathbf{1} \end{bmatrix} \quad (2)$$

A similar calculation is analysed to determine the shadow price, which is direction specific, in the congested line connecting between the nodes ' $i$ ' and ' $j$ '. The aim is to perturb the outputs of the marginal generators at nodes ' $l$ ' and ' $m$ ' by incremental amounts  $\Delta P_A$  and  $\Delta P_B$  so as to increase the flow in the congested line between the nodes ' $i$ ' and ' $j$ ' by 1 MW, while maintaining the energy balance.

The quantities must satisfy the system of equations:

$$\begin{bmatrix} \Delta Flow_{(i-j)l} & \Delta Flow_{(i-j)m} \\ \mathbf{1} & \mathbf{1} \end{bmatrix} * \begin{bmatrix} \Delta P_A \\ \Delta P_B \end{bmatrix} = \begin{bmatrix} \mathbf{1} \\ \mathbf{0} \end{bmatrix} \quad (3)$$

For any pair of nodes, ' $i$ ' and ' $j$ ', a relation between locational marginal price and shadow price (**SP**) for the congested lines (**cl**) can be formulated as

$$LMP_j - LMP_i = \sum SP_{cl} * (PTDF_{(h-k)j} - PTDF_{(h-k)i}) \quad (4)$$

Calculation based on the method of shift factors (**SF**), Lagrangian multipliers where **c** is the bidding price vector of generation, **P** is the energy vector, **A** is the bus unit incidence matrix and **B** is the bus-load incidence matrix.

$$\text{Minimize } c^T * P$$

$$\text{subject to } \sum_j P_{D_j} - \sum_i P_i = 0$$

$$PL = SF * (A * P - B * P_D) \leq PL_{\max} \pi^+$$

$$-PL = -SF * (A * P - B * P_D) \leq PL_{\max} \pi^-$$

$$P_{\min} \leq P \leq P_{\max} \text{ for all generators.}$$

So,

$$LMP = \lambda - SF^T * (\pi^+ - \pi^-) \quad (5)$$

where

$$LMP_{\text{energy}} = \lambda$$

and

$$LMP_{congestion} = -\mathbf{SF}^T * (\pi^+ - \pi^-)$$

$$PI = \sum_{l=1}^L \left( \frac{P_l}{P_l^{lim}} \right)^{2n} \tag{6}$$

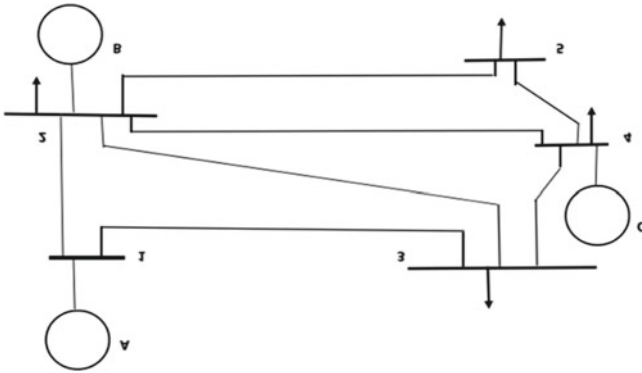
where

- $L$  Number of lines.
- $P_l^{lim}$  MW limit capacity of the line.
- $n$  a positive integer.

The cost of power transmission of a transmission line between the two nodes ‘ $i$ ’ and ‘ $j$ ’ is formulated as

$$t_{ij} = LMP_j - LMP_i \tag{7}$$

### 3 An Illustration with Five-Bus Network



#### 3.1 Generating Units and Load Information

See Table 1.

**Table 1** Generating units and load information

Bus	Cost (\$/MWh)	$P_{\min}$ (MW)	$P_{\max}$ (MW)	$P_D$ (MW)	Type
1	15	0	1000	0	Slack
2	17	100	400	120	P-V
3	–	–	–	100	P-Q
4	19	50	300	80	P-V
5	–	–	–	120	P-Q

**Table 2** Line parameter information

Line	From (bus)	To (bus)	$X_{pu}$ (reactance)	$PL_{\max}$ (MW)
$L_1$	1	2	$j0.06$	150
$L_2$	1	3	$j0.24$	100
$L_3$	2	3	$j0.12$	50
$L_4$	2	4	$j0.18$	100
$L_5$	2	5	$j0.12$	120
$L_6$	3	4	$j0.03$	100
$L_7$	4	5	$j0.24$	100

### 3.2 Information of Line Parameters

See Table 2.

## 4 Results and Discussions

### 4.1 Base-Case Power Flows in MW Under Economic Dispatch

Flow 1–2	Flow 1–3	Flow 2–3	Flow 2–4	Flow 2–5	Flow 3–4	Flow 4–5
197.453 (constrained)	72.547	46.359	34.056	97.038	18.906	22.962

**4.2 Correction of Overloading in the Lines Only Through Scheduling of Generators Under Security-Constrained Economic Dispatch**

Minimize  $15 * P_{G1} + 17 * P_{G2} + 19 * P_{G4}$   
 subject to,  $P_{G1} + P_{G2} + P_{G4} = \text{Demand} = 120 + 100 + 80 + 120 = 420$   
 –  $150 \leq \text{Flow in line (1 – 2)} \leq 150$   
 –  $50 \leq \text{Flow in line (2 – 3)} \leq 50$   
 $0 \leq P_{G1} \leq 1000$   
 $100 \leq P_{G2} \leq 400$  and  
 $50 \leq P_{G4} \leq 300$

So,

$\Delta P_{G1}^-$ (MW)	$\Delta P_{G2}^+$ (MW)	$\Delta P_{G4}^+$ (MW)
57.4932	53.1337	4.3596

where  $\Delta P_{G1}^-$ ,  $\Delta P_{G2}^+$  and  $\Delta P_{G4}^+$  are the increases and decreases of generation. As two lines are accounted for constraint, there are three marginal generators. So with the generated amount of 212.5068 MW by  $P_{G1}$ , 153.1337 MW by  $P_{G2}$  and 54.3596 MW by  $P_{G4}$ , the congestion has been relaxed. The total cost becomes \$6874/h. So the congestion cost becomes \$174/h.

**4.3 To Calculate the LMPs and the SPs, the Price Signals for the Buses in \$/MWh**

LMP <sub>1</sub>	LMP <sub>2</sub>	LMP <sub>3</sub>	LMP <sub>4</sub>	LMP <sub>5</sub>	SP <sub>1-2</sub>	SP <sub>2-3</sub>
15.0	17.0	19.5	19.0	17.67	-3.1249	-6.7512

**4.4 Transmission Costs in \$/MWh**

$t_{12}$	$t_{13}$	$t_{23}$	$t_{24}$	$t_{25}$	$t_{35}$	$t_{45}$
2	4.5	2.5	2	0.67	-1.83	-1.33

**Table 3** Price indicators with increase or decrease in generation and load curtailments

$\Delta P_{G1}^+$	$\Delta P_{G1}^-$	$\Delta P_{G2}^+$	$\Delta P_{G2}^-$	$\Delta P_{G4}^+$	$\Delta P_{G4}^-$	$\Delta P_{D2}^-$	$\Delta P_{D3}^-$	$\Delta P_{D4}^-$	$\Delta P_{D5}^-$
15	50	17	16	19	18	38	38	38	38

#### 4.5 Correction of Overloading in the Lines Through Scheduling of Generators and Load Curtailment Under Security-Constrained Economic Dispatch

Let the price indications in \$/MWh of either increase or decrease in generation and load curtailments which are denoted by  $\Delta P_{Gi}^+$ ,  $\Delta P_{Gi}^-$  and  $\Delta P_{Dj}^-$  in MW, respectively, at different  $i$ th and  $j$ th buses are tabulated in Table 3:

Minimize

$$15 * \Delta P_{G1}^+ + 50 * \Delta P_{G1}^- + 17 * \Delta P_{G2}^+ + 16 * \Delta P_{G2}^- + 19 * \Delta P_{G4}^+ + 18 * \Delta P_{G4}^- + 38 * \Delta P_{D2}^- + 38 * \Delta P_{D3}^- + 38 * \Delta P_{D4}^- + 38 * \Delta P_{D5}^-$$

subject to

$$\Delta P_{G1}^+ - \Delta P_{G1}^- + \Delta P_{G2}^+ - \Delta P_{G2}^- + \Delta P_{G4}^+ - \Delta P_{G4}^- = -\Delta P_{D2}^- - \Delta P_{D3}^- - \Delta P_{D4}^- - \Delta P_{D5}^-$$

$$(\text{Base flow} + \text{change in Flow in line } L_1) \leq 150$$

$$-(\text{Base flow} + \text{change in Flow in line } L_1) \leq 150$$

$$(\text{Base flow} + \text{change in Flow in line } L_3) \leq 50$$

$$-(\text{Base flow} + \text{change in Flow in line } L_3) \leq 50$$

Minimum capacity  $\leq$  (base generation + change in generation)  $\leq$  maximum capacity for all generator buses.

So,

$\Delta P_{G1}^+$	$\Delta P_{G1}^-$	$\Delta P_{G2}^+$	$\Delta P_{G2}^-$	$\Delta P_{G4}^+$	$\Delta P_{G4}^-$	$\Delta P_{D2}^-$	$\Delta P_{D3}^-$	$\Delta P_{D4}^-$	$\Delta P_{D5}^-$
0	57.4933	54.0057	0	0	0	0	3.4877	0	0

and the total cost amounts to  $(270 - 57.4933) * 15 + 57.4933 * 50 + 154.0057 * 17 + 3.4877 * 38 = \$8813/\text{h}$  for the new uncongested flows in MW which are

Flow 1–2	Flow 1–3	Flow 2–3	Flow 2–4	Flow 2–5	Flow 3–4	Flow 4–5
150	62.51	50	36	98	16	22

**Table 4** Power transactions

Transactions	From bus	To bus	Amount of power
T1	1	5	150
T2	4	2	200
T3	2	5	80
T4	4	5	60
T5	2	3	100
T6	1	4	50

**Table 5** Price indicators with increase or decrease in generation and load curtailment

$\Delta P_{G1}^+$	$\Delta P_{G1}^-$	$\Delta P_{G2}^+$	$\Delta P_{G2}^-$	$\Delta P_{G4}^+$	$\Delta P_{G4}^-$	$\Delta P_{D2}^+$
15	15	17	17	19	19	100
$\Delta P_{D2}^-$	$\Delta P_{D3}^+$	$\Delta P_{D3}^-$	$\Delta P_{D4}^+$	$\Delta P_{D4}^-$	$\Delta P_{D5}^+$	$\Delta P_{D5}^-$
50	100	50	100	50	100	50

#### 4.6 Performance Index (PI) Measurement for Line Outages (of the Order of $10^8$ )

1.9637	1.9638	0.0382	0.0589	0.0358	0.1127	0.1056
--------	--------	--------	--------	--------	--------	--------

Taking the MW limit capacity of the lines as 40 MW, the performance index reveals that it has a very high value and the lines are overloaded. The PI would have been a small number if the lines were within the limits.

#### 4.7 Prioritization and Feasibility of Power Transactions

Let the following transactions in MW occur in the system (Table 4)

The system operator checks whether these transactions are feasible or not. These transactions create congestion in the lines  $L_1$ ,  $L_5$  and  $L_7$  amounting to 165.58, 182.07 and 107.93 MW, respectively.

Let the price indications in \$/MWh of either increase or decrease in generation and load increase or curtailments which are denoted by  $\Delta P_{Gi}^+$ ,  $\Delta P_{Gi}^-$  and  $\Delta P_{Dj}^+$ ,  $\Delta P_{Dj}^-$  in MW, respectively, at different  $i$ th and  $j$ th buses for a feasible transaction are tabulated in Table 5.

For feasibility of the transactions and maintaining the security of the system, the amount of increase or decrease in generation and load in MW holds true.



$\Delta P_{G1}^+$	$\Delta P_{G1}^-$	$\Delta P_{G2}^+$	$\Delta P_{G2}^-$	$\Delta P_{G4}^+$	$\Delta P_{G4}^-$	$\Delta P_{D2}^+$
0	23.7	0	63.2	0	0	0

$\Delta P_{D2}^-$	$\Delta P_{D3}^+$	$\Delta P_{D3}^-$	$\Delta P_{D4}^+$	$\Delta P_{D4}^-$	$\Delta P_{D5}^+$	$\Delta P_{D5}^-$
0	0	0	0	0	0	86.9

The amount of generation and loads in MW for these transactions, to keep the system secure, is tabulated below:

$P_{G1}$	$P_{G2}$	$P_{G4}$	$P_{D2}$	$P_{D3}$	$P_{D4}$	$P_{D5}$
176.33	116.80	260	200	100	50	203.14

The transaction **T3** of 80 MW is cut short by 26.86–53.14 MW and transaction **T4** of demand 60 MW is abolished.

#### ***4.8 Settlement of Financial Transmission Rights by the Market Operator***

Transmission rights				Settlements			
Combinations	From bus	To bus	Amount (MW)	From bus price (\$/MW)	To bus price (\$/MW)	Revenue (\$)	Total (\$)
<i>A</i>	1	3	100	15	19.5	450	802
	1	4	80	15	19	320	
	2	5	48	17	17.67	32	
<i>B</i>	1	2	120	15	17	240	802
	1	3	90	15	19.5	405	
	2	4	78.5	17	19	157	
<i>C</i>	1	5	111	15	17.67	296	802
	1	4	62	15	19	248	
	2	3	100	17	19.5	250	
	2	4	4	17	19	8	
<i>D</i>	1	5	120	15	17.67	320	802
	1	2	66	15	17	132	
	2	3	100	17	19.5	250	
	2	4	50	17	19	100	

The settlement shows four combinations of FTRs that meet the feasibility under the secured operation in this five-bus system. Sometimes settlements for contract of difference can be settled by paying additional amount to the market operator by the market participant right holders as FTRs may acquire a negative value for final settlement.

## 5 Conclusion

One of the significant aspects for an open-access transmission system is congestion in the lines. This leads to transmission congestion cost and losses cost. This congestion creates different prices or LMPs at various buses in the system which has been proved. This key issue makes the market inefficient and forces to exercise market power.

In this paper, the line constraint has been relaxed not only by the scheduling of the generators but also even both by the scheduling of the generators and load curtailments. The security has been maintained by bearing the congestion releasing total costs of \$6874/h and \$8813/h, respectively. Various  $n - 1$  contingency cases had been studied, and the calculated performance index for the line outages reveals that it is a large number if one or more lines are constrained and the system small. It is a small number if the lines are within limits. Though the capacity of the line increases, cost of producing energy may decrease, but the consumer payments, congestion surplus and the profits of the generator may increase. The excess surplus amount is settled by providing financial rights to the market holders by the ISO. Here, it is clearly shown how the market participant holders of the rights collect the amount based on the LMPs of the buses which is equal to the congestion surplus, collected by the system operator before settlement.

## References

1. A.J. Wood, B.F. Wollenberg, *Power Generation, Operation and Control* (Wiley, New York, 1996)
2. Y. Fu, Z. Li, Different models and properties on LMP calculations, in *IEEE Power Engineering Society General Meeting*, Montreal, Canada (2006)
3. M.B. Nappu, Locational marginal prices considering transmission congestion and network losses. *Univ. J. Electr. Electron. Eng.* **2**(3), 132–136 (2014)
4. T.W. Gedra, On transmission congestion and pricing. *IEEE Trans. Power Syst.* **14**(1) (1999)
5. E. Litvinov, Design and operation of the Locational marginal prices-based electricity markets. *IET Gener. Transm. Distrib.* **4**(2), 315–323 (2010)
6. H. Singh, S. Hao, A. Papalexopoulos, Transmission congestion management in competitive electricity markets. *IEEE Trans. Power Syst.* **13**(2) (1998)
7. K.L. Lo, Y.S. Yuen, Congestion management in deregulated electricity markets, in *The International Conference on Electric Utility Deregulation and Restructuring and Power Technologies 2000* (City University, London, 4–7 Apr 2000)
8. A.L. Ott, Experience with PJM market operation, system design and implementation. *IEEE Trans. Power Syst.* **18**(2), 528–534 (2003)

9. R.D. Christie, B.F. Wollenberg, I. Wangensteen, Transmission management in the deregulated environment. *Proc. IEEE* **88**, 170–195 (2000)
10. J.A. Momoh, *Electric Power System Applications of Optimization* (Marcel Dekker, New York, 2000)
11. M. Shahidehpour, H. Yaminand, Z.Y. Li, *Market Operations in Electric Power System* (Wiley, New York, 2002)
12. D.S. Kirschen, G. Strbac, *Fundamentals of Power System Economics* (Wiley, 2004)
13. Z. Alaywan, *Facilitating the Congestion Management Market in California* (California Independent System)
14. T. Gomez, C. Marnay, *Transmission Pricing and Congestion Management in California* (1999)
15. H. Chao, S. Peek, A market mechanism for electric power transmission. *J. Regul. Econ.* **10**(1), 25–29 (1996)
16. M. Hsu, An introduction to the pricing of electric power transmission. *Utilities Policy* **6**(3), 257–270 (1997)
17. X. Ma, D.I. Sun, A. Ott, Implementation of PJM financial transmission rights auction market system, in *IEEE on Power Engineering Society Summer Meeting*, vol. 3 (2002), pp 221–25.
18. X. Ma, D.I. Sun, K.W. Cheung, Evolution toward standardized market design. *IEEE Trans. Power Syst.* **18**(2) (2003)
19. B. Paul, M. Pathak, C. K. Chanda, J. Pal, On transmission congestion and financial rights. *IJESRT* (2017). ISSN 2277-9655
20. B. Paul, M. Pathak, C. K. Chanda, J. Pal, On transmission congestion management strategies and forecasting locational marginal prices in a deregulated competitive power market, in *Universities Power Engineering Conference (AUPEC)*, Melbourne, 2017 (IEEE, 2018). USB ISBN 978-1-5386-2646-7
21. B. Paul, M. Pathak, C. K. Chanda, J. Pal, Physical interpretation of DCOPF based Lagrange multipliers-LMP, shadow prices. *IJARSE* **6**(2) (2017)
22. B. Paul, M. Pathak, C. K. Chanda, J. Pal, A comparison of locational marginal prices and locational load shedding marginal prices in a competitive deregulated power market, in *Calcutta Conference (CALCON)*, Calcutta, 2017 (IEEE, 2018). USB ISBN 978-1-5386-3744-9

# Integration of DSTATCOM and Distributed Generation with Nonlinear Loads



Mukul Anand, Amit Kumar, Rahul Dev and Pradeep Kumar

**Abstract** This paper deals with the distributed generation (DG) widely used in custom power devices. Nowadays, photovoltaic array has been utilized in distribution lines with many devices like DSTATCOM, DVR, UPQC and many more. In this paper, distributed static synchronous compensator (DSTATCOM) has been used with distributed generation solar PV array with MPPT technique. Perturbation and observation (P&O) algorithm has been used in MPPT (maximum power point tracking) technique for consuming maximum power from the solar power. Nonlinear loads on grid side have been connected and three-leg VSI has been used for compensation of power quality problems. The conventional form of control technique has been used for gate pulse generation of VSI. Synchronous reference frame (SRF) control technique has been used to get the signals for controlling the thyristors. The experimental results have been verified in MATLAB Simulink/Simpower environment.

**Keywords** Power quality · MPPT · PV array · DSTATCOM · THD · VSI

## 1 Introduction

With the increase in the use of non-renewable source of energy, we have been neglecting renewable source, but nowadays, non-renewable source of energy is tightening its belt in every field. Distributed generation is also expanding day by day and utilized in every part of engineering applications. In power sector, starting of the use

---

M. Anand (✉) · A. Kumar · R. Dev (✉) · P. Kumar  
Electrical and Electronics Department, NIT Sikkim, Ravangla, Sikkim, India  
e-mail: [m170022@nitsikkim.ac.in](mailto:m170022@nitsikkim.ac.in)

R. Dev  
e-mail: [Phee17003@nitsikkim.ac.in](mailto:Phee17003@nitsikkim.ac.in)

A. Kumar  
e-mail: [m170010@nitsikkim.ac.in](mailto:m170010@nitsikkim.ac.in)

P. Kumar  
e-mail: [pradeep@nitsikkim.ac.in](mailto:pradeep@nitsikkim.ac.in)

© Springer Nature Singapore Pte Ltd. 2020  
K. Maharatna et al. (eds.), *Computational Advancement in Communication Circuits and Systems*, Lecture Notes in Electrical Engineering 575,  
[https://doi.org/10.1007/978-981-13-8687-9\\_2](https://doi.org/10.1007/978-981-13-8687-9_2)

of solar energy with PV array is expanding [1]. Photovoltaic cells have come into use in every device of distributed as well as transmission lines. It can be used as an alternate form of energy which can be used in emergency situations or in far places where non-renewable form of energy sources cannot be transported or not accessible. Today, wind energy, solar energy and even battery can also be used in grid connection for improvement in power quality of lines. Broad area of power system comprises that many more custom power devices which are combined can put up a better result in a more economical way [2, 3]. Photovoltaic array consist of cells which extract solar form of energy and transfer this energy to give out electrical supply and for various uses.

Power quality issues are major forms of problems facing in the present scenario by power system. These problems affect not only the transmission lines but also the distribution lines abruptly [4, 5]. Harmonics, flickers, fluctuations, dip, swell, sag, distortions and many more are the effects of the use of many nonlinear devices and equipment in distribution system and bad weather, sudden lighting, adverse condition in transmission system. Poor power factor and angle correction factor are also concerned nowadays.

Basically custom power devices have been designed to solve these PQ problems of transmission and distribution systems. Some of the custom power devices are distributed static synchronous compensator (DSTATCOM), distributed voltage regulator (DVR), unified power flow controller (UPFC), interline power flow controller (IPFC), unified power quality conditioner (UPQC) and many more. These are mostly used in the present days. Here, DSTATCOM as a custom power device (CPD) taken for power quality improvement on various issues.

In the distribution system, the voltage of buses may be unbalanced if the load connected to the system is nonlinear or unbalanced. DSTATCOM, a kind of voltage source inverter (VSI), has been used as compensator at point of common coupling (PCC) [1, 4, 6–9]. A solar photovoltaic system followed by DC–DC boost converter has been used to charge the capacitor of DSTATCOM also known as shunt active power filter. The MPPT (maximum power point tracking) is used to achieve the maximum efficiency of solar photovoltaic system at a specific value of voltage and current corresponding to MPPT. A DC–DC boost converter has been used to extract maximum power from solar photovoltaic system and to provide constant output DC to the capacitor of DSTATCOM. A control technique is used to provide gate pulse of inverter (DSTATCOM), so that it could generate the three-phase current to meet current demand and to reduce harmonic distortion in grid current by nonlinear load, and DSTATCOM also meets reactive power demanded by nonlinear load which reduces reactive power burden on source, and hence, power factor increases (Fig. 1).

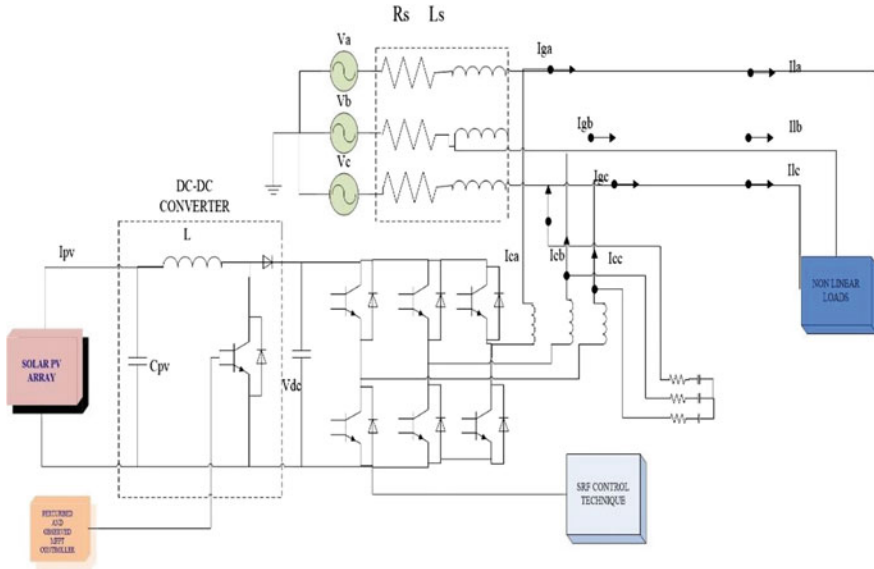


Fig. 1 DSTATCOM integrated with DG

## 2 Configuration of Distributed Generation

### 2.1 MPPT

PV array is used as input to DC–DC boost converter [2, 10]. To optimize the efficiency of PV array, maximum power point technique has been used which extracts maximum power from solar panel. MPPT is based on impedance matching in which maximum power can be extracted when input impedance becomes equal to output impedance. This can be achieved by the varying duty cycles of DC–DC boost converter. The MPPT implemented through boost converter has minimum value of  $D$  limit so that the algorithm needs to calculate the duty cycle below the specified value of  $D$ .

### 2.2 Perturbation and Observation Algorithm

Perturbation and observation control algorithm is mostly used due to simplicity and cost-effective [10]. In this method, we observe the PV array output power, voltage, current, and we modify (increment or decrement) the voltage  $V(n)$  and current  $I(n)$  continuously according to the control algorithm. Hence, the voltage and current change continuously until the maximum power point is obtained fully. We continuously measure the output power  $P(n)$  corresponding to voltage  $V(n)$  and current

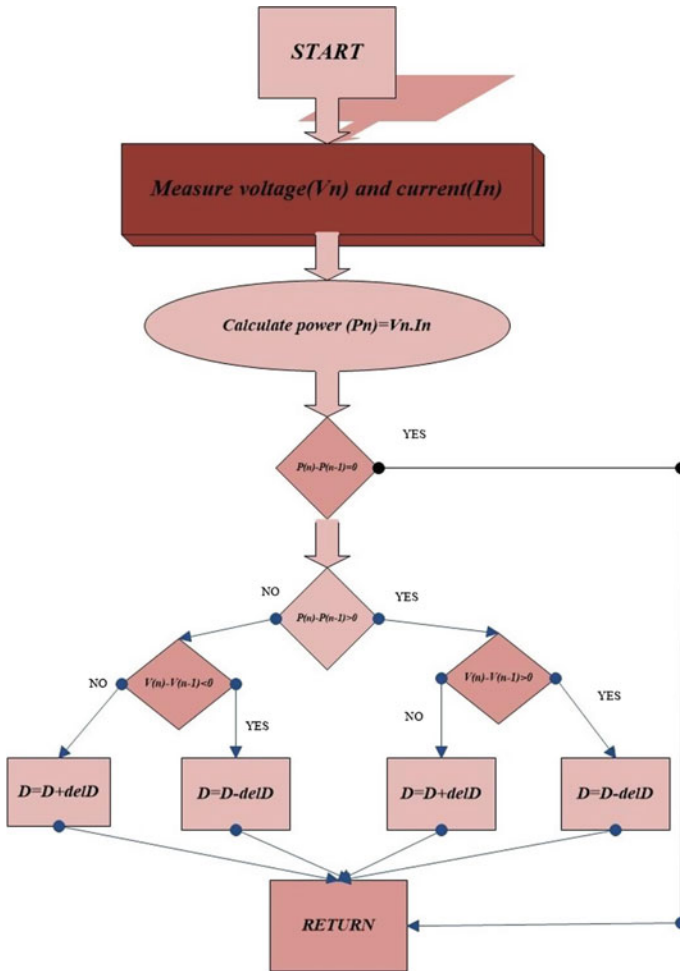


Fig. 2 Perturbation and observation MPPT algorithm

$I(n)$ . Then, we compare the new measured value of power and voltage with the old value. Then in the next step if  $P(n) - P(n - 1)$  which is  $dP(n)$  equal to zero then  $D_{new} = D_{old}$  otherwise  $dP(n)$  is not equal to zero and if  $dP(n)$  and  $dV(n)$  is less than equal to zero ( $dP(n) < 0$  and  $dV(n) < 0$ ) then the duty cycle becomes  $D_{new} = D_{old} - dD$ , if  $dP(n)$  is less than zero and  $dV(n)$  is greater than zero ( $dP(n) < 0$  and  $dV(n) > 0$ ) then the duty cycle becomes  $D_{new} = D_{old} + dD$ , if  $dP(n)$  is greater than zero and  $dV(n)$  is less than zero ( $dP(n) > 0$  and  $dV(n) < 0$ ) then the duty cycle becomes  $D_{new} = D_{old} + dD$ , if  $dP(n)$  is greater than zero and  $dV(n)$  is greater than zero ( $dP(n) > 0$  and  $dV(n) > 0$ ) then the duty cycle becomes  $D_{new} = D_{old} - dD$  as shown in Fig. 2.

### 2.3 DC–DC Boost Converter

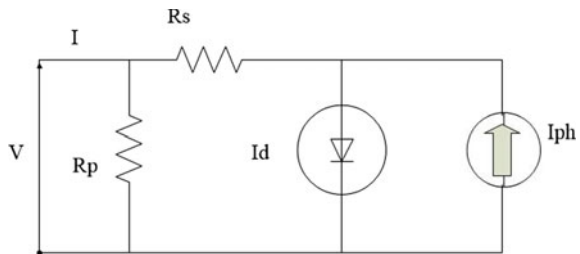
DC–DC boost converter is used to achieve desired average output from an unregulated DC source. It is used to extract the maximum power from PV array by controlling the duty cycle. This converter consists of PV array output voltage as voltage source to converter, inductor L, switch S, diode D, capacitors C1 and C2. Inductor L gets energized when switch S is on, and during this time, continuous conduction of load current is maintained by charge capacitor. When switch S becomes off, inductor reverses its polarity. Inductor voltage and source voltage appear across the load; hence, voltage increases across the load. Voltage across load depends upon the duty cycle. A control algorithm has been developed to generate desired average output voltage. The output voltage  $V_o$  of DC–DC boost converter is inversely proportional to  $(1 - D)$ , and hence, by varying duty cycle we can get desired output voltage of DC–DC converter. A Pulse width modulation (PWM) pulse generator is used based on duty cycle. Duty cycle determines the percentage of pulse period for which output of PWM generator makes switch on. Switching frequency is 5000 Hz for the PWM has been used.

### 2.4 Photovoltaic Array

Solar PV cell works when the sun rays are thrown on the solar cells which convert the light energy into electrical energy. The equivalent diagram of photovoltaic cell consists of mono diode with two resistors one of them connected in series, and other is connected in parallel.  $R_s$  and  $R_p$  shown in Fig. 3 are the two resistors and  $I_{ph}$  is current of photon which is temperature- and irradiance-dependent.  $I_d$  is the current through the diode.  $V$  is the voltage output as DC voltage which is sent to DC–DC boost converter for further rectification. The equation can be written as shown (1) in which  $C_s$  represents cells in series,  $C_p$  cells in parallel,  $D$  is diode ideality factor,  $K$  is Boltzmann constant and  $T$  is the temperature.

$$I_{pv} = C_p I_{ph} - C_p I_0 \left[ e^{\frac{q * v + I_{pv} * R_s}{C_s D * K * T}} \right] \tag{1}$$

Fig. 3 PV cell equivalent diagram





### 3 Design of Controller

SRF control technique has been used in this DSTATCOM [6, 8, 11, 12]. In this control technique, angle is found by PLL (phase-locked loop) and then sent to the Clarke transformation in which the load current is sent initially. Then, this  $dq$  component is passed through the LPF for ripple-free signal and then tuned by PI controller; then, the signals are again transformed to  $a-b-c$  by inverse Clarke transformation; then, it acts as reference, and now, the source voltage is compared and then passed through hysteresis controller to get the gate pulses for three-leg VSI thyristors (Fig. 4).

$$\begin{aligned}
 [I_{LA} I_{LB} I_{LC}] = & \frac{3}{2} * \text{Inverse of} \left[ \cos \theta - \sin \theta \right] \frac{1}{2} \cos \left( \theta - \frac{2\pi}{3} \right) \\
 & - \sin \left( \theta - \frac{2\pi}{3} \right) \frac{1}{2} \cos \left( \theta + \frac{2\pi}{3} \right) \sin \left( \theta + \frac{2\pi}{3} \right) \frac{1}{2} [I_{LD} I_{LQ} I_{L0}]
 \end{aligned}
 \tag{2}$$

Three-phase phase-locked loop is used for the synchronization of signals.

$$I_{Ddc} = I_{D*} + I_{LD} \tag{3}$$

$$I_{LQdc} = I_{q*} + I_{LQ} \tag{4}$$

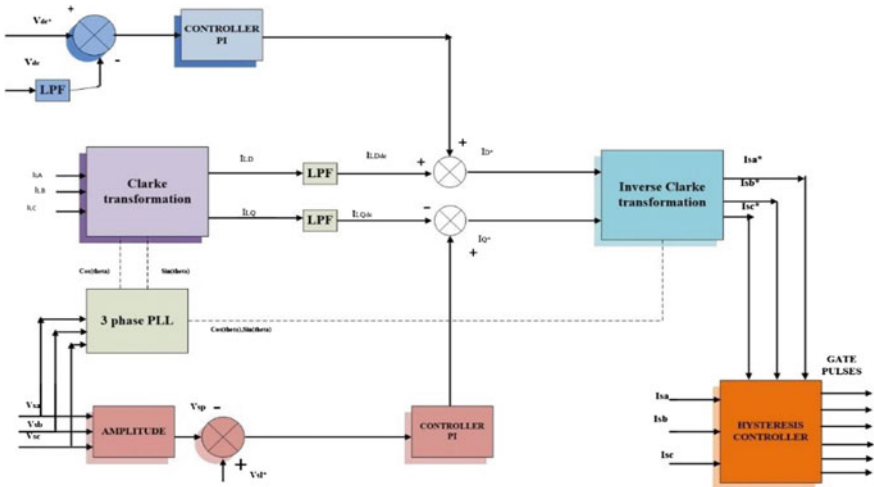
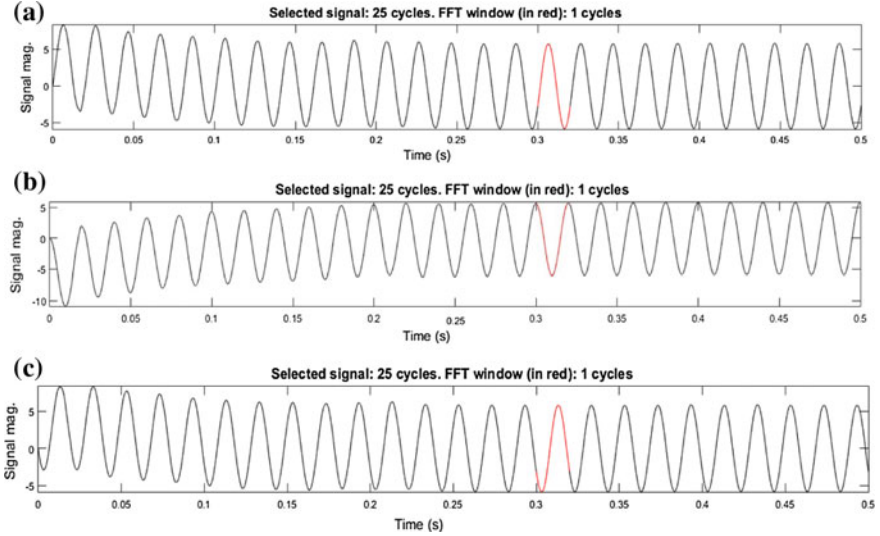


Fig. 4 SRF control technique as Shunt controller

### 4 Simulation Results

Figures 5, 6, 7, 8, and 9 and Table 1.



**Fig. 5** **a** Phase a source current after compensation. **b** Phase b source current after compensation. **c** Phase c source current after compensation

**Table 1** THD of source voltage and source current after compensation

S. No.	Source voltage	THD (%)	Source current	THD (%)
1	$V_{sa}$	2.88	$I_{sa}$	0.20
2	$V_{sb}$	2.88	$I_{sb}$	0.29
3	$V_{sc}$	2.88	$I_{sc}$	0.20

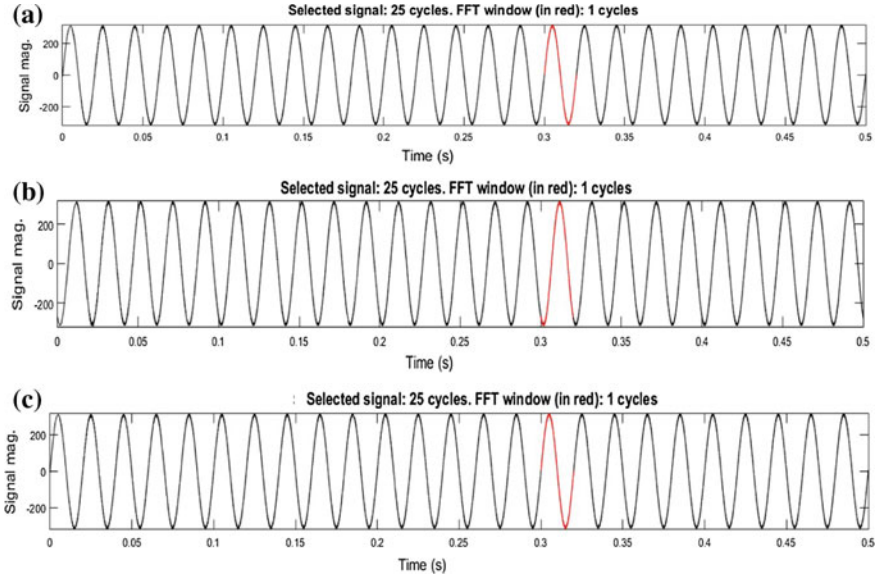


**Fig. 6** **a** Phase a source voltage after compensation. **b** Phase b source voltage after compensation. **c** Phase c source voltage after compensation

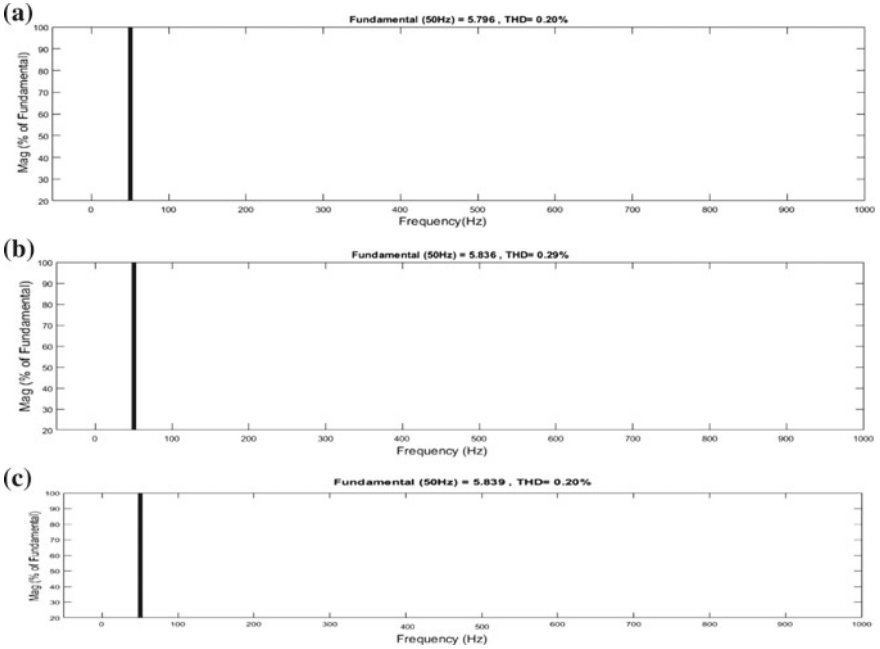


**Fig. 7** **a** Phase a source current THD after compensation. **b** Phase b source current THD after compensation. **c** Phase c source current THD after compensation

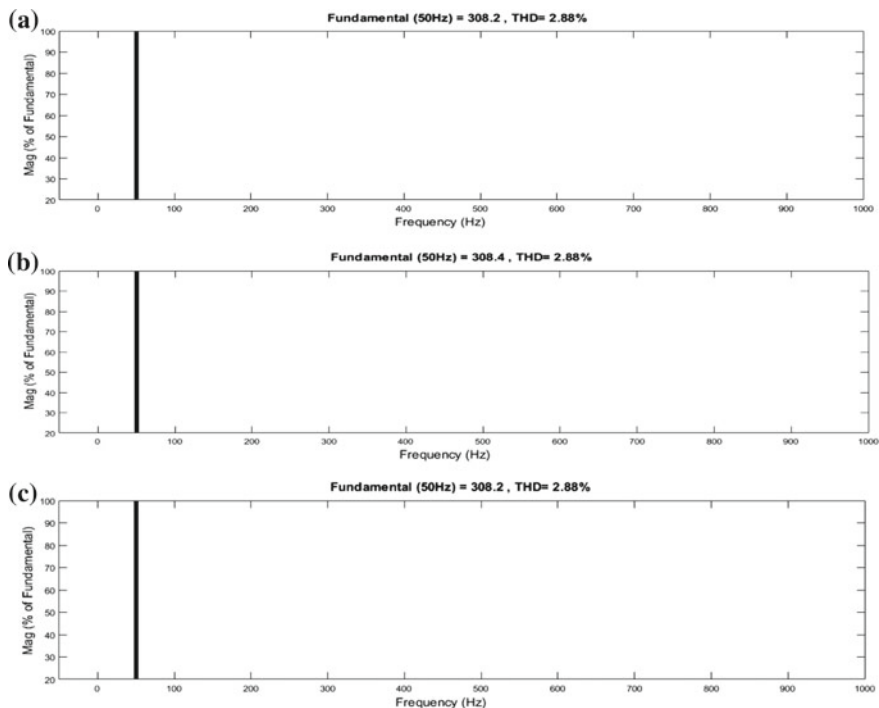


**Fig. 8** a Phase a source voltage THD after compensation. b Phase b source voltage THD after compensation. c Phase c source voltage THD after compensation

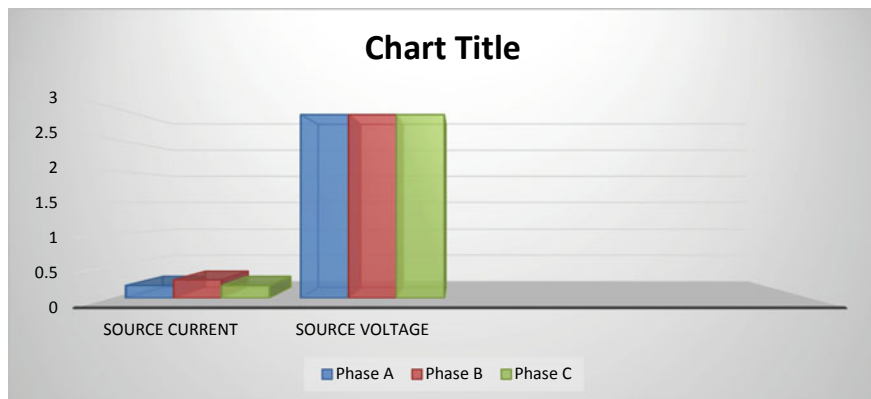


**Fig. 9** Pictorial representation of THD of source voltage and source current

## 5 Conclusion

The DSTATCOM is designed with integration of distributed generation as PV array. It is connected to MPPT and then DC–DC Boost converter for constant DC voltage through DC link capacitor. SRF control technique and distributed generation are combined to reduce the THD at great extent which shows that it is capable of removing power quality problems from the distributed lines which will help the consumers for regulated power supply. THD is reduced to approximately 2.80% in source current and 0.25% in source voltage and meeting the IEEE norms of THD less than 5%.

## References

1. S.K. Khadem, M. Basu, M.F. Conlon, Power quality in grid connected renewable energy systems: Role of custom power devices, in Proceedings for the International Conference on Renewable Energies and Power Quality (ICRE PQ'10), Granada, Spain, 23–35 Mar 2010
2. N. Hamrouni, M. Jraidi, A. Dhouib, A. Cherif, Design of a command scheme for grid connected PV systems using classical controllers. *Electr. Power Syst. Res.* **143**, 503–512 (2017)
3. IEEE Recommended Practices and Requirements for Harmonics control in Electrical Power Systems. IEEE STD 519 (1992)
4. R.C. Dugan, M.F. McGranaghan, H.W. Beaty, *Electric Power Systems Quality*, 2nd edn. (McGraw Hill, New York, 2006)
5. B. Singh, A. Chandra, Kamal-Al-Haddad, *Power Quality Problems and Mitigation Techniques* (Wiley Publications, 2015)
6. K.R. Padiyar, *FACTS Controllers in Power Transmission and Distribution* (New Age International (P) Limited Publishers, New Delhi, 2007)
7. B. Singh, J. Solanki, A comparison of control algorithms for DSTATCOM. *IEEE Trans. Ind. Electron.* **56**(7) (2009)
8. A. Banelji, S.K. Biswas, B. Singh, DSTATCOM control algorithms: A review. *Int. J. Power Electron. Drive Syst.* **2**(3), 285–296 (2012)
9. K.-L. Areerak, K.-N. Areerak, The comparison study of harmonic detection methods for shunt active power filters. *Int. J. Electr. Comput. Energetic Electron. Commun. Eng.* **4**(10) (2010)
10. J. Ahmed, Z. Salam, An improved perturb and observe (P&O) maximum power point tracking (MPPT) algorithm for higher efficiency. *Appl. Energy* **150**, 97–108 (2015)
11. A. Rohani, M. Joorabian, Modeling and control of DSTATCOM using adaptive hysteresis band current controller in three-phase four wire Distribution systems, in *The 5th Power Electronics, Drives Systems and Technologies Conference (PEDSTC 2014)*, Tehran, Iran, 5–6 Feb 2014
12. E. Latha Mercy, R. Karthic, S. Arumugan, A comparative performance analysis of four control algorithms for a three phase shunt active power filter. *Int. J. Comput. Sci. Netw. Secur.* **10**(6) (2010)

# Comparison of Improvement in Technical, Commercial and Environmental Benefits by Optimal Single-Point, Twin-Point and Triple-Point Deterministic PV-Based DG Injection by Jaya Algorithm



Anirban Chowdhury, Ranjit Roy, Kamal Krishna Mandal, Soumyajit Bhattacharya, Priyankar Biswas and Sayani Nandy

**Abstract** Electric distribution networks are characterized by high  $R/X$  ratio. For this reason, the active power losses in the distribution networks are greater as compared to transmission power networks. On the other hand, the fossil fuel reserve is also reducing day by day. For this reason, renewable energy sources like PV, wind, etc., are the best alternatives in order to overcome this crisis. If the power output from renewable energy-based distributed generators can be injected at optimal points of the distribution network, the active power losses, fossil fuel-based energy consumption and environmental emission can be reduced. This paper aims at determining the optimal points of PV-based DG injection by Jaya algorithm with an objective of increasing the technical, commercial and environmental benefits. The capacity of PV-based DG has been calculated by deterministic approach for the location of Kashmir, India.

**Keywords** Distributed generator (DG) · Voltage stability index (VSI) · Voltage profile enhancement index (VPEI) · Benefit–cost ratio (BCR) · Emission cost–benefit index (ECBI) · Jaya algorithm

---

A. Chowdhury (✉) · R. Roy · S. Bhattacharya · P. Biswas · S. Nandy  
Department of Electrical Engineering, Dr. Sudhir Chandra Sur Degree Engineering College,  
Kolkata, India  
e-mail: [anirban.chowdhury@dsec.ac.in](mailto:anirban.chowdhury@dsec.ac.in)

R. Roy  
e-mail: [rroy@dsec.ac.in](mailto:rroy@dsec.ac.in)

K. K. Mandal  
Department of Power Engineering, Jadavpur University, Saltlake Campus, Kolkata, India  
e-mail: [kkm567@yahoo.co.in](mailto:kkm567@yahoo.co.in)

## 1 Introduction

At the present scenario, there has been a huge demand for electric power across the globe and is increasing with the passage of time. There is also a growing demand on the increasing usage of renewable energy sources (i.e., wind energy, photovoltaic energy etc.) with an objective to have ecofriendly technologies to support our electrical energy consumption. The most advanced technology that has gained popularity and shows a lot more advantageous outcomes is the introduction of the PV wind turbine hybrid system. One of the major advantages is that even in cloudy places where the solar panels might not be able to get enough light for producing electrical energy, the wind will serve to the rescue, thereby reducing the dependency on non-conventional sources of energy. The advantages and impact of a distributed voltage control scheme are depicted by Kiprakis, Wallace and Harrison [1]; analyzing the worst-case scenarios and the distributed network operator practice have been illustrated. A proper control strategy for single-stage three-phase PV source using inner current-controlled loop technique has been previously shown by Yazdani and Dash [2] which can be implemented in the unification process of PV into the distribution system. Lo et al. [3] in the journal has provided a better control strategy with the use of a maximum power point tracker (MPPT) for a grid connected PV with a better power factor and lower circuit cost; however, certain challenges related to the battery bank connected with the MPPT have been mentioned along with the solution. Bagheri, Ali and Rizwan [4] have implemented a fuzzy ant colony optimization approach for improving voltage and to mitigate the power losses. Another approach was made by Chen et al. [5] on using distribution static compensation (DSTATCOM) by implementing reactive power voltage compensation techniques for full utilization of the solar radiation in the PV panels, thereby investigating voltage violations in the distribution systems.

## 2 Jaya Algorithm

### 2.1 Jaya—An Overview

Jaya is a fast, powerful and simple algorithm proposed by Venkata Rao [6] for solving both constrained and unconstrained optimization problems. This algorithm is based on the fact that the solution obtained from a problem will move toward the best solution and deviate from the worst. This algorithm has been tested on 24 benchmark problems and the results obtained proved to be very promising. Let us assume  $f(x)$  to be an objective function. The design variables are indicated by ‘ $m$ ’ ( $j = 1, 2, \dots, m$ ), needs to be maximized or minimized. The total number of candidate solutions/size of population is  $n_p$  ( $k = 1, 2, \dots, n$ ). The best- and worst-valued candidates are indicated by  $f(x)$  best and  $f(x)$  worst, respectively, at the  $i$ th iteration. Suppose, if,  $X_{j,k,i}$  indicates the value of the  $j$ th variable of the  $k$ th candidate for the  $i$ th population,

then its updated value as per Jaya algorithm is given by the following equation.  $r_{1,j,i}$  and  $r_{2,j,i}$  are random values between 0 and 1. The term  $r_{1,j,i} * (X_{j,best,i} - |X_{j,k,i}|)$  makes the candidate move toward the best solution and the term  $-r_{2,j,i} * (X_{j,worst,i} - |X_{j,k,i}|)$  deviates the candidate away from the worst solution.

$$X'_{j,k,i} = X_{j,k,i} + r_{1,j,i} * (X_{j,best,i} - |X_{j,k,i}|) - r_{2,j,i} * (X_{j,worst,i} - |X_{j,k,i}|) \quad (1)$$

## 2.2 Jaya—Its Application to the Problem

In this work, Jaya algorithm is used to determine the optimal location of nodes of standard IEEE 33- and 69-bus test systems where PV-based DGs are to be injected at three points. The above problem is subjected to the power flow constraints and maximization of technical, economical and environmental benefits. The same will be discussed in the following article. The flowchart of Jaya algorithm applied to this problem is shown in Fig. 1.

## 3 Cost Modeling, Problem Formulation and Operating Constraints

### 3.1 Voltage Profile Enhancement Index (VPEI)

During power flow in a distribution network, one of the most important performance parameters to be observed is its voltage profile (VP). The nominal voltage ( $V_{nom}$ ) should not violate the upper ( $V^U$ ) and lower ( $V^L$ ) limits. They are to be restricted between 1.1 pu and 0.9 pu, respectively.

$$V_{nom} = \frac{(V^U + V^L)}{2} \quad (2)$$

For a  $k$ th bus, VP is given by

$$VP_k = \frac{4(V_k - V^L)(V^U - V_k)}{(V^U - V^L)} \quad (3)$$

For a radial distribution network, the voltage profile index (VPI) is given by

$$VPI = \frac{1}{N_B} \sum_{k=1}^{N_B} VP_k \quad (4)$$



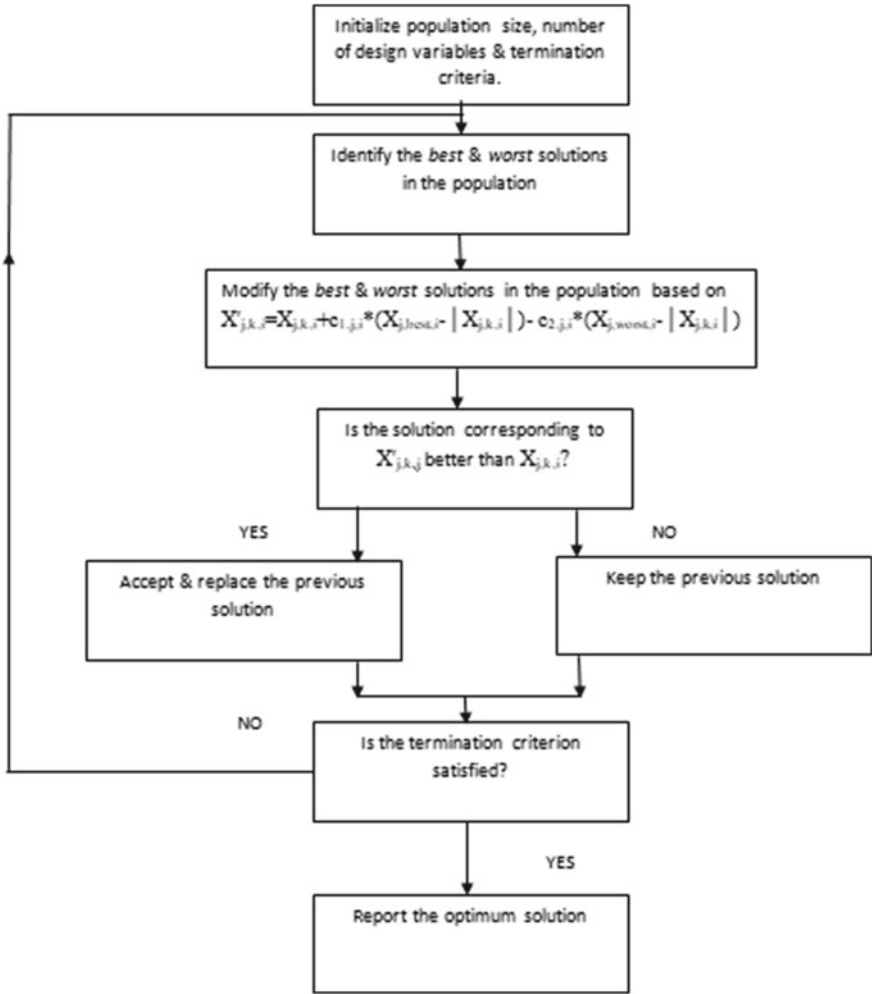


**Fig. 1** Flowchart of Jaya algorithm applied to optimal DG allocation problem

The voltage profile enhancement index (VPEI) for a distribution network is given by

$$VPEI = \frac{(VPI)_{with\ DG}}{(VPI)_{without\ DG}} \tag{5}$$

A value of VPEI less than unity indicates that the network is unstable. A value of VPEI equal to unity indicates that the network is marginally stable. If it is greater than unity, it indicates that the network is stable. It is desirable that after DG injection, the VPEI of the network should be greater than unity.

### 3.2 Benefit-Cost Ratio (BCR)

The benefit in terms of cost savings obtained after installing one or more DG/DGs is indicated by benefit–cost ratio (BCR). The total cost of DG is segregated into three components: (i) investment cost (IC), (ii) hourly working cost (HWC) and (iii) annual maintenance cost (AMC). The cash flow for the newly placed DG/DGs in the coming future must be considered. The inflation rate (IFL) and the interest rate (INR) are necessary in order to predict its current price (CP). It is calculated as

$$CP = \frac{1 + IFL/100}{1 + INR/10} \quad (6)$$

The cumulative current price (CCP) for a specific year-span ( $YR_{span}$ ), is calculated as follows:

$$CCP = \frac{1 - CP^{YR_{span}}}{1 - CP} \quad (7)$$

The cost of DG is calculated in the following way

$$DG_{cost} = IC * P_{DG} + HWC * P_{DG} * PLF * YR_{span} * 8760 * CCP + AMC * CCP * YR_{span} \quad (8)$$

PLF is the plant factor. DG installation results in the reduction of consumption of power from the main grid which, in turn, reduces active and reactive power losses of the distribution network. The benefit of installing DG is calculated by the following equation:

$$DG_{benefit} = \{P_{DG} * PLF + (PLOSS_{w/o} - PLOSS_w)\} * YR_{span} * 8760 * C_h * CCP \quad (9)$$

where  $C_h$  is the cost of power generation,  $PLOSS_{w/o}$  is the power loss of the distribution network without any DG and  $PLOSS_w$  is the power loss of the distribution network after DG installation.

Finally, the BCR of the DG/DGs is

$$BCR = \frac{DG_{benefit}}{DG_{cost}} \quad (10)$$

A value of BCR greater than 1 means that cost saving is generated after DG installation. If BCR is equal to 1, it means that there is no benefit obtained in terms of cost after DG installation. A value of BCR less than 1 will reveal that a financial loss is incurred after DG installation.

### 3.3 Emission Benefit–Cost Index

The twenty-first century is an era of green energy when all the countries, across the globe, are trying to get rid of fossil fuel-based power. It is due to the emission from fossil fuel which is rich in CO<sub>x</sub>, NO<sub>x</sub>, particulate matter, etc. Targets for all the countries are set for zero fossil fuel energy. Renewable energy-based DG injection on a distribution network will reduce power consumption from fossil fuel. In order to ascertain the benefit of a DG with respect to environmental emission, ECBI is formulated as follows:

$$E = E_{\text{grid}} * GP \quad (11)$$

$$EC = \sum_{t=1}^{YR_{\text{span}}} E * E_c * \frac{1}{(1+d)^t} \quad (12)$$

$$ECBI = \frac{EC_{\text{without device}} - EC_{\text{with device}}}{EC_{\text{without device}}} \quad (13)$$

where  $E$ ,  $E_{\text{grid}}$  and  $GP$  represent the amount of CO<sub>2</sub> emission, emission factor and power generated by the main grid, respectively. The variables  $d$  and  $t$  represent the rate of discount/interest and the number of years taken in planning the horizon. If ECBI, after DG injection, turns out to be greater than 0, it indicates that there is reduction in emission due to lower fossil fuel consumption. If ECBI is equal to zero, then there is no change in terms of emission after DG installation.

### 3.4 Formulation of the Objective Function

The objective function (OF) is formulated as a maximizing function, keeping equal weightage on the above three indices, namely VPEI, BCR and ECBI. The values of all the parameters have been taken from [7].

$$OF = \lambda_1 \times VPEI + \lambda_2 \times BCR + \lambda_3 \times ECBI \quad (14)$$

$$\sum_{j=1}^3 \lambda_j = 1 \quad (15)$$

$$\lambda_1 = \lambda_2 = \lambda_3 = 0.333 \quad (16)$$

### 3.5 Operating Constraints

The objective function is subjected to the following constraints.

**Voltage Constraint** The voltage of each node of the radial distribution network must not exceed the maximum and minimum limits of the line.  $V_k$  be the voltage at the  $k$ th node of the distribution network.  $V_k^{\min}$  and  $V_k^{\max}$  are the maximum and minimum voltage limits of the line.

$$V_k^{\min} \leq V_k \leq V_k^{\max} \quad (17)$$

**Line Power Flow Limit** The distribution network must not carry power beyond its power carrying capacity.  $PFL_{mn}$  is the power flow between the points  $m$  and  $n$  of the network, and  $PFL_{mn}^{\max}$  is the maximum power flow limit between the same points.

$$PFL_{mn} \leq PFL_{mn}^{\max} \quad (18)$$

**Active Power Flow Limit** The power output from the main generator must not exceed its specified limits.  $P_G$  is the power output of the main generator.  $P_G^{\min}$  and  $P_G^{\max}$  are the minimum and maximum limits of the main generator.

$$P_G^{\min} \leq P_G \leq P_G^{\max} \quad (19)$$

## 4 Modeling and Calculation of Power Output from Photovoltaic Array

### 4.1 Performance Prediction Model of PV Array

Two most important factors that guide the performance of a PV array are the solar irradiance ( $G$ ) and temperature of the PV module ( $T$ ). The important electrical characteristics of a PV array are the open-circuit voltage ( $V_{oc}$ ), short-circuit current ( $I_{sc}$ ), fill factor (FF) and the peak power output ( $P_{max}$ ).

$$I_{sc} = I_{sc0} \left( \frac{G}{G_0} \right)^\alpha \quad (20)$$

$I_{sc0}$  is the short-circuit current of the PV module under standard solar irradiance  $G_0$ . The nonlinear effects on the photocurrent are indicated by the exponent  $\alpha$ .

$$V_{oc} = \frac{V_{oc0}}{1 + \beta \ln \frac{G_0}{G}} \left( \frac{T_0}{T} \right)^\gamma \quad (21)$$

where  $V_{oc0}$  and  $T_0$  are the open-circuit voltage and temperature of the PV module when exposed to normal solar irradiance.  $\beta$  and  $\gamma$  are technology-specific dimensionless coefficient and coefficient related to nonlinearities in voltage and temperature, respectively.

$$FF = FF_0 \left( 1 - \frac{R_s}{V_{oc}/I_{sc}} \right) \quad (22)$$

$R_s$  and  $v_{oc}$  are the series resistance and normalized open-circuit voltage to the thermal voltage.  $FF_0$  is the ideal fill factor of the PV module. It is given by

$$FF_0 = \frac{v_{oc} - \ln(v_{oc} + 0.72)}{1 + v_{oc}} \quad (23)$$

$$v_{oc} = \frac{V_{oc}}{nKT/q} \quad (24)$$

The ideality factor  $n$  ranges between 1 and 2.  $q$  ( $1.6 \times 10^{-19}$  C) and  $K$  ( $1.38 \times 10^{-23}$  J/K) are the magnitude of electron charge and Boltzmann constant, respectively. The maximum power output of the PV module is given by

$$P_{max} = FF \cdot V_{oc} \cdot I_{sc} \quad (25)$$

If  $N_P$  and  $N_S$  are the numbers of modules in parallel and series, respectively, then

$$P_A = N_P \cdot N_S \cdot P_M \quad (26)$$

where  $P_A$  and  $P_M$  are the array and module power outputs, respectively.

## 4.2 Calculated Power Output of PV Array

The power output from the PV array is calculated [8] with the help of the following parameters in Table 1. The location chosen is Srinagar, India. The calculated power output of the PV array which is to be injected at IEEE 33-bus test system is 348.34 kW. In case of IEEE 69-bus test system, the calculated power output is 1006.7 kW.

## 5 Simulation and Results

The simulation work is done in MATLAB v8.3. The configuration of the PC used is Intel(R) Core(TM) i3-7100 CPU @ 3.91 GHz, 4 GB DDR3 RAM, Windows 10 Professional 64 Bit OS. The calculated power output of the PV array is divided

**Table 1** Values of different parameters for calculation of power output from PV array

Parameters	Values	Parameters	Values
$\alpha$	1.21	$G$	192.917 W/m <sup>2</sup>
$\beta$	0.058	$V_{oc0}$	21 V
$\gamma$	1.15	$I_{sc0}$	6.5 A
$n$	1.5	$R_s$	0.012 $\Omega$
$T_0$	298 K	$N_s, N_p$ (for IEEE 33-bus test system)	10, 10
$T$	288 K	$N_s, N_p$ (for IEEE 69-bus test system)	17, 17
$G_0$	1000 W/m <sup>2</sup>		

equally in three optimal points of standard IEEE 33-bus and 69-bus test systems for triple-point DG injection. The same power is divided equally into two in case of double-point DG injection. The optimal points of DG injection has been calculated by means of Jaya algorithm by maximizing the technical, economic and environmental benefits subjected to the operating constraints as discussed in this paper. The number of iterations and population are taken as 100 and 50, respectively.

### 5.1 Results of IEEE 33-Bus Test System

The power output of the PV array (348.34 kW) is injected at optimal single-point, twin-point and triple-point of IEEE 33-bus test system. In Fig. 2, the convergence characteristics of Jaya algorithm is shown and it is very evident that Jaya algorithm has very high rate of convergence. Figure 3 shows the VSI characteristics of IEEE 33-bus test system for single-point, twin-point and triple-point DG allocation. In each of the cases, the values of VPEI, BCR, ECBI, OF and the active power losses before and after DG allocation are tabulated in Table 2. It is observed that the overall value of OF is improved as shown in Table 2. There is improvement in VSI characteristics after triple-point PV-based DG injection as shown in Fig. 3. The active power loss of the network has been reduced as shown in Table 2. Figure 2 shows that Jaya algorithm has very fast convergence characteristics.

### 5.2 Results of IEEE 69-Bus Test System

The power output of the PV array (1006.7 kW) is injected at optimal single-point, twin-point and triple-point of IEEE 69-bus test system. Figure 4 shows the convergence characteristics of Jaya algorithm, and it is very evident that Jaya algorithm

**Fig. 2** Convergence characteristics of Jaya algorithm for IEEE 33-bus test system

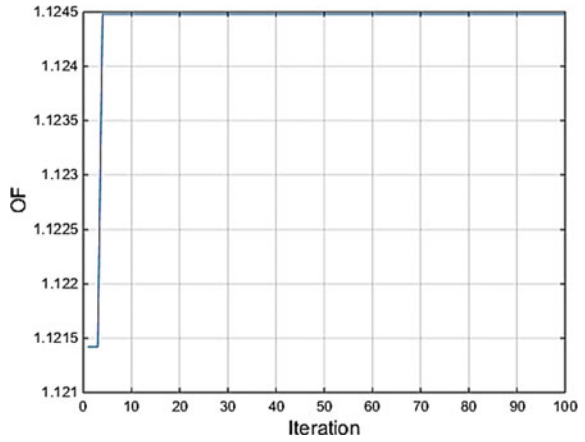


**Fig. 3** VSI characteristics of IEEE 33-bus test system for single-point, twin-point and triple-point DG allocation

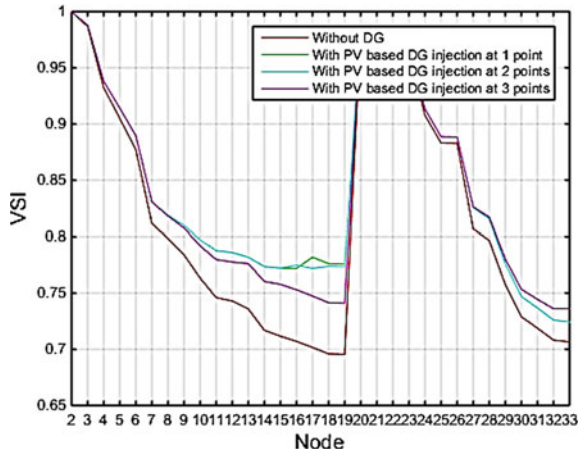


**Table 2** Comparison of results after single-point, twin-point and triple-point DG allocation of IEEE 33-bus test system

Points of DG injection	VPEI	BCR	ECBI	OF	PLOSS before DG installation (kW)	PLOSS after DG installation (kW)
17, 18, 33	1.1467	2.1412	0.0889	1.1245	201.8925	160.3897
18, 33	1.1394	2.1412	0.0889	1.1220	201.8925	160.3910
17	1.1594	2.1067	0.0889	1.1172	201.8925	162.4578

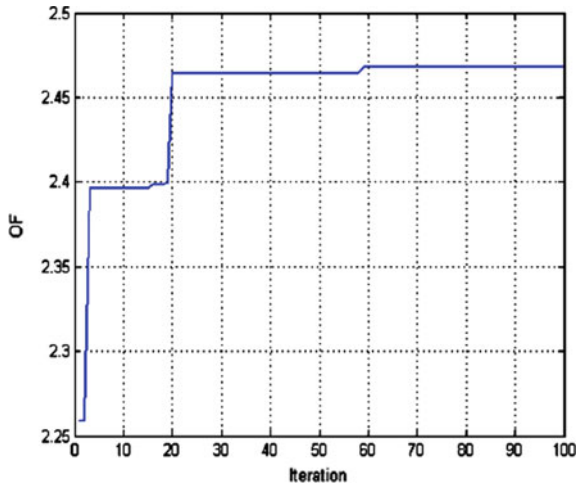


**Fig. 4** Convergence characteristics of Jaya algorithm for IEEE 33-bus test system

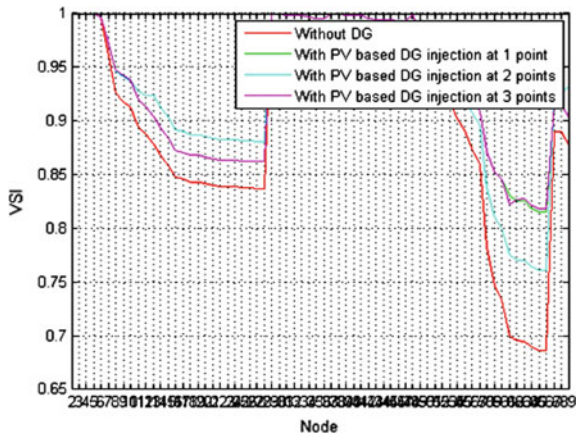


**Fig. 5** VSI characteristics of IEEE 69-bus test system for single-point, twin-point and triple-point DG allocation

has very high rate of convergence. Figure 5 shows the VSI characteristics of IEEE 69-bus test system for single-point, twin-point and triple-point DG allocation. In each of the cases, the values of VPEI, BCR, ECBI, OF and the active power losses before and after DG allocation are tabulated in Table 3. It is observed that the values of VPEI, BCR and ECBI are improved as shown in Table 3. There is improvement in VSI characteristics after triple-point PV-based DG injection as shown in Fig. 5. The active power loss of the network has been reduced as shown in Table 3. Figure 4 shows that Jaya algorithm has very fast convergence characteristics.



**Table 3** Comparison of results after single-point, twin-point and triple-point DG allocation of IEEE 69-bus test system

Points of DG injection	VPEI	BCR	ECBI	OF	PLOSS before DG installation (kW)	PLOSS after DG installation (kW)
61,62,64	1.0944	6.0703	0.2483	2.4686	224.5935	110.0362
61,64	1.0947	6.0677	0.2483	2.4678	224.5935	173.1456
64	1.0934	6.0603	0.2483	2.4649	224.5935	173.0359

## 6 Conclusion

It has been shown that the values of the objective functions are maximum in the cases of triple-point DG injection for both IEEE 33-bus and IEEE 69-bus test systems. So, the technical, commercial and environmental benefits are maximized in both the test systems for the case of triple-point DG injection. In both the test systems, the active power losses are also minimum for the case of triple-point DG injection.

## References

1. P.N. Vovos, A.E. Kiprakis, A. Robin Wallace, G.P. Harrison, Centralized and distributed voltage control: impact on distributed generation penetration. *IEEE Trans. Power Syst.* **22**, 476–483 (2007)
2. A. Yazdani, P. Dash, A control methodology and characterization of dynamics for a photovoltaic system interfaced with a distribution network. *IEEE Trans. Power Deliv.* **24**, 1538–1551 (2009)
3. Y.-K. Lo, T.-P. Lee, K.H. Wu, Grid connected photovoltaic system with power factor correction. *IEEE Trans. Ind. Electron.* **55**, 2224–2227 (2008)
4. H. Bagheri Tolabi, M.H. Ali, M. Rizwan, Simultaneous reconfiguration, optimal placement of DSTATCOM and photovoltaic array in a distribution system based on Fuzzy-ACO approach. *IEEE Trans. Sustain. Energy* **6**, 210–218 (2015)
5. C.-S. Chen, C.-H. Lin, W.-L. Hsieh, Enhancement of PV penetration with DSTATCOM in Taipai distribution system. *IEEE Trans. Power Syst.* **28**, 1560–1567 (2013)
6. R. Venkata Rao, Jaya: a simple and new optimization algorithm for solving constrained and unconstrained optimization problems. *Int. J. Ind. Eng. Comput.* **7**, 19–34 (2016)
7. S.R. Ghatak, S. Sannigrahi, P. Acharjee, Comparative performance analysis of DG and DSTATCOM using improved PSO based on success rate for deregulated environment. *IEEE Syst. J.* **PP(99)**, 1–12 (2017)
8. P. Kayal, C.K. Chanda, Placement of wind and solar based DGs in distribution system for power loss minimization and voltage stability improvement. *Int. J. Electr. Power Energy Syst.* **53**, 795–809 (2013)

# Optimal Reactive Power Dispatch Incorporating Solar Power Using Jaya Algorithm



Tanmay Das, Ranjit Roy, Kamal Krishna Mandal, Souren Mondal,  
Soumayoy Mondal, Paresh Hait and Moloy Kumar Das

**Abstract** Optimal reactive power dispatch (ORPD) is the most functional part of reactive power dispatch technique, by which an effective solution of power flow can be befitted and the system parameters can be arranged in such a value, so that network power losses could be minimized. The ORPD problem can be solved as a single-objective as well as multi-objective optimization problem with the help of various conventional techniques as well as modern developed techniques like differential evolution, particle swarm optimization, genetic algorithm, Jaya algorithm, etc. This paper is an attempt to minimize transmission line power losses by introducing solar energy sources in addition to the existing conventional sources to power network system along with adjusting the reactive power controlled parameter without violating technical equality constraints and inequality constraints. The proposed designed model has been analyzed for IEEE 14-bus and IEEE 30-bus test systems by using Jaya algorithm. The simulation result with comparing others' existing result with and without the inclusion of solar energy has shown that the proposed designed model is effective and profitable for planning an interconnected reliable power system network.

**Keywords** Differential evolution · Genetic algorithm · Jaya algorithm · ORPD · Particle swarm optimization (PSO) · Photovoltaic (PV) · Renewable energy · Solar energy

---

T. Das · R. Roy (✉) · S. Mondal · S. Mondal · P. Hait · M. K. Das  
Department of Electrical Engineering, Dr. Sudhir Chandra Sur Degree Engineering College,  
Kolkata, India  
e-mail: [roy@dsec.ac.in](mailto:roy@dsec.ac.in)

T. Das  
e-mail: [tanmaydas@dsec.ac.in](mailto:tanmaydas@dsec.ac.in)

K. K. Mandal  
Department of Power Engineering, Jadavpur University, SaltLake Campus, Kolkata, India  
e-mail: [kkm567@yahoo.co.in](mailto:kkm567@yahoo.co.in)

## 1 Introduction

Economical operation on power system network has two objectives, one is active power regulation and another is reactive power dispatch. Both the objectives can be improved by introducing renewable sources to the system. Nowadays, renewable sources play an important role on the performance of interconnected power system. They not only minimize harmful green house gas emissions and dependency on fossil fuel but also reduce long-term generation cost of electric power. This article will also show the importance of renewable sources to minimize the active power losses in the system. An interconnected power system is modeled with the help of IEEE 14-bus and IEEE 30-bus test system and is analyzed with ORPD problem by using Jaya algorithm. Jaya algorithm is simple yet powerful optimization algorithm, which is based on the objective that the solution finding out from a problem should be the best solution and should avoid the worst solution. The main objective is to improve the performance of the power system by introducing renewable sources to the system along with controlling the reactive power flow and hence minimizing transmission losses and increasing reliability of the system. The ORPD equation has been formulated with considering the injection of renewable unit to the system, and the best solutions of controlled parameter value (i.e., generator bus voltage, tap changer of transformer, reactive power source) have been found out using Jaya algorithm without violating the equality constraints and inequality constraints. Hence, the best solution for minimizing active power losses has been evaluated. More emphasis is given in the generation of power using renewable energy along with conventional sources in order to reduce the generation cost and to preserve the non-replenishable sources for high demand period. There is an increasing penetration of renewable energy in the system. Thus, in this paper, the solar energy has been incorporated into the IEEE bus test system where the power output from photovoltaic (PV) arrays are integrated along with the existing thermal power to the generator bus in order to minimize the transmission line power loss in the system [1–5].

## 2 Problem Formulation

### 2.1 The ORPD Problem

The objective of the ORPD problem is minimization of active power loss, and it is solved by determining the optimal location of the control variables without the violation of any constraints. The objective function of the problem is expressed as follows [3]:

$$\text{Min } P_{\text{loss}} = \sum_{k \in \text{NL}} g_l (V_a^2 + V_b^2 - 2V_a V_b \cos \delta_{ab}) \quad (1)$$

where  $P_{\text{loss}}$  is the total active power loss in the transmission lines, NL denotes number of transmission lines,  $g_l$  depicts conductance of branch  $l$ ,  $V_a$ ,  $V_b$  are magnitude of the bus voltages the  $a$ th and  $b$ th buses, respectively, and  $\delta_{ab}$  is the phase difference between these voltages. There are few equality constraints given below [6]:

$$P_{Ga} - P_{Da} - V_a \sum_{b=1}^{\text{NB}} V_b [G_{ab} \cos \theta_{ab} + B_{ab} \sin \theta_{ab}] = 0 \quad (2)$$

$$Q_{Ga} - Q_{Da} - V_a \sum_{b=1}^{\text{NB}} V_b [G_{ab} \sin \theta_{ab} + B_{ab} \cos \theta_{ab}] = 0 \quad (3)$$

where NB denotes the number of buses,  $P_{Da}$  and  $Q_{Da}$  are the active and reactive load demands of bus  $a$ .  $P_{Ga}$  and  $Q_{Ga}$  are the active and reactive powers generated at the  $a$ th bus, respectively.  $G_{ab}$  and  $B_{ab}$  are the conductance and susceptance the between  $a$ th and  $b$ th buses, respectively.

There are few inequality constraints given below [6]:

The inequality constraints of the independent variables are:

$$V_{Ga}^{\min} \leq V_{Ga} \leq V_{Ga}^{\max}, \quad a = 1, \dots, N_{\text{GB}} \quad (4)$$

$$Q_{Ca}^{\min} \leq Q_{Ca} \leq Q_{Ca}^{\max}, \quad a = 1, \dots, N_{\text{SC}} \quad (5)$$

$$T_a^{\min} \leq T_a \leq T_a^{\max}, \quad a = 1, \dots, N_{\text{T}} \quad (6)$$

where  $V_{Ga}^{\min}$  and  $V_{Ga}^{\max}$  are the maximum and minimum generator voltages of the  $a$ th bus, respectively.  $Q_{Ca}^{\min}$  and  $Q_{Ca}^{\max}$  are the maximum and minimum reactive power injection of the  $a$ th shunt compensator, respectively, and  $T_a^{\min}$ ,  $T_a^{\max}$  are the maximum and minimum tap settings of the  $a$ th transmission line, respectively.  $N_{\text{GB}}$  is the total number of generator buses,  $N_{\text{SC}}$  is the number of shunt compensators and  $N_{\text{T}}$  is the number of tap-changing transformers. The inequality constraints of the dependent variables are:

$$V_{La}^{\min} \leq V_{La} \leq V_{La}^{\max}, \quad i = 1, \dots, N_{\text{LB}} \quad (7)$$

$$Q_{Gi}^{\min} \leq Q_{Gi} \leq Q_{Gi}^{\max}, \quad i = 1, \dots, N_{\text{C}} \quad (8)$$

$$S_{Li} \leq S_{Li}^{\max}, \quad i = 1, \dots, \text{NL} \quad (9)$$

where  $V_{La}^{\min}$  and  $V_{La}^{\max}$  are the minimum and maximum voltages of the load bus  $a$ , respectively.  $Q_{Gi}^{\min}$  and  $Q_{Gi}^{\max}$  are the minimum and maximum reactive power generations of the  $i$ th generator bus, respectively.  $S_{La}^{\max}$  depicts the maximum apparent power flow in the  $a$ th line and NLB denotes the number of load buses.

## 2.2 Inclusion of PV Unit to the System

In this paper, the study is done by considering the PV unit to be situated at the generator buses and their active power outputs are added to the power output of the conventional generators situated at the generated buses of the standard systems. The power output of the solar PV arrays are determined by using the simplified method of estimating the output of the PV modules under different operating conditions.

## 2.3 Performance Prediction Model of PV Array

The factors that are mostly responsible for the performance of a PV array are the temperature of the PV module ( $T$ ) and solar irradiance ( $E$ ) of the area. The electrical characteristics which are important for the operation of PV array are open-circuit voltage ( $V_{oc}$ ), short-circuit current ( $I_{sc}$ ), the peak power output ( $P_{max}$ ) and fill factor (FF) [7].

$$I_{sc} = I_{sc0} \left( \frac{E}{E_0} \right)^x \quad (10)$$

where  $E_0$  is the solar irradiance and  $I_{sc0}$  is the short-circuit current of the PV module under  $E_0$ .  $I_{sc}$  is the short-circuit current of the PV module under the solar irradiance  $E$ . The nonlinear effects on the photocurrent are indicated by the exponential term  $x$ . The open-circuit voltage  $V_{oc}$  under a given condition is given by

$$V_{oc} = \frac{V_{oc0}}{1 + y \ln \frac{E_0}{E}} \left( \frac{\tau_0}{\tau} \right)^z \quad (11)$$

where  $V_{oc0}$  is the open-circuit voltage of the PV module when exposed to normal solar irradiance at temperature  $\tau_0$ ,  $y$  is a coefficient of technology-specific of PV module technology which is dimensionless and  $z$  is used for considering all the nonlinear effects of voltage and temperature. Fill factor FF is dimensionless and it helps in measuring the deviation of the actual  $I$ - $V$  characteristic from the ideal one. The equation for calculating FF is given below:

$$FF = FF_0 \left( 1 - \frac{R_s}{V_{oc}/I_{sc}} \right) \quad (12)$$

where  $R_s$  is the series resistance,  $FF_0$  is the ideal fill factor of the PV module and  $v_{oc}$  is the normalized value of open-circuit voltage to the thermal voltage.  $FF_0$  and  $v_{oc}$  are given by

$$FF_0 = \frac{v_{oc} - \ln(v_{oc} + 0.72)}{1 + v_{oc}} \quad (13)$$

$$v_{oc} = \frac{V_{oc}}{nK\tau/e} \tag{14}$$

where  $n$  is the ideality factor and it ranges between 1 and 2,  $e$  is the charge of an electron ( $1.6 \times 10^{-19}$  C) and  $K$  is the Boltzmann constant ( $1.38 \times 10^{-23}$  J/K). The maximum power output of the PV module is given by

$$P_{max} = FF \cdot V_{oc} \cdot I_{sc} \tag{15}$$

If there are  $N_S$  number of series and  $N_P$  number of parallel PV modules and  $P_M$  be the module power output, then the array power output is given by

$$P_A = N_P \cdot N_S \cdot P_M \tag{16}$$

### 2.4 Calculated Power Output of PV Array

The active power output from the PV array is calculated using the following parameters from Table 1 [7]. The location chosen in this problem is Srinagar, India, and data is taken from the year 2012 [8]. The calculated power output of the PV array is 348.35 kW.

In this paper, the model of each PV unit has been considered to have 10 modules in both series and parallel and generates around 348.35 kW of power. A total of 20 units can be combined to generate a power of 6.967 MW of power at a particular generator bus. Thus, this power from the PV system is combined to that of the power from the thermal generators at all the generator buses of the system.

**Table 1** Values of the different parameters of PV array

Parameters	Values	Parameters	Values
$x$	1.21	$E$	192.917 W/m <sup>2</sup>
$y$	0.058	$V_{oc0}$	21 V
$z$	1.15	$I_{sc0}$	6.5 A
$n$	1.5	$R_s$	0.012 Ω
$\tau_0$	298 K	$N_P$	10
$\tau$	288 K	$N_S$	10
$E_0$	1000 W/m <sup>2</sup>		

### 3 Implementation of Jaya Algorithm

The Jaya algorithm is a metaheuristic algorithm developed by Rao [9] to solve the objective functions of stochastic optimization techniques. The objective of the algorithm is to proceed toward the best solution and keep avoiding the worst solution. The algorithm keeps on updating the values of the control variables wherever it obtains a better solution compared to the previous iteration. Let  $f(x)$  be an objective function which needs to be minimized. Let 'v' be the number of design variables (i.e.,  $a = 1, 2, \dots, m$ ) and  $i$  be a particular iteration for which the number of candidate solutions be 'c' (i.e., population size,  $b = 1, 2, \dots, c$ ). Let  $f(x)_{\text{best}}$  and  $f(x)_{\text{worst}}$  be the best and worst solutions of the function  $f(x)$  and the candidates obtaining the best and worst solutions be recorded as the best and the worst candidates, respectively. Let value of the  $a$ th variable be  $A_{a,b,i}$  for the  $a$ th candidate in the  $i$ th iteration. The modified value is represented as:

$$A'_{a,b,i} = A_{a,b,i} + r_1(A_{a,\text{best},i} - |A_{a,b,i}|) - r_2(A_{a,\text{worst},i} - |A_{a,b,i}|) \quad (17)$$

where  $A_{a,\text{best},i}$  is the best candidate value of the  $a$ th variable and  $A_{a,\text{worst},i}$  is the worst value of the  $a$ th variable.  $A'_{a,b,i}$  is the updated value of  $A_{a,b,i}$  and  $r_1$  and  $r_2$  are two random numbers in the range  $[0, 1]$ .

#### 3.1 Effectiveness of Jaya Algorithm

The Jaya algorithm has proved to be a superior algorithm over many metaheuristic algorithms in determining the optimal solution of the active power loss in the ORPD problem like PSO, DE, ABC and DE-ABC [10]. Here, the Jaya algorithm is used to determine the active power loss in the transmission lines by incorporating the solar energy into the system, and then, it is comparing with the results of those from the actual system without PV.

## 4 Simulation Results

The ORPD problem is solved using the Jaya algorithm for minimization of the objective function of active power loss. The algorithm is tested on IEEE 14-bus and IEEE 30-bus test system for two different cases for each system. In the first case, the active power output is considered to be delivered only from the conventional generators and then the real power losses are calculated for the ORPD problem using both PSO and Jaya algorithms. In the second case, the bus data of the systems are modified by adding the active power output from the PV blocks to the power output from the generators at the generator buses. Again, the real power losses are

calculated for the ORPD problem using both PSO and Jaya algorithms, and the results are compared. The results for both cases applying the two algorithms are compared, and the results are given below.

#### **4.1 IEEE 14-Bus Test System**

There are 5 generators in IEEE 14-bus test system which are situated at buses 1, 2, 3, 6 and 8 where bus 1 is the slack bus and the others are the PV buses. It has 20 numbers of branches with 3 branches (4–7, 4–9 and 5–6) having tap-changing transformers connected to them. The initial active power loss of the transmission line of the network for the base case is 13.49 MW [11]. The load flow for the system is run by taking the line data and bus data from [12]. The case studies for the test system are as follows:

Case 1:

The number of control variables considered for this case is 10 and their details are listed below [13]:

- (a) 5 numbers of generator voltages at the PV buses 1 (slack bus), 2, 3, 6 and 8. Their range is [0.9, 1.1] p.u.
- (b) 3 numbers of tap-changing transformers connected in the lines between (4–7, 4–9 and 5–6). Their range is within [0.9, 1.1] p.u.
- (c) 2 numbers of static VAR compensators (SVCs) situated at buses 9 and 14. Their range is [0, 0.18] p.u.

Here, the power from the PV unit is not included in the system.

Case 2:

In this case, the control variables and their limits were kept unchanged, only the active power output from PV system has been added to the generator bus data along with the power of the thermal generators. A total of 6.967 MW power is added to all the generator buses (1, 2, 3, 6 and 8) individually.

The ORPD problem has been solved for all the cases using both PSO and Jaya algorithms and their results along with the comparison of the convergence characteristics for both the cases are shown in Table 2 and Fig. 1, respectively.

#### **4.2 Effectiveness of PV on ORPD for Minimization of Active Power Loss and Voltage Deviation**

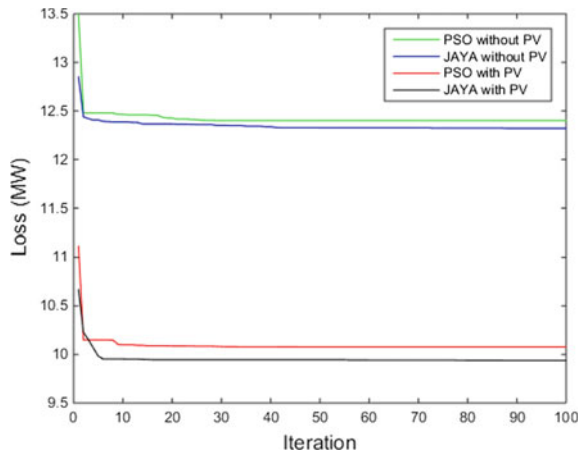
The results obtained from Table 2 and Fig. 1 prove that the penetration of solar power has reduced the active power loss in the system largely, and specifically, the results from Jaya algorithm depict the superiority of the algorithm in determining



**Table 2** Comparative results of IEEE 14-bus test system

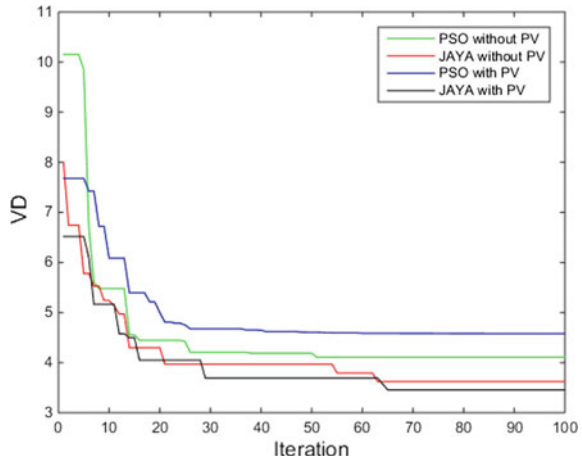
Control variables (p.u.)	PSO (without PV system, case 1)	Jaya (without PV system, case 1)	PSO (with PV system, case 2)	Jaya (with PV system, case 2)
$V_{G1}$	1.1	1.1	1.1	1.1
$V_{G2}$	1.1	1.0973	1.1	1.0973
$V_{G3}$	1.0634	1.0609	1.0634	1.0609
$V_{G6}$	1.0408	1.1	1.0412	1.1
$V_{G8}$	1.1	1.1	1.1	1.1
$T_{4-7}$	1.0865	1.0093	1.0884	1.0093
$T_{4-9}$	1.0661	0.9442	1.0682	0.9442
$T_{5-6}$	1.1	0.9969	1.1	0.9969
$Q_{sc9}$	18	18	18	18
$Q_{sc14}$	18	18	18	18
<b>Total <math>P_{loss}</math> (MW)</b>	<b>12.4023</b>	<b>12.3215</b>	<b>10.0773</b>	<b>9.9389</b>

**Fig. 1** Convergence characteristics of PSO and Jaya algorithms for power loss for both the cases on the IEEE 14-bus test system



the optimal solution over PSO. Since, the PV cannot deliver reactive power, but its contribution in active power in the lines helps in reducing the voltage deviation in the buses as shown in Fig. 2 and thus improves the voltage profile of the system. Thus, Jaya algorithm has the ability to successfully reduce the power loss as well as the voltage deviation in the buses to a greater extent compared to PSO.

**Fig. 2** Convergence characteristics of PSO and Jaya algorithms for voltage deviation for both the cases on the IEEE 14-bus test system



### 4.3 IEEE 30-Bus Test System

The standard IEEE 30-bus test system comprises of total of 6 generators that are situated at the buses 1, 2, 5, 8, 11 and 13 out of which bus 1 is the slack bus and the others are PV buses. There are 41 numbers of branches in which 4 numbers of adjustable transformers are connected in branches (6–9, 6–10, 4–12 and 28–27). The load flow for the system is run by taking the line data and bus data from [11]. Initially, transmission line active power loss is 17.8984 MW for the base case [11]. The two case studies for the test system are as follows:

Case 1:

The number of control variables considered in this particular case for the optimization problem is 12. The variables along with their limits are listed below [13]:

- (a) 6 numbers of generator voltages at the PV buses 1 (slack bus), 2, 5, 8, 11, 13. Their range is [0.9, 1.1] p.u.
- (b) 4 numbers of tap-changing transformers connected in the lines between (6–9, 6–10, 4–12 and 28–27). Their range is within [0.9, 1.1] p.u.
- (c) 2 numbers of static VAR compensators (SVCs) situated at buses 10 and 24. Their ranges are [0, 0.2] p.u. and [0, 0.04] p.u., respectively.

Here, the power from the PV unit is not included in the system.

Case 2:

The control variables in this case has been kept unchanged along their limits. Here, only the active power output from the PV system is included along with the power of the thermal generators in the generator bus data. A total of 6.96 MW power is added to all the generator buses (1, 2, 5, 8, 11 and 13) individually. Both PSO and Jaya algorithms are used to solve the ORPD problem of minimization of active power

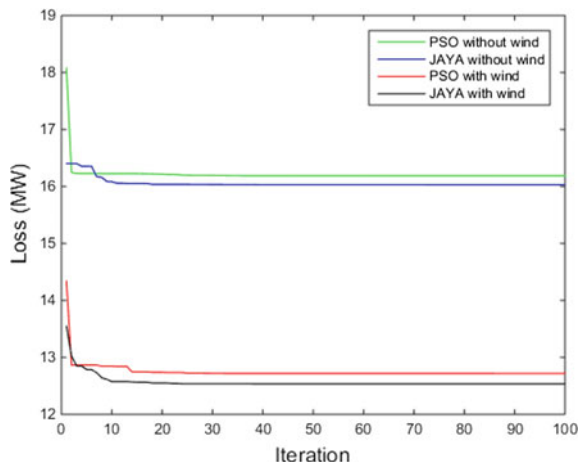
losses of the transmission lines. The results along with the convergence characteristics compared for both the cases are shown in Table 3 and Fig. 2, respectively.

The results obtained from Table 3 and Fig. 3 for the above-mentioned cases imply that the addition of power from the solar energy has helped in reducing the active power losses in the transmission lines to a great extent. Thus, the penetration of the solar energy in the system helps in getting a better result of the ORPD problem. Moreover, the convergence characteristics prove that Jaya is superior in determining

**Table 3** Comparative results of IEEE 30-bus test system

Control variables (p.u.)	PSO (without PV system, case 1)	Jaya (without PV system, case 1)	PSO (with PV system, case 2)	Jaya (with PV system, case 2)
$V_{G1}$	1.1	1.1	1.1	1.1
$V_{G2}$	1.0976	1.0953	1.0976	1.0953
$V_{G5}$	1.1	1.0555	1.1	1.0555
$V_{G8}$	1.0463	1.0921	1.0463	1.0921
$V_{G11}$	1.1	1.1	1.1	1.1
$V_{G13}$	1.1	1.0985	1.1	1.0985
$T_{6-9}$	1.0997	1.0460	1.0997	1.0460
$T_{6-10}$	1.1	0.9	1.1	0.9
$T_{4-12}$	1.08	0.9758	1.08	0.9758
$T_{28-27}$	1.0263	0.9535	1.0263	0.9535
$Q_{sc10}$	0.2	0.2	0.2	0.2
$Q_{sc24}$	0.04	0.04	0.04	0.04
<b>Total <math>P_{loss}</math> (MW)</b>	<b>16.1872</b>	<b>16.029</b>	<b>12.7176</b>	<b>12.5347</b>

**Fig. 3** Convergence characteristics of PSO and Jaya for both the cases on the IEEE 30-bus test system



the optimal solution to the problem and also minimizes the objective function largely compared to the other mentioned algorithm in the literature.

## 5 Conclusion

In this paper, the output from the PV system is added with that of the initial output from the conventional thermal generators of the respective standard systems. The results from the solutions of the ORPD problem from the case studies prove that the transmission line power loss is reported to be lower when the solar power is integrated to the system compared to that of the result when there is no intervention of solar power into the system. Thus, the penetration of additional renewable energy (solar energy in this paper) in the system helps in reducing the power loss in the transmission lines in the ORPD problem. On the other hand, the Jaya algorithm seems to have minimized the objective function largely compared to the other reported algorithm and thus is much more efficient, consistent and superior in determining the optimal solutions to the objective function. In other terms, it is a better choice compared to PSO in finding out the optimal values of control variables in the ORPD problem and thus optimizing the problem faster when tested on the different case studies for the standard IEEE 14- and 30-bus test systems.

## References

1. W. Nakawiro, I. Erlich, J.L. Rueda, A novel optimization algorithm for optimal reactive power dispatch: a comparative study, in *4th International Conference on Electric Utility Deregulation and Restructuring and Power Technologies (DRPT)* (2011)
2. K. Abaci, V. Yamaçlı, Optimal reactive-power dispatch using differential search algorithm. *Electr. Eng.* **99**, 213–225 (2017)
3. M. Ghasemi, S. Ghavidel, M.M. Ghanbarian, A. Habibia, A new hybrid algorithm for optimal reactive power dispatch problem with discrete and continuous control variables. *Appl. Soft Comput.* **22**, 126–140 (2014)
4. S. Pandya, R. Roy, Particle swarm optimization based optimal reactive power dispatch, in *IEEE International Conference on Electrical, Computer and Communication Technologies (ICECCT)* (2015)
5. P.P. Biswas, P.N. Suganthan, G.A.J. Amaratunga, Optimal power flow solutions incorporating stochastic wind and solar power. *Energy Convers. Manage.* **148**, 1194–1207 (2017)
6. M. Mehdinejad, B. Mohammadi-Ivatloo, R. Dadashzadeh-Bonab, K. Zare, Solution of optimal reactive power dispatch of power systems using hybrid particle swarm optimization and imperialist competitive algorithms. *Electr. Power Energy Syst.* **83**, 104–116 (2016)
7. W. Zhou, H. Yang, Z. Fang, A novel model for photovoltaic array performance prediction. *Appl. Energy* **84**, 1187–1198 (2007)
8. P. Kayal, C.K. Chanda, Placement of wind and solar based DGs in distribution system for power loss minimization and voltage stability improvement. *Electr. Power Energy Syst.* **53**, 795–809 (2013)
9. R. Venkata Rao, Jaya: a simple and new optimization algorithm for solving constrained and unconstrained optimization problems. *Int. J. Ind. Eng. Computations* **7**, 19–34 (2016)

10. T. Das, R. Roy, Optimal reactive power dispatch using JAYA algorithm, in *IEEE International Conference on Emerging Trends in Electronic Devices and Computational Techniques (EDCT)* (2018)
11. P. Subbaraj, P.N. Rajnarayanan, Optimal reactive power dispatch using self-adaptive real coded genetic algorithm. *Electr. Power Syst. Res.* **79**, 374–381 (2009)
12. Washington University. <https://www2.ee.washington.edu/research/pstca/>
13. Y. Li, Y. Wang, B. Li, A hybrid artificial bee colony assisted differential evolution algorithm for optimal reactive power flow. *Electr. Power Energy Syst.* **52**, 25–33 (2013)

# Bat-Algorithm-Based Transmission Expansion Planning



P. Das, P. S. Bera and P. Biswaas

**Abstract** This paper presents a TEP problem solution technique based on bat algorithm for standard 6 bus system and a real system of 400 kV, WBSEDCL. The objective of the work is to reduce the cost of proposed new lines for economic and reliable supply. DC power flow has been used to maintain the power balance at buses and line constraints. The line flow constraints are considered while optimizing the objective function. The method has been successfully applied to the system and satisfactory results have been found.

**Keywords** Transmission expansion planning · Cost function · DC load flow model · Bat algorithm

## 1 Introduction

In the last few years, the problem of optimal power flow (OPF) has received into attention. To solve the expansion planning of transmission network, several computer software based on different mathematical techniques have been developed to satisfy the needs of future generation and load. Computer software deals with new circuits addition with minimum cost function in an expansion of transmission system.

It is difficult to develop an effective algorithm for OPF as it is a high-constraint nonlinear optimization problem. Over a decade, research has been carried out in this particular area where Garver [1] first made linear programming algorithm which was used very successfully to determine the power flows in the lossless network and

---

P. Das (✉) · P. Biswaas  
JIS College of Engineering, Kalyani, West Bengal, India  
e-mail: [parthadasee@gmail.com](mailto:parthadasee@gmail.com)

P. Biswaas  
e-mail: [papunbiswas@gmail.com](mailto:papunbiswas@gmail.com)

P. S. Bera  
Kalyani Government Engineering College, Kalyani, West Bengal, India  
e-mail: [parthabera1977@gmail.com](mailto:parthabera1977@gmail.com)

to add new lines where largest overload exists and process will be continuous till overload remains. The nonlinear programming optimization algorithm deals with problem involving nonlinear objective and constraint functions [2–6]. To solve those researchers proposed different modern optimization techniques based on artificial intelligence, genetic algorithm, particle swarm optimization, and many more.

This paper introduces the application of bat algorithm to DC-power-flow-based model for solving TEP. The proposed approach has been examined and tested on Garver [1] test system and a real system of WBSEDCL [2, 3].

## 2 Problem Formulation

Using DC power flow model when the power grid is represented, the mathematical model for the one stage transmission expansion problem can be formulated as follows [7]:

Subject to

Minimize

$$v = \sum_{(i,j)} C_{ij} n_{ij} + \alpha \sum_{(k)} r_k \quad (1)$$

$$sf + g + r = d \quad (2)$$

$$f_{ij} - \gamma_{ij}(n_{ij}^0 + n_{ij})(\theta_i - \theta_j) = 0 \quad (3)$$

$$|f_{ij}| \leq (n_{ij}^0 + n_{ij}) \bar{f}_{ij} \quad (4)$$

$$0 \leq g \leq \bar{g} \quad (5)$$

$$0 \leq r \leq d \quad (6)$$

$$0 \leq n_{ij} \leq \bar{n}_{ij} \quad (7)$$

$n_{ij}$  integer,  $f_{ij}$  and  $\theta_j$  unbounded

$$(i,j) \in \Omega, k \in \Gamma$$

where  $C_{ij}$  = cost of a circuit that can be added to right of way  $i$ - $j$ ,  $\gamma_{ij}$  = susceptance of the circuit,  $n_{ij}$  = no of circuits added in right of way  $i$ - $j$ ,  $n_{ij}^0$  = number of circuits in the base case,  $\bar{f}_{ij}$  = power flow,  $v$  = total investment.

$S$  = branch-node incidence matrix,  $f$  is a vector with elements  $f_{ij}$ ,  $g$  is a vector with elements  $g_k$  whose maximum value is  $= \bar{g}$ ,  $\bar{n}_{ij}$  maximum number of circuits that can be added in right of way  $i$ - $j$ ,  $\Omega$  = set of all right of ways,  $\Gamma$  = set of indices

for load buses. The constraint in Eq. (2) represents the conservation of power in each node if we think in terms of an equivalent DC network, this constraint models in on based on Kirchhoff’s current (KCL) law.

The constraint in Eq. (3) is an expression of ohm’s law for the equivalent DC network. The transmission expansion problem can be formulated as an integer non-linear problem (INLP). It is a difficult combinational problem which can lead to a combinational explosion on the number of alternatives that have to be searched.

### 3 Data Sets

In this section, two systems are presented for TEP. For testing a novel algorithm, the system one is Garver [1] system and system two is real system of WBSEDCL [3].

#### 3.1 6 Bus System

The well-known Garver existing system is shown in Fig. 1. The constraints for the 6 bus system with increased load as shown in Fig. 2. The demand is of 760 MW and the relevant data are given in Tables 1 and 2. This system has six buses and 15 rights of ways for the addition of new circuits. Generation and system data are given in Tables 1 and 2.

**Fig. 1** Existing Garver system

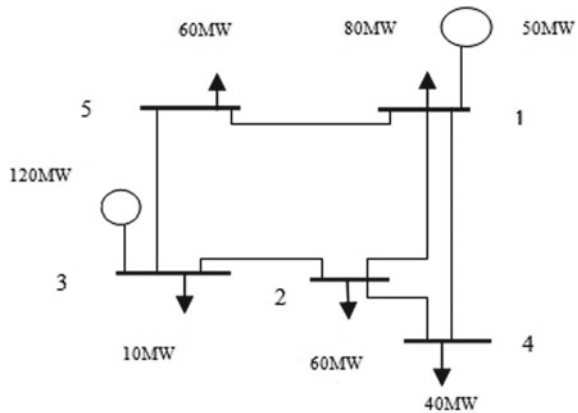




**Fig. 2** Existing Garver system with increased load

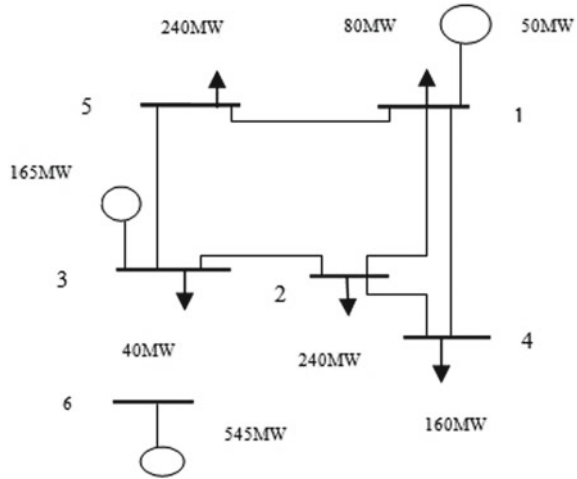


**Table 1** Net generation minus load data for Garver system

Bus	Generation	Load	Net
1	50	80	-30
2	0	240	-240
3	165	40	125
4	0	160	-160
5	0	240	-240
6	545	0	545
Total	760	760	0

### 3.2 WBSIEDCL 400 kV System

The 400 kV system of WBSIEDCL [2, 3] under eighth plan shows in Fig. 3. In Fig. 4, the future condition with the increased load and generation is shown as per the ninth plan of WBSIEDCL. As per the ninth plan of WBSIEDCL three new buses have been added to the existing system. Here, the problem is how to connect these three buses to existing system so that it would be more economic configuration with system constraint maintained. Scheduled generation and loads are shown in Fig. 3 and system data are given in Tables 3 and 4.

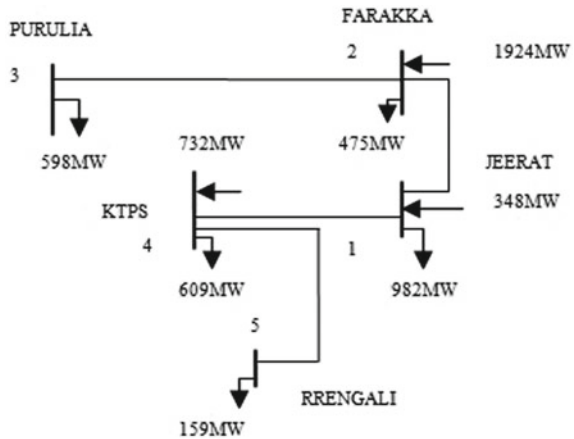
## 4 Bat Algorithm

For optimization problems, nowadays, nature-inspired algorithms are the most powerful tools. Yang proposed a new nature-inspired metaheuristic algorithm, namely

**Table 2** Circuit data for 6 bus system

Terminals	No of baseline ( $n_{ij}^0$ )	$X$ (p.u.)	Capacity (MW)	Cost (\$)
1-2	1	0.40	100	40
1-3	0	0.38	100	38
1-4	1	0.60	80	60
1-5	1	0.20	100	20
1-6	0	0.68	70	68
2-3	1	0.20	100	20
2-4	1	0.40	100	40
2-5	0	0.31	100	31
2-6	0	0.30	100	30
3-4	0	0.59	82	5
3-5	1	0.20	100	20
3-6	0	0.48	100	48
4-5	0	0.63	75	63
4-6	0	0.30	100	30
5-6	0	0.61	78	61

**Fig. 3** Existing system of WBSEDCL



Bat algorithm [8] based on the echolocation behavior of bats. Bats are the mammals which have wings and having high capacity of echolocation. To detect the objects surrounding bats and find their way in night time, they radiate a sound signal called sonar/echolocation. Practically, the sonar/echolocation sound signal is very loud so that they can be able to listen to the sound of echo that bounces back from the surrounding objects.

Bats use short frequency modulated signals in most of the cases. Such echolocation behavior of microbats makes it possible to formulate new optimization algorithm.

**Fig. 4** Existing system with future and demand

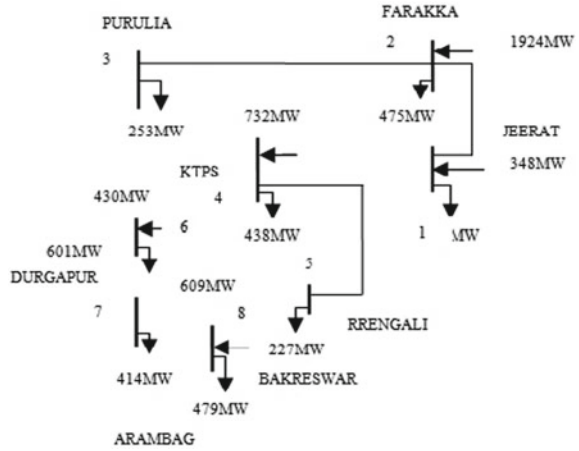


**Table 3** Net generation minus load data for WBSEDCL system

Bus	Generation	Load	Net
1	348	982	-634
2	1924	679	1245
3	0	253	-253
4	762	438	324
5	0	227	-227
6	430	601	-171
7	0	414	-414
8	609	479	130
Total	4073	4073	0

**Table 4** Circuit data for WBSEDCL system

Terminals	No of baseline ( $n_{ij}^0$ )	X (p.u.)	Capacity (MW)	Cost (\$)
1-2	1	0.236	900	236
1-4	1	0.134	900	134
2-3	1	0.249	900	249
4-5	1	0.360	900	360
3-6	1	0.015	900	15
4-6	1	0.132	900	132
4-8	1	0.112	900	112
5-8	1	0.132	900	132
5-7	1	0.140	900	140
6-7	1	0.120	900	120

Such a way that it can be associated with the objective function to be minimized. After idealize some of the echolocation characteristics, we can develop bat algorithm. For simplicity, we are considering some rules:

- The use of echolocation to sense distance is done by all bats, and it is also “known” the distance between prey/food and background barriers in some way.
- Bats are flying with a velocity  $V_i$  at position  $X_i$  with a fixed value of frequency  $f_{\min}$ . The varying wavelength and loudness  $A_0$  to search for prey. The wavelength of emitted pulse is adjusted automatically by them and the rate of pulse emission  $r$  in the range of  $[0, 1]$ , depending on the proximity of their target.
- In many ways, loudness can be varied; here, we are assuming that the loudness varies from a large (positive)  $A_0$  to a minimum constant value  $A_{\min}$ .

In search space of algorithm, we have defined the rules for updating the positions  $Z_i$  and the velocities  $V_i$ . The new solutions, i.e., position and velocity are given by:

$$f_i = f_{\min} + (f_{\max} - f_{\min})\alpha \quad (8)$$

$$v_i^0 = v_i + (z_i - z_0)f_i \quad (9)$$

where  $\alpha$  is the random number varies between  $[0, 1]$  and the current best location is  $z_0$ . Then, the new solution or position for the bat can be generated by the equation below:

$$z_i^t = z_i + v_i \quad (10)$$

Once a solution is selected among the current best solutions, a new solution for each bat is generated locally using random walk

$$z_{\text{new}} = z^{\text{old}} + A^t \mu \quad (11)$$

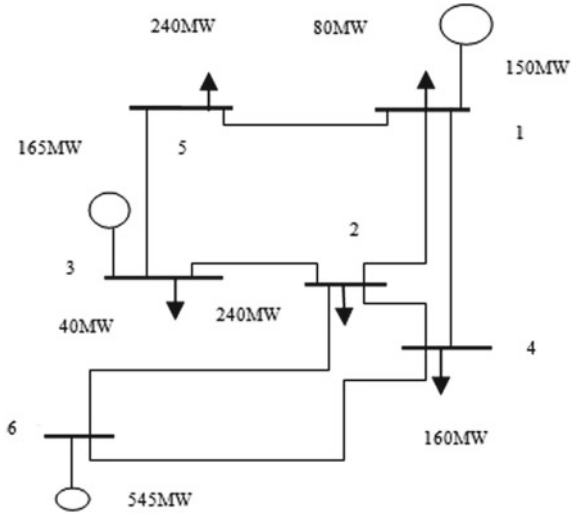
$\mu$  is a random number between  $[0, 1]$  and average loudness of bats is  $A^t$ .

## 5 Results and Discussion

### 5.1 6 Bus System

In existing standard 6 bus Garver system Fig. 1, there are 5 buses and 6 lines are already connected. Now, Bus 6 has to be connected with the existing system with increased load Fig. 2 so that the overall cost function should be minimized. Eight rights of ways have been considered here for new circuit addition. Here, in this case, lines 1-6, 4-5, 5-6, 3-6, 3-4, 1-3, 2-6, 4-6 can be considered for new circuit addition. Within those, lines 1-6, 4-5, 5-6, 3-6, 3-6, 3-4 are not considered here as they are not

**Fig. 5** Optimum route for Garver system



feasible and from remaining three rights of ways (1-3, 2-5 and 4-6) lines are only to be connected. For these three rights of ways, eight combinations are possible and for each combination, the value of cost function has been calculated and minimum cost is found when line 2-6, 4-6 are connected in the system. Figure 5 shows the modified network with optimum route connection for Garver system.

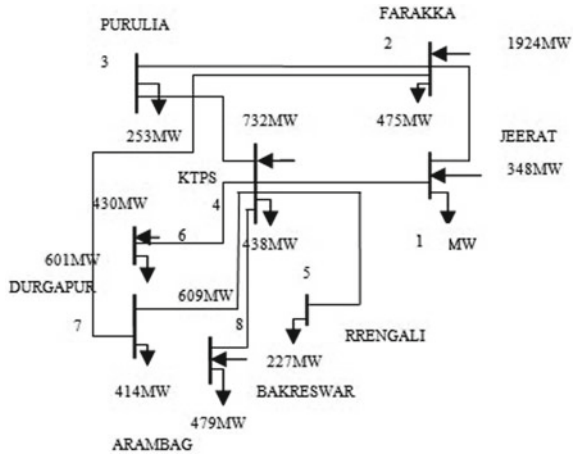
### 5.2 400 kV System of WBSEDCL

As per eighth plan, the existing 400 kV system of WBSEDCL, there are 5 buses and 4 lines shown in Fig. 3. Now in the ninth plan of WBSEDCL, the future condition with increased load and generation shown in Fig. 4 where there are 8 buses. So, there can be 28 rights of ways to minimize the cost function. Here in this case, lines 1-3, 1-4, 1-7, 2-8, 2-5, 5-8, 2-6, 2-7, 2-4, 3-6, 3-1, 3-4, 6-7, 6-1, 1-7, 4-6, 5-7, 4-8 can be considered for new circuit addition. Within those, only 5 lines 2-7, 3-4, 4-6, 4-7, 4-8 are considered. For these five rights of ways, 63 combinations are possible and for each combination, the value of cost function has been calculated and minimum cost which is shown in Fig. 6 with optimum route connection for WBSEDCL system.

## 6 Conclusions

In this paper, systematic approach has been followed for transmission expansion planning (TEP) problem solution technique. Here, TEP problem is formulated as

**Fig. 6** Optimum route for WBSEDCL



an optimization problem and solved by a bio-inspired bat algorithm. While minimizing the cost function, this method considers all the right of ways. The proposed method has been applied to standard 6 bus representative system and 400 kV, 8 bus WBSEDCL real system and the result found satisfactory.

## References

1. L.L. Garver, Transmission network estimation using linear programming. *IEEE Trans. Power Syst.* PAS **89**(7), 1688–1697 (1970)
2. P.K. Das, An application of network optimization technique for transmission expansion planning to a real system, in *National Conference on trends and Advances in Computer Aided Design and Engineering (TACADE-2007)*, Kalyani Government Engineering College, 16–17 Feb 2007, pp. 387–404
3. P.K. Das, P. Roy, P. Bera, S. Halder, A novel approach for transmission expansion to a real system (400 kV system of WBSEDCL), in *International Conference on Control, Instrumentation, Energy and Communication*, 978-1-4799-2044-0/14/\$31.00©2014IEEE, pp. 436–440
4. E.L. Silva, H.A. Gil, J.M. Areiza, Transmission network expansion planning under an improved genetic algorithm, in *21st International Conference on power Industry Computer Applications—PICA*, Santa Clara, CA, May 1999
5. M.C. da Rocha, J.T. Saraiva, A discrete evolutionary PSO based approach to the multiyear transmission expansion planning problem considering demand uncertainties. *Electr. Power Energy Syst.* **45**, 427–442 (2013)
6. R.A. Gallego, A.B. Alves, A. Monticelli, R. Romero, Parallel simulated annealing applied to long term transmission network expansion planning. *IEEE Trans. Power Syst.* **12**, 181–188 (1997)
7. R. Romero, A. Monticelli, A. Gracia, S. Haffner, Test system and mathematical models for transmission network expansion planning. *IEE Proc. Gener. Transm. Distrib.* **140**(1), 27–36 (2002)
8. S. Biswal, A.K. Barisal, A. Behera, T. Prakash, Optimal power dispatch using bat algorithm. *IEEE Trans.* 1018–1023 (2013) (978-1-4673-6150-7/13)

9. P. Maghouli, S.H. Hosseini, M.O. Buygi, M. Shahidehpour, A multi-objective framework for transmission expansion planning in deregulated environments. *IEEE Trans. Power Syst.* **24**, 1051–1061 (2009)
10. J. Contreras, F.F. Wu, Coalition formation in transmission expansion planning. *IEEE Trans. Power Syst.* **14**, 1144–1152 (1999)
11. J. Contreras, F.F. Wu, A kernel-oriented coalition formation algorithm for transmission expansion planning. *IEEE Trans. Power Syst.* **15**, 919–925 (2000)
12. G.B. Shrestha, P.A.J. Fonseca, Congestion-driven transmission expansion in competitive power markets. *IEEE Trans. Power Syst.* **19**, 1658–1665 (2004)
13. O.B. Tor, A.N. Guven, M. Shahidehpour, Congestion-driven transmission planning considering the impact of generator expansion. *IEEE Trans. Power Syst.* **23**, 781–789 (2008)
14. X. Min, Z. Jin, F.F. Wu, Multiyear transmission expansion planning using ordinal optimization. *IEEE Trans. Power Syst.* **22**, 1420–1428 (2007)
15. M. Rahmani, M. Rashidinejad, R. Romero, Efficient method for AC transmission network expansion planning. *Electr. Power Syst. Res.* **80**, 1056–1064 (2010)
16. T. Chung, K. Li, G. Chen, J. Xie, G. Tang, Multi-objective transmission network planning by a hybrid GA approach with fuzzy decision analysis. *Int. J. Electr. Power Energy Syst.* **25**(3), 187–192 (2003)

# Emergency Restoration Based on Priority of Load Importance Using Floyd–Warshall Shortest Path Algorithm



Dipu Sarkar, Maitrayee Chakrabarty, Abhinandan De and Sanjay Goswami

**Abstract** This work presents a novel algorithm for service restoration with an aim to provide power to each important load by the black-start generator during emergency after an immediate blackout. In this process of the restoration, total network must be clustered satisfying all of the electrical constraints based on load priority. To achieve the above objectives, priority-based Floyd–Warshall all-pair shortest path algorithm (FWA) has been utilized. This algorithm will provide the shortest distance between all the pairs of the buses (i.e., vertices in graph theory). Simulation on IEEE 14 bus system has been carried out. The result shows that the proposed method can effectively determine the cluster by means of shortest path algorithm for the reenergizing network after the blackout satisfying all constraints in a very small operating time.

**Keywords** Blackout · Disaster recovery · Power system restoration planning · FWA

---

D. Sarkar (✉) · M. Chakrabarty  
Department of Electrical and Electronics Engineering, National Institute of Technology,  
Nagaland, Dimapur 797103, India  
e-mail: [dipusarkar5@rediffmail.com](mailto:dipusarkar5@rediffmail.com)

M. Chakrabarty  
e-mail: [moitry29@gmail.com](mailto:moitry29@gmail.com)

A. De  
Department of Electrical Engineering, Indian Institute of Engineering Science and Technology,  
Shibpur, Howrah, West Bengal, India  
e-mail: [abhinandan.de@gmail.com](mailto:abhinandan.de@gmail.com)

S. Goswami  
Department of Computer Applications, Narula Institute of Technology, Kolkata, India  
e-mail: [sanjay.goswami@nit.ac.in](mailto:sanjay.goswami@nit.ac.in)



## 1 Introduction

Deficiency of generation, transmission insufficiency, irregular security monitoring, etc., are causes behind a tragic blackout. Power system blackouts are rare phenomena [1, 2], but when it happens, its consequences on the economy of the country, industry, transportations, hospitals, and on the life of the people can be austere. To minimize these ill effects of a blackout, we should focus on restoring the electrical services as early as possible in the power system network [2, 3]. In order to diminish the effect of the blackout on the economy and society, the majority of electric utility companies have pre-established guidelines and operating procedures to re-establish the power system network. Power system restoration generally achieved in two steps. In paper no [4], first step is to search of an optimal path connection configuration and second step is to determine the switching operation sequence of different state. Jaw-Shyang Wu et al. proposed the Petri net model for the power system restoration (PSR). PN model incorporates two sets of nodes, i.e., place (P) node and transition (T) node, with some conditions that have to be met before an action can be taken. In this technique, ‘place’ node represents the power system components, and the ‘transition’ nodes are used to change the state of the power system during power system restoration [5]. T. D. Sudhakar et al. used the Dijkstra algorithm for the restoration of the power supply in the distribution side network and used the Dijkstra algorithm for finding the shortest path from a single source to the entire node in the power system network [6]. Sudhakar et al. consider distribution network used Prim’s algorithm for the searching of optimal power flow path in paper no [7]. S. Hemalatha and P. Valsalal have applied the Bellman–Ford algorithm to find out the optimal path and also the several alternative paths for the restoration of power in the transmission network after a power outage or blackout. As after a power outage, there may be many possible paths with the given set of the generation unit, load, and transmission path [8].

## 2 Application of Graph Theory for Power System Restoration

Power system restoration is a complex phenomenon. So from the past few years, many researchers have dedicated their sincere efforts and come up with various methods for power system restoration which can be broadly classified into different subgroups like knowledge-based approach [4, 9] and mathematical programming techniques [10]. T Sakaguchi et al. proposed some knowledge-based approach in the paper no [4] and discussed how to solve the restoration issues after a failure of a power plant resulting in a blackout and utilized the heuristic knowledge of the operators, guidelines, and manuals about restoring the power system. In the mathematical programming approach, first find out an objective function along with the constraints and solve the objective function with the help of different like optimization method,

graph theory, etc. With the advent of the computer-based system for the restoration, computation becomes very easy and so the knowledge-based approach becomes redundant. As the restoration using the optimization method generally consists of a large complex problem and without the use of a computer, this seems very difficult. But consider some constraints to this optimization method as the computation time increases exponentially with the increase in the number of buses in the network. Graph theory techniques can be used effectively for the power system restoration. This technique helps to minimize the shortcomings of the optimization techniques in which computation time increases exponentially with the addition of buses in the system. Here search time increases linearly with the increase in the de-energized area. The shortest path algorithm used for finding the optimal path for restoration. In graph theory, shortest path algorithms are used to find the path with the minimum weight, i.e., optimal path between two vertices (or nodes). If there are only one source and one destination, then it is called as single-pair shortest path problem. *Dijkstra* algorithm can be used to find the solution of the single-pair shortest path problem. This method can also be used for finding the shortest path from all vertices to a single destination. But Floyd–Warshall algorithm can be used to find the entire pairs' shortest path among every vertices present on the graph. In [11] Hemalatha et al. have found out the shortest path between all pairs of vertices by using Floyd Warshall algorithm in C Sharp programming platforms. In the present article aim to find out the optimum shortest path between generating sources to all the load nodes. It also considers priority load, and four black-start generators capacity (MW, Mvar) supplied separately as a zone-wise.

### 3 Mathematical Formulations

A power system restoration planning is depended upon different objectives and optimization technique. The overall PSR planning can be done with help of the following objective functions and system network constraints. Clustering the overall system in different subsystem depends upon black-start units or cranking unit capacity and cranking load consumption capacity based on nearest shortest path and consider important load priority for solving the blackout problem.

#### 3.1 Loss Minimization

To supply the cranking power source to the load, shortest electric paths are required to flow the power. This shortest path helps to minimizing the power losses, line losses, and voltage drop. The transmission line impedance help to find out the shortest path distance. If power flows, this optimal path line loss are reduced. The impedance value is varying with respect to the distance.

### 3.2 Line Limit

Every line has some power flow capacity limit. The power flow capacity should not exit the above power flow limit.

### 3.3 Power Balance

The cranking unit or black-start unit power generation capacity should be equal or less than the load consumption capacity.

$$P_B \geq P_{\text{load}} + P_{\text{loss}} \quad (1)$$

$$Q_B \geq Q_{\text{load}} + Q_{\text{loss}} \quad (2)$$

Here  $P_B$  and  $Q_B$  are active and reactive power of black-start unit,  $P_{\text{load}}$  and  $Q_{\text{load}}$  are active and reactive power of load, and  $P_{\text{loss}}$  and  $Q_{\text{loss}}$  are active and reactive power of losses of the system.

### 3.4 Load Priority

During the process of disaster restoration, the important loads are restored as per priority basis. Load priority is given by

$$f_1 = \max \sum_{i \in V_z} P_i \quad (3)$$

where  $P_i$  is the priority of the restored load, connected at  $i$ th bus.  $V_z$  is the set of restored bus in a subsystem,  $Z$ . Load priority depends upon the available paths, and higher weight age is given to the important load bus within the restorative path. The proposed algorithm is applied to IEEE 14 Bus network.

## 4 Floyd–Warshall Algorithm

This algorithm computes all the pair's shortest path from all vertices in a weighted graph. In a weighted graph, every edge has some weights. On traversing from a node to another, the total weight will be the sum of all weights of the edge in the route. Shortest path algorithm will compute the path with the minimum weight.

A weighted graph  $G$  of  $v$  vertices is described by a  $n \times n$  matrix  $D = [d_{ij}]$ , where

$d_{ij}$  = length (or distance or weight) of the directed edge and from the vertex  $i$  to vertex  $j$ , and

$d_{ij} \geq 0$ , when there is an edge between  $i$  and  $j$  vertices

$d_{ii} = 0$ , loop edge within the same vertex

$d_{ij} = \infty$ , if there is no edge between  $i$  and  $j$ .

#### 4.1 Pseudocode for Floyd–Warshall Algorithm

This pseudocode assumes an input graph of  $v$  vertices [11].

```

for i = 1 to v
for j = 1 to v
Where one edge between i to j
 $d_{ij}$  = the weight of the edge from i to j
else
 $d_{ij}$  = infinity
for k = 1 to N
for i = 1 to N
for j = 1 to N
 $d_{ij}^k = \min(d_{ij}^{k-1}, d_{ik}^{k-1} + d_{kj}^{k-1})$ 

```

The output of this program will be the shortest distance between any two vertices (or nodes) and from the predecessor matrix; the shortest path among any two vertices (or nodes) can be constructed.

Algorithm for extracting shortest path:

```

path(i, j) = path from vertex i to vertex j
pred[i, j] = predecessor matrix
path(i, j)
if(pred[i, j] == nil)
output (i, j)
else
path(i, pred[i, j])
path(pred[i, j], j)

```

#### 4.2 Implementation of Floyd–Warshall Algorithm in Power System Restoration

The program for the proposed technique has been developed in MATLAB environment in such a way that the distance between any generator to load with highest priorities should make individual cluster. If distance is less between generation source

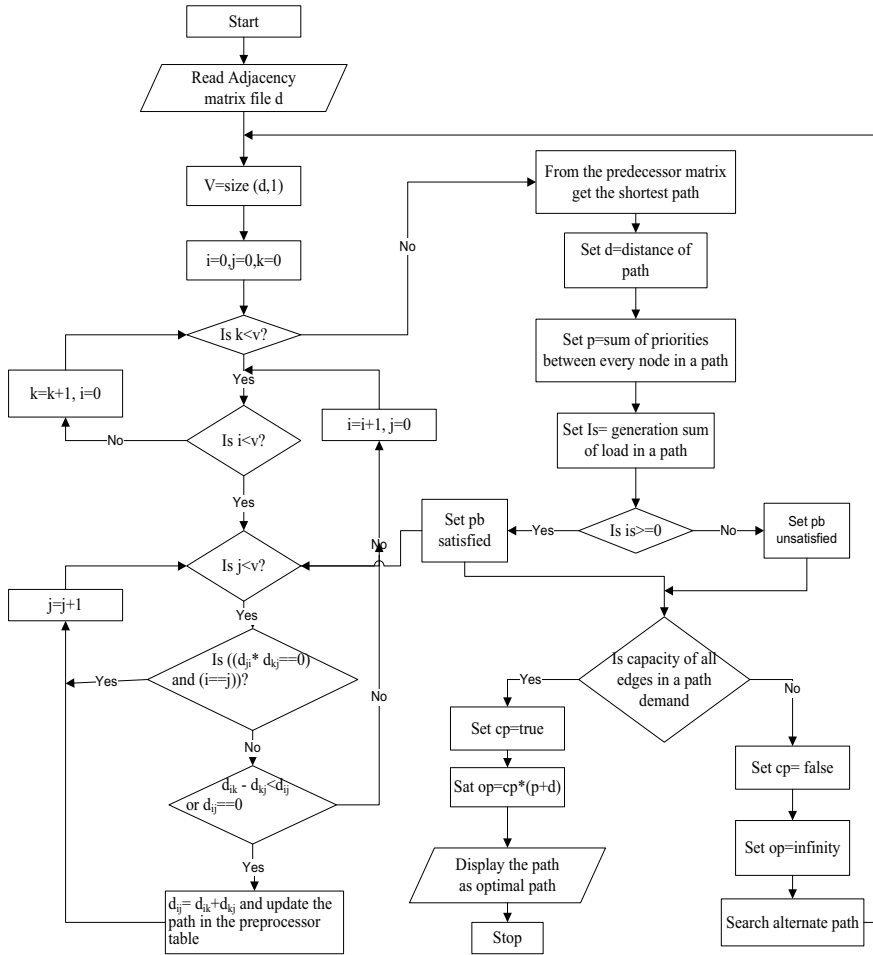


Fig. 1 Flowchart for identification of optimal path [11]

and load, then power losses and voltage drop will be less. The main objective of the present work is to find different cluster which consist of at least one black start and with loads of highest priorities subject to active and reactive power balancing between black-start unit and loads in the cluster (Fig. 1).

### 5 Results and Discussion

To see the effectiveness of the proposed algorithm, load priority-based Floyd–Warshall algorithm has been applied to a modified IEEE 14 bus network as shown in

Fig. 2. Line data and load data with priority have been given in Tables 1 and 2, respectively. In the modified IEEE 14 bus network, four black starts have been connected at bus numbers 1, 3, 8, and 13, respectively. The generation capacity of the black start is given in Table 3.

Adjacency matrix obtained from the impedance data of the test system is shown in Table 4.

The impedance of the line is considered as the weight of adjacency matrix. With the help of Floyd–Warshall algorithm, distance matrix has been found in Table 5. After a blackout immediately has to restore the important load as per priority order but each black-start unit, having own limitation of power capacity. Hence, the entire network has to be divided into different number of clusters and each black start will provide power to nearer loads. During clustering, two important conditions such as finding the nearer loads and the power balance equation as cited in equations (i) and (ii) have been maintained.

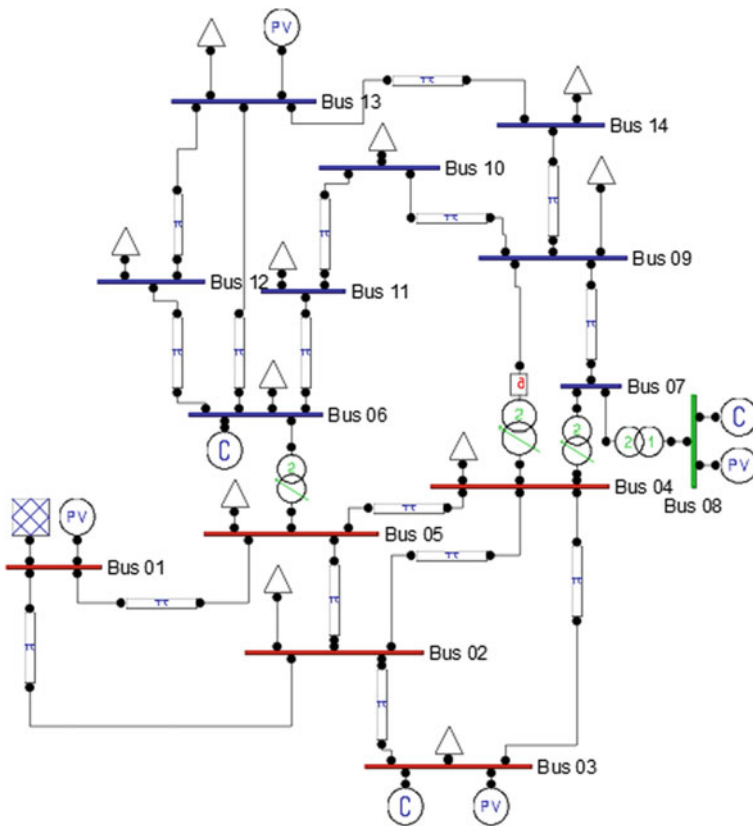


Fig. 2 IEEE 14 bus system

**Table 1** Line data for modified IEEE 14 bus systems

From bus	To bus	Active power (p.u.)	Reactive power (p.u.)
1	2	0.01938	0.01838
1	5	0.05403	0.04953
2	3	0.04699	0.04461
2	4	0.05811	0.05069
2	5	0.05695	0.05469
3	4	0.06701	0.06523
4	5	0.01335	0.00921
4	7	0.22412	0.20912
4	9	0.57896	0.55618
5	6	0.28236	0.25202
6	11	0.09498	0.09235
6	12	0.12291	0.10234
6	13	0.06615	0.04613
7	8	0.19658	0.17615
7	9	0.14569	0.11001
9	10	0.03181	0.0245
9	14	0.12711	0.10038
10	11	0.08205	0.05207
12	13	0.22092	0.19988
13	14	0.17093	0.12802

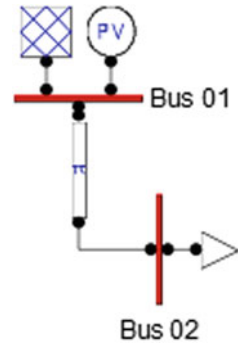
**Table 2** Load details with priority load

Bus No.	Active power [MW]	Reactive power [MVar]	Priority of load
2	2.17	12.7	0.57
3	9.42	19	0.17
4	4.78	-3.9	0.55
5	7.6	1.6	0.54
6	1.12	7.5	0.56
9	2.95	16.6	0.47
10	9	5.8	0.45
11	3.5	1.8	0.43
12	6.1	1.6	0.34
13	1.35	5.8	0.14
14	1.49	5	0.18

**Table 3** Black-start details

Bus No.	Black-start unit	MW capacity
1	B <sub>1</sub>	3
3	B <sub>2</sub>	23
8	B <sub>3</sub>	12
13	B <sub>4</sub>	11

**Fig. 3** Cluster with black-start unit 1



This equation will be satisfied following the load priority. Thus, there is a need to find the shortest path finding algorithm. In the present study, the distance matrix as shown in Table 5 has been utilized to find the distance between any black start and load. For any element,  $a_{ij}$  in the matrix indicates the distance between  $i$  and  $j$  buses. In our test case, the load connectivity has been shown in Table 2.

For an example, if we want to find the connectivity of a load which is connected at bus number 4, then we have to search the lowest distance mapping between row (black start) number, i.e.,  $i = 1, 3, 8, 13$  and column (load),  $j = 4$ . Now,  $a_{14} = 0.2478$ ,  $a_{34} = 0.18360$ ,  $a_{84} = 0.38527$ ,  $a_{134} = 0.39812$ . Among all mapping data,  $a_{34} = 0.18360$  is the lowest possible mapping between load 4 and other black-start unit. Hence, load 4 will connect with black start 3. Similarly, the other loads will be connected as per the result as shown in Table 6. The cluster comprises one black start and the load is obtained from the same table.

To validate the algorithm, steady-state load flow analysis has been performed for each of the clustered systems. For cluster 1, one black-start unit connected on the bus no 1 and supply highest priority load which is connected on bus no 2 as shown in Fig. 3.

For Cluster 2, another black-start unit is connected on bus no 3 for disaster relief and supply highest priority load which is connected on buses no 4, 5, and 3 as shown in Fig. 4.

For Cluster 3, black start is connected on bus no 8 and supply highest priority load which is connected on load buses no 9, 10, and 11. Bus no 7 is not a load bus; it only provided as a shortest path as shown in Fig. 5.



**Table 4** Adjacency matrix for IEEE 14 bus system

Node	1	2	3	4	5	6	7	8	9	10	11	12	13	14
1	0	0.0622	0	0	0.2294	0	0	0	0	0	0	0	0	0
2	0.0622	0	0.2034	0.1856	0.1829	0	0	0	0	0	0	0	0	0
3	0	0.2034	0	0.1836	0	0	0	0	0	0	0	0	0	0
4	0	0.1856	0.1836	0	0.04417	0	0.20912	0	0.5562	0	0	0	0	0
5	0.2294	0.1829	0	0.04417	0	0.25202	0	0	0	0	0	0	0	0
6	0	0	0	0	0.25202	0	0	0	0	0	0.2204	0.2838	0.1461	0
7	0	0	0	0.20912	0	0	0	0.17615	0.11001	0	0	0	0	0
8	0	0	0	0	0	0	0.17615	0	0	0	0	0	0	0
9	0	0	0	0.5562	0	0	0.11001	0	0	0.09028	0	0	0	0.2987
10	0	0	0	0	0	0	0	0	0.09028	0	0.2088	0	0	0
11	0	0	0	0	0	0.2204	0	0	0	0.2088	0	0	0	0
12	0	0	0	0	0	0.2838	0	0	0	0	0	0	0.2979	0
13	0	0	0	0	0	0.1461	0	0	0	0	0	0.2979	0	0.3877
14	0	0	0	0	0	0	0	0	0.2987	0	0	0	0.3877	0

**Table 5** Distance matrix after final interfacing of IEEE 14 bus system

Node	1	2	3	4	5	6	7	8	9	10	11	12	13	14
1	0	0.0622	0.2656	0.2478	0.2294	0.48142	0.45692	0.63307	0.56693	0.65721	0.70182	0.76522	0.62752	0.86563
2	0.0622	0	0.2034	0.1856	0.1829	0.43492	0.39472	0.57087	0.50473	0.59501	0.65532	0.71872	0.58102	0.80343
3	0.26560	0.20340	0	0.18360	0.22777	0.47979	0.39272	0.56887	0.50273	0.59301	0.70019	0.76359	0.62589	0.80143
4	0.24780	0.18560	0.18360	0	0.04417	0.29619	0.20912	0.38527	0.31913	0.40941	0.51659	0.57999	0.44229	0.61783
5	0.22940	0.18290	0.22777	0.04417	0	0.25202	0.25329	0.42944	0.36330	0.45358	0.47242	0.53582	0.39812	0.66200
6	0.48142	0.43492	0.47979	0.29619	0.25202	0	0.50531	0.68146	0.51948	0.42920	0.22040	0.28380	0.14610	0.53380
7	0.45692	0.39472	0.39272	0.20912	0.25329	0.50531	0	0.17615	0.11001	0.20029	0.40909	0.78911	0.65141	0.40871
8	0.63307	0.57087	0.56887	0.38527	0.42944	0.68146	0.17615	0	0.28616	0	0.58524	0.96526	0.82756	0.58486
9	0.56693	0.50473	0.50273	0.31913	0.36330	0	0	0.28616	0	0.09028	0.29908	0.80328	0.66558	0.29870
10	0.65721	0.59501	0.59301	0.40941	0.45358	0.42920	0.20029	0.37644	0.09028	0	0.20880	0.71300	0.57530	0.38898
11	0.70182	0.65532	0.70019	0.51659	0.47242	0.22040	0.40909	0.58524	0.29908	0.20880	0	0.50420	0.3665	0.59778
12	0.76522	0.71872	0.76359	0.57999	0.53582	0.28380	0.78911	0.96526	0.80328	0.71300	0.50420	0	0.29790	0.68560
13	0.62752	0.58102	0.62589	0.44229	0.39812	0.14610	0.65141	0.82756	0.66558	0.57530	0.36650	0.29790	0	0.38770
14	0.86563	0.80343	0.80143	0.61783	0.66200	0.53380	0.40871	0.58486	0.29870	0.38898	0.59778	0.68560	0.38770	0

**Table 6** Cluster data

Black-start unit	Black-start position	Nearest load
1	Bus 1	2
2	Bus 3	4, 5, 3
3	Bus 8	9, 10
4	Bus 13	6, 12, 13, 14

**Fig. 4** Cluster with black-start unit 2

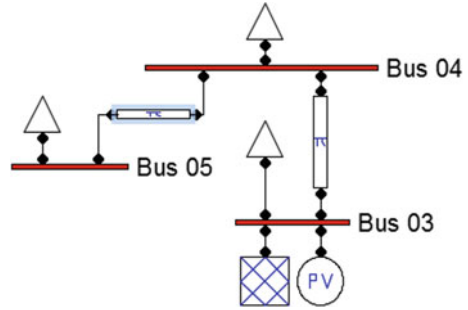


**Fig. 5** Cluster with black-start unit 3

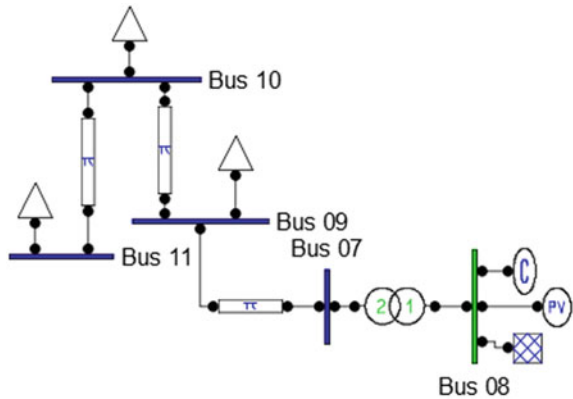


**Fig. 6** Cluster with black-start unit 4

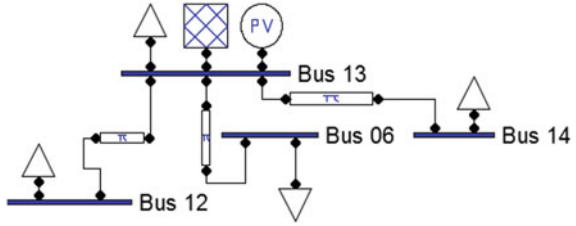


**Table 7** Voltage at different buses overall power losses after clustering with black-start unit 1

S. No.	Bus No.	Voltage magnitude (p.u.)	Overall power losses (p.u.)	
			Active (MW)	Reactive (MVar)
1	Bus 1	1	0.00092	-0.01798
2	Bus 2	0.98476		

**Table 8** Voltage at different buses overall power losses after clustering with black-start unit 2

S. No.	Bus No.	Voltage magnitude (p.u.)	Overall power losses (p.u.)	
			Active (MW)	Reactive (MVar)
1	Bus 3	1.06	0.01283	0.0176
2	Bus 4	0.99095		
3	Bus 5	0.98882		

**Table 9** Voltage at different buses overall power losses after clustering with black-start unit 3

S. No.	Bus No.	Voltage magnitude	Overall power losses (p.u.)	
			Active (MW)	Reactive (MVar)
1	Bus 7	0.98271	0.00047	0.03895
2	Bus 8	1.06		
3	Bus 9	0.94006		
4	Bus 10	0.92416		
5	Bus 11	0.91443		

For Cluster 4, black start is connected on bus no 13 and supply highest priority load which is connected on buses no 6, 12, 13, and 14 as shown in Fig. 6.

The load flow for each of the cluster has been shown in Tables 7, 8, 9, and 10. The voltage magnitude for each of the bus is under acceptable limit and losses also tolerable.

**Table 10** Voltage (p.u.) at different buses overall power losses after clustering with black-start unit 4

S. No.	Bus No.	Voltage magnitude (p.u.)	Overall power losses (p.u.)	
			Active (MW)	Reactive (MVar)
1	Bus 6	0.97524	0.12875	0.26163
2	Bus 12	0.97601		
3	Bus 13	1		
4	Bus 14	0.32533		

## 6 Conclusion

This paper investigates various types of shortest path distance and clustering scheme for service restoration based on Floyd–Warshall algorithm. The proposed algorithm implemented on IEEE 14 bus system for recovering loads finally investigates the optimal cluster or different subsystem for practical implementation. A novel approach for suitable location of cranking units for supply disaster recovery planning implementing the proposed algorithm presented here. Present strategy avail to prove the minimum amount of minimum number of switching operation and active and reactive power loss when black-start units are connected in different clusters.

## References

1. M.M. Adibi, Power system restoration—a task force report. *IEEE Trans. Power Syst.* **2**(2), 271–277 (1987)
2. M.M. Adibi, in *Power System Restoration Methodologies & Implementation Strategies*. IEEE Press Power Engineering Series (2000)
3. A. Bretas, A. Phadke, Power system restoration methodologies & implementation strategies, book review. *IEEE Comput. Appl. Power* **14**, 58–59 (2001)
4. K. Matsumoto, T. Sakaguchi, R. Kafka, M.M. Adibi, Knowledge-based systems as operational aids in power system restoration. *Proc. IEEE* **80**(5), 689–697 (1992)
5. J.S. Wu, C.C. Liu, K.L. Liou, R.F. Chu, A petri net algorithm for scheduling of generic restoration actions. *IEEE Trans. Power Syst.* **12**(1), 69–76 (1997)
6. T.D. Sudhakar, N.S. Vadivoo, S.M.R. Slochanal, S. Ravichandran, Supply restoration in distribution networks using Dijkstra’s algorithm, in *2004 IEEE International Conference on Power System Technology, PowerCon 2004*, vol. 1, pp. 640–645 (2004)
7. T.D. Sudhakar, K.N. Srinivas, Power system reconfiguration based on Prim’s algorithm, in *IEEE 1st International Conference on Electrical Energy Systems (ICEES)*, pp. 12–20 (2011)
8. S. Hemalatha, P. Valsalal, Identification of optimal path in power system network using Bellman Ford algorithm. *Model. Simul. Eng.* **28** (2012)
9. T. Sakaguchi, K. Matsumoto, Development of a knowledge-based system for power system restoration. *IEEE Trans. Power Apparatus Syst.* (2), 320–329 (1983)

10. T. Nagata, H. Sasaki, M. Kitagawa, Power system restoration by joint usage of expert system and mathematical programming approach. *Electr Eng. Jpn.* **117**(2), 41–54 (1996)
11. S. Hemalatha, P. Valsalal, Restorative path selection for power system network using Floyd Warshall algorithm. *ARPN J. Eng. Appl. Sci.* **7**(4), 472–477 (2012)

# Fault Detection During Power Swing Using Fast Discrete $S$ -transform



Arkadeep Mondal, Sayan Das and Bikash Patel

**Abstract** This paper presents a method for detection of fault during power swing on the transmission line using fast discrete  $S$ -transform (FDST). The energy of FDST coefficients is calculated in one-cycle moving window for each of the three-phase current signals. This FDST energy is considered as fault detection index. A 400 kV 9-bus IEEE system is simulated in EMTP, and three-phase fault currents are recorded at one end of the transmission line to find the fault detection index. In this paper, various kinds of faults are diagnosed quickly and accurately for different locations, fault resistances with various fault inception times. It will be shown that the fault detection delay is less than a cycle in both noisy and noise-free condition.

**Keywords** Fault detection · Power swing · Fast discrete  $S$ -transform (FDST) · Transmission lines

## 1 Introduction

Power swing is a phenomenon which occurs in the power system due to any abrupt changes in the system like disconnection of lines, large loads and alternators. Due to oscillation of voltage and current during power swing, the impedance seen by the distance relay changes. This may lead to unwanted tripping of the relay. Hence, it must be blocked during power swing. But when a fault occurs during power swing, this blocking has to be removed immediately to trip the relay.

---

A. Mondal (✉) · S. Das · B. Patel  
Electrical Engineering Department, Kalyani Government Engineering College, Kalyani,  
West Bengal, India  
e-mail: [arkadeep.ee@gmail.com](mailto:arkadeep.ee@gmail.com)

S. Das  
e-mail: [sayandas2011@gmail.com](mailto:sayandas2011@gmail.com)

B. Patel  
e-mail: [biks.ee@gmail.com](mailto:biks.ee@gmail.com)

© Springer Nature Singapore Pte Ltd. 2020  
K. Maharatna et al. (eds.), *Computational Advancement in Communication Circuits and Systems*, Lecture Notes in Electrical Engineering 575,  
[https://doi.org/10.1007/978-981-13-8687-9\\_7](https://doi.org/10.1007/978-981-13-8687-9_7)

There are many methods for detection of fault during power swing. Wavelet transform (WT) plays an important role for the protection of power system [1, 2]. But WT cannot detect fault under noisy condition. The faults during power swing can also be detected by applying  $S$ -transform (ST). Article [3] uses ST to detect the stable and unstable swing for correct distance relay operation. The Prony [4] method detects the symmetrical faults from power swing very fast. This method was based on the calculation of the decaying DC components. In article [5], support vector machine is applied to distinguish faults from power swing to prevent the maloperation of distance relay. Fault during power swing is also detected by calculating the transient monitor index [6]. This method detects the fault during power swing when the transient monitor index exceeds the pre-calculated threshold value. Another method is based on the combination of  $S$ -transform and probabilistic neural network (PNN) [7]. Mathematical morphology-based method is proposed [8] for ultra-high-speed detection of fault during power swing condition on a series compensated transmission line. Using the current phasor information for forward travelling wave tends to provide good indices for the detection of fault during power swing. To distinguish faults from power swing, data-mining-based intelligent differential relay scheme is used in [9]. In [10], moving window averaging of current signal-based method is proposed for detection of faults and power swing. The article [11] presents a fault detection method during power swing using least-square curve-fitting technique.

The present article demonstrates a method for fault detection during power swing using FDST energy. This method is tested on a 9-bus IEEE system at different fault conditions. Its performance is also tested under noisy condition considering 20 dB signal-to-noise ratio. A comparative analysis with a conventional method is also carried out.

## 2 Fast Discrete Stockwell Transform (FDST) Energy

$S$ -transform represents a signal in time-frequency domain and suitable for non-stationary signal analysis. For a signal with frequency  $f$ , ST can be represented as

$$S(\tau, f) = \int_{-\infty}^{+\infty} h(t) \frac{|f|}{\sqrt{2\pi}} \exp\left(-\frac{(\tau - t)^2}{2f^2}\right) \exp(-i2\pi ft) dt \quad (1)$$

The discrete version of  $S$ -transform (DST) can be represented as

$$\begin{aligned} S[j, n] &= \sum_{m=0}^{N-1} H(m+n) \exp\left(-\frac{2\pi^2 m^2}{n^2}\right) \exp\left(\frac{i2\pi mj}{N}\right) \quad \text{for } n \neq 0 \\ &= \frac{1}{N} \sum_{m=0}^{N-1} h[k] \quad \text{for } n = 0 \end{aligned} \quad (2)$$

where  $H[.]$  is the discrete Fourier transform (DFT) of  $h[.]$ .

For a discrete signal of length  $N$ , DST has  $N^2$  number of coefficients and large computational complexity of  $O(N^3)$ . This computational complexity can be reduced by introducing FFT algorithm [12]. This is known as fast DST (FDST) where the computational complexity reduces to  $O(N \log N)$  and only  $N$  numbers coefficients are generated. These coefficients are localized in both the time and the frequency domains. Each FDST coefficient measures a specific feature of a signal. The energy of FDST coefficients is used for fault detection, which represent during power swing, and it is found as the sum of square of absolute values of the coefficients.

$$E = \sum_{k=1}^N |S|^2 \tag{3}$$

### 3 System Simulation and Fault Detection

In this paper, a 400 kV 9-bus IEEE system as shown in Fig.1 is used for detection of fault during power swing. The total length of the transmission line between bus 7 and bus 8 is 200 km. Three alternators are connected to the transmission system through three transformers. Total 1115 MW load is connected at three different buses. Power swing is created on the line 7-8 by disconnecting the line 5-7 at 0.2 s after a three-phase fault at the middle of the later line. During this power swing condition, faults are created at different locations on the transmission line 7-8 for different fault resistances ( $R_f$ ) and fault inception times (FIT). This system is simulated in EMTP, and fault current is recorded at bus 7 with a sampling frequency 1 kHz.

FDST energy (FDSTE) is calculated at each sample point for the previous one-cycle data from each of the three-phase current signals. During power swing condi-

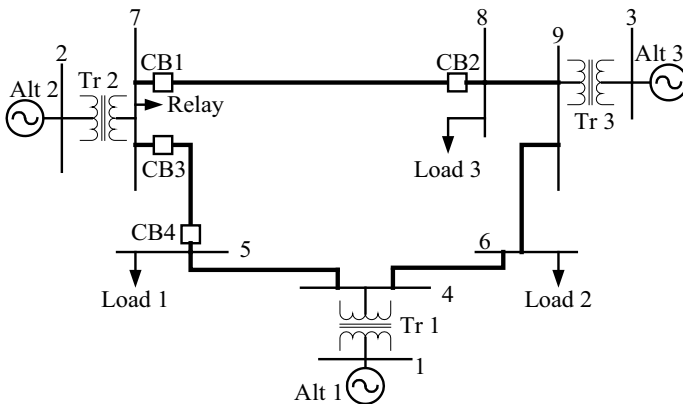
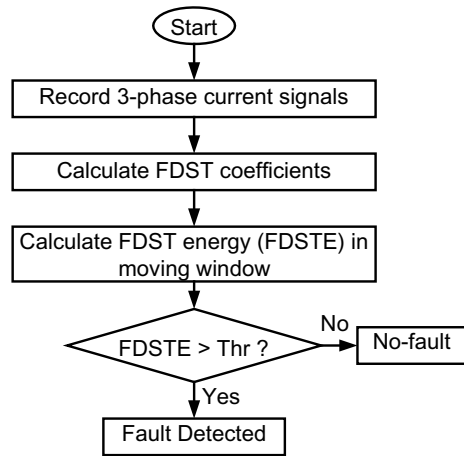


Fig. 1 Single-line diagram of IEEE 9 bus system



**Fig. 2** Flow chart for fault detection during power swing



tion, FDSTE remains below a threshold which is set based on the various simulations at different conditions. But FDSTE crosses the threshold with the inception of a fault, and the fault is detected at the instant when FDSTE exceeds its threshold for any of the three-phase currents. The flow chart of the fault detection method during power swing is shown in Fig. 2. The fault detection delay is calculated by taking the difference between the time instants of fault detection and that of the fault.

## 4 Result and analysis

During power swing condition, FDST energy oscillates within a threshold limit. But when a fault occurs during power swing, FDSTE suddenly rises. Based on a large number of simulation results, a threshold value of FDSTE is set at 50 to detect fault during power swing. For testing, a three-phase, short-circuit fault is simulated at 50 km from bus 7 with FIT 838.3 ms. Current and voltage signals and FDST energies for three phases are shown in Fig. 3 for this fault condition. From these figures, it is clear that after the inception of the fault, the FDSTE rises sharply for all three phases and it crosses the threshold with a time delay of 9 ms for phase B current signal.

The proposed method is tested for one symmetrical fault and three unsymmetrical faults at each fault condition. The faults are simulated at five locations on the transmission line for three fault resistances ( $R_f$ ) and three fault inception times (FIT) as shown in Table 1. The average of fault detection time delays of four types is calculated at each condition. The noise effect on the proposed method is also considered by impregnating 20 dB SNR white Gaussian noise to the fault current signals. The noisy signal does not affect the performance of the proposed method as the average delay is same for without noise condition and noisy condition for most of the cases as seen from Table 1. This is one of the important advantages of this method.

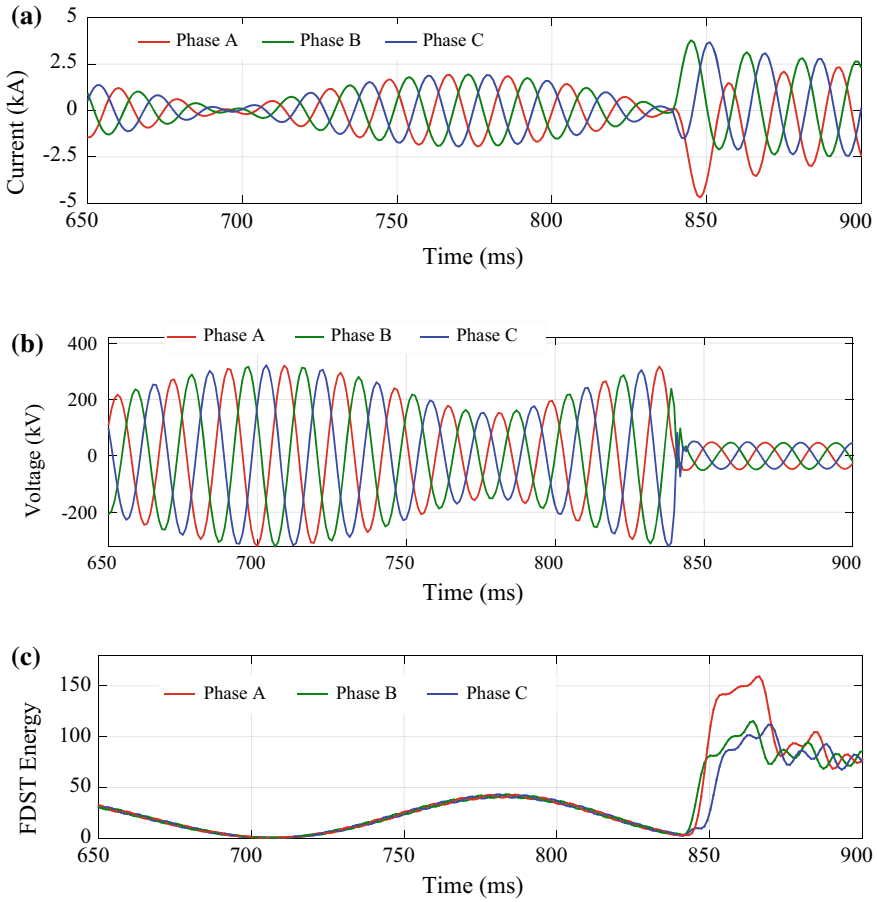


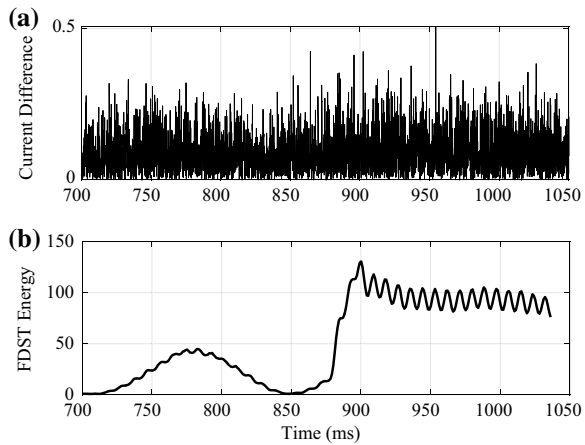
**Fig. 3** Three phases: **a** current signals, **b** voltage signals and **c** FDST energy for three-phase fault at 50 km with  $R_f = 0 \Omega$ , FIT = 838.3 ms

The performance of the method is compared with the conventional sample-to-sample comparison method. The sample-to-sample comparison method performs satisfactorily when there is no noise in the fault signals. But there will be noise in the real-time-recorded fault signals. Sample-to-sample comparison method is not reliable for relay application as it fails to detect fault under noisy condition. The difference of current between two successive samples and FDST energy is shown in Fig. 4 for a three-phase fault at 5 km from bus 7 with FIT 876.2 ms. From this figure, it is clearly observed that the proposed method detects the fault within 6 ms, but the sample-to-sample comparison method is unable to distinguish the fault from power swing under noisy condition as no significant change is observed in the difference of current between two successive samples at fault condition.

**Table 1** Fault detection results at different conditions

Fault location (km)	Fault resistance ( $\Omega$ )	FIT (ms)	Average delay (ms)	
			Without noise	With noise
5	0	838.3	8.25	8.25
5	5	876.2	6.25	6.25
5	20	909.5	6.5	6
50	0	838.3	9.25	9.25
50	5	876.2	7.25	7.25
50	20	909.5	7	6.75
100	0	838.3	10.25	10
100	5	876.2	7.75	8
100	20	909.5	7.75	7.5
150	0	838.3	11.5	11.75
150	5	876.2	8.5	8.5
150	20	909.5	14.25	10
195	0	838.3	14	14
195	5	876.2	9	9.25
195	20	909.5	13	10.25

**Fig. 4** **a** Current difference for sample-to-sample comparison method and **b** FDST energy for proposed method for three-phase fault at 5 km with  $R_f = 5 \Omega$ , FIT = 876.2 ms



## 5 Conclusion

The article presents a method for detection of fault during power swing on the transmission line using fast discrete  $S$ -transform (FDST). A 400 kV 9-bus IEEE system is simulated in EMTP, and three-phase fault currents are recorded. The energy of FDST coefficients is calculated in one-cycle moving window for each of these current signals. This FDST energy is considered as fault detection index. The proposed

method is tested for different types of faults, fault resistances and fault inception times at different locations on the transmission line and detects the faults accurately within one cycle. Another advantage of this method is that it can detect faults for noise-impregnated signal up to a noise level of 20 dB SNR. A relay compatible sampling frequency of 1 kHz is used in this article. This is useful for implementation in digital relays.

## Reference

1. R. Dubey, S.R. Samantaray, Wavelet singular entropy-based symmetrical fault-detection and out-of-step protection during power swing. *IET Gener. Transm. Distrib.* (2013)
2. C. Pang, M. Kezunovic, Fast distance relay scheme for detecting symmetrical fault during power swing. *IEEE Trans. Power Del.* **25**(4) (2010)
3. N.Z. Mohamad, A.F. Abidin, I. Musirin, Intelligent power swing detection scheme to prevent false relay tripping using S-Transform. *Int. J. Emerg. Electr. Power Syst.* (2014)
4. S. Lotfifard, J. Faiz, M. Kezunovic, Detection of symmetrical faults by distance relays during power swings. *IEEE Trans. Power del.* **25**(1) (2010)
5. K. Seethalekshmi, S.N. Singh, S.C. Srivastava, A classification approach using support vector machines to prevent distance relay maloperation under power swing and voltage instability. *IEEE Trans. Power del.* **27**(3) (2012)
6. J. Khodaparast, M. Khederzadeh, Three-phase fault detection during power swing by transient monitor. *IEEE Trans. Power. Syst.* **30**(5) (2015)
7. Z. Moravej, J.D. Ashkezari, M. Pazoki, An effective combined method for symmetrical faults identification during power swing. *I. J. Electr. Power Energy Syst.* (2014)
8. M. Daryalal, M. Sarlak, Fast fault detection scheme for series-compensated lines during power swing. *I. J. Electr. Power Energy Syst.* (2017)
9. R. Dubey, S.R. Samantaray, B.K. Panigrahi, V.G. Venkoparao, Data-mining model based adaptive protection scheme to enhance distance relay performance during power swing. *I. J. Electr. Power Energy Syst.* (2016)
10. J.G. Rao, A.K. Pradhan, Power-swing detection using moving window averaging of current signals. *IEEE Trans. Power Del.* **30**(1) (2015)
11. A.P. Morais, G.C. Júnior, L. Mariotto, G. Marchesan, A morphological filtering algorithm for fault detection in transmission lines during power swings. *I. J. Electr. Power Energy Syst.* (2015)
12. Y. Wang, J. Orchard, Fast discrete orthonormal stockwell transform. *Soc. Ind. Appl. Maths.* (2009)

# Detection and Classification of Faults on the Transmission Line Using Lissajous Figure



Sayan Das, Arkadeep Mondal and Bikash Patel

**Abstract** This paper represents a method to detect and classify faults on the transmission line using Lissajous pattern of voltage and current signals. Three-phase fault voltage and current signals are recorded at one end of the transmission line, and the Lissajous figure is obtained for each phase. The area of the Lissajous figures is calculated at each point for its previous cycle. By calculating the change in this area, indices for fault detection and classification are obtained. The method is tested on a hybrid transmission line consisting of an overhead line and four underground cable sections for different fault conditions and found fast and accurate to detect and classify faults. Electromagnetic transient program (EMTP) and MATLAB software are used for power system simulation and computation, respectively.

**Keywords** Lissajous pattern · Transmission line · Fault detection · Fault classification

## 1 Introduction

Fault detection and classification on the transmission lines are important tasks for the safeguard of electric power systems. There are several techniques in the literature for fault detection and classification on the transmission line. Different techniques based on wavelet transform (WT) [1–4] and Park's vector approach [5] are applied to extract the transient energy from the fault signals to detect and classify different types of shunt faults on the transmission line or micro grids [4]. The detection and localization

---

S. Das (✉) · A. Mondal · B. Patel

Electrical Engineering Department, Kalyani Government Engineering College, Kalyani, West Bengal, India

e-mail: [sayandas2011@gmail.com](mailto:sayandas2011@gmail.com)

A. Mondal

e-mail: [arkadeep.ee@gmail.com](mailto:arkadeep.ee@gmail.com)

B. Patel

e-mail: [biks.ee@gmail.com](mailto:biks.ee@gmail.com)

© Springer Nature Singapore Pte Ltd. 2020

K. Maharatna et al. (eds.), *Computational Advancement in Communication Circuits and Systems*, Lecture Notes in Electrical Engineering 575, [https://doi.org/10.1007/978-981-13-8687-9\\_8](https://doi.org/10.1007/978-981-13-8687-9_8)

of high impedance, permanent single-phase earth faults in the medium-voltage (MV) distribution networks (20 kV) are proposed in [6, 7]. The drawback of the method is that the normal system activity and intermittent disturbances may cause changes to the neutral voltage and residual currents similar to the real faults in the feeders. Extension of sequential decision method [8] which is probabilistic approach is also used for fault detection and classification. A technique based on S transform (ST) and Hilbert transforms (HTs) is used to detect faults on the transmission line [9]. To detect fault in STATCOM connected transmission networks, a fault detection technique is proposed based on estimated reactive power factor (ERF) and differential current [10]. The article [11] proposes a fault detection and localization method in a micro-grid using mathematical morphology (MM) and recursive least square (RLS) method. There is another technique for fault detection and localization on the transmission lines using only voltage measurements obtained from wide area measurement systems (WAMS) [12] and the network bus admittance matrix based on change in injected current at various buses following the line fault.

This paper presents a new approach for fault detection and classification on transmission lines using Lissajous patterns on a multi-terminal hybrid transmission line. The proposed fault detection method is tested for different resistances, fault inception angles at different locations on the transmission line.

## 2 Lissajous Figure and Fault Detection

Lissajous figure is a pattern which shows a sinusoidal signal as a function of another sinusoidal signal. Instantaneous voltage and current signals of a power system are represented as Eqs. (1) and (2).

$$v = V_m \sin(\omega t) \quad (1)$$

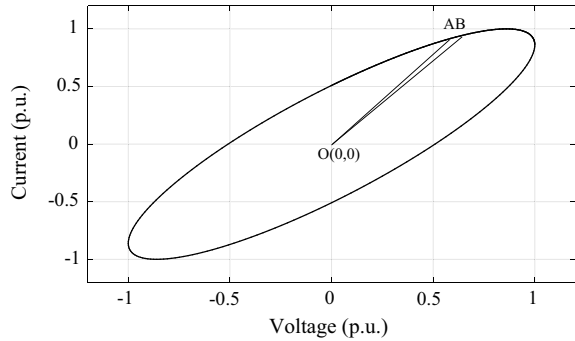
$$i = I_m \sin(\omega t + \delta) \quad (2)$$

where  $v$ ,  $i$  are instantaneous values and  $V_m$ ,  $I_m$  are the maximum values of voltage and current signals,  $\omega$  is frequency, and  $\delta$  is the phase difference between voltage and current signal. Now, replacing Eq. (1) in Eq. (2), we have

$$\begin{aligned} \frac{i}{I_m} &= \sin \omega t \cos \delta + \cos \omega t \sin \delta \\ \text{or, } \frac{i}{I_m} &= \frac{v}{V_m} \cos \delta + \sqrt{1 - \frac{v^2}{V_m^2}} \sin \delta \\ \text{or, } \frac{i}{I_m} - \frac{v}{V_m} \cos \delta &= \sqrt{1 - \frac{v^2}{V_m^2}} \sin \delta \end{aligned} \quad (3)$$

Squaring and rearranging both sides,

**Fig. 1** Area calculation of Lissajous figure



$$\frac{i^2}{I_m^2} + \frac{v^2}{V_m^2} - \frac{2iv}{I_m V_m} \cos \delta = \sin^2 \delta \tag{4}$$

This equation represents an ellipse inclined to the axes of the coordinates. Thus resulting variations of the two sinusoidal signals will be in general elliptical in nature. Depending on the value  $\delta$ , the resultant figure can be either straight line, or circle or ellipse or other complex figure. The shape of the curve also depends on the time period, ratio of the frequency and amplitude of the two constituent signals.

Once we get the Lissajous figure for a given signal, the area of the Lissajous figure is calculated at each point for its previous cycle. If A and B are two adjacent points on the Lissajous figure and O is the origin, then a triangle  $\Delta ABO$  is formed as shown in Fig. 1. The entire Lissajous figure is comprised of a number of such small triangles. The number of triangles in a Lissajous figure loop depends on the number of sample in one cycle. For  $N$  number of samples in a cycle, there will be  $(N - 1)$  number of small triangles. The area of the Lissajous figure can be calculated by summing the area of all these small triangles. A fault detection index ( $D\_Index$ ) is derived at each point by calculating the percentage of change of the area of Lissajous figure from its one cycle earlier value. A fault detection threshold ( $D_{th}$ ) is a set based on the simulation results. During normal condition, fault detection index remains nearly equal to zero. But with the inception of a fault, the index rises sharply and the fault is detected. In the present study, to detect the fault, the threshold  $D_{th}$  is set at 20%.

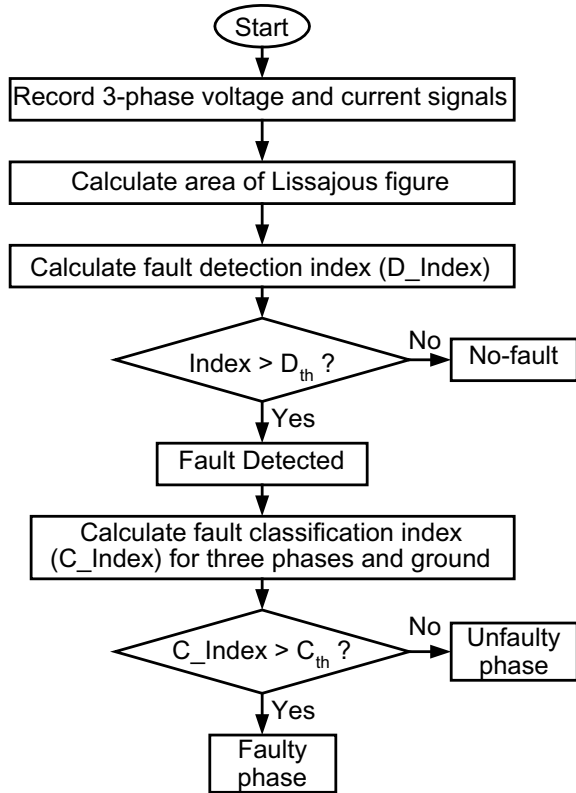
For classification purpose, the area of the Lissajous figure for half-cycle duration after detection of the fault is calculated for each phase and ground where ground voltage ( $V_g$ ) and ground current ( $I_g$ ) are calculated according to (5) and (6).

$$V_g = V_a + V_b + V_c \tag{5}$$

$$I_g = I_a + I_b + I_c \tag{6}$$

where  $V_a, V_b, V_c$  and  $I_a, I_b, I_c$  are the instantaneous value of voltage and current for three phases. These areas for three phases ( $A_a, A_b,$  and  $A_c$ ) and ground ( $A_g$ ) are converted to per unit value by dividing each area by the maximum value among  $A_a,$

**Fig. 2** Flowchart of the proposed method



$A_b$ , and  $A_c$  to obtain the fault classification index ( $C\_Index$ ). These per unit values denoted as  $F_a$ ,  $F_b$ ,  $F_c$ , and  $F_g$  are considered as fault classification indices for three phases and ground, respectively. For the present study, a threshold ( $C_{th}$ ) of  $C\_Index$  is set at 0.45. If  $C\_Index$  exceeds the threshold for a particular phase, then that phase is detected as the faulty phase. The flowchart of the proposed method is shown in Fig. 2.

### 3 System Simulations

In this paper, a 400 kV multi-terminal hybrid line as shown in Fig. 3 is used for detection and classification of fault. Two alternators are connected to the transmission line through two transformers. The total length of the transmission line between bus B1 and B2 is 150 km consisting of one overhead section and four underground sections. Length of the overhead section is 110 km, and its characteristic impedance is 298.208  $\Omega$ . Lengths of 4 underground sections are 10 km each with characteristic



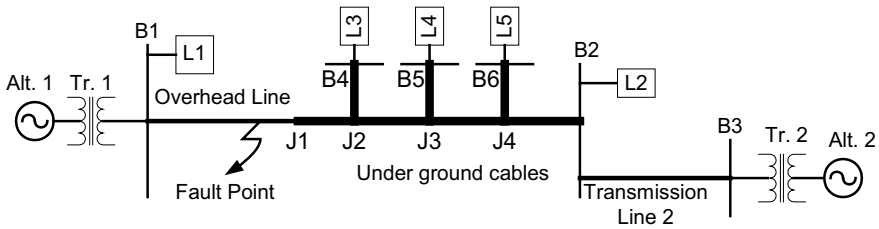


**Fig. 3** Single-line diagram of a multi-terminal hybrid transmission line

impedances 48.795, 50, 47.559, and 51.176  $\Omega$ , respectively. A total load of 1100 MW is connected at four different terminals. During normal condition, faults are created at different locations ( $L_f$ ) on the transmission line for different fault resistances ( $R_f$ ) and fault inception angles (FIA). The system is simulated in EMTP, and voltage and current signals are recorded at bus B1 with a sampling frequency 10 kHz.

### 4 Results and Analysis

During normal condition, fault detection index ( $D\_Index$ ) remains nearly equal to zero. But when fault occurs, the index rises sharply. Based on the simulation of faults at different conditions, the fault detection threshold ( $D_{th}$ ) value is set at 20% and classification index ( $C_{th}$ ) is set at 0.45. For testing, a three-phase fault has been triggered at 70 km from B1 on the transmission line with fault inception angle (FIA)  $90^\circ$  and fault resistance 20  $\Omega$ . Waveforms of voltage and current signals and fault detection index ( $D\_Index$ ) are shown in Fig. 4 for this fault condition. From these figures, it is clear that after the inception of the fault, the  $D\_Index$  rises sharply for all three phases and it crosses the threshold with a time delay of 0.8 ms for phase A.

The proposed method is tested for ten types of faults as shown in Table 1 where  $a$ ,  $b$ ,  $c$ , and  $g$  represent three phases and ground, respectively. The faults are simulated at five locations (1, 70, 115, 133, and 149 km) on the transmission line for two fault resistances ( $R_f$ ) and three fault inception angles (FIA) as shown in Table 1. The proposed method detects the faults accurately with the maximum fault detection time delay of 4.1 ms. The faulty phase is also accurately identified as the values of  $F_a$ ,  $F_b$ ,  $F_c$ , and  $F_g$  are found above the threshold of 0.45 as shown in the last four columns of Table 1.

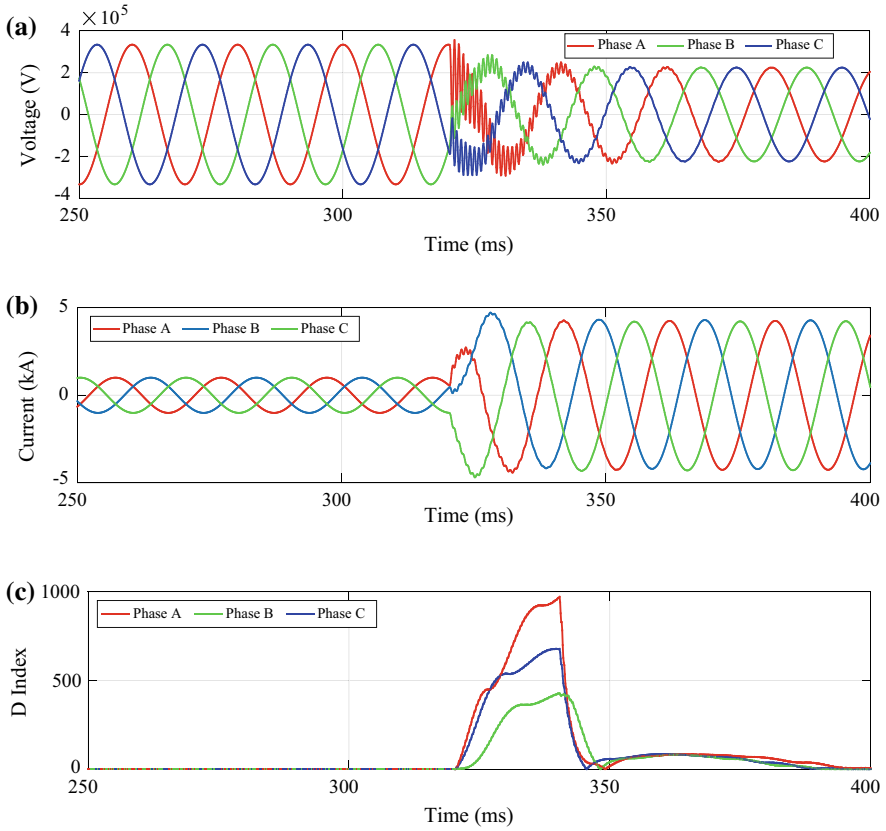


**Fig. 4** **a** Voltage signals, **b** current signals, **c** fault detection index for a three-phase fault at 70 km with fault resistance 20  $\Omega$ , FIA 90°

## 5 Conclusions

This paper demonstrates a method for detection and classification of faults on the hybrid transmission line consisting of an overhead line and four underground cable sections using Lissajous pattern of voltage and current signals. A 400 kV multi-terminal hybrid transmission line is simulated in EMTP, and three-phase fault voltage and current signals are recorded at one end of the transmission line. The area of the Lissajous figure is calculated at each point for its previous cycle using the voltage and current signals. Indices for fault detection and classification are developed by calculating the change in the area of Lissajous figure for each phase. The proposed method detects and classifies the faults on the transmission line at different conditions. This method is fast and accurate for detection of symmetrical and unsymmetrical faults at different locations on the transmission line for different fault resistances and fault inception angles.

**Table 1** Fault detection and classification results at different conditions

Fault type	$L_f$ (km)	$R_f$ ( $\Omega$ )	FIA ( $^\circ$ )	Delay (ms)	Classification features			
					$F_a$	$F_b$	$F_c$	$F_g$
<i>ab</i>	1	10	45	0.5	1.00	0.79	0	0
<i>ac</i>	1	10	45	1.9	0.87	0	1.00	0
<i>bc</i>	1	10	45	4.1	0	1.00	0.86	0
<i>ag</i>	1	10	45	0.5	1.00	0.29	0.05	4.65
<i>acg</i>	1	20	90	0.6	1.00	0.38	0.95	4.60
<i>bc</i>	70	10	0	0.7	0	1.00	0.72	0
<i>abc</i>	70	20	90	0.8	1.00	0.50	0.81	0
<i>abg</i>	70	20	90	0.8	1.00	0.87	0.03	0.92
<i>ag</i>	70	20	90	0.9	1.00	0.20	0.18	2.52
<i>bg</i>	70	20	90	4	0.03	1.00	0.12	2.24
<i>cg</i>	70	20	90	1	0.08	0.08	1.00	2.19
<i>abc</i>	115	10	45	1	1.00	0.77	0.49	0
<i>acg</i>	133	10	0	2.3	1.00	0.07	0.72	0.92
<i>bcg</i>	149	20	45	2.8	0.01	1.00	0.85	0.69

## References

1. M. Singh, B.K. Panigrahi, R.P. Maheshwari, Transmission line fault detection and classification, in *Proceedings of ICETECT* (2011)
2. X.H. Wang, Y.H. Song, Sheath fault detection and classification based on wavelet analysis. *Euro. Trans. Electr. Power* **16**, 327–344 (2006)
3. M. Jamil, R. Singh, S.K. Sharma, Fault identification in electrical power distribution system using combined discrete wavelet transform and fuzzy logic. *J. Electr. Syst. Info. Tech.* **2**, 257–267 (2015)
4. M. Gracia-Gracia, A. Montañés, N. El Halabi, M.P. Comech, High resistive zero-crossing instant faults detection and location scheme based on wavelet analysis. *Electr. Power Syst. Res.* **92**, 138–144 (2012)
5. R. Escudero, J. Noel, J. Elizondo, J. Kirtley, Microgrid fault detection based on wavelet transformation and Park’s vector approach. *Electr. Power Syst. Res.* **152**, 401–410 (2017)
6. S. Hanninen, M. Lehtonen, Method for detection and location of very high resistive earth faults. *Educ. Technol. Endors. Progr.* **9**(5) (1999)
7. A. Ghaderi, L. Ginn III Herbert, H.A. Mohammadpour, High impedance fault detection: a review. *Electr. Power Syst. Res.* **143**, 376–388 (2017)
8. W. Rebizant, J. Szafran, Power system fault detection and classification using probabilistic approach. *Educ. Technol. Endors. Progr.* **9**(3) (1999)
9. R. Perveen, N. Kishor, S.R. Mohanty, Fault detection and optimal coordination of overcurrent relay in offshore wind farm connected to onshore grid with VSC–HVDC. *Int. Trans. Electr. Energy Syst.* **26**, 841–863 (2016)
10. O.H. Gupta, M. Tripathy, ERF-based fault detection scheme for STATCOM-compensated line. *I. Trans. Electr. Energy Syst.* (2016)

11. T. Gush, S.B.A. Bukhari, R. Haider, S. Admasie, Y.S. Oh, G.J. Cho, C.H. Kim, Fault detection and location in a microgrid using mathematical morphology and recursive least square methods. *Electr. Power Energy Syst.* **102**, 324–331 (2018)
12. S. Das, S.P. Singh, B.K. Panigrahi, Transmission line fault detection and location using wide area measurements. *Electr. Power Syst. Res.* **151**, 96–105 (2017)

# Design and Fabrication of Solar-Powered Water Pumping Unit for Irrigation System



Pronami Mukherjee and Tapas Kumar Sengupta

**Abstract** One of the utmost concerns in the energy system of this world is the limited sources of energy and outraging pollution as an outcome of its extensive use that seeks a solution for a long-range energy woe going on presently. Sun is the ultimate source of energy; then why solar power cannot be utilized for the production of electricity is content of research for so many days. Either by directly using photovoltaic (PV) or indirectly using concentrated solar power, solar energy can be derived from sunlight. This paper deals with an aspect in the agricultural field where a particular application has been emphasized that can ease of cultivation sector efficiently. A solar water pumping system is discussed here along with the fabrication of a hardware model to show how the model actually works in the irrigation sector in the near future. Here, a mini model is experimented and validated so that it can further be implemented to large-scale application.

**Keywords** Solar panel · Photovoltaic · Centrifugal pump · Inverter

## 1 Introduction

In a country like India where a huge resource of renewable solar energy is available, non-utilizing it or under-utilization of such energy is nothing but ignoring its own assets. And its vastness is the cause why the rate of electrification is not up to the mark so far its expanding population, urbanization, and industrialization are of concern, this has resulted in the increasing difference between demand and supply of electricity

---

P. Mukherjee (✉)

Department of Electrical Engineering, Kalyani Government Engineering College, Kalyani, Nadia, West Bengal, India

e-mail: [mukherjee.pronami95@gmail.com](mailto:mukherjee.pronami95@gmail.com)

T. K. Sengupta

Department of Electrical Engineering, Supreme Knowledge Group of Institutions, Maulana Abul Kalam Azad University of Technology, Erstwhile West, Bengal University of Technology, Hooghly, West Bengal, India

© Springer Nature Singapore Pte Ltd. 2020

K. Maharatna et al. (eds.), *Computational Advancement in Communication Circuits and Systems*, Lecture Notes in Electrical Engineering 575, [https://doi.org/10.1007/978-981-13-8687-9\\_9](https://doi.org/10.1007/978-981-13-8687-9_9)

wherever required. It is a burden to the government as it is not very easy to keep pace with the demand of electricity all the time.

People usually get used to with fossil fuels like kerosene and diesel for their daily energy needs, and thus heavy recurring expenditure is happening to almost every house of India. Especially, the rural areas suffer the most in this context as the power supply is many a time of unreliable nature to those areas hampering the cultivation and farmers are in bad need of an uninterrupted power supply. During the critical farming period, it becomes a major concern. As per the report, India gets almost 5,000 (Five thousand) trillion unit of solar energy per year with an average solar incidence of 4–7 units of solar energy daily per square meter [1]. It is considerably more than that of the total energy consumption of this country. Further, most parts of the country experience approximately 240–290 sunny days in a year [2], which makes solar energy to be an important alternative these days.

Sun is the ultimate resource of all kind of energies. And solar is renewable in nature, that is, sustainable as well as inexhaustible, unlike that from fossil fuels which are finite. Moreover, it does cost nothing to get into utilization except the solar panels as it does not require any kind of fossils or anything as input. Solar energy has a minimum pollution level as well and there is no chance of any greenhouse gases to be emitted as a byproduct when there is production of electricity from solar energy is happening.

Thus, solar electricity can supplement the entire or partial energy consumption. And due to its economic nature and numerous benefits to be discussed later, it is indeed becoming an alternative source of energy (Fig. 1).

Utilization of solar energy can be in two ways [3]:

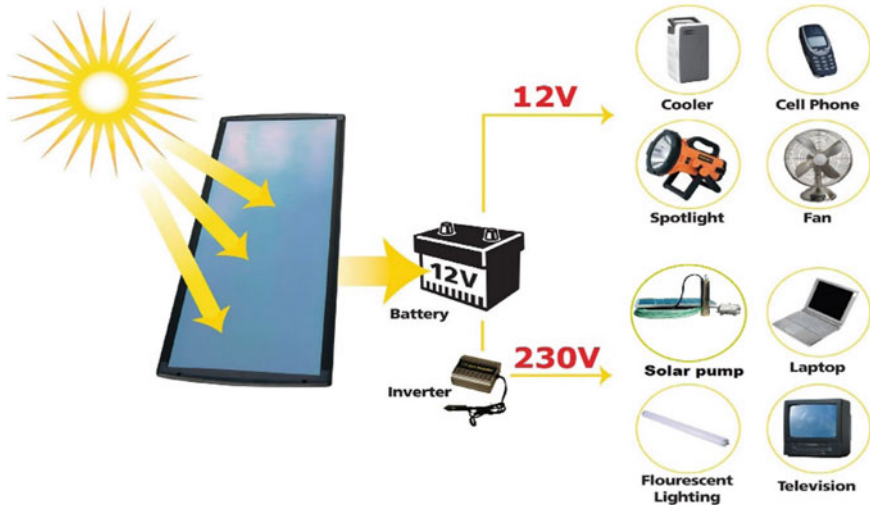


**Fig. 1** Various uses and applications of solar power. *Source* [homesolarenergys.blogspot.in/2014/02/how-to-make-solar-systems-for-homes.html](http://homesolarenergys.blogspot.in/2014/02/how-to-make-solar-systems-for-homes.html)

- **Solar Thermal (ST):** In this technology, the energy gets utilized in heating/cooling/drying. The devices mainly used for village communities include solar heaters/cookers/driers.
- **Solar Photovoltaic (SPV):** This system converts sunlight into electricity through lighting, pumping, communication, and refrigeration.

## 2 Solar Cells and Solar Arrays

The operation of solar cells is based on the principle of the photovoltaic effect, i.e., the formation of charge carrier inside a material by absorbing the energy obtained from the solar radiation that is incident on it [4]. The efficiency of solar cells is meant by how much energy obtained from the sunlight can be converted into electricity via photovoltaic. Solar cells have an efficiency of 18–24% which can be used in case of driving DC motors [5].

Silicon is most commonly used as a material for making solar cells. Other materials used in this case include cadmium sulfide or gallium arsenate. The fabrication process involves a large number of steps. After the junction formation, wafer forms the anti-reflection coating on the active surface of the cell. The outer surface of the panel is protected by a tempered-glass designed especially for this purpose. It provides a high level of transmittance of sunlight so that the efficiency can be enhanced.

Basically, a solar cell behaves like a low-voltage battery whose charge is continuously reinstated at a rate proportional to that of the incident solar radiation. Such cells get connected in any type of series or parallel configuration that results in the photovoltaic modules or solar arrays in producing high current and voltages. The solar arrays produce approximately 75–125 Watts of power from a square meter of the panel. This photovoltaic power is utilized in conventional electrical appliances like DC electric motors, etc. When a number of solar panels get combined, a solar array is formed. It is mounted on a simple frame having provisions for adjusting the whole setup of panels according to the position of the sun [6].

## 3 Different Types of Pumps and the Use of Solar Energy to Install Them

### 3.1 *Centrifugal Pumps—Surface Types*

These types of pumps are suitable in areas where the water level is within 7 m below ground level. It is normally placed at the top ground. The pump is used for pumping water from shallow bore wells, reservoirs, lakes, and canals. The solar pump is driven by a DC motor connected directly to an array of solar panels [7].

### ***3.2 Submersible Pumps***

This type of pumps is installed underwater. The pumps consist of an electric motor and everything is combined into a single unit. The shape of the pump looks like a long cylinder that can fit inside the casing of any well. Although all submersible pumps can be installed in a well, while many of them can also be laid inside a lake or stream [7].

### ***3.3 Turbine Pumps***

It is basically a centrifugal pump mounted underwater and attached by a shaft to a motor mounted above the water. The shaft is extended to the center of a large pipe. These are very efficient indeed and are extensively used for large-rated applications. Multiple stages are sometimes installed where each stage is essentially a pump stacked on top of another one below it. It works like a multiple engine driven train. [7].

### ***3.4 Different Types of Pump Sets Using Photovoltaic Power***

One such unit consists of a solar array, a DC electric motor and a unit for pumping. Along with these, electrical control and some tracking mechanism are also installed. Many types of pump insets may be used with PV systems, a vertical centrifugal pump may be coupled to a submersible DC electric motor or an ordinary volute centrifugal pump can be close-coupled to a horizontal DC motor. However, the submersible version is more suitable for the PV system than any other types. The arrangement removes any sort of suction pipe and foot valve and results in the more efficient pumping unit. A layer of silicon carbide mechanical seal is used to make the submersible pumps leak proof.

The output of the array varies with the intensity of the incoming solar radiation and many other factors. Hence, matching its output with the motor speed that is run by solar energy is very much necessary. At least one PV pumping set utilizes a maximum power control that works as an integral part of the system, in order to counterpart the load on the pump [8].

The power output of the system varies in direct proportion to the number of solar cells and the surface area of the panel exposed to the sun. The discharge of a solar pump varies from 6 to 8 L/s at a head of 5 m. With this irrigation to 1.5–2 ha of land, approximately with crops having moderate irrigation requirements is possible [9].



## 4 Advantages of Solar Photovoltaic (SPV) Pumps

- **Cost-Effectiveness:** The long-lasting life cycle and the lower cost make the SPV systems cost-effective in comparison with conventional systems.
- **Reliability:** As compared to the conventional power system, SPV is much more reliable, consistent, and predictable power option in rural areas.
- **No Fueling:** Sunlight is the main fuel source of the SPV system. Thus, it is available inexhaustibly, and also a reliable and free energy source indeed.
- **Low Maintenance:** The system requires a little servicing and there is no need for repeated refueling unlike the cases in conventional systems that increase its popularity in remote areas.
- **Local Power Generation:** The SPV system makes use of local resource which is sunlight. This provides greater energy security.
- **Easy Transportation:** SPV systems consist of modular setup and it can easily be transported in several pieces/components. These are also expandable to enhance capacity and vice versa.
- **Water conservation:** The SPV sets are highly advantageous when they are combined with water conservation methods like drip-irrigation and nocturnal water distribution. It leads to optimum exploitation groundwater.
- **Environment-Friendly Nature:** Using sunlight as fuel leads to green and clean technique, that is, eco-friendly and decentralized generation of energy. It saves the exploitation of fossil fuel and controls deforestation to save the very nature.

## 5 Case Study with Fabrication of Model

Here, a model is fabricated and its operation is checked to validate the effectiveness of using a solar-powered pump.

The first and foremost thing to fabricate the model is to choose proper components for the setup. Here, a common rated pump [10] is used whose rating is:

Voltage – 165–220 V,  
50 Hz, Power – 18 W(0.025 hp)  
Head – 6 m, Output – 20 L/m

Apart from this pump, the other main components are a transformer, an inverter, a battery, and a solar panel. The battery is chargeable by nature and it is charged by the solar panel both of which are selected as per the requirements here. To select the ratings, a particular load is added to the pump. Although the prime objective is to watering in the irrigation sector, here a miniature model is set up to check whether the system can perform its main work, i.e., to pump out water.

Firstly, it has been checked if the pump can water out from one bucket to another, and next the same pump is projected to pump out water from a reservoir to fill an

empty tank (600 L). Only after successful operation in these two cases, the system can be said to be validated and can be implemented on large scale, i.e., for pumping purpose in agricultural field.

Here, the above two cases have been checked by the first-hand experiment. As per the pump rating and load demand, the battery, inverter, and the solar panel have been designed.

Following are the steps of designing the whole setup and the justification of proper choices of selecting battery rating and solar panel rating.

### 5.1 Load and Running Hour Calculation

- Load requirement = 600 L/day from the depth of 10 ft.
- So, the amount of water to be pumped/day ( $L$ )

$$L = 600 \text{ L} \quad (1)$$

- Total dynamic head is  $6 + 4 = 10$  ft. or 3.05 m which is well within the limit of the pump motor used.

$$\text{Maximum flow rate}(F) = 20 \text{ L/min} \quad (2)$$

So, the required running hour per day ( $H$ ), i.e.,

$$\begin{aligned} H &= L/F \\ &= 600/(20 \times 60) \\ \text{Therefore, } H &= 0.5 \text{ hour per day} \end{aligned} \quad (3)$$

### 5.2 Design of Inverter

Designing of the inverter is a crucial part to obtain the desired result. When AC is not possible to be obtained to feed the pumps, for using the commercially available pumps, inverters are used. As DC is produced from the PV cells, DC pump may be used. But these are suitable for the low-power application. For more than 5 W, there is no choice except using AC pump in the context of cost and maintenance problems occurred in case of DC ones.

In this case, first, a smaller model is fabricated to get the result so that it can be used further for any larger application.

To design an inverter [11] (input being 12 V DC), the components required are

- One battery (12 V).

- MOSFET (IRF 630)-2.
- 2N2222 transistors-2.
- 2.2uf capacitors-2.
- Resistors.
- Center-tapped step up transformer.
- Wires and breadboard.

The circuit diagram and the actual connection diagram are shown here in Figs. 2 and 3.

The circuit consists of three things: (1) oscillator, (2) Amplifier, and (3) transformer. An oscillator of 50 Hz is used as the frequency of AC supply has to be 50 Hz.

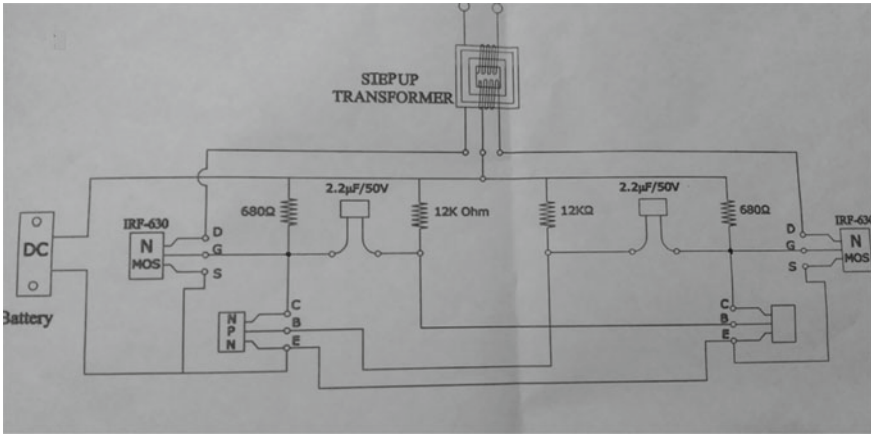


Fig. 2 Circuit diagram for inverter design

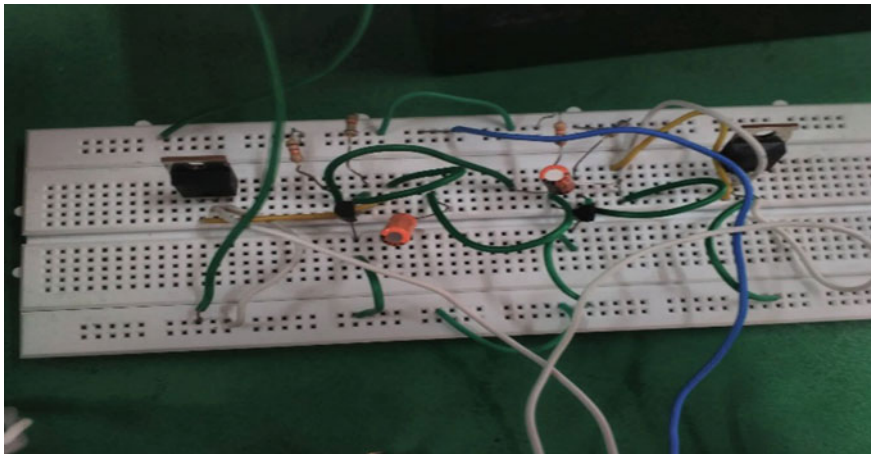


Fig. 3 Actual connection diagram for inverter design

This can be achieved by constructing an A stable multivibrator that produces a square wave at 50 Hz. In the circuit, the oscillator is formed by suitable choices of resistors, viz.  $R_1, R_2, R_3, R_4$ , the capacitors, viz.  $C_1, C_2$ , and transistors  $T_2$  and  $T_3$  (as shown in Fig. 3). Each of the transistors produces inverting square waves. The values of  $R_1, R_2$ , and  $C_1$  ( $R_4, R_3$ , and  $C_2$  are identical) will select the frequency.

The frequency of square wave generated by a stable multivibrator [11] is given by:

$$F = 1/(1.38 \times R_2 \times C_1). \quad (4)$$

The inverting signals formed and produced by the oscillator are amplified by using the power MOSFETS T1 and T4. These amplified signals are given to the step up transformer. The turn ratio of the transformer is chosen to be 1:19 in order to convert 12–220 V. The transformer steps up the inverting signals to a 220 V alternating square wave output.

The selection of this input of 12 V depends upon the capacity of the solar panel to charge a battery which will be designed further.

### 5.3 Selection of Battery and Solar Panel

- Motor full load current = 0.15 A
- Motor input voltage = 220 V
- These are supplied by the inverter designed in the above section through step up transformer of turn ratio 1:19.
- So before stepping up the inverter, output are 2.85 and 11.60 V. Inverter is fed from a 12 V DC supply through a battery which has to be selected properly.
- The load current of the battery is in this case 2.62 A. On a higher side, this value is taken to be 3 A by rounding off for the determination of maximum loading.
- Thus, the load current = 3 A and required running hour per day = 0.5 from Eq. (1)
- So, required ampere hour per day (AhpD), i.e.,

$$\text{AhpD} = 3 \times 0.5 = 1.5 \text{ Ah/day} \quad (5)$$

- Thus, a standard sealed lead acid battery is chosen having the following specifications:

12 V, 7 Ah

Charge parameters-constant voltage charge with voltage regulation (27 °C)  
3.6–13.8 V

Cycle used: 14.1–14.4 V

Maximum initial current: 1.4 A

- Choosing the solar panel also includes few a calculations to obtain the best choice. The factors determining the modeling of the solar panel are: solar radiation per day, sunshine hours per day, maximum load, battery efficiency, and PV panel efficiency.
- In the instant case, solar radiation per day ( $R$ ), i.e., [12].

$$R = 6 \text{ kwh/m}^2 \tag{6}$$

$$\text{Sunshine hour per day} = 8 \text{ h} \tag{7}$$

*(The above two data are taken in case of April month as the experiment has been taken place during April) [12, 13].*

$$\text{Possible max load}(L_{\text{max}}) = 1.5 \text{ Ah/day} \tag{8}$$

- From Eq. (5), battery efficiency for charging and discharging = 90%
- PV module efficiency due to temperature = 30% [14]

$$\begin{aligned} \text{The loss factor(LF)} &= (1/\text{battery efficiency}) \times (1/\text{temperature efficiency}) \\ &= 1/(0.9 \times 0.30) \\ &= 4 \text{ approx.} \end{aligned} \tag{9}$$

- Estimated Ah requirement from PV module is  $Ah_{\text{estt.}}$

$$\begin{aligned} Ah_{\text{estt.}} &= P_{\text{max}} \times LF \\ &= 1.5 \times 4 = 6 \text{ Ah} \end{aligned} \tag{10}$$

- Total Ampere requirement from PV module = (Estimated Ah requirements from PV module)/total sunshine hour during the month which is April in this instant case.

$$\begin{aligned} &= Ah_{\text{estt.}}/8 \text{ from Eq. (7)} \\ &= (6/8) \text{ A} \\ &= 0.75 \text{ A} \end{aligned}$$

- So, PV module system voltage ( $V$ ) = 12 V and PV module system current ( $i$ ) = 0.75 A  
Thus, the required PV module power capacity

$$\begin{aligned} P &= Vi \\ &= 12 \times 0.75 \\ &= 9 \text{ W} \end{aligned}$$



**Fig. 4** Measurement of voltage obtained from solar cell

- So, a solar panel of 10 W is sufficient for this application. The solar panel used in this case has the following specifications:

Open - circuit voltage – 21.6 V  
Rated voltage – 17.2 V  
Power output – 10 W

Open-circuit voltage measurement is shown in Fig. 4.

### 5.4 Experimental Setup

The hardware setup of the system has been demonstrated in Fig. 5.

The red colored pump will be pumping out water from the reservoir to the 600 L tank. A 12 V, 7 Ah battery is connected to the inverter which is fabricated on a breadboard and the inverter output is stepped up by using a transformer to feed the 18 W, 220 V AC pump. The commercially available pumps are well discussed in [15].

The block diagram for this pumping system is shown in Fig. 6. The reason for a battery to be connected is that the battery is chargeable by nature. It is a lead acid battery that is charged through the solar panel. Solar panel may be inserted directly. But it may not work in the bad weather condition like a cloudy atmosphere. So, it is necessary to implement a storage device which can supply the inverter input at any time.

Next, the circuit connection is made through wires. Charged up battery supplies DC input to the inverter. The inverter is already designed on a breadboard. Then, the

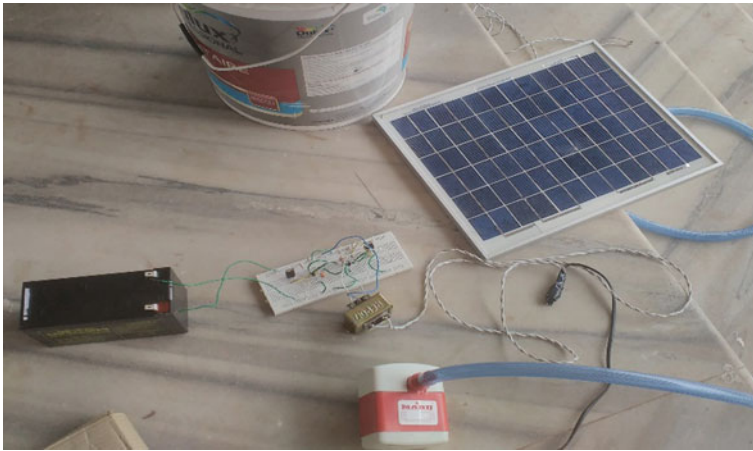


Fig. 5 Hardware model of solar pump—connection diagram

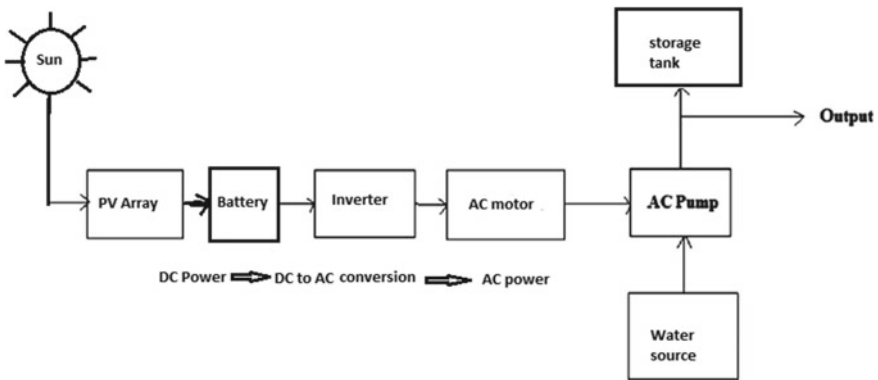


Fig. 6 Block diagram of how an AC pump works on solar energy

small AC output is stepped up by using a 20–220 V AC transformer for obtaining the required voltage needed by the pump to work on.

Once the pump gets fed by its required voltage, it starts watering. Working of the pump is shown in Fig. 7.

The left-hand side bucket, as shown in Fig. 7, wherein the pump is situated, is replaced with the reservoir and the right-hand side bucket will be replaced with 600 L tank that will be filled by this pump.

The technical specification for a solar-AC induction motor pump system is given in Table 1 [16, 17].



**Fig. 7** Pump in working condition (watering out from one bucket to another)

**Table 1** Technical specification for a solar-powered-AC pump

S. No.	PV AC Induction motor pump	Shallow well (surface) PV pumping system		Deep well (submersible) PV pumping system	
		Model-I	Model-II	Model-III	Model-IV
1.	PV array (Wp)	1800	2700	3000	4800
2.	Motor capacity (hp)	2	3	3	5
3.	Shut off dynamic head (m)	15	25	70	70
4.	Water output (L/day)	180,000	148,000	57,000	91,000
5.	Total head in m	10	20	50	50

## 6 Proposed Control Scheme and Future Advancement

- Filter Circuit Design:** Basically, this system that has been fabricated and experimented is a bit ideal in nature. The motor being a very low rated and it being a miniature model, this design is okay only to serve the experiment purpose. In the real world, there is never a sinusoidal waveform achieved from an inverter. Rather a quasi-sinusoidal waveform is always obtained consisting of a large quantity of harmonics which may lead to the poor performance of the motor (low efficiency, heating phenomenon due to increased harmonics, etc.). Thus, to die out those harmonics, design of filter circuit [18] is essential. Therefore, in large-scale application, there will be a filter block between inverter output and motor input in Fig. 6.
- MPPT Controller:** Another control technique may be applied by inserting a MPPT controller in the design. **MPPT** or **maximum power point tracking** is used to extract maximum power that is available from a PV panel under certain circum-



stances [19]. PV module produces maximum power at a voltage called “maximum power point.” This maximum power varies with solar radiation and ambient temperature as well as **solar cell** temperature. Here, an algorithm is used to determine the control technique which varies the electrical operating point to get the desired result [20].

This controller checks and compares the output of a PV module with the battery voltage (that is to be charged by the PV panel). Here, the main objective is to find the best result in respect of the best voltage and power. The best power that PV module can produce to energize the battery is fixed up and the best voltage to get the maximum amount of current into battery is obtained. Typically, during winter or cloudy days with less than the normal availability of sunlight or during when the battery gets heavily discharged, this MPPT controller can be best utilized.

## 7 Conclusion

As the pump works satisfactorily, the first conclusion that must be drawn is that a solar pump can actually work without any sort of hard effort. And there being advantages of no pollution like that in case of using other source of energy, no complexity, no heavy machinery, it can really justify the fact of using alternative energy sources like solar energy.

At any weather condition or at any place where sunlight is available in abundance or at least to that extent to charge the device for storing energy, this system can be installed.

When the agriculture of the whole country is suffering not being fed by sufficient power supply, excessive water pumping in dry areas leads to grid failure, and demand for an alternative source is essential. This application proves that solar energy can be a good option to meet such kind of demand and is very much economical indeed. Here, in this case, a particular miniature model of SPV driven pump is described and fabricated, and it is well observed that the pump is meeting its expectation to do the job of pumping out water. Thus, in this paper, it is discussed how the validation of the pump by using a mini model has successfully experimented and from that, it can be concluded that it might well be implemented in large-scale agricultural application with higher rating including the filtering and controlling units as proposed above.

**Acknowledgements** The authors acknowledge with sincere thanks for the assistance obtained from the department of Electrical Engineering, Supreme Knowledge Foundation Group of Institutions (SKFGI) West Bengal, Pranabesh Sarkar, B. Tech., SKFGI, WB, Dr. Partha Sarathi Bera Prof. in Department of Electrical Engineering, Kalyani Government engineering college, West Bengal. Deep regards also go to my fellow seniors and friends in my department.

## References

1. T. Muneer, M. Asif, S. Munawwar, Sustainable production of solar electricity with particular reference to the Indian economy. *Renew. Sustain. Energy Rev.* **9**, 444–473 (2005)
2. T.V. Ramachandra, R. Jain, G. Krishnadas, Hotspots of solar potential in India. *Renew. Sustain. Energy Rev.* **15**, 3178–3186
3. B. Eker, Solar powered water pumping systems. *Trakia J. Sci.* **3**(7), 7–11 (2005)
4. R. Hantula, *Science and Curriculum Consultant: Debra Voegel. How Do Solar Panel Works*
5. M. McGehee, *An Overview of Solar Cell Technology*. Mater Sci Eng. Global Climate and Energy Project, Center for Advanced Molecular Photovoltaics, Precourt Institute, Stanford University
6. C. Protoger, S. Pearce, Laboratory evaluation and system sizing charts for a second generation direct PV-powered, low cost submersible solar pump. *Sol. Energy* **68**, 453–474 (2000)
7. Irrigation tutorials, [www.irrigationtutorials.com](http://www.irrigationtutorials.com)
8. A. Sengar, Solar photovoltaic water pumping system, in *A project report on Solar PV Water Pumping System*
9. V. Shinde, S. Wandre, Solar photovoltaic water pumping system for irrigation: a review. *Afr. J. Agr. Res.* **10**(22), 2267–2273 (2015)
10. P. Mukherjee, K. Rakib, A. Mukherjee, D. Ghosh, P. Sarkar, Solar powered pumping system, B. Tech final project under guidance of Dr. Tapas Kumar Sengupta
11. M.H. Rashid, *Power Electronics Circuits, Devices and Applications*, 3rd edn. Prentice Hall of India
12. M.S. Kyi, L. Maw, H.M. Tun, Study of solar PV sizing of water pumping system for irrigation of asparagus. *Int. J. Sci. Technol. Res.* **5**(06) (2016)
13. World Meteorological Organization, Weather base record: the solar electricity handbook website
14. M.A. Green, K. Emery, Y. Hishikawa, W. Warta, E.D. Dunlop, Solar cell efficiency tables (Version 45). *Prog. Photovolt. Res. Appl.* **23**, 1–9 (2015)
15. N. Chandrasekaran, K. Thyagarajah, Modeling and performance study of single phase induction motor in PV fed pumping system using MATLAB. *Int. J. Electr. Eng.* **5**(3), 305–316 (2012)
16. Technical specifications for solar photovoltaic water pumping systems. [www.mnre.gov.in/file-manager/technical-specification\\_spwps\\_2013\\_14.pdf](http://www.mnre.gov.in/file-manager/technical-specification_spwps_2013_14.pdf)
17. S.S. Chandel, M. Nagaraju Naik, R. Chandel, Review of solar photovoltaic water pumping system technology for irrigation and community drinking water supplies. *Renew. Sustain. Energy Rev.* **49**, 1084–1099 (Elsevier Journal)
18. A. Ale Ahmed, A new design procedure for output LC filter of single phase inverters, in *International Conference on Power Electronics and Intelligent Transportation System*, China
19. B. Pakkiraiah, G. DurgaSukumar, A new modified MPPT controller for solar photovoltaic system, in *IEEE International Conference on Research in Computational Intelligence and Communication Networks (ICRCICN)* (2015)
20. B.R. Sanjeeva Reddy, P. Badari Narayana, P. Jambholkar, K. Srinivasa Reddy, MPPT algorithm implementation for solar photovoltaic module using microcontroller, in *Annual IEEE India Conference* (2011)

# Power Grid Generation with Tectonic Mechanism Wind Energy Resources



Pratyusha Biswas Deb, Susmita Das, Arnima Das, Ronojit Bose, Aritra Das and Maitreyi Ray Kanjilal

**Abstract** The availability of natural non-conventional resources such as wind, water, sunlight, and other renewable sources of energy has been a boon to the human being and the society. If these sources of energy can be utilized in a proper way with energy conservation policy, a pollution-free environment can be achieved to change the world and society. Scientific process implementation of the sources can create an eco-friendly world along with the sustainable source of development. Nature has gifted the numerous numbers of scopes and a wide range of resources such as solar, wind, water, tidal, and geothermal. In this project, the application of wind energy is the prime concern through which the other natural components can be used to drive a more amount of energy for our daily needs and to reduce the harmful consequence as an absorption by the ecosystem. In this era of the advanced technological environment, our modern life has become more advanced in the fields of operating various plant operations and daily life needs too. But sometimes, it really affects our earth and depletes other natural components which can cause the natural disaster or can unbalance the ecosystem. Thus, to overcome the problem, people should be more aware and take a step forward to the planned use of natural energy sources. The

---

P. B. Deb (✉) · R. Bose · A. Das  
Electrical Engineering, Narula Institute of Technology, Kolkata, W.B, India  
e-mail: [pratyusha.biswasdeb@nit.ac.in](mailto:pratyusha.biswasdeb@nit.ac.in)

R. Bose  
e-mail: [Ronojit12@gmail.com](mailto:Ronojit12@gmail.com)

A. Das  
e-mail: [aritrad915@gmail.com](mailto:aritrad915@gmail.com)

S. Das  
Electronics and Instrumentation Engineering, Narula Institute of Technology, Kolkata, W.B, India  
e-mail: [susmita.das@nit.ac.in](mailto:susmita.das@nit.ac.in)

A. Das  
Electronics and Communication Engineering, Narula Institute of Technology, Kolkata, W.B, India  
e-mail: [arnima.das@nit.ac.in](mailto:arnima.das@nit.ac.in)

M. Ray Kanjilal  
Narula Institute of Technology, Kolkata, W.B, India  
e-mail: [principal.nit@jisgroup.org](mailto:principal.nit@jisgroup.org)

© Springer Nature Singapore Pte Ltd. 2020  
K. Maharatna et al. (eds.), *Computational Advancement in Communication Circuits and Systems*, Lecture Notes in Electrical Engineering 575,  
[https://doi.org/10.1007/978-981-13-8687-9\\_10](https://doi.org/10.1007/978-981-13-8687-9_10)

project work is mainly concerned about the non-conventional sources of energy and the effective use of it to extract energy through several mechanisms. It also focuses on the distribution and access to groundwater for drinking and irrigation purpose. The idea is to solve some of the problems which are faced by human beings in daily life.

**Keywords** Wind energy · Energy conversion · Power generation · Hydroelectricity

## 1 Introduction

This paper discusses the power generation from wind energy using tectonic mechanism. This mechanism produces energy using renewable sources which be get in the form of electricity that can be made available to the grid while pumping fresh-water from the ground. The energy absorbed in the form of sunlight by the earth's atmosphere differs from place to place and time to time. Due to this uneven heating of the atmosphere, low- and high-pressure regions are generated and wind currents start to flow from the high-pressure zones to low-pressure zones. The air currents caused by these pressure differences are intermittent and difficult to predict accurately, but modern forecasting can help. Wind sites are classified by their average wind speed. The amount of energy available increases with the cube of the wind speed, and a slight increase or decrease in the wind speed can cause a huge difference in the available wind power. Wind speeds vary with altitude, so further we move away from the sea level, the available wind power increases. Establishing a wind farm at higher altitude is also beneficial because closer to the sea level the farm is the higher presence of humidity and pollution particles. This rough atmospheric condition causes acceleration in the corrosion and fatigue of wind blades. The condition may further deteriorate the closer we get to the sea. Total global wind power available is much larger than total power demand, but the level of the resource varies from region to region. Further prospecting is required to narrow down the regions suitable to establish a wind farm keeping in account the aforesaid parameters.

## 2 Methodology

This initiative is an interdisciplinary work of electrical, mechanical, and electronics engineering, and it provides a sustainable enhancement in the emergent countries. The viewpoint of the project work lies on the use of wind energy which in turn generates electricity, and further, it can drive water from the groundwater level by pumping it with a piston on the basis of shaft engineering method including a hydraulic system. While the water is being pumped up with the kinetic force with which it is going up, it can drive the turbine where hydroelectric power may be generated. That groundwater

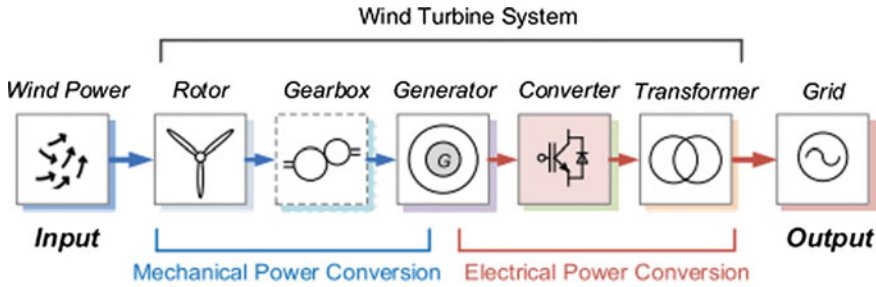


Fig. 1 Schematic diagram of the proposed work

can be used for drinking for living beings and irrigation purpose for crop yielding. But the 60% pumped out water can be used for drinking water supply purpose, and the other 40% can be recycled by bypassing a channel from where water can be streamed with a potential from a height to a reservoir which will be the main source of hydroelectric power. That amount of water shall not be wasted; in turn, it will aid the groundwater level and will definitely compensate the depletion of water level, thus maintaining a good balance in the water quantity of the earth (Figs. 1, 2 and 3).

The wind energy shall drive the shaft mechanism to drive water from underground which will in turn drive the turbines, as well as the wind energy shall also generate electricity. From a few meters above the ground level, the water shall be transported for drinking and irrigation and for other utilities. The total water pumped out shall go through a channel in which 60% shall be transported for drinking purpose and the other 40% will be used for recycling of the groundwater and that 40% of the water will be dropped from a height with high potential which shall also help to generate electricity by hydroelectric method (Fig. 4).

1.1 Specification of prototype model:

- Generator rating: Voltage rating: 12 V
- Current rating: 5 A
- Speed: 2000 rpm

1.2 Blade of windmill specification: length: 13 cm and width: 5 cm

3 Results and Discussion

See Tables 1, 2 and 3.

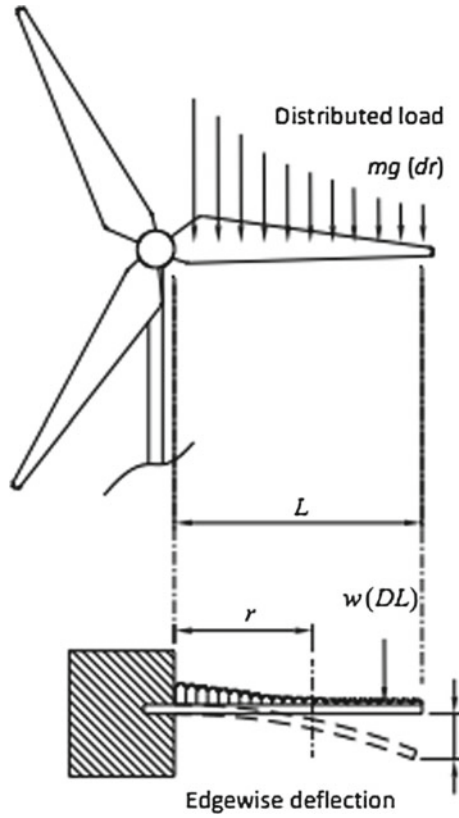


Fig. 2 2D functional diagram of the proposed work

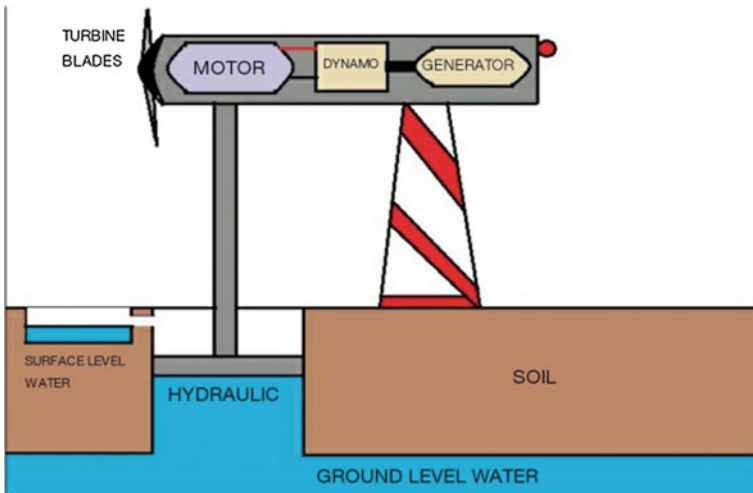


Fig. 3 CAD of the work effort



Fig. 4 Pictorial representation of the proposed prototype of the model

Table 1 Selection of turbine size and weight configuration

Turbine name	Pitch or stall	Rotor dia (m)	No. of blades	Nacelle and rotor weight (kg)	Weight per swept area (kg/m <sup>2</sup> )
Mitsubishi MWT-1000 (1 MW)	P	57	3	Unspecified	
Norder N90(2.3 MW)	P	90	3	84,500	13.3
Nordex N80 (2.5 MW)	P	80	3	80,500	16
Repower 5M (5 MW)	P	126	3	Unspecified	
Siemens SWT-3.6-107 (3.6 MW)	P	107	3	220,000	24.5
Siemens SWT-2.3-93 (2.3 MW)	P	93	3	142,000	20.9
Gamesa G90-2 MW(2 MW)	P	90	3	106,000	16.7
Gamesa G58-850 (850 kW)	P	58	3	35,000	13.3
Enercon E82(2 MW)	P	82	3	Unspecified	
GE wind 3.6sl (3.6 MW)	P	111	3	Unspecified	
Vestas V164 (7.0 MW)	P	164	3	Unspecified	
Vestas V90 (2 MW)	P	90	3	106,000	16.7
Vestas V82 (1.65 MW)	P	82	3	95,000	18

**Table 2** Information of the manufacturers of rotor diameter and power ranges

Rank	Manufacturer	Global market shares (%)	Rotor diameter (m)	Power range (MW)
1	Goldwind (China)	12.5	70–121	1.5–3
2	Vestas (Denmark)	11.8	90–136/164	1.8–3.45/8
3	GE Wind (USA)	9.5	83–137/150	1.7–3.8/6
4	Siemens Wind (Denmark/Germany)	8.0	101–142/154	2.3–4/6–8
5	Gamesa (Spain)	5.4	80–132/132	2–3.3/5
6	Enercon (Germany)	5.0	44–141	0.8–4.2

**Table 3** Output measurement of the prototype model

S. no.	Wind speed(rpm)	Output voltage(v)
1	600	1
2	700	1.5
3	800	2
4	1000	2.2

## 4 Conclusions

The excessive use of non-renewable sources of energy will cause its depletion. The optimum use of renewable sources of energy with simple mechanisms is a vital solution. Pollution-free environment and creation of an eco-friendly nature and green earth are our future aim. Hydro-wind power can be generated both simultaneously in greater amount so that there will be a balance with the use of non-renewable source of energy. Recycling the groundwater in a 60–40 ratio will eventually aid to the groundwater level to maintain equilibrium in the water level. The rainwater harvesting can be used in the reservoir, which will also improve the groundwater level. No electricity or man power is required to generate the initial mechanism.

## References

1. J. Rodriguez, S. Bernet, B. Wu, J.O. Pontt, S. Kouro, Multilevel voltage-source converter topologies for industrial medium voltage drives. *IEEE Trans. Ind. Electron.* **54**(6), 2930–2945 (2007)
2. S. Kouro et al., Recent advances and industrial applications of multilevel converters. *IEEE Trans. Ind. Electron.* **57**(8), 2553–2580 (2010)
3. A. Faulstich, J.K. Stinke, F. Wittwer, Medium voltage converter for permanent magnet wind power generators up to 5 MW. in *Proceeding of EPE*, (2005), pp. 1–9



4. J. Rodriguez, S. Bernet, P.K. Steimer, I.E. Lizama, A survey on neutral-point-clamped inverters. *IEEE Trans. Ind. Electron.* **57**(7), 2219–2230 (2010)
5. B. Engel, M. Victor, G. Bachmann, A. Falk, 15 kV/16.7 Hz energy supply system with medium frequency—Transformer and 6.5 kV IGBTs in resonant operation. in *Proceedings of EPE*, (Toulouse, France, 2003, Sep)
6. S. Inoue, H. Akagi, A bidirectional isolated DC–DC converter as a core circuit of the next-generation medium-voltage power conversion system. *IEEE Trans. Power Electron.* **22**(2), 535–542 (2007)
7. F. Iov, F. Blaabjerg, J. Clare, O. Wheeler, A. Rufer, A. Hyde, UNIFLEX-PM-A key enabling technology for future European electricity networks. *EPE J.* **19**(4), 6–16 (2009)
8. A.Q. Huang, M.L. Crow, G.T. Heydt, J.P. Zheng, S.J. Dale, The future renewable electric energy delivery and management (FREEDM) system: The energy Internet. *Proc. IEEE* **99**(1), 133–148 (2011)
9. M. Davies, M. Dommaschk, J. Dorn, J. Lang, D. Retzmann, D. Soerangr, HVDC plus—basics and principles of operation. Siemens, Munich, Germany, Tech. Rep (2008)
10. A. Lesnicar, R. Marquardt, An innovative modular multilevel converter topology suitable for a wide power range. in *Proceedings of IEEE Bologna Power Tech Conference* (2003, Jun), pp. 1–6
11. K. Ma, F. Blaabjerg, The impact of power switching devices on the thermal performance of a 10 MW wind power NPC converter. *Energies* **5**(7), 2559–2577 (2012)
12. R. Jakob, C. Keller, B. Gollentz, 3-Level high power converter with press pack IGBT,” in *Proceedings of EPE*, (2007, Sep), pp. 2–5. [72] R. Alvarez, F. Filsecker, S. Bernet, Comparison of press-pack IGBT at hard switching and clamp operation for medium voltage converters. in *Proceedings of EPE*, (2011), pp. 1–10
13. U. Scheuermann, Reliability challenges of automotive power electronics. *Microelectron. Rel.* **49**(9–11), 1319–1325 (2009). [74] U. Scheuermann, R. Schmidt, A new lifetime model for advanced power modules with sintered chips and optimized al wire bonds. in *Proceedings of PCIM*, (2013), pp. 810–813
14. J. Biela, M. Schweizer, S. Waffler, J.W. Kolar, SiC versus Si—Evaluation of potentials for performance improvement of inverter and DC–DC converter systems by SiC power semiconductors. *IEEE Trans. Ind. Electron.* **58**(7), 2872–2882 (2011)
15. L. Yang, T. Zhao, J. Wang, A.Q. Huang, Design and analysis of a 270 kW five-level DC/DC converter for solid state transformer using 10 kV SiC power devices. in *Pro*
16. G. Boyle, *Renewable Electricity and the Grid: The Challenge of Variability*. (Earthscan, London, 2007). Print
17. Irena. ETSAP. Renewable Energy Integration in Power Grids (n.d.). Int. Renew. Energy Agency 1–36 (2015, Apr). Web
18. A. Keyhani, *Design of Smart Power Grid Renewable Energy Systems*. (Wiley, Hoboken, NJ, 2011). Web
19. S. Jahdi, L. Loi, *Grid Integration of Wind-solar Hybrid Renewables Using AC/DC Converters as DG Power Sources* (IEEE, 2011), pp. 1–7. Web
20. A. Anees, *Grid Integration of Renewable Energy Sources: Challenges, Issues and Possible Solutions* (IEEE, 2012), pp. 1–6. Web

**Part II**  
**Cloud Computing, Internet  
on Things, Machine Learning  
and Big Data Analytics**

# Mining Social Network Data for Predictive Personality Modelling by Employing Machine Learning Techniques



Arjun Sengupta and Anupam Ghosh

**Abstract** Facebook, Twitter, LinkedIn and Tumblr are online social networking platforms where the users send and receive messages on the topic of their choice and express their sentiments. The usage of these sites has exponentially increased over the last few years, thereby increasing the information posted on online social media sites. The quantity of information/tweets keeps increasing on a daily basis. Twitter has become a stable platform to identify personality-related indicators and encrypted in user profiles and pages related to a subject. In this proposed work, we present a scalable real-time system for sentiment analysis of Twitter data. This work will collect tweets of the users in real time and thus provide a basis to identify each tweet into either positive or negative based on the mind-set of the user, thereby providing a real-time analysis of the users regarding a certain topic. The system relies on feature extraction from the tweets generated in real time. A supervised learning approach based on ensemble learning is used to train various classifiers based on the features extracted. A design and implementation in Flask and Celery has been carried out which contains the feature extraction and classification tasks. The system is scalable with respect to the size of the input data and the rate of data arrival. The merits of the proposed system in terms of scalability, performance and classification accuracy was evaluated experimentally.

**Keywords** Opinions · Real time · Sentiments · Twitter · Ensemble

---

A. Sengupta (✉)

Tata Consultancy Services Ltd, Candor Kolkata One Hi-Tech Structures Pvt. Ltd IT/ITES SEZ,  
Block G III, 5th Floor Tower B-II, New Town, Kolkata 700160, India  
e-mail: [sengupta.arjun@tcs.com](mailto:sengupta.arjun@tcs.com)

A. Ghosh

Department of Computer Science & Engineering, Netaji Subhash Engineering College,  
Techno City, Garia, Kolkata 700152, India  
e-mail: [anupam.ghosh@rediffmail.com](mailto:anupam.ghosh@rediffmail.com)

© Springer Nature Singapore Pte Ltd. 2020

K. Maharatna et al. (eds.), *Computational Advancement in Communication  
Circuits and Systems*, Lecture Notes in Electrical Engineering 575,  
[https://doi.org/10.1007/978-981-13-8687-9\\_11](https://doi.org/10.1007/978-981-13-8687-9_11)

## 1 Introduction

Among all varieties of social media, Facebook is a valuable asset for data mining because of its prevalence and recognition all over the globe [1]. The social media is an important source of learning of influences, subjectivity, assessments, opinions, discussions, sentiments, approaches, remarks, evaluation, observations, feelings, reviews, news, reactions, blogs or some other references [2]. The discovery of opinions expressed online can be extracted using traditional methods, but conversely this is inadequate considering the fact that there is a large corpus of information which is being generated every nanosecond on all social media sites at present [3]. The definition of social network analysis is the various linkages between interacting units and the vital importance of social relationships among the interacting units [4]. Many domains such as collaboration, ecommerce, e-learning and information filtering use personalized systems which would benefit greatly from a user interface that would adapt to the personality of a user according to the interactions of the user (e.g. interaction modalities, recommendations, motivational strategies, etc.) [5]. Data mining is a powerful tool which assists to find various types of relationships and patterns within the data by discovering latent information from big databases [6]. Many business activities utilize social networks to increase their business like development of a new product and to strengthen public relations, idea generation, customer service, co-innovation and general marketing, employee communications, etc. [7]. The Big Five model is established as the most popular personality model out of the many that have been proposed till now [8].

## 2 Related Work

A model was proposed for the classification of the tweets as either negative or positive [9]. A sentiment analysis classifier based on maximum entropy model and Naïve Bayes method was implemented by collection of tweets using the Twitter API which automatically labelled the tweets using emoticons. [10]. A paper was presented which used models like SVM, maximum entropy and Naïve Bayes classifier [11]. A feature space consisting of POS, unigrams and bigrams was created. SVM outperformed other models, and it was concluded that in terms of features unigrams were more effective. A tree kernel-based model was proposed wherein all the tweets were represented in the form of a tree, and it gave a better performance in comparison with the other two models (one being a feature-based model using 100 features and the other a unigram model using over 10,000 features) [12]. A classification model involving sentiment analysis was implemented which uses user-defined hashtags in tweets as a type of style of classification using single words, patterns, punctuations and n-grams as different types of features which were combined as a single feature vector [13]. A paper was presented wherein various types of variations of Naïve Bayes classifier were used for the detection of the polarity of English tweets. Baseline and Binary were the two different types of Naïve Bayes classifier which were built [14].

### 3 Methodology

#### 3.1 System Framework of the Proposed Model using Ensemble Learning

We present a model which will collect data from pages of Twitter and provide the required business intelligence. A total of six machine learning algorithms were used for this ensemble. They are as follows:

I. Logistic regression, II. linear SVC, III. multinomial NB, IV. ridge classifier, V. MLP classifier and VI. SGD classifier (Fig. 1).

There are mainly four layers in this work:

##### Data Collection Module:

Raw data is collected from Twitter Application Programming Interface (API) in real time.

The raw data is then stored in a .csv file for data pre-processing.

##### Data Pre-processing Module:

Meta-attributes were extracted from the tweets, and the information was divided into grammatical information and social information which includes the average number of positive and negative words, average length of text, etc.

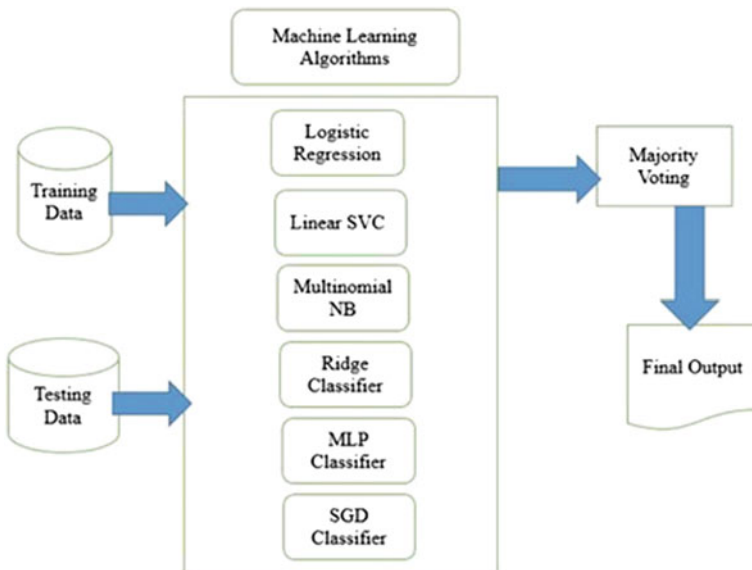


Fig. 1 Block diagram of the proposed ensemble learning algorithm

**Transformation Module:**

The multilabel problem was transformed into a binary classification problem in this module. From the previous module, the meta-attributes were used to construct a feature vector and each position in the vector was mapped to a meta-attribute which was then used in the classification module whose output was either '0'(negative) or '1'(positive).

**Classification Module:**

The classification module uses an ensemble for classification of the tweets. The module receives a training set which has been already transformed along with a test set. The model compares the test feature vector with its training feature vectors. The result of each classifier is either a '1' (positive) or '0' (negative) based on whether the vectors match or not.

**Recommendation module:**

In this module, the data is split up into training/test to run on the models and recommending users on basis of their likes/posts/comments and suggesting them various sites/groups according to their personality.

### 3.2 Algorithms used for Ensemble Learning

**Logistic Regression**

This model is used as a linear model for classification and is also known by other names such as maximum entropy classification model. In this model, a logistic function is used wherein the outcome of a single trial is described by its probabilistic outcome. The implementation fits a one-vs-rest multiclass regression with an optional L1 or L2 regulation. The following cost function [9] is minimized using L2 penalized logistic regression.

$$\min_w, c \frac{1}{2} w^T w + C \sum_{i=1}^n \log(e^{(-y_i(x_i^T w + c))} + 1) \quad (1)$$

The L1 regularized logistic regression can solve the following problem of optimization in a similar fashion:

$$\min_w, c ||w|| + c \sum_{i=1}^n \log(e^{(-y_i(x_i^T w + c))} + 1) \quad (2)$$

## Linear SVC

Support vector machine (SVM) is supervised machine learning method used for regression, classification and detection models. Generally, for multiclass specification, SVCs are used. Linear SVC is built on linear models, but Nu-SVC and SVCs are generally similar [15]. These SVCs take two input array ‘X’ of size [samples, feature] and array ‘Y’ of size [samples]. Linear SVC implements “one-vs-rest” scheme, whereas Nu-Svc implements “one-against-once” scheme for multiclass; hence, it provides consistent interface with other classifiers [11].

## Multinomial NB

The usage of the Naïve Bayes algorithm is expanded by the multinomial Naïve Bayes algorithm. It implements Naïve Bayes for multinomial data distribution and for the purposes of text classification also uses one its version [16]. The distribution data was parameterized by vectors for every ‘y’, where ‘n’ gives the total feature (equivalent to the size of vocabulary for next classification) and probability  $p(x_i|y)$  of each ‘i’ that appears in the sample of class ‘y’ is  $\theta_{yi}$  and then used the smoothed version of maximum likelihood for estimation of parameters  $\theta_{y1}$  which is relative frequency of counting [7].

$$\theta_{yi} = (\theta_{yi} \dots \theta_{yn}) \quad (3)$$

$$\theta_{yi} = \frac{N_{yi} + \alpha}{N_{yi} + \alpha n} \quad (4)$$

where  $N_{yi}$  represents number of times ‘i’ appeared in any sample of class ‘y’ which belongs to training sample  $T$ .

$$N_{yi} = \sum_{i=0}^T N_{yi} \quad (5)$$

The equation (v) gives the total number of features in class ‘y’. To prevent zero probabilities for further calculations, smoothing priors  $\alpha \geq 0$  was added for features that are not present in any learning samples.

## Ridge Regression Classifier

Ridge regression classifier or commonly known as ridge regression in statistics named after Andrey Tikhonov is one of the most commonly used functions of regularization of ill-posed problems.

## MLP Classifier

MLP classifier or multilayer perceptron classifier is a class of feed-forward artificial neural network. Multilayer perceptron consists of at least three layers of nodes.

Except for the input nodes, each node acts like a neuron which functions as a nonlinear activation function. For training purposes, it uses back-propagation, a supervised learning technique [16, 17]. The MLP is different from a linear perceptron by the fact that it uses its multiple layers and nonlinear activation and distinguishes data that is not separable linearly [18].

### SGD Classifier

Stochastic gradient descent (SGD) classifier uses an optimized method to solve unconstrained optimization problems. To minimize the error function, it updates a set of parameters in an iterative fashion. Rather to run through all the samples from training set before updating, the SGD classifier uses only one training sample and in this way the linear classifier converges quickly and favoured for particularly large datasets. The classifier acts like SVM or maximum entropy classifier by using convex loss functions [19].

### Collecting raw data from Twitter

Raw data is collected in real time from the Twitter using Twitter’s API (Fig 2).

### Cleaning raw data

After cleaning the raw data, the cleaned dataset is then stored for running various ML algorithms and the accuracy of various models is checked.

Data Preparation: HTML decoding, URL links, UTF-8 BOM (Byte Order Mark), hashtag/numbers (Figs. 3 and 4).

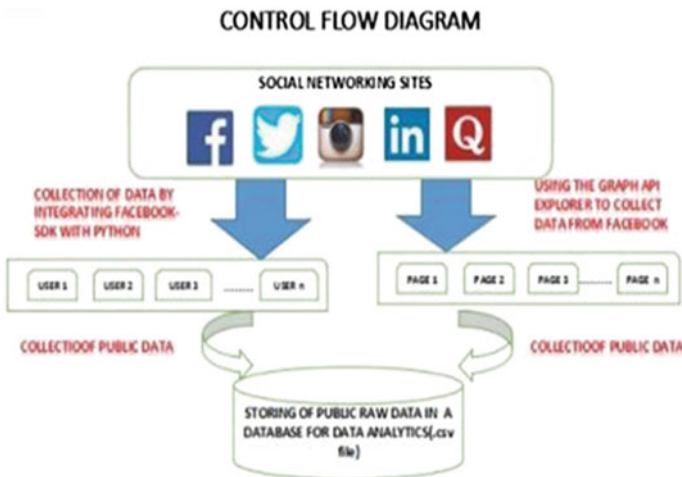


Fig. 2 Control flow diagram for collection of user data from social networking sites and storing them on a database





Fig. 3 Control flow diagram for cleaning and filtering the raw data by removing the emoticons, removing repetitive words and storing the final .csv for running the machine learning algorithms

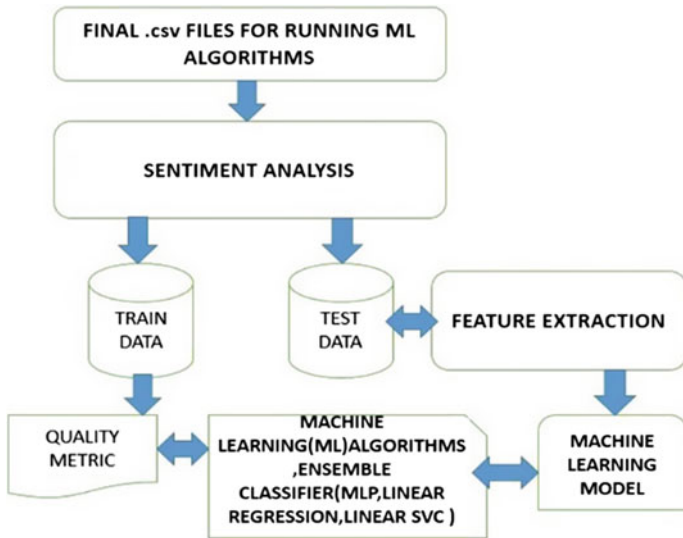


Fig. 4 Control flow diagram of sentiment analysis tool and its working prototype implemented in this project



## CountVectorizer

With CountVectorizer, we merely count the appearance of the words in each text. For example, let us say we have three documents in a corpus: “I love dogs”, “I hate dogs and knitting” and “Knitting is my hobby and my passion”.

### Stop words

Stop words are words which do not contain important significance, such as “the” and “of”. It is often assumed that removing stop words is a necessary step and will improve the model performance. CountVectorizer is run with three types (unigram, bigram and trigram), and each type was run with three different conditions with logistic regression classifier: • without stop words, • with stop words and • with custom stop words (“to”, “the”, “my”, “it”, “and”, “you”, “not”, “is”, “in”, “for”).

## 4 Result

### 4.1 Description of the Dataset

Name of the Dataset: Sentiment140 Dataset

Dataset Description: The dataset can be downloaded from the below link.

<http://cs.stanford.edu/people/alecmgo/trainingandtestdata.zip>

It contains 1,600,000 tweets extracted using Twitter API. The tweets have been annotated (0 = negative, 2 = neutral, 4 = positive). The size of the dataset is 77.6 MB. Another Twitter-Data Sentiment-Dataset used was of size 200 MB.

### 4.2 Analysis of the Result

#### Accuracy Result for Ensemble

Null accuracy: 50.64%; accuracy score: 79.60%; model is 28.97% more accurate than null accuracy; train and test time: 2245.30 s

*Creating Frequency data frame using Zipf's Law (Fig. 7).*

## 5 Validation of the Result

**Result of Unigram Without Stop Words (Table 1).**

**Result of Unigram with Stop Words (Table 2).**

Out[49]:

	negative	positive	total
to	313160	252566	565726
the	257836	265998	523834
my	190774	125955	316729
it	157448	147786	305234
and	153958	149642	303600
you	103844	198245	302089
not	194724	86865	281589
is	133435	111191	244626
in	115541	101160	216701
for	98999	117369	216368

**Fig. 7** Indexes are the token from the tweets dataset (“Sentiment140”), and the numbers in “negative” and “positive” columns represent how many times the token appeared in negative tweets and positive tweets

**Table 1** Result of unigram without stop words

No. of features	Null accuracy (%)	Accuracy score (%)	Train and test time(s)
20,000	50.64	75.51	157.83
40,000	50.64	75.67	247
60,000	50.64	75.62	242.92
80,000	50.64	75.65	227.56
100,000	50.64	75.68	265.55

**Table 2** Result of unigram with stop words

No. of features	Null accuracy (%)	Accuracy score (%)	Train and test time(s)
20,000	50.64	77.81	293.56
40,000	50.64	77.83	299.02
60,000	50.64	77.81	422.04
80,000	50.64	77.79	378.99
100,000	50.64	77.78	485.64

**Table 3** Result of unigram with custom stop words

No. of features	Null accuracy (%)	Accuracy score (%)	Train and test time(s)
20,000	50.64	76.83	193.56
40,000	50.64	77.05	261.11
60,000	50.64	77.1	315.69
80,000	50.64	77.14	299.74
100,000	50.64	77.19	310.86

**Table 4** Result of bigram with stop words

No. of features	Null accuracy (%)	Accuracy score (%)	Train and test time(s)
20,000	50.64	79.04	383.34
40,000	50.64	79.42	572.71
60,000	50.64	79.37	755.17
80,000	50.64	79.18	841.847
100,000	50.64	79.28	871.97

**Table 5** Result of trigram with stop words

No. of features	Null accuracy (%)	Accuracy score (%)	Train and test time(s)
20,000	50.64	78.98	2891.41
40,000	50.64	79.62	3717.013
60,000	50.64	79.3	6610.117
80,000	50.64	79.25	5863.75
100,000	50.64	79.15	6959.32

**Table 6** Result of TF-IDF vectorizer with unigram

No. of features	Null accuracy (%)	Accuracy score (%)	Train and test time(s)
20,000	50.64	77.71	143.37
40,000	50.64	77.82	160.75
60,000	50.64	77.89	171.19
80,000	50.64	77.88	179.32
100,000	50.64	77.94	184.35

**Result of Unigram with Custom Stop Words** (Table 3).

**Result of Bigram with Stop Words** (Table 4).

**Result of Trigram with Stop Words** (Table 5).

**Result of TF-IDF Vectorizer with Unigram** (Table 6).

**Result of TF-IDF Vectorizer with Bigram** (Table 7).

**Table 7** Result of TF-IDF vectorizer with bigram

No. of features	Null accuracy (%)	Accuracy score (%)	Train and test time(s)
20,000	50.64	78.99	232.1
40,000	50.64	79.62	250.55
60,000	50.64	79.73	276.66
80,000	50.64	79.62	277.56
100,000	50.64	79.88	289.16

**Table 8** Chart of algorithm name, accuracy and train test time using TF-IDF vectorizer

Algorithm name	Accuracy score (%)	Train and test time(s)
Logistic regression	79.7025042365	1391.8473668099
Linear SVC	79.0874286073	2852.5113706589
Linear SVC with L1-based feature selection	79.1313625808	3788.4052898884
Multinomial NB	77.6125023536	3464.3178443909
Bernoulli NB	76.2505491747	4009.3094704151
Ridge classifier	79.0748760434	3994.2744159699
AdaBoost	68.0411724095	5310.3148405552
Perceptron	72.2839389945	8347.0656085014
Passive-aggressive	76.2944831482	6820.8820326328
Nearest centroid	70.9408146614	4047.182826519

**TF-IDF Vectorizer Accuracy of Various Algorithms** (Table 8).

## 6 Output of the Tweet Analysis Module

The model is saved locally on disc via the python package “pickle”. Then, predictions are made by loading the model and making predictions on whether the tweet is positive or negative. The predictions along with their tweets are stored via pandas data frame as a .csv file. The screenshot of that .csv file is as follows (Figs. 8 and 9):

*Tweet ID versus Prediction Graph* (Figs. 10 and 11).

## 7 Application

The application leverages a variety of technologies to visualize a real-time stream of twitter data using sentiment analysis and word vector space mapping via Word2vec. It runs on a local Flask instance with a Redis/Celery back end and uses Socket.IO to

Predictor	Tweet-Text
0	1 getting ready for new week hope it goes fast could use nap now
1	0 got job interview tomorrow and fucken hate centrelink lol its just gives me the shits
2	1 had to unhook twitter from facebook because all my facebook cronies were complaining
3	0 lol unfortunately
4	1 often want to respond to your l) posts but am not your friend the gist of this one is
5	1 hey you
6	0 heyyyyyy not on myspace at all right now
7	0 wtf is it raining thought it was summer not spring
8	0 lol yes the warm due was killing my throat have ic now
9	0 just woke up we got paid today and am broke need moneyz
10	1 mmm had to make one for my daughter those smell so good
11	0 dont have no brain food think thats why cant sleep
12	0 no one owns twitter hashtags you can wish for it but you can not be rid of me tcot
13	0 doing homework for the rest of my life
14	0 my son had tubes put in but since one has fallen out he has had ear infections already this year
15	1 its my birthday weekend am spending it by relaxing of course will pamper myself love being independent every woman should be
16	0 time to get out of bed
17	1 thx watching ducking
18	0 awww
19	0 sad day
20	1 more daysss
21	0 has not had nookie for while

Fig. 8 Screenshot of .csv file containing the predictions of the tweet texts after running the model

Fig. 9 Unigram accuracy of “without stop words” versus “with stop words” versus “with custom stop words”

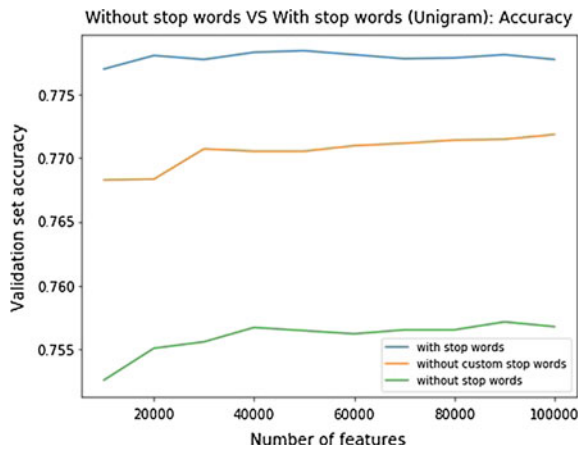
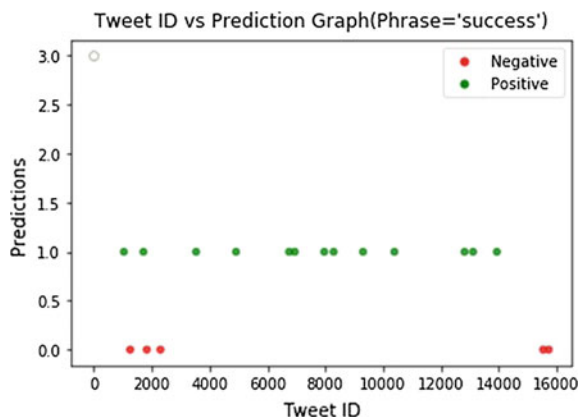


Fig. 10 Tweet ID versus Prediction Graph for phrase = “success” in real time



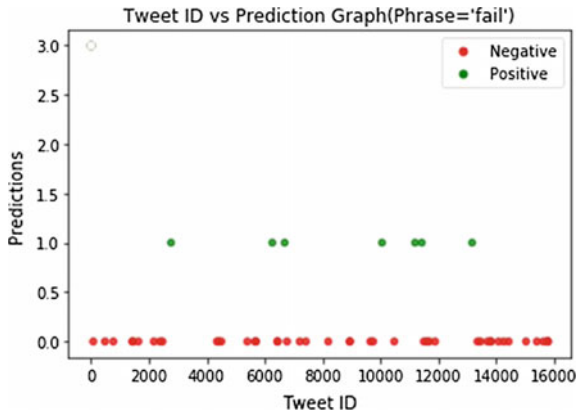


Fig. 11 Tweet ID versus Prediction Graph for phrase = “fail” in real time

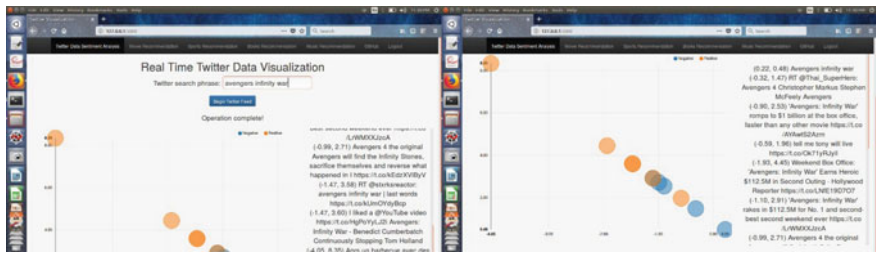


Fig. 12 Real-time Twitter data visualization with search phrase = “avengers infinity war”

push events to the Web client. Twitter integration is managed by the pattern library. NVD3 is used on the front end to create the visualization.

The snapshots of the application are as follows (Fig. 12):

## 8 Conclusion and Future Work

In this work, a system which analyses the tweets in real time was proposed for the identification of the sentiment in Twitter as either negative or positive using ensemble learning. It was concluded that if the data was cleaner, then the results obtained would be more accurate. The future scope of the project lies in the aspect that the sentiment analysis module can be integrated with other modules such as “Movie Recommender”, “Sports Recommender”, “Music Recommender”, “Book Recommender” to analyse the behaviour of a person and to group the people into clusters with common behaviour so that better and more accurate recommendations can be made which will benefit the society at large.



## References

1. I. Hemalatha, G.P.S. Varma, A. Govardhan, Social network analysis and mining using machine learning techniques. *Assoc. Adv. Artif. Intell.* **0020-0190**, 603–607 (2012)
2. B. Liu. Sentiment Analysis and Opinion Mining. *Assoc. Advancement of Artif. Intell.* 1947–4040 (2013)
3. M.A. Olowe, M.M. Gaber, F. Stahl. A Survey of data mining techniques for social media analysis. *ICAISC, Int. Conf. Artif. Intell. Soft Comput. J. Data Mining Digital Humanit. ACM Sigmod Record* **34(2)**, 18–26 (2014)
4. B. Pang, L. Lee, Opinion mining and sentiment analysis. *Found. Trends Inform. Retrieval* **2(1–2)**, 1–135 (2008)
5. D. Markovikj, S. Gievska, M. Kosinski, D. Stillwell. Mining facebook data for predictive personality modelling. *Assoc. Advancement Artif. Intell.* ([www.aaai.org](http://www.aaai.org)), **110(15)**, 5802–5805 (2013)
6. C. Costea, D. Joyeux, O. Hasan, L. Brunie. *A Study and Comparison of Sentiment Analysis Methods for Reputation Evaluation*. A. Collomb. Laboratoire d'Informatique en Image et Systèmes d'information, Rapport de Recherche, RR-LIRIS-2014-002 (2014)
7. E.F.G.M. Beig. Data mining techniques for web mining: A review. *Appl. Math. Eng. Manage. Technol.* **3(5)**, 81–90 (2015)
8. L.R. Goldberg. A broad-bandwidth, public domain, personality inventory measuring the lower-level facets of several five-factor models. 7–29 (1992)
9. K. Tao, C. Hauff, G.J. Houben, F. Abel, G. Wachsmuth. Facilitating twitter data analytics: platform, language and functionality. *IEEE Int. Conf.* 421–430 (2014)
10. A. Pak, P. Paroubek. Twitter as a corpus for sentiment analysis and opinion mining. in *Proceedings of the Seventh Conference on International Language Resources and Evaluation*, (2010), pp. 1320–1326
11. R. Parikh, M. Movassate. Sentiment analysis of user-generated twitter updates using various classification techniques. CS224 N Final Report (2009)
12. A. Go, R. Bhayani, L. Huang. Twitter sentiment classification using distant supervision. Stanford University, Technical Paper (2009)
13. A. Agarwal, B. Xie, I. Vovsha, O. Rambow R. Passonneau. Sentiment analysis of twitter data. in *Proceedings of the ACL 2011 Workshop on Languages in Social Media*, (2011), pp. 30–38
14. D. Davidova, A. Rappoport. Enhanced sentiment learning using twitter hash tags and smiley's Cooling: Poster. 241–249 (2010)
15. B. Wagh, J.V. Shinde, P.A. Kale, A Twitter sentiment analysis using NLTK and machine learning techniques. *Int. J. Emerg. Res. Manage. Technol.* **6(12)**, 2278–9359 (2017)
16. F. Rosenblatt, *Principles of neurodynamics: Perceptrons and the theory of brain mechanisms* (Spartan Books, Washington DC, 1961)
17. D.E. Rumelhart, G.E. Hinton, R.J. Williams. Learning internal representations by error propagation. *Parallel Distributed Processing: Explorations in the Microstructure of Cognition*, vol. 1 (Foundation, MIT Press, 1986)
18. G. Cybenko. Approximation by superpositions of a sigmoidal function. *Mathematics Control, Signals Syst.* **2(4)**, 303–314 (1989)
19. A.O. Steinskog J.F. Therkelsen. Characterizing Twitter data using sentiment analysis and topic modeling. Artificial Intelligence Group Department of Computer and Information Science Faculty of Information Technology, Mathematics and Electrical Engineering. Master's Thesis, Spring (2016)

# An Ensemble Learning-Based Language Identification System



Himadri Mukherjee, Sahana Das, Ankita Dhar, Sk. Md. Obaidullah,  
K. C. Santosh, Santanu Phadikar and Kaushik Roy

**Abstract** Speech recognition from multilingual voice signals is a challenging task. It is essential to distinguish the language of the spoken phrases prior to recognizing them. This is known as automatic language identification. Automatic language identification is very much important for multilingual countries like India as people often use more than a single language while talking. In this paper, a language identification system for seven different languages from the IIIT-H Indic Speech Databases is presented. We have used line spectral frequency-based features for modelling the languages. The highest accuracy of 99.71% has been obtained with ensemble learning-based classification technique.

**Keywords** Language identification · Line spectral frequency · Ensemble learning

---

H. Mukherjee (✉) · A. Dhar · K. Roy  
Department of Computer Science, West Bengal State University, Kolkata, India  
e-mail: [himadrim027@gmail.com](mailto:himadrim027@gmail.com)

A. Dhar  
e-mail: [ankita.ankie@gmail.com](mailto:ankita.ankie@gmail.com)

K. Roy  
e-mail: [kaushik.mrg@gmail.com](mailto:kaushik.mrg@gmail.com)

S. Das  
Department of Computer Applications, Narula Institute of Technology, Kolkata, India  
e-mail: [sahana.das@nit.ac.in](mailto:sahana.das@nit.ac.in)

Sk. Md. Obaidullah  
Department of Computer Science & Engineering, Aliah University, Kolkata, India  
e-mail: [sk.obaidullah@gmail.com](mailto:sk.obaidullah@gmail.com)

K. C. Santosh  
Department of Computer Science, The University of South Dakota, Vermillion, USA  
e-mail: [santosh.kc@usd.edu](mailto:santosh.kc@usd.edu)

S. Phadikar  
Department of Computer Science & Engineering, Maulana Abul Kalam Azad University of Technology, Kolkata, India  
e-mail: [sphadikar@yahoo.com](mailto:sphadikar@yahoo.com)

## 1 Introduction

There have been multifarious advances in the field of speech recognition. Though different speech recognition-based solutions to our daily lives have come up, residents of multilingual countries like India have not been fully able to take advantage of the same. Here, people often use phrases from different languages while talking which makes speech recognition difficult. A system which can identify the language of the spoken phrases can help towards better recognition by invoking the language-specific recognizers. This task of identifying the spoken language by machine is termed as automatic language identification.

Bekker et al. [1] used NIST language recognition challenge data set comprising of 50 languages for the purpose of their experiment. Language identification was carried out by training deep neural network using intra-cluster training technique. The said network consisted of two hidden layers of 200 and 100 neurons, respectively. Softmax output layer was used in conjunction with ReLU activation function together with mini back stochastic gradient descent technique with momentum for optimization. Confusion matrix-based cluster technique provided the most desirable result. Aarti et al. [2] employed ANN on 75 h of data from nine different Indian languages such as Marathi, Hindi, Bangla, Gujarati, Tamil, Malayalam, Assamese, Kannada and Telugu for the language identification. They achieved an accuracy level of 44.61% by using MFCC-based features including delta and double-deltas.

Revathi et al. [3] performed experiment on a corpus comprising of 1000 sentences from each of Hindi, Kannada, Bangla, Malayalam, Marathi, Tamil and Telugu, recorded in a studio environment. The obtained accuracy was 99.4%. Halder et al. [4] used particle swarm optimization feature selection method on four different languages, with contribution from 20 people. They used MFCC and LPC features. ANN was used for classification. The accuracy level was 88%. Koolagudi et al. [5] worked with 15 different Indian languages. Their system identified the languages using MFCC and GMM. From each language, 5 min of speech data was collected for training, and 1.5 min data each was used for testing. Validation was done using a clip of 2 s from each language.

Mukherjee et al. [6] presented a system for identifying three languages in the thick of English, Bangla and Hindi. They had used multiple devices for data collection and experimented with different scenarios. MFCC-based features and an artificial neural network-based classification technique produced the highest accuracy of 98.39% in their experiments. YouTube music videos were used by Chandrasekhar et al. [7] in an effort to identify 25 languages using content-based audio–visual features. Classification was done using SVM. For training and testing, 18,750 and 6250 videos were used, respectively. They obtained an accuracy of 48%. Mohanty [8] used SVM classifier to distinguish between four Indian languages using a single manner and 10 place features. He used corpora of 500 words for each language and obtained an accuracy of 89.75%.

In this paper, a system is proposed for the distinction of seven Indian languages from audio clips. The system uses line spectral frequency-based features and ensem-

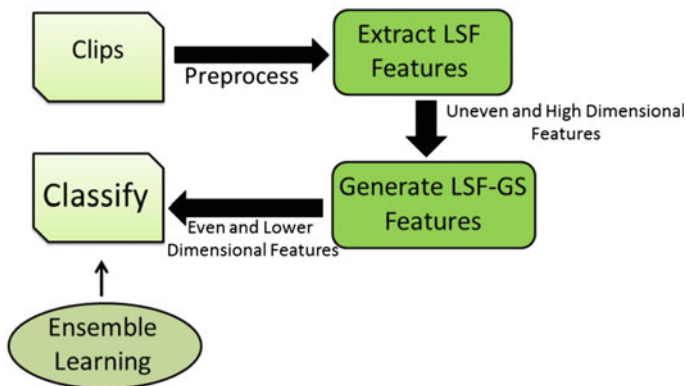


**Fig. 1** Block diagram of the proposed system

ble learning-based classification. The system is pictorially illustrated in Fig. 1. In the rest of the paper, the data set details and proposed methodology are presented in Sects. 2 and 3. The results are presented in Sect. 4, and we have concluded in Sect. 5.

## 2 Data Set

Speech and Vision Lab of IIT-H developed the Indic speech database [9] to design speech synthesis system in Indic languages. The database encompasses 7 languages in the thick of Marathi, Bengali, Kannada, Hindi, Malayalam, Telugu and Tamil. One of the reasons for choosing these languages was the large number of texts present in Wikipedia for each of these languages which was used as text corpus. The other reason was the accessibility on the campus of the people whose mother tongue was these languages. There are various dialects of each of these languages. Initially, speeches were recorded in the dialect of the language with which the speaker was comfortable. From each language, 1000 sentences were selected in such a way as to cover 5000 most common words. Studio environment was used to record the speech data from native speakers. They used a standard headset microphone connected to a Zoom handy recorder for recording the speech segments. Such a device was chosen primarily due to the fact that it was easy to operate. Headset was used to maintain a constant recording level by keeping a fixed distance between the microphone and the mouth. The length of data per language is tabulated in Table 1.

**Table 1** Details of the data set

Language	Bangla	Hindi	Malayalam	Tamil	Marathi	Telugu	Kannada
Duration (HH:MM)	1:39	1:12	1:37	1:28	1:56	1:31	1:41

### 3 Proposed Method

#### 3.1 Pre-processing

Manifold frequency components of audio signal always fluctuate for the total length. This interferes with the frequency-based analysis of the signal. To handle this, the signal is segregated into smaller frames. The spectral features within these frames incline to be pseudo-stationary. Continuity of two consecutive frames is ensured by framing the signals in overlapping fashion. If a signal has  $x$  points, then it can be subdivided into  $y$  frames of size  $z$  with  $o$  overlap points. The mathematical expression is demonstrated as below. The signals were divided into 256 samples point wide frames with an inter-frame overlap of 100 points due to the effectiveness as established [9].

$$y = \left\lceil \frac{x - z}{o} + 1 \right\rceil \quad (1)$$

Jitters should be removed from the frames as it causes spectral leakage during the analysis. In order to achieve this, the frames are generally multiplied with windowing function. Here, we used Hamming window ( $H(n)$ ) [10] which is illustrated below where  $n$  ranges from start to end of a frame of size  $N$ .

$$H(n) = 0.54 - 0.46 \cos\left(\frac{2\pi n}{N - 1}\right) \quad (2)$$

#### 3.2 Line Spectral Frequency—Graded Statistical (LSF-GS) Extraction

An exclusive method of representing linear predictive coefficient named line spectral frequency (LSF) was formulated by Itakura et al. [11]. It guaranteed both high interpolation and effective quantization policy.

Here, a signal is presented as the output of  $H(z)$  which is an all-pole filter whose inverse  $X(z)$  is shown below, where  $x_{\{1..T\}}$  are the predictive coefficients up to  $T$ th order.

$$X(z) = 1 + x_1 z^{-1} + \dots + x_T z^{-T} \quad (3)$$

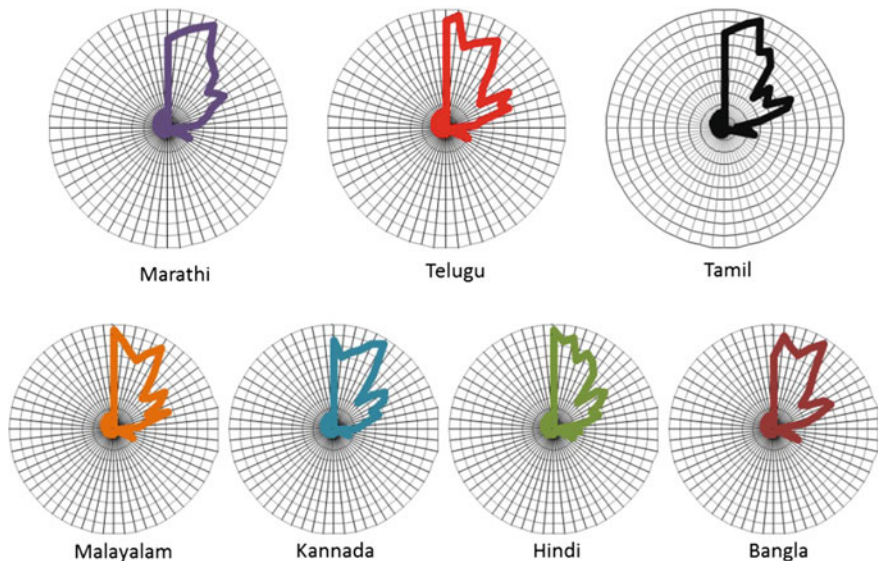


**Fig. 2** Trend of the of F4 (best result) for all the seven languages

The LSF representation is obtained by decomposing  $X(z)$  into  $X_1(z)$  and  $X_2(z)$  which are presented in the equations as under.

$$X_1(z) = X(z) + z^{-(T+1)}X(z^{-1}) \tag{4}$$

$$X_2(z) = X(z) - z^{-(T+1)}X(z^{-1}) \tag{5}$$

Five-, 10-, 15-, 20- and 25-dimensional frame-wise LSFs were extracted for the clips in our experiment which are denoted as  $F1-F5$ .

Since the clips were of different lengths, features of different dimensions were obtained. A clip of only 3 s produced 1320 overlapping frames. When only five-dimensional values were extracted for the clip, a feature of 6600 (1320 \* 5) dimension was obtained. In order to obtain features of even and lower dimension, the band values were graded based on total energy content in descending order which were used as features. Along with this, the mean and standard deviation values of the bands were also appended which produced the final feature set. Thus for the same case, a feature of 15 dimension (5 grade values, 5 mean values, 5 standard deviation values) was obtained which was independent of clip length. The trend of feature values for  $F4$  is presented in Fig. 2.

### 3.3 Ensemble Learning-Based Classification

In ensemble learning [12], multiple learners called ‘base learners’ are trained to produce classification on the same problem. The essence of ensemble-based decision-making or group-based decision is almost a second nature to humans and is thus a natural decision-making process. No decision-maker is perfect; i.e., every decision has a nonzero variability.

There are two components in any classification error: bias which signifies the accuracy and variance, which signifies the precision when multiple training sets are involved. Classifiers that have low bias usually have high variance and vice versa. Averaging tends to reduce the variance. The aim of the ensemble learning is to produce different classifiers that have a similar bias. Their outputs are combined by averaging to reduce the bias.

Random forest [13] is a bagging classifier with an ensemble of trees. For classification, an ensemble of trees each cast a vote for the predicted class. We have taken a bootstrap sample of size  $N$  from the training data set  $X = \{x_1, x_2, \dots, x_N\}$ . Samples are continuously selected from the training set and fit into the random forest tree  $T_b$ . The training set coupled with the recursive splitting technique is used to grow the tree. Pruning of the tree to an optimal size is done with cross validation. New observations ( $X$ ) are characterized by passing them down to a terminal node followed by majority voting. Output is the ensemble of trees  $\{T_b\}_1^B$ .  $(x_b, y_b)$  represents the sample classification pair for the ensemble  $b$ . A regression tree  $f_b$  is trained on the pair  $(x_b, y_b)$ . Once the training is complete, prediction for the new sample  $x_n$  is done by taking the average of the predictions from all the individual  $T_b$  on  $x_n$ . The prediction for the new point is

$$f^B(x_n) = \frac{1}{B} \sum_{b=1}^B T_b(x) \quad (6)$$

As part of evaluation, we had used  $k$ -fold cross validation. The value of  $k$  was varied whose details are presented in the next section.

## 4 Result and Discussion

### 4.1 Our Results

The obtained accuracies for  $F1$ – $F5$  using fivefold cross validation with all default parameters is presented in Table 2. It is observed that the highest accuracy was obtained for  $F4$ . We thus further experimented with this feature set.

The number of folds of cross validation was varied from 2 to 10 whose results are presented in Table 3.

**Table 2** Obtained accuracies for the different feature sets

Feature set	F1	F2	F3	F4	F5
Accuracy	95.60	99.34	99.54	99.69	99.61

**Table 3** Obtained accuracies for F4 using different folds of cross validation

Folds	2	3	4	5	6
Accuracy	99.50	99.66	99.70	99.69	99.71
Folds	7	8	9	10	
Accuracy	99.70	99.70	99.69	99.57	

**Table 4** Obtained accuracies for F4 and different training iterations with sixfold cross validation

Iteration	100	200	300	400	500
Accuracy	99.71	99.69	99.66	99.64	99.64

**Table 5** Obtained accuracies on F4 for different bag sizes

Bag size (As % of training set size)	25	50	75	100
Accuracy	99.51	99.64	99.61	99.71

It is seen that the best result was obtained for sixfold cross validation which points to the fact that the distribution of instances in the testing and training set was even in terms of variations in data.

Next, the number of training iterations was also varied from 100 to 500 which was evaluated with sixfold cross validation technique. The obtained results presented are in Table 4 where it can be seen that higher number of training epochs led to overfitting which ultimately brought down the accuracy.

The size of each bag during training was also varied based on the size of the training set. The size of the bags as a percentage of the training set size with the obtained accuracies is presented in Table 5 where it can be seen that the best result was obtained when the bag size was equal to the training set.

The confusion matrix of the best result (F4) after parameter tuning, i.e., sixfold cross validation at 100 epochs with a bag size equal to that of the training set, is presented in Table 6.

It is observed that Telugu and Hindi were recognized with 100% accuracy. Bangla and Telugu constituted the highest confused pair. Clips for these two languages were chosen randomly from the data sets, and it was observed that some of them had name of places and people and resources like “India” and “Wikipedia” to name a few. This could have led to such confusions.



**Table 6** Confusion matrix for F4 for sixfold cross validation with 100 training iterations and a bag size equal to that of the training set

	Marathi	Telugu	Tamil	Malayalam	Kannada	Hindi	Bangla
Marathi	999	1	0	0	0	0	0
Telugu	0	1000	0	0	0	0	0
Tamil	0	0	994	0	0	0	6
Malayalam	1	0	1	996	0	0	2
Kannada	0	0	0	0	999	0	1
Hindi	0	0	0	0	0	1000	0
Bangla	1	0	5	0	2	0	992

**Table 7** Recognition of individual languages by our system as compared to that of Revathi et al. [3]

	Marathi	Telugu	Tamil	Malayalam	Kannada	Hindi	Bangla	Total
Revathi et al. [3]	99.22	99.44	98.89	99.67	98.67	100	99.78	99.38
Our method	99.90	100	99.40	99.60	99.90	100	99.20	99.71

## 4.2 Comparative Study

Revathi et al. [3] have worked with the same data set. They have used different features and reported the highest accuracy of 99.38% (900 test instances per language). Our system performed better than the same, and we obtained the highest accuracy on 99.71%. The individual language-based accuracies for the two systems are presented in Table 7. It can be observed that a lowest accuracy of 98.67% was obtained for Kannada by Revathi et al. [3] while the lowest accuracy for our system was 99.20% for Bangla. Both the systems were able to achieve 100% recognition; only Hindi in the case of Revathi et al. [3], Telugu and Hindi for our system.

We further experiment with some popular classifiers in the thick of RBF, Naïve Bayes, SVM and LibLINEAR from WEKA [14]. The performance of the classifiers is presented in Fig. 3.

## 5 Conclusion

Here, a system is present for identification of seven Indic languages from the IIIT-H Indic speech databases. We have obtained an encouraging accuracy with a precision of 0.997. We will experiment with a larger data set and observe the robustness of the system by introducing noise. We also plan to an active learning [15] -based approach for handling live audio streams. In the future, we will use deep learning-

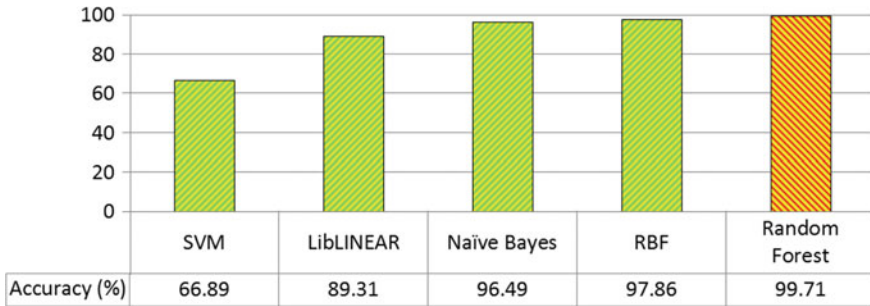


**Fig. 3** Results of different classifiers on F4

based approaches and incorporate voice activity detection [16] in our system as well to obtain better results. We will also use different feature selection techniques to reduce the feature dimension and obtain computational speedup.

## References

1. A.J. Bekker, I. Opher, I. Lapidot, J. Goldberger, Intra-cluster training strategy for deep learning with applications to language identification, in *Proceedings of MLSP-2016* (2016), pp. 1–6
2. B. Aarti, S.K. Koppurapu, Spoken Indian language classification using artificial neural network—An experimental study, in *Proceedings of SPIN-2017*, (2017), pp. 424–430
3. A. Revathi, C. Jeyalakshmi, T. Muruganantham, Perceptual features based rapid and robust language identification system for various Indian classical languages. *Comput. Vision and Bio Inspired Comput.* 291–305 (2018)
4. R. Haldar, P.K. Mishra, A novel approach for multilingual speech recognition with back propagation artificial neural network. *Int. J. Recent Innov. Trends Comput. Commun.* 4(5), 312–318 (2016)
5. S.G. Koolagudi, D. Rastogi, K.S. Rao, Identification of language using mel-frequency cepstral coefficients (mfcc). *Procedia Eng.* 38, 3391–3398
6. H. Mukherjee, A. Dhar, S. Phadikar, K. Roy, RECAL-A language identification system, in *Proceedings of ICSPC-2017* (2017), pp. 300–304
7. V. Chandrashekar Automatic language identification in music videos with low level audio and visual features, in *Proceedings of ICASSP-2011*, (2011) pp. 5724–5727
8. S. Mohanty, Phonotactic model for spoken language identification in Indian language perspective, *Int. J. Comput. Appl.* 19(9), pp. 18–24
9. K. Prahallad, E.N. Kumar, V. Keri, S. Rajendran, A.W. Black, The IIT-H Indic Speech Databases, in *Proceedings of INTERSPEECH-2012*, (2012), pp. 2546–2549
10. H. Mukherjee, S. Phadikar, K. Roy, An ensemble learning-based Bangla phoneme recognition system using LPCC-2 features, in *Proceedings of FICTA-2017*, (2017), pp. 61–69
11. F. Itakura, Line spectrum representation of linear predictor coefficients of speech signals. *J. Acoustical Soc. Am.* 57(S1), S35–S35 (1975)
12. T.G. Dietterich, *Ensemble Learning. The Handbook of Brain Theory and Neural Networks*, vol. 2, (2002), pp. 110–125
13. L. Breiman, Random forests. *Machine Learn.* 45(1), 5–32 (2001)
14. M. Hall, E. Frank, G. Holmes, B. Pfahringer, P. Reutemann, I.H. Witten The WEKA data mining software: An update. *ACM SIGKDD Explor. Newsletter* 11(1), 10–18 (2009)

15. M.R. Bouguelia, S. Nowaczyk, K.C. Santosh, A. Verikas, Agreeing to disagree: active learning with noisy labels without crowd sourcing. *Int. J. Mach. Learn. Cybern.* 1–13 (2017)
16. H. Mukherjee, S.M. Obaidullah, K.C. Santosh, S. Phadikar, K. Roy, Line spectral frequency-based features and extreme learning machine for voice activity detection from audio signal. *Int. J. Speech Technol.* 1–8 (2018)

# Kinect Sensor Based Single Person Hand Gesture Recognition for Man–Machine Interaction



Biswarup Ganguly, Priyanka Vishwakarma, Shreya Biswas and Rahul

**Abstract** The advancement of cameras and sensors has made a skyline for man–machine interaction (MMI). This paper aims to present an improved man–machine interaction by single person hand gesture recognition using Microsoft’s Kinect sensor. Using the skeletal images obtained from the sensor, six features are extracted from 20 body joints’ coordinates in 3D space. Artificial neural network with back-propagation learning algorithm is employed for classification. The proposed work outperforms the state-of-the-art algorithms and produces a recognition rate of 97.8%.

**Keywords** Kinect sensor · Gesture recognition · Artificial neural network · Backpropagation · MMI

## 1 Introduction

Gestures are visible body actions used for non-verbal communications to convey important messages. Gesture recognition [1] is a technology for the extraction of human’s meaningful expressions with mathematical interpretations through computing devices. Gestures can be of static and dynamic type. This technology has been implemented in various domains such as person identification [2], athletic performance analysis, robot control, surveillance, health care [3]. Single person hand gesture recognition is a significant topic in man–machine interaction (MMI) [4], which constitutes every possible communication way between a human and a machine.

---

B. Ganguly (✉) · P. Vishwakarma · S. Biswas · Rahul  
Department of Electrical Engineering, Meghnad Saha Institute of Technology, Kolkata, India  
e-mail: [bganguly@msit.edu.in](mailto:bganguly@msit.edu.in)

P. Vishwakarma  
e-mail: [vpriyanka705@gmail.com](mailto:vpriyanka705@gmail.com)

S. Biswas  
e-mail: [shreyabiswas2013@gmail.com](mailto:shreyabiswas2013@gmail.com)

Rahul  
e-mail: [singhbashu279@gmail.com](mailto:singhbashu279@gmail.com)

© Springer Nature Singapore Pte Ltd. 2020  
K. Maharatna et al. (eds.), *Computational Advancement in Communication Circuits and Systems*, Lecture Notes in Electrical Engineering 575,  
[https://doi.org/10.1007/978-981-13-8687-9\\_13](https://doi.org/10.1007/978-981-13-8687-9_13)

Saha et al. [5] have presented an improved human–computer interaction by Kinect sensor. Six Euclidean distances, i.e., distances between spine and centroids of six triangles formed by several hand joints, are extracted for building the feature space. Support vector machine is used for classification, and 88.7% accuracy is obtained. Varshini et al. [6] have used Kinect sensor for generating a depth map from which dynamic hand gestures are recognized by several algorithms. Hand detection using convex hull followed by finger identification followed by gesture classification is done to recognize dynamic gestures.

Pal et al. [7] have introduced Kinect sensor to recognize dynamic hand gestures for robotic link control. Skin and motion detection techniques are implemented, and Hu’s moments are taken as features from the input image. Finally, hidden Markov model is employed for recognizing gestures. Lai et al. [8] have established a system to detect fingertips and recognize hand gestures using Kinect sensor based on discrete curve evolution with an accuracy of 97.5%. Hussain et al. [9] have proposed an algorithm for hand gesture recognition based on deep learning using six static and eight dynamic hand gestures with 93.09% accuracy. Hand shapes are recognized followed by tracing the detected hands. In this work, 25 single person hand gestures, both single and double, are taken to generate a new data set, apart from [5], that can be used for better man–machine interaction. Instead of taking the RGB image and depth map as inputs in [7] and [8], our proposed work uses only the skeletal information of the subject and several complexities have been culminated and here lies the novelty of our work.

This paper aims to present hand gesture recognition for single person using Microsoft’s Kinect sensor. Out of 20 body joints, six body joints, i.e., shoulder center, spine, elbow right and left, hand right and left are used for making the feature space. Four Euclidean distances and two angles are extracted as features in 3D feature space per frame. For each input gesture, a 4-s video is recorded to extract the features. Artificial neural network with backpropagation learning algorithm is used for classification which yields an accuracy of 97.8%.

Section 2 describes the fundamental ideas of the proposed work. The algorithm and experimental results are illustrated in Sects. 3 and 4, respectively. The conclusion is drawn in Sect. 5.

## 2 Fundamental Ideas

The data acquisition is done by Kinect sensor [9, 10], which is a combination of an RGB camera, an IR emitter and receiver. The sensor is able to capture human skeleton along with twenty body joints’ coordinates in 3D space at a frame rate of 30. The sensor has a resolution of  $640 \times 480$  and can measure the depth at a range of 1.2–3.5 m.

Artificial neural network (ANN) [11] is an electrical analog of biological nervous system. It has a wide application in pattern recognition and classification problems. ANN with backpropagation (BP) learning algorithm [12] is a popular supervised

learning algorithm, where a number of hidden layers along with input and output layers are formed. This BP algorithm is based on the rule of gradient descent learning.

### 3 Proposed Algorithm

The block diagram of the proposed work is shown in Fig. 1. Let number of subjects selected are  $N$ , number of gestures executed by each person are  $G$ , and each gesture are taken for  $K$  instances. For each  $t$ th ( $1 \leq t \leq T$ ) frame, six body joints, e.g. spine (S), shoulder center (SC), elbow left (EL), elbow right (ER), hand left (HL) and hand right (HR), are selected for the proposed work. From these joints, Euclidean distances between S and EL, S and ER, SC and HL, SC and HR; angles formed by SC, EL, HL and SC, ER, HR are extracted as features.

The features are calculated using Euclidean distances and angles between six joints for a particular frame. Since the distance between subject and sensor plays a major role, normalization is applied on the average value of the  $z$  coordinate from  $S^t$  and respective body joints. Thus for  $t$ th frame, the six features are:

$$F_1^t = \frac{\|S^t - ER^t\|}{(S^{t,z} + ER^{t,z})/2} = 2 \times \frac{\|S^t - ER^t\|}{(S^{t,z} + ER^{t,z})} \quad (1)$$

$$F_2^t = 2 \times \frac{\|S^t - EL^t\|}{(S^{t,z} + EL^{t,z})} \quad (2)$$

$$F_3^t = 2 \times \frac{\|SC^t - HR^t\|}{(SC^{t,z} + HR^{t,z})} \quad (3)$$

$$F_4^t = 2 \times \frac{\|SC^t - HL^t\|}{(SC^{t,z} + HL^{t,z})} \quad (4)$$

$$F_5^t = \text{angle}(SC, EL, HL) \quad (5)$$

$$F_6^t = \text{angle}(SC, ER, HR) \quad (6)$$

For each input gesture performed by a subject, total frames produced are  $T$  and six features are extracted from each frame. Therefore, the feature space dimension becomes  $T \times 6$ . Since the database is comprised of  $N$  subjects and  $G$  gestures, the total dimension becomes  $N \times G \times T \times 6$ . Whenever an unknown gesture is performed in front of the Kinect sensor, the testing data dimension becomes  $T \times 6$ . For classification purpose, ANN with backpropagation learning is implemented as already stated in Sect. 2.

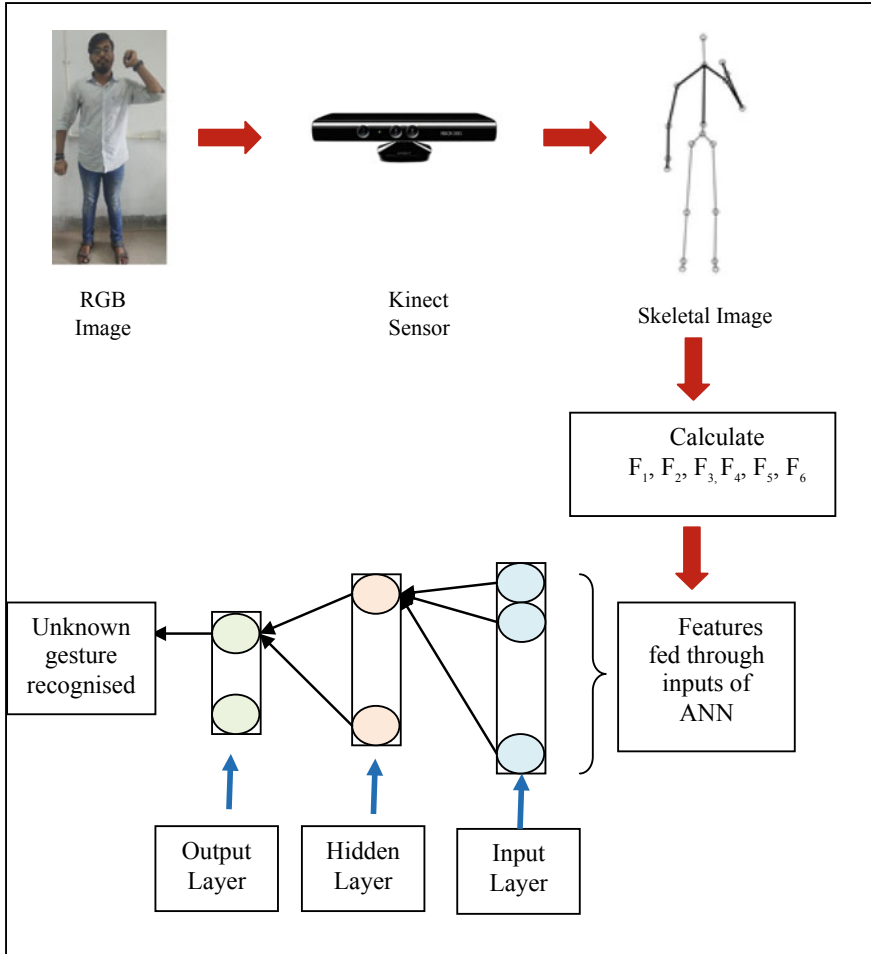


**Fig. 1** Block diagram for single person hand gesture recognition using artificial neural network

## 4 Experimental Results

In the proposed work, five new single person hand gestures, viz. clenched fist, crossed fingers, loser, praying and hand heart, are taken including the gestures in [5]. A number of participants taken are 80 in the age between 25 and 40 years, and each interaction is recorded for 4 s, i.e.  $T = 30 \text{ fps} \times 4 \text{ s} = 120$  frames. The calculation of features with three different frames is explained in Table 1. The performance of the proposed work is compared with  $k$ -nearest neighbor ( $k$ -NN), support vector machine (SVM) and ensemble decision tree (EDT) algorithms as given in Fig. 2.

**Table 1** Computation of features for unknown gesture

Frame no.	Feature no.	Feature value
12	1	0.1987
	2	0.2245
	3	0.6573
	4	0.6787
	5	144
	6	167
45	1	0.1944
	2	0.2265
	3	0.6518
	4	0.6639
	5	56
	6	168
95	1	0.2816
	2	0.2320
	3	0.7192
	4	0.1308
	5	13
	6	163

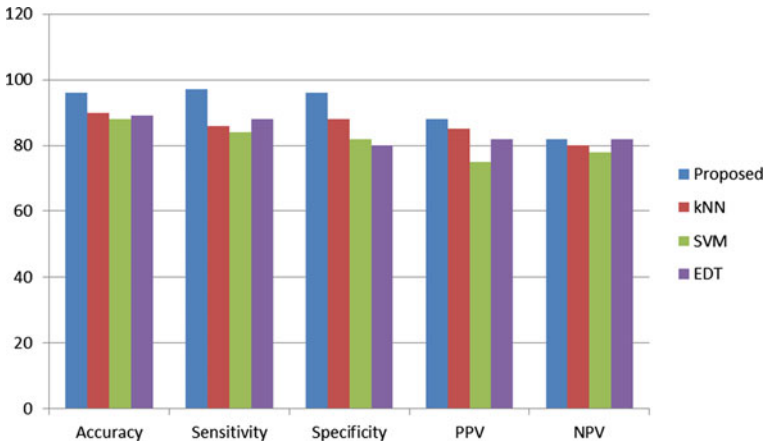


**Fig. 2** Performance comparison with standard classifiers



## 5 Conclusion

The proposed work recognizes 25 single person hand gestures to explore an enhanced man–machine interaction in an efficient way using Kinect sensor. Apart from the previous research [5], five new hand gestures have been incorporated to the data set for achieving increased accuracy and robustness of the system. A recognition rate of 97.8% has been achieved by employing backpropagation neural network which outperforms the state-of-the-art methods. The proposed research finds its application from man–machine interaction to gesture-based intelligent gaming. In the future, some statistical models like hidden conditional random field can be implemented for real-time gesture recognition.

**Acknowledgements** The research work is supported by Artificial Intelligence Laboratory, Department of Electronics and Tele-communication Engineering, Jadavpur University, India.

## References

1. S. Mitra, T. Acharya, Gesture recognition: a survey. *IEEE Trans. Syst. Man Cybern. Part C (Appl. Rev.)* **37**(3), 311–324 (2007)
2. A. k. Sadhu, S. Saha, A. Konar, R. Janarthanan, Person identification using Kinect sensor, in *2014 International Conference on Control, Instrumentation, Energy and Communication (CIEC)* (IEEE, 2014), pp. 214–218
3. Erik E. Stone, Marjorie Skubic, Fall detection in homes of older adults using the Microsoft Kinect. *IEEE J. Biomed. Health Inf.* **19**(1), 290–301 (2015)
4. T. Kapuscinski, M. Wysocki, Hand gesture recognition for man-machine interaction, in *2001 Proceedings of the Second International Workshop on Robot Motion and Control* (IEEE, 2001), pp. 91–96
5. S. Saha, B. Ganguly, A. Konar, Gesture based improved human-computer interaction using Microsoft’s Kinect sensor, in *2016 International Conference on Microelectronics, Computing and Communications (MicroCom)* (IEEE, 2016), pp. 1–6
6. M.R.L. Varshini, C. M. Vidhyapathi. Dynamic fingure gesture recognition using KINECT, in *2016 International Conference on Advanced Communication Control and Computing Technologies (ICACCCT)* (IEEE, 2016), pp. 212–216
7. D.H. Pal, S.M. Kakade, Dynamic hand gesture recognition using Kinect sensor, in *2016 International Conference on Global Trends in Signal Processing, Information Computing and Communication (ICGTSPICC)* (IEEE, 2016), pp. 448–453
8. Z. Lai, Z. Yao, C. Wang, H. Liang, H. Chen, W. Xia, Fingertips detection and hand gesture recognition based on discrete curve evolution with a Kinect sensor, in *Visual Communications and Image Processing (VCIP)* (IEEE, 2016), pp. 1–4
9. S. Hussain, R. Saxena, X. Han, J.A. Khan, H. Shin. Hand gesture recognition using deep learning, in *2017 International SoC Design Conference (ISOCC)* (IEEE, 2017), pp. 48–49
10. M.R. Andersen, T. Jensen, P. Lisouski, A.K. Mortensen, M.K. Hansen, T. Gregersen, P. Ahrendt, Kinect depth sensor evaluation for computer vision applications. *Tech. Rep. Electron. Comput. Eng.* **1**(6) (2015)
11. T.T. Dao, H. Tannous, P. Pouletaut, D. Gamet, D. Istrate, M.C. Ho Ba Tho, Interactive and connected rehabilitation systems for e-health. *IRBM* **37**(5–6), 289–296 (2016)
12. Lin Wang, Yi Zeng, Tao Chen, Back propagation neural network with adaptive differential evolution algorithm for time series forecasting. *Expert Syst. Appl.* **42**(2), 855–863 (2015)

# Artificial Intelligence-Based Economic Control of Micro-grids: A Review of Application of IoT



Promila Das, Sandip Chanda and A. De

**Abstract** India is a developing country, and the economic conditions of Indian citizen in some rural areas are ambiguous. It is extremely important to reduce the financial burden so that people can use electricity. Incorporation of solar and wind energy in a micro-grid along with a small storage unit can be used to feed a whole block of rural electricity demand which is absolutely pollution free and maintenance less. The only problem is the initial investment and recurring cost of misutilization of electricity. The micro-grids can be operated as an autonomous unit or may be used to share the load with the main grid for the area. During load shedding, which is a common phenomenon during summer, a storage unit will be used as a backup. These micro-grids are connected with bus bars that are directly connected with remote terminal unit which can feed us the necessary data for optimization. As several units are a part of this optimization, artificial intelligence (AI) may be used for a quicker and improved solution with the available data bank of the resources. The data bank can be optimized in a cloud-based server, and the whole electrical network can be controlled by a cyber-physical network or Internet of things (IoT) technology. Optimization can be used to upload the data in the cloud computing server. This paper presents a review of excellent endeavors in the field of IoT-based micro-grid control in the recent past. The review also includes a conceptualization of a method which may substantially reduce the budget of electricity in rural areas of a process that may be beneficial for people dwelling in rural areas.

**Keywords** IoT · Micro-grids · Artificial intelligence · RES

---

P. Das (✉) · S. Chanda

Electrical Engineering Department, Narula Institute of Technology, Kolkata, India  
e-mail: [promiladas27@gmail.com](mailto:promiladas27@gmail.com)

S. Chanda

e-mail: [sandipee1978@gmail.com](mailto:sandipee1978@gmail.com)

A. De

Electrical Engineering Department, IEST Shibpur, Shibpur, India  
e-mail: [abhinandan.de@gmail.com](mailto:abhinandan.de@gmail.com)

© Springer Nature Singapore Pte Ltd. 2020

K. Maharatna et al. (eds.), *Computational Advancement in Communication Circuits and Systems*, Lecture Notes in Electrical Engineering 575,  
[https://doi.org/10.1007/978-981-13-8687-9\\_14](https://doi.org/10.1007/978-981-13-8687-9_14)

## 1 Introduction

Electricity is a major form of energy that is continuously being required for nearly all the operations nowadays. It is quite a dreadful that even now the penetration of solar power has not reached the rural India. Due to the vastness of the country, it is not commercially viable always to erect transmission lines to dispatch electrical energy in the furthest corners of the country.

Moreover, the traditional way of generating electricity is causing profound environmental concern which is also considerable in enlightening the darkened part of the country. Micro-grid can be a solution because it can be designed to be environment friendly and also does not require the support of traditional transmission unit to reach the consumer end [1].

The reliability of electricity is one of the major concerns apart from the above, which should be taken care of, so as to provide seamless power supply to the consumer end. The consumer end faces serious interruption of power due to the booming occurrences of load shedding. These frequent occurrences of load shedding cause eloquent losses of power, thus striking the economic growth of the country [2].

Having stated that, another phenomenon comes into focus. Connecting a micro-grid with the main grid system can also be counterfeit as a conglomeration of numerous transmission lines congests at one period. This conglomeration can result in congestion in transmission lines, thus resulting in reduction of efficiency and an increment in expenditure and transmission line losses.

This phenomenon arises a question to the functionality of existing transmission line system and also speculates the idea of reducing transmission losses and in turn reducing the expenditure of electricity consumption. To implement this perception in the substantial world, it is necessary to create an algorithm using artificial intelligence in such a way that all the transmission lines can be monitored and the precise transmission line can be chosen which can provide the abbreviated pathway for transmitting electricity to the micro-grid. The program formulated based on Particle Swarm Optimization (PSO) or genetic algorithm (GA) or evolutionary algorithm (EU) will be done in two stages, first is to choose the transmission lines suitable for micro grid interconnection and also in the second to optimize the micro grid operation. A lot of data will be needed from the traditional grid and the micro-grid for this optimization. To generate the data, sensors have been used receivers, transmitters will be required forming an Internet of all these things (IoT) so that it can be accessed from any domicile of the world.

This facility is supposed to enable the user or the end consumer to develop its own characteristics known as demand response which is beneficial for them as the same will minimize their payment cost. It is also beneficial for the whole system as the same will reduce the wastage of electricity. A micro-grid consumer can monitor its own system and accordingly control the overall power system optimization by providing their anticipated demand for the next frame of time suitable for the next hour. This paper is an accumulation of research work in the field of micro-grid and application of IoT in controlling the operation of such grid in an optimized way.

Research work in the relevant field has been presented in this paper to highlight the major contribution in this field and also a discussion pertinent to each of these relevant works. A conceptualization in the same direction led by the most important works has been also presented in this paper. For the sake of the review of the works, it was imperative to also conduct a review of traditional micro-grid optimization techniques, which is also presented at the preamble of the work.

## 2 Review of Works Related to Micro-grid

### 2.1 Traditional Micro-grids

An excellent in endeavor has been presented in [3] where the energy storage system will be able to control the voltage provided by the bus, which is being fed by a DC source, independent of the operating micro-grid and the operating value is set with respect to the energy management rules (Fig. 1).

Advantages: (1) The approach which is conferred in the paper presented facilitates the utilization of protractible consumption and generation patterns for various components inculcated in a micro-grid. (2) The theory presented will sustain the elimination of time critical control mode changes, culminating from distortions occurring in a grid or energy management conditions, thus enabling recurring budget curtailment. Disadvantages: If this approach was implemented along with IoT, then it could have been accessed from any domicile of the world so that we can control and reroute the

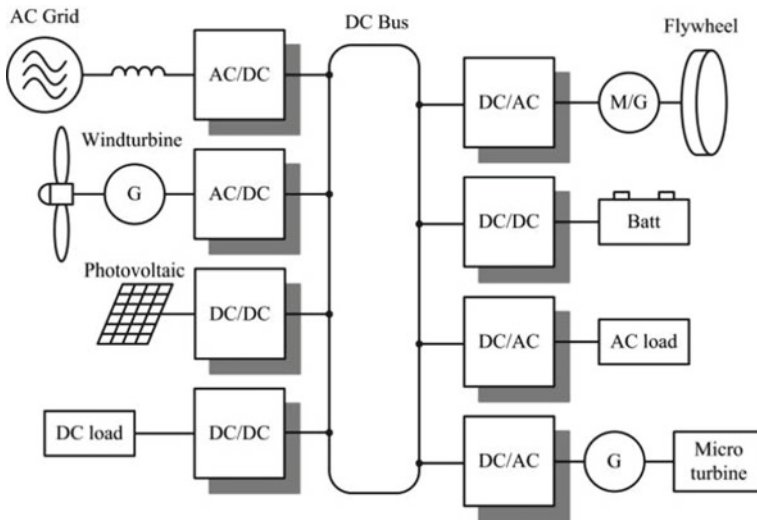


Fig. 1 DC voltage control (source [3], p. 2)

path of transmission and the optimization can be performed according to people's contentment.

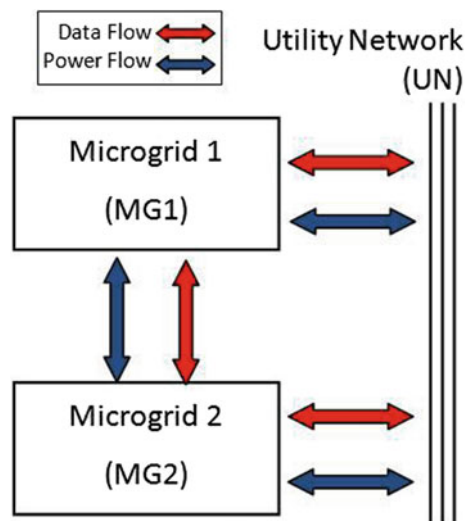
An excellent endeavor has been presented in [4] where simulation has been performed and interconnection made depending on random variable required for temporary storage and cost associated with generation and coordination action for triennial controlling between the central controllers of micro-grid (Fig. 2).

*Advantages:* (1) The interconnection between micro-grid will be able to determine and propose voltage control mechanism for transmitting power from DC generation to utility grid. (2) The combination of battery and super condensers has been presented that allow rapid respond and a bulk energy output. *Disadvantages:* A micro-grid connected with bus bars can be directly connected with remote terminal unit which can feed us the necessary data for Optimization. A program formulated based on particle swarm optimization can be used to upload the data in the cloud system of the IoT so that it can be accessed from any domicile of the world, thus achieving the objective of reducing the budget of transmission system so that people dwelling in rural domicile all around the globe can be benefitted.

An excellent endeavor in the similar field has been presented in [5] where AC-DC hybrid micro-grid has been developed to incorporate renewable energy sources in the grid (Fig. 3).

*Advantages:* (1) With the accelerating implementation of distributed generation/storage element interfacing converters, unbalances in harmonics and voltage distortions can be controlled. (2) The renewable generation and its effective collaboration with DC systems make it more efficient than the conventional AC system. This AC-DC hybrid system also enables the user to integrate each power source with one another. *Disadvantage:* Though this work has prudently addressed an efficient way of integrating non-conventional energy sources, it has not been objected

**Fig. 2** Power interconnection scheme of utility network and micro-grids (source [4], pp. 3–4)



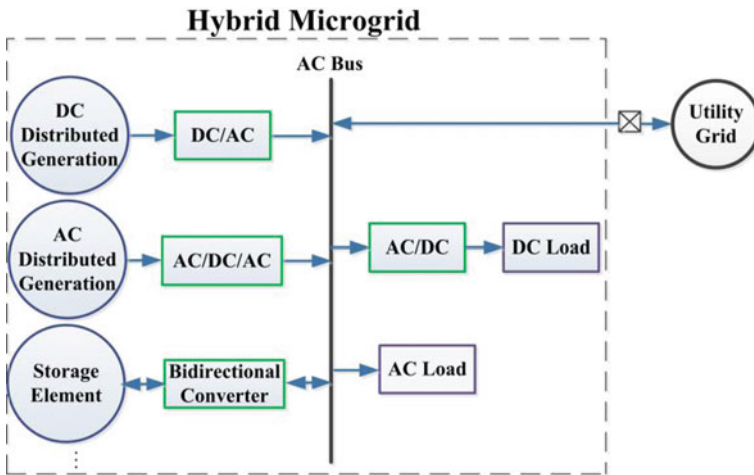


Fig. 3 AC-DC hybrid micro-grid (source [5], p. 2)

toward minimization of investment charge and subsequent recurring cost of the system. Connection of main grid system with micro-grids is a prevalent phenomenon which can be seen nowadays. But the main objective will be to reduce the cost of transmission so that the people of developing India can be benefited. In that case, just having made a model of hybrid AC or DC system cannot give us a complete balanced output so as to serve Indian citizen. It is much more important to optimize the transmission lines in such a way and so that the faults in the transmission lines can be detected and the most abbreviated pathway for transmitting the electricity can be chosen so that the budget of electricity consumption can be reduced and also that it can be accessed from any domicile of the world so that we can control and reroute the path of transmission and the optimization can be performed according to people’s contentment.

Indian rural micro-grid based on Arduino system focusing on distributed generation agent system has been presented in [6] which cynosures on monitoring and control of a micro-grid system (Fig. 4).

Advantages: (1) The nomenclature illustrates a compressed and abridged design as admissible parameter from a micro-grid is taken into consideration. (2) As implementation of the system if done using an Arduino microcontroller, the inputs from the various distributed generation agent are appropriately processed and channeled to the distribution agent. Disadvantage—It is a compacted and simplified design micro-grid along with a small storage unit can be used to feed a whole block, and during load shedding, this storage unit will be used as a backup. These micro-grids are connected with bus bars that are directly connected with remote terminal unit which can feed us the necessary data for optimization. A program is being formulated based on particle swarm optimization and can be used to upload the data in the cloud system of the IoT so that it can be accessed from any domicile of the world,

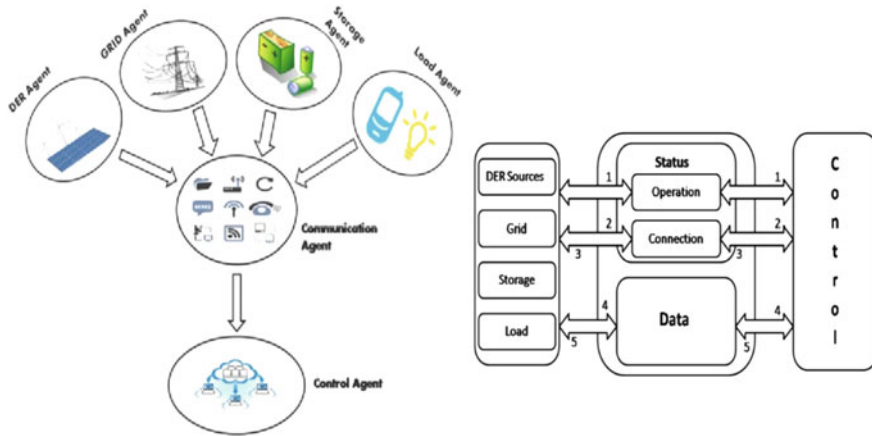


Fig. 4 Multi-agent collaboration schematic (source [6], pp. 2–3)

whereas in an Arduino system, an artificial intelligent system has to be installed so as to achieve the objective of reducing the budget of transmission system so that people dwelling in rural India can be benefitted. Moreover, these grid systems cannot be accessed from any domicile of the world, whereas the proposed theory in this paper of incorporating IoT can help monitor this multi-agent system from any domicile of the world.

Similar work has been found as [7] where an economically feasible architecture has been presented which is able to provide electricity to populace residing off the grid system (Fig. 5).

Advantage: (1) The model presented can connect relatively smaller and weaker with the grid power system and can also connect self-feeding communities with the weaker grid. (2) The proposed theory of dispersed generation sources can eloquently control and distribute power to the off-grid populace. Disadvantages: Firstly, having a DC micro-grid connected with the main grid system can be a conglomeration of numerous wires, which may cause congestion in the transmission system. Using Newton Raphson algorithm with the PMU can only be beneficial for power management. But this model will not be able to distinguish the abbreviated route nor will it be able to detect fault in the lines. Instead, if RTUs are connected with each bus bar, and a much effective optimization technique (PSO) is used, both fault analysis and budget reduction can be achieved.

## 2.2 Artificial Intelligence and IoT-Based Micro-grids

An excellent endeavor in the field of multi-agent residential DC micro-grid enabled with Internet of things (IoT) is presented in [8] where minimization of electricity

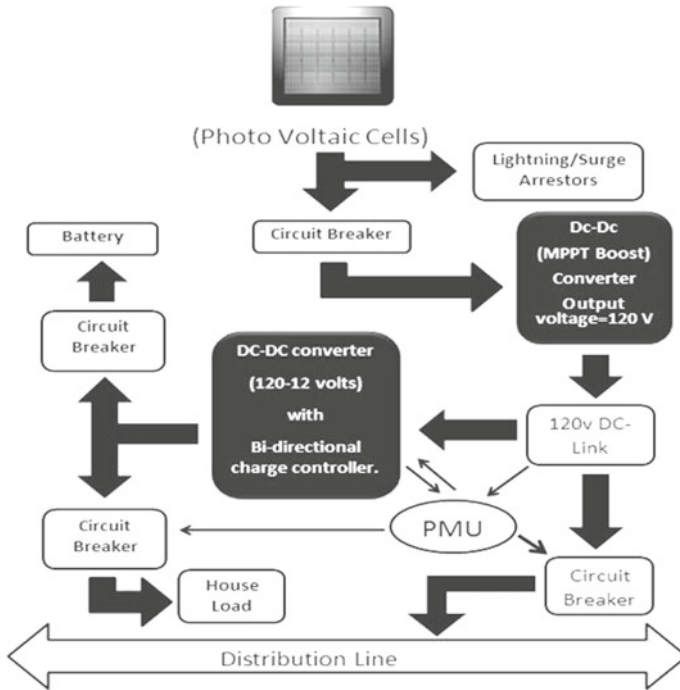


Fig. 5 DC distribution line connected to one isolated house (source [7], p. 1)

budget is achieved alleviating the peak load of the RDCNG. Advantages: (1) The proposed system will be able to provide the necessary reinforcement of power for a whole apartment even if the grid system faces major outages or blackout. (2) This multi-agent system has been objected toward minimization of investment charge and subsequent recurring budget of the system (Fig. 6).

Disadvantage—Incorporating Internet of things enables multi-agent system for residential DC micro-grid consisting of smart home agents can be beneficial for a group of people living in urban India who have the ability to cope up with different situation and can spend an enormous amount of money without any kind of hesitation. But if the same is implemented in rural India where the people earns money with agricultural means only are not benefited by this kind of Smart home techniques. So in order to reduce the budget of transmission and also to reduce the budget of electricity consumption for a vast group of people living in India, it is much more important to optimize the transmission line in such a way that it can detect faults and also to reduce the area by which the electricity is transmitted so that the losses can be reduced, and thus, the electricity consumption can be reduced. An intelligent RTU system is being attached to the bus bars which can provide us with the basic data of the transmission and a smart algorithm is being formulated and uploaded in the cloud system of an IoT, which can be accessed from any domicile of the world



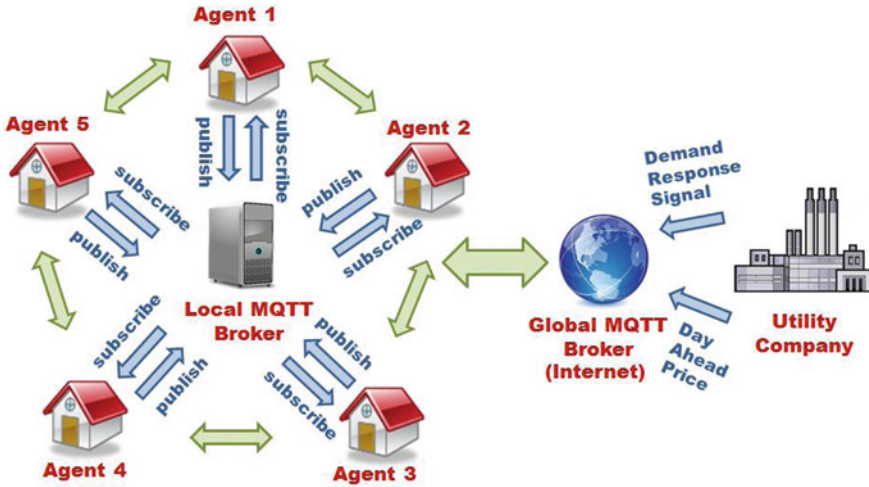


Fig. 6 Proposed IoT-enabled MAS communication architecture (source [8], pp. 3–4)

so that we can control and reroute the path of transmission and the optimization can be performed according to people’s contentment.

Similar work has been found as [8] where a system is automated with the help of IoT in such a way, so that it can constantly monitor each and every parameter relating to electrical engineering, in a DC micro-grid [9]. Advantages: (1) During fault condition, this system detects and alerts occurrences of various fault condition and ensures the clearance of these faults whenever necessary. (2) As the system is developed using the concept of Internet of things, the detection and clearance of the fault condition can be accessed and control from domicile of the world. Disadvantages: If a small storage unit would have been implemented along with the DC micro-grid, then during load shedding people would not have suffered from the scorching heat of summers in India. Only the clearance of faults will not be able to solve the dilemma of people dwelling in rural India. If the congestions in the transmission line system can be eliminated and the flow of current through the transmission lines can be rerouted to the abbreviated path, then the budget of transmission line will also be reduced and people in rural India will be benefitted.

A cloud-based optimization methodology has been depicted in [10] to control power flow in micro-grids in a possible efficient manner. Unlike the previous work [9], this work operates only with renewable energy sources forming islanded network or micro-grid.

Advantages: (1) This noble technology administers profusion in the DC transmission lines, thus saving the micro-grid system from major power cuts. (2) This noble approach minimizes deprivation, thus reducing losses occurring in a power grid. Disadvantages: Firstly, an optimal routing should be able to optimize the faults and also be able to detect the shortest route for transmitting electricity; this can not only reduce the cost of transmission, but also detect faults in line and reroute the flow of

electricity through the next abbreviated pathway. Being a cloud based approach the work also is efficient and it results is also easily accessible but it does not substantiate the method of optimization in case of simultaneous operation of different modules of micro grid (Fig. 7).

An excellent approach has been presented in [11] where integration of renewable energy sources in a smart grid infrastructure has been optimized with the help of an artificial intelligent algorithm. Advantages: (1) Incorporation of renewable source of energy revamps the standard of electric power supply with highest reliability at minimum prize. (2) Optimum utilization of resources such as generator characteristic,

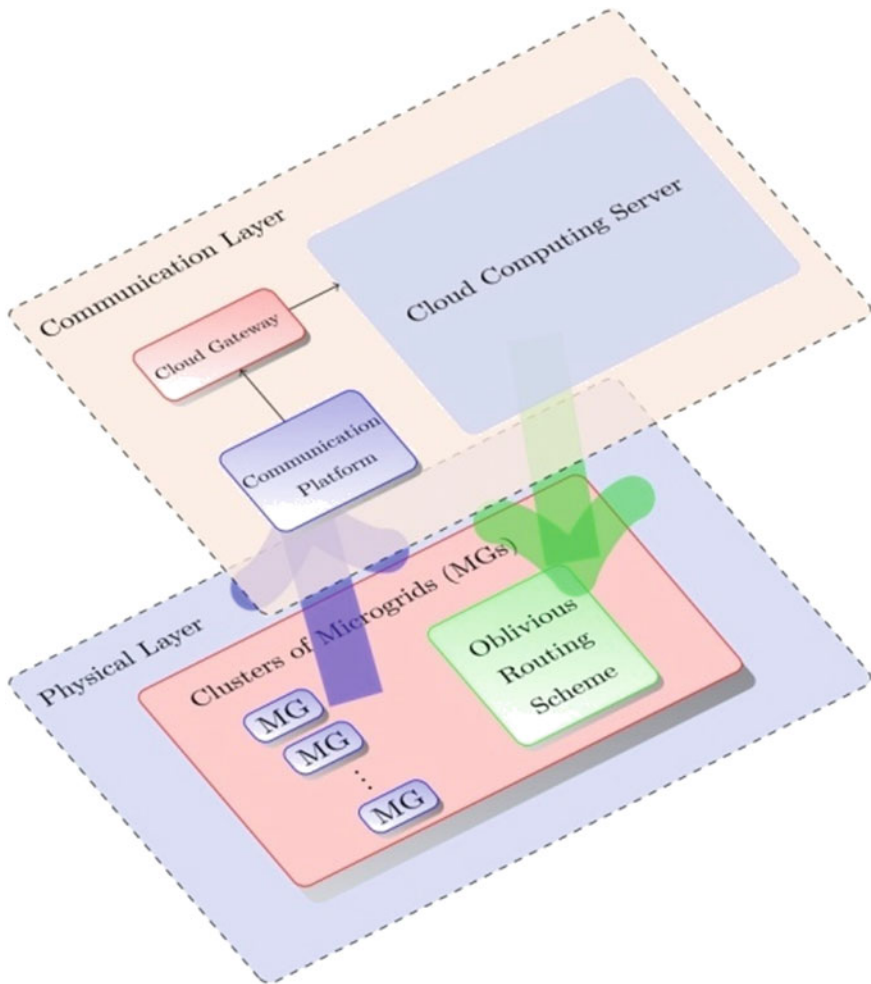


**Fig. 7** Cloud-based simulation platform for incognizant routing of DC micro-grids (source [10], pp. 4–5)

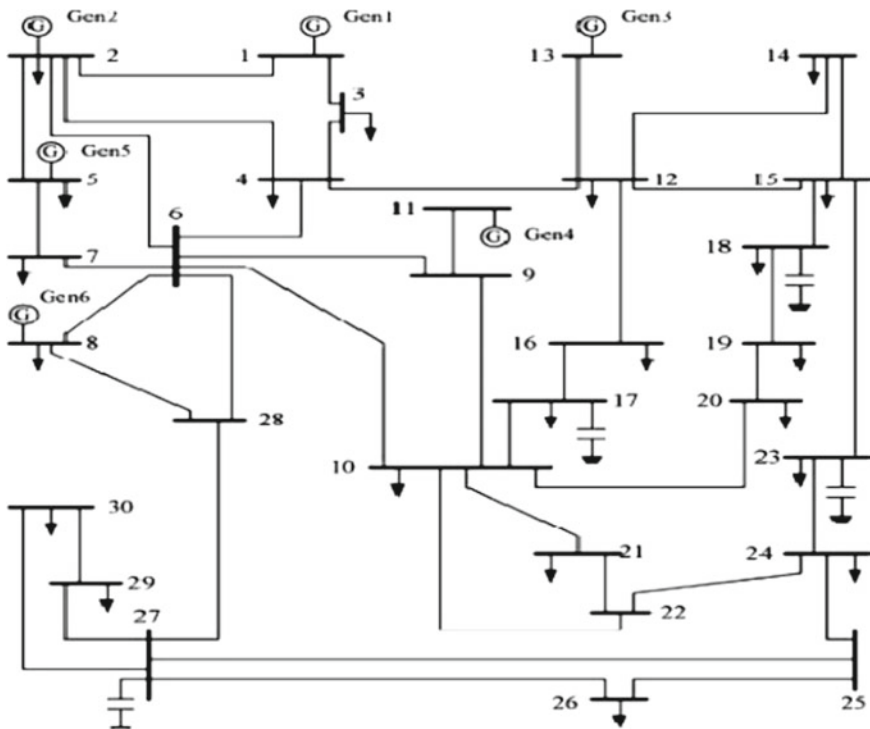


Fig. 8 Standard IEEE 30 bus system (source [11], pp. 7–8)

demand response, optimizing load curtailment, cost of generation transmission line loss and congestion can be optimized with a single artificially intelligent algorithm. Disadvantages: The only disadvantage this approach lacks is the implementation along with IoT so that it could have been accessed from any domicile of the world (Fig. 8).

### 3 Conclusion

India is a developing country, and the economic conditions of Indian citizen in some rural areas are ambiguous. Still now majority of people dwelling in rural areas are without the access of electricity and its benefits. The proposed methodology is an endeavor of integration between two most promising renewable source of energy that is solar and wind. This hybrid micro-grid is optimized in such a way that optimum utilization of micro-grid resources can be achieved with the purpose of social welfare. In order to accomplish the objective of monitoring the transmission lines, remote terminal units are attached with the bus bars. These RTUs are devices used for remote

monitoring and control of various devices and system for automation. Without the presence of this kind of innovative budget discovery mechanism and methodology, both the optimality of economic operation and reliability of power supply cannot be maintained.

The use of artificial intelligence is procured in this paper so as to optimize the transmission lines in such a way that the most abbreviated pathway for transmitting electricity can be selected and also the faults in a particular transmission line can also be detected so that the optimum utilization of power can be achieved, thus reducing the budget of transmission. This formulated artificially intelligent algorithm is then uploaded in the cloud system of an IoT which can be accessed from any domicile of the world so that the path of transmission can be controlled and rerouted and optimization can be performed according to people's contentment. Thus, the budget of transmission will also be reduced and the people dwelling in rural areas of the world will also be benefited.

## References

1. ABB on the Indian Subcontinent, <https://new.abb.com/indian-subcontinent>
2. A.H. Pasha, W. Saleem, The impact and cost of power load shedding to domestic consumers, USAID, Pakistan (2012)
3. L.E. Zubietta, Power management and optimization concept for DC micro grids, in *IEEE Conference*, Oakville, Ontario, Canada (2015)
4. J. Mírez, A modeling and simulation of optimized interconnection between DC micro grids with novel strategies of voltage, power and control, in *IEEE*, Lima, Peru (2017)
5. F. Nejabatkhah., Overview of power management strategies of hybrid AC/DC micro grid. *IEEE J.*, 0885–8993 (2013)
6. D. Purusothaman, R. Rajesh, K.K. Bajaj, V. Vijayaraghavan, Implementation of Arduino-based multi-agent system for rural Indian micro grids, in *IEEE Conference ISGT Asia* (2013)
7. R. Farooq, L. Mateen, M. Ahmad, S.Q. Akbar, H.A. Khan, N.A. Zaffar, Smart DC microgrids: modeling and power flow analysis of a DC micro grid for off-grid and weak-grid connected communities, in *IEEE Conference*, Lahore, Pakistan (2014)
8. A. Adhikaree, H. Makani, J. Yun, W. Qiao, T. Kim, Internet of Things-enabled multiagent system for residential DC microgrids, in *IEEE Conference*, USA (2017)
9. S. Sujeeth, O.V. Gnana Swathika, IoT based automated protection and control of DC microgrids, in *ICISC* (2018). ISBN 978-1-5386-0807-4
10. M. Hadi Amini, K.G. Boroojeni, T. Dragičević, A. Nejadpak, S.S. Iyengar, F. Blaabjerg, A comprehensive cloud-based real-time simulation framework for oblivious power routing in clusters of DC microgrids, in *IEEE Conference* (2017). ISBN 978-1-5090-4479-5/17
11. S. Chanda, A. De, An artificially intelligent algorithm and methodology to integrate renewable energy sources in the smart grid infrastructure: a demand response approach, in *IEEE* (2017)

# Analysis of Heart Rate Variability to Understand the Immediate Effect of Smoking on the Autonomic Nervous System Activity



Prerana Talukdar, Suraj Kumar Nayak, Dibyajyoti Biswal, Anilesh Dey and Kunal Pal

**Abstract** Over the past few decades, the heart rate variability (HRV) analysis has gained importance as a noninvasive technique for understanding the autonomic nervous system (ANS) activity. The work presented in this paper aims to identify the immediate change in the ANS activity because of smoking using HRV analysis. The ECG signals were collected from 17 male volunteers before and after smoking. The RR intervals (RRIs) were extracted and subjected to HRV analysis, resulting in the extraction of 29 HRV parameters. Both linear and nonlinear methods were employed to detect the statistically important HRV parameters. The interpretation of the statistically important features suggested that smoking reduced the parasympathetic activity, thereby suggesting the alteration in the ANS activity. ANN classification of the statistically significant HRV parameters with accuracies  $\geq 90\%$  further evinced the alteration in the ANS activity.

**Keywords** Electrocardiogram · RR intervals · Smoking · Heart rate variability

## 1 Introduction

The addiction of people to smoking is increasing day-by-day worldwide. Plenty of research has been performed to understand the harmful effects of smoking on human health like cancer, emphysema, and cardiovascular diseases. Over the decades,

---

P. Talukdar · S. K. Nayak · D. Biswal · K. Pal (✉)

Department of Biotechnology and Medical Engineering, National Institute of Technology, Rourkela 769008, India

e-mail: [kpal.nitrkl@gmail.com](mailto:kpal.nitrkl@gmail.com)

P. Talukdar

Department of Biomedical Engineering, JIS College of Engineering, Kolkata 741235, India

A. Dey

Department of Electronics and Communication Engineering, Narula Institute of Technology, Kolkata 700109, India

e-mail: [anilesh.dey@gmail.com](mailto:anilesh.dey@gmail.com)

© Springer Nature Singapore Pte Ltd. 2020

K. Maharatna et al. (eds.), *Computational Advancement in Communication*

*Circuits and Systems*, Lecture Notes in Electrical Engineering 575,

[https://doi.org/10.1007/978-981-13-8687-9\\_15](https://doi.org/10.1007/978-981-13-8687-9_15)

smoking has emerged as a major preventable reason of cardiovascular diseases (e.g., myocardial infarction, ventricular fibrillation, and even sudden death) [1]. On the basis of the recent evidences, it has been predicted that the deaths due to smoking will be more than 8 million per year by 2030 [2]. This may be attributed to the steady increase in the number of smokers worldwide even after the occurrence of antismoking campaigns as well as the expected global expansion of the tobacco epidemic in the upcoming years [3]. The cardiac electrophysiology is controlled by the ANS through its vagal and sympathetic nerve innervations to the sinoatrial node [4]. These two nerve innervations have opposite actions. The parasympathetic nerves try to reduce the heart rate by releasing acetylcholine, whereas the sympathetic nerves are responsible for increasing the heart rate by releasing norepinephrine. At resting condition, the activation of both parasympathetic and sympathetic nerves should be akin. The higher activity of sympathetic nerves or the reduced parasympathetic activity at resting condition hints the susceptibility to various pathological conditions, whereas the higher vagal tone at resting condition indicates good cardiac health and lower biological age.

Therefore, the understanding of the ANS activity has emerged as a tool to divulge information about the various cardiac abnormalities. Among the different techniques used to study the ANS activity, the HRV analysis has gained much importance due to its noninvasive nature. The occurrence of any abnormality in the HRV has been reported to be linked to the cardiovascular diseases and divulge prognostic information about the harmful outcomes [1]. The HRV analysis aims at studying the alteration in the time duration of successive cardiac cycles [5]. It involves the study of the parameters computed from the RR interval (RRI) signals using time, frequency and nonlinear methods. The time-domain HRV parameters are extracted using the statistical or geometric analysis of the instantaneous heart rate or the RRI signal. On the other hand, the frequency-domain HRV parameters are obtained from the distribution of power/variance of the RRI signal as a function of frequency. Both the parametric (e.g., autoregressive model) and nonparametric techniques (e.g., fast Fourier transform (FFT)) have been used to estimate the frequency-domain HRV parameters. The nonlinear HRV parameters are helpful to identify the hidden patterns in the RRI signal which may be looking like a random signal and the techniques of dynamical system analysis are used for the extraction of the nonlinear HRV parameters. The analysis of HRV has been reported to be useful for indicating the current occurrence of a disease and a marker of the upcoming cardiac diseases [6]. Apart from this, the HRV has been widely explored for understanding the alteration in the sympathovagal balance due to stimuli like smoking. It has been reported by researchers that the HRV of smokers may vary in an age-dependent manner. The smokers of age  $\geq 30$  years have shown to have lower HRV than the smokers having an age of  $\leq 30$  years [1]. The smoking cessation programs are being conducted worldwide nowadays to encourage the people to abstain from smoking. Harte and Meston examined the HRV of 62 male smokers to understand the influence of smoking cessation on the ANS activity [7]. The volunteers were undergoing an 8-week long smoking cessation program, where they were treated with a transdermal nicotine patch. The HRV of the volunteers was analyzed before the starting of the smoking cessation program, in the middle

of the program and 4 weeks after the completion of the program. The results suggested that the volunteers, who quit smoking, had enhanced HRV than those, who were found to relapse smoking at follow-up during and after the smoking cessation program. Thus, the study supported the fact that the abstaining from smoking can improve the HRV and hence the ANS activity. Taralov et al. (2015) [8] examined the variation in the ANS activity among the smokers and the non-smokers through HRV analysis [8]. The study involved 14 smokers and 21 non-smokers, whose 4-channel ECG signals were acquired along with blood pressure (BP) and pulse oximetry. The RRI signals were extracted for 5 min, and cubic spline interpolation method was used to convert the RRI signals to a uniformly sampled signals. The HRV parameters were estimated using Kubios HRV analyzer, and their statistical importance was analyzed using t-test. The results suggested a decrease in the time domain and the nonlinear HRV parameters of the smokers. The interpretation of the results hinted for an increased heart rate (HR) and decreased HRV in case of the smokers. Considering the outcomes of the study, the authors concluded that the HRV analysis may be used in medical practice to identify the modification in the ANS physiology. Nayak et al. (2015) [9] performed the HRV analysis of smokers and non-smokers along with the time domain and wavelet-based processing of their ECG signals. The authors chose 40 volunteers among which 20 volunteers were smokers, and the rest 20 volunteers were non-smokers. The interpretation of the short-term HRV parameters obtained from 5-min ECG signals exhibited the dominance of the sympathetic nervous system in the smokers. The HRV as well as the ECG parameters could be classified with an accuracy of  $\geq 85\%$ , further confirming the variation in the ANS and the cardiac activity [9]. Ohta et al. (2016) [10] studied the alteration in the HRV along with BP and HR of hypertensive patients due to cigarette smoking. The authors found that the BP and the HR were elevated but the high-frequency (HF) component of the HRV was decreased in daytime more during the smoking time as compared to the non-smoking time. On the other hand, no significant variation was found in the low-frequency (LF) components and LF/HF ratio. Based on the interpretation of the results, the authors suggested that the obtained variations in the blood pressure, heart rate and HRV were associated with the reduction of the parasympathetic nervous system activity [10]. Ahmadian et al. (2018) reported the use of HRV analysis method for understanding the effect of waterpipe smoking on cardiac autonomic function at rest as well as after following an anaerobic exercise [11]. The waterpipe, also regarded as hookah, is a method of consuming tobacco in which the heating of tobacco takes place at temperature  $<200$  °C in contrast to cigarette where tobacco is heated at several hundred degrees temperature. The authors observed that the smokers had a reduced overall HRV due to the decline in the parasympathetic activity and/or relative increment in the sympathetic activity. Although a number of studies have conducted using HRV analysis to recognize the long-term consequence of smoking on the ANS physiology of smokers, we did not come across much literature describing the immediate consequence of smoking on the ANS physiology. Taking the motivation from the

above-mentioned facts, this study attempts to understand the immediate change in the ANS physiology of smokers due to smoking.

## 2 Methodology

The study involved the acquisition of ECG signals from 17 male Indian volunteers (20–22 years old), who were regular cigarette smokers. The approval for acquisition of ECG signals was received from the Institute Ethical Clearance (IEC) committee of NIT Rourkela (office order no. NITRKL/IEC/FORM/2/25/4/11/001, dated 13/12/2013). After getting their written consent for the participation in our study, the ECG signal acquisition was carried out for 5 min both before and after smoking. The basal ECG signals were categorized under “Category C”, whereas the ECG signals acquired after smoking a cigarette were categorized as “Category S”. The digitization of the ECG signals was performed at a sampling rate of 1000 Hz, and the signals were stored into a computer. Thereafter, the 5-min ECG signals were analyzed to obtain the corresponding RRI signals. The RRI signals were subjected to HRV analysis to extract 29 HRV parameters, which comprised of both the linear and the nonlinear parameters. The t-test, classification and regression tree (CART), boosted tree (BT), and random forest (RF) methods were used to assess important parameters, which have statistically different values in Category C and Category S. The statistically significant parameters were employed as the input used for the ANNs. The popular neural networks, namely radial basis function (RBF) and multilayer perceptron (MLP), were implemented to classify the HRV data.

## 3 Results and Discussion

The HRV analysis is a popular noninvasive method to detect any alteration in the ANS activity and has been extensively used for quantifying the risk of numerous cardiac and non-cardiac diseases [12]. In this study, the HRV parameters were estimated from the RRI signals using the time, frequency, and nonlinear domain techniques. The time-domain HRV parameters included the mean and the standard deviation (SD) values of the RRI signals, mean and SD values of the heart rate, RMSSD (i.e., square root of the average of the squared variation of successive RRIs), NN50 (i.e., the number of adjacent RRIs having time interval variation of  $\geq 50$  ms), PNN50, HRV triangular index and triangular interpolation of RRI histogram (TINN). PNN50 indicates the result of dividing NN50 with the total number of RRIs. The HRV triangular index represents the ratio of the entire RRI density to the maximum of RRI density distribution in the RRI histogram, whereas TINN indicates the baseline width of the RRI histogram (measured as the base of a triangle) [12]. The frequency-domain



HRV parameters, namely very-low-frequency (VLF), LF, and HF components of the power spectral distribution (PSD) of the RRI signals, were computed using FFT and AR techniques. Among the frequency-domain parameters, the HF and the VLF power are considered to be a marker of the parasympathetic activity, whereas the LF power along with the LF/HF ratio is indicative of the sympathetic activity [13]. These parameters were expressed in terms of absolute values, relative values (in percentage of total power) and normalized values [14]. The nonlinear HRV analysis was performed using Poincare plot, which provided the parameters SD1 and SD2. The SD1 parameter is considered to be an indicative of the parasympathetic activity, whereas the SD2 parameter is considered to be inversely related to the sympathetic activity [15].

The statistically important HRV parameters were identified using t-test, CART, BT and RF. The t-test is a linear technique for comparing the existence of significant difference among the average values of the parameters obtained from two groups. The t-test could not detect any statistically vital parameter. This suggested the existence of nonlinear relationship among the parameters. The CART method represents the primitive decision tree-based method, which can be used for both classification and regression problems. The HF n.u.-FFT (i.e., HF power calculated using FFT method and expressed in normalized units) was obtained as an important predictor from the CART analysis (Table 1). Its mean value was higher in Category S in comparison to Category C suggesting the alteration in the sympathovagal balance due to smoking. Although the increase in HF n.u.-FFT value after smoking may contradict the fact reported in the literature that parasympathetic activity decreases with smoking, similar results have also been reported by Lee and Chang [16]. From the BT analysis, HR mean, NN50, HF power-FFT, and HF power-AR were obtained as the important predictors. All these parameters had lower mean values in Category C as compared to Category S. The lower values of HF power in Category S, computed using both FFT and AR methods, suggested the alteration in the sympathovagal balance, which may be attributed to the reduction in the parasympathetic activity [17]. The RF analysis is an ensemble learning based widely used decision tree method, which provides higher performance than the conventional decision tree methods [18]. The VLF power-FFT was obtained as the parameter with statistical importance from the RF analysis, whose mean value was higher in Category S as compared to Category C. However, some researchers have reported that the physiological explanation of the VLF power is less defined and also the VLF power measured from the short-term ECG signals may be regarded as a dubious measure [19]. Hence, the VLF power was not taken into consideration during the interpretation of the HRV results. The prevalence of these statistically important HRV parameters suggested that the ANS activity of the volunteers varied considerably after smoking. Further, the interpretation of the clinical significance of the important HRV parameters indicated an alteration in the sympathovagal balance due to the reduction in the parasympathetic activity after smoking.

To ascertain the variation of the ANS activity due to smoking, ANN classification was performed using MLP and RBF networks, where the important HRV predictors were used as the inputs. The MLP network is a feed-forward ANN that comprises of

**Table 1** Statistically important HRV parameters

Methods	HRV parameters	Mean $\pm$ SD		Predictor importance
		Category C	Category S	
CART	HF n.u.-FFT	42.24 $\pm$ 11.59	44.02 $\pm$ 17.00	1.00
BT	HR mean	91.94 $\pm$ 13.29	91.23 $\pm$ 13.76	1.00
	NN50	60.94 $\pm$ 56.53	49.69 $\pm$ 46.73	0.97
	HF power-FFT	252.90 $\pm$ 247.05	244.11 $\pm$ 258.52	0.95
	HF power-AR	240.97 $\pm$ 220.71	217.40 $\pm$ 242.52	0.96
RF	VLF power-FFT	67.70 $\pm$ 64.51	86.18 $\pm$ 134.26	1.00

at least three layers of nodes, namely an input layer, one or more hidden layers, and an output layer [20]. The RBF network is another popular ANN network that uses only a single layer of hidden neurons along with the input and the output layer of neurons [21]. The MLP 5-9-2 network classified the HRV parameters with the classification efficiency of 91.00% when HF n.u.-FFT, HR mean, HF power-FFT, HF power-AR, and NN50 were used as the inputs. The training of the network was performed using Broyden–Fletcher–Goldfarb–Shanno (BFGS) 37 algorithm. Sum of squared error (SOS) acted as the error function (EF). The hidden activation function (HAF) and the output activation function (OAF) were logistic and identity functions, respectively. However, the RBF 5-9-2 network resulted in a classification accuracy of 88.00% with the parameters HF n.u.-FFT, HF power-FFT, HF power-AR, VLF power-FFT, and NN50 as the inputs. The training of the RBF network was performed using RBFT algorithm. Entropy was considered as the EF of the RBF network. The HAF and the OAF of the RBF network were Gaussian and Softmax functions, respectively. The details and classification performance of these ANNs have been tabulated in Table 2.

## 4 Conclusion

In the present study, the HRV analysis, of 5-min ECG signals, which were acquired before and after smoking from 17 Indian male smokers, was performed to understand the immediate effect of smoking on the ANS activity. The HRV analysis resulted in 29 parameters among which a number of parameters were found to be significantly different among Category C and Category S. The in-depth interpretation of the significant HRV parameters suggested an alteration in the ANS activity due to the reduction in the parasympathetic activity. Further confirmation of the alteration in the ANS activity was provided by the ANN classification of the HRV parameters which showed classification accuracy of  $\geq 90\%$ .

**Table 2** Details of the MLP 5-9-2 and RBF 5-9-2 networks

Networks	Features used	Training efficiency (%)	Testing efficiency (%)	Classification efficiency (%)	Algorithm	EF	HAF	OAF
MLP 5-9-2	HF n.u.-FFT, HR mean, HF power-FFT, HF power-AR and NN50	89.28	100.00	91.00	BFGS 37	SOS	Logistic	Identity
RBF 5-9-2	HF n.u.-FFT, HF power -FFT, HF power-AR, VLF power-FFT and NN50	85.71	83.33	88.00	RBFT	Entropy	Gaussian	Softmax

## References

1. R. Yuksel et al., Autonomic cardiac activity in patients with smoking and alcohol addiction by heart rate variability analysis. *Clin. Invest. Med.* **39**, 147–152 (2016)
2. P.C. Dinas et al., Effects of active and passive tobacco cigarette smoking on heart rate variability. *Int. J. Cardiol.* **163**, 109–115 (2013)
3. J. Mackay et al., *The Tobacco Atlas* (World Health Organization, 2002)
4. J.E. Hall, *Pocket Companion to Guyton & Hall Textbook of Medical Physiology E-Book* (Elsevier Health Sciences, 2015)
5. G. Ernst, *Heart Rate Variability* (Springer, 2014)
6. H. ChuDuc et al., A review of heart rate variability and its applications. *APCBEE procedia* **7**, 80–85 (2013)
7. C.B. Harte, C.M. Meston, Effects of smoking cessation on heart rate variability among long-term male smokers. *Int. J. Behav. Med.* **21**, 302–309 (2014)
8. Z. Taralov et al., The effect of smoking on the autonomic heart regulation in young “healthy” male smokers. *J. IMAB–Ann. Proc. Sci. Pap.* **21**, 718–721 (2015)
9. S.K. Nayak et al., Automated neural network based classification of HRV and ECG signals of smokers: a preliminary study, in *Advancements of Medical Electronics* (Springer, 2015), pp. 271–279
10. Y. Ohta et al., Effects of cigarette smoking on ambulatory blood pressure, heart rate, and heart rate variability in treated hypertensive patients. *Clin. Exp. Hypertens.* **38**, 510–513 (2016)
11. M. Ahmadian, S. Ghorbani, V.D. Roshan, A.S. Leicht Influence of waterpipe smoking on cardiac autonomic function at rest and following high-intensity anaerobic exercise. *Acta Gymnica* **48**(1), 36–43 (2018)
12. M.P. Tarvainen et al., Kubios HRV–heart rate variability analysis software. *Comput. Methods Programs Biomed.* **113**, 210–220 (2014)
13. R.E. Kleiger et al., Heart rate variability: measurement and clinical utility. *Ann. Noninvasive Electrocardiol.* **10**, 88–101 (2005)
14. S.K. Nayak et al., Effect of Cannabis consumption on ANS and conduction pathway of heart of Indian paddy field workers, in *2016 IEEE Annual India Conference (INDICON)*, 2016, pp. 1–5
15. M.M. Corrales et al., Normal values of heart rate variability at rest in a young, healthy and active Mexican population. *Health* **4**, 377 (2012)
16. C.-L. Lee, W.-D. Chang, The effects of cigarette smoking on aerobic and anaerobic capacity and heart rate variability among female university students. *Int. J. Women’s Health* **5**, 667 (2013)
17. G. Yadu et al., Effect of a motivational song on the autonomic nervous system and the heart of indian male volunteers, in *Design and Development of Affordable Healthcare Technologies* (IGI Global, 2018), pp. 299–317
18. C.C. Hau, *Handbook of Pattern Recognition and Computer Vision* (World Scientific, 2015)
19. A. Camm et al., Heart rate variability: standards of measurement, physiological interpretation and clinical use. Task Force of the European Society of Cardiology and the North American Society of Pacing and Electrophysiology. *Circulation* **93**, 1043–1065 (1996)
20. I.N. Da Silva et al., *Artificial Neural Networks* (Springer International Publishing, Cham, 2017)
21. K. Gurney, *An Introduction to Neural Networks* (CRC press, 2014)

# Recurrence Quantification Analysis of Electrocardiogram Signals to Recognize the Effect of a Motivational Song on the Cardiac Electrophysiology



Swatilekha Paul, Gitika Yadu, Suraj Kumar Nayak, Anilesh Dey and Kunal Pal

**Abstract** Listening to music has been reported to provide health benefits. This has inspired the researchers to recognize the effect of music on various organs like the heart. In the past few decades, analysis of the electrocardiogram (ECG) signals has been widely used to divulge information about the cardiac activity not only for the diagnosis of the cardiovascular diseases but also during the exposure to a stimulus like music. This study attempts to identify the occurrence of any change in the cardiac activity due to the exposure to a motivational song. The ECG signals were acquired before and after exposing 18 volunteers to the motivational song. The recurrence plot analysis and recurrence quantification analysis (RQA) of the ECG signals were performed. The statistical analysis of the RQA features suggested a variation in the cardiac activity, which was further evinced by the classification of the RQA features using the artificial neural network (ANN) with an accuracy of >85%.

**Keywords** Music · Electrocardiogram · Recurrence plot · Recurrence quantification analysis

---

S. Paul · G. Yadu · S. K. Nayak · K. Pal (✉)  
Department of Biotechnology and Medical Engineering, National Institute of Technology,  
Rourkela 769008, India  
e-mail: [kpal.nitrkl@gmail.com](mailto:kpal.nitrkl@gmail.com)

S. Paul  
Department of Biomedical Engineering, Netaji Subhash Engineering College, Kolkata,  
West Bengal 700152, India

A. Dey  
Department of Electronics and Communication Engineering, Narula Institute of Technology,  
Kolkata 700109, India

## 1 Introduction

Listening to music is one of the well-known leisure activities of people since a long time. A strong emotion is associated with the music. This may be attributed to the fact that the auditory system of human has the ability to elicit information from the sound and generate relevant emotions associated with them. Recent few studies have also comprehensively surveyed the therapeutic effects of music [1, 2]. For example, to countervail anxiety, music has been used as an intervention. Music has been found to be utilized for the maintenance and the treatment of diseases [3]. Previous studies have found that both the motivational music and the oudeterous music produce affective responses in a person [4]. Due to the widespread benefits of music on human health, the recent decades have witnessed much interest among the researchers to understand the alteration induced by music on the physiology of various organs [5, 6]. Among the different organs, the research on understanding the effect of music on the heart physiology is gaining prominence in recent years [7]. The ECG signals are widely used as a clinical tool to detect various abnormalities related to the heart. However, they have also been used to analyze the heart physiology after the exposure to different stimuli [8]. Over the decades, a plethora of linear and nonlinear techniques have been developed for the analysis of the ECG signals. Among them, the recurrence plot represents a simple nonlinear method proposed by Eckmann et al. [9], which aims at a visual representation of the hidden recurrence (i.e., repeatedly occurring) patterns present in a signal by analyzing its phase space trajectory. However, the recurrence plot suffers from the demerit of having the qualitative nature. The RQA has been proposed by researchers to compute the measures of complexity on the basis of the small-scale structures appearing in the recurrence plots [10]. Hence, the RQA features provide a measure of nonlinearity and complexity present in the signal. In recent years, numerous studies have been performed, employing RQA features of the ECG signals for detecting the effect of external stimuli on the heart activity as well as for cardiovascular disease diagnostic applications. Chen et al. [8] used the RQA method for detecting the influence of the exposure to low-frequency noise on the RR interval signals (also called as HRV signals). The authors exposed 16 male volunteers to a 63 Hz noise of different intensities, and ECG signals were simultaneously recorded. The corresponding RR intervals were extracted, and RQA-based parameters were computed. Some of the RQA features exhibited higher values in the noisy environment as compared to the noise-free situation. The values of the RQA features also varied with the change in the intensity levels of the noise. Thus, the authors proposed that RQA may act as an effective tool to analyze the variations in the HRV signals due to noise. Sudden cardiac death (SCD) refers to the unexpected immediate death of a person, which is mainly caused by ventricular fibrillation. Violence causes serious mental and physical effects on the victims. It increases the stress level of the victim, reduces the self-esteem and also leads to suicide. Ferdinando et al. [11] utilized RQA along with bivariate empirical mode decomposition (BEMD) analysis of ECG signals to detect violence. The authors acquired 6 s ECG signals from 12 pupils and extracted the RQA and BEMD-based features of the ECG signals. The K-nearest neighbor (K-NN) classifier was used

for the classification purpose. The results suggested that the analysis of the ECG signals can act as a potential candidate for the detection of violence. Acharya et al. [12] reported the use of RQA and Kolmogorov complexity features of the HRV signals to perform automated diagnosis of SCD. The authors extracted the RR interval signals, and the RQA and Kolmogorov complexity-based features were computed. The important features were identified using t-test and were used for classification. The K-nearest neighbor (K-NN) classifier was able to classify the features of the normal people and the sudden cardiac death patients with the average efficiency of 86.8%. Thus, the authors suggested that their proposed methodology may aid in the automated diagnosis of cardiovascular diseases. Deasi et al. [13] also extracted the RQA features of ECG signals for the diagnosis of three different types of arrhythmia. The RQA features were ranked using ANOVA and subjected to classification using a decision tree, random forest and rotation forest classifiers. The maximum classification efficiency of 98.37% could be achieved using the rotation forest method. Thus, the authors proposed that their developed methodology can find applications in automated diagnosis of fatal cardiovascular diseases. Billeci et al. [14] performed the RQA of the RR interval signals along with HRV analysis to perform seizure prediction in advance. The time and frequency domain HRV features and RQA features of RR interval signals were extracted. All the features were segmented into ictal, preictal and interictal states. The important features were selected, and classification of the selected feature set was performed using a support vector machine (SVM). The SVM classifier provided a sensitivity of 89.06%. The results suggested that seizure may be predicted in advance using the proposed approach. Taking the inspiration from the facts discussed above, in this study, we have tried to recognize whether the exposure to a motivational song alters the cardiac activity using RQA of the ECG signals.

## 2 Methodology

In this study, 18 healthy undergraduate students of National Institute of Technology, Rourkela were invited for voluntary participation. The age range of the volunteers was 20–23 years. The selection of the volunteers was done such that none of them were neither involved in smoking nor had any pre-ailment record. Moreover, the volunteers were not involved in any kind of athletic or swimming activities and had no past record of neurological disorder. After describing them about the study, their written consent for the participation in this study was taken. Prior permission for acquiring the ECG signals was obtained from the Institute Ethical Clearance (IEC) Committee of NIT Rourkela. The volunteers were advised not to take food 1 h prior the acquisition of the ECG signals. They were advised to comfortably sit on a chair, and the ECG signals were recorded in Lead-I configuration for 6 min at 1000 Hz sampling frequency. These signals were categorized as Category-N (representing the pre-stimulus condition). After the resting period of 45 min, the volunteers were suggested to listen to a motivational song “Salaam India” from the bollywood movie

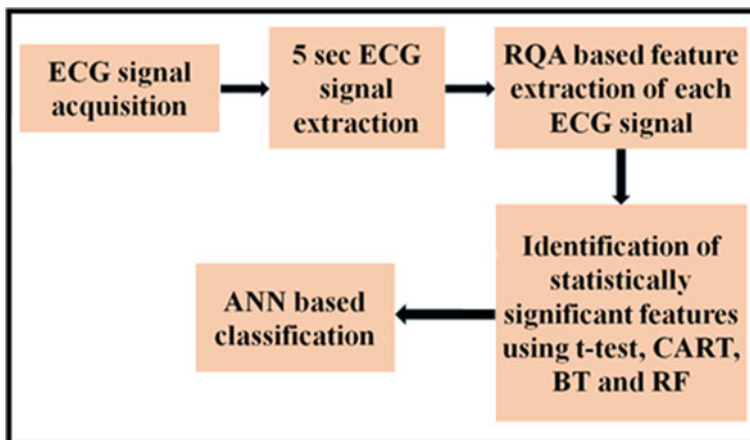


**Fig. 1** Block diagram representation of the analysis of ECG signals using RQA

Mary Kom. Subsequently, the ECG signals were again acquired for 6 min. This category of the ECG signals was regarded as Category-M, which represented the post-stimulus situation. Eckmann et al. [15] proposed the concept of recurrence plot. It is a powerful tool used for the characterization of the signal behavior in the phase space. On the basis of the recurrence plot, the RQA method has been developed, which eliminates the shortcoming of the qualitative nature of the recurrence plot. The ECG signals of 5 s duration of both the categories, i.e., Category-N and Category-M, were extracted. These signals were imported to MATLAB (R2014a, MathWorks Inc., USA) and were used for drawing the recurrence plots as well as for computing several quantitative RQA features using a custom-built MATLAB program [16, 17]. The RQA of the ECG signals provided six features. The extracted RQA features were initially analyzed for their statistical importance using t-test. Thereafter, the decision tree methods, namely classification and regression tree (CART), boosted tree (BT) and random forest (RF), were also implemented for understanding their statistical importance. The classification of the resulting features was performed using ANN. The conventional ANN, namely radial basis function (RBF), was used for the classification purpose. The block diagram representation of the steps followed for the RQA of the ECG signals has been shown in Fig. 1.

### 3 Results and Discussion

In order to recognize the influence of the afore-mentioned musical stimulus on the cardiac activity, the recurrence plots and the RQA of the ECG signals were carried out. The recurrence plot represents an analytical tool, which provides the qualitative visualization of the recurrent patterns hidden within a signal. In our study, the recur-



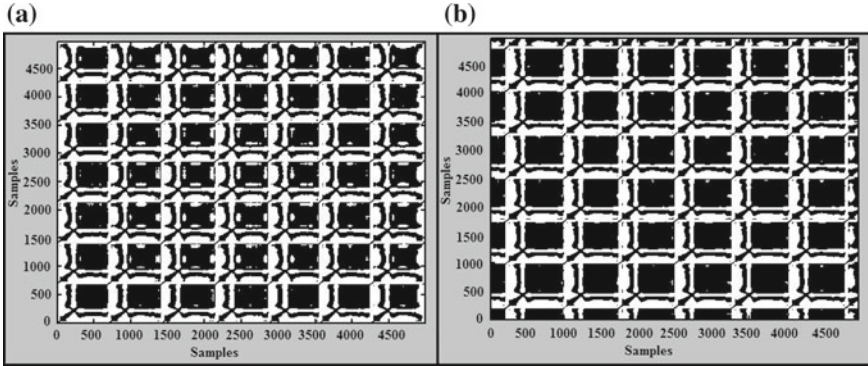


**Fig. 2** Typical recurrence plots: **a** category-N and **b** category-M

recurrence plots of the 5 s ECG signals (both Category-N and Category-M) are constructed as shown in Fig. 2. It is evident from the recurrence plots that visually distinguishable variations exist between the recurrence patterns of Category-N and Category-M.

The quantification of the recurrence plot is known as RQA, which performs the quantification of the recurrence patterns observed in the recurrence plot. The RQA can be accomplished on the basis of the small structures present in the recurrence plot. As the recurrence plot is usually symmetrical, only the vertical lines are taken into consideration for the determination of the RQA features. The RQA features provide the measure of the nonlinearity and complexity, which are present in the signal. The RQA features computed for our study were determinism (DET), length of the longest diagonal line (LMAX), entropy (ENT), trend (TND), laminarity (LAM) and trapping time (TT) [9]. However, instead of using all the RQA features, the statistically important features were identified for utilizing in the further analysis. The t-test of the RQA features could not find out any statistically significant feature. The t-test is a linear method to find out the existence of the significant variation between the mean values of features corresponding to two groups. Therefore, nonlinear relationship between the RQA features was expected, which could not be identified through the t-test [18]. In addition to the t-test, the nonlinear decision tree-based methods (i.e., CART, BT and RF) were also implemented. The CART method represents the conventional decision tree method, which can be useful in both classification and regression problems [19]. It suggested TT as the important feature (Table 1). The feature TT provides the information about how long the signal remains in a particular state by calculating the mean length of the vertical lines. Mathematically, TT is given by Eq. 1 [9].

$$TT = \frac{\sum_{v=v_{\min}}^N vP(v)}{\sum_{v=v_{\min}}^N P(v)} \tag{1}$$

**Table 1** Statistically important RQA features of ECG signals

Methods	RQA features	Mean $\pm$ SD		Predictor importance
		Category-N	Category-M	
CART	TT	199.04 $\pm$ 79.63	191.63 $\pm$ 75.51	1.00
BT	LMAX	99.97 $\pm$ 0.02	99.97 $\pm$ 0.03	1.00
	DET	128.29 $\pm$ 27.37	127.40 $\pm$ 27.55	0.99
RF	TT	199.04 $\pm$ 79.63	191.63 $\pm$ 75.51	1.00

where  $\nu$  = length of the vertical lines and  $P(\nu)$  = number of vertical lines of length  $\nu$ .

The BT analysis is another decision tree method with improved performance due to the use of a gradient decent algorithm. The RQA features, namely DET and LMAX, were identified as the important predictors from the BT analysis. The recurrence plot contains diagonal lines. The percentage of recurrence points forming the diagonal lines and exhibiting the periodicity nature is regarded as determinism (DET) (Eq. 2) [9]. On the other hand, LMAX represents the maximum length of the vertical lines occurring in the recurrence plot. Furthermore, in the RF analysis, TT was again obtained as the important feature. The RF analysis represents the popularly used ensemble learning-based decision tree method [20]. The occurrence of the nonlinearly related statistically important RQA features suggested the variation in the cardiac activity because of the exposure to the musical stimulus.

$$DET = \frac{\sum_{l=\min}^N lP(l)}{\sum_{i,j=1}^N R(i,j)} \quad (2)$$

where  $l$  represents the length of the diagonal lines and  $P(l)$  represents the number of horizontal lines of length  $l$ .

The statistically significant predictors thus obtained were considered as inputs for the ANN-based classification. The commonly used RBF neural networks were implemented for this purpose. When TT, LMAX and DET were applied as the categorical inputs, the RBF architecture attained the maximum classification efficiency (CE) of 86.11%. The network architecture details of RBF 3-17-2 network have been given in Table 2. The training of the RBF 3-17-2 network was performed using RBFT algorithm. It is a well-known fact that the RBF network uses the backpropagation algorithm for improving the classification accuracy, which requires the proper selection of an error function (EF). In our proposed network, the entropy function played the role of the EF. The hidden activation function (HAF) and output activation function (OAF) also have an important role in deciding the performance of the ANN. Here, Gaussian and softmax functions were employed as the HAF and the OAF, respectively. In the classification of the ECG signals, an accuracy  $\geq 85\%$  has

**Table 2** Details of RBF 3-17-2 network

Network	Features	Classification accuracy	Algorithm	EF	HAF	OAF
RBF 3-17-2	TT	86.11%	RBFT	Entropy	Gaussian	Softmax
	LMAX					
	DET					

been regarded as significant [21]. Thus, the results of the ANN classification also supported the hypothesis drawn from the statistically significant RQA features that listening to music had altered the cardiac activity.

### 4 Conclusion

In this study, the ECG signals were acquired from 18 volunteers to analyze the effect of the musical stimulus on the heart activity. The acquisition was performed before and after the exposure to a motivational song. The ECG signals were used to construct the recurrence plots, whose visual analysis suggested the existence of the variation in the ECG signals of Category-N and Category-M from visual observation. Thus, the RQA was implemented to quantify the variation in the cardiac activity. Several RQA features varied significantly between Category-N and Category-M, suggesting the alteration in the cardiac activity due to the musical stimulus. The variation was again confirmed from the classification performance of the RBF networks.

### References

1. Y.Z. Tan et al., The effect of relaxing music on heart rate and heart rate variability during ECG GATED-myocardial perfusion scintigraphy. *Complement. Ther. Clin. Pract.* **21**, 137–140 (2015)
2. C.-H. Ko et al., Effect of music on level of anxiety in patients undergoing colonoscopy without sedation. *J. Chin. Med. Assoc.* **80**, 154–160 (2017)
3. L.J. Labrague, D.M. McEnroe-Petitte, Influence of music on preoperative anxiety and physiologic parameters in women undergoing gynecologic surgery. *Clin. Nurs. Res.* **25**, 157–173 (2016)
4. D. Elliott et al., The effect of motivational music on sub-maximal exercise. *Eur. J. Sport Sci.* **5**, 97–106 (2005)
5. L.O. Bonde, T. Theorell, *Music and Public Health: A Nordic Perspective* (Springer, 2018)
6. L.O. Bonde et al., in *10th European Music Therapy Conference*. Music and Public Health: Music in the Everyday Life of Adult Danes and Its Relationship with Health (2016)
7. S.K. Nayak et al., in *Pattern and Data Analysis in Healthcare Settings*, ed. by IGI Global. Effect of Odia and Tamil Music on the ANS and the Conduction Pathway of Heart of Odia Volunteers (2017), pp. 240–263
8. S.-T. Chen et al., in *Advanced Materials Research*. Recurrence plot analysis of HRV for exposure to low-frequency noise (2014)

9. S. K. Nayak et al., A review on the nonlinear dynamical system analysis of electrocardiogram signal. *J. Healthc. Eng.* **2018** (2018)
10. N. Marwan et al., Recurrence-plot-based measures of complexity and their application to heart-rate-variability data. *Phys. Rev. E* **66**, 026702 (2002)
11. H. Ferdinando et al., Violence detection from ECG signals: a preliminary study. *J. Pattern Recogn. Res.* **1**, 7–18 (2017)
12. U.R. Acharya et al., in *2015 IEEE International Conference on Systems, Man, and Cybernetics (SMC)*. Automated Prediction of Sudden Cardiac Death Risk Using Kolmogorov Complexity and Recurrence Quantification Analysis Features Extracted from HRV Signals (2015), pp. 1110–1115
13. U. Desai et al., Diagnosis of multiclass tachycardia beats using recurrence quantification analysis and ensemble classifiers. *J. Mech. Med. Biol.* **16**, 1640005 (2016)
14. L. Billeci et al., Patient-specific seizure prediction based on heart rate variability and recurrence quantification analysis. *PLoS ONE* **13**, e0204339 (2018)
15. J.P. Eckmann, Recurrence plots of dynamical systems. *Europhys. Lett.* **5**, 973–977 (1987)
16. H. Yang, Multiscale recurrence quantification analysis of spatial cardiac vectorcardiogram signals. *IEEE Trans. Biomed. Eng.* **58**, 339–347 (2011)
17. Y. Chen, H. Yang, Multiscale recurrence analysis of long-term nonlinear and nonstationary time series. *Chaos Solitons Fractals* **45**, 978–987 (2012)
18. H. Hsu, P.A. Lachenbruch, *Paired t Test* (Wiley StatsRef: Statistics Reference Online, 2014)
19. L. Breiman, *Classification and Regression Trees* (Routledge, 2017)
20. C.C. Hau, *Handbook of Pattern Recognition and Computer Vision* (World Scientific, 2015)
21. S.K. Nayak et al., in *Advancements of Medical Electronics*. Automated Neural Network Based Classification of HRV and ECG Signals of Smokers: A Preliminary Study (Springer, 2015), pp. 271–279

**Part III**  
**Communication**

# Meteorological Parameter Studies During 6 December 2016 Indonesia Earthquake ( $M_w$ 6.5)



Pranab Hazra, Suman Paul, Shreya Chatterjee and Anindita Chandra

**Abstract** The atmosphere near the ground surface is affected more than the ionospheric region in terms of ionization by the electromagnetic emissions caused by various reasons. One such occurrence is the emission of radon ( $Rn^{222}$ ) from lithosphere through the deformities of the earth crust during the earthquakes. This creates atmospheric anomalies before any strong seismic activities which seem to be present in the meteorological parameters. The evidence for atmospheric anomalies has yet to be meticulously analysed. The data for analysis can be recorded by receiving through L-type antenna and a detector module having a local oscillator, power amplifier, IF amplifier and data acquisition card. But in this work, the data are satellite data. Here, the event of Indonesia earthquake occurred on 6 December 2016 with magnitude  $M_w$  6.5 analysed for observing the anomalies in meteorological parameters, viz. air temperature, relative humidity, atmospheric pressure and wind speed before and after this earthquake. The variations of these parameters might help to predict the occurrence of the earthquake 2–3 days prior to its occurrence. We obtain certain anomalies in temperature, relative humidity, pressure and wind speed observations. Also, we have found that 30-km depth is very sensitive for Indonesia.

**Keywords** Ionosphere · Radon · Temperature · Humidity · Pressure · Wind speed · Tectonic plate · Strain energy

---

P. Hazra (✉) · S. Chatterjee · A. Chandra  
Electronics & Communication Engineering, Narula Institute of Technology, Agarpara, Kolkata,  
India  
e-mail: [pranabhazra2007@gmail.com](mailto:pranabhazra2007@gmail.com)

P. Hazra · S. Paul  
Centre of Advanced Study in Radio Physics and Electronics, University of Calcutta, Kolkata, India  
e-mail: [Paul\\_suman30@yahoo.co.in](mailto:Paul_suman30@yahoo.co.in)

S. Paul  
Department of Physics, Rishi Bankim Chandra Evening College, Naihati, India

## 1 Introduction

An earthquake occurred at the tectonic plate boundary, south-west of Sumatra on 6 December 2016 with  $M_w$  6.5. The 8000-km-tectonic fault line extended from Papua towards the west of Himalaya where the large earthquakes occurred at Sumatra. The fault zone of Indian Ocean is considered as events which are Chagos-Laccadive Ridge and the Sumatra Trench due rotation between the Indian and the Australian plates [1–3]. Predominant strike-slip and left lateral mechanism both are characterized of the events on 11th April, 2012. The depth of the main shock is about 18–27 km .

Fault ruptures can trigger the event of seismic activity. The observations on the earthquake insist the scientists to trust that the event is based on changes in the state of stress around the volcano due to the release of energy from the rupture of the fault and vice versa. On and from 15 September 2013, the volcanic activity is continuing till today.

The relation between earthquakes and volcanic eruption is understood, and reasons of dormancy of volcanoes are still a question for scientists but the assumption again comes into light. Mount Sinabung has several volcanoes along in Sumatra Trench which is the subduction zone of the Indian Ocean. It is also part of the Ring of Fire. Map of the location of volcanoes in relation to Sumatra Trench is shown in Fig. 1. The Lake Toba Caldera is about 40 km south-east of Mount Sinabung which is the site of the last known super-volcanic eruption on earth about 75,000 years ago. According to the data, the three mega-earthquakes occurred in this region during 2005–2007 with  $M_w$  8.6 in 2005,  $M_w$  7.9 in 2007 and  $M_w$  8.4 in 2007 which are triggered to the most recent volcanic activity at Mount Sinabung. Large subduction-type earthquakes can reactivate volcanic arcs because they change the types and amounts of tectonic stress underground which are released after a subduction, and this can lead to strike and slip motions and other types of tectonic stress. This can further open new channels for magma flow and increase the overall permeability of the volcanic system causing magma to erupt. The long-term pulses of increased volcanic activity have observed after megathrust earthquakes in other regions of the world including Chile and Japan.

Sumatra earthquake is the largest earthquake of the contributory era of 6 December 2016  $M_w$  6.5 earthquake offshore. This large earthquake occurs due to the differential rotation of Indian and Australian plates. Strike-slip fault rupture triggered a complex variable westward-propagating order and inherited NNE Sumatra offshore earthquake striking the sea floor as a cloth to be associated with reactivation. Temporary dynamic triggering mechanism and fluid interaction between surface waves can be from stress perturbations. Sumatra Earthquake: an N-S Ocean westward sequential seismic fabric, Geophysical evidence of rupture associated with reactivation (Sumatra Aftershocks” team, 26th December, 2004 Sumatra-Andaman Earthquake: co-seismic and post-seismic motions in northern Sumatra). The pressure in the recent

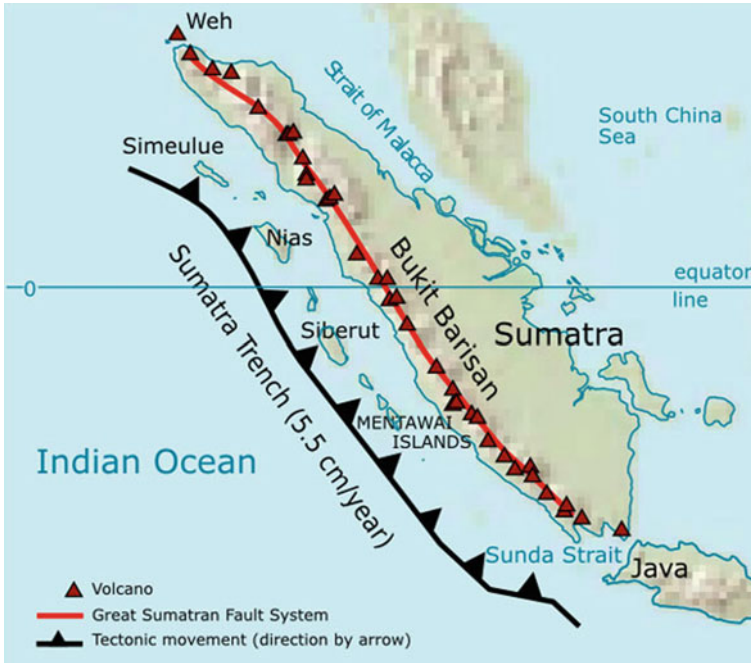


**Fig. 1** Location of volcanoes in relation to Sumatra Trench

past, the high tsunami run-ups along the south coast of Java, the two large, shallow earthquakes and tsunamis organized [4–6].

Attempts to predict earthquakes set up long ago, using different methods and analysing data from various stations all over the globe. Predicting the earthquakes deals with geophysical anomaly on the earth surface, thermal anomalies, ELF-VLF signal anomalies, ionospheric and sub-ionospheric signal propagation disorders, electron density fluctuations [7–15]. Over the past few decades, great efforts have been presented all over the world, of impending earthquake precursory signals in search of potential—both geophysical and geochemical methods in a variety of different natures have been adopted in non-seismic monitoring parameters. In all methods of radon gas as a pre-seismic signal, geochemical monitoring of its facilities, as well as the detection of highly deformed tectonic zone, has proven to be very promising because of its direct connection [16, 17]. In this paper, we analyse the satellite data to investigate the nature of variations of different atmospheric parameters, viz.



air temperature, humidity, pressure and wind speed during earthquake preparation and exploration. Significant variations are observed; those are presented below and discussed.

## 2 Data

- [https://www.wunderground.com/history/wmo/96009/2016/12/6/DailyHistory.html?req\\_city=Reuleuet&req\\_state=AC&req\\_statenam=Indonesia&reqdb.zip=00000&reqdb.magic=1932&reqdb.wmo=96009](https://www.wunderground.com/history/wmo/96009/2016/12/6/DailyHistory.html?req_city=Reuleuet&req_state=AC&req_statenam=Indonesia&reqdb.zip=00000&reqdb.magic=1932&reqdb.wmo=96009)
- <https://geoazur.oca.eu/spip.php?rubrique787>
- <https://earthquake.usgs.gov/earthquakes/eventpage/us10007ghm#region-info>
- <http://www.sagaingfault.info/>
- <http://legacy-www.swpc.noaa.gov/alerts/k-index.html>
- <https://www.spaceweatherlive.com/>.

## 3 Observational Results and Analyses

Different tectonic plates of various unified components Sumatra–Andaman plate start to move along the fault line, and strain energies are released. At 60 km depth most strain accumulation and subduction occurred along the Sunda-Mega-Thrust (SMT) plate subducting lithosphere has relation with the release of the Indo-Australian plate. A slab of less than 300 kilometres and less than 150 km along the Andaman Islands Sumatra deep earthquake or distortion associated with the release of the subducting deformation is evidence of a deep stretch.

The pressure of two plates is moving north-west along the diagonal of the growing convergence of a series transformation and normal faults along the crustal seismicity. In this context, we have enlisted the major earthquakes ( $M_w > 5.8$ ) in Indonesia since 1976, which are shown in Table 1, to have an idea about the distribution in terms of depth of occurrences.

The data of air temperature, relative humidity, atmospheric pressure and wind speed variations are taken from Indonesia Meteorological Department official website (reference link is given in Data Section). Relative humidity, atmospheric pressure and wind speed variations with daily air temperature during the pre- and post-seismic periods of this earthquake from 20 November 2016 to 20 December 2016 are plotted in panels (a) to (l) of Figs. 2, 3 and 4, respectively. Eight days of data earlier to and three days of data after the occurrence of the earthquake are shown here along with the earthquake day plot. Results of the data with respect to Indian Standard Time

(IST) and their variations are presented. In each panel, data have been plotted in three-hour interval. Some data are missing in all the plots due to non-availability. Relative humidity attained minimum and maximum value before and after the occurrence of the earthquakes. During the period, temperature variation was seen between 23 and 31 °C. Relative humidity variations were noticed between 65 and 98%. Figure 3 reveals a variation in atmospheric pressure from 1005 to 1113 mb, while wind speed variation is in between 2 and 15 kmh<sup>-1</sup> which is shown in Fig. 4. All these are observed 5–7 days before the day of occurrence of the earthquake. These variations are found to continue up to 2–3 days for this region of occurrence of the earthquake station; the variations of temperature, humidity, pressure and wind speed do not show ample variations but follow some common trends. Figure 5 shows the *M*-value plot against depth along with Gaussian fit curve which is discussed later in detail. Now the question is whether these variations are within the normal range of magnitudes of air temperature, humidity, pressure and wind speed or not. One simple technique is to check the values of standard deviation ( $\sigma$ ). The threshold value is  $2\sigma$ , within which the variation is said to be normal and beyond which the variation will be said to be anomalous one. Panels (a) and (b) in Fig. 6 show the variations of air temperature mean and standard deviation and average relative humidity and standard deviation, by the black-coloured solid line joining square blocks and the blue-coloured solid line joining blue square blocks, respectively. Abscissa indicates number of day counts; i.e. 1–31 means 20 November 2016 to 20 December 2016. Also, Fig. 6c, d represents pressure mean and standard deviation, and wind speed mean and standard deviation by the black-coloured solid line joining square blocks and the blue-coloured solid line joining blue square blocks, respectively.

**Table 1** Major earthquakes ( $M_w > 5.8$ ) in Indonesia since 1976

Date	Position (latitude, longitude)	Depth (km)	<i>M</i> -value
14 July 1976	8.277°S, 114.775°E	25.4	6.5
17 December 1979	8.49°S, 115.75°E	15	6.3
25 December 1982	8.36°S, 123.07°E	10	5.9
17 November 1984	0.20°N, 98.03°E	33	7.2
11 December 1992	8.48°S, 121.896°E	28	7.8
15 February 1994	4.967°S, 104.302°E	23	7
6 October 1995	2.045°S, 101.436°E	33	6.8
1 January 1996	0.729°N, 119.931°E	24	7.9
17 February 1996	0.95°S, 136.94°E	20	8.2
4 June 2000	4.61°S, 102.06°E	35	7.9
10 October 2002	1.757°S, 134.297°E	10	7.6
2 November 2002	2.824°N, 96.085°E	30	7.3

(continued)

**Table 1** (continued)

Date	Position (latitude, longitude)	Depth (km)	<i>M</i> -value
26 May 2003	2.354°N, 128.855°E	31	7
1 January 2004	8.310°S, 115.788°E	44.5	5.8
5 February 2004	4.0°S, 135.1°E	10	7.4
11 November 2004	8.152°S, 124.868°E	10	7.5
26 November 2004	3.68°S, 135.41°E	24	7.1
26 December 2004	3.316°N, 95.854°E	30	9.1–9.3
28 March 2005	2.09°N, 97.15°E	30	8.6
5 July 2005	1.90°N, 97.10°E	30	6.7
14 March 2006	3.595°S, 127.214°E	30.1	6.7
26 May 2006	8.07°S, 110.35°E	15	6.4
17 July 2006	9.33°S, 107.32°E	25.3	7.7
21 January 2007	1.08°N, 126.36°E	23.5	7.5
12 September 2007	4.520°S, 101.374°E	30	8.4
20 February 2008	2.768°N, 95.964°E	26	7.4
25 February 2008	2.245°S, 99.808°E	25	6.7
16 November 2008	3.89°N, 126.39°E	20	7.3
4 January 2009	0.5°S, 132.74°E	30	7.7
12 February 2009	0.5°S, 132.74°E	30	7.6
16 August 2009	1.397°S, 99.473°E	44.8	6.7
2 September 2009	7.778°S, 107.328°E	49	7
30 September 2009	0.71°N, 99.97°E	90	7.6
1 October 2009	2.482°S, 101.524°E	9	6.6
6 April 2010	2.38°N, 97.05°E	31	7.8
9 May 2010	3.775°N, 96.055°E	45	7.2
16 June 2010	2.22°N, 136.58°E	15	7
25 October 2010	3.464°S, 100.084°E	20.6	7.7
5 September 2011	2.965°N, 97.893°E	91	6.7
7 July 2013	4.698°N, 96.687°E	10	6.1
27 July 2015	52.376°N, 169.658°W	11.9	6.9
2 March 2016	4.908°S, 94.275°E	24	7.8

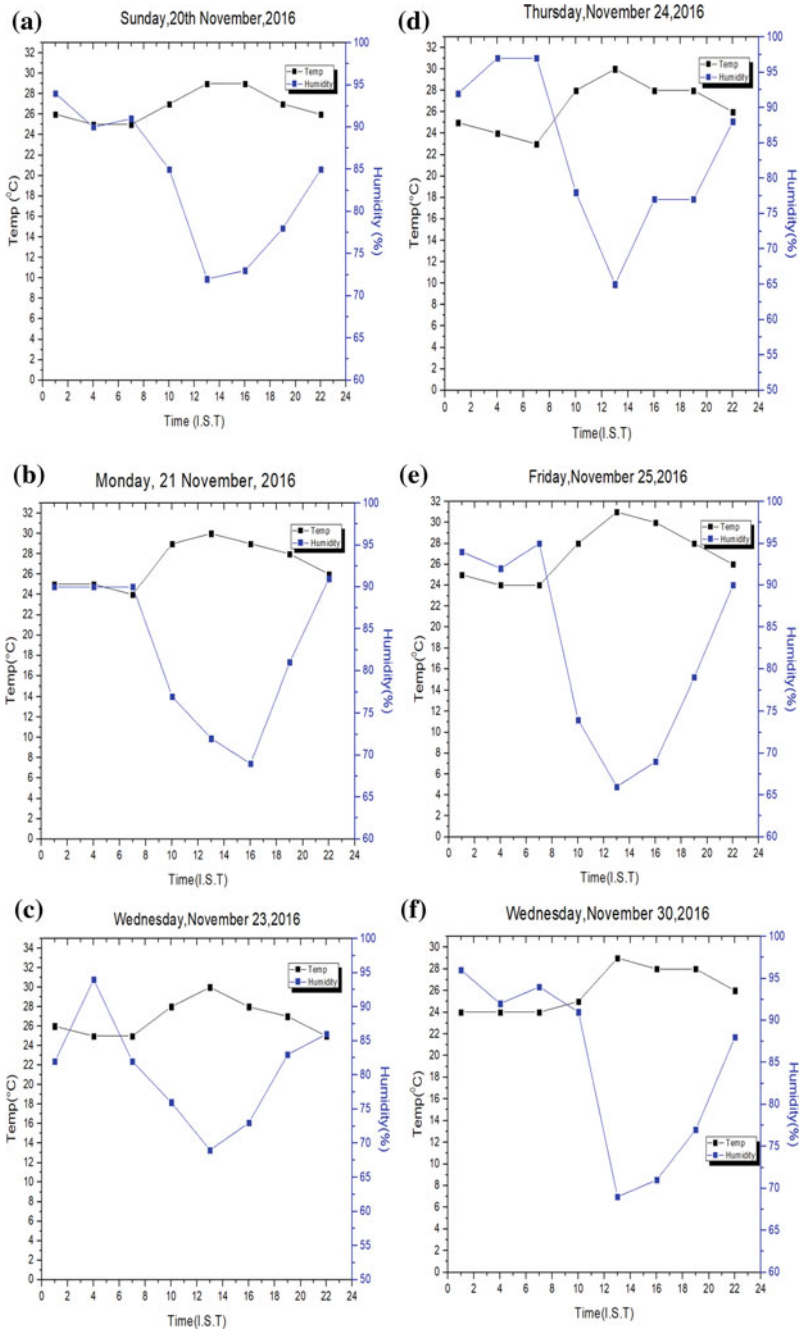


**Fig. 2** Temperature and relative humidity variations during the pre- and post-seismic periods of 6 December 2016 Indonesia earthquake, from 20 November 2016 to 20 December 2016 (black-coloured solid line joining black square blocks represents temperature, and blue-coloured solid line joining blue square blocks represents relative humidity)

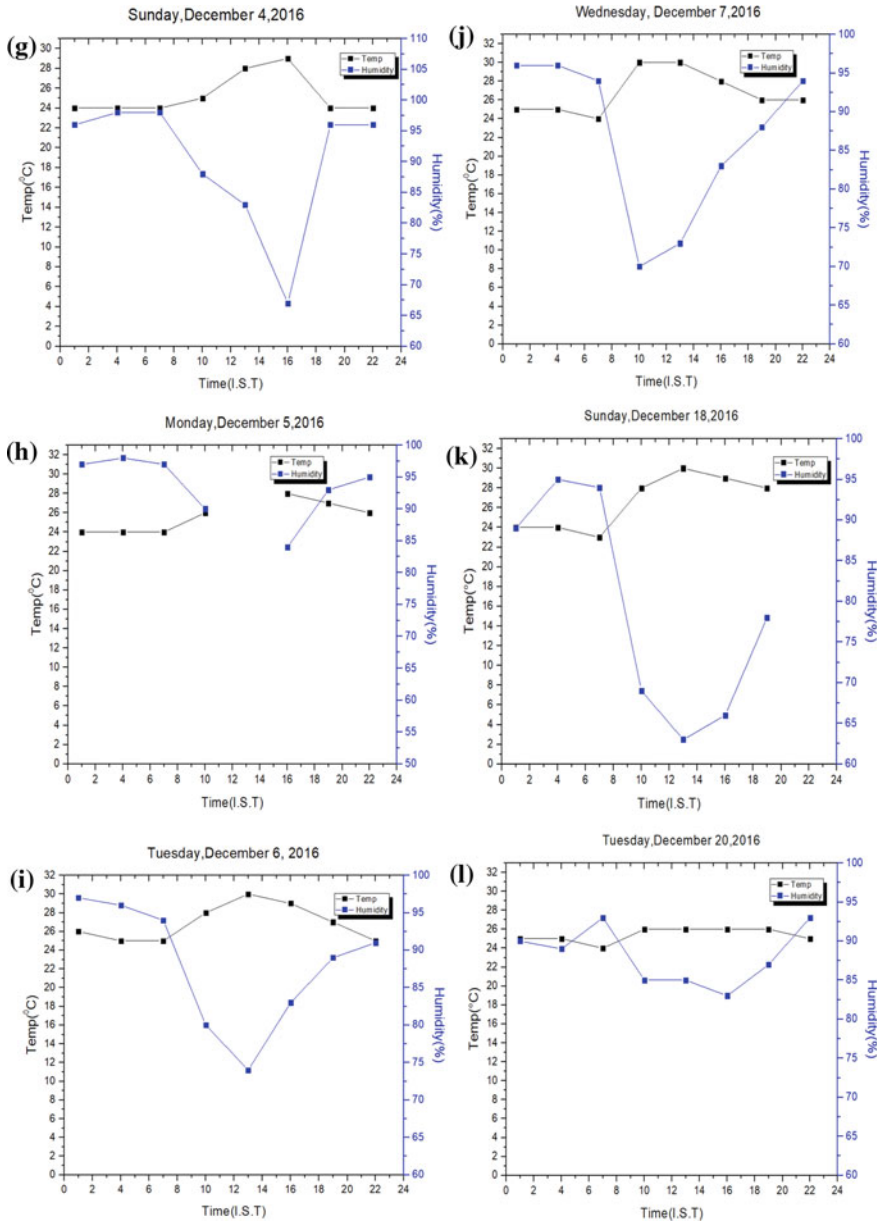
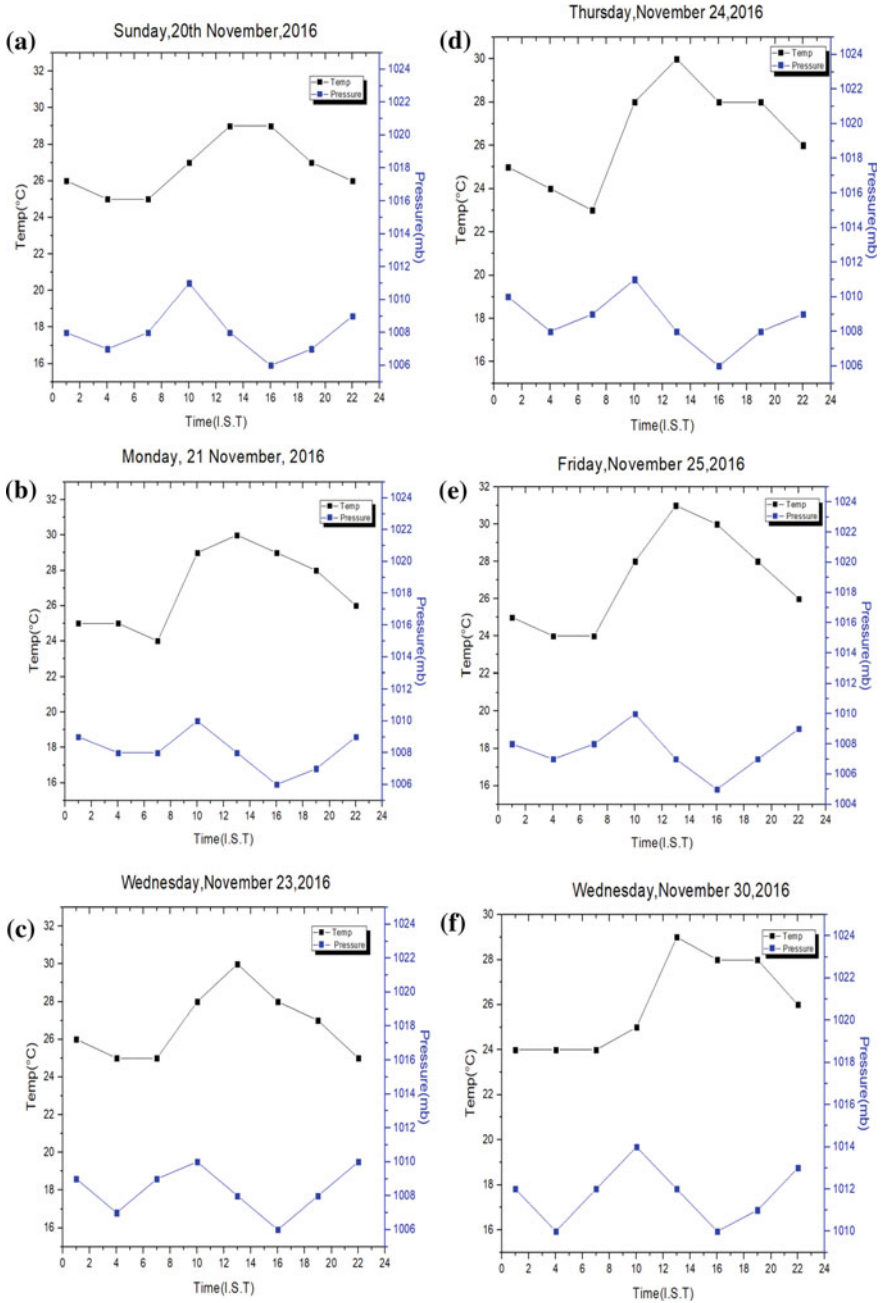


Fig. 2 (continued)



**Fig. 3** Temperature and atmospheric pressure variations during the pre- and post-seismic periods of 6 December 2016 Indonesia earthquake, from 20 November 2016 to 20 December 2016 (black-coloured solid line joining black square blocks represents temperature, and blue-coloured solid line joining blue square blocks represents atmospheric pressure)

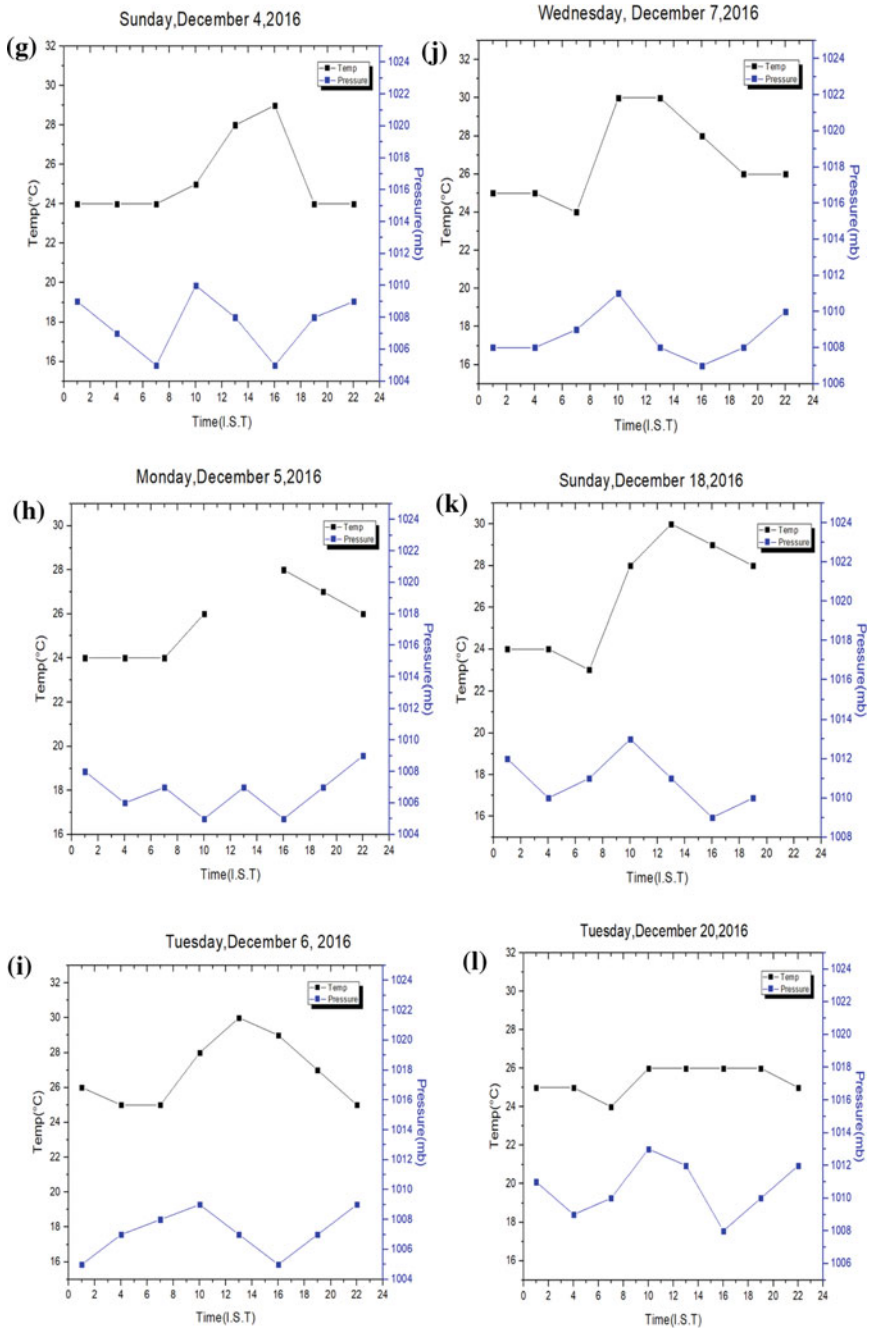


Fig. 3 (continued)

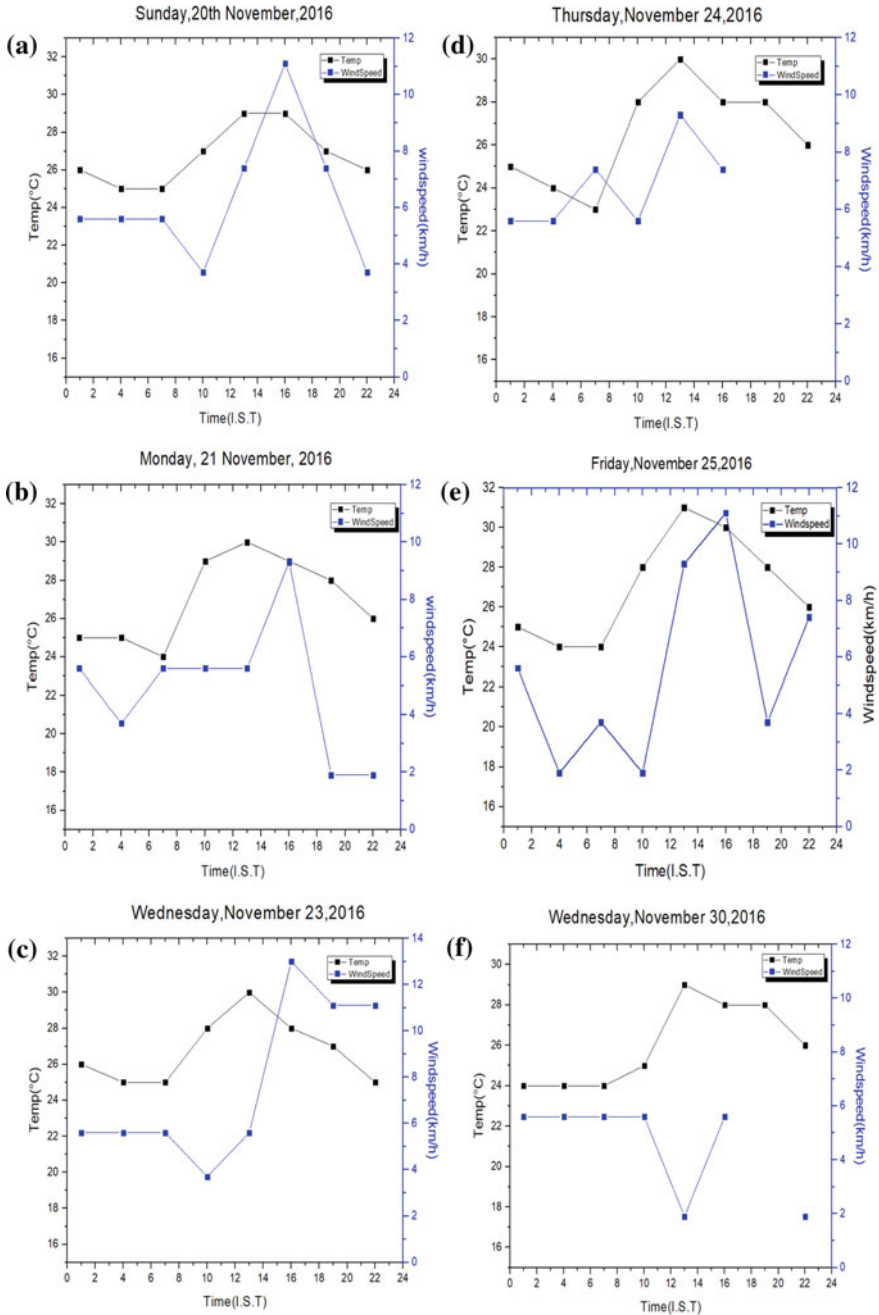


Fig. 4 Temperature and wind speed variations during the pre- and post-seismic periods of 6 December 2016 Indonesia earthquake, from 20 November 2016 to 20 December 2016 (black-coloured solid line joining black square blocks represents temperature, and blue-coloured solid line joining blue square blocks represents wind speed)



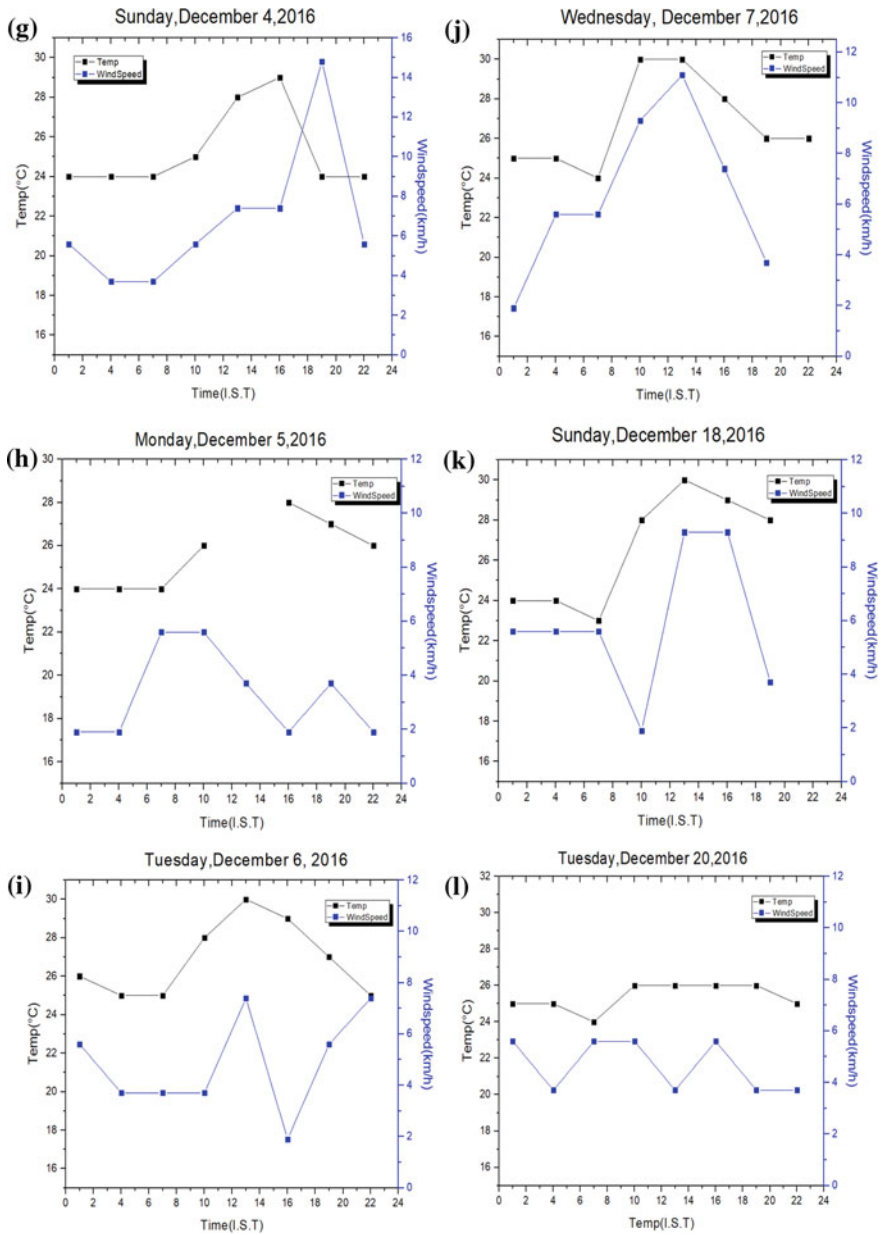


Fig. 4 (continued)

### 4 Discussion and Conclusion

As said in an earlier section, we have enlisted the major earthquakes ( $M_w > 5.8$ ) in Indonesia since 1976 (Table 1), and to investigate the main region having the depth of occurrences of different earthquakes, we have plotted  $M$ -value against depth along with Gaussian fit curve (Fig. 5). Relevant fit equation is shown, and the different parameters are given in Table 2. Here, ‘ $x$ ’ is a vector of earthquakes (with  $M$ -value),  $x_c$  is mean of  $x$ ,  $w$  is the standard deviation, and  $y_0$  is the amount of bias value or adjustment value which is required to fit for a minimum amount of error. We have found that 30-km depth is very sensitive for Indonesia.

$$y = y_0 + \frac{A}{w\sqrt{\frac{\pi}{2}}} e^{-2\left(\frac{x-x_c}{w}\right)^2}$$

It was observed after the analyses that air temperature starts to increase gradually (5–7 days before) as it approaches the event of earthquake date and it reaches

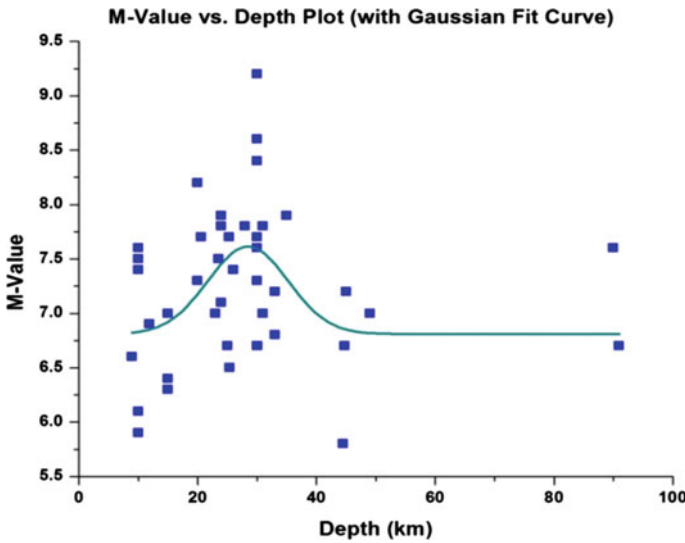


**Fig. 5**  $M$ -value versus depth (km) of major earthquakes ( $M > 5.8$ ) in Indonesia since 1976. Blue squares are for different events, and green solid line is the Gaussian fit curve for the data

**Table 2** Nonlinear Gaussian fit parameters

	Value	Standard error
$y_0$	6.81058	0.23469
$x_c$	28.46364	2.81767
$w$	13.54804	9.53482
$A$	13.63907	11.24089

maximum (from 23 to 31 °C) on the day of event and remains almost in the same position 2–3 days as shown by Fig. 2. On the day of occurrence of earthquake, relative humidity decreases from 95% to 75% (Fig. 2i), and pressure increases from 1005 mb to 1009 mb and again decreases (Fig. 3i), while wind speed fluctuates within the range of 2–7 kmh<sup>-1</sup> (Fig. 4i). It generally shows the chance of repetition of earthquakes after the main shock near the epicentre, but fortunately no such occurrences are reported within a couple of days. From Fig. 6, visual representation shows that standard deviations ( $\sigma$ ) for temperature, relative humidity and pressure except wind speed are not only well away from mean but also in the opposite direction. Thus, it may be concluded that there is an anomaly in meteorological parameters during this earthquake. To ascertain that the daily variations of air temperature, relative humidity, atmospheric pressure and wind speed as described in this work are related solely to this earthquake and not caused by any geomagnetic activity and other natural processes, we checked the diurnal variation of  $K_p$  index for the stated duration, and in Fig. 7 we present the  $K_p$  index for 6 December 2016.  $K_p$  index ranges between 0 and 9. Values between 0 and 4 indicate quiet magnetic conditions. The highest  $K_p$  index values on the day of earthquake occurrence are 3, while the average is smaller

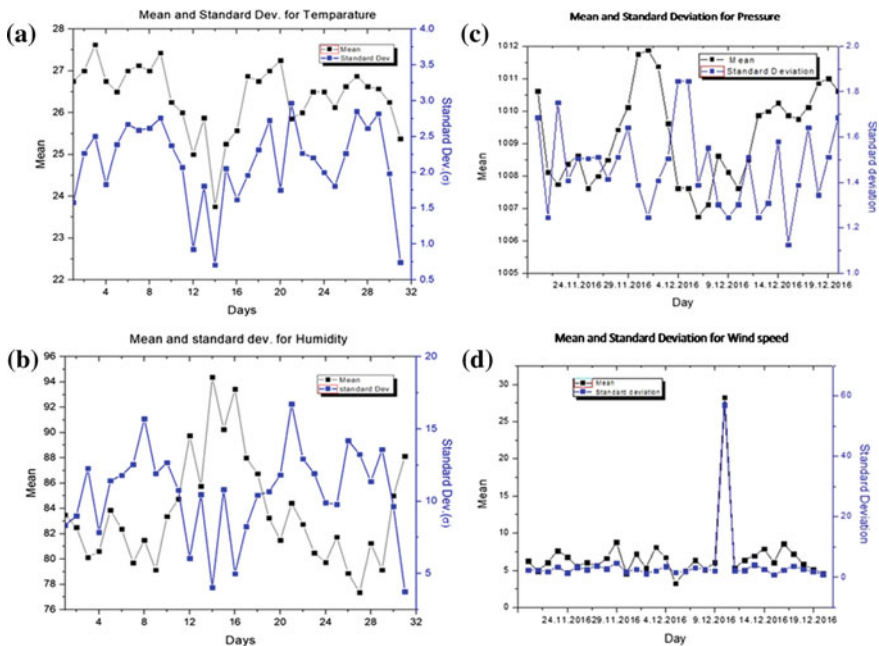


**Fig. 6** **a** Variations of air temperature mean and its standard deviation against number of day counts, **b** variations of the average relative humidity and its standard deviation against number of day counts, **c** pressure mean variations and its standard deviation against observation dates and **d** wind speed mean variations and its standard deviation against observation dates (black-coloured solid line joining black square blocks represents mean, and blue-coloured solid line joining blue square blocks represents standard deviation)

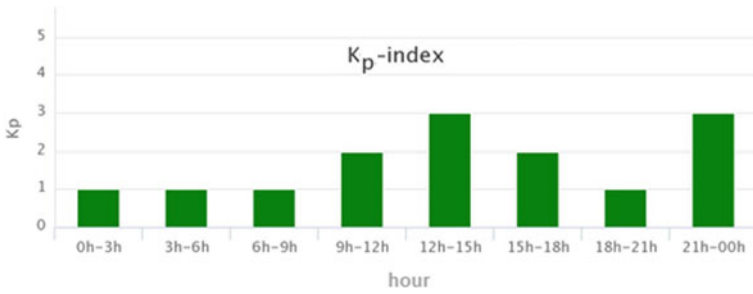


**Fig. 7**  $K_p$  index on 6 December 2016

than this, which implies that the day was geomagnetically quiet. This confirms that the anomalies presented in this work may be due to this earthquake event and not due to any other natural or geomagnetic activities.

A study reveals that earthquake lights (EQLs) occur before, during and occasionally after any earthquakes [18]. In relation to meteorological anomalies presented in this event, our assumption is that strong electric currents are produced inside the earth during earthquakes. It results in different configurations of current dipoles inside the earth. Jansky and Pasko showed that a large-scale dipole with poles located in earth crust at 5 and 15 km beneath the earth’s surface requires energy significantly higher than the total seismic wave energy in major earthquakes. From the long duration data (Table 1), we found that 30-km depth is very sensitive for Indonesia. Thus, this theory could be applied to this set of data. Besides, radon ( $Rn^{222}$ ) is carried by different gases like helium, methane, hydrogen and carbon dioxide from the earth crust. So, this radioactive gas needs to be considered because of its potential relevance.

We here suspect the effect of this radioactive gas to the environment before a strong earthquake. There was a rock deformation due to the movement of Indian Plate beneath the Eurasian Plate. From this deformity area, radon starts to emit and air ionization starts which turns into the effect of temperature change as well as relative humidity, atmospheric pressure and wind speed modification. But the soil radon ( $Rn^{222}$ ) and also thoron ( $Tn^{220}$ ) concentrations could be recorded at the earthquake-prone zone like Indonesia to study the sources of the radon emissions, earthquake precursors and the influence of meteorological parameters on the radon emission. Then, the observations and analyses and prediction could be justified. Various sophisticated instruments are available now to monitor radon and meteorological parameters like Radon Monitor RMT 1688-2, and direct correlation could be studied with radon and meteorological parameters.

**Acknowledgements** The authors gratefully acknowledge the support of the Narula Institute of Technology, 81, Nilgunj Road, Agarpara, Kolkata-700 109, India, in carrying out this work. This research did not receive any specific grant from any funding agencies in the public, commercial or not-for-profit sectors. The authors are also acknowledging the support from Head of this institute (Narula Institute of Technology) as well as from Head of the Department (Electronics and Communication Engineering).

## References

1. D.A. Wiens, C. DeMets, R.G. Gordon, S. Stein, D. Argus, J.F. Engeln, D.F. Woods, A diffuse plate boundary model for Indian Ocean tectonics. *Geophys. Res. Lett.* **12**, 429–432 (1985)
2. M. Delescluse, N. Chamot-Rooke, Instantaneous deformation and kinematics of the India-Australia Plate. *Geophys. J. Int.* **168**, 818–842 (2007)
3. J.C. Sibuet, C. Rangin, X. Le Pichon, S. Singh, A. Cattaneo, D. Graindorge, J.L. Schneider, 26th December 2004 great Sumatra-Andaman earthquake: co-seismic and post-seismic motions in northern Sumatra. *Earth Planet. Sci. Lett.* **263**, 88–103 (2007)
4. C. Satriano, E. Kiraly, P. Bernard, J.P. Vilotte, The 2012  $M_w$  8.6 Sumatra earthquake: evidence of westward sequential seismic ruptures associated to the reactivation of a N-S ocean fabric. *Geophys. Res. Lett.* **39**, 1–6 (2012)
5. D. Graindorge, F. Klingelhoefer, M.G. Gutscher, Sibuet, J.C., McNeill, L., Henstock, T., Singh, S.: in *European Geosciences Union Meeting, Austria*. Lower Plate control of Upper Plate Deformation at the Toe of the NW Sumatra Convergent Margin from Swath Bathymetry (2007)
6. M. Vallée, J. Charléty, A.M. Ferreira, B. Delouis, J. Vergoz, SCARDEC: a new technique for the rapid determination of seismic moment magnitude, focal mechanism and source time functions for large earthquakes using body-wave deconvolution. *Geophys. J. Int.* **184**, 338–358 (2011)
7. A.U. Maksudov, M.A. Zufarov, Measurement of neutron and charged particle fluxes toward earthquake prediction. *Earthquake Sci.* **30**, 283–288 (2017)
8. P. Hazra, S. Barui, S.S. De, S. Paul, Studies on the influence of two large earthquakes ( $M > 6$ ) upon 9 kHz sferics recorded from Kolkata. *Rom. J. Phys.* **60**, 1218–1224 (2015)
9. P. Hazra, S.S. De, S. Paul, G. Guha, A. Ghosh, Thermal anomalies around the time of nepal earthquakes M 7.8 April 25, 2015 And M 7.3 may 12, 2015. *Int. J. Geotech. Earthquake Eng.* **8**, 8–73 (2017)
10. M.A. Novianta, M.S. Achmad, E. Setyaningsih, in *Wireless Earthquakes Feature Monitoring Based on Acceleration and Magnetic Measurements Using MEMS Sensor*. ICETIA (2014), pp. 189–192
11. Z.M. Zeren, X.M. Zhang, X.H. Shen, W.H. Sun, D.M. Ning, Y. Ruzhin, in *General Assembly Scientific Symposium, (URSI GASS), XXXIth URSI. IEEE*. VLF Radio Signal Anomalies Associated With Strong Earthquakes (2014)
12. S.S. De, B.K. De, B. Bandyopadhyay, S. Paul, D.K. Haldar, A. Bhowmick, S. Barui, R. Ali, Effects on atmospherics at 6 kHz and 9 kHz recorded at Tripura during the India-Pakistan Border earthquake. *Nat. Hazards Earth Syst. Sci.* **10**, 843–855 (2010)
13. S.S. De, B. Bandyopadhyay, T.K. Das, S. Paul, D.K. Haldar, B.K. De, G. Chattopadhyay, Studies on the anomalies in the behaviour of transmitted subionospheric VLF electromagnetic signals and the changes in the fourth Schumann resonance mode as signatures of two pending earthquakes. *Indian J. Phys.* **85**, 447–470 (2011)
14. S.S. De, B.K. De, B. Bandyopadhyay, S. Paul, D. De, S. Barui, M. Sanfui, P. Pal, T.K. Das, Studies on the precursors of an earthquake as the vlf electromagnetic sferics. *Rom. J. Phys.* **56**, 1208–1227 (2011)
15. S.S. De, S. Paul, D.K. Haldar, D. De, A.K. Kundu, S. Chattopadhyay, S. Barui, Analyses of the effects of several earthquakes on the sub-ionospheric VLF-LF signal propagation. *J. Atmos. Sol.-Terr. Phys.* **81–82**, 20–26 (2012)
16. A. Deb, M. Gazi, C. Barman, Anomalous soil radon fluctuations—signal of earthquakes in Nepal and eastern India regions. *J. Earth Syst. Sci.* **125**, 1657–1665 (2016)
17. S.K. Sahoo, M. Katlamudi, J.P. Shaji, K.M. Krishna, G.U. Lakshmi, Influence of meteorological parameters on the soil radon ( $Rn^{222}$ ) emanation in Kutch, Gujarat, India. *Environ. Monit. Assess.* **190**, 111–115 (2018)
18. J. Jánský, V.P. Pasko, Earthquake lights: mechanism of electrical coupling of earth's crust to the lower atmosphere. *J. Geophys. Res. Atmos.* <https://doi.org/10.1029/2018jd028489> (2018)

# WARP Test Bed Implementation of Lag Order and Data Length-optimized AR Spectrum Estimation Algorithm



Debashis Chakraborty and Salil Kumar Sanyal

**Abstract** Recently, efficient spectrum estimation has become a fundamental requirement for any wireless communication technology. Accurate detection of spectrum in a populated and noisy environment reduces spectrum scarcity problem. Even though theoretical formulation is sufficient, physical realization and its real-time performance analysis are rare to find out. So, in this work we have investigated thoroughly the autoregressive (AR) modelling of a received signal using Yule-Walker (YW) method with the concept of confidence interval (CI) and Levinson–Durbin algorithm (LDA). The received signal strength has been observed extensively with variations of different radio gain parameters, data length and lag order along with the *statistical analysis*. Nonlinear curve fitting technique has been used to characterize the correlation between them. The physical study and real-time application of these algorithms have been implemented and verified on an FPGA-based platform by Rice University’s Wireless Open-Access Research Platform test bed in association with WARPLab.

**Keywords** Autoregressive · Yule-Walker · Levinson–Durbin algorithm · WARP · Statistical analysis

---

D. Chakraborty (✉)

Department of Electronics and Communication Engineering, Future Institute of Engineering and Management, Kolkata, India

e-mail: [debashisc77@gmail.com](mailto:debashisc77@gmail.com)

S. K. Sanyal

Department of Electronics and Communication Engineering, Narula Institute of Technology, Kolkata, India

e-mail: [s\\_sanyal@ieee.org](mailto:s_sanyal@ieee.org)

© Springer Nature Singapore Pte Ltd. 2020

K. Maharatna et al. (eds.), *Computational Advancement in Communication*

*Circuits and Systems*, Lecture Notes in Electrical Engineering 575,

[https://doi.org/10.1007/978-981-13-8687-9\\_18](https://doi.org/10.1007/978-981-13-8687-9_18)

## 1 Introduction

Efficient spectrum estimation (SE) is an emerging topic in the era of wireless communication. The estimation process is broadly categorized as nonparametric and parametric methods. In the nonparametric approach, we use fast Fourier transform (FFT) techniques, but the implementation of FFT method on hardware components is often complex and requires lots of memory elements. Whereas in the Parametric approaches, we always try to incorporate or assume a model for spectrum estimation. Sometimes, one has more knowledge about the particular process from which the data samples are taken. This a priori information or assumption permits the appropriate selection of an exact model for the process that generated the samples. In addition, the parametric models can combine and respond simultaneously to design constraints. The ability to estimate spectrum with very few samples (especially short data length) makes the parametric approach suitable for various applications like accurate spectrum estimation, channel modelling, prediction of a process or some natural phenomena, and waveform analysis of biological activity.

Therefore, for efficient and accurate SE we have selected the YW parametric technique [1]. Once we apply the concept of LDA [2] along with YW, the required lag order is reduced to a reasonable value, but this is not sufficient to implement the model. Accordingly, we have further opted for *statistical analysis* method for efficient and most optimized SE implementation of WARP test bed.

In this work, we have optimized lag order and data length using the exhaustive nonlinear curve fitting technique [3] against various radio board parameters for best optimized SE. We have chosen Rice University's Wireless Open-Access Research Platform (WARP) [4] board for prototyping. The sinusoidal signal is generated using WARPLAB commands, and the communication is established between the designated radio boards via JTAG and USB cables. The MATLAB program executes the algorithm to obtain the spectrum using above-said methods, whereas the OriginLab Pro [5] statistical software performs the regression analysis to find out the optimum lag order and data length. The approach can be considered as a software-defined radio (SDR) too. Flexibility and programmability of WARP board make it easier to implement the AR algorithms with minimum design turnaround time. The entire process of efficient estimation has been depicted in Fig. 1.

The paper is organized as follows. Section 2 deals with the development of AR model using LDA and CI along with logistic curve fit. The WARP board and its features as a test bed are described in Sect. 3. The implementation of WARP test bed has been demonstrated in Sect. 4. Section 5 explains the statistical approach. The

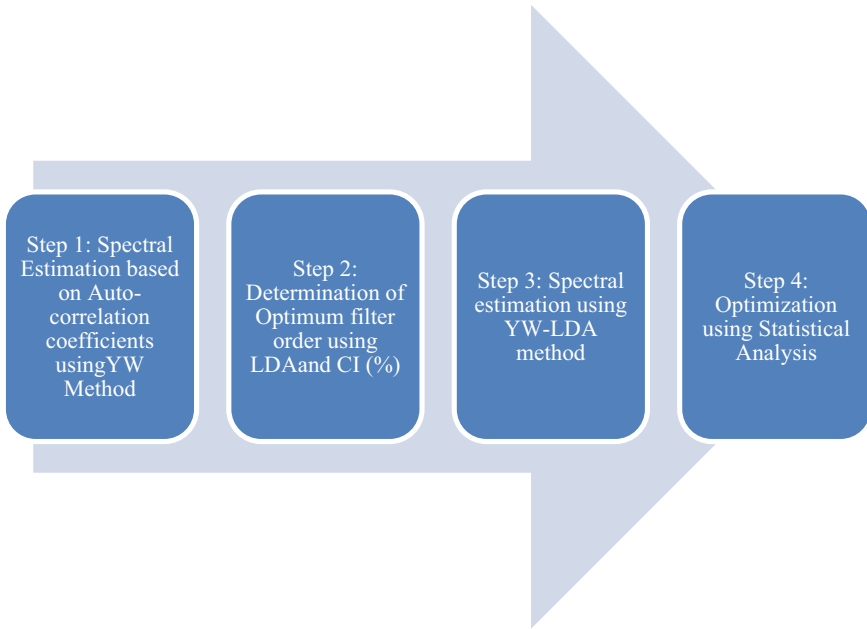


Fig. 1 Estimation procedure

experimental results with *statistical analysis* and related discussions are presented in Sect. 6. The conclusion and future scope of work is reviewed in Sect. 7.

## 2 Mathematical Modelling and Curve Fitting

### 2.1 Computation of AR Model

A rational power spectral density (PSD) is a function of the ratio of two polynomials having degrees  $m$  and  $n$ , respectively, provided the degrees are chosen large enough. Typically, we would like to estimate the PSD of the signal  $y(t)$ , which is obtained by filtering the white noise  $e(t)$  of power  $\sigma^2$  through the rational, asymptotically stable and causal filter with the transfer function

$$H(\omega) = \frac{B(\omega)}{A(\omega)} \tag{1}$$

where

$$A(\omega) = 1 + a_1 e^{-j\omega} + \dots + a_n e^{-jn\omega} \tag{2}$$



$$B(\omega) = 1 + b_1 e^{-j\omega} + \dots + b_m e^{-jm\omega} \tag{3}$$

The PSD estimation procedure has been depicted in Fig. 1. It is basically a four-step process.

The time series model of step 1 for the above filtering can be represented as:

$$y(t) + \sum_{i=1}^n a_i y(t - i) = \sum_{j=0}^m b_j e(t - j), \quad \text{where, } a_1 = b_0 = 1 \tag{4}$$

Now, multiplying both sides of (4) by  $y^*(t - k)$  and taking expectation yield:

$$r(k) + \sum_{i=1}^n a_i r(k - i) = \sigma^2 \sum_{j=0}^m b_j E\{e(t - j)y^*(t - k)\} \tag{5}$$

where  $r(k)$  is the auto-correlation of the output signal and  $0 \leq k \leq N - 1$

Simplifying successively, we obtain:

$$\begin{bmatrix} r(0) & r(-1) & \dots & r(-n) \\ r(1) & r(0) & \dots & r(-n + 1) \\ \vdots & \vdots & \ddots & \vdots \\ r(n) & r(n - 1) & \dots & r(0) \end{bmatrix} \begin{bmatrix} 1 \\ a_1 \\ \vdots \\ a_n \end{bmatrix} = \begin{bmatrix} \sigma^2 \\ 0 \\ \vdots \\ 0 \end{bmatrix} \tag{6}$$

$\triangleq R_{n+1}$

Equation (6) is popularly known as Yule-Walker equation [6]. This equation provides the desired estimation of auto-correlation coefficients of step 2.

If  $\{r(k)\}_{k=0}^n$  are known, we could solve for:

$$\theta = [a_1 a_2 \dots a_n]^T \tag{7}$$

More precisely, by using all the rows in (6) excepting the first one Eq. (6) could be reduced to:

$$\begin{bmatrix} r(1) \\ \vdots \\ r(n) \end{bmatrix} + \begin{bmatrix} r(0) & \dots & r(-n + 1) \\ \vdots & \ddots & \vdots \\ r(n - 1) & \dots & r(0) \end{bmatrix} \begin{bmatrix} a_1 \\ \vdots \\ a_n \end{bmatrix} = \begin{bmatrix} 0 \\ \vdots \\ 0 \end{bmatrix} \tag{8}$$

$\triangleq r_n \qquad \qquad \qquad \triangleq R_n \qquad \qquad \qquad \triangleq \theta$

Thus,  $[r_n] + [R_n][\theta] = 0$  and once  $\theta$  is found  $\sigma^2$  could be found using the first row of (8). Now to explicitly show the dependence of  $\theta$  and  $\sigma^2$  on the order n, we can write Eq. (8) as:

$$R_{n+1} \begin{bmatrix} 1 \\ \theta \end{bmatrix} = \begin{bmatrix} \sigma^2 \\ 0 \\ \vdots \\ 0 \end{bmatrix} \quad (9)$$

## 2.2 Logistics Curve Fit

Logistics curve [7] has the nature that drops off towards “0” and ascends towards “1” values more gradually. The formula which produces such a curve is the logistic formula as given in Eq. (10)

$$p = \frac{1}{1 + e^x} \quad (10)$$

The formula is simple in the form and has a number of key interpretational advantages to provide flexibility, which can be modified as follows:

$$p = \frac{1}{1 + e^{-(a+bx)}} \quad (11)$$

where  $a$  and  $b$  determine the logistic intercept and slope.

As the relationship between  $p$  and  $x$  is nonlinear, the slope varies as  $x$ . When  $p = \frac{1}{2}$ , the slope is  $\frac{b}{4}$ . It is to be noted that both  $a$  and  $b$  have the same qualitative effect on the logistic regression relationship like the linear cases. The correlation between *lag order* and *data length* has been demonstrated using this curve along with suitable *regression* analysis.

## 3 WARP as a Test Bed

A traditional hardware-defined radio has fixed architecture, and its characteristics could only be changed by adjustment through physical intervention. In contrast to SDR, Rice University’s WARP board provides a scalable and configurable platform employing programmable hardware mainly designed to run various communication algorithms. Its programmability and flexibility make it easier to implement various physical and network layer protocols.

The important components associated with the architecture are highlighted.

### ***3.1 Custom Hardware***

It mainly consists of two functional sub-units, namely Virtex-4 FPGA and PowerPC (PPC). The Xilinx Virtex-4 FX100 [8] provides scalable interconnects to run high-speed DSP intensive algorithms under the reconfigurable scenario. PowerPC handles the relevant protocols for establishing the communication between the WARP board and the desktop-running programs in MATLAB environment through USB.

### ***3.2 Platform Support Packages***

This involves the commands for configuring various radio boards. It could be added to the standard MATLAB library to enable seamless use of WARP board at all layers of wireless network design [9]. It is a central archive for all source codes, models and hardware design files. The full contents will be available under a Berkeley Software Distribution (BSD) like open-source licence. Implementations of novel algorithms are enabled by the custom hardware and platform support packages. Full systems incorporating novel algorithms can be rapidly built using the standard building block modules provided in the repository.

### ***3.3 Open-Access Repository***

Open-access repository and research applications [10] provide the standard programs like Xilinx iMPACT board configuring files (\*.ipf) required to configure WARP board v 2.2 as either SISO or MIMO mode. Once the platform is configured, the MATLAB program depicting the specific algorithm such as AR Yule-Walker method of SE could be executed on the desktop computer in association with WARP node connected via USB port.

## **4 Test Bed Implementation of AR Model**

The major steps for the implementation are described in Fig. 2 and are as follows.

### ***4.1 Generating Baseband Signal***

The baseband signal being a sinusoidal one has been generated using MATLAB with amplitude ranging between  $-1$  and  $+1$  V at various frequencies such as 4 and 8 MHz.

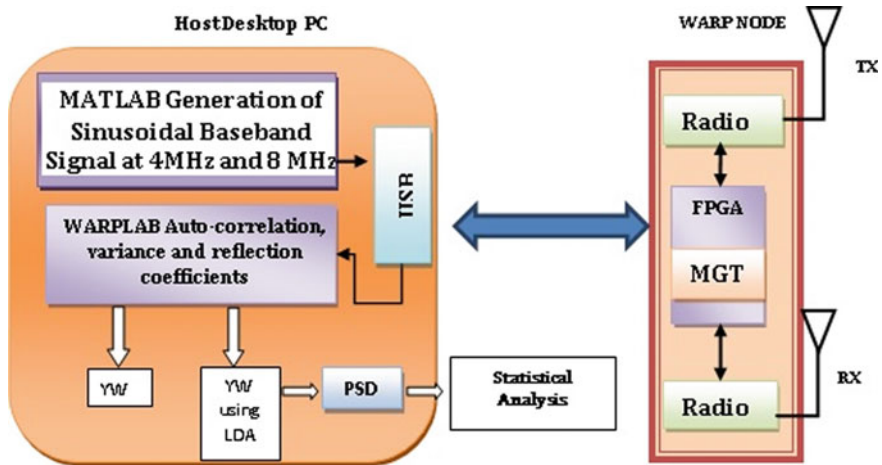


Fig. 2 WARP test bed implementation

The numbers of samples for all the radio boards could be varied to a maximum value of  $2^{14}$  as specified by the manufacturer.

#### 4.2 Configuring and Connectivity of Radio Boards on WARP Node

The digital baseband samples to be transmitted over the air have been generated by the user in the MATLAB program as mentioned earlier. Xilinx iMPACT program via USB JTAG cable configures FPGA and its peripheral processor using \*.bit file. Once the node is configured, a trigger is sent to transmitter and receiver boards. Upon reception of the trigger signal, samples stored in transmitter buffers are transmitted over the transmitting antenna in real time. The transmitter radio board performs two jobs successively [11]. First, it performs the job of DAC and secondly up-conversion to analog RF. The receiver radio board performs the reverse job, and captured baseband samples are stored in the received buffers in WARP node. The received data is then sent to the workspace and processed offline using MATLAB commands.

### 5 Statistical Approach

Estimation of a parameter or parameter vector by using statistical approach has been quite a good method for modelling either a phenomenon or an available spectrum as in

our experimental set-up. To reach the optimum value, we have initially employed the standard estimators like Yule-Walker using LDA and subsequently using the notion of confidence interval, which specifies a random set covering the true parameter value with some specified high probability of occurrence. Even though we apply the above-mentioned approaches for practical applications using WARP test bed, it is not always assured to produce the best result of estimating the spectrum with minimum error probability. Accordingly, to achieve the optimal values of WARP transmitter and receiver gain parameters, data length and lag order we have performed the following *statistical analysis* among these correlated design parameters to obtain the best optimized spectrum using WARP test bed.

### ***5.1 Maximum Likelihood Estimation***

The method of least squares [12] has an appealing intuitive interpretation as it depends only on the knowledge of the mean and covariance of the observed samples. The Gauss–Markov theorem [13] also uses least squares estimation technique by showing its natural property of minimum variance amongst unbiased linear estimators. Least squares or maximum likelihood leads to the desired value, often referred to as a point estimate. As it is obvious that goodness of accuracy lies in their large-numbered sample behaviour, which may lead to the exact value or the true value, hence it is important to bear the idea of the probable accuracy of the estimator. The criterion which permits verifying the mean square convergence, also considers not to identify the limit of the sample length. Maximum likelihood estimation [14] depends on the assumption of a particular distributional form of the observed data.

Verification of the above properties on our sample data leads to the estimation performance of the gain parameters of WARP boards. Different performance characteristics with variations of lag order, data length and receiver–transmitter gain parameters have exhaustively been measured experimentally. Finally, statistical software has been utilized to achieve the best optimized value of the above parameters.

### ***5.2 Statistical Parameters for Optimum Performance of WARP Test Bed***

The parametric method of SE as undertaken in this work is absolutely based on the knowledge of auto-correlation coefficients of the data samples as provided by the radio transmitter of WARP test bed. Since *statistical analysis* has been adopted over and above the results obtained through YW, YW-LDA, YW-LDA with CI to adjudicate the best optimized fit of the WARP parameter for SE, knowledge of some common statistical deterministic parameters, namely *R*-value, *R*-squared value, adjusted *R*-square and  $\chi^2$  (chi – square) [15], is extremely necessary to estimate

the spectrum. Accordingly, OriginLab Pro software along with MATLAB has been exhaustively used to access the SE process.

Here, we incorporate various statistical parameters as mentioned above for the assessment of the fitment of different WARP parameters as well as lag order and data length. As discussed earlier, the  $R^2$  measures the per cent of variation on the “dependent” variable that can be accounted for or “explained” by the “independent” variables. The estimate represents the software’s attempt to find the equation that best summarizes the data under observation. The minimization of the standard errors like standard deviation (SD) or mean square error (MSE) and chi-square determines the quality of estimate [16]. So, this concept of statistical fitment encourages us to investigate the best optimum values of related design parameters for achieving efficient SE using WARP test bed. The contemporary literature describes the method by theoretical optimization analysis only. However, our study of various parameters employing statistical analysis leads us to a new dimension of achieving optimum SE using a real test bed. Different nonlinear curve fitting techniques have been employed for best describing the dependencies on various parameters. In the following section, we shall observe their behaviour with best statistical fit of the parameters based on statistical analysis techniques and tabulated after every fitment method.

## 6 Experimental Results and Analysis

### 6.1 Generation and Detection of Waveforms

As described earlier, the real-time sinusoidal signals are generated using WARPLAB environment at two frequency values, such as 4 and 8 MHz. One of the transmitted waveforms is shown in Fig. 3a, along with the received noisy signal in Fig. 3b. Here we observe that the received signal is highly affected by *white Gaussian noise* present in the environment. Therefore our job is to detect the frequency components present in this waveform using YW method.

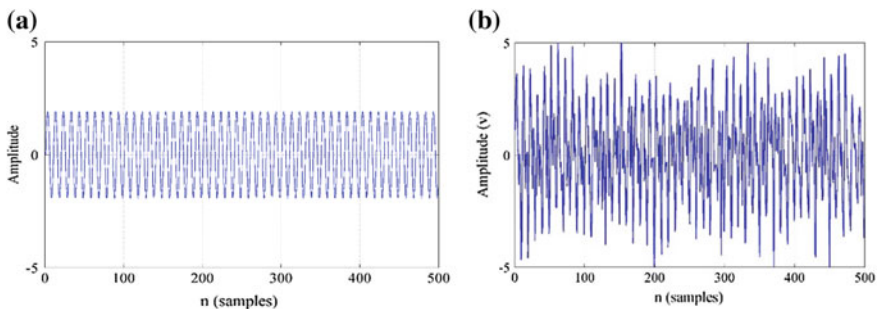


**Fig. 3** **a** Transmitted signal, **b** received noisy signal

### 6.2 Dependency of Lag Order and Received Signal Strength on Data Length

The variation of lag order with data length has been plotted in Fig. 4. We observe that the lag order has a minimum value at a data length of around 200 and gradually increases up to 64 at a data length of 10,000. The plotted graph has been empirically fitted using nonlinear curve fitting technique using the statistical software OriginLab Pro. Both the YW-LDA-CI and the statistical approach (YW-LDA-CI-SA) have been shown in Fig. 4 with a 95% of CI (both upper and lower) to the experimental plot. The relevant fitment parameters are described by Eq. (12). The goodness of fit is justified in Table 1 with fit status of 100% achieved in only 5 iterations. It is also to be noted that most optimized (very close to 1) values of different statistical parameters such as  $R$ ,  $R$ -square and adjusted  $R$ -square have been achieved for 100% fit status.

$$y = \frac{a}{1 + \exp(-k * (x - x_c))} \tag{12}$$

where  $a = \text{amplitude}$ ,  $x_c = \text{curve centre}$  and  $k = \text{coefficient}$ .

In our fitted curve, we obtain the values of these parameters against WARP board as given in Table 2.

Another interesting point to be noted that, in case of YW-LDA-CI-SA the received signal strength is comparatively very high than nonparametric periodogram approach as shown in Fig. 5. This feature makes it easier for signal detection and estimation employing statistical approach in a hostile environment. The signal strength also improves significantly with increased data length up to 10,000.

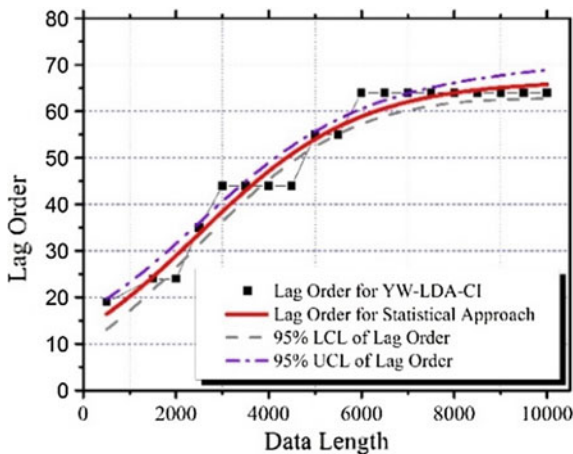


Fig. 4 Variation of lag order with data length

**Table 1** Fitment parameters for YW-LDA-CI

Number of points	19
Degrees of freedom	16
Reduced chi-square	10.92129
Residual sum of squares	174.7406
R-value	0.98033
R-square (COD)	0.96104
Adj. R-square	0.95618
Root MSE (SD)	3.30474
Number of iterations	5
Fit status	Succeeded (100%)

**Table 2** Parameters for the fitted using logistic curve for lag order against data length Logistic curve

Parameter	Value
$a$	66.66324
$x_c$	2459.65982
$k$	5.72E-04

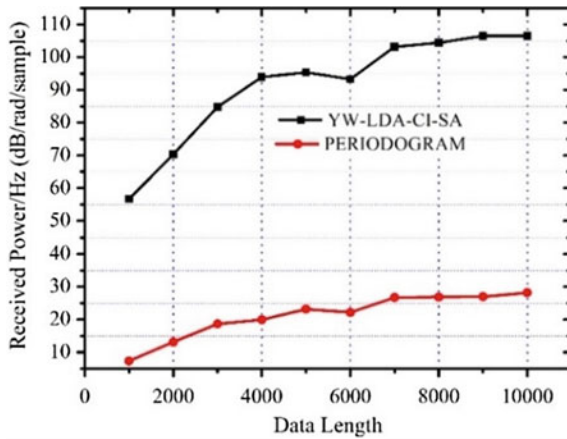


**Fig. 5** Variation of signal with data length



### 6.3 Optimization of Lag Order and Data Length

Figure 6 shows the step-by-step optimization of the lag order, starting from using YW only to *statistical analysis* including LDA and CI. As observed by us, the lag order requirement is around 494 for YW to implement the SE. However, when we apply LDA and CI it is reduced to 78. But this is still very high to implement the filter. Hence, we employ the *statistical analysis* to achieve minimum lag order of 19 only as depicted in Fig. 6. Figure 7 indicates a reduction in data length to 200 only, starting from 1000 as required in ordinary YW method.

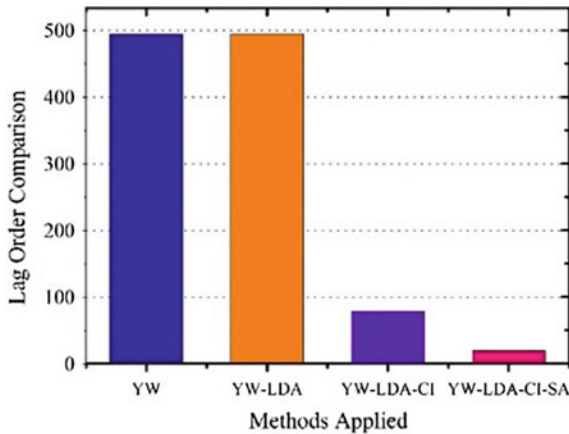


Fig. 6 Optimization of lag order

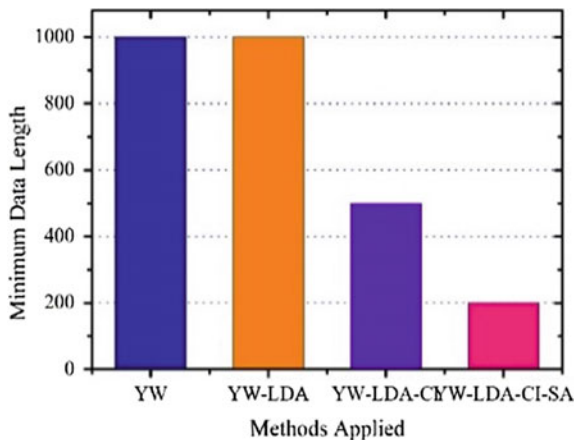
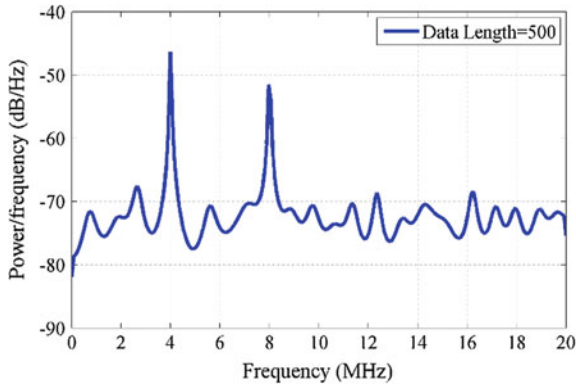


Fig. 7 Optimization of data length



**Fig. 8** Received signal spectrum

### 6.4 Received Signal Spectrum

Finally, we have plotted the received signal spectrum with the optimized values of lag order and data length. The sinusoidal signals at frequencies of 4 and 8 MHz have sharp peaks estimated by the statistical approach based on YW-LDA-CI method as indicated in Fig. 8.

## 7 Conclusion

In this work, AR YW method of SE is established using WARPLAB in real time. Our work is unique in the sense of considering real-world constraints and performance criteria like gain parameters available at transmitter and receiver. An excellent real-time output has been shown, which is a valid prototype of the parametric estimation model or process under consideration. In this work, the optimal modelling of the signal has been done using LDA and CI efficiently and it has also been validated on the test bed. The comparison of performance study has been experimented as well, which contributes a better performance analysis in favour of the parametric approach along with *statistical analysis*. Evidently, *statistical analysis* of the WARP board gain parameters gives us the robust model for optimum detection. In the present set-up, we have implemented a SISO model with sinusoidal signals having frequencies of 4 and 8 MHz, whereas using at least two nodes with four radio boards a complete MIMO model could be conceived with greater complexity and much real-life environment, which leads to the concept of cognitive radio in the true sense of the term.

## References

1. S.U. Pillai, T.I. Shim, *Spectrum Estimation and System Identification* (Springer Science & Business Media, 2012)
2. S.S. Haykin, *Adaptive Filter Theory* (Pearson Education India, 2008)
3. T.A.N.G. Jia-de, Nonlinear curve fitting based on MATLAB. *Comput. Modernization* **6**, 15–19 (2008)
4. J. Ansari et al., in *Wireless Communications and Networking Conference (WCNC), 2011 IEEE*. A flexible MAC Development Framework for Cognitive Radio Systems (2011)
5. Pro, Origin. 8 (2007). *About Origin Pro 8 SRO, V8. 0724 Software, Copyright 1991–2007* (Origin Lab Corporation, 2007)
6. J. Liew, S.L. Marple, in *IEEE International Conference on Proceedings (ICASSP'05), Acoustics, Speech, and Signal Processing, IEEE*. Three-Dimensional Fast Algorithm Solution for Octant-Based Three-Dimensional Yule-Walker Equations, vol. 2 (2005)
7. N.M. Nasrabadi, Pattern recognition and machine learning. *J. Electron. Imaging* **16**(4), 049901 (2007)
8. C. Lavin et al., in *2010 International Conference on Field-Programmable Technology (FPT). IEEE*. Rapid Prototyping Tools for FPGA Designs: RapidSmith (2010)
9. A. Khattab et al., WARP: a flexible platform for clean-slate wireless medium access protocol design. *ACM SIGMOBILE Mob Comput. Commun. Rev.* **12**(1), 56–58 (2008)
10. M. Duarte, Full-duplex wireless: design, implementation and characterization. Ph.D. Dissertation, Rice University, 2012
11. O. Gustafsson et al., in *2010 Proceedings of the Fifth International Conference on Cognitive Radio Oriented Wireless Networks & Communications (CROWNCOM). IEEE*. Architectures for Cognitive Radio Testbeds and Demonstrators—An Overview (2010)
12. S. Širca, in *Method of Least Squares*. Probability for Physicists (Springer, Cham, 2016), pp. 227–258
13. S. Brooks et al., eds. *Handbook of Markov Chain Monte Carlo* (CRC Press, 2011)
14. F.W. Scholz, *Maximum Likelihood Estimation* (Wiley StatsRef: Statistics Reference Online, 2014)
15. R.H. Shumway, S.S. David, in *Time Series Regression and Exploratory Data Analysis*. Time Series Analysis and Its Applications (Springer, New York, 2011), pp. 47–82
16. D.C. Montgomery, *Introduction to Statistical Quality Control* (Wiley, New York, 2009)

# Detection of Black Hole Attack in Delay-Tolerant Network



Chandrima Chakrabarti, Ananya Banerjee, Anirban Das,  
Souradip Ganguly, Somraj Mukherjee, Rohan Dutta and Jagriti Chourasia

**Abstract** In spite of modernization of humanity, in emergency situations like after any natural calamity our infrastructure-based network backbone gets affected first. Disaster relief volunteers face the immense pain to set up a communication system, due to the failure of telecommunication infrastructure and long-standing power. Smartphones are the most preferable devices, operating and acting in delay-tolerant mode through Bluetooth/Wi-Fi, for setting up a peer-to-peer network enabling communication in post-disaster network. It is now popularly known as delay-/disruption-tolerant network (DTN). In this network, a node can misbehave and fail to establish a route or direct the data to neighbor node due to its malicious activity to decrease the performance of overall network. If a node suddenly drops messages after receiving, then it is known as black hole node. Black hole nodes do not forward any messages and can also destroy the message forever. A node may also act as a partially black hole node with the character of selective dropping. However, black hole nodes can hamper the overall performance of the network. In this paper, we have proposed a

---

C. Chakrabarti (✉) · A. Banerjee · A. Das · S. Ganguly · S. Mukherjee · R. Dutta · J. Chourasia  
Computer Science and Engineering Department, Narula Institute of Technology, Agarpara,  
Kolkata 700109, WB, India  
e-mail: [chandrima.chakrabarti@nit.ac.in](mailto:chandrima.chakrabarti@nit.ac.in)

A. Banerjee  
e-mail: [ananya.banerjee@nit.ac.in](mailto:ananya.banerjee@nit.ac.in)

A. Das  
e-mail: [anirbandas.gst@gmail.com](mailto:anirbandas.gst@gmail.com)

S. Ganguly  
e-mail: [souradip.g.21@gmail.com](mailto:souradip.g.21@gmail.com)

S. Mukherjee  
e-mail: [iamsomraj@gmail.com](mailto:iamsomraj@gmail.com)

R. Dutta  
e-mail: [rohanduttaperfect@gmail.com](mailto:rohanduttaperfect@gmail.com)

J. Chourasia  
e-mail: [jagritichourasia47@gmail.com](mailto:jagritichourasia47@gmail.com)

method to detect and avoid the malicious nodes forming black hole attack in DTN. We also evaluate the scheme using ONE simulator.

**Keywords** Disruption-tolerant network · Black hole · Delay · Hopping · Mobility · Opportunistic · Protocols · Security · Scalability

## 1 Introduction

Currently in the era of advancement, delay-tolerant network (DTN) is one of the most budding areas of research in post-disaster environment where infrastructure is absent. In DTN, mobile nodes are operating together [1] and acting as router without any central authority. Delay is unavoidable in DTN as there is no fixed route from sender to receiver node. Messages are transferred bundle-wise in multi-hop manner. DTN has a widespread application in disaster environment, space, remote areas, emergency situation where fixed network fails to establish or is unaffordable. DTN is distinguishable from other networks due to its store–carry–forward method [2–4]. Messages are stored by any intermediate node first. Then, message is carried by the intermediate node until the next forwarder node is found. Lastly, message is forwarded to the next forwarder node. Messages can also be forwarded without knowing the actual location of receiver due to multi-hop communication. Routing is very challenging in DTN due to different mobility patterns of nodes. For a better understanding of network characteristics, a sample scenario of a DTN is presented here in Fig. 1. In this paper, we are considering applications of DTN in post-disaster communication.

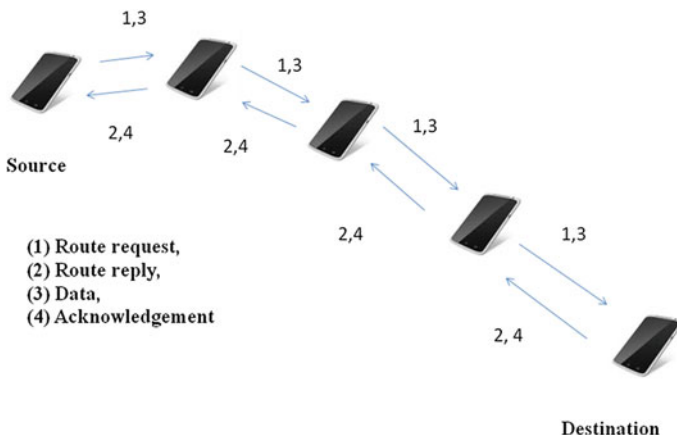


**Fig. 1** Multi-hop communication in delay-tolerant network

Delay-tolerant network is a new approach of communication where the signal connectivity may lack continuousness. It is now popularly known as disruption-tolerant network. In this network, a node can misbehave and fail to establish a route or direct the data to neighbor node due to its malicious activity to decrease the performance of overall network [2–4].

Quite similar to a black hole in space, a black hole node in delay-tolerant network is a node which receives any incoming message or data and blindly drops it without further forwarding or transmitting. When it is done so in any emergency time, this dropping of information can badly affect the whole network architecture. Thus, the performance of the DTN highly depends upon the detection of the black hole nodes and then taking proper measures for lowering the effect on them on the whole ad hoc architecture. We discuss the literature survey, i.e., existing related work in Sect. 2. Section 3 describes our proposed black hole node detection and avoidance scheme. How our system is implemented and results are evaluated are discussed in Sect. 4. Our paper is concluded with a direction of future work in Sect. 5.

## 2 Related Work

Popularity and usefulness of DTN are increasing day by day among researchers. Here, we incorporate some of the survey works. Banerjee proposed a mechanism in [5] where the source before sending any data preludes a message to destination, too aware of the communication. Now after receiving the message, the receiver sends a postlude message. It contains the number of total data packets received. If data is lost, then the detection and removal procedure are initiated on the malicious node, after getting neighboring nodes' information in the network.

In [6], the authors described a solution for avoiding multiple black holes by modifying the AODV protocol. Here, every participating node has assigned a reliability level. The node which has 0 reliable values is termed as a malicious node. Malicious nodes are removed from the network. In this paper, nodes' reliability levels are maintained based on their cooperation and involvement. When the packet is received by the destination, it must send an acknowledgement toward source; instantly, the level of the intermediate node will be upgraded. If there is no acknowledgement, the level of the intermediate node will be reduced. The major disadvantage of this scheme is delay in processing throughout the network. Kurosawa in [7] projected a black hole detection approach based on statistics. This scheme is based on received RREPs, and differences of the destination sequence numbers are also calculated. The scheme is low cost as extra routing traffics are eliminated, and existing protocols are not modified. Nevertheless, false positives are not detected using this scheme.

In [8], Bhattacharyya et al. proposed that rushing attack can be solved by using Secured Dynamic MANET On-Demand (SEDYMO), where routing information must be added while transmitting messages by intermediate nodes. Intermediate nodes are not allowed to delete any routing information from the previous node. Hash chains and digital signatures are used to protect identity of nodes.

In [9–11], the authors proposed a method of providing a tier architecture of ad hoc network depending on the barriers at the affected site by using different types of communicating devices according to strength, like cheaper devices in bottom of the building and costlier devices when lower devices cannot be handled.

In [12], Hegde and Sreenivas proposed the technique of steganography for hiding the message before transmission to neighbor node. The scheme maintains different levels of security. Message-specific key is used to hide message in an image. Then, the pictures are divided into  $r$  no. of pixels. First group of pixels is formed by extracting first pixel of all images. Similarly, second group of pixels is formed by extracting second pixel of all images and so on. Using neighborhood key, all the pixels are encrypted and forwarded to next node. Any intermediate node can decrypt the message as well as encrypt the message with the next node's key and can forward it. Delosières and Nadjm-Tehrani in [13] used store-and-forward technique in DTN routing. The BATMAN store-and-forward scheme enables routing of packets in both mesh and delay-tolerant sub-networks instead of different mobility patterns of nodes.

Uddin et al. in [14] used post-disaster mobility (PDM) model to describe different mobility patterns of nodes in post-disaster network. The authors described mobility pattern on a given city map. It designs two major groups after a disaster, i.e., survivors and rescue workers. The authors simulated PDM in the opportunistic network environment (ONE) simulator. The authors also compared connectivity characteristics and mobility model between PDM and ONE simulator. In [15], Zhang et al. discovered a reputation scheme for DTN to provide score on node behavior. The scheme includes bundle forwarding protocol, behavior recording mechanism and computation model. Piggybacking is used for acknowledgement purpose.

Gao et al. in [16] proposed PMDS, a probabilistic misbehavior detection scheme for DTN, to adaptively detect misbehaviors in DTN. After successfully forwarding and passing TA's investigation, every node must claim compensation from trusted authority (TA). Otherwise, the particular node will be punished by TA node [16].

Zhu et al. in [17] proposed an algorithm SUCCESS, and forwarding evidence and authentication are used to ensure nodes' participation. A separate message signed by next hop node's public key is known as forwarding evidence. They also introduced the concept of *reputation ticket* [17].

Lu et al. in [18] discovered Pi protocol to find behavior of selfish node in DTN. Pi protocol has four parts: initialization of system, generation of bundle, forwarding of bundle, and finally charging and rewarding of nodes. After successful bundle forwarding, cooperating nodes will get reputation and rewards. On the contrary, non-cooperating nodes will be punished.

In [19], Zhu et al. presented iTrust scheme for misbehavior detection. The scheme is used for calculating trustworthiness of nodes in the network. The iTrust scheme works in two phases. First, routing evidences of nodes are collected and based on that reputations are assigned. After that, auditing is performed to find actual cause of misbehavior. It may be intentional or unintentional.

In [20], Asplund et al. described the network challenges in post-disaster environment. However, the presence of black hole nodes may hamper delivery ratio of the

network. Inspired by these works, we implemented a scheme to detect black hole attack in DTN.

### 3 System Model

In this section, we discuss how our system will detect and avoid black hole nodes.

#### 3.1 Black Hole Attack Detection

Black hole nodes can be defined as a node that drops the message immediately without forwarding them. If a node drops all the messages after receiving, then it is known as fully black hole node. On the other hand, if a node drops some messages according to its choice, then it is known as a partially black hole node. We implement our scheme in post-disaster scenario where due to intermittent connectivity message delivery gets delayed. Due to the presence of black hole nodes in the network, message delivery gets immense delay. So, our objective is to detect black hole nodes in the network and avoid them during message exchange. In our proposed model, firstly the sender tries to send the data to any nearby neighboring nodes within the range of 100 m. If the waiting time in case is greater than the value of scheduled time ( $t1$ ), the sender sends a warning message just to identify if the neighboring node is a black hole node or not. If our counter  $c$  is increased by two, then the neighboring node is a black hole node and thus that node will further be avoided by other neighboring nodes. If it is not a black hole node, then the initial sender will receive an acknowledgement from the neighboring node preferably within the time period  $t1$ . Then,  $c$  is reinitialized to zero and the same process gets repeated for the intermediate neighboring nodes as well until the final receiver receives the message.

#### Declaration of variables used in the algorithm

$S$ —sender node,  $N$ —neighbor node,  $R$ —receiver node, WT—waiting time,  $C$ —counter variable, ACK—acknowledgement.

In our model, we have assumed the following:

Sender is the person who sends the data, and receiver is the person who receives the message. There can only be one starting sender and final receiver.

There are  $n$  number of neighboring nodes in between starting sender and final receiver to transmit any given data. Neighboring nodes can be a sender or a receiver at any instance of time. All the neighboring nodes are moving continuously.

Waiting time is the time until which a sender waits for the receiver to give the acknowledgement to the sender (here, we are considering WT is  $t1$  min at maximum). Here,  $C = 0$ . Acknowledgement (ACK) variable stores the next node's name with the copy of the report.



**Algorithm 1: Detection of Black hole attack**

1. Start.
2. Starting sender sends the data information or report to the neighboring nodes within the range of 100 m.
3. For the starting sender, if WT is greater than  $t_1$  min, then the starting sender will give a warning message to all the neighbors nearby within the range of 100 m to really warn that respective node is not responding.
4. And,  $C$  is incremented by one.
5. Else, the starting sender will get ACK from the neighboring nodes (who are acting like a receiver in that time).
6. Repeat the steps 3–5 until  $C$  becomes 2.
7. Reinitialize  $C$  to 0.
8. The group of neighboring nodes sends the data information or report to the next group of neighboring nodes within the range of 100 m.
9. If WT is greater than  $t_1$  min, then the sender neighbors ( $S$ ) will give a warning message to all the receiver neighbors ( $R$ ) nearby within the range of 100 m to really warn that the respective node ( $N$ ) is not responding.
10. And,  $C$  is incremented by one.
11. Else, the sender neighbors ( $S$ ) will get ACK from the neighboring nodes ( $R$ ) (who are acting like a receiver in that time).
12. The steps 8–11 get repeated until  $C$  becomes 2.
13. Repeat the steps 7–12 until the final receiver gets the report.
14. Stop.

**3.2 Black Hole Attack Avoidance**

The neighboring nodes that are having a value of  $C$  as 2 should be eliminated, so that the network remains connected throughout. Receiver node will determine which nodes need to be eliminated from the network. A broadcast message will be sent by the final receiver node to all the nodes in the network that the respective node/nodes will not be included in the network further.

In our system, each node needs to maintain neighbor table and update the table time to time. Neighbor table should be updated time to time to avoid black hole nodes in the network. In our system, a node before sending actual packet must send test packet to all neighbor nodes based on neighbor table. If a neighbor node drops the test packet and does not give any acknowledgement within time, that neighbor node needs to be avoided. If any other neighbor node has given ACK within time, that node may be chosen as the next forwarder node.

A sample neighbor table is displayed in Table 1 maintained by node  $N_1$ . Before forwarding any message, each node needs to consult this neighbor table.

As shown in Table 2, node  $N_1$  will choose  $N_2$  as the next forwarder as it is not black hole node.  $N_1$  will not choose  $N_3$  as the next forwarder as it is black hole node.

**Table 1** A sample neighbor table maintained by node *N1*

Neighbor node id	Within range (Y/N)	Last meeting time	Black hole node (Y/N)
<i>N2</i>	Y	<i>T1_N1_N2</i>	N
<i>N3</i>	Y	<i>T1_N1_N3</i>	Y

For any newly joined node, there is no available status of the node whether it is black hole or not. So, a new node may be chosen as the next forwarder based on the initial test message ACK verification method.

## 4 Simulation

ONE stands for opportunistic network environment [21] which is a simulator based on Java and is mainly used for research work related to the delay-tolerant network (DTN). Using ONE simulator, simulation can be done in a flexible manner. Statistical reports can also be generated efficiently from the previous simulations. The ONE simulator runs on various different platforms supporting Java like Linux and Windows. The simulator can be downloaded from the official site with free license to use.

In our model, we have designed our relief team comprising total 61 nodes or members. We have divided our total team into five subgroups as shown in Table 2.

**Table 2** Configuration of our proposed approach in simulation

Group name	Group id	Number of hosts	Movement speed (m/s)	Buffer size (MB)	Interface	Purpose/need
Control station	Cs	1	0	5000	High speed	Monitoring, located outside of disaster zone
Shelter	Sh	4	0	2000	High speed	Relief camp in the disaster zone
Shelter workers	Sw	8	0	100	Bluetooth	Workers in shelter camp
Volunteers	Vol	40	Min. 7, max. 10	50	Bluetooth	Relief workers outside shelter
Vehicle	Veh	8	Min. 10, max. 20	1000	Bluetooth	Carrying relief stuffs to victims

We used group movement model: shortest path map-based movement; router: “spray and wait router”; and message TTL: 300 max.

### **Algorithm 2: Steps followed in simulation**

1. Start.
2. Prepare “delivered message report” // to store the successful delivery of data packets, along with the number of times a node is being used while delivering data packets.
3. Prepare “message stats report” // to check the delivery probability and latency of delivered messages between nodes.
4. Prepare “final report” through inheriting “delivery messages report” data to count the number of times each node being used as intermediate one in data transfer.
5. Now run the simulation with the source file, “defaults\_settings.txt” for 12 h duration. After simulation, the reports are automatically generated. Study the reports carefully.
6. From “final report,” we are able to see that which nodes are being used as an intermediate one in the total simulation. If some nodes are not yet used in the whole simulation time, then we can guess those nodes may be black hole one. But for that, we have carried another simulation.
7. Picked up those nodes specifically whose participation in message transfer was “0”. Designed another source file as “defaults\_settings2.txt”. Now we have carried out simulating those nodes with message creation and transfer.
8. If after simulation still we get delivery probability, overhead ratio, latency all value null that confirms those nodes are really black hole one, else due to close distance between sender and receiver those nodes are not used as an intermediate one in the first simulation.
9. End.

Algorithm 2 discusses how the black hole nodes are detected in the actual simulation environment. We create the simulation environment using ONE simulator and follow the steps as mentioned in algorithm 2 to detect and avoid black hole nodes in the network.

We have obtained the observations after the simulation. The delivery probability decreased significantly due to the presence of black hole nodes. In Fig. 2, the graph of delivery probabilities obtained from the reports is given.

The overhead ratio decreased significantly due to the presence of black hole nodes, as most of the nodes are not taking part in the transfer of messages. In Fig. 3, the graph of overhead ratio obtained from the reports is given.

The latency also decreased significantly due to the presence of black hole nodes. In Fig. 4, the graph of average latency is obtained from the reports.

We have successfully implemented black hole detection mechanism. We also avoid black hole nodes during communication and message exchange. So, after removal of black hole nodes, our scheme performs better than the scheme with black

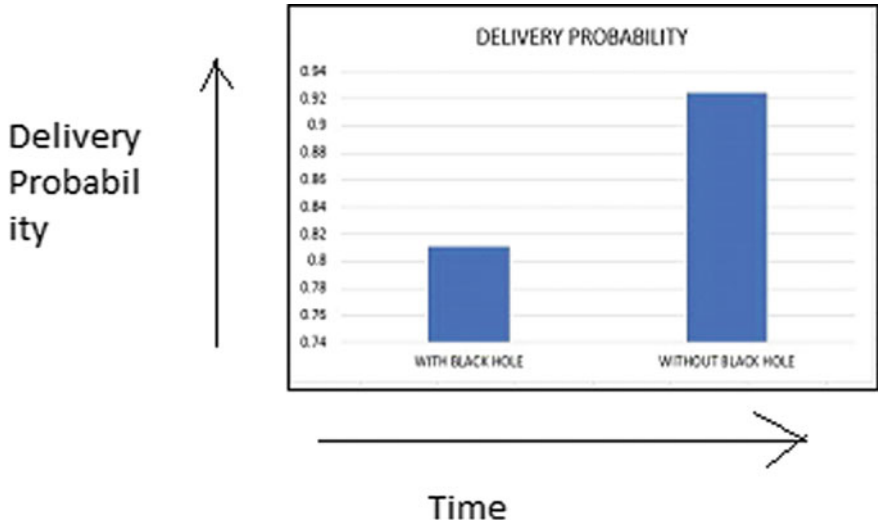


Fig. 2 Delivery probability with respect to time

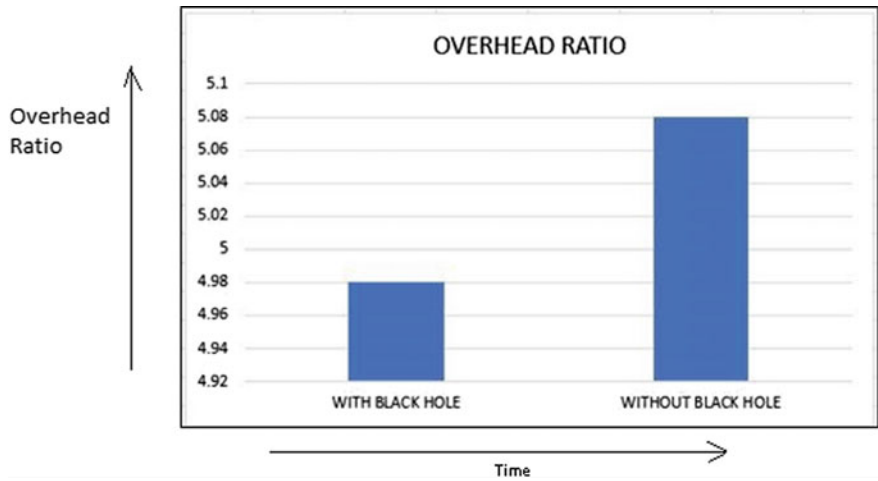


Fig. 3 Overhead ratio with respect to time

hole nodes. If black hole nodes are present in the network, delivery probability will decrease drastically. But, overhead ratio and average latency will increase. Therefore, black hole nodes need to be detected and avoided for increasing overall performance of the network.

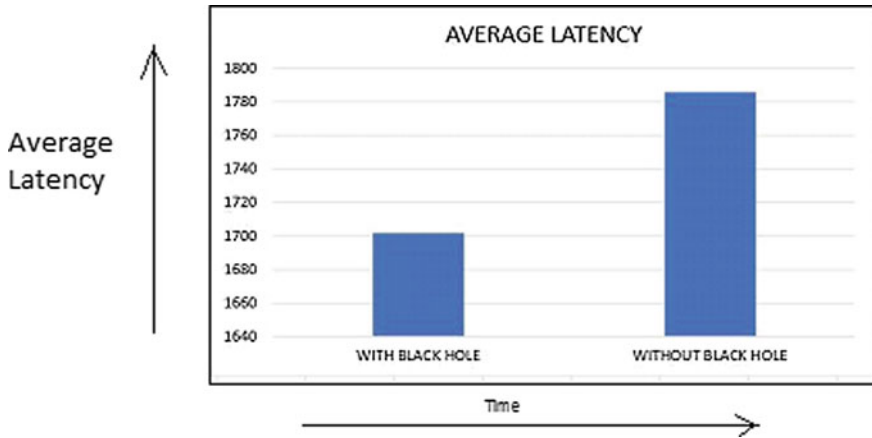


Fig. 4 Average latency with respect to time

## 5 Conclusion

The acknowledgement and the report if combined can sufficiently determine and identify the black hole nodes at every step of data transmission. Thus by detecting the black hole nodes, we can avoid or eradicate black hole nodes from the network. In the absence of black hole node, we can see a huge decrease in delivery probability and minor increase in latency and overhead ratio. Thus through the proposed approach, we can say that black hole nodes have a deep impact on DTN infrastructure and can minimize the effects to a great extent.

In the future, we are planning to work on the mitigation process of black hole attack in delay-tolerant network, as black hole nodes significantly worsen the delivery probability on the network which is the most important parameter in post-disaster scenario.

## References

1. Image Source: <https://www.jpinfotech.org/provest-provenance-based-trust-model-delay-tolerant-networks/>
2. C. Chakrabarti, S. Roy, Adapting mobility of observers for quick reputation assignment in a sparse post-disaster communication network, in *IEEE Proceedings of AIMoC* (2015), pp. 29–35
3. C. Chakrabarti, S. Roy, S. Basu, Intention aware misbehavior detection for post-disaster opportunistic communication over peer-to-peer DTN, in *Peer to Peer Networking and Applications* (Springer, 2018), pp. 1–19
4. C. Chakrabarti, A. Banerjee, S. Roy, An observer-based distributed scheme for selfish-node detection in a post-disaster communication environment using delay tolerant network, in *Proceedings of AIMoC* (2014), pp. 151–156

5. S. Banerjee, Detection/removal of cooperative black and gray hole attack in mobile ad-hoc networks, in *World Congress on Engineering and Computer Science*, October (2008), pp. 337–342
6. L. Tamilselvan, V. Sankaranarayanan, Prevention of co-operative black hole attack in MANET. *J. Netw.* **3**(5), 13–20 (2008)
7. S. Kurosawa, Detecting blackhole attack on AODV-based mobile ad hoc networks by dynamic learning method. *Proc. Int. J. Netw. Secur.* (2006)
8. A. Bhattacharyya, D. Bose, A. Banerjee, H. Saha, D. Bhattacharjee, Different types of attacks in Mobile ADHOC Network: prevention and mitigation techniques. *Int. J. Commun. Netw. Syst.* 22 Sep 2012
9. Bhattacharjee, S., Basu, S., Roy, S., Das Bit, S.: Best-effort delivery of emergency messages in post disaster scenario with content-based filtering and priority-enhanced Prophet over DTN, in *2016 8th International Conference on Communication Systems and Networks* (2016)
10. S. Saha, V.K. Shah, R. Verma, R. Mandal, S. Nandi, Is it worth taking a planned approach to design ad hoc infrastructure for post disaster communication, in *CHANTS'12*, Istanbul, Turkey, 22 August 2012
11. S. Saha, S. Patra, A. Sheldekar, S. Nandi, Post disaster management using delay tolerant network, in *3rd International Conference on Wireless & Mobile Networks*, Ankara, Turkey, 26–28 June 2011
12. R. Hegde, T.H. Sreenivas, Steganography in ad hoc networks. *Int. J. Comput. Sci. Inf. Technol.* **6**(6), 5405–5408 (2015)
13. L. Delosières, S. Nadjm-Tehrani, BATMAN store-and-forward: the best of the two worlds, in *IEEE* (2012)
14. Y.S. Uddin, D.M. Nicol, T.F. Abdelzaher, R.H. Kravets, A post-disaster mobility model for delay tolerant networking, in *Proceedings of WSC* (2009), pp. 2785–2796
15. X. Zhang, X. Wang, A. Liu, Q. Zhang, C. Tang, Reputation-based scheme for delay tolerant networks, in *2011 International Conference on Computer Science and Network Technology* (2011)
16. Z. Gao, H. Zhu, S. Du, C. Xiao, R. Lu, PMDS: A probabilistic misbehavior detection scheme in DTN, in *IEEE ICC 2012—Wireless Networks Symposium*
17. H. Zhu, S. Du, Z. Gao, M. Dong, Z. Cao, A secure user centric and social-aware reputation based incentive scheme for DTNs, In final form 12 March (2012)
18. R. Lu, X. Lin, H. Zhu, X. Shen, B. Preiss, Pi: a practical incentive protocol for delay tolerant networks. *IEEE Trans. Wireless Commun.* **9**(4), April (2010)
19. H. Zhu, S. Du, Z. Gao, M. Dong, Z. Cao, A probabilistic misbehavior detection scheme toward efficient trust establishment in delay-tolerant networks. *IEEE Trans. Parallel Distrib. Syst.* **25**(1), 22–32 (2014)
20. M. Asplund, S. Nadjm-Tehrani, J. Sigholm, *Emerging Information Infrastructures: Cooperation in Disasters*, Lecture Notes in Computer Science, vol. 5508 (Springer, Berlin, 2009)
21. A. Keranen, J. Ott, T. Karkkainen, The ONE simulator for DTN protocol evaluation, in *Proceedings of SIMUTools* (2009), Article No. 55

# Unvoiced Speech Recognition Using Dynamic Analysis of EMG Signal



Paromita Das, Biswarup Neogi, Aniruddha Chandra and Anilesh Dey

**Abstract** The current study is an initiative taken to recognize the speech by observing the muscle associated with speech (Locks et al. in Motriz, Rio Claro 21(1):15–22, 2015, [1]). It will realize unvoiced communication; guarantee the participation of inarticulate people in society. Electromyography (EMG) sensor is used to track and recognize various intramuscular signals for accurate and precise recognition of the subjects. In this aspect, letter ‘A’ and digit ‘1’ are performed in sign language by volunteers and the EMG signals are collected for four muscles, i.e. Lumbrical muscles, Hypothenar muscles, Thenar muscles and Flexor carpi muscles of palm and hands. The nonlinear study of these signals proved to be an efficient method of sign recognition.

**Keywords** Nonlinear dynamics · Recurrence plot · Isometry · Consecutive isometry · Sign language

---

P. Das (✉)

Department of Electronics and Communications, Amity University, Kolkata, West Bengal, India  
e-mail: [wrt2paromita@gmail.com](mailto:wrt2paromita@gmail.com)

B. Neogi

Department of Electronics, JIS College of Engineering and Communications, Nadia, West Bengal, India  
e-mail: [biswarupneogi@gmail.com](mailto:biswarupneogi@gmail.com)

A. Chandra

Department of Electronics and Communication Engineering, National Institute of Technology, Mahatma Gandhi Avenue, Durgapur 713209, West Bengal, India  
e-mail: [aniruddha.chandra@ieee.org](mailto:aniruddha.chandra@ieee.org)

A. Dey

Department of Electronics and Communication Engineering, Narula Institute of Technology, 81 Nilgunj Road, Agarpara, Kolkata 700109, India  
e-mail: [anilesh.dey@nit.ac.in](mailto:anilesh.dey@nit.ac.in)

© Springer Nature Singapore Pte Ltd. 2020

K. Maharatna et al. (eds.), *Computational Advancement in Communication Circuits and Systems*, Lecture Notes in Electrical Engineering 575, [https://doi.org/10.1007/978-981-13-8687-9\\_20](https://doi.org/10.1007/978-981-13-8687-9_20)

217

## 1 Introduction

Sign language (SL) is a movement language which expresses certain semantic information through series of hands, arms' motion, facial expressions and head–body postures. It is the basic means of communication for the deaf people. An interpreter is required to establish the communication between an ordinary person and hearing impaired one. Unfortunately, the availability of trained interpreter is inadequate [2]. The role of sign language recognition system is to ensure equality of opportunity and full participation of inarticulate people in the society. Sign language recognition is decoding and understanding the information embedded in the hand shapes and generating a meaningful word without the need for an interpreter.

The electromyography is the representation of intramuscular activities in terms of voltages. The EMG patterns extracted with the help of proper pattern recognition system proceed to a good computer interface that improves the quality of life of inarticulate [3]. In the recognition of ASL gesture, the surface electromyography (sEMG) signal of user's forearm evaluated by mahalanobis distance criteria revealed 97.7% of the inspected gesture recognized correctly [4]. Subject-dependent recognition with 99.82% accuracy was achieved using accelerometer and sEMG sensors in the field of German sign language (GSL) [5].

In another approach, sEMG signal applying Levenberg–Marquardt-algorithm-based ANN proved to be efficient and fast gesture identification system [3] with 83.5% of accuracy. Double-handed Chinese sign language gesture can be recognized with sEMG and accelerometer outperforms the prior SLR method in subword level [6]. A more recent approach includes sEMG sensors along with three-axis accelerometer and three-axis gyroscope offers 95.94% recognition rate [7]. The SLR system was engaged in analysing sEMG signal and 26 alphabets were recognized with 90% accuracy [8] under offline condition. A more accurate system was implemented when bagged trees classifier is used for the classification of the SLR output in case of online and offline ASL recognition [9]. Neuro-fuzzy system was applied on different sEMG signals generated from Lumbrical muscles, Thenar muscles, Hypothenar muscles and Flexor carpi radialis muscles in a model to get more accurate recognition [10]. We can conclude that all these are focused on static characteristic analysis of EMG signals.

Considering all the aforementioned facts, current study proposed the consecutive isometric analysis of sign language EMG signal which can lead to a more accurate and precise recognition of sign language. The qualitative analysis of the EMG signals for 'A' and '1' on the basis of recurrence analysis of RRISeries is to state the outcome towards improving capability of silent and to propose future directions for research in this area.

In this aforesaid literature survey, it is noticed that all the analyses are basically local analyses done in time-domain or frequency- or time–frequency-domain. Naturally, new contribution to improve the literature survey, i.e. to discuss the global analysis of the signal from the reconstructed space and not from the context.



## 2 Data Collection and Processing

Eight (8) male volunteers (age 20–23 years) were appointed for the study. They were informed about the details of the study and an informed consent form was obtained from them as an evidence. RMS Aleron 201, a 2/4 channel EMG machine was employed, and the electrodes were attached to the aforementioned muscles of those eight volunteers in the Electronics and Communication Engineering Department, JIS College of Engineering, Kalyani, Nadia, West Bengal.

## 3 Methodology

Phase space approach was used to investigate the nonlinear properties of the EMG signals. A phase space was reconstructed for each speech signal with appropriate time delay and proper embedding measurement.

### 3.1 Recurrence

Recurrence is a basic characteristic of a dynamic process, represents the process behaviour into phase space. Phase space mainly involved in dynamic process defined as a space that represents all its possible values, with different unique points. Among different ways of measuring and representing isometry, the present study involved consecutive isometry. Isometry can be defined as the recurrence of vectors (sequences created from the given time series of a dynamic process) of the same length. The vector length is calculated as the square root of the sum of squares of its elements. The number of data points involved in each vector (i.e. dimensionality) is also identified as embedding. Two vectors are considered as isometric when the absolute value of the difference between their lengths is lower than a cut-off radius (expressed in % of the range of the time series). Isometry is calculated as the number of isometric recurrences expressed as a percentage of the total number of pairs of vectors compared in the sample (i.e. % isometry) [11]. Consecutive isometry is another quantifier of recurrence calculated in terms of per cent of the isometry. It is known as the number of recurrences that follows each other, i.e. if the vector  $x_t$  is recurrent with  $x_{t+m}$ , then the vector  $x_{t+1}$  is recurrent with  $x_{t+m+1}$ . Consecutive isometry has been reported as a measure of causality [12].

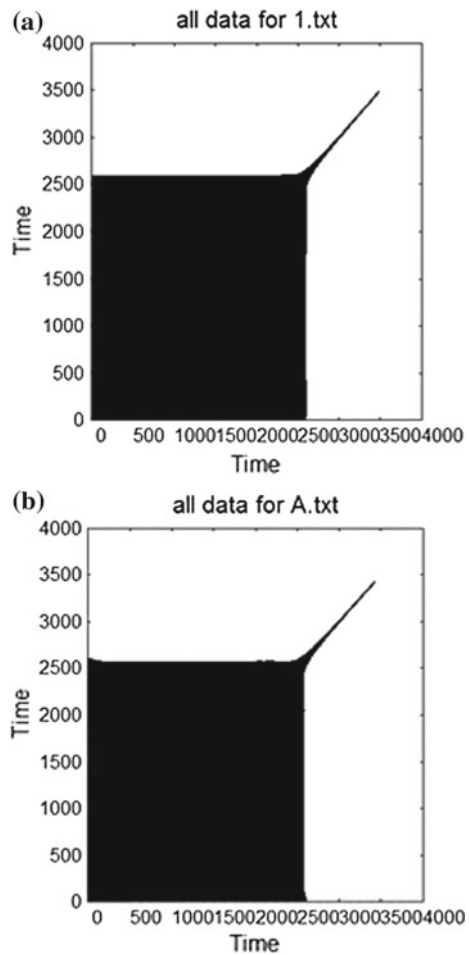
### 3.2 Recurrence Plot Analysis

Recurrence Plot (RP) is one of the efficient graphical methods designed to find the hidden nonlinear structure of the phase spaces, introduced by Eckmann et al. [12]. For any two points  $x_i, x_j$  in a phase space, the distance among  $x_i$  and  $x_j$  can be calculated by  $\|x_i - x_j\|$ . Then, the recurrence between two points  $x_i$  and  $x_j$  is given by

$$R_{ij} = \Theta(\varepsilon - \|x_i - x_j\|) \tag{1}$$

where  $\Theta$  represents Heaviside function.

**Fig. 1** **a** Recurrence plot of electromyography signal of '1' with proper time delay and embedding dimension. **b** Recurrence plot of electromyography signal of 'A' with proper time delay and embedding dimension



From the definition, it follows that the entries of the matrix  $(R_{ij})_{N \times N}$  ( $N$  being the span of the trajectory of the phase space) are either 1 or 0. The number '1' is represented by a black dot. On the other hand, '0' is represented by a white dot. So, an RP is a visual representation of a phase space by two colours. From the structure of the RP, various dynamical patterns of a complex dynamics can be described, such as periodicity, quasi-periodicity, noise effect, non-stationary behaviour and chaotic nature. It indicates that classification between two different dynamics can be made by RP analysis. Figure 1a, b shows the recurrence plot of the EMG signals for "1" and "A", respectively.

If two points  $x_i$  and  $x_j$  are recurrent, we say that there is an isometry. Two points  $x_i$  and  $x_j$  in a phase space are said to be in consecutive isometry if

$$R_{ij} = \Theta(\varepsilon - \|x_{i+L} - x_{j+L}\|) \quad (2)$$

where  $L \in Z^+$ .

Since periodicity and aperiodicity of a phase space are the reflections of isometry, the nature of the dynamics can be described by it. In fact, complexity of the RP decreases as the consecutive isometry increases [13, 14].

## 4 Numerical Experiments and Results

### 4.1 Noise-Free Environment

As stated above, isometry is the measure of recurrence in any phase space. It is calculated as

$$\text{Isometry} = \frac{1}{N^2} \sum_{i,j=1}^N R_{i,j}(\varepsilon) \quad (3)$$

where,  $N$  is the numeral of speech samples and  $R_{i,j}(\varepsilon)$  is the repetition matrix equivalent to a threshold of  $\varepsilon$ . Isometry is represented as the quantity of isometric recurrences articulated as a fraction of the entire quantity of pairs of vectors contrast in the sample (i.e. %isometry) [15]. The design of %isometry or any of its copied frameworks as a function of embedding dimension is considered as an embedding plot. The embedding plot of %consecutive isometry, represented in Fig. 2a, b, shows the %consecutive isometry of two EMG signals for "1" and "A" in noise-free environment.

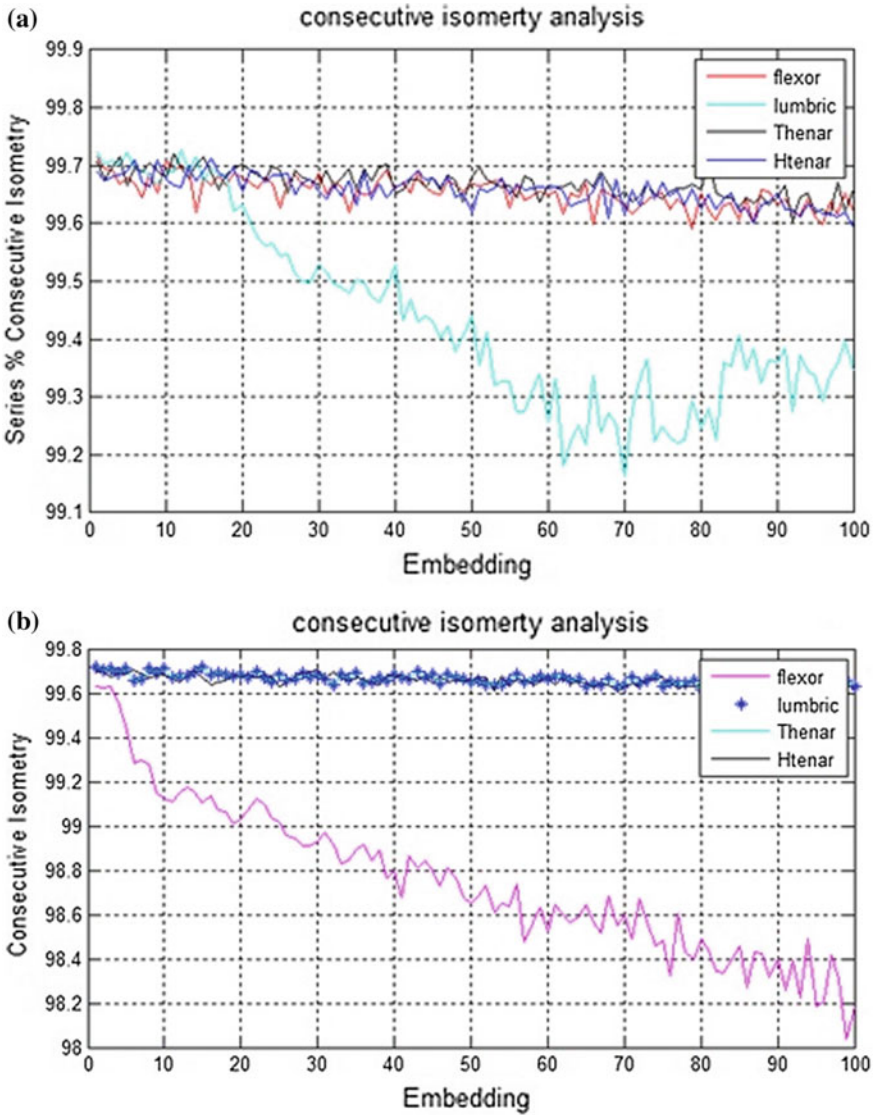


**Fig. 2** **a** Embedding plot of %consecutive isometry with proper time delay for 'l' in noise-free environment. **b** Embedding plot of %consecutive isometry with proper time delay for 'A' in noise-free environment. **c** Embedding plot of %consecutive isometry with proper time delay for 'l'. **d** Embedding plot of %consecutive isometry with proper time delay for 'A'

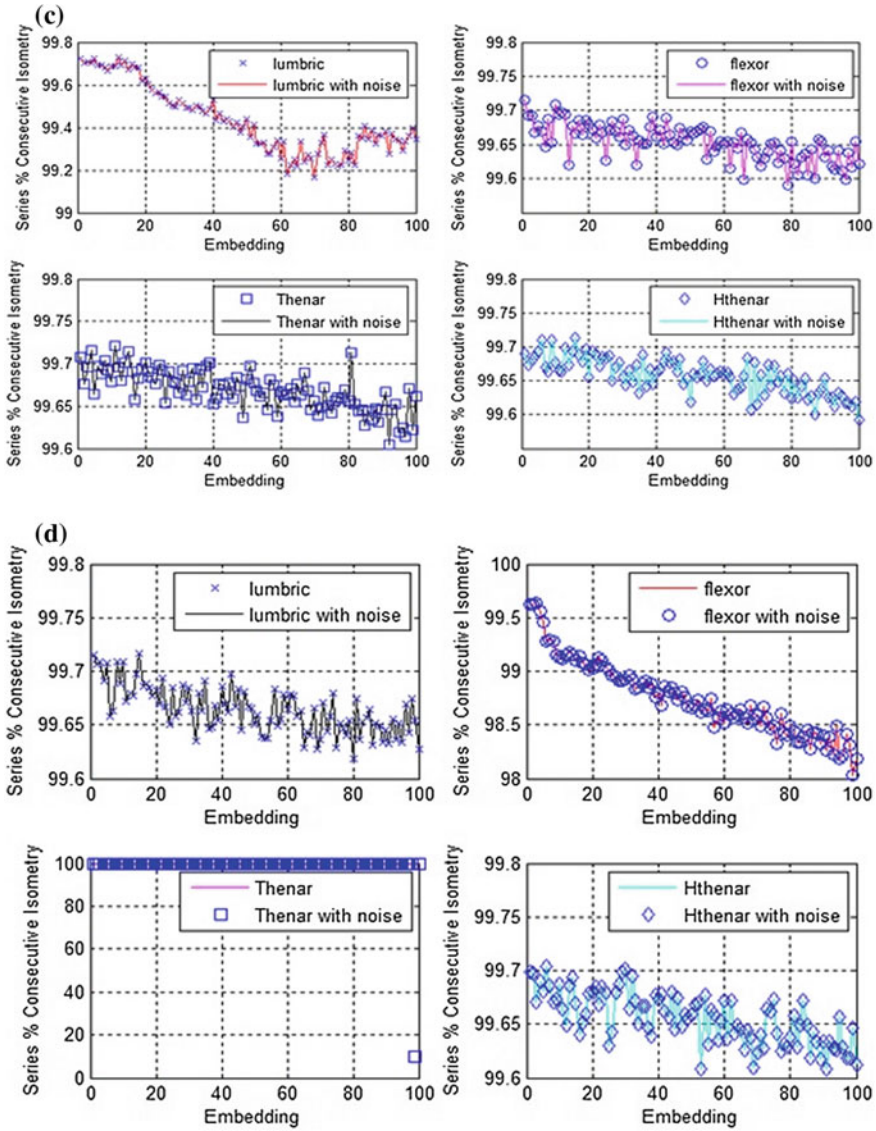


Fig. 2 (continued)

## 4.2 Noisy Environment

To investigate the effect of noise on the isometry, a Gaussian noise was added, given by

$$\phi(\xi) = e^{-\frac{\xi^2}{2}}, \quad (4)$$

where  $\xi$  is a random variable.

A very close review of the past sign recognition system guided us to invent a robust, cost-effective system without compromising the throughput. The detailed study reveals the fact that nonlinear analysis of EMG signals for different sign language recognition assures more and more participation of deaf–mute people in the society.

## 5 Conclusion

Motor neuron is employed to control the movement of skeleton muscle fibre. EMG sensors detect the electrical energy produced due to motor movements. Aforementioned muscles on hand and palm produced corresponding EMG signals. The signal is received at the electrode and amplified. Exclusion of low frequency and high frequency noise is necessary before being displayed. Recurrence analysis was performed on the EMG signals to classify the signs performed. The recurrence plots were drawn and correlated parameters, specifically %isometry and %consecutive isometry, were calculated for the EMG signals acquired for these two signs in noise-free and noisy environments. In both the environments, %isometry and %consecutive isometry values are identical. Hence, it is concluded that these parameters are robust to environmental noise and can be used in any biomedical analysis of inarticulate. Our final goal is to identify the total alphabet and numerical series with the help of this proposed system.

## References

1. F. Locks, H.H. Santos, L.C. Carvalho, L.R.O.G. Stolt, J.J.A. Ferreira, Neural adaptations in isometric contractions with EMG and force biofeedback. *Motriz*, Rio Claro **21**(1), 15–22 (2015). <https://doi.org/10.1590/S1980-65742015000100003>
2. B.E. Jones, Competencies of K–12 educational interpreters: what we need versus what we have, ed. by E.A. Winston Ed. 1st edn. (Gallaudet University Press, New York, 2004)
3. H.S.D. Eldin, P. Manimegalai, Hand gesture recognition based on EMG signals using ANN. *Int. J. Comput. Appl.* **3**(2), 31–39 (2013)
4. E.K. Vasiliki, J.H. Leontios, M.P. Stavros, Evaluation of surface EMG features for the recognition of American Sign Language gestures, in *Proceedings of the 28th IEEE EMBS Annual International Conference*, New York City, USA (2006), pp. 6197–6200

5. K. Jonghwa, W. Johannes, R. Matthias, A. Elisabeth, Bi-channel sensor fusion for automatic sign language recognition. Paper presented at 8th IEEE International Conference on Automatic Face & Gesture Recognition, 17–19 September (2008)
6. L. Yun, C. Xiang, Z. Xu, W. Kongqiao, Z.J. Wang, A sign-component-based framework for Chinese sign language recognition using accelerometer and sEMG data. *IEEE Trans. Biomed. Eng.* **59**(10), 2695–2704 (2012)
7. W. Jian, T. Zhongjun S. Lu, E. Leonardo, J. Roozbeh, Real-time American sign language recognition using wrist-worn motion and surface EMG sensors. JBHI-00032-2016. University of Texas at Dallas, Richardson, TX, USA (2015)
8. S. Celal, S. Ferat, Real-time American sign language recognition system by using surface EMG signal. Paper presented at 14th International Conference on Machine Learning and Applications (2015), pp. 497–502. <https://doi.org/10.1109/ICMLA.2015.212>
9. S. Celal, S. Ferat, American Sign Language Recognition system by using surface EMG signal. Paper presented at IEEE International Conference on Systems, Man, and Cybernetics, Budapest, Hungary (2016), pp. 2872–2877
10. D. Paromita, P. Sudipta, G. Joydev, P.B. Shilpi, N. Biswarup, G. Ankur, An approach towards the representation of sign language by electromyography signals with fuzzy implementation. *Int. J. Sens. Wirel. Commun. Control* **7**(1), 19–25 (2017)
11. M.B. Kennel, H.D. Abarbanel, False neighbors and false strands: a reliable minimum embedding dimension algorithm. *Phys. Rev. E* **66**, 026209 (2002)
12. J.P. Eckmann, S. Oliffson Kamphorst, D. Ruelle, Recurrence plots of dynamical systems. *EPL (Europhys. Lett.)* **4**, 973–977 (1987)
13. N. Marwan, M. Carmen Romano, Marco Thiel, Jürgen Kurthsl, Recurrence plots for the analysis of complex systems. *Phys. Rep.* **438**, 237–329 (2007)
14. K.N. Suraj, P. Karan, K.P. Pratyush, N. Shikshya, J.P. Shankar, A. Arfat, D. Anilesh, P. Kunal, Understanding the effect of cannabis abuse on the ANS and cardiac physiology of the Indian women paddy-field workers using RR interval and ECG signal analyses. Paper presented at IEEE International Conference APSIPA ASC 2017, Aloft Kuala Lumpur Sentral Sentral, Kuala Lumpur, 12–15 December 2017. <https://doi.org/10.1109/apsipa.2017.8282047>
15. H. Sabelli, A. Lawandow, Homeobios: the pattern of heartbeats in newborns, adults, and elderly patients. *Nonlinear Dyn. Psychol. Life Sci.* **14**, 381 (2010)

# Study the Effect of Cognitive Stress on HRV Signal Using 3D Phase Space Plot in Spherical Coordinate System



Sudhangshu Sarkar, Pallav Dutta, Aniruddha Chandra and Anilesh Dey

**Abstract** In this article, the effect of stress on heart rate variability (HRV) is analysed, while a human mind is subjected to different stressful situations. The subjects had to go through a series of challenges that exaggerate their mental stress. The subjects had been given specific tasks which are both time bound and without any limitation of time. The HRV signals are taken before and after the completion of tasks. The quantification is done by fitting an ellipse on the constructed a 2D phase space of the HRV signal. But the 2D phase space plot is not able to distinguish HRV signals on normal and stressful conditions for all the time. In this paper, we introduce a 3D phase space plot in a spherical coordinate system which can distinguish normal and stressed conditions significantly. It has been observed that the volume of the cluster in reconstructed space increased drastically on stressed condition. The volume of the fitted ellipsoid on the reconstructed space is a proper quantification tool which can clearly distinguish two aforesaid conditions. Our experimental result provides a satisfactory result in this context.

**Keywords** 3D phase space plot · Cognitive stress · HRV signal

---

S. Sarkar (✉) · P. Dutta

Department of Electrical Engineering, Narula Institute of Technology, 81 Nilgunj Road, Agarpara, Kolkata, India

e-mail: [sudhangshu.sarkar@nit.ac.in](mailto:sudhangshu.sarkar@nit.ac.in)

P. Dutta

e-mail: [Pallav.dutta@nit.ac.in](mailto:Pallav.dutta@nit.ac.in)

A. Chandra

Department of Electronics and Communication Engineering, National Institute of Technology, Mahatma Gandhi Avenue, Durgapur 713209, West Bengal, India

e-mail: [aniruddha.chandra@ieee.org](mailto:aniruddha.chandra@ieee.org)

A. Dey

Department of Electronics and Communication Engineering, Narula Institute of Technology, 81 Nilgunj Road, Agarpara, Kolkata 700109, India

e-mail: [anilesh.dey@nit.ac.in](mailto:anilesh.dey@nit.ac.in)

© Springer Nature Singapore Pte Ltd. 2020

K. Maharatna et al. (eds.), *Computational Advancement in Communication*

*Circuits and Systems*, Lecture Notes in Electrical Engineering 575,

[https://doi.org/10.1007/978-981-13-8687-9\\_21](https://doi.org/10.1007/978-981-13-8687-9_21)



## 1 Introduction

Stress is increasing day by day and also affecting badly to human physiology as well as psychology. It affects the human brain, heart and other major parts of the body. So, collecting and analysing the signal of heart in cognitive mode with HRV analysis is very essential for the precaution of different harmful diseases of a human being. The HRV signal is fundamentally identified with the physiological condition of the human being. Physiological systems normally contain various subsystems that show both highly nonlinear deterministic, and in addition, arbitrary characteristics, and are managed progressively. These systems produce signals that show complex characteristics, for example, touchy reliance on little unsettling influences, long memory, extraordinary varieties and non-stationary (i.e. mean and fluctuation change with time). Brandimonte et al. [1] have explained the meaning of the word cognition which is given as the psychological activity or process including cognizant scholarly movement, for example, securing information, considering, thinking, learning, critical thinking, recollecting and in like manner. These parts of comprehension are critical in consistent life. An enormous number of studies have been led to various cognitive tasks in a previous couple of decades under different circumstances [2–4]. Rosas et al. [5] explains the real goals of such investigations which give psychological recovery to the patients who are experiencing distinctive sorts of intellectual debilitation, for example, stroke, bipolar turmoil, Alzheimer’s malady and related dementias, lupus, various sclerosis, incessant weakness disorder, schizophrenia, Parkinson’s and Huntington’s illnesses, significant depressive issue, rheumatoid joint inflammation, Lyme ailment, etc.

It is found that most of the people used to suffer from ‘work stress’ [6] which reduces the efficiency of day-to-day life [7]. Ursin and Eriksen [8] describe the relationship between brain and mental stress with the help of cognitive activation theory of stress (CATS). HRV analysis in long- and short-term process [9] has been studied previously to detect mental stress. In several studies, pupil dilation has been considered as a signal for stress. The studies from Sharma and Gedeon [10] reveal that change in the diameter of pupil shows the level of stress in a subject. Larger the diameter more is the stress.

In this paper, we mainly focused on to study the effect of cognitive stress on HRV. The cognitive tasks considered are mostly related to the puzzle solving or problem-solving capabilities of the subjects. The goal of this work is to determine the changes of HRV with the use of a 3D phase space plot in the spherical coordinate system [11]. At first, all the subjects are asked to perform three different types of cognitive tasks so as to develop cognitive stress in their brain. We know from the term of homoeostasis that if any external stimuli effects any part of the body that reflects other organs of the body also. So our objective is to find out the effect of the cognitive stress on sympathetic and parasympathetic activities on the heart. Our experimental analysis gives a satisfactory result in this context.

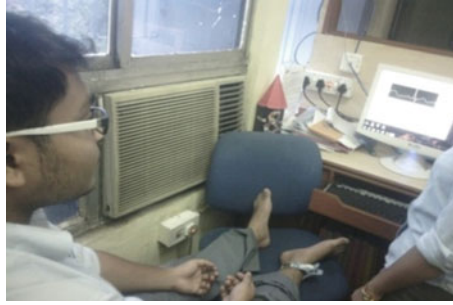


**Fig. 1** HRV signals were collected

## **2 Methodology**

### **2.1 Accusation of Signal**

At first, ECG signals of six volunteers (three male and three female) age between 18 and 22 years (mean 20 years) were collected. The signals were collected from our own designed HRV data logger machine. All signals are of 10 min duration at Department of Electrical Engineering, Narula Institute of Technology, under normal room temperature and least noisy environment as shown in Fig. 1. At the first stage, ECG signals are collected at normal condition, and in the next stage, ECG signals were taken when subjects (after getting their written consent for the participation in our study) were in stress condition. Next all recorded ECG signals are processed by LabVIEW2013 software, and ECG signals were converted into HRV signals shown in Fig. 2.

### **2.2 Generation of Cognitive HRV**

A series of experiments have been conducted on six subjects (three male and three female), where it is intended to generate stress based on different conditions and situations and monitoring their cardiac activity.

Firstly, subjects were shown a riddle based on the generic prisoners red and blue cap problem where the solution is also given to them. The same problem was executed among the subjects. Initially, the cardiac cavities were duly monitored and asked to perform the following experiment as shown in Fig. 3.

Secondly, a medium-level Sudoku puzzle has been given to each of the subjects. The rules and regulation of the game were explained and asked to solve the puzzle without any limitation of time. The Sudoku puzzle is given in Fig. 4.

The rules and regulations of a generic chess game were explained, and the contestants were divided into three groups consisting of two subjects. One group consists

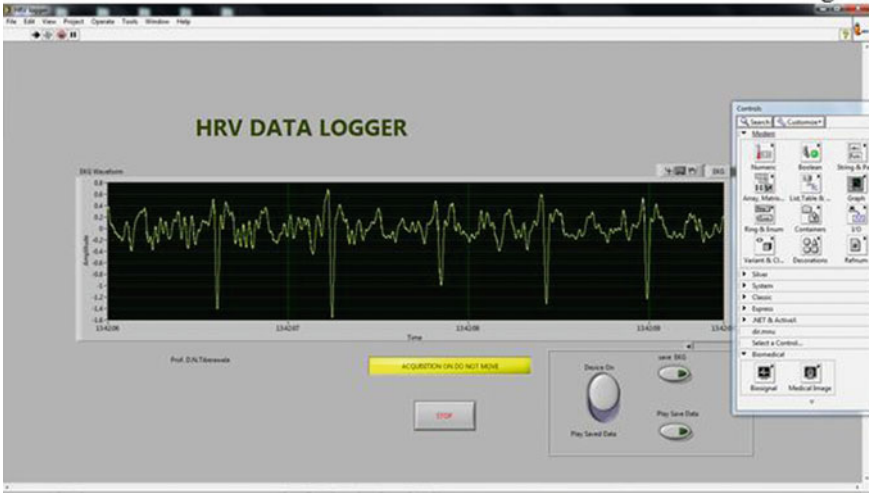


Fig. 2 DAQ software made using LabVIEW

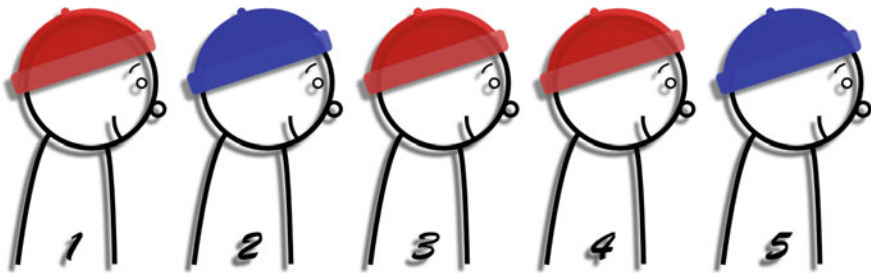
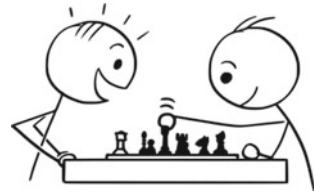


Fig. 3 Prisoners red and blue cap problem

Fig. 4 Sudoku puzzle problem

5	3			7				
6			1	9	5			
	9	8					6	
8				6				3
4			8		3			1
7				2				6
	6					2	8	
			4	1	9			5
				8			7	9

**Fig. 5** Chess game generating stress



of two male candidates, the second one consists of two female candidates and the third one consists of one male and one female subject. But the rules of the games are slightly changed as the candidates will have to take their move only within 20 s (Fig. 5).

After completion of the following experiment, the cognitive stress level of the subjects was monitored, and the results of the tasks are given in Sect. 3.

### 2.3 3D Phase Space Plot of HRV Signal in Spherical Coordinate System

Discrete signals like HRV can be analysed in the time domain with phase space plot. Nonlinear structure in the discrete signal can be identified in the geometrical way. Thus, the notion of a 3D phase space plot can be done in a spherical coordinate system. The values of  $\theta_n$  and  $\varphi_n$  can be calculated for every pair of successive  $R$ - $R$  interval in the aspherical coordinate system. The calculations are given below,

$$r_n = \sqrt{RR_n^2 + RR_{n+1}^2 + RR_{n+2}^2}$$

$$\theta_n = \tan^{-1} \left( \frac{\sqrt{RR_n^2 + RR_{n+1}^2}}{RR_{n+2}} \right)$$

$$\varphi_n = \tan^{-1} \left( \frac{RR_{n+2}}{RR_n} \right)$$

The spherical coordinate plot is then defined as

$$\zeta_n = r_n(\theta_n + \varphi_n)$$

Finally, phase space is constructed with the points  $(\zeta_n, \zeta_{n+1}, \zeta_{n+2})$ . This is called 3D spherical coordinate plot.

‘Ellipsoid fit’ method is generally a mode of quantification of 3D phase space plot [12]. Changes in energy dynamics of HRV is strongly indicated by axes of the ellipsoid. Figure 6 depicts how an ellipsoid is fitted into the region of the phase space which is dense.

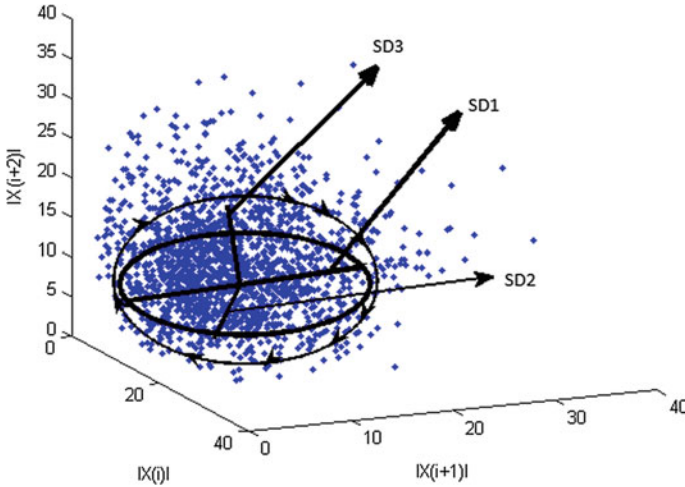


**Fig. 6** SD1, SD2 and SD3 are the axes of the ellipsoid, where ellipsoid fit applied on dense region

Let  $\{X(j)\}_{j=1}^N$  be a discrete HRV signal. The 3D frequency-delay plot be made by subdividing this signal into three groups ( $x^+, x^-, x^{--}$ ) with the same time delay, where

$$x^+ = \{|X(j)|\}_{j=1}^{N-2\tau}, \quad x^- = \{|X(j)|\}_{j=1+\tau}^{N-\tau},$$

$$x^{--} = \{|X(j)|\}_{j=1+2\tau}^N, \quad \tau = 1, 2, \dots, (N - 1)$$

Now, this coordinate system is moderated by a 3D rotation with same angle  $\frac{\pi}{4}$  with respect to X-, Y- and Z-axis [12]. The transform is given by,

$$\begin{pmatrix} x_m \\ x_n \\ x_p \end{pmatrix} = \begin{pmatrix} \cos \frac{\pi}{4} \cos \frac{\pi}{4} \cos \frac{\pi}{4} \sin \frac{\pi}{4} - \cos \frac{\pi}{4} \sin \frac{\pi}{4} \cos \frac{\pi}{4} \cos \frac{\pi}{4} \sin \frac{\pi}{4} + \sin \frac{\pi}{4} \sin \frac{\pi}{4} \cos \frac{\pi}{4} \cos \frac{\pi}{4} \\ \cos \frac{\pi}{4} \sin \frac{\pi}{4} \cos \frac{\pi}{4} \cos \frac{\pi}{4} + \sin \frac{\pi}{4} \sin \frac{\pi}{4} \sin \frac{\pi}{4} \cos \frac{\pi}{4} - \cos \frac{\pi}{4} \sin \frac{\pi}{4} + \cos \frac{\pi}{4} \sin \frac{\pi}{4} \sin \frac{\pi}{4} \\ -\sin \frac{\pi}{4} \cos \frac{\pi}{4} \sin \frac{\pi}{4} \cos \frac{\pi}{4} \sin \frac{\pi}{4} \cos \frac{\pi}{4} \cos \frac{\pi}{4} \end{pmatrix} \begin{pmatrix} x^+ \\ x^- \\ x^{--} \end{pmatrix}$$

$$= \frac{1}{2\sqrt{2}} \begin{pmatrix} 2\sqrt{2} & -(\sqrt{2}-1) & (\sqrt{2}+1) \\ 2\sqrt{2} & (\sqrt{2}+1) & -(\sqrt{2}-1) \\ -2 & \sqrt{2} & \sqrt{2} \end{pmatrix} \begin{pmatrix} x^+ \\ x^- \\ x^{--} \end{pmatrix}$$

Hence,

$$x_m = \frac{1}{2}.x^+ + \left(\frac{1}{2\sqrt{2}} - \frac{1}{2}\right).x^- + \left(\frac{1}{2\sqrt{2}} + \frac{1}{2}\right).x^{--}$$

$$= \frac{2\sqrt{2}.x^+ - (\sqrt{2}-1).x^- + (\sqrt{2}+1).x^{--}}{2\sqrt{2}}$$

$$x_n = \frac{1}{2}.x^+ + \left(\frac{1}{2\sqrt{2}} + \frac{1}{2}\right).x^- + \left(\frac{1}{2\sqrt{2}} - \frac{1}{2}\right).x^{--}$$

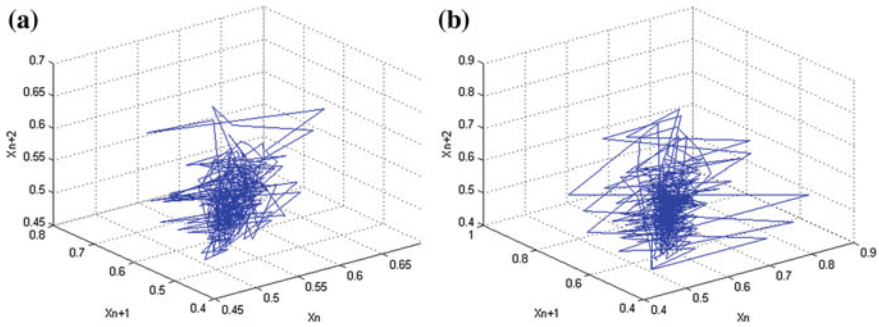


Fig. 7 a Noise free normal condition, b noisy normal condition

$$\begin{aligned}
 &= \frac{2\sqrt{2}.x^+ + (\sqrt{2} + 1).x^- - (\sqrt{2} + 1).x^{--}}{2\sqrt{2}} \\
 x_p &= \left(-\frac{1}{\sqrt{2}}\right).x^+ + \frac{1}{2}.x^- + \frac{1}{2}.x^{--} \\
 &= \frac{-2.x^+ + \sqrt{2}.x^- + \sqrt{2}.x^{--}}{2\sqrt{2}}
 \end{aligned}$$

Thus, there is a formation of a new  $x_m, x_n, x_p$  coordinate system.

Let  $\bar{x}_m = \text{Mean}(x_m)$ ,  $\bar{x}_n = \text{Mean}(x_n)$ ,  $\bar{x}_p = \text{Mean}(x_p)$  and  $SD_1 = \sqrt{\text{Var}(x_m)}$ ,  $SD_2 = \sqrt{\text{Var}(x_n)}$ ,  $SD_3 = \sqrt{\text{Var}(x_p)}$ . Lastly, an ellipsoid centered at  $(\bar{x}_m, \bar{x}_n, \bar{x}_p)$  with three axes of length  $SD_1, SD_2$  and  $SD_3$  is taken for quantification of the existing 3D phase space.

### 3 Result and Discussion

From the above phase space plot, it is clear that the cluster volume increases significantly. Figure 7a represents the cognitive stress level observed from the HRV signals in normal condition, while Fig. 7b represents the HRV signals observed from the stressed condition and the cluster volumes are highly distinguishable. The volume of these clusters is measured by placing an ellipsoid over the main cluster, and a huge difference is noticed in the volume of the ellipsoid. The analytics are given in a tabular form in Table 1, where the difference in volume is clearly visible.

To check the robustness of the system, we have plotted the same data signals in phase space plot with the inclusion of noise, and the phase space model in normal condition including noise is exposed in Fig. 8a, b explains the plotting of the statistics signals that are received in a stressed condition. Observation of both the phase space plotting reveals that the volume of the cluster in a stressed condition is much more

**Table 1** Three-dimensional spherical coordinate data sheet for normal and stress condition

Signal	Normal condition			Stress condition				
	SD <sub>1</sub>	SD <sub>2</sub>	SD <sub>3</sub>	Volume	SD <sub>1</sub>	SD <sub>2</sub>	SD <sub>3</sub>	Volume
1	0.065345425	0.067708849	0.023806206	0.000330903	0.071333157	0.072974409	0.024647457	0.000403073
2	0.052756199	0.056454053	0.029840314	0.000279204	0.064944239	0.068772839	0.039563316	0.000555137
3	0.068448777	0.07202936	0.042883829	0.00066423	0.081928164	0.090513582	0.058490386	0.001362641
4	0.068134712	0.070653751	0.045142651	0.000682717	0.069291544	0.078250059	0.048419869	0.000824781
5	0.080755635	0.089935441	0.053803624	0.001227623	0.085113413	0.09223983	0.056627555	0.001396671
6	0.031992206	0.033119576	0.015083782	0.000050210	0.041792294	0.045103308	0.023096255	0.000136772

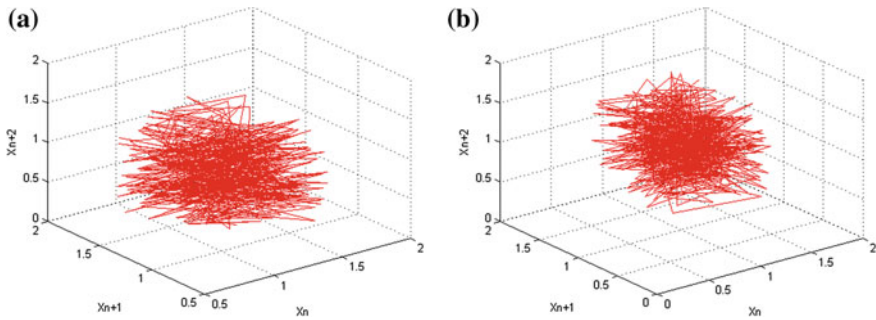


**Fig. 8** **a** Noise free stress condition, **b** noisy stress condition

than that in the normal condition. Thus, it can be proposed that the system similar properties in both noisy and noiseless condition, confirming its robustness. Tabulation provided in Table 2 shows the drastic increase in volume at stressed condition than that of the normal condition again aiding the fact that the system is robust in every situation.

## 4 Conclusion

It is established that cognitive task has an effect on the autonomic nervous system. Volume of the fitted ellipsoid increasing also indicates that it has an effect of sympathetic activity on the autonomic nervous system. There are different methods of global analysis of HRV data, but some methods do not work successfully in giving the best results in case of cognitive stress on HRV 3D phase space plot. In the spherical coordinate system, with volume fitted ellipsoids as the quantifying parameter, gives best results for HRV data on cognitive stress. It is evident from the previous result analysis that cognitive stress level of human beings can be rendered according to the level of activities done in their daily life. If the level of cognitive stress further increased, it may cause severe anomalies in heart signals. Prolonged exposure to such stress can affect normal human activities and can be a cause for several medical issues. Such stress levels can be easily diminished by simple measures like listening to soothing music, or by just simply giving a break to mental activities. The above methodology can be used to determine severe medical problems due to stress, and the effective measures can be taken in time with proper medical assistance. The robustness of the methodology ensures the accuracy of the stress-level measurement. Thus, implementation of the system can be done in a broad spectrum.



**Table 2** Three-dimensional spherical coordinate data sheet for normal and stress condition with noise

Signal	Normal condition				Stress condition			
	SD <sub>1</sub>	SD <sub>2</sub>	SD <sub>3</sub>	Volume	SD <sub>1</sub>	SD <sub>2</sub>	SD <sub>3</sub>	Volume
1	0.382578440	0.395316203	0.282109493	0.134039463	0.403938371	0.398171579	0.297499931	0.150321849
2	0.378574433	0.38550583	0.287005515	0.131589836	0.40645294	0.405635254	0.307438555	0.159240732
3	0.391046358	0.377420314	0.298557989	0.138430595	0.403122393	0.415620447	0.280218456	0.147496066
4	0.388065656	0.390000195	0.286383533	0.136165771	0.372159561	0.404925694	0.2910588	0.137795527
5	0.38085063	0.392107746	0.296445502	0.139076848	0.412076284	0.413290606	0.298786873	0.159861742
6	0.384347638	0.392039217	0.287402721	0.136048725	0.385061741	0.401242246	0.291806947	0.141638893

## References

1. M.A. Brandimonte, N. Bruno, S. Collina, *Psychological Concepts: An International Historical Perspective* (Psychology Press, Hove, UK, 2006)
2. M. De Vos, S. Debener, Mobile EEG: towards brain activity monitoring during natural action and cognition. *Int. J. Psychophysiol.: Off. J. Int. Organ. Psychophysiol.* **91**(1), 1–2 (2014)
3. N. Lally, P.G. Mullins, M.V. Roberts, D. Price, T. Gruber, C. Haenschel, Glutamatergic correlates of gamma-band oscillatory activity during cognition: a concurrent ER-MRS and EEG study. *Neuroimage* **85**, 823–833 (2014)
4. A.C. Marshall, N.R. Cooper, R. Segrave, N. Geeraert, The effects of long-term stress exposure on aging cognition: a behavioral and EEG investigation. *Neurobiol. Aging* (2015)
5. H.D. Rosas, N.D. Hevelone, A.K. Zaleta, D.N. Greve, D.H. Salat, B. Fischl, Regional cortical thinning in preclinical Huntington disease and its relationship to cognition. *Neurology* **65**(5), 745–747 (2005)
6. T. Chandola, A. Heraclides, M. Kumari, Psychophysiological biomarkers of work-place stressors. *Neurosci. Biobehav. Rev.* **35**, 51–57 (2010)
7. P. Melillo, M. Bracale, L. Pecchia, Nonlinear Heart Rate Variability features for real-life stress detection. Case study: students under stress due to university examination. *Biomed. Eng. Online* **10**, 1–13 (2011)
8. H. Ursin, H. Eriksen, The cognitive activation theory of stress. *Psychoneuroendocrinology* **29**, 567–592 (2004)
9. R. Castaldo, P. Melillo, U. Bracale, M. Caserta, M. Triassi, L. Pecchia, Acute mental stress assessment via short term HRV analysis in healthy adults: a systematic review with metaanalysis. *Biomed. Signal Process. Control* **18**, 370–377 (2015)
10. N. Sharma, T. Gedeon, Objective measures, sensors and computational techniques for stress recognition and classification: a survey. *Comput. Methods Programs Biomed.* **108**, 1287–1301 (2012)
11. S.K. Nayak, A. Bit, A. Dey, B. Mohapatra, K. Pal, A review on the nonlinear dynamical system analysis of electrocardiogram signal. *J. Healthc. Eng.* **2018** (2018)
12. M. Das, T. Jana, P. Dutta, R. Banerjee, A. Dey, D.K. Bhattacharya, M.R. Kanjilal, Study the effect of music on HRV signal using 3D Poincare plot in spherical co-ordinates—A signal processing approach, in *International Conference on Communication and Signal Processing*, India, 2–4 April 2015

**Part IV**  
**Network Security & Cryptography**

# MVTRNG: Majority Voter-Based Crossed Loop Quantum True Random Number Generator in QCA Nanotechnology



Arindam Sadhu, Kunal Das, Debashis De and Maitreyi Ray Kanjilal

**Abstract** True random number generator, commonly known as TRNG, is an important candidate in today's cryptography process. TRNG is only innovative design which can generate non-deterministic and unique digital bit stream to any communication systems or secured system. Quantum cellular automata (QCA) technology is adopted to design TRNG due to its low area, ultra high operating frequency, and low power dissipation. This article presents a QCA majority voter-based TRNG, which is comprised of crossed loop circuit and seed circuit. The random bits are extracted from crossed loop circuit which is composed of "OR" gate. Again the seed circuits are used here to enhance the unpredictability of generated number sequence and quality of random number. The proposed TRNG design is verified through QCA Designer tool 2.0.3, and its architecture is passed industry standard successfully. In area, latency, and energy point of view, the proposed 8-bit TRNG is consumed  $0.36 \mu\text{m}^2$  area, 1 QCA clock cycle latency, and 49.7 meV energy (per bit). So, proposed TRNG will be interpreted as a promising design in next-generation cryptography domain.

**Keywords** TRNG · Crossed loop · Seed · QCA · MV

---

A. Sadhu (✉) · K. Das · M. R. Kanjilal  
Narula Institute of Technology, 81, Nilganj Road, Agrapara, Kolkata 700109, West Bengal, India  
e-mail: [arindam.hit1@gmail.com](mailto:arindam.hit1@gmail.com)

K. Das  
e-mail: [kunal.das@nit.ac.in](mailto:kunal.das@nit.ac.in)

M. R. Kanjilal  
e-mail: [maitreyi.kanjilal@nit.ac.in](mailto:maitreyi.kanjilal@nit.ac.in)

D. De  
West Bengal University of Technology, BF-142, Salt Lake, Kolkata, India  
School of Physics, University of Western Australia, M013 35, S.H., Crawley, Perth, Australia

# 1 Introduction

In the last four decades, the required features are high density, low power, and high speed in VLSI design. All requirements are fulfilled by complementary metal oxide semiconductor (CMOS) technology. But, after scaling down, CMOS devices face lots of problem like high power dissipation, hot electron effect. So, today's world has been concentrated to identify proper alternative of CMOS technology without affecting the merits of CMOS technology. Different types of nano-electronic technology have been introduced in the present decades as possible alternative candidate of CMOS technology. In this article, the main focus is on quantum cellular automata (QCA) technology. The QCA technology is introduced by C. S. Lent in the year of 1993 due to its low power consumption (meV range), low covering area ( $\text{nm}^2$  range), and high operating frequency (THz range) [1, 2]. This technology is also known as zero-current technology as there is not any flow of electron. Information is transferred from one QCA cell to another in the form of electrostatic charge due to columbic interaction. Because of the above benefits, QCA technology could be a possible alternative of bulk CMOS technology. Many fruitful efforts have been made to design different QCA circuit. Same way in this assignment, our major concern is to design a true random number generator (TRNG) in QCA domain.

In modern security techniques, random number generator (RNG) is an indispensable ingredient. These techniques have been adopted to get maximum security without affecting user access and productivity of device. So, RNG design is a prime aspect for secured device and communication. RNG is a hardware device or a programmable device which can generate random bit sequence. Although any programme generated, bit streams are quite periodic and predictable as it has deterministic algorithm. This is commonly known as pseudo-random number generator (PRNG) [3]. So, totally unpredictable sequence generators are most important in today's era for getting more security. This phenomenon can be obtained from hardware device which has not any specific algorithm. This unique and unpredictable sequence generator is called true random number generator (TRNG) [4–6]. TRNG is a revolutionary invention in hardware cryptography.

In this article, our prime concern is to design area–delay–energy efficient majority voter (MV)-based QCA TRNG. The proposed MV-based TRNG is based on unexpected oscillation in cross-looped MV circuit. So that similar QCA crossed loop structure can be implemented to design proposed TRNG but dissimilar in outputs.

The remaining portion of this assignment is presented as follows: Physical and logical behaviour of QCA devices is discussed in Sect. 2. Section 2 also contains the basic idea about RNG. In Sect. 3, our proposed MV-based crossed loop circuit and seed circuit are explained. Proposed 8-bit MV-based TRNG design is also illustrated in Sect. 3.3. Result and discussion are presented in Sect. 4. Finally, we concluded this assignment in Sect. 5.

## 2 Preliminaries

### 2.1 QCA Basics

QCA cell architecture is the most interesting architecture where quantum physical features are hidden. Each cell consists of four-quantum dot bounded in a square shape box as shown in Fig. 1a. In each,  $(4n + 2)$  numbers of electrons are entangled in dots. The surplus electrons cannot move outside the cell, but they can tunnel between dots within the cell. Whenever the external biasing influences the cell, the excess electrons are placed two farthest dots of a cell, i.e., in diagonal position due to columbic repulsion. Each QCA cell has bistable state. Each state is defined by cell polarization ( $P$ ) and polarization of a QCA cell ( $P$ ) is measured by Eq. (1) where  $q_i$  is the probability of the presence of an electron in quantum dot  $i$ . Polarization “+1” defined the logical state “1”, whereas logical “0” state is defined by “-1” polarization as shown in Fig. 1a [2].

$$P = \frac{\rho_1 + \rho_2 - \rho_3 - \rho_4}{\rho_1 + \rho_2 + \rho_3 + \rho_4} \tag{1}$$

Prime members of QCA circuits are QCA wire, QCA inverter. and majority voter. If QCA cells are arranged in a line, then it could form a QCA chain. Again QCA logic gates are totally different from classical logic gates. QCA NOT gate, i.e., QCA inverter, could be formed by arranging QCA cell diagonally as shown in Fig. 1b. Another important QCA gate is majority voter that consists of three input driver cell, one device cell and one output cell. The device cell is bounded by input and output cell as depicted in Fig. 1c. The device cell is depolarized depending on majority polarization of driver cell, and signal is extended to output cell and rest of the circuit. If  $A, B, C$  are the inputs of a MV, then the logical expression of MV is expressed in Eq. (2).

$$\text{Maj}(A, B, C) = Y = AB + BC + CA \quad \text{where } Y = \text{output} \tag{2}$$

Now let input  $C = 0$ , then MV acts as two input “AND” gate and expression is

$$Y = AB \tag{3}$$

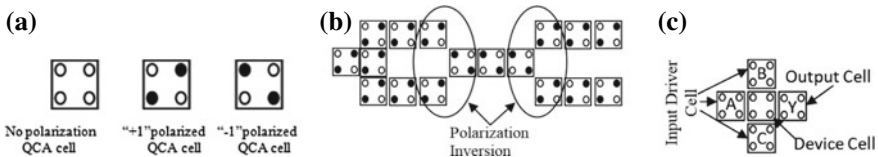
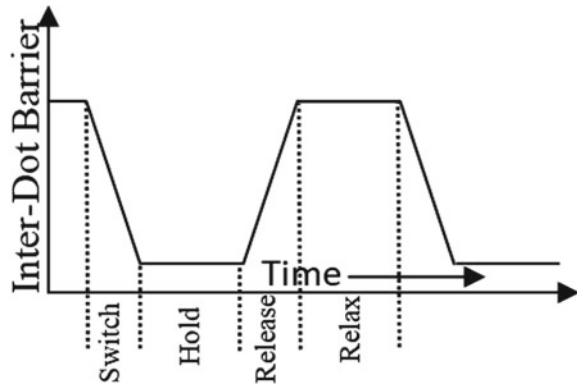


Fig. 1 a QCA cell with different polarization. b QCA inverter circuit. c QCA majority voter (MV)

**Fig. 2** QCA clocking scheme with different clocking zone descriptions



Again 0 input  $C$  is fixed at '+1' static input, then MV will be converted into two input OR gate and expression is

$$Y = A + B \quad (4)$$

In QCA technology, clocking scheme is a very vital phenomenon. Single period of a QCA clock consists of four clock zones, i.e., clock 0, clock 1, clock 2, and clock 3, and they are 90-degree phase shifted with each other, with the consecutive next. Again each clock is an integration of four zones, i.e., switch, hold, release, relax [7]. Each zone is shown in Fig. 2.

## 2.2 RNG Basics

One of the vital candidates of a secured and safe system is RNG. The strength of any random number generator is specifically related to unpredictability of successive numbers and undeterministic level of generated number also enhances the security level of device or communication [8]. Random number generator can be classified broadly in two categories—software-based RNG and hardware-based RNG.

The software-based RNG is a random number generator and is based on predefined algorithm. As it follows a deterministic algorithm, then its generated random numbers have a specific period; i.e., after a specific time, numbers will repeat. Thus, software-based RNG is commonly named as pseudo-random number generator (PRNG) [3]. If anybody has the knowledge about generating algorithm, then generated numbers are quiet easily predictable. So, PRNG is not suitable for high secured device.

There is another type of random generator, i.e., hardware RNG which is capable of generating random number without following any predefined algorithm. So, generated numbers are truly random as they do not have any specific period and are totally unpredictable. That is why hardware TRNG is commonly known as true random

number generator (TRNG). Commonly used initial input sources to TRNG, named as seed, are clock fitter, quantum phenomenon, noise, radioactive decay, etc. Here in this assignment, quantum phenomenon is used as seed of our proposed TRNG. Output sequence of TRNG is arbitrary and non-deterministic in nature, as the seeds are unpredictable. So, output sequence cannot be predicted by anybody, even internal circuit design is known to them. Again TRNG design is much easy in analogue circuit technology [9, 10] than digital technology domain [11]. Thus, it is more desirable to design TRNG in digital domain. Digital TRNG can be obtained and classified according to their randomness sources such as ring oscillator [12–14], metastability [15, 16], oscillator sampling [17, 18]. All types of TRNG are already implemented in CMOS technology. Now, it is desirable to design in next-generation emerging technology like QCA.

Different TRNG circuits are already introduced in different nano-electronic emerging technologies such as memristor [19, 20], carbon nanotube field effect transistor (CNTFET) [21], nanoscale diode [6], quantum cellular automata (QCA) [1, 2], magnetic tunnel junction [22, 23]. In this assignment, QCA technology is used to design TRNG due to its low covering area, low power, and high frequency. However in this specific QCA domain, there are only three works [24–26]. The first work [24] is related to PRNG, whereas [25] is not guaranteed to generate unpredictable bit. The work [26] gave us a cross-coupled loop TRNG in QCA technology. This work [26] is verified by statistical test, and test results are also very impressive. Consequently, more TRNG design is need to explore in QCA technology in respective of area-delay-energy.

### 3 Proposed MV-Based TRNG in QCA

In this section, proposed QCA majority voter-based TRNG is presented to generate unpredictable and non-deterministic number sequence. It is composed of two proposed elements: cross-looped MV circuit and QCA seed circuit. The crossed loop MV circuit is illustrated firstly as random list generator, and then, QCA seed circuit is discussed in order to obtain arbitrary logical outputs. Finally, proposed 8-bit TRNG is explained in QCA technology.

#### 3.1 Crossed Loop MV Circuit

The crossed loop MV circuit consists of two “OR” gate shown in Fig. 3. This cross-looped MV circuit is achieved by connecting two QCA OR gate back to back inverted. At the same time, other inputs of both MV are driven by the same seed input. As seed input oscillates randomly, so generated output bit sequence at output port ( $X$ ) is also non-deterministic as shown in Fig. 3. It consists of 43 QCA cell in an area of  $0.04 \mu\text{m}^2$  and latency of 1 QCA clock cycle. One seed input is fixed output port



starts to oscillate randomly with inverted feedback loop. QCA layout of cross-looped MV circuit is depicted at Fig. 4. When  $clk = 0$ , output is stable with  $X_t = (X_{t-1})$ . Meanwhile if  $clk = 1$ , then output will be fixed at '1'.

It consists of 43 QCA cells in an area of  $0.04 \mu\text{m}^2$  and latency of 1 QCA clock cycle. Whenever, seed input is fed into circuit, output port starts to oscillate randomly with inverted feedback loop.

### 3.2 QCA Seed Circuit

To generate more unpredictable state in QCA technology, a set of QCA cells are arranged into a specific configuration as shown in Fig. 5a–c are our proposed seed generator and Fig. 5c is reported at [26]. In this assignment, Fig. 5a, b are our proposed

**Fig. 3** Schematic diagram of proposed crossed loop MV circuit

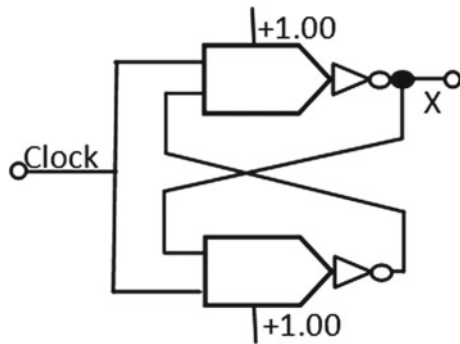
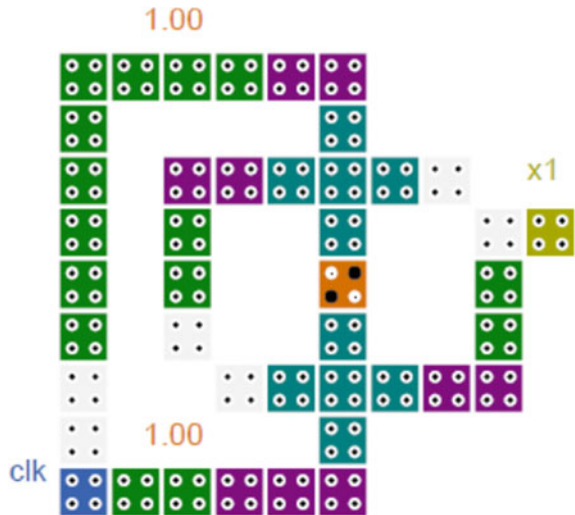


**Fig. 4** QCA layout of proposed crossed loop MV circuit



seed generator circuit. But in energy point of view, our proposed seed generator is more fruitful than Fig. 5c. Seed generators are named as SEED1, SEED2, and SEED3, and they are shown in Fig. 5a–c respectively.

The functionality of all seed generator can be illustrated theoretically based on principle of integrated electrostatic charge. As per QCA technology, device cell will always be polarized according to majority polarization. But to get unpredictable state always two inputs and one output port is used here. In Fig. 5a, if both are same, then output will be polarized as per input, but if they are different, then output will be static at either ‘1’ or at ‘0’ which is quite unpredictable. In Fig. 5b, c, device cell of both figures will inversely get polarized with input polarization.

But in energy point of view, Fig. 5a, b have energy benefit than Fig. 5c. Here in this assignment, Fig. 5a, c are used as seed input of our proposed TRNG circuit. Table 1 shows comparison table of energy dissipation in energy ratio 0.5.

### 3.3 Majority Voter-Based Quantum TRNG Design

In this section, our proposed MV-based TRNG is discussed. The straightforward MV-based QCATRNG is achieved by arranging proposed QCA structure discussed in the previous subsection. The proposed 8 bit crossed loop MV based QCATRNG is depicted in Fig. 6. This feedforward architecture is arranged to increase the circuit complexity that enhances the randomness of number.

By connecting the outputs of two crossed loop MV structure in each column through a single QCA seed input. On this proposed structure, seed1 and seed2, both type seed inputs, are used. There are not any specific algorithms to connect the seed; any body can connect the seed input by the previous discussed type seed circuit. The

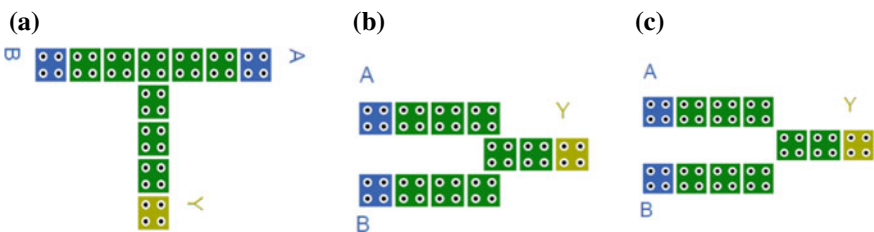


**Fig. 5** a QCA layout of SEED1. b QCA layout of SEED2. c QCA layout of SEED3

**Table 1** Energy dissipation comparison table between different SEED circuit for energy ratio 0.5

QCA circuits	Avg. leakage power dissipation (mev)	Avg. switching power dissipation (mev)
SEED1	2.60	9.33
SEED2	2.73	7.88
SEED3	4.16	12.54

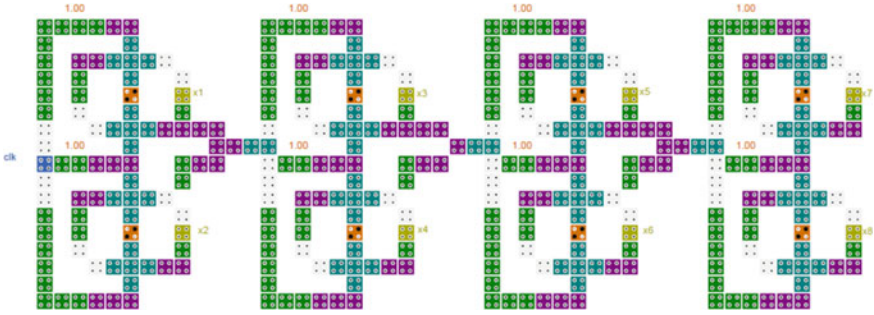


Fig. 6 QCA layout of 8-bit proposed QCA MV-based TRNG

output is connected to the seed input of next column, and this process will continue till end. The circuit complexity, area, and latency of proposed TRNG are 339 QCA cell,  $0.36 \mu\text{m}^2$  and 1 QCA clock cycle, respectively. Since our feed forward structure is crossover free and straight forward then easily expandable to required bits.

## 4 Result and Discussion

In this, the proposed TRNG design is evaluated to check the functionality. Proposed circuit is evaluated by QCAD designer, and power analysis is calculated by QCAPro.

### 4.1 Simulation Outcome with Parameter Specification

In this article, all performance analysis is completed using QCAD Designer 2.0.3 [27] under both coherence and bistable approximation engines. Again simulation parameters are taken as default value. Simulation outcome of our proposed 8-bit TRNG is shown in Fig. 7. The single random numbers are considered after calculating the sum of electrostatic polarization of fourth clock zone operated output cell of individual.

In this article, 10-bit majority voter-based TRNG is designed as a particle implemented example. The output random number is taken as same as single 8-bit proposed TRNG. All 10-bit TRNG is operated by some input clock. The randomly generated ten numbers from each 10 bit TRNG (out 1-out 10) are unpredictable and non-deterministic natures, as shown in Fig. 8.

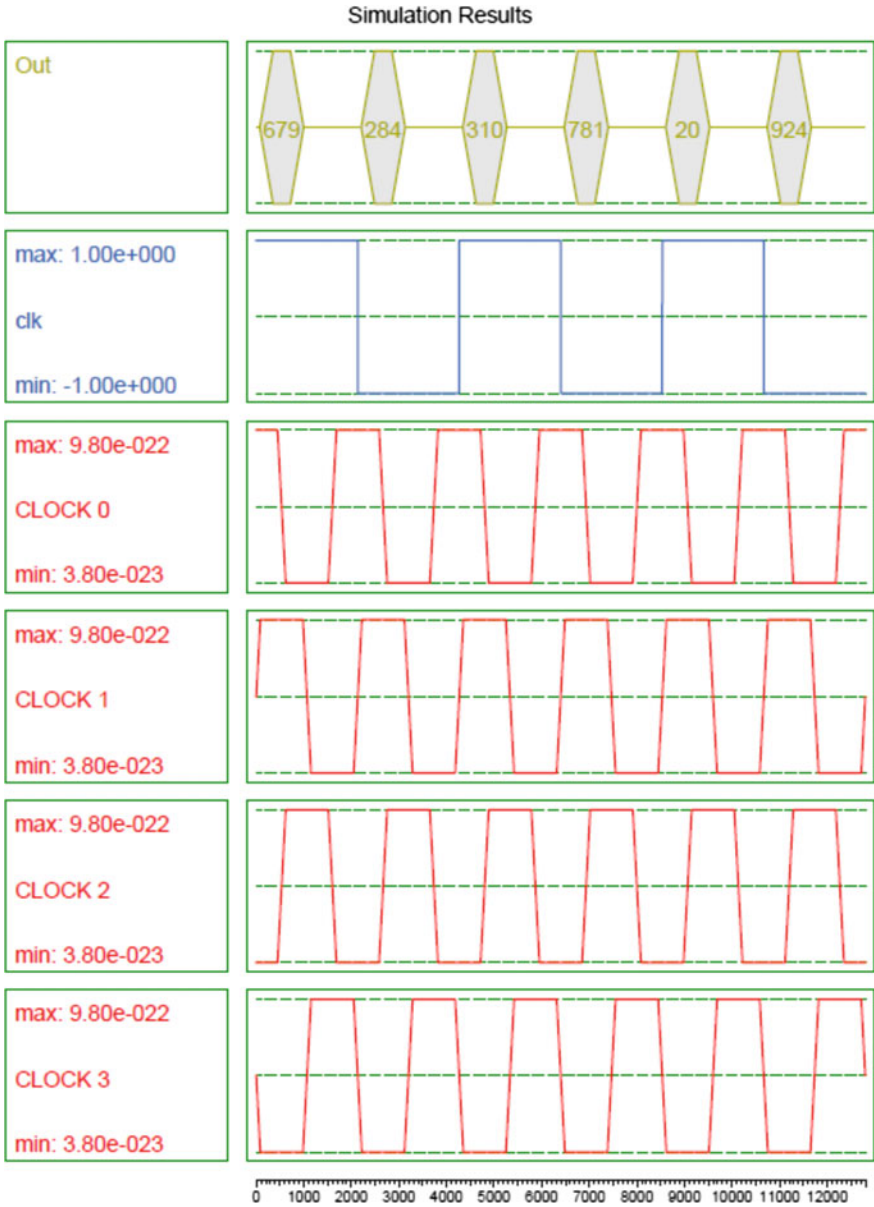
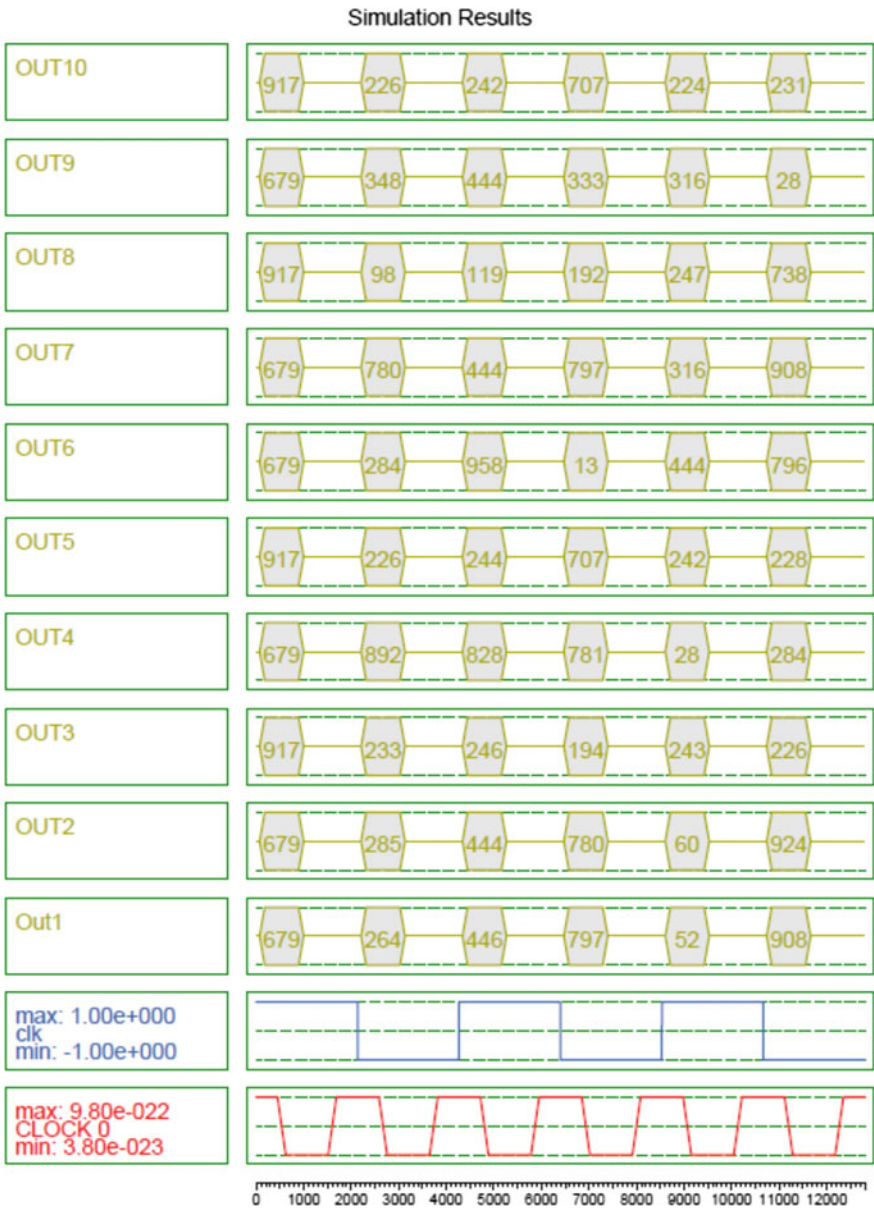


Fig. 7 Simulation outcome of proposed 8-bit TRNG from QCA Designer



**Fig. 8** Simulation outcome of ten 10-bit TRNG from QCADesigner as a practical implementation

**Table 2** NIST test report

TEST name	<i>p</i> -value
Frequency test	0.9862
Frequency block test	0.9149
Run test	0.8741

### 4.2 Statistical Test

There are several statistical test batteries to verify the industry standard design like Diehard, NIST. Here in this article, the most popular statistical test suite, National Institute of Standards and Technology (NIST) is adopted to verify that our proposed design is industry standard or not. As per NIST guideline, if *p*-value of NIST test battery lies in between 0.01 and 0.99 for 16 statistical tests, then the TRNG design will meet industry standard.

In this assignment, Table 2 is described the NIST test report of our proposed TRNG design for first three statistical test. In this Table 2, *p*-value is proved that our proposed design met industry standard due to high score.

### 4.3 Power Analysis with QCAPro Tool

Energy dissipation calculation of TRNG design is our one of the prime concerns with area and delay. So, all energy dissipation is calculated by very precise QCAPro [28]. In Table 3, average leakage energy and average switching energy dissipation are described of proposed circuits for energy ratio of 0.5, 1.0, and 1.5. From Table 3, it can be easily concluded that proposed TRNG is consumed very less energy.

**Table 3** Power dissipation data

QCA circuits	Avg. leakage power dissipation (mev)			Avg. switching power dissipation (mev)		
	0.5	1.0	1.5	0.5	1.0	1.5
Crossed loop MV circuit	14.60	42.95	75.99	3.75	3.01	2.44
SEED1	2.60	7.94	14.08	9.33	8.02	6.76
SEED2	2.73	7.82	13.91	7.88	4.54	3.93
SEED3	4.16	11.98	20.60	12.54	10.12	8.14
8-bit TRNG (per bit)	16.89	46.92	83.03	10.23	8.47	6.89

## 5 Conclusion

In this article, QCA TRNG has been proposed based on QCA physical properties. Our proposed MV-based TRNG is area–delay–energy efficient design which is proved in the previous section. The proposed architecture is presented based on unpredictable polarization in output QCA cell using cross-looped QCA ‘OR’ gate and non-deterministic seed input. Random bits are generated from cross-looped QCA ‘OR’ gate, whereas the unpredictable seed input circuit is enhanced the randomness possibility. 8-bit proposed TRNG consists of 339 QCA cell with the area of 0.36  $\mu\text{m}^2$ . The TRNG circuit can generate a random number in a single QCA clock cycle, so latency is very low and operate at high frequency range. Now, average energy dissipation point of view, 8-bit proposed TRNG, is consumed 49.7 meV energy (per bit). Again as per NIST standard, our proposed MV-based TRNG sturdily meet desired industry standard. Again, as this architecture is very straightforward, then anybody can extend the design up to required bit. So it is easily concluded that the proposed MV-based TRNG will play a big role in next-generation nano-electronic cryptography due to its low covering area, ultra high frequency, and ultra low energy dissipation.

**Acknowledgements** The authors Dr. Kunal Das, Arindam Sadhu are grateful to the Science and Engineering Research Board (DST-SERB), Government of India, for providing with the grant for accomplishment of the project under the Project File No. CR/2016/000613.

## References

1. C. Lent, P. Tougaw, W. Porod, G. Bernstein, Quantum cellular automata. *Nanotechnology* **4**(1), 49–57 (1993)
2. P. Tougaw, C. Lent, Dynamic behavior of quantum cellular automata. *J. Appl. Phys.* **80**(8), 4722–4736 (1996)
3. S. Hedayatpour, S. Chuprat, Random number generator based on transformed image data source. *Adv. Comput. Commun. Control Autom.* **121**, 457–464 (2011)
4. L. Zhang, Z. Kong, C. Chang, PCKGen: a phase change memory based cryptographic key generator, in *IEEE International Symposium on Circuits and Systems* (2013), pp. 1444–1447
5. L. Zhang, X. Fong, C. Chang, Z. Kong, K. Roy, Optimizing emerging non-volatile memories for dual-mode applications: data storage and key generator. *IEEE Trans. Comput. Aided Des. Integr. Circuits Syst.* **34**(7), 1176–1187 (2015)
6. U. Rührmair, C. Jaeger, M. Bator, M. Stutzmann, P. Lugli, G. Csaba, Applications of high-capacity crossbar memories in cryptography. *IEEE Trans. Nanotechnol.* **10**(3), 489–498 (2011)
7. S.E. Frost, T.J. Dysart, P.M. Kogge, C.S. Lent, Carbon nanotubes for quantum-dot cellular automata clocking, in *4th IEEE Conference on Nanotechnology* (2004), pp. 171–173
8. National institute of standards and technology (NIST), A Statistical test suite for random and pseudorandom number generators for cryptographic applications, Special Publication 800–822 (2010)
9. W. Holman, J. Connelly, A. Dowlatbadi, An integrated analog/digital random noise source. *IEEE Trans. Circuits Syst. I Fundam. Theory Appl.* **44**, 521–528 (1997)

10. M. Bucci, L. Germani, R. Luzzi, A. Trifiletti, M. Varanonuovo, A high-speed oscillator-based truly random number source for cryptographic applications on a smart card IC. *IEEE Trans. Comput.* **52**, 403–409 (2003)
11. B. Sunar, W. Martin, D. Stinson, A provably secure true random number generator with built-in tolerance to active attacks. *IEEE Trans. Comput.* **56**(1), 109–119 (2007)
12. D. Schellekens, B. Preneel, I. Verbauwhede, FPGA vendor agnostic true random number generator, in *International Conference on Field Programmable Logic and Applications (FPL)*, 2006, pp. 1–6
13. K. Wold, C. Tan, Analysis and enhancement of random number generator in FPGA based on oscillator rings. *Int. J. Reconfigurable Comput.* **4** (2009)
14. P. Bayon, L. Bossuet, A. Aubert, V. Fischer, F. Poucheret, B. Robisson, P. Maurine, Contactless electromagnetic active attack on ring oscillator based true random number generator. *COSADE* **7275**, 151–166 (2012)
15. S. Mathew, S. Srinivasan, M. Anders, H. Kaul, S. Hsu, F. Sheikh, R. Krishnamurthy, 2.4 Gbps, 7 mW all-digital PVT-variation tolerant true random number generator for 45 nm CMOS high-performance microprocessors. *IEEE J. Solid-State Circuits* **47**(11), pp. 2807–2821 (2012)
16. C. Tokunaga, D. Blaauw, T. Mudge, True random number generator with a metastability-based quality control. *IEEE J. Solid-State Circuits* **43**(1), 78–85 (2008)
17. T. Amaki, M. Hashimoto, T. Onoye, A process and temperature tolerant oscillator-based true random number generator. *IEICE Trans. Fundam. Electron. Commun. Comput.* **97**(12), 2393–2399 (2014)
18. M. Bucci, R. Luzzi, Fully digital random bit generators for cryptographic applications. *IEEE Trans. Circuits Syst. I Regul. Pap.* **55**(3), 861–875 (2008)
19. Y.T. Chiu, A memristor true random-number generator. *IEEE Spectr.* (2012)
20. T. Zhang, M. Yin, C. Xu, X. Lu, X. Sun, Y. Yang, R. Huang, High-speed true random number generation based on paired memristors for security electronics. *Nanotechnology* (2017)
21. W. Gaviria Rojas, J. McMorro, M. Geier, Q. Tang, C. Kim, T. Marks, M. Hersam, Solution-processed carbon nanotube true random number generator, *Nano Lett.* **17**(8), 4976–4981 (2017)
22. Y. Wang, H. Cai, L. Naviner, J. Klein, J. Yang, W. Zhao, A novel circuit design of true random number generator using magnetic tunnel junction, in *IEEE/ACM International Symposium on Nanoscale Architectures (NANOARCH)* (2016), pp. 123–128
23. Y. Qu, J. Han, B. Cockburn, W. Pedrycz, Y. Zhang, W. Zhao, A true random number generator based on parallel STT-MTJs, in *Design, Automation & Test in Europe Conference & Exhibition (DATE)* (2017), pp. 606–609
24. T. Purkayastha, D. De, K. Das, A novel pseudo random number generator based cryptographic architecture using quantum-dot cellular automata. *Microprocess. Microsyst.* **45**, 32–44 (2016)
25. A. Keikha, C. Dadkhah, M. Tehrani, K. Navi, A novel design of a random generator circuit in QCA. *Int. J. Comput. Appl.* **35**(1), 30–36 (2011)
26. M.M. Abutaleb, A novel true random number generator based on QCA nanocomputing. *Nano Commun. Netw.* **17**, 14–20 (2018)
27. K. Walus, T. Dysart, G. Jullien, R. Budiman, QCADesigner: a rapid design and simulation tool for quantum-dot cellular automata. *IEEE Trans. Nanotechnol.* **3**, 26–31 (2004)
28. S. Srivastava, A. Asthana, S. Bhanja, S. Sarkar, QCAPro: a novel power estimation tool for QCA circuit design, in *IEEE International Symposium of Circuits Systems* (2011), pp. 2377–2380



# Applying Encryption Algorithm on Text Steganography Based on Number System



Kunal Kumar Mandal, Siddhartha Chatterjee, Avishek Chakraborty, Saptarshi Mondal and Saikat Samanta

**Abstract** Nowadays as there is huge transfer of information throughout the world so there are adequate chances of leakage of information. Standard algorithms fail to protect data/information. This is the primary purpose for developing a number system-based technique for data/information hiding. This is a combination of art and science where the original data is hidden, which appears as nonexistent, so keeping it out of sight. All the characters, numbers can be hidden by using a novel method, and so it is applicable to any language. Any message can be hidden by transmitting it in the encoded form over any electronic media. This work is not a comparison or improvement of the previous works but it is a different approach to text Steganography to hide the information. A superb blend of number, word to hide information. For developing the application, this paper could be very useful for any defence, force to transmit highly secret data securely.

**Keywords** Steganography · Number system · AES algorithm · Information hiding

---

K. K. Mandal

Department of Computer Science, Mankar College, Mankar, India  
e-mail: [kunal@turiyan.com](mailto:kunal@turiyan.com)

S. Chatterjee (✉)

Department of Computer Application, DSMS Group of Institutions, Durgapur, India  
e-mail: [siddhartha.chatterjee31@gmail.com](mailto:siddhartha.chatterjee31@gmail.com)

A. Chakraborty

Department of Basic Science, Narula Institute of Technology, Kolkata, India  
e-mail: [tirtha.avishek93@gmail.com](mailto:tirtha.avishek93@gmail.com)

S. Mondal

Indian Railways, New Delhi, India  
e-mail: [rishi.crj@gmail.com](mailto:rishi.crj@gmail.com)

S. Samanta

Department of Computer Science and Engineering, Bengal College of Engineering, Durgapur, India  
e-mail: [ssamanta.wb@gmail.com](mailto:ssamanta.wb@gmail.com)

© Springer Nature Singapore Pte Ltd. 2020

K. Maharatna et al. (eds.), *Computational Advancement in Communication Circuits and Systems*, Lecture Notes in Electrical Engineering 575,  
[https://doi.org/10.1007/978-981-13-8687-9\\_23](https://doi.org/10.1007/978-981-13-8687-9_23)

255

## 1 Introduction

Internet is an immense process of changing ideas throughout the globe. Communication medium is present days like SMS reaches around 350 billion per month. An amalgam of Facebook and WhatsApp messenger covers around 60 billion data transfer inform of text for transmitting the expansive capacity of data lead us to evolve such kind of technique [1, 2]. Here we are working with the English language only. Other languages can also be included if it was synchronized with a lingo. To protect messages from intruder attacks or interference in an extraordinary way, here a commonly known approach is used called Steganography. By this technique, a way to predict recipient to recognize this subsistence of the message is done [3, 4]. This is done to overshadow a message, video, image or file. In other words, Steganography is a way in which a text is enclosed by another text, so that no one can easily recognize the original one. Through a pre-determined address, the messages can only be perceived. According to Trithemius, polygraphia and Steganographia are a grand encryption. The term “Steganography” was first stated by Trithemius. This term is derived from to Greek word “steganos” meaning “covered” and “graphein” meaning “to write” [5–7]. We make come to know about the black and white facts of Steganography by disclosing the story of legendary Herodotus, who use to send messages on the shaved heads of his slaves. Intruder attacks are increasing day by day over the Internet. So securing the information is very much needed to prevent theft of data/information. Now this is a big time to turn aside the invader for the sake of privacy, secrecy and integrity of data [8, 9]. Until now, a huge amount of work is done in this area but plenty to be done yet. “Need is the mother of invention” and this is our duty to manifest the proverb. Our innovative technique can rescue data/information far better than the existing one through several safety measures like cryptography, Steganography. It is a blend of art by keeping important information concealed through the process of hiding information. Generally, the message is encoded in such a way that it remains concealed from unintended users. Steganography is the supreme approach in concealed communication data as if compare with other present data communication system [10, 11]. The main motive of this technique is not to make sure to others or not make them familiar with the concealed data, but to make assurance about the presence of data. When a digital image is attached with it then only Steganographic application can be significant, which includes copy write protection, feature tagging and secret communication. To identify as intellectual property, copy write notice or watermark can be implanted inside as an image. By the help of this watermark any kind of unauthorized attempt to use the image can be recognized [12, 13]. Steganography is an approach in which a message is kept out of sight by which the dispatcher of that message and the subsistence of the message is his beneficial counterpart recognition. It does not make a centre of consideration for the hackers and it is the beauty of this process [14]. The term Steganography is not a new process, it was coined even in the ancient era, and these primeval techniques are specified physi-

cal Steganography. Several sketches are there for such process where the messages are concealed in various supplementary modes, in secret links messages are carved messages are kept in envelopes in different areas covered by stamps. This venerable process is known as digital Steganography. In inclusion, network Steganography is drawn on the networks of telecommunication. This comprises the method of resembling the Steganography and WLAN Steganography [15, 16]. It can be categories depending on its importance and goals. Different kinds of diagram of Steganography are shown. Technical Steganography and Linguistic Steganography are the main two types of Steganography. Basically, we are working with technical part which can again subdivide into two part, method-based and cover-based Steganography. The covered-based technical technique is a text Steganography. The advantages of text Steganography is the whole message which is to be transferred through image, audio or video. Due to covering the secret message, the video requires huge space in a descending manner the audio, image and text are kept [17, 18]. Cryptography is the art of “hide from view” of any data. On another side, Steganography organizes a hidden message in such a way that only the receiver and the sender are aware with the existence of the message. In Steganography, the reality of the message is only known to the sender and the receiver, whereas in cryptography the outlive of the encoded message is free to be seen to the world. Steganography disposes of all unnecessary attention of hidden message. Specifically, Steganography deals with hiding both the message and the content, while in cryptography method always try to protect the subject of the message [2, 19].

## 2 Previous Work

In this segment, several attempts are related here to illustrate this information hiding by the side of their disadvantages and advantages.

### 2.1 Markup Lingo

In text Steganography, the markup language is used as an existing service that is provided to hide any data or information. Any HTML document can be an example of the features of it, and this is in the care of in attentiveness of tags. Suppose for example, the <BR> tags may be as <Br> or it can also be as <br>. Steganography, as per thoughts, may be utilized as may one or two the tags. In this case, the text which is within two tags can be in a hidden form. It may contain normal text in the first and third tags. It may not be possible for an intruder to find out where Steganography is used in HTML files. A key can be said so that only purposive receiver can see the proper text. By this suitable function, we can dig up all the hidden information. Anyhow this technique does not exercise for all other markup languages same like WML. In the first text Steganography, it may not be engaged on it but the second text

Steganography process may work. In some certain condition only it is useful [14, 20].

## ***2.2 Specific Characters in Words***

In this type, we choose one of the few words or a group of words from some or all paragraphs. For example, we can say a secret message is formed in such a way that the initial word of every paragraph is chosen. By placing, the first character of a specific word side by side is a process. An undesired receiver may find variance in the text. Same as a chain of text after an interim may decide on hiding Steganography [15, 21].

## ***2.3 Line Shifting Procedure***

This type of system includes, vertically sifting of lines of the text to some extent of degrees. For example, few elected appearances are being altered. In the particular text and information, it can be 1/695 inch up or down, it is hidden by generating a secret unique nature of the text. This is always kept unknown to others. This converted text cannot be seen with naked eyes. Though in this process, distance can be measured using some particular instruments and necessary modifications can be initiated to knock out the hidden data. Text is also retyped or character program (OCR) is in use, would find demolish the hidden information [4, 22].

## ***2.4 Genetic Algorithm Scheme***

In this paper, authors have focused on Genetic Algorithm (GA) to protect stego text from third party [17]. Maximum time has been seen that generated stego text produces a doubtful stego text which can be measured by Jaro Winkler measurement. Many researchers focused on images, audio and video Steganography but GA provides the optimized solution compared to the others. It takes less memory for communication compared to video Steganography.

## ***2.5 Syntactic Proposal***

For finding the meaning of a sentence, punctuation symbols are also essential. In this entire significance modification of punctuations can be done. But changing the punctuation like full stop “(.)” and comma (,) has been kept in right places. In this

technique can be used to hide information. Here is an example: “when I dance well, ladies feel seek”, so after changing the punctuation we can see, “when I dance, well ladies feel seek”. In this case, the application of the word changes in nature. Now in a text file, one can hide information.

## ***2.6 Semantic Proposal***

In semantic scheme, by using the words synonyms of particular words we can hide information within the text. The protection of the information is the fore more priority, improvement and significant of the scheme [7]. In case of using OCR program or retyping, it can be violated. Anyhow the significance of the documentation makes change.

## ***2.7 Feature Coding***

Some characters in between the text can be altered in this method. For example, hiding information in text may be elongated or shortened of the last part of some character like h, d, b or so on. In this process, without making the reader aware of the existence of the information in text a enlarge volume of information is kept hidden in the text [13, 22]. By keeping the characters in a fixed form the main information is disappeared. The hidden information has been destroyed by using OCR program or retyping the text.

## ***2.8 Abbreviation***

The use of abbreviation is another method for hiding information. Very small-scale information can be kept concealed in the text in this method. As for example, among several kilobytes in a file only a few bits can be hidden, for example, like regular basis normal abbreviation such as PFA (Please Find Attachment), PTO (Please Turn Over) [12].

## ***2.9 Missing Letter Puzzle***

In this paper, author discusses about missing letter puzzle [9], which means one or more letters missing in each word. A question mark is used on misplaced position or certain position in a word. Replaced each question mark by an appropriate letter in each word, so as to make the words meaningful. Words in a missing letter puzzle can

be of different span and various domains, i.e., terminologies of various fields or can be proper nouns or a combination of both. Each character of undisclosed message is out of sight in a word of certain length by missing one or few letters in it. So, length of words depends on the value of characters to be hidden, the words are energetically generated. There is no prearranged cover file. In such a way, the technique is designed that the Steganography file is formed without the cover medium.

### 3 Proposed Method

We find for text Steganography, we discover a lot of miscellaneous approaches. A techniques is been used in this paper, in which through a cover media of number system a secret message will pass through, on Indian languages for the proposed scheme. In this paper, it proposes a scheme where implanting of secret message is done by applying a skilful model of the number system. This is not the motive to say that the set of symbol have been used like digits of system. As in the decimal system similar 10 digits means 0–9 are used [23], but in this system the demonstration is in altered way. This time the representation is in an order of pair of two number in which any number is represented. Here, calculate the final value of the number the two numbers are put in a specific formula. After looking at the given example, the concept will be more prominent.

Let us suppose, a decimal number system says 859. So, the number is computed as  $(8 * 100 + 5 * 10 + 9)$ . Same as if this number 859 is put in some other number system suppose base “ $i$ ”, then it is value will come out as  $(8 * i * i + 5 * i + 9)$ .

Thus we can see that in every number system it requires to work on the digits to get the final value. Similarly to get the final value my system also operates on digits but somehow the computation is different. The number like 859 of decimal is written as (40,39) in my system. And the computation is done by the formula  $((Y * (Y + 1) / 2) + Z)$  for an ordered pair (Y,Z). So the value of (40,39) is given by  $((40 * 41) / 2) + 39 = ((20 * 41) + 39) = 820 + 39 = 859$ . Here every component like Y and Z are treated as decimal [20–22]. Now this is a concept where counting is done in a different way. We all know the people of ancient time used to barter their commodities in exchange of other commodities. So in terms of standard they could not represent the quantity. By dividing quantity in group of 10 in decimal system the counting is done. A number of groups containing 10 units of each commodity are divide, for any two digits which can be visualized (1,2,3,4,.....10), (11,12,13,.....20), .....

Thus the group of number is identical to the 10 digits of the number and the unit digits of the number are marked by the extra quantity of number left (>10). Here the division is done in a different way in my system. In this system, we consider any quantity of a commodity and the counting starts as,

Proposed Number System

Group	Number in group	Group element
1	1	(1)
2	2	(2,3)
3	3	(4,5,6)
4	4	(7,8,9,10)
5	5	(11,12,13,14,15)
6	6	(16,17,18,19,20,21)
7	7	(22,23,24,25,26,27,28)
.....	.....	.....
.....	.....	.....
14	14	(92,93,94,95,96,97,98, 99,100,101,102, 103,104,105)
15	15	(106,107,108,109,110, 111,112,113,114,115, 116,117,118,119,120)
.....	.....	.....
.....	.....	.....
.....	.....	.....
N	N	.....

That is, we divide the group table in a way that group number 1 carry only one unit, group number 2 carry two unit and *n*th group contain *n*th unit. So if the number is given by 10 in 13th group is to be represented then it is done like (12, 10). So the value of it by the given formula is  $(12 * 13 / 2 + 10) = 78 + 10 = 88$ . By counting the place of the italic and red colour 10 given below it can be verified. From the left, it is the 88th number. Thus the pair order (*Y*, *Z*) is defined as:

- Y* including the number being considered the number of group have fully completed.
- Z* left the number of extra element.

Thus if in 7th group we considered number 7 then along with that “7” and we get 7 complete group. So *X* = 7, beside this no extra element is left with us, so *Y* = 0. So the given number will be (7, 0).

### 4 Technical and Theoretical Background

In this paper, recipient only knows about the secret message, way to hide the message and how to extract the information. Sender also knows about the encoding technique and how is applied to hide the secret message inside the text. This scenario also

repeats at receivers end and recipient also knows about the decoding technique and also grasps the knowledge about how to extract the secret message within the text. The recreation of the method can be described in fashion is distinctive in nature. The cover message is made here so simple that may not be understood by the intruder. And our secret message is “PARMANU”. Which is encrypted at the sender end and simultaneously decrypted at the receiver end, the whole process is described in Fig. 1.

### 4.1 Encoding Algorithm

- “P” is the first character of the secret message and its hexadecimal value is 50 and  $50 = (9, 5)$  where  $Y = 9$  and  $Z = 5$ .
- “A” is the next character of the secret message and its hexadecimal value is 41 and  $41 = (8, 5)$  where  $Y = 8$  and  $Z = 5$ .
- Next character is “R”, and its hexadecimal value is 52 and  $52 = (9, 7)$  where  $Y = 9$  and  $Z = 7$ .
- Next character is “M” and its hexadecimal value is 4D, first it will be converted octal value, which is 115 and  $115 = (14, 10)$  where  $Y = 14$  and  $Z = 10$ .
- Next character is “A” and its hexadecimal value is 41 and  $41 = (8, 5)$  where  $Y = 8$  and  $Z = 5$ .
- Next character is “N” and its hexadecimal value is 4E, first it will be converted octal value, which is 116 and  $116 = (14, 11)$  where  $Y = 14$  and  $Z = 11$ .

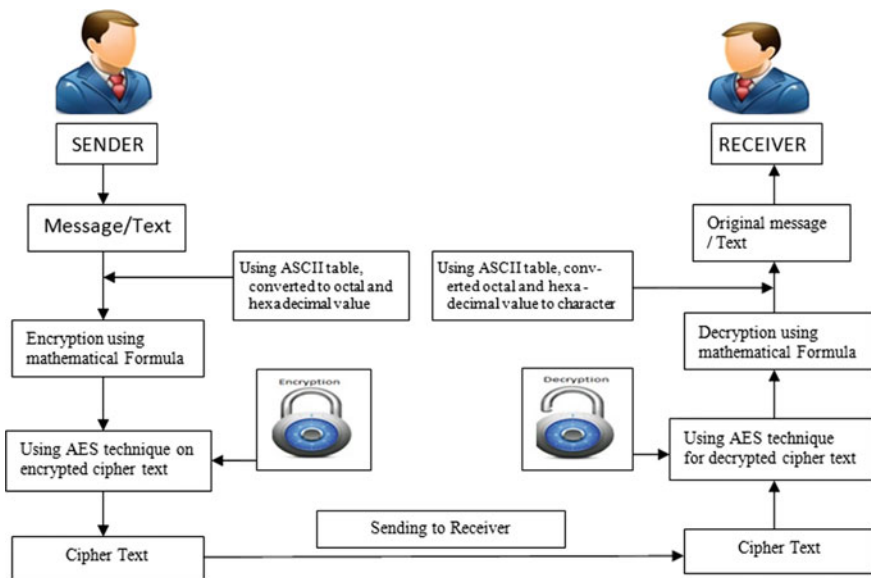


Fig. 1 Message sending and receiving technique



- Next character is “U” and its hexadecimal value is 55 and  $55 = (9, 10)$  where  $Y = 9$  and  $Z = 10$ .

Now it will look like,

Char	P	A	R	M	A	N	U
Hexadecimal	50	41	52	4D	41	4E	55
If there is a character in suffix on hexadecimal value, then find out the corresponding octal value	50	41	52	115	41	116	55
Using our formula (table)	(9, 5)	(8, 5)	(9, 7)	(14, 10)	(8, 5)	(14, 11)	(9, 10)

Like all the above coordinator are valid coordinator and contain the secret message. After getting all above coordinators, we will apply AES encryption technique on it for making it more secure the cipher text message with ECB mode and 128 bits size of key. Then sender sends the cipher text message to receiver end.

Receiver received the cipher text message, applying AES decryption technique on it and will get all the coordinators like (9, 5), (8, 5), (9, 7), (14, 10), (8, 5), (14, 11), (9,10). We are applying our mathematical technique on the above coordinator and get the original message.

## 4.2 Decoding Algorithm

- Step 1: Receiver scan start all the coordinators that is (9, 5) (8, 5) (9, 7) (14, 10) (8, 5) (14, 11) (9, 10) according to left to right direction.
- Step 2: A pair like (9, 5) provides  $Y = 9$  and  $Z = 5$ .
- Step 3: Decoder accumulates all  $Y, Z$  value, applying  $y$  and  $z$  value in the formula  $[Y * (Y + 1) / 2 + Z]$  and extract the hexadecimal value.
- Step 4: Extract hexadecimal value using same procedure and if needed then convert octal value to hexadecimal value (Fig. 2).

In our example, first pair is (9, 5). So,  $Y = 9, Y + 1 = 10$ , and  $Z = 5$ .  
 So,  $(9 * 10) / 2 + 5 = 50$ .

- Step 5: Collect the hexadecimal value (50) and alter the character using hexadecimal to character revision. In our first case, hexadecimal value is 50 and corresponding character is P (hexadecimal value of P is 50).
- Step 6: This process will be continuing (Step 1–5) until decryption for the rest of the pairs.

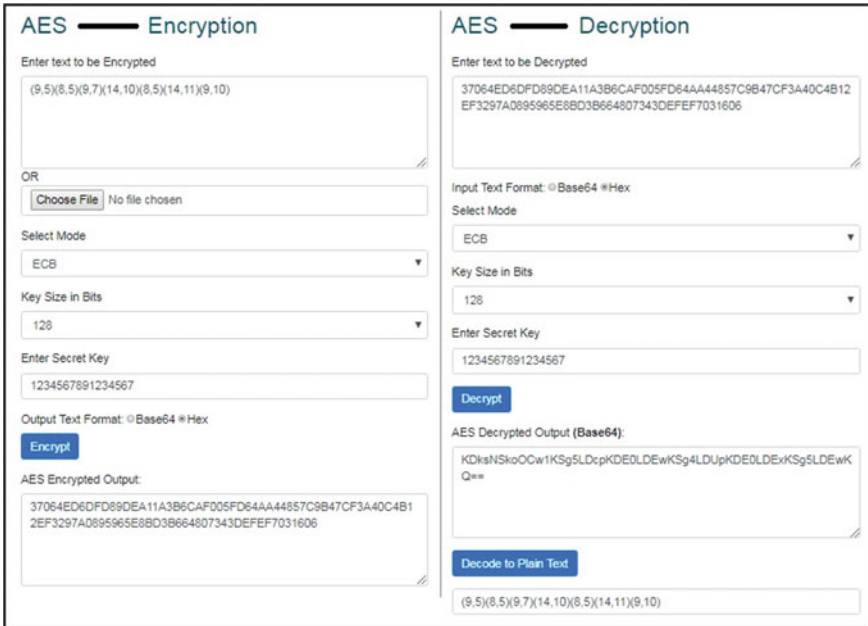


Fig. 2 AES encryption and decryption technique

## 5 Conclusion

In this paper, demonstration of mathematical formula with the number system and using AES algorithm where Steganography is a method and text message is used as a cover medium. This structure is fascinating the advantage of the continuation of numerous unusual types of Steganographic approach in a variety of languages. The basic encouragement at the raise of this technique is exploited for hiding the secret information in a number system devoid of using any conventional algorithm.

## 6 Future Scope

Future research is a big challenging of any researchers to find out cover medium and expand the various kind of medium founded on number system and revise it to sparse the secret message. In everywhere, security is the major challenge or concern in any data hiding procedure, hence enhancing novel security features and modifies it from time to time is a great challenge.

## References

1. C. Cachin, An information-theoretic model for steganography, in *Proceedings of 2nd Information Hiding Workshop*, vol. 1525, 1998, pp. 306–318
2. N.T. Johnson, S. Jajodia, Staganalysis: the investigation of hiding information, in *IEEE*, 1998, pp. 113–116
3. K. Thangadurai, G. Sudha Devi, An analysis of LSB based image steganography techniques, in *ICCCI*, 3–5 Jan 2014
4. T.S. Chen, M.W. Cheng, A new data hiding scheme in binary image, in *Proceedings of Fifth International Symposium on Multimedia Software Engineering*, 2003, pp. 88–93
5. D. Artz, Digital steganography: hiding data within data, in *IEEE Internet Computing*, May–Jun 2001, pp. 75–80
6. Herodotus, *The Histories*, trans. by A. de Selincourt (Penguin Books, London, 1996)
7. J.C. Judge, Steganography: past, present, future. SANS white paper, 30 November 2001, <http://www.sans.org/rr/papers/index.php?id=552>
8. G. Simmons, The prisoners problem and the subliminal channel, in *CRYPTO*, 1983, pp. 51–67
9. M. Agarwal, Text steganographic approaches: a comparison. *Int. J. Netw. Secur. Appl. (IJNSA)* **5**(1), 2013
10. M. Shirali Shahreza, An improved method for steganography on mobile phone. *WSEAS Trans. Syst.* **4**(7), 955–957 (2005)
11. K. Gopalan, Audio steganography using bit modification, in *Proceedings of the IEEE International Conference on Acoustics, Speech, and Signal Processing (ICASSP '03)*, vol. 2, 6–10 April 2003, pp. 421–424
12. G. Doërr, J.L. Dugelay, A guide tour of video watermarking. *Sig. Process. Image Commun.* **18**(4), 263–282 (2003)
13. N. Provos, P. Honeyman “Hide and seek”: an introduction to Steganography, in *IEEE Security and Privacy*, May/June 2003, pp. 32–44
14. G. Doërr, J.L. Dugelay, Security pitfalls of frame by frame approaches to video watermarking. *IEEE Trans. Signal Process. Suppl. Secure Media* **52**(10), 2955–2964 (2004)
15. J.T. Brassil, S. Low, N.F. Maxemchuk, L. O’Gorman, Electronic marking and identification techniques to discourage document copying. *IEEE J. Sel. Areas Commun.* **13**(8), 1495–1504 (1995)
16. K. Bennett, Linguistic steganography: survey, Analysis, and robustness concerns for hiding information in text, Purdue University, CERIAS Tech. Report 2004-13
17. B. Osman, A. Yasin, M.N. Omar, An analysis of alphabet-based techniques in text steganography. *J. Telecommun. Electron. Comput. Eng.* **8**(10), pp. 109–115 (2015)
18. S.H. Low, N.F. Maxemchuk, J.T. Brassil, L.O’Gorman, Document marking and identification using both line and word shifting, in *Proceedings of the Fourteenth Annual Joint Conference of the IEEE Computer and Communications Societies (INFOCOM '95)*, 2–6 April 1995, vol. 2, pp. 853–860
19. T. Moerland, Steganography and steganalysis, 15 May 2003, [www.liacs.nl/home/tmoerlan/privtech.pdf](http://www.liacs.nl/home/tmoerlan/privtech.pdf)
20. S. Koley, K.K. Mandal, A novel approach of secret message passing through text steganography, in *International Conference on “Signal Processing, Communication, Power and Embedded System (SCOPES—2016)”*, Issue—III, 3–5 Oct 2016, pp. 21–26. 978-1-5090-4620-1/16/\$31.00 ©2016 IEEE, ISBN CPF16H12-PRT/978-1-5090-4619-5

21. K.K. Mandal, S. Koley, S. Mondal, Number system oriented text steganography in English Language for short messages: a decimal approach, in *Intelligent Computing and Information and Communication. Advances in Intelligent Systems and Computing*, vol. 673, ed. by S. Bhalla, V. Bhateja, A. Chandavale, A. Hiwale, S. Satapathy (Springer, Singapore, 2018)
22. S. Koley, K.K. Mandal, Number system oriented text steganography in various language for short messages, in *Computational Intelligence, Communications, and Business Analytics. CICBA 2017. Communications in Computer and Information Science*, vol. 775, ed. by J. Mandal, P. Dutta, S. Mukhopadhyay (Springer, Singapore, 2017)
23. K.K. Mandal, A. Jana, V. Agarwal, A new approach of text Steganography based on mathematical model of number system, in *Circuit, Power and Computing Technologies (ICCPCT)*, IEEE, 20–21 March 2014, pp. 1737–1741

**Part V**  
**VLSI and Image Processing**

# Four-Directional Detection-Based Gaussian Noise Removal



Shubhendu Banerjee, Aritra Bandyopadhyay, Rajib Bag and Atanu Das

**Abstract** Detection of gaussian noise is an exigent task, especially at high noise density levels. This paper proposes a four-directional noise detection scheme towards the noise removal process. A calculated threshold value is undertaken in the detection scheme. Moreover, a four-stage segmentation scheme is applied to check the noise contamination level of the pixel using the calculated threshold value. A binary flag image is generated after identifying the noise contamination and ultimately sequentially combined mean–median filter (SCMMF) is used for the removal purpose. Results of the computer simulations demonstrate the effectiveness of the proposed methods even at high noise density levels.

**Keywords** Gaussian noise · Detection · Image restoration · SCMMF

## 1 Introduction

Arbitrary variation of pixel values generates noise in images. Generally, those noisy images are caused by defective cameras, inexperienced operators, during transmission and image acquisitions [1]. The primary objective is to find out the types of degradation for the noise corrupted images as different types of causes generate dif-

---

S. Banerjee

Computer Science and Engineering, Narula Institute of Technology, Agarpara, Kolkata, India  
e-mail: [shankushubhendu@gmail.com](mailto:shankushubhendu@gmail.com)

A. Bandyopadhyay (✉) · R. Bag

Computer Science and Engineering, Supreme Knowledge Foundation Group of Institutions,  
Mankundu, India  
e-mail: [aritra.d90@gmail.com](mailto:aritra.d90@gmail.com)

R. Bag

e-mail: [rajib.bag@gmail.com](mailto:rajib.bag@gmail.com)

A. Das

Computer Science and Engineering, Netaji Subhash Engineering College, Garia, Kolkata, India  
e-mail: [atanudas75@yahoo.co.in](mailto:atanudas75@yahoo.co.in)

© Springer Nature Singapore Pte Ltd. 2020

K. Maharatna et al. (eds.), *Computational Advancement in Communication Circuits and Systems*, Lecture Notes in Electrical Engineering 575,  
[https://doi.org/10.1007/978-981-13-8687-9\\_24](https://doi.org/10.1007/978-981-13-8687-9_24)

269

ferent types of noises like salt and pepper noise [2], rayleigh noise, poisson noise, gaussian noise and gamma noise. Gaussian noise is an additive white noise having a gaussian-like distribution to introduce in each image pixel a value with mean ( $\mu$ ) and varying standard deviation ( $\sigma$ ) [3–7]. The noise level is directly proportional to the value of  $\sigma$ . Generally, gaussian noise is caused by poor illumination or high temperature. The gaussian distribution is denoted by a probability density function where  $z$  represents the grey level,  $\mu$  is the average value of  $z$ ,  $\sigma$  is the standard deviation and is variance [8]. There exist many approaches for de-noising the images affected by gaussian noise, e.g. mean filter (MF) [9], standard median filter (SMF) [10, 11], Wiener filter (WF) [8], alpha trimmed [12], bilateral filter (BF) [13], tri-lateral filter (TF) [14], filter proposed by Vijaykumar [15], adaptive window median filter (AWMDF) [16] and so on. In the MF, the pixels are replaced by the arithmetic mean of the neighbourhood pixels [17]. In the SMF, the pixels are replaced by the median of the corresponding window [18]. Both mean and median filters are effective in low-density impulse noise removal [19]. Wiener filter basically minimizes the mean square error for images affected by additive noises. But this filter requires ‘a priori’ knowledge about the original signal and noise spectra to generate optimal threshold value which is not obtainable in the real-time images [15]. To overcome the limitation of previous filters, bilateral filter is introduced by Tomasi [13]. Though at high noise density, it shows staircase effect and false edge in the images. Afterwards, Garnett [14] proposes a trilateral filter for removing various types of noises, but it does not give satisfactory result in case of gaussian noise. Moreover, recent filters like AWMDF [16] and a filter proposed by Vijaykumar [15] tried to remove gaussian noise with less computational complexity with edge preservation, but the results are not satisfactory at high noise density level. In this paper, a four-stage subdivision pattern is applied for checking the noise corruption level of the pixel. A threshold value is calculated by the average deviation between the pixels and used for the detection purpose. Thereafter, a sequentially combined mean–median filter (SCMMF) is incorporated for the removal. Apart from gaussian noise, this process also experimentally worked for the salt and pepper noise and random valued impulse noise.

The remaining paper is as follows. Review of SCMMF is described in the next section. After that, the proposed algorithm is stated briefly. The simulated results are discussed in the results and discussion part. Finally, the conclusion is drawn in the last section.

## 2 Review of SCMMF

### 2.1 Outline

Sequentially combined mean–median filter is the combination of mean and median operations. At first, a plus (+)-type operation is introduced to restore the noisy pixels by the nearest uncorrupted pixel intensities. The rest noisy pixels are then replaced by

neighbourhood mean operation and to enhance the image quality median operation is used. At last, border operation is used to maintain the same size of the image.

A salt and pepper noise corrupted image  $X_1$  ( $M \times N$ ) is taken where is the pixel value at location  $(i, j)$ . A same size binary flag image  $F_1$  ( $M \times N$ ) is generated where is the pixel value at location  $(i, j)$ .

## 2.2 Noise Detection

if  $(x_{i,j} == 0 \parallel x_{i,j} == 255)$  then

$f_{i,j} = 0$  and  $x_{i,j} = 0$ ;

else

$f_{i,j} = 1$ ;

After completion image  $X_2$  and  $F_1$  is generated and used in next level.

## 2.3 Plus Operation

if  $(x_{i,j} == 0 \ \&\& \ (x_{i-1,j} + x_{i+1,j} + x_{i,j-1} + x_{i,j+1}) \neq 0)$  then

$x_{i,j} = \frac{x_{i-1,j} + x_{i+1,j} + x_{i,j-1} + x_{i,j+1}}{f_{i-1,j} + f_{i+1,j} + f_{i,j-1} + f_{i,j+1}}$ ; [where  $i = 2$  to  $M - 1$  and  $j = 2$  to  $N - 1$ ]

$f_{i,j} = 1$ ;

After completion image  $X_3$  and  $F_2$  is generated and used in next level.

## 2.4 Neighbourhood Mean Operation

if  $(x_{i,j} == 0)$  then

$x_{i,j} = \frac{\sum_{k=i-1}^{i+1} \sum_{r=j-1}^{j+1} x_{k,r}}{\sum_{k=i-1}^{i+1} \sum_{r=j-1}^{j+1} f_{k,r}}$

After completion image  $X_4$  is generated and used in next level.

## 2.5 Neighbourhood Median Operation

Consider a set  $E$  taking the pixels of a  $3 \times 3$  matrix centring  $x_{i,j}$  where  $x_{i,j}$  is the corresponding pixel of  $f_{i,j}(= 0)$  in the binary flag image  $F_1$ .

Replace  $x_{i,j} = \text{median}\{E\}$

After completion image  $X_5$  is generated and used in next level.



### 2.6 Border Operations

if  $(x_{i,j} == 0)$  then  
 $x_{1,j} = x_{2,j}$  [where  $j = 2$  to  $N - 1$ ]  
 if  $(x_{M,j} == 0)$  then  
 $x_{M,j} = x_{M-1,j}$  [where  $j = 2$  to  $N - 1$ ]  
 if  $(x_{i,1} == 0)$  then  
 $x_{i,1} = x_{i,2}$  [where  $i = 1$  to  $M$ ]  
 if  $(x_{i,N} == 0)$  then  
 $x_{i,N} = x_{i,N-1}$  [where  $i = 1$  to  $M$ ]

After completion final output image  $X_6 (M \times N)$  is generated.

### 3 Proposed Method

Consider  $(i, j) \in A \equiv \{1, 2, 3, \dots, M\} \times \{1, 2, 3, \dots, N\}$  and be the grey level intensity value of the pixel location  $(i, j)$  of a noise-free image  $X (M \times N)$ .  $X_1 (M \times N)$ , the Gaussian noisy image is considered for the two parts algorithm (i) Detection (ii) Removal using SCMMF. Simultaneously, a same-size binary flag image  $F_1$  is generated where firstly all pixel values are 1 (true).

#### 3.1 Detection Part

A  $5 \times 5$  matrix has been created taking of  $X_1$  as a centre. A fixed threshold value ( $T$ ) has been taken to detect the pixel is a noisy one or not by four-directional detection surrounding the said pixel.

$T = \frac{\sum |X - \mu|}{N}$ , where  $\mu = \text{mean}$ ,  $X = \text{each pixel value}$ ,  $N = \text{number of pixel in } 5 \times 5$ .

Left Side

$$m_1 = \frac{\left| \left[ \sum_{r=i-2}^{i+2} |(x_{r,j} - x_{r,j-1})| - \sum_{r=i-2}^{i+2} |(x_{r,j-1} - x_{r,j-2})| \right] \right|}{5} \tag{1}$$

Right Side

$$m_2 = \frac{\left| \left[ \sum_{r=i-2}^{i+2} |(x_{r,j+1} - x_{r,j})| - \sum_{r=i-2}^{i+2} |(x_{r,j+2} - x_{r,j+1})| \right] \right|}{5} \tag{2}$$

Upper Side

$$m_3 = \frac{\left[ \sum_{k=j-2}^{j+2} |(x_{i,k} - x_{i-1,k})| - \sum_{k=j-2}^{j+2} |(x_{i-1,k} - x_{i-2,k})| \right]}{5} \quad (3)$$

Lower Side

$$m_4 = \frac{\left[ \sum_{k=j-2}^{j+2} |(x_{i+1,k} - x_{i,k})| - \sum_{k=j-2}^{j+2} |(x_{i+2,k} - x_{i+1,k})| \right]}{5} \quad (4)$$

Evaluate  $m_1$ ,  $m_2$ ,  $m_3$  and  $m_4$  from Eqs. 1, 2, 3, 4, respectively. If any value of above said any  $m \leq T$ , then  $x_{i,j}$  will be considered as a correct pixel otherwise noisy one. If  $x_{i,j}$  is a noisy one, then put in the corresponding  $f_{i,j} = 0$  in the binary flag image  $F_1$ . Completing the above process, an image  $X_2$  and a new flag image  $F_2$  are generated.

### 3.2 Illustration of the Detection Part

Consider a  $5 \times 5$  matrix,  $X_1$  has been created taking  $x_{i,j}$  as a centre from the noisy image.

$$X_1 = \begin{bmatrix} x_{i-2,j-2} & x_{i-2,j-1} & x_{i-2,j} & x_{i-2,j+1} & x_{i-2,j+2} \\ x_{i-1,j-2} & x_{i-1,j-1} & x_{i-1,j} & x_{i-1,j+1} & x_{i-1,j+2} \\ x_{i,j-2} & x_{i,j-1} & x_{i,j} & x_{i,j+1} & x_{i,j+2} \\ x_{i+1,j-2} & x_{i+1,j-1} & x_{i+1,j} & x_{i+1,j+1} & x_{i+1,j+2} \\ x_{i+2,j-2} & x_{i+2,j-1} & x_{i+2,j} & x_{i+2,j+1} & x_{i+2,j+2} \end{bmatrix}$$

Here,  $m_1$  is calculated according to Eq. 1 taking the pixels from the marked pixels in the matrix.

$$m_1 = \begin{bmatrix} x_{i-2,j-2} & x_{i-2,j-1} & x_{i-2,j} & x_{i-2,j+1} & x_{i-2,j+2} \\ x_{i-1,j-2} & x_{i-1,j-1} & x_{i-1,j} & x_{i-1,j+1} & x_{i-1,j+2} \\ x_{i,j-2} & x_{i,j-1} & x_{i,j} & x_{i,j+1} & x_{i,j+2} \\ x_{i+1,j-2} & x_{i+1,j-1} & x_{i+1,j} & x_{i+1,j+1} & x_{i+1,j+2} \\ x_{i+2,j-2} & x_{i+2,j-1} & x_{i+2,j} & x_{i+2,j+1} & x_{i+2,j+2} \end{bmatrix}$$

Here,  $m_2$  is calculated according to Eq. 2 taking the pixels from the marked pixels in the matrix.

$$m_2 = \begin{bmatrix} x_{i-2,j-2} & x_{i-2,j-1} & \boxed{x_{i-2,j}} & \boxed{x_{i-2,j+1}} & \boxed{x_{i-2,j+2}} \\ x_{i-1,j-2} & x_{i-1,j-1} & \boxed{x_{i-1,j}} & \boxed{x_{i-1,j+1}} & \boxed{x_{i-1,j+2}} \\ x_{i,j-2} & x_{i,j-1} & \boxed{x_{i,j}} & \boxed{x_{i,j+1}} & \boxed{x_{i,j+2}} \\ x_{i+1,j-2} & x_{i+1,j-1} & \boxed{x_{i+1,j}} & \boxed{x_{i+1,j+1}} & \boxed{x_{i+1,j+2}} \\ x_{i+2,j-2} & x_{i+2,j-1} & \boxed{x_{i+2,j}} & \boxed{x_{i+2,j+1}} & \boxed{x_{i+2,j+2}} \end{bmatrix}$$

Here,  $m_3$  is calculated according to Eq. 3 taking the pixels from the marked pixels in the matrix.

$$m_3 = \begin{bmatrix} \boxed{x_{i-2,j-2}} & \boxed{x_{i-2,j-1}} & \boxed{x_{i-2,j}} & \boxed{x_{i-2,j+1}} & \boxed{x_{i-2,j+2}} \\ \boxed{x_{i-1,j-2}} & \boxed{x_{i-1,j-1}} & \boxed{x_{i-1,j}} & \boxed{x_{i-1,j+1}} & \boxed{x_{i-1,j+2}} \\ \boxed{x_{i,j-2}} & \boxed{x_{i,j-1}} & \boxed{x_{i,j}} & \boxed{x_{i,j+1}} & \boxed{x_{i,j+2}} \\ x_{i+1,j-2} & x_{i+1,j-1} & x_{i+1,j} & x_{i+1,j+1} & x_{i+1,j+2} \\ x_{i+2,j-2} & x_{i+2,j-1} & x_{i+2,j} & x_{i+2,j+1} & x_{i+2,j+2} \end{bmatrix}$$

Here,  $m_4$  is calculated according to Eq. 4 taking the pixels from the marked pixels in the matrix.

$$m_4 = \begin{bmatrix} x_{i-2,j-2} & x_{i-2,j-1} & x_{i-2,j} & x_{i-2,j+1} & x_{i-2,j+2} \\ x_{i-1,j-2} & x_{i-1,j-1} & x_{i-1,j} & x_{i-1,j+1} & x_{i-1,j+2} \\ \boxed{x_{i,j-2}} & \boxed{x_{i,j-1}} & \boxed{x_{i,j}} & \boxed{x_{i,j+1}} & \boxed{x_{i,j+2}} \\ \boxed{x_{i+1,j-2}} & \boxed{x_{i+1,j-1}} & \boxed{x_{i+1,j}} & \boxed{x_{i+1,j+1}} & \boxed{x_{i+1,j+2}} \\ \boxed{x_{i+2,j-2}} & \boxed{x_{i+2,j-1}} & \boxed{x_{i+2,j}} & \boxed{x_{i+2,j+1}} & \boxed{x_{i+2,j+2}} \end{bmatrix}$$

If any  $m_r \leq T$ , then  $x_{i,j}$  is correct; where  $r = 1, 2, 3, 4$ .

### 3.3 Removal Part

The removal is processed by the above-stated algorithm SCMMF [5] where the input image is  $X_2$  and the used flag image is  $F_2$ . The final output image  $X_6$  can be obtained by the step-by-step processes of SCMMF starting from plus (+) operation till the end.

## 4 Results and Discussion

This section illustrates the comparison of the proposed method with other existing methods. The simulation is done in MATLAB 7.12 (R2011a), on a standard PC with 2.8-GHz CPU, 2 GB RAM and other requirements. The simulation is carried out on a number of acknowledged  $512 \times 512$  images like Lena, Goldhill, Cameraman and Man. These images are tested on the range of standard deviation 10–50 with an interval of 10. The quantitative performance is evaluated by peak-signal-to-noise ratio (PSNR) and mean square error (MSE) for image Lena corrupted by additive white gaussian noise as defined in Eqs. (5) and (6), respectively.

$$\text{MSE} = \left( \sum_{M,N} \frac{\left( I(m, n) - \hat{I}(m, n) \right)^2}{M \times N} \right). \quad (5)$$

$I$  = Original image,  $\hat{I}$  = De-noised image,  $M$  = Number of rows,  $N$  = Number of columns.

$$\text{PSNR} = 10 \log_{10} \frac{255^2}{\text{MSE}} \quad (6)$$

The qualitative performance is judged by structural similarity index measurement (SSIM) and mean structural similarity index measurement (MSSIM) as defined in Eqs. (7) and (8), respectively.

$$\text{SSIM}(x, y) = \frac{(2\mu_x\mu_y + C_1)(2\sigma_{xy} + C_2)}{(\mu_x^2 + \mu_y^2 + C_1)(\sigma_x^2 + \sigma_y^2 + C_2)} \quad (7)$$

$$\text{MSSIM}(x, y) = \frac{1}{M} \sum_{m=1}^M \text{SSIM}(x_m, y_m) \quad (8)$$

where  $\mu_x$  is the mean of image  $x$  and  $\sigma_x$  is the standard deviation of image  $x$ , similarly  $\mu_y$  is the mean of image  $y$  and  $\sigma_y$  is the standard deviation of image  $y$ ,  $C_1, C_2$  are the constants  $\sigma_{xy}$  is the co-variance of  $x$  and  $y$ , given by:

$$\mu_x = \frac{1}{N} \sum_{i=1}^N x_i \quad \sigma_x = \left[ \frac{1}{N-1} \sum_{i=1}^N (x_i - \mu_x)^2 \right]^{\frac{1}{2}} \quad \sigma_{xy} = \left( \frac{1}{N-1} \sum_{i=1}^N (x_i - \mu_x) \right)$$

Table 1 shows the PSNR values for the Lena image for standard deviation varies from 10 to 50 and demonstrates the assessment of performance of the proposed algorithm over the existing methods. The figure confirms the significance of the proposed method. The qualitative assessment is shown in Fig. 2 for Lena image

**Table 1** PSNR for different filters for Lena image at different standard deviations ( $\sigma$ )

SD ( $\sigma$ )	MF	WF	Alpha trimmed	BF	TF	Vijaykumar [15]	NLM [20]	Proposed algorithm
10	26.72	32.14	30.62	31.88	30.83	32.91	32.89	<b>34.24</b>
20	25.84	28.76	29.02	29.11	28.45	31.27	30.21	<b>32.83</b>
30	24.86	26.83	27.73	28.92	27.17	28.41	29.55	<b>31.17</b>
40	23.67	24.12	24.67	25.34	24.43	26.36	27.41	<b>29.60</b>
50	21.52	22.32	21.25	23.91	22.31	25.49	26.75	<b>28.13</b>

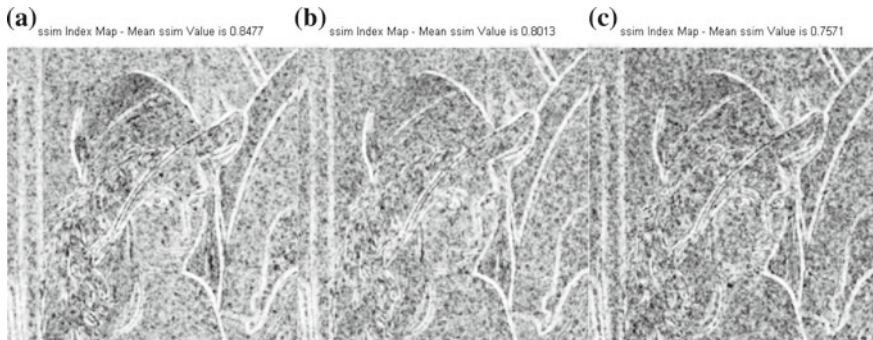


**Fig. 1** SSIM index map (MSSIM) of Lena image at standard deviation. **a**  $\sigma = 30$  (MSSIM = 0.8477), **b**  $\sigma = 40$  (MSSIM = 0.8013), **c**  $\sigma = 50$  (MSSIM = 0.7571)

where existing method’s result is compared with the proposed method. The structural information is analysed by mean structural similarity index measurement (MSSIM) as shown in Fig. 1.

## 5 Conclusion

A gaussian noise detection scheme is proposed in this paper. The importance is given on the noise detection part having a four-directional mechanism. For the filtration process, the removal part of SCMMF algorithm is used. Two different fixed windows ( $5 \times 5$  and  $3 \times 3$ ) are used for the detection and removal part. From the qualitative, quantitative, and structural symmetry analysis, it can be concluded that this method produces significant result over many existing methods. With few changes over this detection scheme, this methodology can be applied over salt and pepper, random valued and poisson noise to acquire an enhanced result.

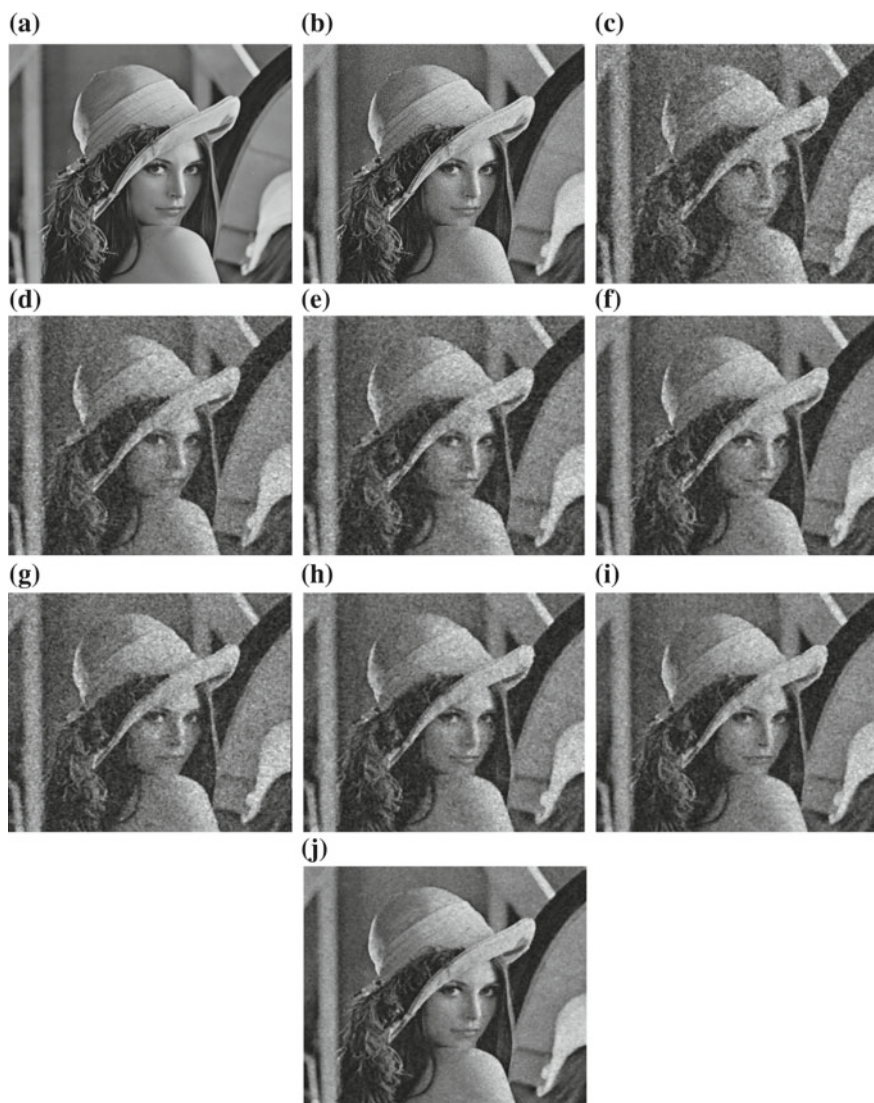


**Fig. 2** a Original image. b Noisy image  $\sigma = 40$ . c Mean filter. d Wiener filter. e Alpha trimmed. f Bilateral filter. g Trilateral filter. h V. R. Vijaykumar filter. i AWMDf filter. j Proposed method

## References

1. A. Bandyopadhyay, M. Kumari, Pooja, A. Das, R. Bag, Detection and removal of high density random valued impulse noise. *CiiT Int. J. Digital Image Process.* **7**(8), 242–246 (2015)
2. A. Bandyopadhyay, K. Chakraborty, R. Bag, A. Das, High density salt and pepper noise removal by selective mean filter, in *Foundations and Frontiers in Computer, Communication and Electrical Engineering* (Taylor & Francis Group, CRC Press, Boca Raton, 2016), pp. 191–194
3. S. Banerjee, A. Bandyopadhyay, R. Bag, A. Das, A deviation based identification of random valued impulse noise towards image filtering using neighbourhood approximation, in *Foundations and Frontiers in Computer, Communication and Electrical Engineering* (Taylor & Francis Group, CRC Press, Boca Raton, 2016), pp. 217–220
4. S. Banerjee, A. Taraphdar, R. Bag, A. Das, Binary expansion based denoising algorithm for an image corrupted by Gaussian noise, in *CSI Transaction on ICT* (Springer, Berlin, 2016), pp. 1–5. <https://doi.org/10.1007/s40012-016-0151-7>
5. S. Banerjee, A. Bandyopadhyay, R. Bag, A. Das, Sequentially combined mean-median filter for high density salt and pepper noise removal, in *IEEE ICRCICN*, pp. 21–26 (2015)
6. N. Dey, B.A Roy, M. Pal, FCM based blood vessel segmentation method for retinal images. *IJCSN* **1**(3) (2012)
7. S.A. Ashour, S. Samanta, N. Dey, N. Kausar, B.W. Abdesslemkaraa, E.A. Hassanien, Computed tomography image enhancement using cuckoo search: a log transform based approach. *JSIP* **6**(3), 244–257 (2015)
8. W. Gonzalez, *Digital Image Processing*, 2nd edn. (Prentice Hall, New Jersey, 2001)
9. A. Kundu, K.S. Mitra, P.P. Vaidyanathan, Application of two-dimensional generalized mean filtering for removal of impulse noises from images. *IEEE Trans. Acoust. Speech Signal Process.* **32**(3), 600–609 (1984)
10. W.J. Tukey, *Exploratory Data Analysis*, preliminary edn. (Addison-Wesley, Reading, MA, 1971)
11. W.J. Tukey, *Explanatory Data Analysis* (Addison-Wesley, Menlo Park, 1977)
12. J. Bednar, L.T. Watt, Alpha-trimmed means and their relationship to median filters. *IEEE Trans. Acoust. Speech, Signal Process.* **32**(1), 145–153 (1984)
13. C. Tomasi, R. Manduchi, Bilateral filtering for gray and color images, in *IEEE International Conference Computer Vision*, pp. 839–846 (1998)
14. R. Garnett, T. Huegerich, C. Chui, A universal noise removal algorithm with an impulse detector. *IEEE Trans. Image Process.* **14**(11), 1747–1754 (2005)
15. R.V. Vijaykumar, T.P. Vanathi, P. Kanagasabapathy, Fast and efficient algorithm to remove Gaussian noise in digital images. *IAENG Int. J. Comput. Sci.* **37**(1), 78–84 (2010)
16. S. Meheta, J. Vajpai, C.B.S. Gaur, Gaussian noise reduction using adaptive window median filter. *Int. J. Comput. Appl.* 0975–8887
17. S. Banerjee, A. Bandyopadhyay, R. Bag, A. Das, Neighborhood based pixel approximation for high level salt and pepper noise removal. *CiiT Int. J. Digit. Image Process.* **6**(8), 346–351 (2014)
18. A. Bandyopadhyay, S. Banerjee, A. Das, R. Bag, A relook and renovation over state-of-art salt and pepper noise removal techniques. *Int. J. Image Graph Signal Process.* **7**(9), 61–69 (2015)
19. S. Banerjee, A. Bandyopadhyay, R. Bag, A. Das, Moderate density salt & pepper noise removal. *IJECT* **6**(1) (2015)
20. Y. Jin, W. Jiang, J. Shao, J. Lu, An improved image denoising model based on nonlocal means filter: mathematical problems in engineering. *Hindawi* **2018**, Article ID. 8593934 (2018)

# Comparative Analysis of 6-T SRAM Cell in Terms of Power Using CMOS and DGMOS



Srabani Das (Roy), Saradindu Panda and Gourav Chakraborty

**Abstract** As we know for current industry, downscaling of MOSFET is a very essential factor, but due to downscaling, the performance of MOS degrades. For robust design, it is very much required to downscale the MOS length keeping the performance of MOSFET intact. The multigate MOS model has been introduced for keeping the MOS performance intact as well as reducing the channel length. In this paper, the comparison of 6-T single bit SRAM cell has been done using single-gate MOS and double-gate MOS in terms of power using CMOS technology and 90-nm channel length in SYMICA environment. SYMICA is an electronic design automation (EDA) tool for the analog and mixed-signal integrated circuit design. In this paper, we have simulated CMOS and DGMOS SRAM cell and compare the power dissipation of DGMOS SRAM cell and CMOS SRAM cell. It proves that the dynamic power consumption of DGMOS SRAM cell is much smaller than CMOS SRAM cell for a particular input voltage and channel length.

**Keywords** SRAM · DGMOS · CMOS · Power dissipation

## 1 Introduction

Static random access memory (SRAM) cells are bistable circuits to hold data bit. A low-power SRAM cell has been designed by two inverters connected back to back. Here, we use CMOS inverter with low-power dissipation for designing SRAM

---

\*No academic titles or descriptions of academic positions should be included in the addresses.

---

S. Das (Roy) (✉) · S. Panda · G. Chakraborty  
Department of ECE, Narula Institute of Technology, Kolkata, India  
e-mail: [roysrabani.roy@gmail.com](mailto:roysrabani.roy@gmail.com)

S. Panda  
e-mail: [saradindupanda@gmail.com](mailto:saradindupanda@gmail.com)

G. Chakraborty  
e-mail: [gouravchakraborty7@gmail.com](mailto:gouravchakraborty7@gmail.com)

© Springer Nature Singapore Pte Ltd. 2020  
K. Maharatna et al. (eds.), *Computational Advancement in Communication Circuits and Systems*, Lecture Notes in Electrical Engineering 575,  
[https://doi.org/10.1007/978-981-13-8687-9\\_25](https://doi.org/10.1007/978-981-13-8687-9_25)



cell. In this paper, we have designed and simulated circuit of CMOS static random access memory cell using 90 nm channel length for double-gate MOS as well as single-gate MOS using SYMICA tools. For double-gate MOS, we have used 90nm\_bulk.pm model file keeping GEOMOD = 0, and for single-gate MOS, we have used 90nm\_bulk model file. The purpose of this paper is to reduce power dissipation, reducing leakage current, short-channel effects, etc., by using double-gate MOSFET in place of conventional CMOS.

## 2 SRAM Cell

Static random access memory is used to store single-bit binary information. The 6-T SRAM cell is used in IC industry due to its lower static power dissipation and better noise margin. A typical 6-T SRAM cell is shown in Fig. 1. It consists of two cross-coupled inverters latch and two access transistors. The gate terminal of access transistors is connected to the word line, and the source terminal is connected to bit and bit bar line. For reading and writing operation, the access transistor must be switched on.

For designing CMOS SRAM cell,  $W/L$  ratio is a very important factor. The  $W/L$  ratio should be as such as the data read operation should never destroy the stored information. Here, we use  $W/L$  ratio = 1.

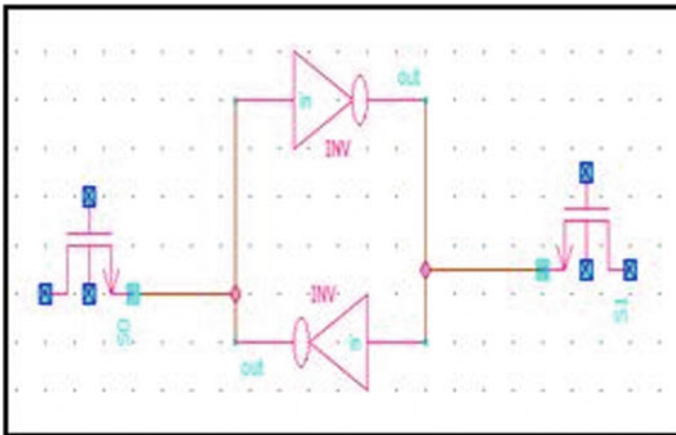


Fig. 1 Simple SRAM cell

### 3 6-T SRAM Bit Cell (1 Bit) Using CMOS and DGMOS

As we know, the requirement of MOS downscaling is essential for the current industry, for the fabrication of much more transistors in a single wafer, but the limitations arise due to downscaling of MOSFET. Due to downscaling of MOSFET, the operational performance of device degrades like leakage-current effects and short-channel effects. But still, we need lower power dissipation and nanoscale technology to get the multiple features and to fabricate much more transistor in a single substrate. So to get rid of the short-channel effects or leakage current effects due to downscaling, the alternate method is multigate MOS. In this paper, we compare the power consumption of a single-bit 6-T SRAM (1 bit) cell with double-gate SRAM cell.

### 4 6-T SRAM Cell (1 Bit) Using CMOS

See Fig. 2.

### 5 Output

See Fig. 3.

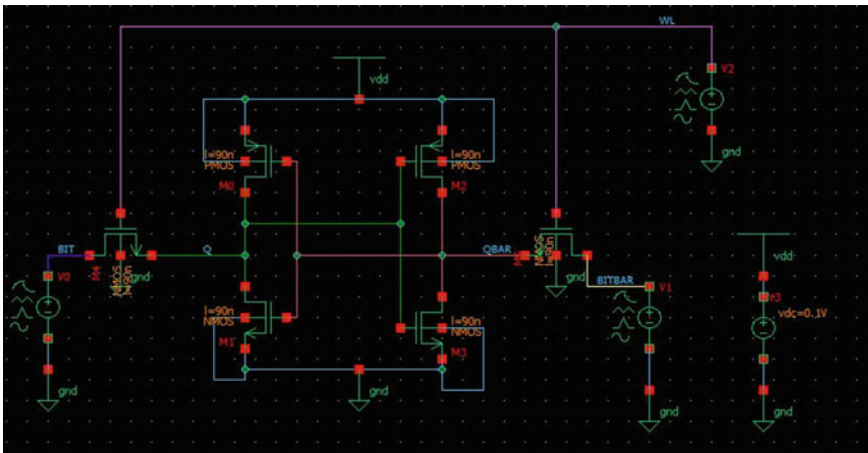


Fig. 2 Schematic CMOS-based SRAM (6-T) cell using 90nm\_bulk model

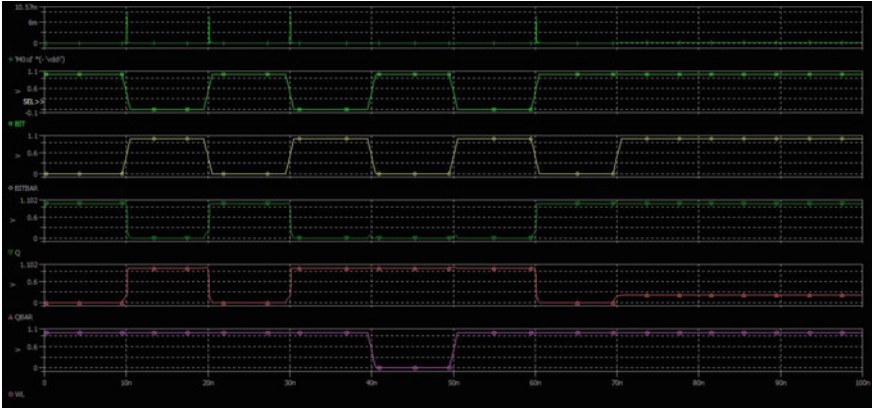


Fig. 3 Simulated output of CMOS SRAM at  $V_{dd} = 1\text{ V}$

## 6 SRAM 6-T Cell Using DGMOS

See Fig. 4.

## 7 Output

See Fig. 5.

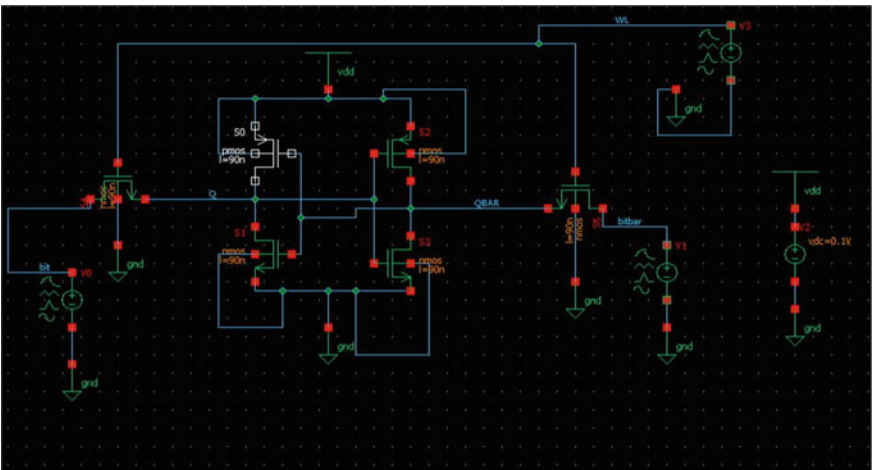


Fig. 4 Schematic diagram of 6-T SRAM cell using DGMOS, 90nm\_bulk.pm model

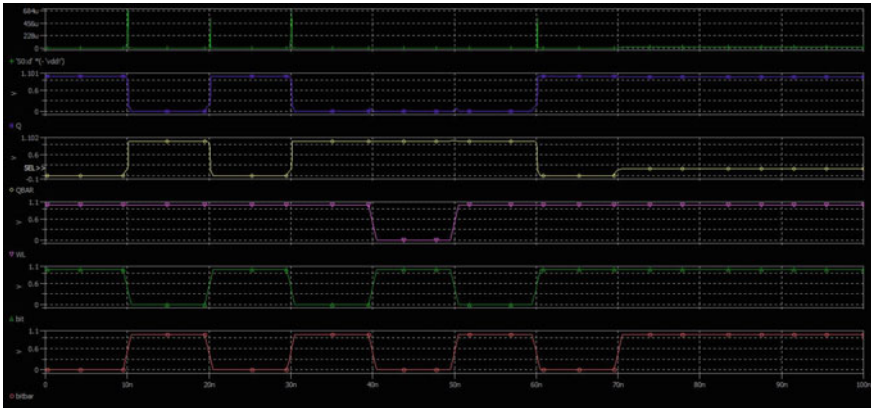


Fig. 5 Simulated output of DGMOS SRAM at  $V_{dd} = 1\text{ V}$

### 8 6-T SRAM Bit Cell (1 Bit) Using CMOS and DGMOS

Mainly, there are two categories of power dissipation: (i) static and (ii) dynamic [1]. The main factor of dynamic power dissipation is due to switching that is changing its state. The dynamic power can be expressed by  $P_{dynamic} = \alpha CV_{dd}^2 f_{sw}$ , where  $\alpha$  = activity factor,  $f_{sw}$  = input frequency.  $V_{dd}$  = supply voltage,  $C$  = load capacitance. And due to short-circuit current, power dissipation takes place and is expressed as  $P_{short\ circuit} = V_{dd}I$ . But when the circuit is not in active mode, the leakage current flows and causes static power dissipation of the circuit which depends on gate length and gate oxide thickness and power dissipation expressed as  $P_{static} = I_{leakage}V_{dd}$ . In this paper, we have analyzed and compared the dynamic power dissipation of SRAM cell (1 bit) using double-gate MOSFET and CMOS.

### 9 Table for Graph

See Table 1.

### 10 Output Graph

See Fig. 6.

**Table 1**  $V_{dd}$  versus dynamic power dissipation

$V_{dd}$ (V)	Dynamic power for DGMOS (mW)	Dynamic power for SGMOS (mW)
0.1	9.38768E-06	5.69603E-05
0.2	9.72753E-05	0.001181762
0.3	0.00230443	0.022902128
0.4	0.016820497	0.239294185
0.5	0.039115965	0.723723962
0.6	0.080600788	1.353213513
0.7	0.167282781	2.403804474
0.8	0.294862167	4.060642487
0.9	0.466860431	6.278648247
1	0.683410677	9.10619107
1.1	0.944319832	12.54729133
1.2	1.257119672	16.52033339
1.3	1.621762598	21.44729066
1.4	2.045193141	26.89849195
1.5	2.501662967	33.13390908
1.6	3.028602391	39.54835206
1.7	3.607399241	47.64512739
1.8	4.084557998	55.30589535
1.9	4.890399895	64.46302523
2	5.628401838	73.50371586

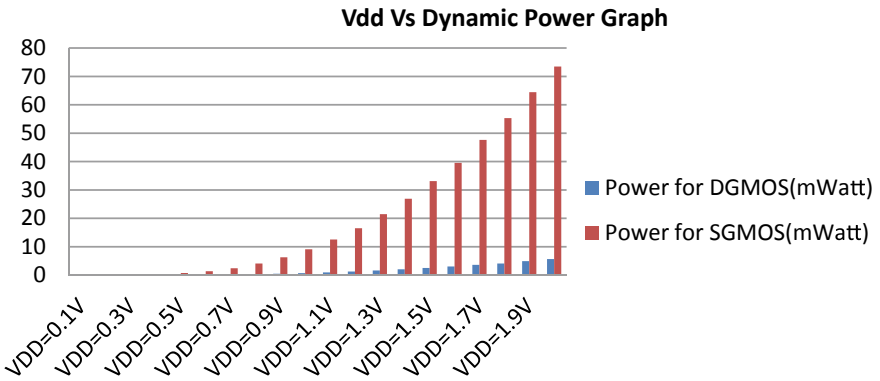


**Fig. 6**  $V_{dd}$  versus power bar graph for DGMOS and CMOS SRAM Cell

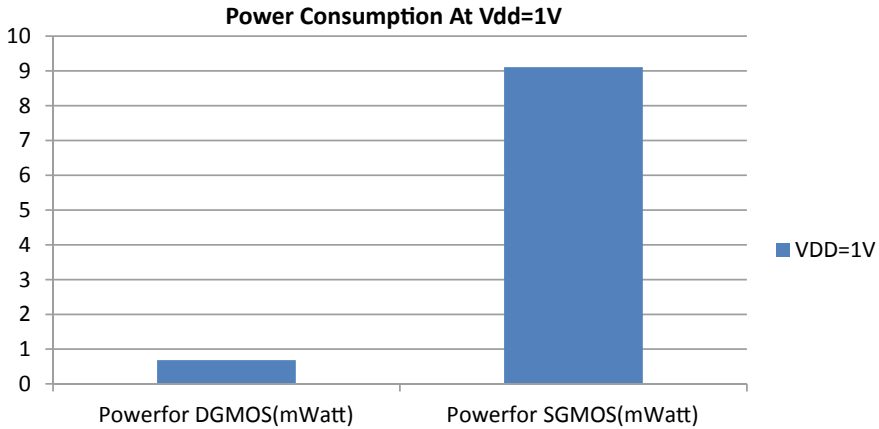


Fig. 7  $V_{dd}$  versus power bar graph for DGMOS and CMOS at  $V_{dd} = 1\text{ V}$

## 11 Output Graph

See Fig. 7.

## 12 Conclusion

It is clear from Graph 1 and Graph 2 that as  $V_{dd}$  increases power also increases, but the power consumption of 6-T SRAM cell using CMOS technology is much higher than the power consumption of 6-T SRAM cell using double-gate MOS technology. It is found from Graph 2 that at  $V_{dd} = 1\text{ V}$ , the power consumed by CMOS SRAM cell is 9.106 mW, whereas power consumed by DGMOS SRAM cell is 0.683 mW.

## References

1. R. Gatkal, G. Mali, Low power CMOS inverter in nanometer technology, in *International Conference on Communication and Signal Processing*, April 6–8, 2016, India, November 19 (2013)
2. K. Kuhn et al., Managing process variation in Intel's 45 nm CMOS Technology. *Intel Technol.* **12**(2), 92–110 (2008)
3. K. Bernstein, D.J. Frank, A.E. Gattiker, W. Haensch, B.L. Ji, S.R. Nassif, E.J. Nowak, D.J. Pearson, N.J. Rohrer, High-performance CMOS variability in the 65-nm regime and beyond. *IBM J. Res. Dev.* **50**(4.5), 433–449 (2006)
4. A. Islam, M. Hasan, T. Iqbal, M.A. Kafeel, Variability analysis of MTJ-based circuit, in *IEEE 3rd International Conference on Computer and Communication Technology (ICCCT)*, pp. 57–62 (2012)

5. S.G. Alie, T.A. Chandel, J.R. Dar, Power and delay optimized edge triggered D flip-flops for low power microcontroller. *Int. J. Sci. Res. Publ.* 4(5) (2014)
6. Q. Wang, S. Vrudhula, Static power optimization of deep sub-micron CMOS circuits for dual VT technology

# Low-Power FPGA-Based Hardware Implementation of Reversible Watermarking Scheme for Medical Image



Poulami Jana and Amit Phadikar

**Abstract** The data security and authenticity with good image quality are very much important in medical imaging applications. The goal of hardware-based watermarking techniques is to achieve low power consumption, real-time performance, reliability, and ease of integration with the existing consumer electronic devices. In this paper, the hardware architecture of reversible watermarking for medical images and its implementation in field-programmable gate array (FPGA) is proposed. The difference expansion (DE) method for watermarking in lifting-based DWT domain and channel coding is implemented in hardware to achieve the goal. The simulation result shows that the designed architecture consumes 44.66% less power and 44.67% higher operating frequency (operating speed) than the similar implementation.

**Keywords** Reversible watermarking · Lifting-based DWT · VLSI · FPGA

## 1 Introduction

In recent days, digital watermarking becomes very much essential and powerful tool for data security. The adding of the watermark usually introduces distortion, although it may be quite small. For some applications like medical imaging, the irreversible degradation of the original data is not permitted. In this field, the reversibility of the watermarking technique is significant. A good number of reversible watermarking algorithms found in the literature are implemented in the spatial domain [1] or in the transform domain [2]. Among those entire techniques, the transform domain algorithms are more robust and secured compared to the spatial domain but they

---

P. Jana

Department of Electronics and Communication Engineering, Maulana Abul Kalam Azad University of Technology, Kolkata, India  
e-mail: [poulami.mtech@gmail.com](mailto:poulami.mtech@gmail.com)

A. Phadikar (✉)

Department of Information Technology, MCKV Institute of Engineering, Liluah, India  
e-mail: [amitphadikar@rediffmail.com](mailto:amitphadikar@rediffmail.com)

© Springer Nature Singapore Pte Ltd. 2020

K. Maharatna et al. (eds.), *Computational Advancement in Communication Circuits and Systems*, Lecture Notes in Electrical Engineering 575,  
[https://doi.org/10.1007/978-981-13-8687-9\\_26](https://doi.org/10.1007/978-981-13-8687-9_26)

287



are complex in nature. Moreover, maximum data hiding techniques found in the literature are implemented in software.

Some undeniable reasons like less area, low execution time, low power, real-time performance, high reliability, and also ease of integration with the existing consumer electronic devices motivate researchers to move toward hardware implementation of watermarking algorithms. Over the past decade, numerous efforts have been made to develop a hardware system for security and copyright protection of image and video signals. The merits of hardware implementation are defined on the parameters like power consumption, operating speed, and compactness of the design. Hardware designs may be synthesized in the platforms like ‘custom integrated circuit’ (IC) [3], ‘tri-media processor board’ [4], or ‘field-programmable gate array’ [5]. With the advent of ‘very-large-scale integration’ (VLSI), the high-speed hardware in the form of ‘field-programmable gate array’ (FPGA) has made the transform domain watermarking techniques feasible for real-time implementation.

An FPGA architecture is proposed by Maity and Maity [5], using modified reversible contrast mapping (RCM) algorithm that achieves an operating frequency of 95.3 MHz. Shete et al. [6] proposed an FPGA architecture for steganography, using ‘least significant bit’ (LSB) technique in the DWT domain. The scheme achieved the maximum frequency of 183.756 MHz. Das et al. [7] proposed a VLSI architecture to implement ‘difference expansion’ (DE)-based watermarking scheme for an image block of  $(8 \times 8)$ . The authors demand that the scheme consumes 150 mW power on an average while operating at a frequency of 150 MHz. Hazra et al. [8] implemented a reversible watermarking algorithm by ‘histogram bin shifting’ (HBS) in FPGA. The watermarking encoder module and decoder module operate at a maximum frequency of 445.330 and 201.824 MHz, respectively, and consume 1.215 and 0.104 W of power, respectively. Ghosh et al. [9] proposed a VLSI implementation of ‘spread spectrum’ image watermarking in the transform domain. Xilinx 14.1, Virtex 4 XC4v1x200-11ff1513, is used to get a max frequency of 90.131 MHz. Darji et al. [10] proposed a watermarking architecture with and without pipeline which is synthesized using Xilinx’s integrated synthesis environment (ISE) for FPGA and also in a semi-custom integrated chip using UMC 0.18  $\mu\text{m}$  technology standard cell library.

Most of the reversible watermarking schemes which are found in the literature are in the spatial domain for avoiding the complex hardware design. Our aim is to design the hardware architecture of the reversible watermarking scheme based on our previous work [2] and implemented in FPGA. Lifting-based DWT offers some advantages while design in hardware. The optimized hardware design is done using Xilinx FPGA (Spartan-6 device family XC6SLX75-2FGG676). The main objective is to design an optimized VLSI architecture for the encoder to achieve multifarious intent.

The main contributions of the proposed method are summarized as follows:

- *Minimal resource utilization*: Efficient architectural design and advanced Xilinx Synthesis Technology (XST) synthesis tool stimulate minimal resource utilization. Encoding for a cover image of size  $(256 \times 256)$  requires 998 number of slices, 464 number of slice registers, and 76 bonded input/output buffers (IOBs).

- *Very low power consumption:* The power requirement is calculated using Xilinx XPower analyzer. According to this analysis, the proposed encoder consumes 57 mW power for an image size (256 × 256).

The rest of the paper is organized as follows: Sect. 2 describes the scheme which is chosen for hardware implementation, while in Sect. 3, the proposed hardware data path of the scheme is presented. In Sect. 4, the performance evaluation of the encoder is demonstrated. Finally, conclusions are drawn in Sect. 5 along with the scope of the future work.

## 2 Reversible Algorithm

This scheme describes the watermarking scheme which is selected for the hardware implementation. The algorithm is chosen as it is fully reversible and also very robust [2]. In this reversible watermarking algorithm, a binary watermark (encoded patient record) is embedded in the lifting-based DWT domain and extracted in the receiver side using the reverse process.

### 2.1 Image Encoding

The encoding block diagram is shown in Fig. 1. The host image is partitioned by lifting-based DWT. A binary watermark is permuted by a user defining a secret key and encoded by convolution coding. Convolution coding is done to increase the robustness of the scheme. Then, the coded watermark is embedded using Algorithm 1.

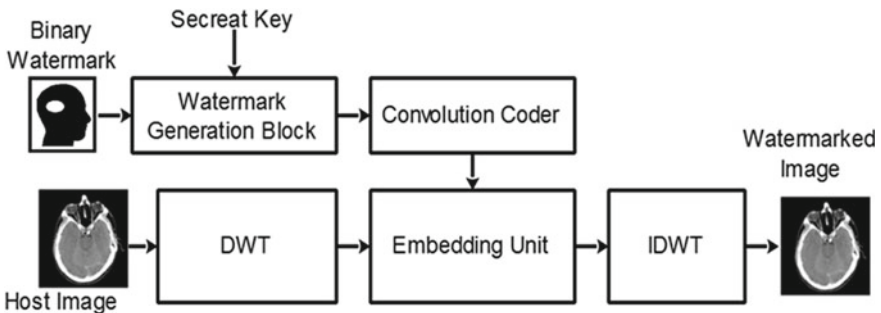


Fig. 1 Watermark embedding

**Algorithm 1** Image Encoding Process.**Inputs:** Watermark ( $w$ ), Key ( $k$ ), Image Pixel ( $P_x$ )

1. Calculate Permuted Watermark:  $[(w') = w \oplus k]$ .
3. Apply channel coding on the permuted watermark bits  $w'$  and get coded watermark bits ( $w_c$ ).
2. Calculate lifting based 2-D DWT on image pixel ( $P_x$ ) to get the coefficients.
3. Select coefficients from LH and HL sub-band.
4. Calculate average ( $l$ ) and difference ( $d$ ) of a coefficient pair  $c_1$  and  $c_2$ .

$$\left[ l = \frac{c_1 + c_2}{2} \right]; \quad \left[ d = \frac{\text{mod}(c_1 - c_2)}{2} \right].$$

5. Embed the coded watermark bit in the difference value ( $d$ ). The new difference value is ( $d'$ ).

$$[d' = 2d + w_c].$$

6. Calculate the watermarked coefficient pair from the watermarked difference ( $d'$ ) and the average value ( $l$ ).

$$\left[ c'_1 = l + \frac{d' + 1}{2} \right]; \quad \left[ c'_2 = l - \frac{d'}{2} \right].$$

7. Compute lifting based 2D-Inverse DWT.

**Output:** Watermarked Pixels ( $P'_x$ ).

## 2.2 Image Decoding

The block diagram representation of the decoder is depicted in Fig. 2. In the decoder unit, the lifting-based DWT is applied to the received watermarked image. The original host image is restored, and the original binary watermark is extracted by Algorithm 2.

**Algorithm 2** Image Decoding Process.**Inputs:** Watermarked Pixels ( $P'_x$ ), Key ( $k$ )

1. Calculate lifting based 2-D DWT on watermarked image pixel ( $P'_x$ ) to get lifting coefficients.

- Calculate average ( $l$ ) and difference ( $d$ ) of the watermarked coefficient pair  $c'_1$  and  $c'_2$  from LH and HL sub-bands.

$$\left[ l = \frac{c'_1 + c'_2}{2} \right]; \quad \left[ d = \frac{\text{mod}(c'_1 - c'_2)}{2} \right].$$

- Calculate the original difference value ( $d$ ):  $\left[ d = \left\lfloor \frac{d'}{2} \right\rfloor \right]$ .
- Extract the coded watermark bit ( $w_c$ ):  $\left[ w_c = 2d - d' \right]$ .
- Calculate the recovered coefficient pair from the difference ( $d$ ) and average value ( $l$ ).

$$\left[ c_1 = l + \left\lfloor \frac{d+1}{2} \right\rfloor \right]; \quad \left[ c_2 = l - \left( \frac{d'}{2} \right) \right].$$

- Compute 2D-Inverse Integer Wavelet Transform.
- Apply viterbi decoding on the extracted watermark bits ( $w_c$ ) and get back ( $w'$ ).
- Recover the original binary watermark  $w$  by the secret key:  $\left[ w = w' \oplus k \right]$ .

**Outputs:** Retrieved Image pixel ( $P_x$ ), Extracted watermark ( $w$ ).

### 3 The Proposed VLSI Data Path

The data path of the proposed DWT (lifting)-based encoder for the medical image is elaborated in this section. A reversible encoder of the proposed scheme is designed using ‘Very-High-Speed-Integrated-Circuit-Hardware-Description-Language’ (VHDL) and implemented in Xilinx Zynq (XC7Z020-

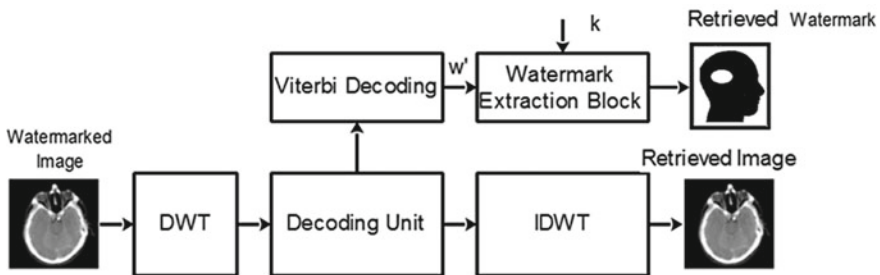


Fig. 2 Watermark decoding

CLG484-1) FPGA. The new power-efficient architecture is constructed by configuring different modules separately. The encoder architecture is constructed in a symmetric fashion. The proposed encoder module consists of ‘Image\_RAM,’ lifting-based ‘DWT-256’ and ‘IDWT-256,’ ‘convolution encoder,’ ‘watermark permutation,’ ‘watermark embedding unit,’ and a finite-state machine (FSM)-based ‘control unit.’ All the individual hardware components are designed, tested, and optimized separately before integrating together to perform the embedding operation.

### 3.1 Watermark Encoder

The encoding algorithm is applied to different host images of size  $(256 \times 256)$  for the prototype implementation. Figure 3 describes the data path for watermark encoder.

The prototype design of the encoder considers the preloaded  $(N \times N)$  image pixels in ‘Image\_RAM.’ The user can interface an external input bus with Image\_RAM for the real-time implementation. Watermark and random key are the inputs to the encoder. Lifting-based two-dimensional DWT is performed on each  $(256 \times 256)$  sized image block. The output DWT coefficients are then stored back into the ‘Image\_RAM.’ Depending on ‘Algorithm 1,’ the selected coefficient of ‘Image\_RAM’ is modulated by a convolution-coded watermark ( $w_c$ ).

The detailed encoding process is described below:

- **Step 1:** The image pixels are stored in the ‘Image\_RAM.’
- **Step 2:** The ‘DWT\_256’ hardware unit applies lifting-based DWT on the output pixel values from the RAM.
- **Step 3:** The binary watermark is permuted by the user defining the binary key ( $k$ ).
- **Step 4:** In the embedding unit, one bit of watermark is embedded within the difference value of one coefficient pair using the algorithm depicted in Sect. 2.1.

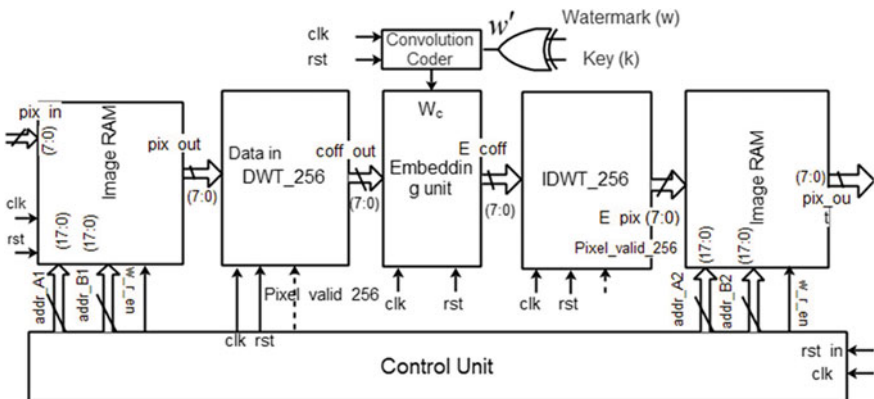


Fig. 3 VLSI data path for the encoder

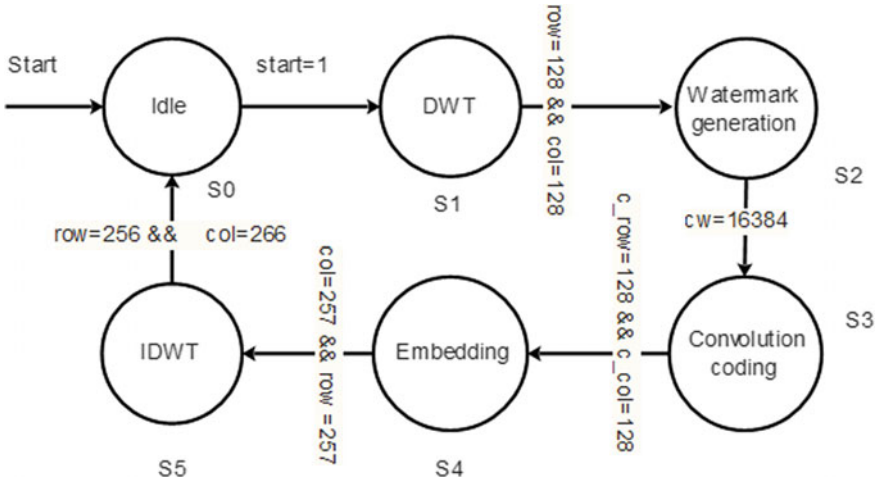


Fig. 4 VLSI data path for the encoder control states

One pair of watermarked coefficient value is calculated from the difference and average values of that pair of coefficients.

- **Step 5:** The 'IDWT\_256' unit converts the watermarked coefficients to watermarked pixels which are stored in the 'Image\_RAM.'

The VLSI 'control unit' generates genuine timing and control sequence for the smooth completion of the encoding process. This is maintained by designing the 'control unit' based on a finite-state machine (FSM). Figure 4 represents the FSM control states for the encoder. The FSM flow of control signals for encoding operation is performed by five distinct steps, i.e., 'S0' to 'S5'.

The 'Start' signal initiates the encoding operation. The state 'S1' calculates the DWT and accumulates the coefficients in 'Image\_RAM.' Then, the watermark generation is done in 'S2' and the convolution coding is done in state 'S3'. The coded watermark is embedded in the DWT coefficients at 'S4'. The 'S5' state enables IDWT operation with the activation of IDWT block. The state 'S5' verifies all conditions and computes IDWT. After the completion of the IDWT, the 'program control' (PC) moves to 'S0', i.e., the idle state.

#### 4 Hardware Realization: Results and Discussion

The implementation and synthesis of the above hardware architecture are done in 'Xilinx Zynq XC7Z020-CLG484-1 FPGA board.' 'Xilinx ISE 14.5' synthesis tool is assigned to fabricate the utilization of logic and performance outline of the encoder. Some of the test images are shown in Fig. 5.

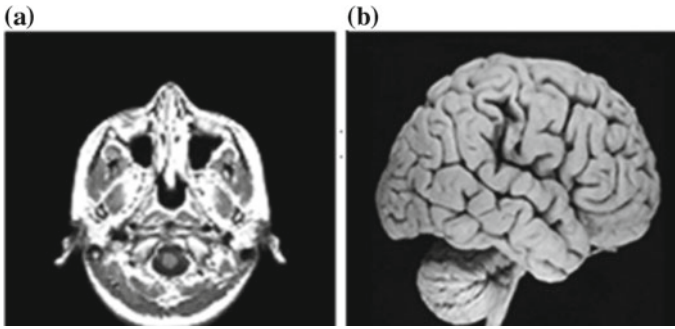


**Fig. 5** Test images: **a** brain and **b** MRI

**Table 1** Resource utilization table of an encoder for image size  $(256 \times 256)$  and comparison with the similar work

Serial No.	Parameters	Encoder	Encoder
		The proposed architecture	Maity and Maity [11]
1	Target board details	Xilinx Zynq (XC7Z020-CLG484-1)	Xilinx Spartan-3E XC3S1600E-4FG320
2	Image size	$(256 \times 256)$	$(32 \times 32)$
3	Number of slice LUTs	998	11,291
4	Number of slice registers	464	9347
5	Number of fully used LUTs	198	9881
6	Bonded IOBs	76	NA
5	Number of block RAM	1	3
7	Number of DSP 48E1 s	9	NA

The logic utilization and performance summary of different units are depicted in Table 1. The result proves that the resource utilization of the proposed scheme is lesser for bigger image size compared to the related work [11]. The results in Table 2 depict the power utilization and frequency comparison of different schemes found in the literature with the proposed hardware architecture for the encoder. The estimation of power consumption is done using ‘Xilinx XPower analyzer’ (XPA). The results of power consumption summary are given in Table 2. The total analyzed power is 57 mW for the encoder module by the power-aware design. It is seen that the proposed design consumes 95.30% less power than [8], 62% less power than [7], and 44.66% less power than [10]. The power consumption results (Table 2) and resource utilization results (Table 1) depict that the methodology is better than the peers. Table 3 gives various data hiding hardware from the current literature.

**Table 2** Power comparison

Schemes	Working domain	Total power (mW)	Clock (MHz)	Percentage of extra power with respect to the proposed scheme
Hazra et al. [8]	Spatial	1215	454.33	95.30%
Das et al. [7]	Spatial	150	150	62%
Darji et al. [10]	DWT	103	87.82	44.66%
Phadikar et al. [12]	IWT	65.20	11302	12.57%
The proposed scheme	IWT	57	127.05	NA

**Table 3** Data hiding hardware from the current literature

Related work	Working domain	Chip statistic
Phadikar et al. [12]	LWT	Xilinx Zynq XC7Z020-CLG484-1, 127.161 MHz
Gosh et al. [9]	Spatial	Xilinx Virtex 4 XC4vlx200-11ff1513, 90.131 MHz
Hazre et al. [8]	Spatial	Xilinx Virtex 7 (xc7vx485t-ffg1761-1), 201.824 MHz
Das et al. [7]	Spatial	Xilinx Zynq-7000 (xc7z030-3ffg676), 150 MHz
The proposed scheme	LWT	Xilinx Zynq XC7Z020-CLG484-1, 127.161 MHz

LWT Lifting-based DWT

## 5 Conclusions and Scope of the Future Work

This paper proposes the hardware architecture of reversible watermarking encoder which is suitable for medical imaging applications. The encoder hardware uses only 998 slice lookup tables (LUTs) and consumes the power of 57 mW while operating at a frequency of 127.05 MHz. The power consumption of the scheme is quite low compared to other methods found in the literature which makes it suitable for portable devices. The future work will be done by designing decoder architecture on FPGA for large size images such that the benefit of the low-power architecture can fit into the available consumer electronic gazettes in the market.

## References

1. N.H. Divecha, N.N. Jani, Reversible watermarking technique for medical images using fixed point pixel, in *Fifth International Conference on Communication Systems and Network Technologies*, vol. 1 (2015), pp. 725–730. <https://doi.org/10.1109/csnt.2015.287>



2. A. Phadikar, P. Jana, B.S. Phadikar, G.K. Maity, Reversible watermarking using channel coding and lifting for cultural heritage and medical image. *Int. J. Inf. Comput. Secur.* **8**(1), 34–54 (2016). <https://doi.org/10.1504/IJICS.2016.075308>
3. S.P. Mohanty, N. Ranganathan, K. Balakrishnan, A dual voltage frequency VLSI chip for image watermarking in DCT domain. *IEEE Trans. Circuits Syst. II Express Briefs* **53**, 394–398 (2006). <https://doi.org/10.1109/TCSII.2006.870216>
4. M. Maes, T. Kalker, J.P. Linnartz, J. Talstra, F.G. Depovere, J. Haitsma, Digital watermarking for DVD video copy protection. *IEEE Signal Process. Mag.* **17**, 47–57 (2000). <https://doi.org/10.1109/79.879338>
5. H.K. Maity, S.P. Maity, FPGA implementation for modified RCM-RW on digital images. *J. Circ. Syst. Comput.* **26**(3), 1750044 (2017)
6. K.S. Shete, M. Patil, J.S. Chitode, Least significant bit and discrete wavelet transform algorithm realization for image steganography employing FPGA. *Int. J. Image Graph. Sig. Process. (IJIGSP)* **8**, 48–56 (2016). <https://doi.org/10.5815/ijigsp.2016.06.06>
7. S. Das, R. Maity, N.P. Maity, VLSI-based pipeline architecture for reversible image watermarking by difference expansion with high-level synthesis approach. *Circ. Syst. Signal Process.* **37**, 1575–1593 (2018). <https://doi.org/10.1007/s00034-017-0609-3>
8. S. Hazra, S. Ghosh, S. De, H. Rahaman, FPGA implementation of semi-fragile reversible watermarking by histogram bin shifting in real time. *J. Real-Time Image Proc.* **14**, 193–221 (2018). <https://doi.org/10.1007/s11554-017-0672-9>
9. S. Ghosh, S. Talapatra, J. Sharma, N. Chatterjee, H. Rahaman, S.P. Maity, Dual mode VLSI architecture for spread spectrum image watermarking using binary watermark. *Procedia Technol.* **6**, 784–791 (2012). <https://doi.org/10.1016/j.protcy.2012.10.095>
10. A.D. Darji, T.C. Lad, S.N. Merchant, A.N. Chandorkar, Watermarking hardware based on wavelet coefficients quantization method. *Circ. Syst. Signal Process.* **32**, 2559–2579 (2013). <https://doi.org/10.1007/s00034-013-9550-2>
11. H.K. Maity, S.P. Maity, FPGA implementation of reversible watermarking in digital images using reversible contrast mapping. *J. Syst. Softw.* **96**, 93–104 (2014). <https://doi.org/10.1016/j.jss.2014.05.079>
12. A. Phadikar, G.K. Maity, T.L. Chiu, H. Mandal, FPGA implementation of lifting-based data hiding scheme for efficient quality access control of images. *Circ. Syst. Signal Process.* **1**, 1–27 (2018). <https://doi.org/10.1007/s00034-018-0893-6>

# A New Approach Toward Invariant Shape Descriptor Tools for Shape Classification Through Morphological Analysis of Image



Soumen Santra and Surajit Mandal

**Abstract** The study of image classification is based on various aspects. One of the dimension-based image classifications is shape description technique. This region-based multidimensional descriptor acts as a morphometric tool for contour analysis of close convex images. However, in some cases, we may get same information from extrinsic structural feature components of different cluster-based regions as well as different hidden information from several intrinsic structural components of the same cluster region. At the same time, the problem becomes severe if the image undergoes homogeneous transformations, such as translation, rotation and shearing. Analyzing the image object using an invariant shape descriptor may alleviate such problems. In this paper, we introduce a new class of invariant shape descriptor tool known as circularity which works locally and globally throughout the image texture pattern. A comparative study on variant and invariant transformations which work on multiresolution, multilateral and multicluster image texture has also been discussed.

**Keywords** Shape classification · Invariant shape descriptor · Circularity · Geodesic transformation

## 1 Introduction

At the very initial learning stage of life, novices are taught about different types of geometrical shapes and structures; thus, they can identify different types of objects and recognize them by their structures based on shape [1]. So, it is necessary to know about different types of geometrical structures and how they differ from one

---

S. Santra

Department of Computer Application, Techno International New Town, Kolkata, India  
e-mail: [soumen70@gmail.com](mailto:soumen70@gmail.com)

S. Mandal (✉)

Department of Electronics and Communication Engineering, B.P. Poddar Institute of Management and Technology, Kolkata, India  
e-mail: [surajitmandal@yahoo.co.in](mailto:surajitmandal@yahoo.co.in)

© Springer Nature Singapore Pte Ltd. 2020

K. Maharatna et al. (eds.), *Computational Advancement in Communication Circuits and Systems*, Lecture Notes in Electrical Engineering 575,  
[https://doi.org/10.1007/978-981-13-8687-9\\_27](https://doi.org/10.1007/978-981-13-8687-9_27)

297

another. Images can be classified in terms of shape and size because the shape is defined by various feature contents based on two-dimensional region [2]. The region-based shape descriptor is one of the most significant factors in the field of shape classification. An image is separated from its background by the edges of various shapes which may be continuous or discrete in nature (Fig. 1).

A grayscale image may be considered as a two-dimensional matrix where each element or cell may have some intensity value in the range from 0 to 255. Based on these values, an image separates itself from its background through its edges [3–5]. The contents of the cells bounded by the edges appear as different shapes and signify a meaningful sense which gives an idea to the user's mind about the image. Based on these shapes, we can identify or classify an image through the structuring elements which may be a triangle, circle or rectangle. In most of the cases, these structuring elements combine with each other in some ratios and form various complex shapes. The circularity or boundary of shape also depends on these basic geometric figures. Even though a particular image rotates, translates or changes through deformations, some of the properties of the basic figures remain unaltered and the proportion of the constituent structuring elements in the deformed image always remains same like before.

Cluttered identifications are also possible using putative point matching feature, but it does not always work for all types of rotations, translations and deformations. In this communication, we propose a new approach which is a homogeneous transformation and unwavering in nature.

The field of image processing for medical diagnosis, robotics, aeronautics, administrative purpose, etc., depends upon computer vision and pattern analysis [6]. The

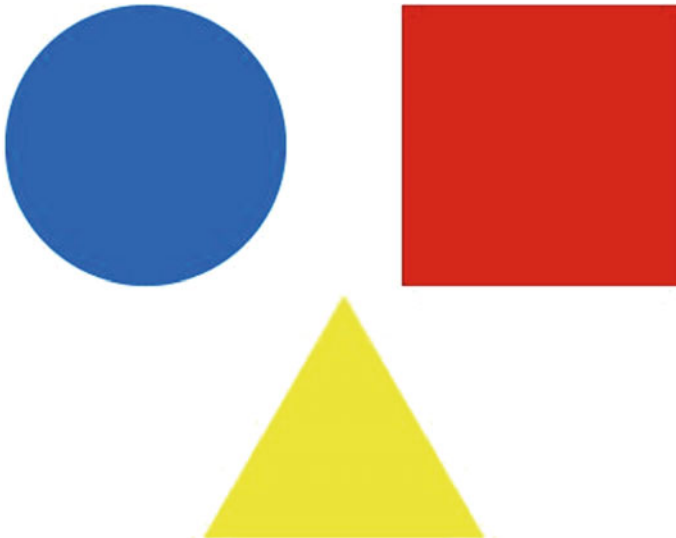


**Fig. 1** Basic geometric figures

technique for image analysis is always changing day by day and time to time where one technique overrides another to resolve the drawback of the previous one. Gonzalez et al. [1] described how to classify an image by using multiresolution pattern in the local region. A brief architecture of shape descriptor based on 2D and 3D perspective view was reported by Zhang et al. [2]. Dougherty et al. [3] proposed the idea of pattern spectrum in the noisy shapes of the image based on granulometries. Many other researchers studied morphological techniques for similar or dissimilar shape classification using many factors such as boundary, height function, common structure skeleton graph, etc., which explain image analysis [4, 5, 7, 8] in space domain. Using shape, we can identify unique images and also retrieve them by matching factor which was also shown by Guang et al. [9] for microstructure image objects. Maragos [6] explained the pattern spectrum and introduced it into the taxonomy form of shape concept through opening and closing filter for multilateral and multipattern images. In this communication, Sects. 2, 3, and 4 explain the concept of descriptor, shape descriptor and invariant shape descriptor of image, whereas Sect. 5 analyzes the results.

## 2 Descriptor of Image Object

It is a feature of the image by which we can describe the region of image contents. These descriptors are classified as four types on the basis of local and global spatial region.

### 2.1 *Color Descriptors*

**Dominant Color**—It is based on a color which plays a dominant role in the image.

**Color Layout**—It is essentially based on the primary color on block-by-block.

**Scalable Color**—It is essentially known as color histogram.

**Color Structure**—It is also known as local color histogram where color spaces make things interoperable.

### 2.2 *Texture Descriptors*

**Texture Browsing Descriptor**—This defines granularity/coarseness, regularity and direction.

**Homogeneous Texture Descriptor**—This is based on Gabor filter [10].

**Edge Histogram**—This is based on pixel continuity and defines the variation of edge.

### 2.3 *Shape Descriptors*

Region-based Descriptors—These are scalar attributes of shape under consideration such as area and eccentricities.

Semantic-based Descriptor—It is based on semantic region of image object.

Contour-based Descriptor—It captures the actual characteristic shape features and 3D descriptors.

### 2.4 *Motion Descriptors for Video*

Camera Motion (3D camera motion parameters)—It is based on motion trajectory (tracking of objects in the scene).

Parametric Motion—It allows the description of motion of the scene. But it can be a more complex model to be applied on various objects [10], e.g., motion vector.

## 3 **Shape Descriptor**

It is a tool by which we can predict and classify the shape or appearance of the image or the constituent of the image. Basically, we compare the shapes of the objects which are bounded by edges with shape of basic figures. These descriptors are classified as local and global descriptors where we mainly illustrate the local descriptor which is based on local spatial region. Local shape descriptor needs connecting edges where it meets uncertainty of spatial region and differentiates a shape from another one. When we classify the shapes for one or more structuring elements, then we can also define the nature of the shape. Based on this shape, we can identify the edge as well as segmentation of the image object. There are certain filters, such as opening and closing filters by which we can determine the structuring elements that are present in the image object. Using this technique, multilateral and multiregional shapes can easily be identified because sometime one or more regional shapes spread throughout the image object spatially. But when we change the object, i.e., image through homogeneous transformations (rotation, translation and shearing), the shape of the object will also change. As a result, its predictable shape also changes. This shape descriptor also cannot find out any discreteness in shape properly [11]. This thing creates shape discontinuity, and more than one type of basic shapes merge together to form holes or image crater blocks or bays. We can also describe shape properties by measuring the number or size of concavities in the shape [11]. For doing this, first we find the convex hull of the shape and then subtract it from the shape itself. We go on subtracting the convex hull from the difference for multiple times. Finally, holes (“lakes”) or concavities (“bays”) are formed [11]. This might



Fig. 2 Image bay or holes

be useful in distinguishing the letter “O” from “C”, etc., as shown in Fig. 2. The resulting structure is a concavity tree.

### 4 Invariant Shape Descriptor

Due to rotation, translation or any other transformation of image, the corresponding edge may change due to fragmentation, loosing of edges or occlusion. Most of the shape descriptors are bounded by planes, so if two points of the same shape region lie in different planes due to transformation, then they cannot be identified by the shape descriptor. So we need invariant shape descriptor to eradicate this problem. Putative point matching is one of the techniques of image analysis which is region-based, and it identifies the image object based on shape but does not work if we apply transformations on the image. But another shape descriptor tool is geodesic-based which works invariantly throughout any transformation. In Fig. 3, we have shown that variant shape descriptor also fails to detect object through matching shape for symmetric image object which is not true for invariant shape descriptor.

SOURCE IMAGE	OBJECT IMAGE	INLINE PLANE	OUTLINE PLANE	CROP OBJECT	REMARKS
					SUCCESSFULLY DETECTED
					SUCCESSFULLY NOT DETECTED

Fig. 3 Drawback of putative point matching method for object detection. It works on first image (brain image) but not for second image (hole image)

## 5 New Approach for Invariant Shape Descriptor: Circularity

Since all previously mentioned shape detectors fail to produce the desired output, we focus on invariant shape descriptor. Here, we consider circularity feature of the image as the invariant shape descriptor which means how a circular path can completely surround an object.

If circularity of the object  $< 1.2$ , then the object is a circle.

If circularity of the object  $< 1.53$ , then the object is a rectangle.

If circularity of the object  $< 1.35$ , then the object is a square.

Using this feature, we can predict which basic shapes form this image object and the difference of one object from another. It also helps us to create a class of the same types of object, and we can predict the types of image object.

## 6 Output and Analysis

Using Fig. 4, we can predict the classes of different datasets and identify their features because all different letters show different values but the same letters with different

















SET1	SET2	SET3	SET4
 Rectangle(1.398) Triangle(1.566)	 Rectangle(1.429) Triangle(1.86)	 Rectangle(1.284) Triangle(1.988)	 Rectangle(1.736) Triangle(1.788)
 Rectangle(1.35, 1.265) Triangle(1.539)	 Rectangle(1.42, 1.525) Triangle(1.62)	 Rectangle(1.436, 1.342) Triangle(1.681)	 Triangle(1.583, 1.598, 2.176)
 Rectangle(1.506, 1.293)	 Rectangle(1.453, 1.411)	 Rectangle(1.456, 1.229)	 Rectangle(1.367, 1.211)
 Rectangle(1.244)	 Rectangle(1.278)	 Rectangle(1.263)	 Rectangle(1.299)

Fig. 4 Circularity values of different datasets

transformations produce values which lie in a small range. This feature point of image morphological analysis is shape invariant in nature and one of the most significant shape descriptor tools. This technique may be considered superior over putative point feature which was explained earlier.

## 7 Conclusion

The most encouraging aspect of this technique is its evident capability to solve the various shape detection problems in spite of all the difficulties and adversities posed by real images and in spite of large numbers and great structural overlap of shapes (objects) to be distinguished. Invariant shape descriptor may find applications in multiple domains, and its utilization may further increase by adding more efficient algorithms. What we can do is to try in developing this code so that it can find minute objects with precision and their shapes. Some of the areas where it plays an important role are biomedical image processing, shape recognition, cartography, etc.

## References

1. E. Gonzalez, F. Bianconi, A. Fernandez, An investigation on the use of local multi-resolution pattern for image classification. *Inf. Sci.* (2016). (0020-0255, Elsevier)
2. D. Zhang, G. Lu, Review of shape representation and description techniques. *Pattern Recogn.* **37**, 1–19 (2004). <https://doi.org/10.1016/j.patcog.2003.07.008> (0031-3203)
3. E.R. Dougherty, Y. Cheng, Morphological pattern spectrum classification of noisy shapes: exterior granulometries. *Pattern Recogn.* **28**(1), 81–98 (1995). 0031-3203(94)00083-2
4. X. Yu, X. Lin, Y. Dai, K. Zhu, Image edge detection based tool condition monitoring with morphological component analysis, 0 019-0578/& ISA Published by Elsevier Ltd. (2017)
5. S. Loncaric, A survey of shape analysis techniques. *Pattern Recogn.* **31**(8), 983–1001 (1998). PII: S0031-2023(97)00122-2
6. P. Maragos, Pattern spectrum and multiscale shape representation. *IEEE Trans. Pattern Anal. Mach. Intell.* **11**(7) (1989) (0162-8828/89/0700-0701)
7. W. Shen, Y. Wang, X. Bai, H. Wang, L.J. Latecki, Shape clustering: common structure discovery. *Pattern Recogn.* **46**(2013), 539–550 (2012). (0031-3203, Elsevier Ltd.)
8. X. Wang, Z. Wang, A novel method for image retrieval based on structure elements' descriptor. *J. Vis. Commun. Image Represent.* **24**, 63–74 (2013) (1047-3203/2012, Elsevier Inc.)
9. G.-H. Liu, Z.-Y. Li, L. Zhang, Y. Xu, Image retrieval based on micro-structure descriptor. *Pattern Recogn.* **44**, 2123–2133 (2011). (0031-3203, Published by Elsevier Ltd.)
10. <https://dsp.stackexchange.com/questions/1433/list-of-possible-image-features-for-content-based-image-retrieval/1435>
11. <http://docplayer.net/27418028-Lecture-9-shape-description-regions.html>



# A Variable Delay Circuit to Develop Identical Rise/Fall Time in the Output



Pritam Bhattacharjee and Alak Majumder

**Abstract** Circuit designing of variable delay elements has been in practice for decades. However, these delay circuits have not been able to demonstrate equal rise and fall delays at its output. One of the major reasons for this failure is that the construction of delay circuits is non-symmetric. In this paper, we have attempted in designing a simple symmetric architecture which can produce the delayed output with almost identical rise and fall time. The proposed delay circuit is simulated using 90 nm GPDK in Cadence Virtuoso® initially for an input signal of 1 GHz at power supply  $V_{dd} = 1.1$  V, and the results infer that the contrast ( $\Delta$ ) in rise and fall time is very small even during the input variations.

**Keywords** Variable delay · CMOS · Low power · Rise delay · Fall delay

## 1 Introduction

In modern integrated circuits (ICs), the delay elements play a big role to build the clock networks which facilitate the proper and timely signal transmission in various parts of the IC. Fundamentally, the efficiency of delay element is judged by its capability to manipulate the symmetric rise and fall of the signal without disrupting signal logic level. In fact, the figure of merit of the delay elements is asserted by its operability in the higher-frequency zone. However, the use of variable delay elements (i.e., the delay element where the rise and fall of the signal can be varied) is quite popular in terms of designing application-specific ICs like digital/phase-locked loops (DLL/PLL) [1], switching mode DC/DC converters [2], digitally controlled oscillator

---

P. Bhattacharjee (✉) · A. Majumder  
Integrated Circuit and Systems (i-CAS) Lab, Department of Electronics and Communication Engineering, National Institute of Technology, Arunachal Pradesh, Yupia, District-Papumpare 791112, Arunachal Pradesh, India  
e-mail: [pritam\\_bhattacharjee@live.com](mailto:pritam_bhattacharjee@live.com)

A. Majumder  
e-mail: [majumder.alak@gmail.com](mailto:majumder.alak@gmail.com)

© Springer Nature Singapore Pte Ltd. 2020  
K. Maharatna et al. (eds.), *Computational Advancement in Communication Circuits and Systems*, Lecture Notes in Electrical Engineering 575,  
[https://doi.org/10.1007/978-981-13-8687-9\\_28](https://doi.org/10.1007/978-981-13-8687-9_28)

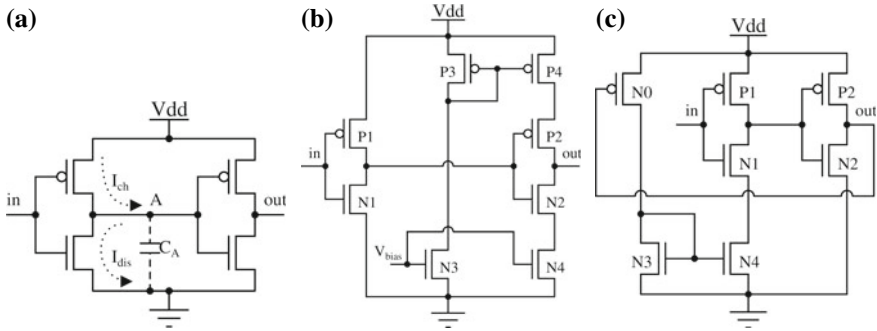


**Fig. 1** Conventional delay elements like **a** cascaded CMOS inverters, **b** current-starved cascaded CMOS inverter and **c** modified current mirror-based current-starved inverter

(DCO) [3], memory circuits [4], and many more. The change in the amount of delay in variable delay elements is usually regulated digitally (known as digitally controlled delay elements, viz. DC-DE) or by analog means. However, the digital approach is more secured and energy-efficient in compared to the analog-based delay elements [5]. Various architectures of DC-DE reported in [6–9] are mainly constructed on the basis of cascaded inverters (in the form of inverter chains), current-starved inverters, external RC elements, dynamic current mirrors, shunt capacitors, and variable resistors. Though these architectures successfully produce variable delay, they are not consistent in delivering equal rise and fall delays at the output in comparison with its input. Therefore, it is very difficult to utilize them for the purpose of clock management in modern ICs as they do not support the equal ON time and OFF time in the clock signal. Usually, the design of delay elements needs to follow up some basic characteristics like having a good tuning range of the delay values, consistency in the delay variability irrespective of the behavior of the input signal, maintaining the proper signal integrity between the input and the delayed signals, and most importantly, the power consumption should be in control.

The major problem with the conventional DC-DEs is in their constructions. The propagation delay ( $\tau$ ) of any circuit is proportionate to the charging and discharging current (i.e.,  $I_{ch}$  and  $I_{dis}$  shown in Fig. 1a) across its output (or the circuitual node ‘A’) and is denoted by  $\tau = \frac{C_A V_{out}(t)}{I}$  (where  $C_A$  is the average value of the capacitances at node ‘A’,  $V_{out}$  is the instantaneous voltage at the output (or at node ‘A’), and  $I$  is either  $I_{ch}$  or  $I_{dis}$  based on the steady state of the input signal). Therefore, the relevancy is that  $I_{ch}$  is equivalent to  $I_{dis}$  to have the equal rise and fall delays through the DC-DE.

In the cascaded CMOS (complementary metal-oxide semiconductor) inverter chain, both the values of  $I_{ch}$  and  $I_{dis}$  are anticipated depending on the individual saturation current in the PMOS and NMOS transistors, assimilating their average current ( $I_{av}$ ) to be  $I_{av} \approx \frac{\beta}{2} V_{dd}^2$ , where  $\beta$  insights the device-dependent factors of the transistors and  $V_{dd}$  corresponds to the power supply of the circuit [10]. The value of  $I_{av}$  relates to the notation of the propagation delay for low to high ( $t_{pLH}$ ) and high to low ( $t_{pHL}$ ) of the output transition in the CMOS inverter. Though the signal integrity

of the circuit is computed by  $I_{av}$ , the rise delay (time difference across 50% of the input and output rising edges) and fall delay (time difference across 50% of the input and output falling edges) strictly depend on the values of  $I_{ch}$  and  $I_{dis}$ , respectively. As the  $I_{ch}$  happens to be because of the pull-up section of CMOS and  $I_{dis}$  is due to the pull-down section, their matchup is a significant point of concern. Moreover, the power dissipation in the cascaded CMOS inverter is critical as the combined effect of the capacitive power, static power, and short-circuit power come into action, which is why this type of delay element is usually not preferred [11]. Another delay element which has been very popular in use is the current-starved cascaded inverter as shown in Fig. 1b. Its design architecture is nearly based on the cascaded CMOS inverters with some additional circuitry comprising transistors P3, P4, N3, and N4. The purpose of fitting P3 and N3 is to keep a control over the extra current from the power supply  $V_{dd}$  so that the delay time is longer. However, the current-limiting property of P4 and N4 also hampers the signal integrity (by blending in supply noise components) within the input and output of the delay element [12], and so the current-starved cascaded inverter is not preferred to be used in the applications where high-frequency operations are concerned. In this context, many designers have tried to incorporate external RC elements across these delay circuits [10] and found good result in terms of achieving noise-free signal transmission with appropriate delay time. But consequently, the approach brings in large power dissipation [13] and so the use of additional RC elements is rarely preferred. Even the designers introduced dynamic current mirror to the current-starved inverter in order to enhance the accuracy of P3 and N3 (of Fig. 1b). The design architecture of dynamic current mirror mentioned in [14] is an implicit modification of the previous version as shown in Fig. 1c. Here the current mirror is set by the NMOS transistors (N3 and N4 of Fig. 1c) instead of P3 and P4 (of Fig. 1b). This incorporation eliminates the direct connection with the  $V_{dd}$ , avoiding the supply noise components. However, the basic issue of this design is that it is unable to provide equal  $I_{ch}$  and  $I_{dis}$  as the weightage of the pull-up and pull-down sections is totally different which affects the individual rise and fall delays. The concept of shunt capacitor-based DC-DE mentioned in [6] is a good approach to resolve this issue, where depending on the values of shunt capacitors, the weightage of both the sections can be managed. But from the practical point of view, the feasibility of fabricating such capacitors is questionable whether it is more an option to fabricate variable resistors and use them by altering the region of operation of the metal-oxide semiconductor (MOS) transistors.

Therefore, in this article, we put in an architecture (comprising MOS capacitors and variable MOS resistor) which can produce a decent amount of symmetric rise and fall delays. Depending on the variability of the ON resistance of the MOS resistors, both the rise and fall delays can be tuned within a range. The construction of this article is in pursuit: In the second section, we talk about our architecture, discuss its operation, and perform the transient analysis of the proposed architecture for 90 nm GPDK [15] and 1 GHz input signal at  $V_{dd} = 1.1$  V in Cadence Virtuoso® platform. In the next section, the circuit performance is verified against the input variations in nominal process corner. Lastly, we conclude the presence of our proposed architecture as a good delay element.

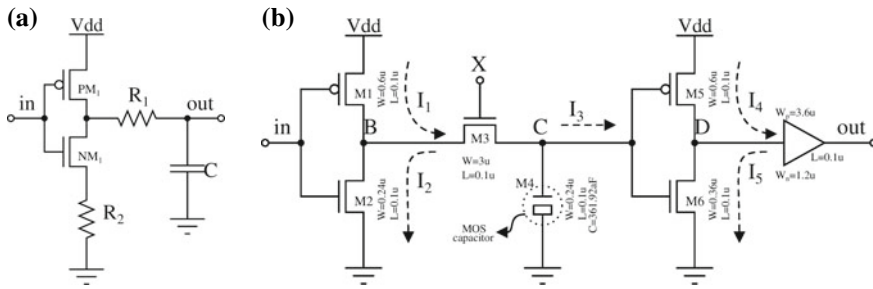


Fig. 2 a Different structure of CMOS inverter [16] and b modified version of Fig. 2a

## 2 Proposed Architecture

In the previous section, we have hinted on implementing MOS capacitor and resistor to build a delay element. This will be a simple modification over the cascaded CMOS inverter circuit incorporated with MOS-based internal RC elements. An approach is already reported by Mondal et al. in [16] where they have used normal RC element adjacent to the first inverter and across its pull-down section as shown in Fig. 2a.

The design has supported good amount of propagation delay while considering the value of  $R_2$  to be zero. But practically, the value of  $R_2$  can never be zero due to its dependency on process technology during physical design. This introduces technical issues in the logic ‘0’ level and in the slope of output fall. Therefore, in Fig. 2b, we have eliminated  $R_2$  and replaced  $R_1$  and  $C$  (of Fig. 2a) with NMOS-based resistor (M3 of Fig. 2b) and capacitor (M4 of Fig. 2b). Here, we have preferred NMOS over PMOS just to utilize its better carrier mobility during the signal transmission. The inverter comprising M5 and M6 is placed to complete the cascading and follow the input at the output. This cascaded CMOS inverter has its own intrinsic delay, addition to which more delay is contributed by M3 and M4. The beauty of the design is that the ON resistance ( $R_{ON}$ ) of M3 can be controlled externally through a control unit by regulating the gate voltage of M3 (marked here as ‘X’). The value of  $R_{ON}$  is inversely proportional to the difference in ‘X’ and the threshold voltage of M3. As the threshold voltage is set by the intrinsic properties and the physical dimensions of the MOS device, this difference is varied only due to the change in the value of ‘X’. The variability in  $R_{ON}$  composes separate circuit delay in each case as shown in Fig. 3a.

However, the rise delays seem to be almost constant though the fall delays are found to be changing for the different values of ‘X’. Looking back to the circuit, we understand that though the charging current ‘ $I_1$ ’ through M1 and the discharging current ‘ $I_2$ ’ through M2 are equal, the voltage at node ‘C’ is divided according to the different  $R_{ON}$  of M3 (i.e., fundamentally due to the potential divider principle [17]). The different voltage division (across the node ‘C’) due to the different values of ‘X’ changes the voltage level of logic ‘1’, whereas the maxima and minima of the voltage level in logic ‘0’ happen to be within the noise margin which is why

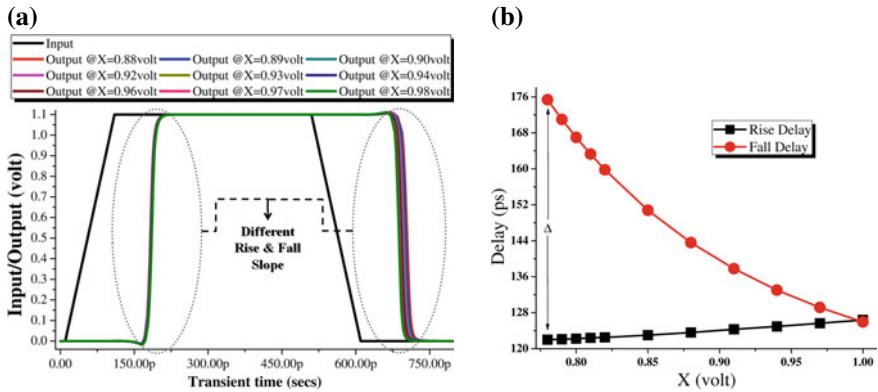


**Fig. 3** Simulation of Fig. 2b in 90 nm GPDK and  $V_{dd} = 1.1$  V, **a** transient response and **b** delta-plot

when the second inverter (made of M5 and M6) inverts the signal of node ‘C’, it is seen that there are multiple falling edges of the signal, and the rising edges have converged to a single unit. Consequently, we see in Fig. 3b that the difference in rise and fall delays (referred as delta—‘ $\Delta$ ’) reduces with the higher values of ‘X’ and get nullified at around ‘X’ = 1 V. But in practical scenario, adjusting the value of ‘X’ ~ 1 V is quite impossible (using any conventional biasing circuit) since the circuit’s  $V_{dd}$  is 1.1 V. Therefore, it may be very difficult to utilize this type of delay element for setting up variable near symmetric values of rise and fall delays.

In Fig. 4a, we improvised the delay element by adding another pair of MOS resistor and capacitor, viz. M7 and M8, respectively, at the end of second inverter. The second inverter has been structured such that the individual charging and discharging current, viz. ‘ $I_4$ ’ and ‘ $I_5$ ’, are equal. But as the input to the second inverter is from node ‘C’, where the logic ‘1’ is already having distinguished voltage levels (in accordance with different values of ‘X’), the inverted output at node ‘D’ will have both multiple rising and falling edges. However, this time, by virtue of potential divider principle, the voltage level at the node ‘E’ across  $R_{ON}$  of M7 will have more advantage in the rising edge (in terms of edge slope). The buffer at the end is therefore adjusted in such a manner that the output has both multiple rising and falling edges in the output (as shown in Fig. 4b) with the variation in ‘X’. In fact, the magnitude of  $\Delta$  in Fig. 4c is observed to be very small in contrast to the one seen in Fig. 3b, and the  $\Delta$  get nullified at around ‘X’ = 820 mV which can be generated by conventional or any newly designed biasing circuits. Moreover, the values of rise and fall delays found in Fig. 4c are comparatively larger than the delay values in Fig. 3b. Therefore, the proposed architecture in Fig. 4a can be considered as a favorable delay element.

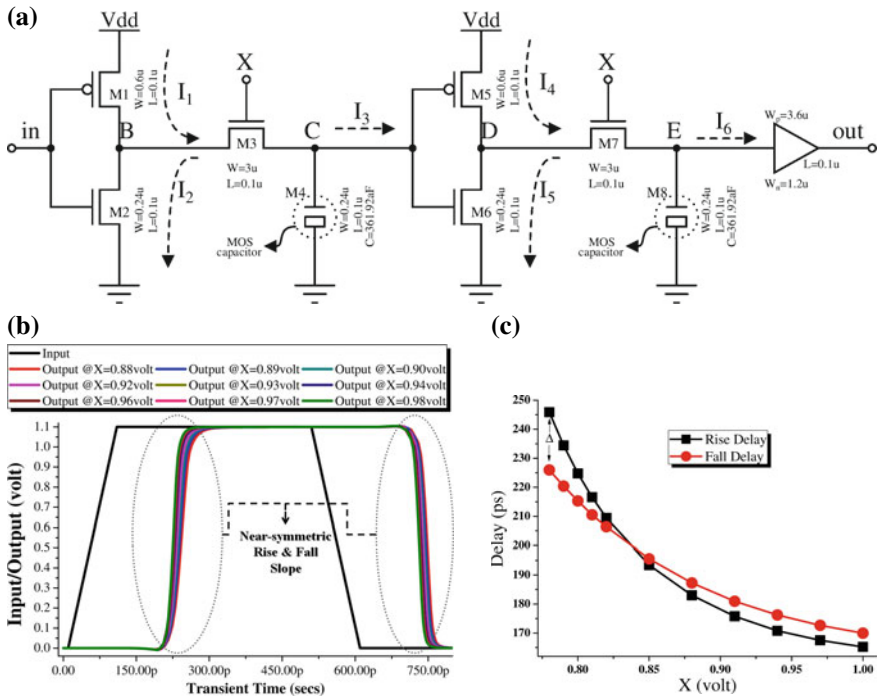


Fig. 4 Proposed delay element, a schematic, b transient response and c delta-plot

### 3 Performance Analysis of the Proposed Delay Element

In this section, we display the results obtained while testing the proposed delay element against parametric variation of the input signal. From previous discussions, we have learnt that most delay elements fail to function appropriately in high-frequency zone. So, the proposed delay circuit is tested for different frequency input signal in nominal process corner and room temperature (27 °C) as shown in Fig. 5a.

It is observed that the  $\Delta$  value increases with gradual rise in the input frequency. This happens mainly due to the steep drop in the value of fall delay, whereas the variation in rise delay is negligible. However, the magnitudes of  $\Delta$  are quite small and do not fluctuate much for the higher input frequencies. In Fig. 5b, we have observed the values of rise and fall delays of a 1 GHz input signal under nominal process corner for different operating temperatures. The magnitude of  $\Delta$  at lower temperatures is very small compared to its value in the high-temperature zone. Therefore, the proposed delay element can be asserted to be a reliable architecture producing near symmetric rise and fall delays.

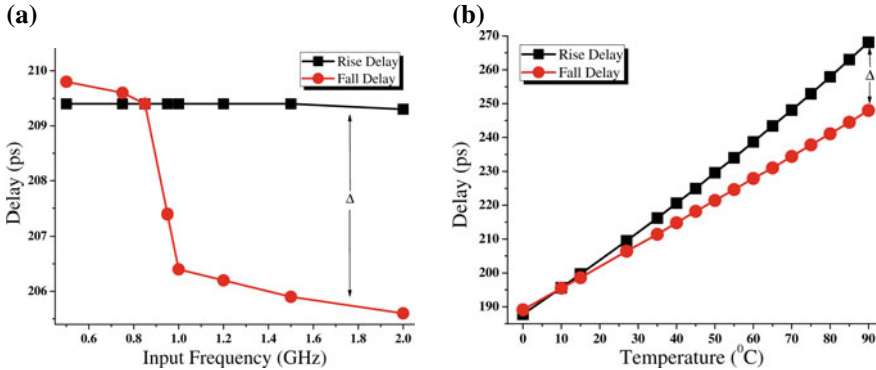


Fig. 5 Delta-plot as the function of **a** input frequency and **b** temperature

### 4 Conclusion

This paper has been dedicated to the development of a delay circuit that will produce nearly equal rise and fall delays. We have designed the delay circuit based on the cascaded inverter approach with few important tweaking like the inclusion of MOS-based internal RC elements. The delay element has successfully resulted in delivering variable delays and  $\Delta$  even in varied input conditions. However, it is realized that the operability of this delay element will be best possible if the MOS-based resistor is efficiently controlled using some programmable biasing circuit.

**Acknowledgements** This work has been supported by MeitY, Government of India, under their Visvesvaraya PhD Scheme and SMDP-C2SD project.

### References

1. M.G. Johnson, E.L. Hudson, A variable delay line PLL for CPU-coprocessor synchronization. *IEEE J. Solid-State Circ.* **23**(5), 1218–1223 (1988)
2. P. Gupta, A. Patra, Hybrid mode-switched controls of DC-DC boost converter circuits. *IEEE Trans. Circ. Syst. II Express Briefs* **52**(11), 734–738 (2005)
3. J.S. Chiang, K.Y. Chen, The design of an all-digital phase-locked loop with small DCO hardware and fast phase lock. *IEEE Trans. Circ. Syst. II: Analog Digit. Sig. Process.* **46**(7), 945–950 (1999)
4. H. Noda, M. Aoki, H. Tanaka, O. Nagashima, H. Aoki, An on-chip clock-adjusting circuit with sub-100-ps resolution for a high-speed DRAM interfaces. *IEEE Trans. Circ. Syst. II: Analog Digit. Signal Processing* **47**(8), 771–775 (2000)
5. E. Burlingame, R. Spencer An analog CMOS high-speed continuous-time FIR filter, in *Solid-State Circuits Conference, 2000, ESSCIRC'00, Proceedings of the 26rd European* (pp. 288–291). IEEE (2000, September)
6. P. Andreani, F. Bigongiari, R. Roncella, R. Saletti, P. Terreni, A digitally controlled shunt capacitor CMOS delay line. *Analog Integr. Circ. Sig. Process.* **18**(1), 89–96 (1999)

7. D.C. Ng, N. Wong, D.K. Kwong, A 0.9 V 2.7  $\mu$ W small-area 100  $\mu$ s + analog CMOS tunable-delay circuit utilizing Miller effect, in *IEEE International Conference on Electron Devices and Solid-State Circuits, 2008. EDSSC 2008*. (2008, December). pp. 1–4
8. M. Saint-Laurent, M. Swaminathan, in A digitally adjustable resistor for path delay characterization in high-frequency microprocessors, in *2001 Southwest Symposium on Mixed-Signal Design, 2001, SSMSD*. IEEE (2001), pp. 61–64
9. M. Maymandi-Nejad, M. Sachdev, A monotonic digitally controlled delay element. *IEEE J. Solid-State Circ.* **40**(11), 2212–2219 (2005)
10. J.M. Rabaey, A. Chandrakasan, B. Nikolic, *Digital Integrated Circuits: A Design perspective 2e Prentice-Hall* (Upper saddle River, NJ, 2002)
11. J.L. Yang, C.W. Chao, S.M. Lin Tunable delay element for low power VLSI circuit design, in *TENCON 2006. 2006 IEEE Region 10 Conference*. IEEE (2006, November), pp. 1–4
12. G. Kim, M.K. Kim, B.S. Chang, W. Kim, A low-voltage, low-power CMOS delay element. *IEEE J. Solid-State Circ.* **31**(7), 966–971 (1996)
13. A. Nabavi-Lishi, N.C. Rumin, Inverter models of CMOS gates for supply current and delay evaluation. *IEEE Trans. Comput. Aided Des. Integr. Circ. Syst.* **13**(10), 1271–1279 (1994)
14. S.B. Kobenge, H. Yang, A power efficient digitally programmable delay element for low power VLSI applications, in *1st Asia Symposium on Quality Electronic Design, 2009. ASQED 2009*. IEEE (2009, July), pp. 83–87
15. 90 nm General Process Design Kit -GPDK090, (n.d.). Bangalore: University Team of Cadence Design Systems. Retrieved from <https://support.cadence.com/>
16. J.A. Mondal, A. Majumder, B.K. Bhattacharyya, P. Chakraborty, A process aware delay circuit with reduce impact of input switching at GHz frequencies. *IEEE VLSI Circ. Syst. Lett.* **3**(2), 6–12 (2017)
17. R. Millar, T. King, Students' understanding of voltage in simple series electric circuits. *Int. J. Sci. Educ.* **15**(3), 339–349 (1993)



# Algorithms for Minimizing Bottleneck Crosstalk in Two-Layer Channel Routing



Tarak Nath Mandal, Ankita Dutta Banik, Kaushik Dey, Ranjan Mehera and Rajat Kumar Pal

**Abstract** Channel routing and crosstalk minimization are important issues while we talk about high-performance circuits for VLSI physical design automation. Interconnection among the net terminals satisfying constraints in an intelligent way is a necessity to realize a circuit in a minimum possible area, as this is a primary requirement to reduce cost as well as to increase yield. In this paper, along with area minimization, the performance of the computed circuits has also been enhanced by computing routing solutions with a specified amount of bottleneck crosstalk in two-layer channel routing. Usually, crosstalk is measured by the amount of overlapping of a pair of nets assigned to adjacent tracks. The crosstalk minimization problem in the reserved two-layer Manhattan channel routing model is NP-hard. Thus, in this paper, heuristic algorithms have been devised to optimize bottleneck crosstalk in order to augment circuit performance in two-layer channel routing. Experimental results obtained are highly encouraging.

**Keywords** Bottleneck crosstalk · Channel routing problem · Crosstalk minimization · Manhattan routing model · NP-hard · Two-layer routing

---

T. N. Mandal (✉) · A. D. Banik · K. Dey · R. K. Pal  
Department of Computer Science and Engineering, University of Calcutta, 700106 JD-2,  
Sector-III, Saltlake, Kolkata, India  
e-mail: [tarak.sap2016@gmail.com](mailto:tarak.sap2016@gmail.com)

A. D. Banik  
e-mail: [duttabanik.ankita@gmail.com](mailto:duttabanik.ankita@gmail.com)

K. Dey  
e-mail: [kaushikdey59@gmail.com](mailto:kaushikdey59@gmail.com)

R. K. Pal  
e-mail: [pal.rajatk@gmail.com](mailto:pal.rajatk@gmail.com)

R. Mehera  
Subex Inc., 12303 Airport Way, Suite 390, Broomfield, CO 80021, USA  
e-mail: [ranjan.mehera@gmail.com](mailto:ranjan.mehera@gmail.com)

# 1 Introduction

Channel routing is a well-defined, important problem in VLSI physical design automation [1, 2]. In this problem, it is required to realize a specified interconnection of a set of terminals present on the periphery of different modules on two opposite sides of a rectangle, primarily using minimum possible area. Incidentally, channel routing is one of the essential existing detailed routing strategies [2, 3].

A *channel* with two open ends, one on the left and one on the right, is a rectangular routing region. The *terminals*, rows of fixed points/pins, are located to the upper and lower sides of the rectangle. Along the length of the channel, the terminals are vertically aligned in *columns*. In general, the columns are spaced apart at equal distances. A *net* is a set of terminals which need to be electrically connected together. Figure 1 represents a *two-terminal net*, where the same terminal number appeared in the upper and lower sides of the rectangular area needs to be electrically connected to complete the routing process. In general, a channel contains multi-terminal nets as well. Non-terminals are represented using the numerical value zero and must be ignored during the routing process.

Rectilinear wiring comprises only *vertical* and *horizontal net segments*. Vertical and horizontal net segments are sets of wires which lie on columns and tracks, respectively. *Tracks* are parallel to the rows of fixed terminals and are usually spaced apart at equal distances.

A *route* for a net connects all the terminals of the net by using both horizontal and vertical net segments scattered across different layers. A *legal wiring or feasible routing solution* of a channel comprises a set of routes which ensures that net segments belonging to different nets do not overlap on the same conducting layer satisfying all well-defined requirements.

The *channel routing problem (CRP)* is modelled by using two  $m$  element vectors *TOP* and *BOTTOM*, and a number  $t$ ; the objective is to find legal wiring for the channel using no more than  $t$  tracks if one exists. Figure 1 shows an instance of CRP with assignments of net intervals limited to four tracks only. Let us define the *interval*

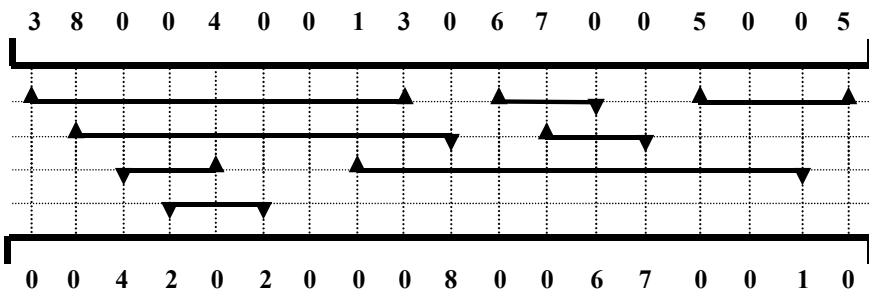


**Fig. 1** An example channel instance that comprises eight two-terminal nets. Arrows indicate the top or bottom terminals to be connected to complete all interconnections of the nets present in the channel

(or *span*) of net  $n_i$  as  $I_i = (L_i, R_i)$ , where  $L_i$  ( $R_i$ ) represents the leftmost (rightmost) column position of the net.

In this work, we have assumed the crosstalk minimization problem as an important high-performance issue. A significant advancement in fabrication technology helped in reducing the feature size and allowed the devices to be placed in close proximity while operating in higher frequencies. As a result, electrical hazards, viz. *crosstalk* between net segments, are evolved, which is proportional to the coupling capacitance that depends on the coupling length (i.e. the total length of overlap between the segments of two different nets). Crosstalk is also proportional to the frequency of operation and inversely proportional to the separating distance between wires. In our work, overlapping between a pair of segments of two different nets is ignored if these are assigned to non-adjacent tracks, as crosstalk is reduced drastically.

Crosstalk introduces signal delay and impacts circuit performance. Therefore, the intent of developing channel routing algorithms is to minimize the number of tracks along with crosstalk. VLSI circuit synthesis demands high performance [2, 4]; therefore, channel routing solution with reduced crosstalk has significant importance.

Thus, it is expected if a routing solution could be computed where the amount of some crosstalk is mostly reduced, which is an NP-complete problem [5]. However, it has been observed that even if some crosstalk is reduced, the performance of the solution may not be achieved due to long overlapping of a pair of nets assigned to adjacent tracks. Hence, a new problem, specifically the bottleneck crosstalk minimization, comes into the picture, which has also been proved to be NP-complete [5]. As a natural consequence, researchers are intended to devise heuristic algorithms or to employ some soft computing technique such that bottleneck crosstalk is taken care of. In this paper, several such experimentations have been performed in order to reduce bottleneck crosstalk in computing two-layer channel routing solutions to enhance the circuit performance.

The paper is organized as follows. Section 2 includes some basics relating to channel routing problem and crosstalk minimization. The problems are formulated in Sect. 3. Algorithms have been devised in Sect. 4. Section 5 comprises the experimental results along with necessary discussions. The paper is concluded in Sect. 6.

## 2 Preliminaries

The channel routing algorithms are developed based on a routing model under consideration. One such most practical and apposite model of routing that IC industries have accepted in designing and fabricating much of the VLSI chips is the grid-based reserved layer non-overlap Manhattan channel routing model [2, 3]. The concept of grid-based routing model has already been discussed in the introductory section. In the two-layer reserved layer routing model, one layer is reserved for horizontal net segments and the other layer is reserved for vertical net segments. Connections between two orthogonal net segments of the same net are achieved by a via, located at the junction point of the grid. This model is, of course, a non-overlap routing model,

as there is no issue of overlapping wire segments of two different nets (assigned to the same track) on adjacent layers. Finally, the Manhattan routing allows only rectilinear wiring for making the interconnections; wherein horizontal net segments are parallel to the two rows of fixed terminals and knock-knees are not allowed [1]. In no-dogleg routing, the horizontal segment of a net is assigned to a track only (and not split into two or more for their assignment to two or more tracks) in a routing solution.

Based on the specified routing model above, the CRP is characterized by two important constraints: horizontal constraints and vertical constraints [2, 3]. The *horizontal constraints* specify if a pair of horizontal segments of two different nets is assignable to the same track, and the *vertical constraints* indicate the assignment of net intervals to tracks along the height of the channel. The graphical representation of these two constraints depicts the *horizontal constraint graph (HCG)* and the *vertical constraint graph (VCG)*, respectively [2, 3]. Incidentally, the HCG is an interval graph, which is triangulated [6]. On the other hand, the VCG is an arbitrary directed graph. A maximum number of nets passing through a column (in a channel) are known as the *channel density*, which is same as the size of the clique in the HCG, and denoted as  $d_{\max}$  [2]. In contrast,  $v_{\max}$  is the length of the longest path in an acyclic VCG [2], and  $\max(d_{\max}, v_{\max})$  is a lower bound on the number of tracks in the above-mentioned two-layer channel routing model [2].

In devising channel routing algorithms, often we view horizontal constraints with the help of *horizontal non-constraint graph (HNCG)*, which is the complement of HCG. We may note that as an HCG is an interval graph, the corresponding HNCG is a comparability graph and the nets belonging to a clique in it can safely be assigned to a track to compute a routing solution [2, 6].

For a given routing solution, we model the crosstalk measure, as an amount of overlap between the horizontal segments placed on adjacent tracks belonging to two different nets. Horizontal crosstalk will be considered nil for non-overlapping intervals.

For any viable routing solution, the bottleneck crosstalk is modelled as the maximum amount of overlap between two horizontal segments belonging to two different nets and is adjacent to the height of the channel. Therefore, for a bottleneck crosstalk minimization problem, the major concern is to find whether a pair of nets (overlapping to each other) is assignable to two adjacent tracks. In other words, the problem of minimizing the bottleneck crosstalk can be restated as, for a given number of tracks find a feasible routing solution such that the maximum amount of crosstalk between a pair of (net) intervals stays within a bound.

In the next section, we briefly formulate the problems under consideration towards devising subsequent algorithms in Sect. 4.

### 3 Formulation of the Problems

#### 3.1 *Computation of Minimum Area Channel Routing Solutions*

The input to the CRP is a netlist that comprises the top vector and the bottom vector of a channel. There are some inherent constraints that have already been stated in the previous section. In this work, horizontal constraints are represented with the help of HNCG and vertical constraints with the help of VCG. Note that, to obtain a feasible routing solution for any two-layer channel routing model specified [2], the VCG needs to be acyclic.

Any channel instance without a vertical constraint guarantees to have a routing solution using density number of tracks [2, 7–9]. However, a general channel instance contains both the constraints that we are supposed to conform in devising any routing algorithm in a model under consideration towards achieving a routing solution.

Note that an HNCG is an undirected comparability graph that can be oriented based on the presence of the nets (or intervals) from left to right along the length of the channel. Here an edge connects a pair of vertices if the associated intervals do not overlap in the channel. Now, there are several factors involving a net in a channel that can be sequenced (in the form of weight tuples) based on some priority of assigning them to tracks [2, 10], or that can be assumed in combination as a single weight to each allied net. Next, the maximum weighted clique computation algorithm of a comparability graph [6] is employed to compute a set of most desirable nets for their assignment to a track under consideration [10]. However, if such nets in a clique are vertically constrained to each other, those cannot be assumed at a time (for their assignment to a track). To resolve this issue, we do the following.

It is very clear that each of the nets whose vertices are source vertices in the VCG is assignable in separation to the topmost track of the channel. However, they might have horizontal constraints among themselves. We may note that all the information relating to horizontal non-constraints are there in the HNCG. So, if possible, a maximum weighted clique in the HNCG is expected to be computed such that the corresponding nets (that comprise a non-overlapping set of intervals) would be considered for their assignment to the (current) topmost track.

Thus, in our formulation what we do, first we compute the set of source vertices from the VCG, then we extract the induced subgraph from the HNCG comprising the said set of source vertices, which are weighted based on some weight metric defined by us and acquired from the channel itself. Then we compute a maximum weighted clique from this induced HNCG (which is a comparability graph) such that the associated nets in the clique are safely assignable to the (current) topmost track.

Clearly, the algorithm is iterative in nature. In each iteration, a set of source vertices is selected for their assignment to the current topmost track. Then these are deleted from the VCG as well as the HNCG to start the next iteration, till all the

nets are assigned to tracks; vertical (net) segments are connected as needed to make the routing complete. Furthermore, the number of such iterations is the same as the number of tracks required for the channel under consideration. This is how probably a minimum area routing solution is computed wherein all the constraints of channel routing are complied with.

### 3.2 *Computation of Bottleneck Crosstalk Routing Solutions*

As some crosstalk minimization in two-layer VH channel routing for general channel instances by permutation of tracks of a feasible routing solution is an NP-hard problem [4, 5], eventually devising a heuristic algorithm may be an immediate choice [11, 12]. There are two heuristic algorithms: one is based on track permutation and the other is based on interchanging nets. A combination of these two may often work better, though in general track interchange is followed by net interchange, and the latter one is essentially greedy in nature.

For any two-layer VH feasible routing solution,  $S$  of  $t$  tracks, another feasible routing solution,  $S'$  with zero crosstalk can be computed by introducing  $t - 1$  blank tracks, where each blank track is introduced in between two adjacent tracks in  $S$ . However,  $S'$  will be a solution with almost  $2t$  tracks and so there is a trade-off between the routing area and the resulting crosstalk in routing a channel, which is not acceptable in general.

In this work, our objective is to develop a variation of the second algorithm such that the new routing solution may contain a maximum of either 60%, or 75%, or 90% bottleneck crosstalk in comparison with the earlier one. This may be achieved by interchanging a pair of nets or by shifting a net interval to a blank space in some other track if the constraints are validated, and crosstalk is also reduced involving the net. Following some logical sequence of nets, intervals are attempted to move for their assignment to some other tracks to achieve the desired bottleneck crosstalk.

In a case when the desired bottleneck crosstalk is not achieved, a blank track is introduced between the associated pair of tracks. This is how compromising channel area (not augmenting beyond an allowable range), a high-performance routing solution is computed wherein we introduce a minimal number of blank tracks, if at all necessary, for reducing the crosstalk to reach the bottleneck value.

In the next section, we introduce the proposed algorithms. Performance of the algorithms is also presented in the subsequent section of experimental results.

## 4 Proposed Algorithms

### 4.1 Algorithms for Computing Minimum Area and Minimum Crosstalk Routing Solutions

Computing a two-layer no-dogleg routing solution with minimum area constraint, in the specified channel routing model, is a hard problem for general channel instances [13]. Anyway, as has been formulated in the earlier section, the proposed heuristic algorithm computes the density of the channel ( $d_{\max}$ ) and the longest path length ( $v_{\max}$ ) in the VCG of a channel, if the VCG is acyclic. Then an iterative algorithm is devised as follows where, in each iteration, an induced HNCG is computed among the set of source vertices in the VCG, wherein an edge is oriented from left to right for each non-overlapping pair of nets along the length of the channel.

Our projected algorithm computes a composite weight for each of the vertices in the HNCG. Thus, from the said induced HNCG, a maximum weighted clique is computed so that the nets in the clique are assigned to the intended (topmost) track under consideration. Then, the VCG and the HNCG are modified after deleting the vertices (along with their associated edges) for the nets just assigned to a track. Afterwards, the next iteration is initiated based on the set of source vertices in the modified VCG. The process continues till all the nets in the channel are assigned to tracks.

When the routing solution is obtained, then primarily the amount of maximum crosstalk between a pair of nets assigned to adjacent tracks is computed. This is because the bottleneck crosstalk is then defined based on this maximum crosstalk between a net pair. More specifically, if the maximum crosstalk between a pair of nets is ten (units), and it is a two-layer routing solution of  $t$  tracks, then in our proposed algorithm, our objective is to find a two-layer routing solution of  $t + k$  tracks for some minimum value of  $k$  (which is expected to be zero), wherein the amount of crosstalk between a pair of nets is no more than six (units). The outlines of the proposed algorithms are given below to see them at a glance.

#### 4.1.1 Algorithm 1: Computation of Minimum Area Routing Solutions

**Procedure** *INITIAL\_ROUTING\_SOLUTION(C)*

**Input:** A channel instance  $C$ .

**Output:** A two-layer minimum area routing solution  $S$  along with horizontal crosstalk.

1. Compute VCG and  $v_{\max}$ , if the VCG is acyclic.
2. Compute HNCG,  $d_{\max}^j$  (of the channel), and the maximum density zone(s) of the channel.
3. Compute oriented HNCG (OHNCG), where the edges are naturally oriented from left to right based on the presence of associated nets along the length of the channel.

```

4. While VCG is not null
    Consider the source vertex set in VCG.
    Compute weight of each of the source vertices using
    either 4.1 or 4.2.
4.1 If  $d_{max} > v_{max}$ , then
    If a source vertex  $v_i$  passes through maximum density
    zone(s) then
        Weight =  $\{\sum zd(v_i)\} \times (\# \text{ maximum density}$ 
        zones) $\}^p + \sum ht(v_i)$ 
    Else
        Weight =  $\sum zd(v_i) + \sum ht(v_i)$ 
    End If
    End If
4.2 If  $d_{max} \leq v_{max}$ , then
    If a source vertex  $v_i$  in VCG has at least one
    path having a height equal to  $v_{max}$ , then
        Weight =  $\{(\sum \text{heights of the source vertex}) \times$ 
         $(\# \text{ paths with height } v_{max})^q\} + \sum zd(v_i)$ 
    Else
        Weight =  $(\sum \text{heights of the source vertex}) +$ 
         $\sum zd(v_i)$ 
    End If
    End If
4.3 Compute the maximum weighted clique  $C_i$  from OHNCG
    among the source vertex set in the current VCG.
4.4 Assign the intervals of the nets corresponding to
    the vertices in  $C_i$  to the current topmost tract  $t$  of
    the horizontal layer of the channel, vertical seg-
    ments of the assigned nets are also placed in the
    vertical layer of the channel.
4.5 Delete all assigned nets from HNCG and VCG.
4.6 Compute  $d_{max}$ ,  $v_{max}$ , and maximum density zone(s) of the
    modified channel.
5. End While
6. Compute  $S$  along with its status of horizontal cross-
    talks.
End Procedure    INITIAL_ROUTING_SOLUTION (C)

```

In this procedure, we have used some symbols that have been briefly explained as follows. Here for a source vertex,  $v_i$ ,  $zd(v_i)$  and  $ht(v_i)$  are the zonal density of the channel within the span of net  $n_i$  and the height of the vertex  $v_i$  in the VCG, respectively [2]. Clearly, if this procedure iterates  $t$  times, then a  $t$ -track two-layer routing solution  $S$  for channel  $C$  is computed. Then for this initial routing solution  $S$ , the crosstalk amount gets computed. In this work, this crosstalk is primarily the maximum amount of crosstalk between a pair of nets assigned to two adjacent tracks (in the horizontal layer) of  $S$ , as subsequently, we are concerned in reducing crosstalk in terms of some bottleneck value (sacrificing more channel area, if at all necessary). An outline of the bottleneck crosstalk minimization algorithm is included in the following section.



#### 4.1.2 Algorithm 2: Computation of Minimum Crosstalk Routing Solutions

As has already been mentioned, the two-layer routing solution  $S$  that is computed in the previous section may contain a maximum amount of overlapping (i.e. crosstalk in the horizontal layer) between a pair of nets beyond a limit, which may degrade the performance of the routing solution. In our next objective, we like to devise an algorithm wherein the bottleneck value is set below the maximum amount of crosstalk obtained in  $S$ , and compute a routing solution that may contain an amount of crosstalk not crossing the bottleneck value (defined by us) in two-layer channel routing.

In our implementation, we like to reach the bottleneck crosstalk to a value, not beyond 60%, or 75%, or 90% of the maximum value of crosstalk between a pair of nets that we obtained in  $S$ . Conceptually, the algorithm tries to move net intervals (in the horizontal layer) that are creating crosstalk beyond this limit satisfying all the constraints present in the channel and the assignment of nets in  $S$ . In doing that, sometimes we may succeed, sometimes we may not. When it is a case of success, routing area is not increased; otherwise, one more track is introduced into the channel (in  $S$ ), and a desired bottleneck crosstalk routing solution is computed compromising on channel area. In brief, the algorithm is as follows to see it at a glance.

##### **Procedure *Bottleneck\_Crosstalk\_Minimization(S)***

**Input:** A two-layer routing solution  $S$  and a bottleneck value  $x$  (in percentage).

**Output:** Another two-layer routing solution  $S'$ , wherein the maximum crosstalk (for a pair of nets assigned to adjacent tracks) is at most  $x\%$  of the maximum crosstalk in  $S$ .

1. Sort the responsible nets in non-ascending order  $P$  based on their maximum crosstalk with some other net and its presence from top to bottom in  $S$ .
2. For each such net  $n_j$  in  $P$ , perform either 2.1 or 2.2.
  - 2.1 **If**  $n_j$  is isolated in VCG, **then** it may be reassigned to a possibly different track in  $S$ , if suitable blank space is found in some other track where crosstalk is reduced to  $x\%$  of the maximum crosstalk in  $S$  or below the same, satisfying both horizontal as well as vertical constraints.
  - 2.2 **If**  $n_j$  is in vertical constraint with  $n_i$  as well as  $n_k$  such that  $(v_i, v_j)$  and  $(v_j, v_k)$  are edges in VCG, and  $n_i$  and/or  $n_k$  are there in  $P$ , while the nets  $n_i$  and  $n_k$  are assigned to tracks  $t_i$  and  $t_k$  in

$S$ , respectively,  $t_i < t_k$ , **then**  $n_j$  may be reassigned to a possibly different track in  $S$ , if a suitable blank space is found in some other track within the range of tracks  $t_{i+1}$  and  $t_k-1$ , where crosstalk is reduced to  $x\%$  of the maximum crosstalk in  $S$  or below the same, satisfying both horizontal as well as vertical constraints.

3. **If** no such track is found where  $n_j$  could be reassigned, **then** a blank track is introduced between the tracks where  $n_j$  and the other responsible net(s) are assigned (immediately above and/or below the track to which  $n_j$  is assigned) that are creating crosstalk in  $S$  beyond the allowable bottleneck (crosstalk) value.
4. Compute  $S'$ , wherein the maximum crosstalk is  $x\%$  of the maximum crosstalk in  $S$  or less.

**End Procedure *Bottleneck\_Crosstalk\_Minimization(S)***

Now, it is clear from the above algorithm (in Step 2.2), when  $v_j$  is a source (sink) vertex,  $v_i$  ( $v_k$ ) is no more there. In such a case,  $v_j$  may be attempted to reassign to a track among the range of tracks 1 ( $t_i + 1$ ) and  $t_k - 1$  (the  $t$ -th track in  $S$ ). Furthermore, if  $t_k - t_i = 2$  and all the nets  $n_i$ ,  $n_j$  and  $n_k$  are in  $P$ , then  $n_j$  is sandwiched in its track  $t_j$ , as  $t_k - t_j = t_j - t_i = 1$ . In such a case, we are forced to introduce blank tracks between  $t_i$  and  $t_j$  and also in between  $t_j$  and  $t_k$ . Of course, in such a case, prior to  $n_j$ , either  $n_i$  or  $n_k$  (that renders more crosstalk with  $n_j$  in  $S$ ) is better to assume earlier for its reassignment to some other track. This completes the bottleneck crosstalk minimization algorithm starting from a two-layer given routing solution  $S$ .

## 4.2 Computational Complexity

In the *Initial\_Routing\_Solution* algorithm, different parameters and eventually the weights for each of the nets can be computed in  $O(n)$  time as there are  $n$  nets in the given channel. The maximum weighted clique in an iteration can be computed in time  $O(n + e)$ , where  $n$  and  $e$  are the order (which is also same as the number of nets in  $C$ ) and size of the HNCG. As the algorithm iterates,  $t$  times for computing a  $t$ -track routing solution  $S$ , the computational complexity that dominates the algorithm is  $O(t(n + e))$ . In this measurement of complexity, when  $e = O(n)$ , then  $t$  is also  $O(n)$ , and when  $e = O(n^2)$ , then  $t$  could be assumed as constant (as the number of tracks in computing  $S$  is reduced radically).

On the other hand, when we measure crosstalk for the nets assigned to two adjacent tracks, if there are  $O(n)$  pairs of nets, this computation takes time  $O(n)$ . So, for a  $t$ -track routing solution  $S$ , the total crosstalk computation time may be overestimated as  $O(nt)$ . In the bottleneck crosstalk minimization algorithm *Bottle-*

*neck\_Crosstalk\_Minimization*, nets are expected to move to some other track (satisfying constraints), only when some suitable blank space is there in some other track for at least one responsible net creating more crosstalk in  $S$ . If no such track is found for such a desired interchange, a blank track is introduced in between eventually to make the earlier crosstalk negligible. This computation never exceeds the worst-case estimation of  $O(n^2)$  for a given channel of  $n$  nets.

## 5 Experimental Results

To judge the novelty of the algorithms devised in this paper, we have randomly generated a huge number of general channel instances wherein the number of nets varies from 20 to 1000. More specifically, for each value of a number of nets, we have randomly generated 200 general channel instances each of which is free from any cyclic vertical constraint. The results we obtain are included in Table 1 following algorithm *Initial\_Routing\_Solution*. Along with crosstalk values on an average for 200 similar instances for a given value of net number ( $n$ ), here we have comprised net wire length information as well of the computed routing solutions since net wire length is also responsible in high-performance routing in terms of delay.

Now, we compute reduced bottleneck crosstalk routing solutions, after algorithm *Bottleneck\_Crosstalk\_Minimization* over each of the two-layer minimum area channel routing solutions  $S$  (based on which the results are included in Table 1), and on an average, the values of crosstalk we obtain for a given value of  $n$  are included in Tables 2, 3 and 4. In Table 2, the bottleneck value is set to 60% of the maximum amount of crosstalk obtained in  $S$ , whereas in Tables 3 and 4, the bottleneck values are set to 75 and 90%, respectively, of the maximum amounts of crosstalk obtained in  $S$ . In each of these newly computed routing solutions  $S'$ , additional tracks are also introduced in order to assure the bottleneck crosstalk value that has also been included in the relevant tables.

These tables also include the percentage reduction of horizontal crosstalk and the percentage reduction of total crosstalk. We may observe that while reducing horizontal crosstalk, vertical crosstalk may increase. However, as the channel length is much more on an average than the channel height, the total crosstalk is eventually reduced along with fulfilling the respective bottleneck values. As we are primarily concerned in attaining bottleneck crosstalk routing solutions, in these tables, we do not include the values against average net wire length obtained in these routing solutions.

Some graphical representations of the variation of bottleneck horizontal crosstalk against the number of nets are shown in Figs. 2 and 3. Figure 2 includes on an average bottleneck horizontal crosstalk versus a number of nets when the bottleneck value is set to 60, 75 and 90% of the maximum amounts of horizontal crosstalk obtained in the minimum area two-layer routing solutions after algorithm *Initial\_Routing\_Solution*. On the other hand, Fig. 3 shows the average percentage reduction in bottleneck horizontal crosstalk after algorithm *Bottleneck\_Crosstalk\_Minimization* against a

**Table 1** Two-layer routing solutions obtained after algorithm *Initial\_Routing\_Solution*

# Nets	Average $d_{\max}$	Average $v_{\max}$	Average # Tracks in $S$	Average horizontal net length	Average vertical net length	Average total net length	Average horizontal crosstalk	Average vertical crosstalk	Average total crosstalk
20	10.025	6.05	10.02	205.79	276.35	482.14	118.34	160.66	279
40	17.04	8.195	18.14	753.85	929.62	1683.57	491.71	569.94	1061.65
60	24.39	9.885	25.75	1682.25	1974.52	3664.72	1174.37	1238.18	2412.55
80	31.77	10.91	33.31	2973.02	3418.62	6391.64	2141.48	2197.22	4338.7
100	38.36	12.35	40.03	4648.23	5202.35	9851.58	3415.12	3361.31	6776.43
140	51.545	13.785	53.41	8819.19	9551.23	18371.4	6720.15	6259.2	12980.4
180	63.93	15.115	65.69	14299.31	15155.22	29455.5	11164.12	10015.2	21179.4
240	82.665	16.395	85.35	24921.02	26048.35	50969.4	19823.23	17370.2	37193.5
320	107.975	18.92	110.5	43929.15	45435.19	89365.24	35543.35	30560.21	66103.56
400	133.945	19.935	136.21	68342.04	70173.03	138515.07	55853.25	47242.12	103095.37
500	164.68	21.85	168.02	106304.28	107970.21	214274.5	87977.9	73058.2	161036.1
600	197.05	22.56	200.67	152328.29	154365.31	306693.6	126956.29	104722.2	231678.31
800	260.245	25.295	264.23	270081.29	272188.2	542269.49	227214.21	185628.25	412842.46
1000	321.75	27.085	326.28	418745.14	419971.52	838716.66	354600.12	287118.13	641718.25

**Table 2** Two-layer reduced crosstalk routing solutions obtained after algorithm *Bottleneck\_Crosstalk\_Minimization* with 60% bottleneck values over the initial minimum area routing solutions

# Nets	Average $d_{max}$	Average $v_{max}$	Average # Tracks in $S'$	# Blank tracks introduced	Average horizontal crosstalk	Percentage reduction in horizontal crosstalk	Average vertical crosstalk	Average total crosstalk	Percentage reduction in total crosstalk
20	10.025	6.05	14.25	4.23	65.32	45	198.4	263.72	5.73
40	17.04	8.195	22.53	4.39	304.45	38.08	696.4	1000.85	5.74
60	24.39	9.885	32.26	6.51	745.65	36.54	1526.24	2271.89	5.84
80	31.77	10.91	41.97	8.66	1391.12	35.03	2712.43	4102.55	5.44
100	38.36	12.35	49.52	9.49	2358.32	30.95	4074.34	6432.66	5.07
140	51.545	13.785	64.25	10.84	4867.87	27.57	7495.02	12362.89	4.76
180	63.93	15.115	77.45	11.76	8408.21	24.68	11824.45	20232.66	4.47
240	82.665	16.395	100.12	14.77	15103.68	23.81	20433.23	35536.91	4.45
320	107.97	18.92	129.47	18.97	27527.43	22.55	35819.05	63346.48	4.17
400	133.94	19.93	158.25	22.04	44038.43	21.15	54853.4	98891.83	4.07
500	164.68	21.85	194.15	26.13	70200.78	20.2	84470.05	154670.8	3.95
600	197.05	22.56	231.12	30.45	101582.3	19.98	120910.2	222492.5	3.95
800	260.24	25.29	299.52	35.29	188185.5	17.17	210700.4	398885.9	3.38
1000	321.75	27.08	361.37	35.09	300984.7	15.12	321096.2	622080.9	3.06

**Table 3** Two-layer reduced crosstalk routing solutions obtained after algorithm *Bottleneck\_Crosstalk\_Minimization* with 75% bottleneck values over the initial minimum area routing solutions

# Nets	Average $d_{max}$	Average $v_{max}$	Average # Tracks in $S'$	# Blank tracks introduced	Average horizontal crosstalk	Percentage reduction in horizontal crosstalk	Average vertical crosstalk	Average total crosstalk	Percentage reduction in total crosstalk
20	10.025	6.05	13.4	3.38	81.2	31.35	185.5	266.7	4.65
40	17.04	8.195	21.32	3.18	378.32	23.01	642.33	1020.65	3.86
60	24.39	9.885	29.34	3.59	917.25	21.89	1404.25	2321.5	3.77
80	31.77	10.91	37.65	4.34	1773.43	17.18	2439.4	4212.83	2.9
100	38.36	12.35	44.21	4.18	2905.32	14.93	3693.33	6598.65	2.62
140	51.545	13.785	58.63	5.22	5863.55	12.75	6815.2	12678.75	2.32
180	63.93	15.115	70.43	4.74	9988.33	10.53	10763.2	20751.53	2.02
240	82.665	16.395	91.32	5.97	17875.43	9.82	18609.34	36484.77	1.9
320	107.97	18.92	117.43	6.93	32493.1	8.58	32515.33	65008.43	1.65
400	133.94	19.935	144.54	8.33	51319.21	8.11	50120.22	101439.4	1.6
500	164.68	21.85	177.76	9.74	81426.29	7.44	77228.1	158654.4	1.47
600	197.05	22.56	210.2	9.53	117944.3	7.09	110373.3	228317.7	1.45
800	260.24	25.29	276.35	12.12	213348.1	6.1	194451.3	407799.4	1.22
1000	321.75	27.08	338.67	12.39	335577.3	5.36	299068.3	634645.6	1.1

**Table 4** Two-layer reduced crosstalk routing solutions obtained after algorithm *Bottleneck\_Crosstalk\_Minimization* with 90% bottleneck values over the initial minimum area routing solutions

# Nets	Average $d_{max}$	Average $v_{max}$	Average # Tracks in $S'$	# Blank tracks introduced	Average horizontal crosstalk	Percentage reduction in horizontal crosstalk	Average vertical crosstalk	Average total crosstalk	Percentage reduction in total crosstalk
20	10.025	6.05	12.34	2.32	96.32	4	174.43	270.75	3.22
40	17.04	8.195	19.45	1.31	430.22	12.42	607.24	1037.46	2.26
60	24.39	9.885	27.32	1.57	1049.24	10.64	1316.43	2365.67	1.94
80	31.77	10.91	35.21	1.9	1965.21	8.22	2308.43	4273.64	1.49
100	38.36	12.35	41.19	1.16	3199.1	6.32	3497.54	6696.64	1.18
140	51.545	13.785	55.43	2.02	6397.32	4.8	6460.43	12857.65	0.94
180	63.93	15.115	67.2	1.51	10724.12	3.94	10289.04	21013.16	0.78
240	82.665	16.395	87.12	1.77	19138.33	3.45	17803.03	36941.36	0.67
320	107.97	18.92	112.45	1.95	34578.32	2.71	31174.64	65752.96	0.53
400	133.94	19.935	139.23	3.02	54438.32	2.53	48122.3	102560.62	0.51
500	164.68	21.85	170.75	2.73	85967.6	2.29	74324.2	160291.8	0.46
600	197.05	22.56	203.45	2.78	124240.32	2.13	106396.3	230637.62	0.45
800	260.24	25.29	267.34	3.11	223486.44	1.64	187985.4	411471.84	0.33
1000	321.75	27.08	329.32	3.04	349839.07	1.34	290070.12	639910.19	0.28

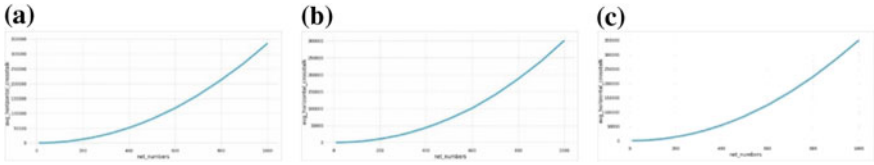


**Fig. 2** Bottleneck horizontal crosstalk against a number of nets when the bottleneck value is set to **a** 60%, **b** 75% and **c** 90% of the maximum amounts of crosstalk obtained in the minimum area two-layer routing solutions after algorithm *Initial\_Routing\_Solution* on an average

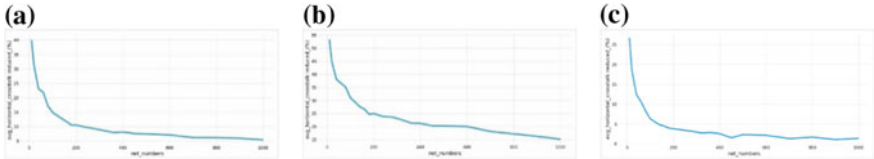


**Fig. 3** Average percentage reduction in bottleneck horizontal crosstalk after algorithm *Bottleneck\_Crosstalk\_Minimization* against a number of nets when the bottleneck values are set to **a** 60%, **b** 75% and **c** 90% of the maximum amounts of crosstalk obtained in the initial minimum area two-layer channel routing solutions

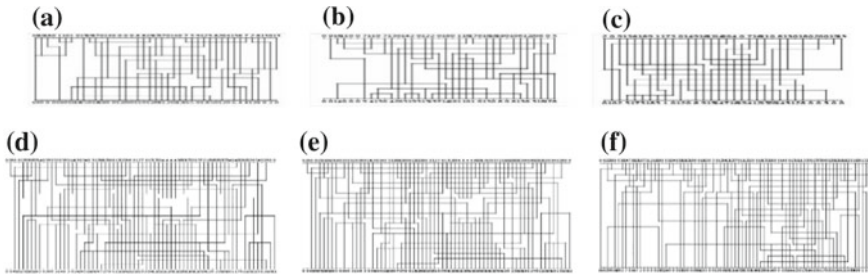
number of nets when the bottleneck value is set to 60, 75 and 90% of the maximum amounts of crosstalk obtained in the initial minimum area two-layer channel routing solutions.

Figure 4 includes only a very few hardcopy routing solutions that have been computed based on the implementation of our proposed heuristic algorithms. None of the minimum area routing solutions after algorithm *Initial\_Routing\_Solution* have shown here. However, only six (out of 2800) routing solutions after the *Bottleneck\_Crosstalk\_Minimization* algorithm have been depicted, out of which no additional (blank) track is introduced to achieve the set bottleneck value for each of the routing solutions in (b), (c) and (f), whereas for the routing solution in (d), five additional blank tracks have been introduced to satisfy the bottleneck value set for reducing the crosstalk.

## 6 Conclusion

This paper focuses on bottleneck crosstalk minimization problem in two-layer channel routing. We know that the area minimization problem in the reserved two-layer Manhattan channel routing model is NP-hard. The defined crosstalk minimization problem is also known to be NP-hard. Thus, devising heuristic algorithms is an immediate step, hopefully, to compute desired routing solutions. In this paper, we have designed and implemented two such heuristic algorithms that are executed one after the other. A large class of random channel instances has been generated for





**Fig. 4** A set of two-layer routing solutions computed with reduced crosstalk after algorithm *Bottleneck\_Crosstalk\_Minimization* against numbers of nets, wherein a pertinent bottleneck value is set based on the maximum amounts of crosstalk obtained in the initial minimum area channel routing solutions after algorithm *Initial\_Routing\_Solution*. **a** The number of nets is 20, and the bottleneck value is set to 10; four blank tracks have been introduced. **b** The number of nets is 20, and the bottleneck value is set to 12; no blank track has been introduced. **c** The number of nets is 20, and the bottleneck value is set to 15; no blank track has been introduced. **d** The number of nets is 40, and the bottleneck value is set to 23; five blank tracks have been introduced. **e** The number of nets is 40, and the bottleneck value is set to 28; two blank tracks have been introduced. **f** The number of nets is 40, and the bottleneck value is set to 34; no blank track has been introduced

analysing the performance of the devised algorithms. Our crosstalk reduction algorithm is implemented for computing routing solutions with 60, 75 and 90% bottleneck consideration over the maximum amount of crosstalk present in an initial minimum area channel routing solution. All these experimental results have been presented in this paper, and a few hardcopy routing solutions have also been illustrated. As an immediate enhancement over the work, we may think of bottleneck crosstalk minimization in three-layer channel routing.

## References

1. N.A. Sherwani, *Algorithms for VLSI Physical Design Automation* (Kluwer Academic Publishers, Boston, 1993)
2. R.K. Pal, *Multi-Layer Channel Routing: Complexity and Algorithms*, Narosa Publishing House, New Delhi (Also published from CRC Press, Boca Raton, USA and Alpha Science International Ltd., UK, 2000)
3. T. Yoshimura, E.S. Kuh, Efficient algorithms for channel routing. *IEEE Trans. CAD Integr. Circ. Syst.* **1**, 25–35 (1982)
4. T. Gao, C.L. Liu, Minimum crosstalk channel routing, in *Proceedings of IEEE International Conference on Computer Aided Design* (1993), pp. 692–696
5. A. Pal, A. Chaudhuri, R.K. Pal, A.K. Datta, Hardness of crosstalk minimisation in two-layer channel routing. *Integr. VLSI J.* **56**, 139–147 (2017). ISSN: 0167-9260
6. M.C. Golumbic, *Algorithmic Graph Theory and Perfect Graphs* (Academic Press, New York, 1980)
7. A. Hashimoto, J. Stevens, Wire Routing by Optimizing Channel Assignment within Large Apertures, in *Proceedings of the 8th ACM Design Automation Workshop* (1971), pp. 155–169

8. R.K. Pal, A.K. Datta, S.P. Pal, A. Pal, Resolving horizontal constraints and minimizing net wire length for VH channel routing, in *Technical Report, no.: TR/IIT/CSE/92/01*, Department of Computer Science and Engineering, IIT, Kharagpur (1992)
9. R.K. Pal, A.K. Datta, S.P. Pal, A. Pal, Resolving horizontal constraints and minimizing net wire length for multi-layer channel routing, in *Proceedings of IEEE Region 10's Eighth Annual International Conference on Computer, Communication, Control and Engineering (TENCON 1993)*, vol. 1 (1993), pp. 569–573
10. R.K. Pal, A.K. Datta, S.P. Pal, M.M. Das, A. Pal, General graph theoretic framework for multi-layer channel routing, in *Proceedings of the Eighth VSI/IEEE International Conference on VLSI Design*, (Jan. 4–7, 1995), pp. 202–207
11. A. Pal, D. Kundu, A.K. Datta, T.N. Mandal, R.K. Pal, Algorithms for reducing crosstalk in two-layer channel routing. *J. Phys. Sci.* **10**, 167–177 (2006). (ISSN: 0972-8791)
12. A. Pal, D. Kundu, A.K. Datta, T.N. Mandal, R.K. Pal, A.K. Datta, A. Chaudhuri, Two algorithms for minimizing crosstalk in two-layer channel routing. *Int. J. Emerg. Trends Technol. Comput. Sci.* **3**(6), 194–204 (2006). (ISSN: 2278-6856)
13. A.S. LaPaugh, *Algorithms for Integrated Circuit Layout: An Analytic Approach*, Ph.D. Thesis, Laboratory for Computer Science (Massachusetts Institute of Technology (MIT), Cambridge, 1980)

# Design and Comparative Analysis of Low-Power, High-Speed, 3-Bit Flash ADC for Biomedical Signal Processing Using 45-nm CMOS Technology



Sk. Firojuddin, Soumen Pal and Puspak Pain

**Abstract** The analog-to-digital converter is the key component for communication and signal processing. This paper describes the design and simulations of a 3-bit flash analog-to-digital converter (ADC) which includes voltage divider network, comparators, and a priority encoder. The proposed circuit is driven by 0.6 V supply voltage with an analog input of 600 mV amplitude and 1 MHz frequency. The proposed architecture is designed, simulated, and analyzed using Cadence Virtuoso IC 6.1.5 Simulator tool in 45-nm CMOS technology. The power consumption of proposed 3-bit flash ADC is 142  $\mu$ W with 12.52 nS delay and output noise of 26.55 nV/sqrt(Hz). In this paper, a high-speed, low-power CMOS flash ADC, suitable for biomedical application, is proposed and analyzed.

**Keywords** Low power · High speed · Flash ADC · 45-nm CMOS · Cadence Virtuoso

## 1 Introduction

In current research on radio frequency, communication device asks for higher integration, with low cost, low power, and high speed. ADC is the most important component in wireless receivers and is one of the applications where low-power dissipation, low noise, and high speed are required in analog-to-digital converter (ADC) for mobile and portable devices. The gain amplifiers and comparators are the performance-limiting factors of such ADC. The conversion from analog to digital is oversampling

---

Sk. Firojuddin (✉) · S. Pal · P. Pain  
Department of Electronics and Communication Engineering, Narula Institute of Technology,  
81, Nilgunj Road, Agarpara, Kolkata 700109, West Bengal, India  
e-mail: [firojsk1122@gmail.com](mailto:firojsk1122@gmail.com)

S. Pal  
e-mail: [soumen.pal@nit.ac.in](mailto:soumen.pal@nit.ac.in)

P. Pain  
e-mail: [puspak.pain@nit.ac.in](mailto:puspak.pain@nit.ac.in)

for wireless application. The flexibility and performance are increased and became popular [1–3].

In the field of biomedical, the maximum signals are the analog signal. This analog signal is converted into one kind of electrical signal. The sensor devices are utilized for the sensing of biomedical signals from the human body like electroencephalography (EEG), electromyography (EMG), and electrocardiography (ECG). In the present-day digital signal processing, the signal required digital form more than analog form. That is why ADC is required for converting the signal. Bio-signals are mostly noisy and its work low–medium frequency. A biomedical signal is mostly in the range of mV [4].

In this paper, flash or parallel ADC is considered since their speed of converting an analog signal to digital signal is faster than other ADCs. This ADC is the most suitable for several applications and hardware implementation of low-resolution, high-speed, modern-day electronic circuit design. It is highly used in data rate, radar, digital oscilloscopes, optical communication, and biomedical signal processing. The conversion operation of flash ADC is parallel, and the maximum possibility of operating frequency is in MHz. Comparator design also challenges for the design of 3-bit flash ADC. The main objective of this paper is to design a 3-bit flash ADC using 45-nm CMOS technology in Cadence Virtuoso environment.

## 2 Architecture of Flash ADC

The flash ADC is the fastest ADC and has parallel architecture among all other types and suitable for high-bandwidth applications.

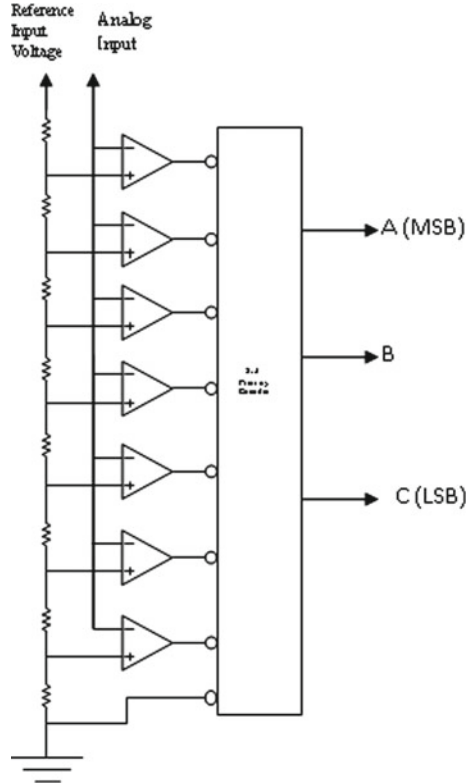
Figure 1 shows a flash ADC block diagram, and it can be seen that  $2N - 1$  comparators are required for an  $N$ -bit converter. The resistor ladder network which is used to generate the +reference voltage for each of the comparator is formed by  $2N$  resistors. The reference voltage for each comparator is 1 least significant bit which is less than the reference voltage for the comparator instantly above it. When the input voltage is above the reference voltage, comparator will generate a 1, otherwise the output of the comparator is 0 [5].

The components of flash ADC are resistor ladder, comparator, and priority encoder.

### 2.1 Resistor Ladder

In a flash ADC, the resistor ladder block is used to generate the reference voltages for the comparators. The block diagram of the resistor ladder is shown in Fig. 2.

**Fig. 1** Basic architecture of flash ADC [6]



## 2.2 Comparator

A comparator is used to detect whether a signal is greater or smaller than a reference signal. The two-stage operational amp is used as a comparator circuit. The comparator has two stages like primary and secondary. The primary stage also has two parts, one is the biasing circuit and another part is a differential amplifier. The second stage is for gain stage; this gain is better than an operational amplifier.

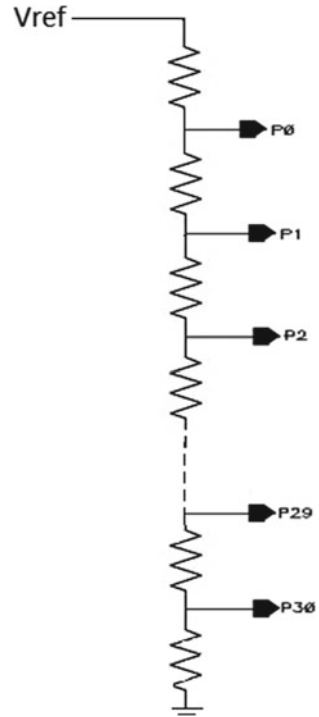
$$V_{INV} > V_{NON-INV} \text{ then output} = V_{ss} = \text{logic '0'}$$

$$V_{INV} < V_{NON-INV} \text{ then output} = V_{dd} = \text{logic '1'}$$

A positive voltage applied at the  $V_P$  input will cause the comparator output to go positive, whereas a positive voltage applied at the  $V_N$  input will cause the comparator output to go negative. The upper and lower voltage limits of the comparator output are defined as  $V_{OH}$  and  $V_{OL}$ , respectively.

A comparator has been defined above as a circuit that has a binary output whose value is based on a comparison of two analog inputs. This is illustrated in Fig. 3b; the output of the comparator is high ( $V_{OH}$ ) when the difference between the non-inverting and inverting inputs is positive, and low ( $V_{OL}$ ) when this difference is negative.

**Fig. 2** Basic architecture of resistor ladder



### 2.3 Priority Encoder

Here used active low-input priority encoder. The output of the comparator is in the encoded form. Therefore, a priority encoder has to be designed in order to convert the encoded signal into bit data (digital) which is a unipolar binary code (Fig. 4; Table 1).

The following equations give the relation between the thermometer-coded data and the binary-coded data for a 3-bit encoder.

$$A = \bar{I}_4 I_5 I_6 I_7 + \bar{I}_5 I_6 I_7 + \bar{I}_6 I_7 + \bar{I}_7 \tag{1}$$

$$B = \bar{I}_2 I_3 I_4 I_5 I_6 I_7 + \bar{I}_3 I_4 I_5 I_6 I_7 + \bar{I}_6 I_7 + I_7 \tag{2}$$

$$C = \bar{I}_1 I_2 I_3 I_4 I_5 I_6 I_7 + \bar{I}_3 I_4 I_5 I_6 I_7 + \bar{I}_5 I_6 I_7 + \bar{I}_7 \tag{3}$$

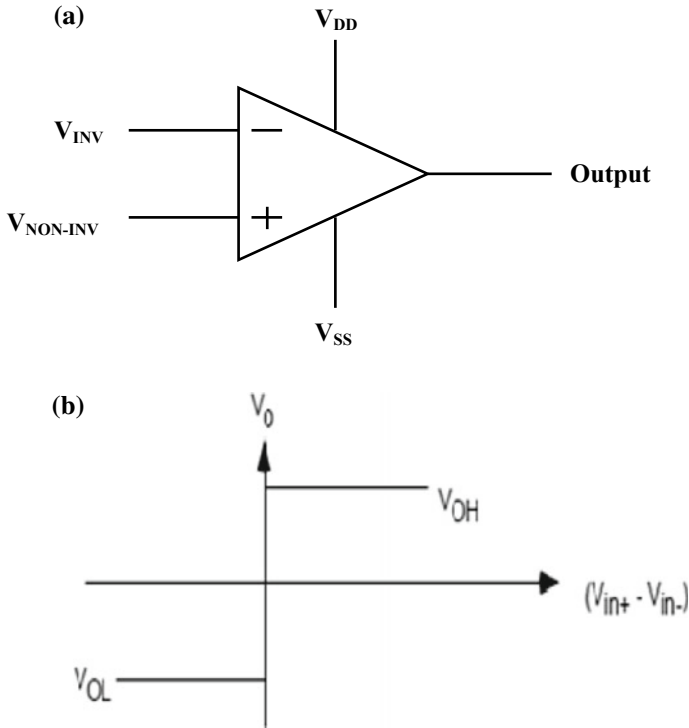
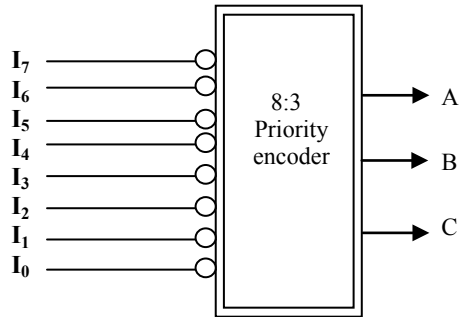


**Fig. 3** a Basic architecture of comparator [6]. b Basic comparator output [6]

**Fig. 4** Basic architecture of active low-input priority encoder



### 3 Proposed Flash ADC

The following Table 2 represents process parameters for the comparator, Table 3 represents specifications for the proposed flash ADC which has been designed as shown in Fig. 1, and the design parameters can be determined as given in Table 4 (Figs. 5 and 6).

**Table 1** Truth table of thermometer code to binary code

$I_0$	$I_1$	$I_2$	$I_3$	$I_4$	$I_5$	$I_6$	$I_7$	A(MSB)	B	C(LSB)
0	1	1	1	1	1	1	1	0	0	0
×	0	1	1	1	1	1	1	0	0	1
×	×	0	1	1	1	1	1	0	1	0
×	×	×	0	1	1	1	1	0	1	1
×	×	×	×	0	1	1	1	1	0	0
×	×	×	×	×	0	1	1	1	0	1
×	×	×	×	×	×	0	1	1	1	0
×	×	×	×	×	×	×	0	1	1	1

× = Don't care condition  
 $I_0, I_1, I_2, I_3, I_4, I_5, I_6,$  and  $I_7$  are the inputs of the priority encoder, and  $A, B,$  and  $C$  are the outputs of the priority encoder, where  $A$  is the MSB and  $C$  is the LSB

**Table 2** Process parameters

Parameters	NMOS	PMOS
Gate oxide thickness ( $t_{ox}$ ) (nm)	2.41	2.4
Mobility ( $\mu$ )( $m^2/volt\text{-}sec$ )	156.718	247.139
Threshold voltage ( $V_{th}$ ) (mV)	349.255	-369.135

**Table 3** Electrical specifications

Electrical parameters	Values
Supply voltage (V)	$\pm 0.6$
Output noise (nV/sqrt(Hz))	26.55
Power consumption (uW)	142
Delay (nS)	12.52
Resolution	3-bit

**Table 4** Design parameters for comparator

Aspect ratio (W/L)	
M1, M2	95/1
M3, M4	21.66/1
M5, M8	1/2
M6	214/1
M7	6/1
M9	2.66/1



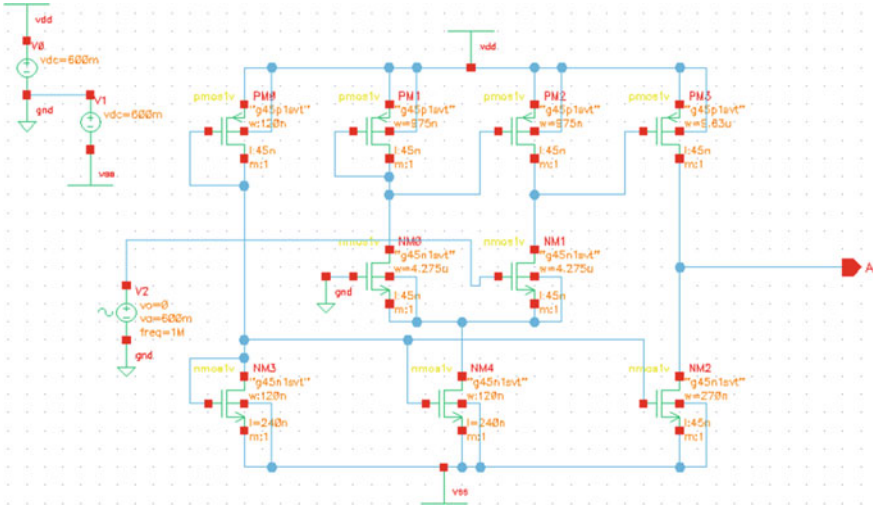


Fig. 5 Schematic diagram of the proposed two-stage comparator using 45-nm CMOS technology

### 4 Simulation Result

The design parameters have been determined in Table 4 for our proposed CMOS comparator and flash ADC with the help of standard design procedure [6] and the process parameters given in Table 2 and the electrical specifications in Table 3, respectively. The SPICE simulation and analysis of our proposed system have been carried out in Cadence Spectre tools, and the results are discussed as follows (Fig. 7).

This figure shows that an input analog signal is converted into digital (a bit). The amplitude of the input signal is 0.6 V. The output varies depending on the amplitude of the input signal (Table 5).

Table 5 Analysis of theoretically expected and simulated analog input voltage level with corresponding digital output word

Analog input voltage level (Volt) (theoretically expected)	Analog input voltage level (Volt) (simulated)	Digital output word
0.0	0.0	000
0.075	0.1052	001
0.150	0.1741	010
0.225	0.2573	011
0.300	0.3260	100
0.375	0.4026	101
0.450	0.4708	110
0.525	0.5582	111

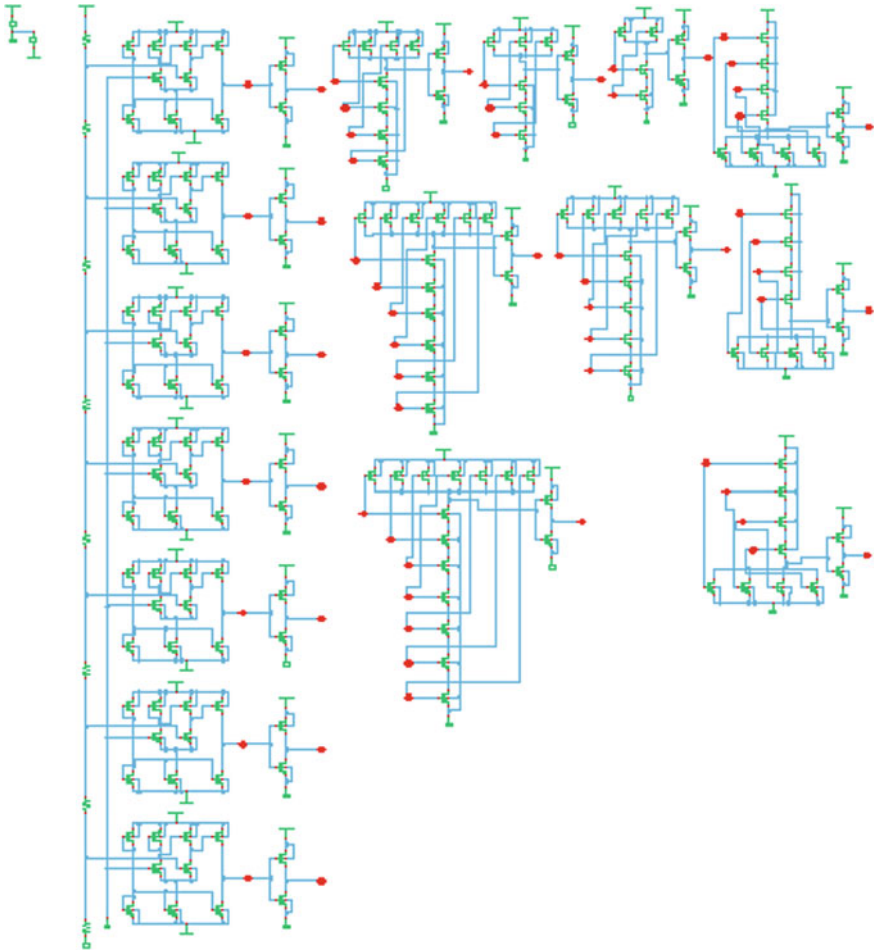


**Fig. 6** Schematic diagram of proposed 3-bit flash ADC using 45-nm CMOS technology

Figure 8 shows if supply voltage increases, the power consumption will also increase.

Figure 9 shows with the increase of supply voltage, delay will decrease (Figs. 10, 11, Table 6).

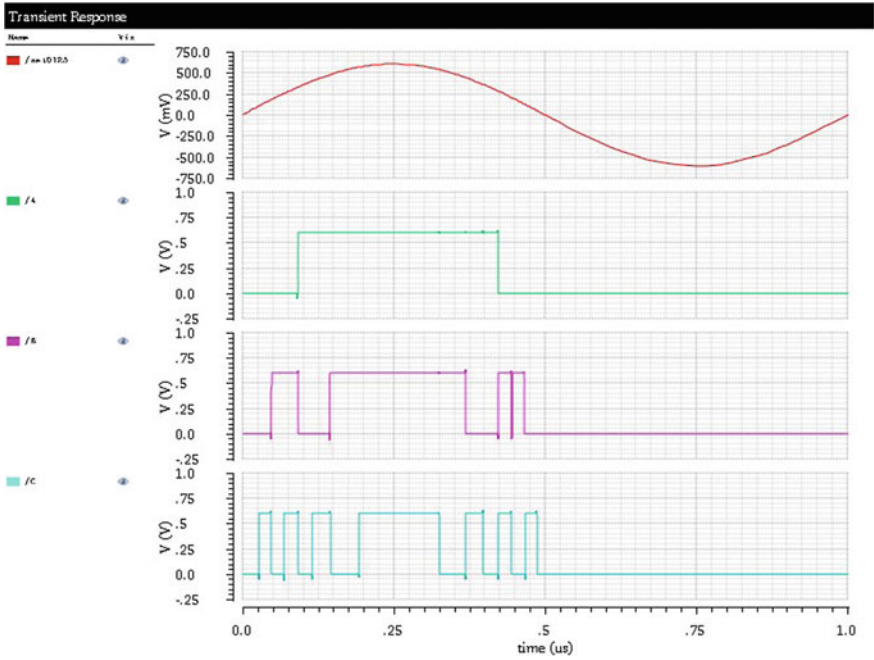


Fig. 7 Transient analysis of flash ADC using designed comparator

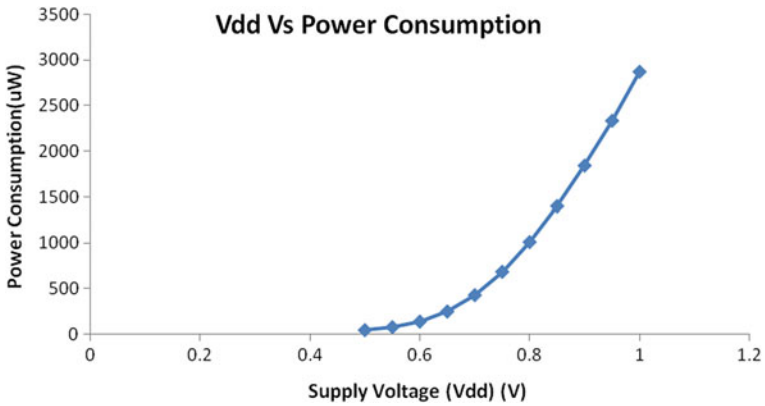


Fig. 8 Supply voltage versus power consumption curve of proposed flash ADC

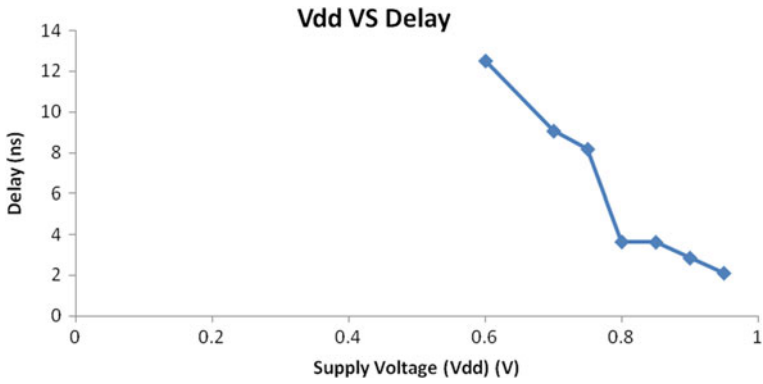


Fig. 9 Supply voltage versus delay curve of proposed flash ADC

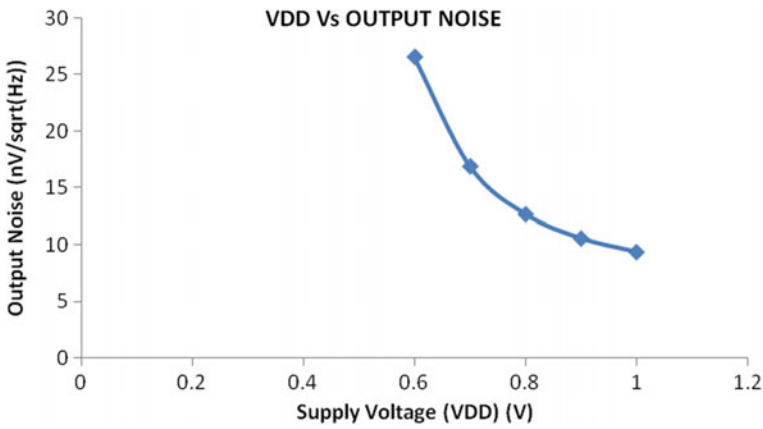


Fig. 10 Supply voltage versus output noise

Table 6 Comparative analysis

References	Technology (nm)	Resolution (in bit)	Power supply (V)	Power consumption
[1]	65	4	1.2	6 mW
[3]	180	3	1.8	179 uW
[7]	45	6	1.2	18 mW
[8]	90	3	0.9	870 uW
This work	45	3	0.6	142 uW

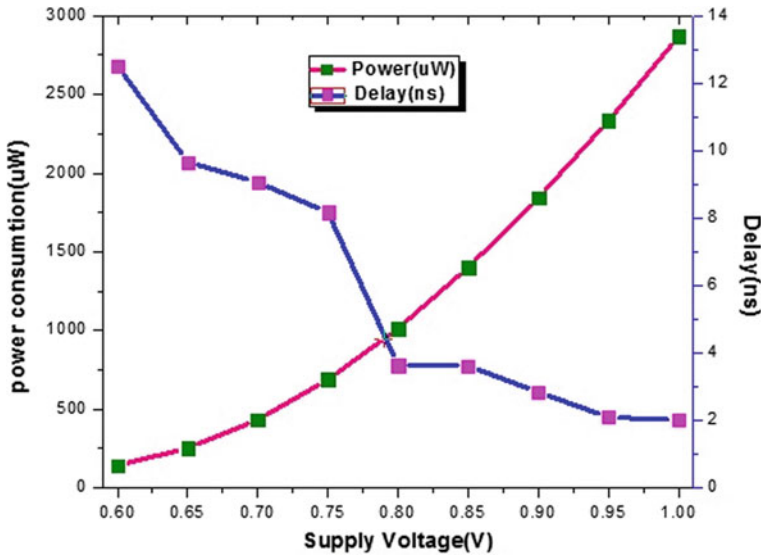


Fig. 11 Supply voltage versus power consumption versus delay curve of flash ADC

## 5 Conclusion

The flash ADC, the faster analog-to-digital converters, ought to optimize its performance through its application-specific design architecture, parameters, and power utilization in the modern, high-speed, low-power era. In this work, the proposed ADC is designed in standard GPDK 45-nm CMOS technology of IC 6.1.5 version using Cadence Virtuoso tool. The proposed 3-bit flash ADC has been operated with an analog input voltage from 0 to 0.6 V for a supply voltage of 0.6 V which consumed the lesser power of 142 uW and squat delay of 12.52 ns with SNR 26.55. The simulated results and comparative analysis of our proposed flash ADC design ascertain its expediency in low-power biomedical signal processing with a variety of high-speed ADC applications. Further diminution in device channel length might be necessary to ensure more integration, and we are looking to intend lesser power ADC in 32-nm technology in the future.

## References

1. A. Mahesh Kumar, V. Tummala, Design of low power variable resolution flash ADC, in *22nd International Conference on VLSI Design (IEEE, 2009)*
2. S.S. Guru, Dr. D.P. Acharya, Design and simulation of SIGMA DELTA ADC. M.Tech thesis, May (2013)

3. S. Mukherjee, D. Saha, P. Mostafa, D. Saha, S. Chatterjee, C.K. Sarkar, A low power, high speed, IF range flash type ADC designed with the concept of TMCC and Binary Counter, in *IEEE* (2012)
4. Pradeep, A, Mahaveera, K, Design and analysis of analog to digital converter for biomedical applications. *Int. J. Innov. Res. Sci., Eng. Technol.* **5**(9) (2016). ISSN: 2319-8753
5. N. Prabhat, A. Yadav, A review of low power flash ADC using different comparator styles & design techniques. *Int. J. Innov. Res. Comput. Commun. Eng.* **4**(Special Issue 4) (2016). ISSN (Online): 2320-9801
6. P.E. Allen, D.R. Holberg, *CMOS Analog Circuit Design*. 2nd edn. (Oxford University Press, 2004)
7. P.S. Nabeel, T.E. Ayoob Khan, Dr. T.A. Shahul Hameed Design of low power high speed flash ADC in 45 nm CMOS. *Int. J. VLSI Syst. Des. Commun. Syst. (IJVDCS)* **03**(05), 0620–0625 (2015). ISSN 2322-0929
8. K. Chaudhary, R.B. Singh, A novel approach to 3-bit flash ADC. *Int. J. Sci. Res. Dev.* **2**(03) (2014) Issn (Online): 2321-0613

**Part VI**  
**Nano Technology**

# Influence of Gate and Channel Engineering on Multigate Tunnel FETs: A Review



Ritam Dutta, Sukumar Chandra Konar and Nitai Paitya

**Abstract** The continuous progress in the development of tunnel field-effect transistors (TFETs) by replacing the conventional metal-oxide field-effect transistors is to satisfy the development of continuous device dimension down-scaling. In this paper, a detailed review is made on non-conventional TFET structures owing to the inbuilt benefit of band-to-band tunneling (BTBT) phenomenon carrier conduction mechanism, thereby reducing short-channel effects (SCEs). The work presents the drain current evaluation of various non-conventional device structures, viz. double-gate tunnel FET (DG-TFET), triple-gate tunnel FET (TG-TFET), double-gate pocket intrinsic tunnel FET (DG-PI-TFET), and triple-gate TFET structures with pocket intrinsic layer (TG-PI-TFET). The variation of drain current for different device parameters has been reviewed and demonstrated with Silvaco TCAD simulator.

**Keywords** DG-TFET · DG-PI-TFET ·  $I_{ON}/I_{OFF}$  ratio · TG-TFET · TG-PI-TFET

## 1 Introduction

Continuous downsizing of metal-oxide semiconductor field-effect transistors (MOS-FETs) have been a real challenge nowadays. Hence, the tunnel field-effect transistors (TFETs) are found to be interesting due to the low leakage current and steep sub-

---

R. Dutta (✉)

Department of Electronics & Communication Engineering, Surendra Institute of Engineering and Management, MAKAUT, Siliguri, West Bengal, India  
e-mail: [ritam\\_siliguri@yahoo.com](mailto:ritam_siliguri@yahoo.com)

S. C. Konar

Department of Research & Development, Narula Institute of Technology, MAKAUT, Kolkata, West Bengal, India  
e-mail: [sckonar55@gmail.com](mailto:sckonar55@gmail.com)

N. Paitya

Department of Electronics & Communication Engineering, Sikkim Manipal Institute of Technology, SMU, Majitar, Sikkim, India  
e-mail: [nitai.p@smit.smu.edu.in](mailto:nitai.p@smit.smu.edu.in)

© Springer Nature Singapore Pte Ltd. 2020

K. Maharatna et al. (eds.), *Computational Advancement in Communication Circuits and Systems*, Lecture Notes in Electrical Engineering 575,  
[https://doi.org/10.1007/978-981-13-8687-9\\_31](https://doi.org/10.1007/978-981-13-8687-9_31)



threshold slope [1, 2]. Since the minimum sub-threshold swing ( $SS$ ) attainable in a MOSFET has been limited to 60 mV/decade, a MOSFET does not behave like an ideal switch. The tunnel FET has the prospect of reducing the sub-threshold swing less than the conventional limit [3–5]. TFETs are ambipolar in nature and also produce low drive current ( $I_{ON}$ ). The ambipolarity can be subdued by increasing doping concentration, and the  $I_{ON}$  can be boosted by introducing gate and channel engineering [6, 7]. This paper mainly focuses on to boost  $I_{ON}$  with best possible sub-threshold swing below 60 mV/decade.

Various TFET structures with multigate have been reviewed, studied, and analyzed to assess the performance improvement of TFET [8–12]. Multigate structure of TFETs has the two-way tunneling junctions to increase the tunneling current compared to single-gate TFET [13, 14].

The incorporation of thin pocket intrinsic doping in the tunnel FET produces another electric field component to the intrinsic channel region of the device. As a result of which the tunneling current of the device improves [15]. Hence, by introducing channel engineering, the ON current can be boosted.

Due to band-to-band tunneling (BTBT) mechanism, the thin pocket intrinsic layers will raise the  $I_{ON}$  for both double-gate and triple-gate pocket intrinsic TFET structures. The maximum  $I_{ON}$  is recorded for TG-PI-TFET as  $1.236 \times 10^{-4}$  A/ $\mu\text{m}$ , whereas for DG-PI-TFET is  $1.018 \times 10^{-4}$  A/ $\mu\text{m}$ .

The paper shows a detailed comparison between double-gate and triple-gate tunnel FET structures. The modifications in channel engineering are also performed by comparing double-gate and triple-gate pocket intrinsic tunnel FETs. The typical device parameters are mentioned in Table 1 [16, 17]. The review on double-gate and triple-gate TFET structures explicitly showcase the limitations on the drive current  $I_{ON}$  after incorporating the gate and channel engineering.

## 2 Device Structures and Simulation

### 2.1 Device Specifications

Figure 1 shows the cross-sectional view of silicon-on-insulator tunnel FET (SOI-TFET) with conventional double-gate structure aiming to boost in the drive current ( $I_{ON}$ ). The double gates are placed in both the front and back of the gate oxide layer of 2 nm thickness. The drain current obtained under transfer characteristics is not satisfactory for fast-switching device.

Since boosting of  $I_{ON}$  has been a real challenge, the structure in Fig. 1 has been modified by incorporating thin pocket intrinsic layers in both the front and back of silicon substrate in Fig. 2, in which the drain region has been extended in order to access overlapping region from 20 to 50 nm.

**Table 1** Typical parameters of various tunnel FET structures

Parameters	DG-TFET	DG-PI-TFET	TG-TFET	TG-PI-TFET
Gate length/intrinsic channel length ( $L_{ch}$ ) (nm)	60	30	60	30
Tunneling length ( $L_t$ )	–	30 nm	–	30 nm
Length of source ( $L_s$ ) (nm)	20	20	20	20
Length of drain ( $L_d$ ) (nm)	20	50	20	50
Length of gate gap ( $L_{gg}$ )	–	–	2 nm	2 nm
Length of every separated gate ( $L_{gm}$ and $L_{gc}$ )				
$[L_{ch} = L_{gm} + L_{gg} + L_{gc}]$	–	–	29 nm	29 nm
Gate oxide thickness ( $T_{oxf}$ ) (nm)	2	2	2	2
Gate oxide thickness ( $T_{oxb}$ ) (nm)	2	2	2	2
Silicon film thickness ( $T_{si}$ ) (nm)	10	10	10	10
P <sup>+</sup> source doping concentration ( $N_a$ )	$1 \times 10^{20} \text{ cm}^{-3}$	$1 \times 10^{20} \text{ cm}^{-3}$	$1 \times 10^{20} \text{ cm}^{-3}$	$1 \times 10^{20} \text{ cm}^{-3}$
N <sup>+</sup> drain doping concentration ( $N_d$ )	$1 \times 10^{17} \text{ cm}^{-3}$	$1 \times 10^{17} \text{ cm}^{-3}$	$1 \times 10^{17} \text{ cm}^{-3}$	$1 \times 10^{17} \text{ cm}^{-3}$
Intrinsic doping concentration ( $N_i$ )	$1 \times 10^{15} \text{ cm}^{-3}$	$1 \times 10^{15} \text{ cm}^{-3}$	$1 \times 10^{15} \text{ cm}^{-3}$	$1 \times 10^{15} \text{ cm}^{-3}$
Pocket intrinsic thickness ( $T_{in}$ )	–	5 nm	–	5 nm
Gate voltage ( $V_{GS}$ )	3 V	3 V	3 V ( $V_{GM} = V_{GC}$ )	3 V ( $V_{GM} = V_{GC}$ )
Supply voltage ( $V_D$ ) (V)	1	1	1	1
Gate work-function ( $\Phi$ ) (eV)	4.8	4.8	4.8	4.8

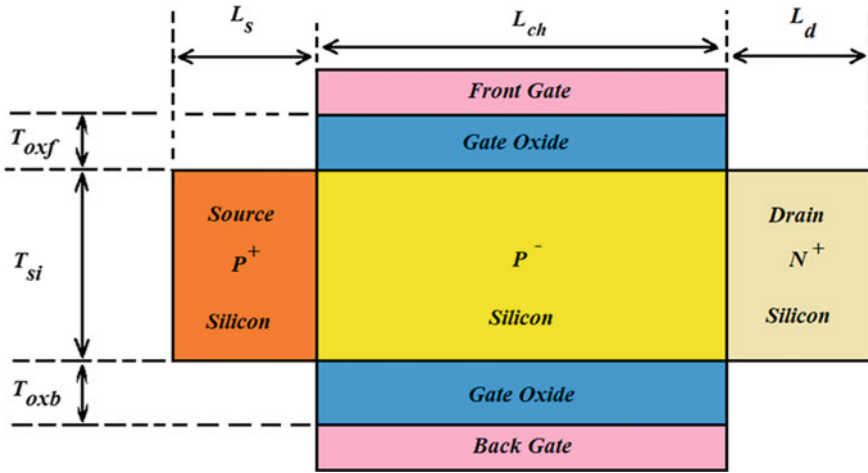


Fig. 1 Cross-sectional view of SOI-TFET with conventional double-gate structure

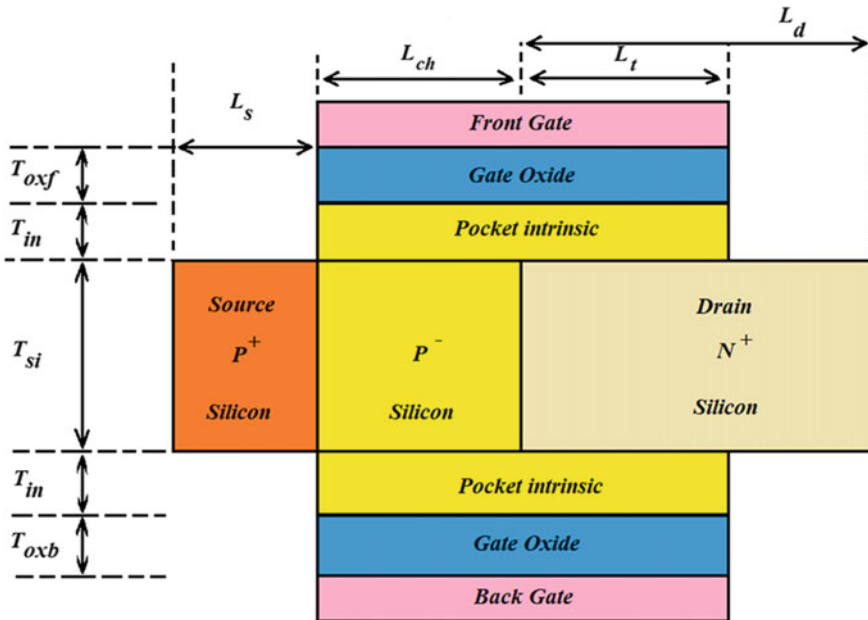


Fig. 2 Cross-sectional view of modified double-gate tunnel FET structure with pocket intrinsic layer (DG-PI-TFET)

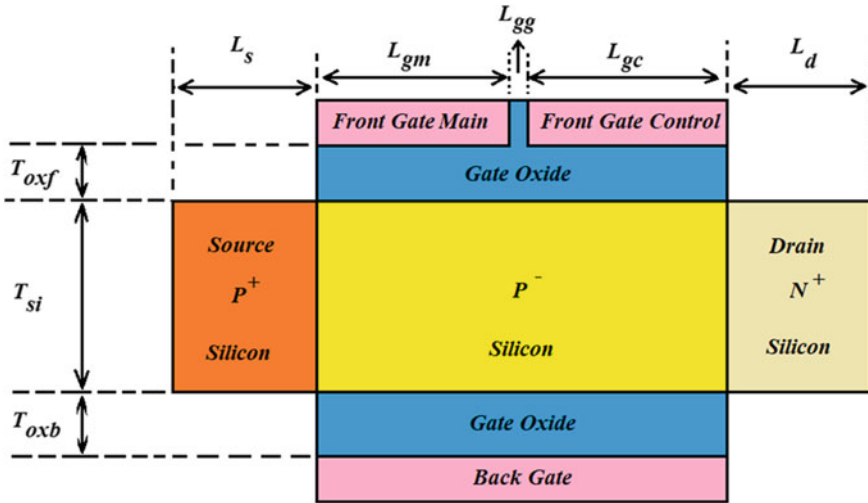


Fig. 3 Cross-sectional view of triple-gate tunnel FET (TG-TFET) structure

The modified DG-TFET structure with pocket intrinsic layer (DG-PI-TFET) shows a considerable increase in the ON current. But the leakage current ( $I_{OFF}$ ) has been an issue as for fast switching, the  $I_{ON}/I_{OFF}$  ratio plays a major role.

Therefore, by introducing gate engineering, the front gate has been redesigned into two lateral poly gates having length of 29 nm each. A narrow vertical gap of 2 nm is created in between of the two freshly separated gates named as front gate main and front gate control. The vertical gap is filled with same gate oxide material, i.e., silicon. The cross-sectional view of triple-gate tunnel FET (TG-TFET) structure is shown in Fig. 3. The modified TFET structure with triple gates enhances better control on the transposition of carriers through quantum BTBT tunneling. This exhibits a high  $I_{ON}/I_{OFF}$  ratio for a channel length of 60 nm compared to DG-TFET.

Although multigate structure of tunnel FET provides better drive current ( $I_{ON}$ ), the leakage current has been an issue for obtaining better switching ( $I_{ON}/I_{OFF}$ ) ratio. Keeping this limitation in view, the thin pocket intrinsic layers are placed similar to that of double-gate pocket intrinsic tunnel FET structure for analyzing  $I_{ON}$ ,  $I_{OFF}$ , and  $I_{ON}/I_{OFF}$  ratio.

Figure 4 shows the cross-sectional view of modified triple-gate structure with pocket intrinsic layer keeping the silicon film thickness and the gate length unaltered, and the drain region has been extended from 30 to 50 nm in order to access overlapping region. In addition to this, the triple gates (i.e., front gate main, front gate control, and back gate) will help to control the barrier width better. This overlapping region has been observed as an effective gate length or tunneling length. By using BTBT quantum tunneling phenomenon, the probability of transposition of carriers from source to drain is increased.

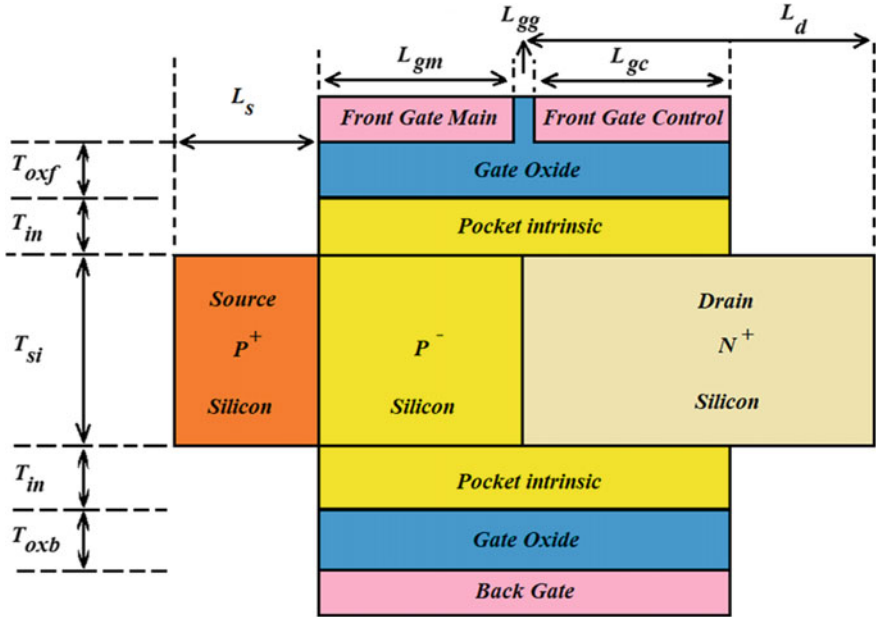


**Fig. 4** Cross-sectional view of modified triple-gate structure with pocket intrinsic layer (TG-PI-TFET)

The modified triple-gate tunnel FET structure with pocket intrinsic layer (TG-PI-TFET) shows a considerable increase in the ON current without degrading the leakage current for obtaining better  $I_{ON}/I_{OFF}$  ratio.

### 2.2 Device and Electrical Parameter Analysis

The DG-TFET, DG-PI-TFET, TG-TFET, and TG-PI-TFET are designed by varying the device and electrical parameters mentioned below. The typical parameters for the above-mentioned tunnel FET structures are summarized in Table 1.

### 2.3 Simulation Framework

The double-gate and triple-gate tunnel FET devices with their modified pocket intrinsic structures, i.e., DG-TFET, DG-PI-TFET, TG-TFET, and TG-PI-TFET, are designed in Silvaco TCAD device simulator. The results have been thoroughly compared and analyzed.

In this paper, the Shockley–Read–Hall (SRH) model is used for the recombination effects at junctions. Velocity saturation in high electric field is modeled using the field-dependent mobility (FLDMOB) model. The band gap narrowing (BGN) model has been used for high doping concentration, and the non-local, band-to-band tunneling (BTBT) model is introduced for the tunneling in lateral ( $X$ -) direction.

### 3 Results and Discussions

#### 3.1 Transfer Characteristics

The  $I_{ON}$  characteristics for all different TFET structures are performed with gate voltage ( $V_{GS}$ ) variation from 0 to 3 V. The drain current was obtained in log scale where the triple-gate PI-TFET attains maximum value of  $I_{ON}$  as  $1.236 \times 10^{-4}$  A/ $\mu\text{m}$ , whereas the conventional DG-TFET, DG-PI-TFET, and TG-TFET provide  $(I_{DS})_{max}$  as  $0.496 \times 10^{-4}$ ,  $1.018 \times 10^{-4}$ , and  $1.110 \times 10^{-4}$  A/ $\mu\text{m}$ , respectively, as shown in Fig. 5.

To analyze the  $I_{OFF}$  characteristics for different multigate TFET structures, the gate voltage ( $V_{GS}$ ) is varied from  $-3$  to 0 V. The drain current was obtained in log scale where the TG-PI-TFET attains minimum value of  $I_{OFF}$  as  $2.135 \times 10^{-5}$  A/ $\mu\text{m}$ , whereas the conventional DG-TFET, DG-PI-TFET, and TG-TFET provide  $(I_{DS})_{min}$

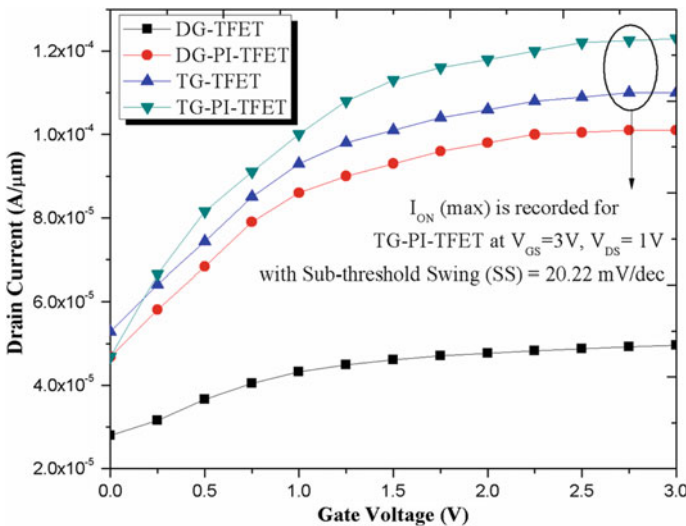


**Fig. 5** Comparison of transfer characteristics ( $I_{ON}$ ) of DG-TFET, DG-PI-TFET, TG-TFET, and TG-PI-TFET. The  $I_D$  versus  $V_{GS}$  curves, where  $I_D$  in log scale and  $V_{GS}$  in linear scale when  $V_{DS} = 1.0$  V

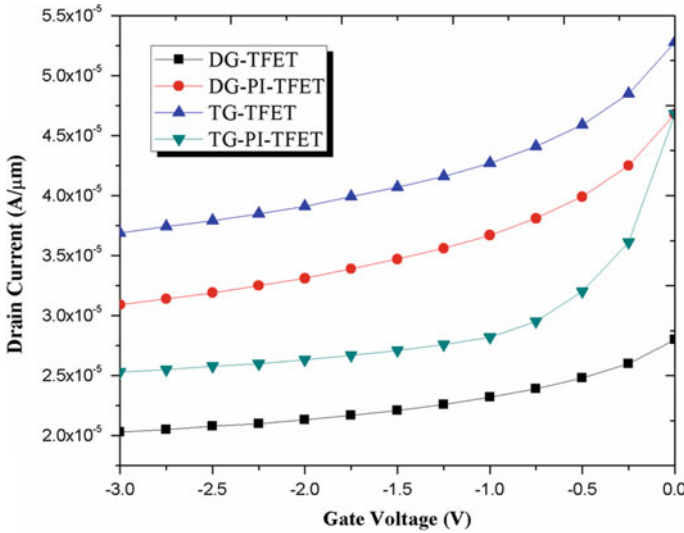


**Fig. 6** Comparison of transfer characteristics ( $I_{OFF}$ ) of DG-TFET, DG-PI-TFET, TG-TFET, and TG-PI-TFET. The  $I_D$  versus  $V_{GS}$  curves, where  $I_D$  in log scale and  $V_{GS}$  in linear scale when  $V_{DS} = 1.0$  V

**Table 2**  $I_{ON}/I_{OFF}$  ratio of DG-TFET, DG-PI-TFET, TG-TFET, and TG-PI-TFET for gate voltage variation with  $V_{DS} = 1$  V

Devices	$I_{ON}$ at $V_{GS}=3$ V	$I_{OFF}$ at $V_{GS}= -3$ V	$I_{ON}/I_{OFF}$ ratio
DG-TFET	$0.496 \times 10^{-4}$ A/ $\mu$ m	$2.035 \times 10^{-5}$ A/ $\mu$ m	2.43
DG-PI-TFET	$1.018 \times 10^{-4}$ A/ $\mu$ m	$3.113 \times 10^{-5}$ A/ $\mu$ m	3.27
TG-TFET	$1.110 \times 10^{-4}$ A/ $\mu$ m	$3.595 \times 10^{-5}$ A/ $\mu$ m	3.09
TG-PI-TFET	$1.236 \times 10^{-4}$ A/ $\mu$ m	$2.135 \times 10^{-5}$ A/ $\mu$ m	5.79

as  $2.035 \times 10^{-5}$ ,  $3.113 \times 10^{-5}$ , and  $3.595 \times 10^{-5}$  A/ $\mu$ m, respectively, as shown is Fig. 6.

The  $I_{ON}/I_{OFF}$  characteristics of DG-TFET, DG-PI-TFET, TG-TFET, and TG-PI-TFET are clearly depicted in Fig. 7.

It can be seen that to boost  $I_{ON}$ , the leakage current ( $I_{OFF}$ ) simultaneously plays very important role for designing fast-switching device. Due to reduction in  $I_{OFF}$  for the TG-PI-TFET structure, the sub-threshold slope can be increased. Table 2 provides the detailed analysis and comparison of  $I_{ON}$ ,  $I_{OFF}$ , and  $I_{ON}/I_{OFF}$  ratio.

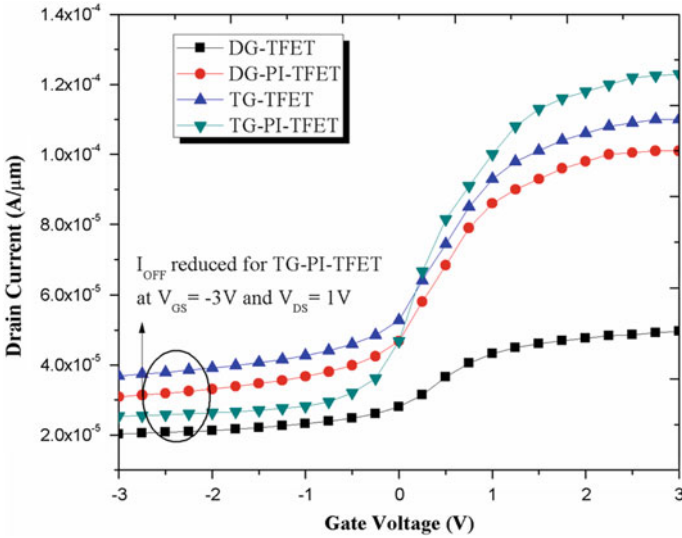


**Fig. 7**  $I_{ON}/I_{OFF}$  characteristics of DG-TFET, DG-PI-TFET, TG-TFET, and TG-PI-TFET. The  $I_D$  versus  $V_{GS}$  curves where  $I_D$  in log scale and  $V_{GS}$  in linear scale when  $V_{DS} = 1.0$  V

### 3.2 Sub-threshold Swing (SS)

Keeping the overall gate length same as 60 nm for all multigate tunnel FET structures, the sub-threshold swing (SS) is also measured and compared at  $V_{DS} = 1$  V,  $T_{si} = 10$  nm,  $T_{ox} = 2$  nm. Since in all the transfer characteristics curves the drain current ( $I_d$ ) is taken in log scale, using the formula for finding SS swing the comparison report is thoroughly investigated.

$$\text{Sub-threshold Swing (SS)} = \frac{dV_g}{d(\log_{10} I_d)} \text{ mV/dec}$$

The comparison report is shown in Table 3.



**Table 3** Sub-threshold swing ( $SS$ ) of DG-TFET, DG-PI-TFET, TG-TFET, and TG-PI-TFET for gate voltage variation  $V_{GS}$  from  $-3$  to  $3$  V with  $V_{DS} = 1$  V

Devices	Sub-threshold swing ( $SS$ ) (mV/dec)
DG-TFET	47.10
DG-PI-TFET	25.05
TG-TFET	22.72
TG-PI-TFET	20.22

The sub-threshold swing ( $SS$ ) provided by the TG-PI-TFET has been recorded as 20.22 mV/dec which is much less than that of other non-conventional TFET structures (DG-TFET, DG-PI-TFET, and TG-TFET).

## 4 Conclusion

In this work, we have reviewed various multigate TFET structures by using 2D TCAD simulations on the performance enhancement of  $I_{ON}$  for the low-power applications.  $I_{ON}/I_{OFF}$  and  $SS$  as figures of merit for DC performance are also investigated.  $I_{ON}/I_{OFF}$  is significantly larger in TG-PI-TFET making the device suitable for low-power sensor applications. So this shows need of optimization throughout the TFET device that could pave the way to operate the TFET consistently even if the gate leakage current is included.

## References

1. N. Thomas, H.S. Philip Wong, The end of Moore's Law: a new beginning for information technology. *IEEE J. Comput. Sci. Eng.* **19**(2), 41–50 (2017)
2. D.E. Nikonov, I.A. Young, Overview of beyond-CMOS devices and a uniform methodology for their benchmarking. *Proc. IEEE* **101**(12), 2498–2533 (2013)
3. A. Seabaugh, C. Alessandri, H.M. Li, P. Paletti, Steep slope transistors: tunnel FETs and beyond, in *Proceedings 46th European Solid State Device Research Conference*, pp. 349–351 (IEEE, 2016)
4. W.Y. Choi, B.G. Park, J.D. Lee, T.J. King Liu, Tunneling field-effect transistors (TFETs) with sub-threshold swing ( $SS$ ) less than 60 mV/dec, *IEEE Electron Dev. Lett.* **28**(8), 743–745 (2007)
5. Q. Zhang, W. Zhao, A. Seabaugh, Low-subthreshold-swing tunnel transistors, *IEEE Electron Dev. Lett.* **27**(4), 297–300 (2006)
6. A.V. Hraziaia, A. Amara, C. Anghel, An analysis on the ambipolar current in Si double-gate tunnel FETs. *Solid-State Electron.* **70**, 67–72 (2012)
7. N. Bagga, S. Sarkhel, S.K. Sarkar, Recent research trends in gate engineered tunnel FET for improved current behavior by subduing the ambipolar effects: a review, in *The Proceedings of IEEE International Conference on Computing, Communication & Automation, India* (2015)
8. A. Pal, A.B. Sachid, H. Gossner, V.R. Rao, Insights Into the design and optimization of tunnel-FET devices and circuits. *IEEE Trans. Electr. Dev.* **58**(4), 1045–1053 (2011)
9. S. Datta, H. Liu, V. Narayanan, Tunnel FET technology: a reliability perspective. *Microelectron. Reliab.* **54**, 861–874 (2014)

10. D. Leonelli, A. Vandooren, R. Rooyackers, S. Gendt, M.M. Heyns, G. Groeseneken, Drive current enhancement in p-tunnel FETs by optimization of the process conditions. *Solid-State Electron.* **65**, 28–32 (2011)
11. K. Boucart, A.M. Ionescu, Length scaling of the double gate tunnel FET with a high-K gate dielectric. *Solid-State Electron.* **51**, 1500–1507 (2007)
12. A.S. Verhulst, B. Sorée, D. Leonelli, W.G. Vandenberghe, G. Groeseneken, Modeling the single-gate, double-gate, and gate-all-around tunnel field-effect transistor. *J. Appl. Phys.* **107**(2), 024518 (2010)
13. J. Seunggyu, K. Hyungtak, C. Hwan, Characteristics of recess structure tunneling field-effect transistor for high on current drivability. *J. Semicond. Technol. Sci.* **18**(3) (2018)
14. S. Wei, G. Zhang, L. Geng, Z. Shao, C.F. Yang, *Comparison of the Performance Improvement for the Twonovel SOI-tunnelFETs with the Lateral Dual-Gate and Triple-Gate* (Microsystem Technologies, Springer, 2018)
15. R. Jhaveri, V. Nagavarapu, J. Woo, Effect of pocket doping and annealing schemes on the source-pocket tunnel field-effect transistor. *IEEE Trans. Electron Dev.* **58**(1), 80–86 (2011)
16. M.J. Kumar, S. Ramaswamy, Double gate symmetric tunnel FET: investigation and Analysis, *IET Circuits, Devices and Systems*, Vol. 11, No. 4, pp. 365–370, (2017)
17. M. Graef, F. Hosenfeld, F. Horst, A. Farokhnejad, F. Hain, B. Iñíguez, A. Kloes, Advanced analytical modeling of double-gate Tunnel-FETs—a performance evaluation. *Solid-State Electron.* **141**, 31–39 (2018)

# Quantitative Structure–Activity Relationship (QSAR) Study of Some DNA-Intercalating Anticancer Drugs



Indrani Sarkar, Sanjay Goswami and Paushali Majumder

**Abstract** Small molecular anticancer drugs bind reversibly to DNA and are used in chemotherapy. The experimental measurements of the inhibition activity of drugs are difficult, expensive, and time-consuming. So, quantitative structure–activity/property relationship method (QSAR) is adopted where the dependency of drug binding affinity with their structural features is exploited. To explore whether molecular descriptors can explain their DNA-binding affinity and toxicity, 23 antitumor molecules, which are being used clinically as drugs, are analyzed by rigorous statistical calculations. The 50% cancer cell growth inhibition constant ( $IC_{50}$ ) for any particular cancer cell line is obtained from the NCI/NIH database. Molecular descriptors (geometrical, physicochemical, and quantum chemical) are calculated for the molecules. A mathematical model is built to predict DNA-drug-binding constant and growth inhibitory concentration by multiple regression which can be useful for rational drug design.

**Keywords** QSAR · Anticancer drugs · Genetic algorithm applications

## 1 Introduction

**QSAR-** (Quantitative Structure Activity Relationship) provides a method to predict the pharmacological activity of a set of compounds. It is based on the relationship between molecular features and activity. Anthracyclines inhibit DNA replication and RNA synthesis by intercalating between base pairs of the DNA/RNA strand,

---

I. Sarkar (✉)

Department of Physics, Narula Institute of Technology, Kolkata, India  
e-mail: [indrani.sarkar@nit.ac.in](mailto:indrani.sarkar@nit.ac.in)

S. Goswami · P. Majumder

Department of Computer Applications, Narula Institute of Technology, Kolkata, India  
e-mail: [sanjay.goswami@nit.ac.in](mailto:sanjay.goswami@nit.ac.in)

P. Majumder

e-mail: [mail2paushalimajumder@gmail.com](mailto:mail2paushalimajumder@gmail.com)

© Springer Nature Singapore Pte Ltd. 2020

K. Maharatna et al. (eds.), *Computational Advancement in Communication Circuits and Systems*, Lecture Notes in Electrical Engineering 575,  
[https://doi.org/10.1007/978-981-13-8687-9\\_32](https://doi.org/10.1007/978-981-13-8687-9_32)

thus preventing the replication of rapidly growing cancer cells. The anthracyclines' family drugs composed of 23 substituted derivatives are studied, and the activity for prediction is the  $\log IC_{50}$  (50% inhibitory concentration). The topological and physicochemical descriptors are studied separately for the investigation of QSAR of these drugs. Multiple linear regressions are performed to find correlation on substituent of *anthracycline* (Table 1; Fig. 1).

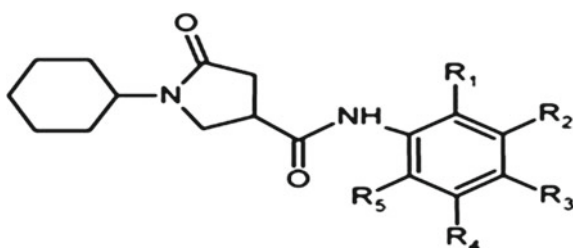
**Table 1** Different *substituents* on 23 compounds

No.	R1	R2	R3	R4	R5	R6	R7
1	OCH <sub>3</sub>	H	H	O	OH	H	COCH <sub>2</sub> OH
2	OCH <sub>3</sub>	H	H	O	OH	H	COCH <sub>3</sub>
3	H	H	H	O	OH	H	COCH <sub>3</sub>
4	OCH <sub>3</sub>	H	H	O	OH	H	COCH <sub>2</sub> OCH <sub>3</sub>
5	OCH <sub>3</sub>	H	H	O	OH	H	COCH <sub>3</sub>
6	OCH <sub>3</sub>	H	H	O	OH	H	COCH <sub>2</sub> OH
7	OCH <sub>3</sub>	H	H	O	OH	H	COCH <sub>2</sub> OH
8	OCH <sub>3</sub>	H	H	O	OH	H	COCH <sub>2</sub> OH
9	OCH <sub>3</sub>	H	H	O	OH	H	COCH <sub>3</sub>
10	OCH <sub>3</sub>	H	H	O	OH	H	COCH <sub>2</sub> OH
11	OC <sub>6</sub> H <sub>5</sub>	H	H	O	OH	H	COCH <sub>3</sub>
12	OCH <sub>3</sub>	H	H	O	OH	H	CHCH <sub>3</sub> OH
13	OCH <sub>3</sub>	H	H	O	OH	H	COCH <sub>2</sub> OH
14	OCH <sub>3</sub>	H	H	NH	OH	H	COCH <sub>3</sub>
15	OCH <sub>3</sub>	H	H	O	OH	H	COCH <sub>2</sub> OH
16	OCH <sub>3</sub>	H	H	O	OH	H	COCH <sub>2</sub> OH
17	OCH <sub>3</sub>	H	H	O	OH	H	COCH <sub>2</sub> OH
18	OCH <sub>3</sub>	H	H	O	OH	H	
19	OCH <sub>3</sub>	H	H	O	OH	H	COCH <sub>2</sub> OH
20	H	H	H	O	OH	H	COCH <sub>2</sub> Br
21	OH	H	H	O	OH	COOCH <sub>3</sub>	CH <sub>2</sub> CH <sub>3</sub>
22	OCH <sub>3</sub>	H	H	O	OH	H	C(NNHCO <sub>6</sub> H <sub>5</sub> (CH <sub>3</sub> ))
23	OCH <sub>3</sub>	H	H	O	OH	H	COCH <sub>2</sub> OCO(CH <sub>2</sub> ) <sub>3</sub> CH <sub>3</sub>

(continued)

**Table 1** (continued)

No.	R8	R9	R10	R11	R12	EXP
1	H	H	NH <sub>2</sub>	OH	H	1.27
2	H	H	NH <sub>2</sub>	OH	H	1.83
3	H	H	OH	OH	H	0.9
4	H	H	NH <sub>2</sub>	OH	H	1.37
5	H	H	N(CH <sub>3</sub> ) <sub>2</sub>	OH	H	1.405
6	H	H	NH <sub>2</sub>	OCH <sub>3</sub>	H	0.94
7	H	H	NH <sub>2</sub>	H	H	1.83
8	H	H	NH <sub>2</sub>	H	H	0.68
9	H	H	OH	OH	H	1.34
10	H	H	N(CH <sub>3</sub> ) <sub>2</sub>	OH	H	1.56
11	H	H	NH <sub>2</sub>	OH	H	2.02
12	H	H	NH <sub>2</sub>	OH	H	0.62
13	H	H	OH	OH	H	1.75
14	H	H	NH <sub>2</sub>	OH	H	0.8
15	H	H	NH(CH(CN)(CH <sub>2</sub> OCH <sub>3</sub> ))	OH	H	0.92
16	H	H	Aromatic side chain	OH	H	0.42
17	H	H	NH <sub>2</sub>	OH	H	0.72
18	H	H	NH <sub>2</sub>	OH	H	0.479
19	H	F	Aromatic side chain	OH	H	0.286
20	H	H	OH	OH	H	2.5
21	H	H	N(CH <sub>3</sub> ) <sub>2</sub>	OH	H	2.23
22	H	H	NH <sub>2</sub>	OH	H	1.13
23	H	H	NHCOCF <sub>3</sub>	OH	H	2.2

**Fig. 1** Schematic representation of different anthracycline drugs (the different functional groups are identified)

## 2 Methodology

### 2.1 Structure-Based Drug Design Steps

The objective of this work is to develop mathematical models in terms of molecular descriptors to encode information about each of the molecular structures. The biological activity of the molecules is measured by  $\log IC_{50}$  (50% inhibitory concentration). The molecular descriptors are used to build statistical or computational neural network models to predict the property or activity of interest [1, 2].

The molecular structure of a chemical compound is related to its properties, but there is no direct method for prediction of the properties. So, indirect approach is used. It has two main parts. In the first part, each molecular structure is used to calculate structural descriptors, and in the second part subset of descriptors are chosen and good models are proposed to predict the properties. This model can be statistical models or neural network models. It depends on a set of structures with experimentally determined properties. These set of known compounds are used to develop the model. The main steps of QSAR study are: Structure entry and molecular modeling  $\rightarrow$  Descriptor generation  $\rightarrow$  Feature selection  $\rightarrow$  Construct Model MLRA or CNN  $\rightarrow$  Model validation.

## 3 Procedure

### 3.1 Molecular Modeling

The molecular structures for 23 anthracycline molecules (Table 2) are searched in the chemical database by pharmacophore selection. The 3D models of structures are generated by the software Avogadro. The structures are subjected to energy minimization with MOPAC. These energy minimized three-dimensional molecular structures are used to generate descriptors by using their topological and geometrical properties. The structures of organic compounds can be represented as graphs. The theorems of graph theory can be applied to generate graph invariants which are known as topological descriptors.

### 3.2 Molecular Descriptor Generation

Topological descriptors selected here are Balaban Connectivity Index, chi connectivity, atomic polarizability, molecular weight, Pauling electronegativity, van der Waals volume, hydrogen bond donor, hydrogen bond acceptor, MlogP, logS, rotat-

Table 2 Descriptors generated

Compound	1st	2nd	3rd	4th	5th	6th	7th	8th	9th	10th	11th
Properties											
MTI (Schultz molecular topographical index)	3173	3173	3543	3543	3173	3173	3543	3543	3543	3543	4173
S (electro-topographical state)	48.35	49.85	56.02	57.52	44.46	49.85	52.13	48.24	51.64	65.6	45.95
LogW	2.8609	2.8609	2.913	2.9133	2.8609	2.8609	2.9133	2.9133	2.9133	3.0298	2.9795
LogP	1.176	0.832	1.424	1.08	1.479	1.231	1.823	2.222	2.126	1.936	0.31
ST	45.4	42.3	42.9	40.2	49.6	46.1	47	51.1	47.5	40.4	60.6
Pol	28.09	30.2	28.03	30.14	29.96	32.07	29.91	31.78	35.21	30.02	30.38
Balaban index	1.50225	1.49622	1.48118	1.50382	1.49175	1.49175	1.48955	1.48955	1.49622	1.48458	1.3026
Balaban connectivity index Jt	3.79827	3.78353	3.75404	3.78188	3.76361	3.78761	3.74789	3.74789	3.78353	3.73517	3.27102
Atomic polarizability	374.5	358	350.4	374.5	380.5	397.02	364.02	364.02	349.62	391.78	414.3
Chi connectivity	2.6596	2.64264	2.62522	2.66035	2.65105	2.67345	2.63627	2.64264	2.64264	2.65006	2.64437
Molecular weight	530.297	502.286	488.279	530.297	526.308	554.319	498.298	498.298	508.267	538.319	562.341
Pauling electronegativity	113.17	107.18	104.14	113.17	112.28	118.27	106.29	106.29	108.47	114.83	119.93
Van der Waals volume	560.826	534.359	522.66	560.826	565.228	591.695	538.761	538.761	529.29	580.662	611.532
Weiner index	4659	4044	3780	4663	4686	5337	4071	4071	4044	5056	5874
First-order Zagreb index	226	216	212	224	226	234	214	214	216	230	244
Second-order Zagreb index	284	270	266	279	282	294	266	266	270	287	302
I2 (substitution in R2)	0	0	1	1	0	0	1	1	1	0	0
I1 (substitution in R1)	0	1	0	1	0	1	0	0	1	0	0
I(1,7) (substitution in R1 and R7)	0	1	0	1	0	1	0	0	1	0	0
I(3,8) (substitution in R3 and R8)	0	0	0	0	0	0	0	0	0	0	0

(continued)

Table 2 (continued)

Compound	12th	13th	14th	15th	16th	17th	18th	19th	20th	21st	22nd	23rd
Properties												
MTI (Schultz molecular topographical index)	4523	4523	4523	4523	6119	5111	4173	4173	4523	4523	3629	4029
S (electro-topographical state)	53.62	5.12	49.73	51.23	70.87	58.02	44.35	45.85	53.52	48.13	50.35	58.02
LogW	3.0265	3.0265	3.0265	3.0265	3.1658	3.0824	2.9795	2.9795	3.0265	3.0265	2.9238	2.7931
LogP	0.902	0.558	1.301	0.957	1.662	-0.58	-0.889	-0.71	-0.462	0.281	-0.058	0.19
ST	57.2	52.5	61.8	56.5	50	54.4	49.3	48.7	47.2	55.7	48.5	46.1
Pol	30.33	32.44	32.2	34.32	32.26	32.16	29.3	31.26	30.96	30.72	32.83	32.78
Balaban index	1.48471	1.48536	1.49622	1.44577	1.28128	1.50393	1.50393	1.28128	1.49226	1.55969	1.28434	1.47705
Balaban connectivity index Jt	3.73455	3.74503	3.78353	3.59369	3.1966	3.79438	3.79438	3.1966	3.76477	3.94492	3.19899	3.70233
Atomic polarizability	358	366.9	360.36	427.14	436.82	361.7	365.6	427.14	360.17	397.02	452.02	424.78
Chi connectivity	2.63249	2.63883	2.64264	2.637	2.63791	2.655	2.655	2.63791	2.63413	2.71891	2.65098	2.66321
Molecular weight	502.286	516.29	500.293	592.347	586.363	521.285	516.293	592.347	556.172	554.319	614.377	594.34
Pauling electronegativity	107.18	110.13	106.78	126.41	125.03	111.16	110.22	126.41	104.55	118.27	131.11	126.81
Van der Waals volume	534.359	549.127	535.025	634.263	642.401	544.338	546.057	634.263	527.116	591.695	665.799	633.597
Weiner index	4079	4392	4044	6764	6756	4334	4334	6756	3758	5162	7654	6648

(continued)





able bonds, Unsaturation Index, hydrophilic groups, Hydrophilic Index, first- and second-order Zagreb index, Wiener Index, Topographical Index, Randic Branching Index, Schultz Molecular Topographical Index, Szeged index, electro-topological state [3–5].

### 3.3 Genetic Algorithm for Selection of Best Descriptors

After calculation of the descriptors, a reduced set of descriptors are selected which are rich in information but smallest in size. The feature selection process is done by the genetic algorithm variable selection technique. A subset of descriptors is selected to relate with  $IC_{50}$  values. MLR regression method determines the root-mean-square error of cross-validation (RMSECV) when using only that subset of variables in a regression model. It is found that  $IC_{50}$  depends highly on Schulz Molecular Topographical Index (MTI), electro-topological state (S), Wiener Index (W), polarizability (Pol), and partition coefficient (logP).

## 4 Results and Discussion

The biological activity  $IC_{50}$  is taken as the dependent variable and the six molecular descriptors as independent variables to build the model. The result found is the geometrical molecular descriptors when taken for univariate correlation are insufficient to describe the structure activity relationship. The low correlation values ( $R = 0.5$ ) are not taken. All the univariate relationship shows very low coefficient. The best statistics is shown by S.

For bivariate correlation, best statistics is shown by MT1 and I2 (substitution at R2). For trivariate correlation, best solution is shown by MT1, logP, and Pol. For tetravariate, MT1, logP, Pol, and logW; for pentavariate, MT1, logP, Pol, logW, and S; and for hexavariate, MT1, logP, Pol, logW, S, and I2 (substitution at position 2 shows best statistics) are the best combinations.

The mathematical model obtained from above variables is given by

$$IC_{50} = 0.0007 MTI - 3.4 \text{ LogW} - 0.45 \text{ LogP} + 0.24 \text{ Pol} - 0.21S - 0.6 I2 + 11.02$$

The above equation is validated for the experimental value of  $\log IC_{50}$  (Table 3).

**Table 3** Observed and calculated values of IC<sub>50</sub>

Compounds	LogIC <sub>50</sub> (obs.)	LogIC <sub>50</sub> (calculated)	Residual
1	1.602	1.4956	0.1063
2	1.23	1.0841	0.1458
3	0.869	1.105	−0.236
4	0.708	0.6935	0.0144
5	0.973	1.5629	−0.5899
6	0.908	1.0841	−0.1761
7	0.301	1.1722	−0.8712
8	0.255	1.2395	−0.9845
9	0.462	0.7952	−0.3332
10	1.114	0.8771	0.2368
11	1	1.8575	−0.8575
12	0.176	1.4711	−1.2951
13	0.58	1.0596	−0.4796
14	0.255	1.5384	−1.2834
15	0.342	1.1269	−0.7849
16	0.544	1.8593	−1.3153
17	1.982	1.2464	0.7355
18	2.587	1.8852	0.7017
19	2.663	1.4737	1.1892
20	1.813	1.0873	0.7256
21	1.875	1.566	0.3089
22	2.58	1.1906	1.3893
23	1.477	1.4644	0.0125

## 5 Conclusion

A mathematical model for anthracycline drugs is obtained by using molecular descriptors, genetic algorithm multiple regression models, and molecular dynamics simulation. This shows the relation of graph theoretical and physicochemical descriptors with their activity.

**Acknowledgements** The authors are thankful to *University Grants Commission, India*, for providing necessary facilities.

## References

1. S. Vahdani, Z. Bayat, A Quantitative Structure Activity Relationship (QSAR) study of anti—cancer Drugs. *Pelagia Res. Lib., Der ChemicaSinica* **2**(4), 235–243 (2011)
2. J. Portugal, Evaluation of molecular descriptors for anti-tumor drugs with respect to no covalent binding to DNA and ant proliferative activity. *BMC Pharmacol.* **9**, 11 (2009)
3. A.T. Balaban, *J. Mol Struc (Theochem)* **165**, 243 (1988)
4. M. Randic, *Croat. Chem. Acta* **66**, 289 (1993)
5. H.P. Schltz, E.B. Schltz, T.P. Schltz, *J. Chem. INF Compute Sci.* **30**, 27 (1990)

# To Explore Compounds as Tuberculosis Inhibitors—A Combination of Pharmacophore Modelling, Virtual Screening and Molecular Docking Studies



Indrani Sarkar, Sanjay Goswami and Paushali Majumder

**Abstract** In the present work, a ligand-based 3D *pharmacophore* and QSAR approach is used for the selection of potentially active compounds for inhibitory action against the enoyl-ACP-reductase (InhA) from *Mycobacterium tuberculosis*, followed by molecular modelling, dynamic simulation and binding energy calculation methods. The biological activity of the molecules is measured by  $\log IC_{50}$  (50% inhibitory concentration). The molecular descriptors are used to build statistical models to predict the biological activity of interest.

**Keywords** QSAR · Pharmacophore modelling · Molecular computing

## 1 Introduction

In order to fight the increasing cases of multi-drug-resistant and extensively drug-resistant strains of *Mycobacterium tuberculosis* (MTb), new antituberculous drugs should be introduced. The enzymes involved in the synthesis of fatty acids are potential targets for drug design. The enoyl-ACP-reductase (InhA) is an enzyme in *M. Tuberculosis* that helps in the synthesis of mycolic acids. Mycolic acids are the main constituents of bacterial cell wall. The TB-specific drug targets the synthesis of mycolic acids by blocking the activity of InhA [1, 2].

Pyrrole derivatives which are known as antibacterial agents also have antitubercular activity. X-ray structure of InhA provided insight into the structural elements to its catalytic mechanism. The active site residues Tyr158 and lysine 165 are known

---

I. Sarkar (✉)

Department of Physics, Narula Institute of Technology, Kolkata, India  
e-mail: [indrani.sarkar@nit.ac.in](mailto:indrani.sarkar@nit.ac.in)

S. Goswami · P. Majumder

Department of Computer Applications, Narula Institute of Technology, Kolkata, India  
e-mail: [sanjaygoswamee@gmail.com](mailto:sanjaygoswamee@gmail.com)

P. Majumder

e-mail: [mail2paushalimajumder@gmail.com](mailto:mail2paushalimajumder@gmail.com)

© Springer Nature Singapore Pte Ltd. 2020

K. Maharatna et al. (eds.), *Computational Advancement in Communication Circuits and Systems*, Lecture Notes in Electrical Engineering 575,  
[https://doi.org/10.1007/978-981-13-8687-9\\_33](https://doi.org/10.1007/978-981-13-8687-9_33)

as catalytic residues. The glycine-rich loop is correlated with the attenuation of correlation of enzymic activities. Crystal structures of InhA in complex with the drug isoniazid refined to 1.40 Å have been reported (PDB 4TRO). InhA binding pocket has high substrate specificity [3, 4].

The number of three-dimensional structures of potential targets is increasing enormously in PDB bank and other databases. So, to deal with such a vast amount of data, we need a computer-aided tool like virtual screening to identify potential leads. Virtual screening can be considered as an *in silico* method which is an alternative to high throughput screening. The complementarity of shape of receptor and drug is important for receptor–drug interaction [5, 6].

A pharmacophore is described by the spatial arrangement of a group of structural elements which are essential for interaction with receptor. This approach of shape complementarity is used to develop a pharmacophore query from a group of inhibitors. This is based on the principle that receptor and drug have certain chemical features that favour interactions.

Molecular docking is another structure-based *in silico* method which uses high-resolution crystal structure of the target. These methods are combined to find a number of new compounds with potent inhibitory activity and also to understand their interaction at the binding site [7, 8].

## 2 Procedure

### 2.1 Dataset

A dataset of inhibitors was taken from ZINC data bank, and IC<sub>50</sub> values were collected from the literature [9]. The dataset contains pyrrole ring (Table 1).

### 2.2 Generation of Pharmacophore Hypotheses

Pharmacophore and 3D QSAR structure was generated using *Schrodinger Suite 9.4*. Six built-in features were used. These are hydrogen bond acceptor, hydrogen bond donor, hydrophobic group, negatively ionic, positively ionic and aromatic. A total of 80 compounds were ranked based on IC<sub>50</sub> values, 20 were test sets and others were training sets.

**Table 1** Compounds used for quantitative structure–activity studies

Compound	R1	R2	R3	R4	R5	IC <sub>50</sub> (micro M)
1	H	H	H	H	H	10.66
2	H	H	Br	H	H	28.02
3	H	Br	H	H	H	0.89
4	H	Cl	H	H	H	1.35
5	H	CF <sub>3</sub>	H	H	H	3.51
6	H	H	CH <sub>2</sub> COOH	H	H	73.58
7	H	NO <sub>2</sub>	H	H	H	10.59
8	Br	H	H	H	H	101.00
9	H	Cl	H	Cl	H	0.39
10	Cl	H	Cl	H	H	56.02
11	Cl	H	H	Cl	H	56.50
12	CH <sub>3</sub>	Cl	H	H	H	23.12
13	H	Cl	F	H	H	14.83
14	H	F	F	H	H	1.49
15	H	CH <sub>3</sub>	H	CH <sub>3</sub>	H	3.14
16	CH <sub>3</sub>	H	H	Cl	H	0.97
17	H	CF <sub>3</sub>	H	CF <sub>3</sub>	H	3.67
18	H	CH <sub>2</sub> (CH <sub>3</sub> ) <sub>2</sub>	H	H	H	5.55
19	H	OCH <sub>3</sub>	H	CF <sub>3</sub>	H	1.30
20	H	Br	H	CF <sub>3</sub>	H	0.85
21	H	CH <sub>3</sub>	H	H	H	16.79
22	H	H	Cl	H	H	101.00
23	H	CH <sub>3</sub>	Br	H	H	37.41

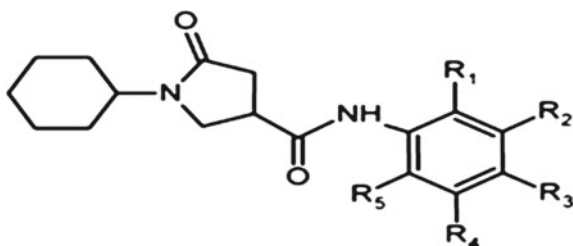
### 2.3 Virtual Screening

VS was carried out using ZINCPharmer ([www.zincpharmer.csb.pitt.edu](http://www.zincpharmer.csb.pitt.edu)). It searches ZINC database of fixed conformers to search for potential inhibitors.

### 2.4 Molecular Structure Preparation

The structures were drawn using *Avogadro* software, and energy-minimized structures of the inhibitor molecules were made. Energy minimization was done until the root-mean-square deviation (RMSD) of potential energy became less than 0.001. The *optimized potentials for liquid simulations (OPLS)* force field was used (Fig. 1).

**Fig. 1** Lead compound and general structure of pyrrolidine carboxamides



## 2.5 Model Building

Three-dimensional molecular models of InhA–inhibitor complexes were constructed from high-resolution (1.4 Å) X-ray crystal structure taken from *Protein Data Bank* (PDB ID 4TRO) (Fig. 2).

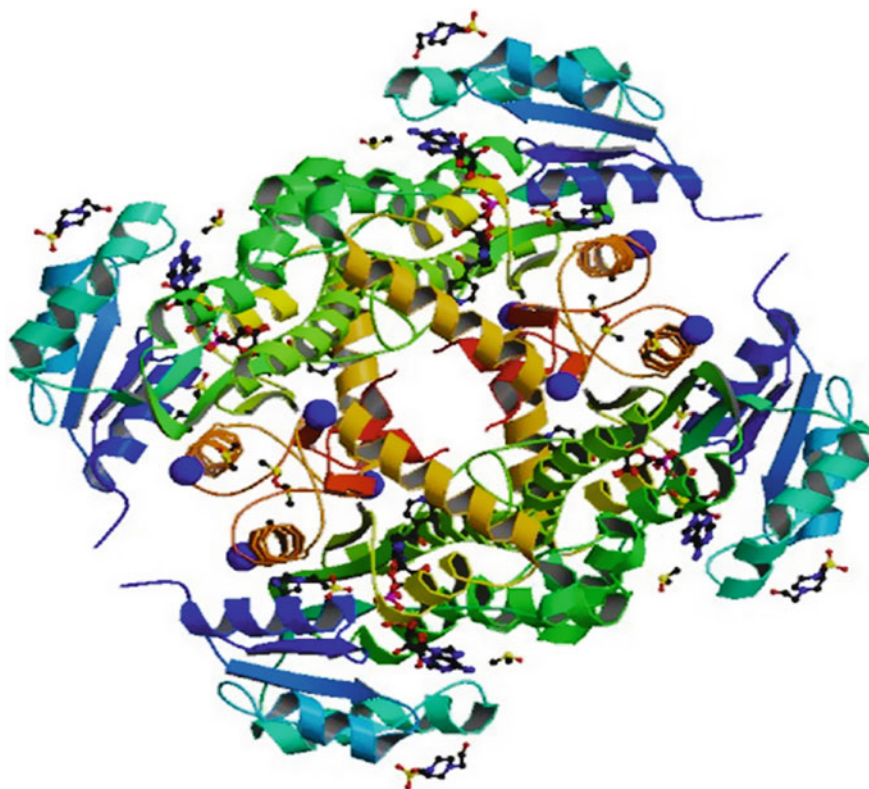


**Fig. 2** Crystal structure of enoyl-ACP reductase of *Mycobacterium tuberculosis* InhA, inhibited with isoniazid at 1.4 Å resolution



## 2.6 Molecular Docking Studies

The active compounds were flexibly docked into the active site of the InhA. All docking simulations were carried out using *AutoDock* program.

## 2.7 Statistical Analysis

The IC<sub>50</sub> values were used as a dependent variable, and the molecular descriptors calculated by *The Chemistry Development Kit* software were used as independent variables for QSAR model. Over 50 descriptors were calculated. To find the correlation between the individual descriptor and the biological activity (IC<sub>50</sub>), the following descriptors were selected by variable selection method. These were hydrogen bond donor, hydrogen bond acceptor, atomic polarizability, molar refractivity and dipole, water-accessible surface areas (WASA), volume, solvation energy and logP (o/w) (the log value of octanol/water partition coefficient of a compound).

## 2.8 Dynamic Simulation

Molecular dynamic simulation revealed the actual dynamic behaviour of the active site in inhibitor binding process. Analysis of dynamic trajectory gave insight about the role of different residues of the receptor protein. Analysis of potential energy, kinetic energy, total energy profile and RMSD/RMSF (root-mean-square deviation and root-mean-square fluctuation with respect to initial minimized structures) explained the global minimum energy of the InhA–inhibitor complexes. Analysis of H-bonding, hydrophobic interactions, salt bridge,  $\pi$ -interaction, electrostatic energy, van der Waals energy predicted the inhibitor binding pattern with the active site of the receptor. MD simulation was done by *Gromacs* software package.

## 2.9 Binding Free Energy Calculation

The binding free energy of the enzyme–inhibitor complex is given by the following equation:

$$\Delta G = \Delta H - T \Delta S$$

where  $T$  is the temperature of the complex. The binding free energy ( $\Delta G$ ) of the complex is given as follows:  $\Delta G = G_{\text{complex}} - [G_{\text{inhibitor}} + G_{\text{enzyme}}]$  where

Gcomplex is the absolute free energy of the complex, Genzyme is the absolute free energy of the enzyme, and Ginhibitor is the absolute free energy of the ligand.

The binding free energy values for potential inhibitors were calculated using the structures of enzyme–ligand complexes during explicit solvent molecular dynamic simulations [10, 11].

### 3 Result and Discussion

The Gly-rich loop of InhA is found to be responsible for the enzymic activity. Tyrosine 158 and lysine 165 are important catalytic residues of InhA. Tyrosine 158 is involved in catalysis, and lysine 165 helps in cofactor binding. The benzene ring of the inhibitor is stabilized in a hydrophobic cavity made up of the following non-polar residues: Met103, Gly104, Phe149, Met155, Pro156, Ala157, Tyr158, Pro193, Met199, Ile202, Leu207, Ala211, Gln214, Ile215 and Leu218. The hydrogen bonding network stabilizes the inhibitor within the binding pocket of InhA. The effect of different substitutions on the benzene ring is studied. The presence of –F and –Cl in R2 and R3 groups increases the potency of the inhibitor. R3 groups include F, Cl, Br and H atoms. Mostly, H atom is found in R3 position. The best substitution in R1 group is –CH<sub>3</sub> and other bulky hydrophobic groups like –OCH<sub>3</sub> and –COOCH<sub>3</sub>. R5 group is mostly –H or a hydrophobic group. This information can be useful in increasing the potency of these compounds.

### References

1. D.A. Rozwarski, Crystal structure of the *Micobacterium tuberculosis* enoyl-ACP reductase, InhA in complex with NAD<sup>+</sup> and a C16 fatty acyl substrate. *J. Biol. Chem.* **274**, 15582–15589 (1999)
2. S.R. Luckner, X ray crystal structure of a slow, tight binding inhibitor of InhA from *M. Tb*. *J. Biol. Chem.* **285**, 14330 (2010)
3. X. He et al., Pyrrolidine carboxamides as a novel class of inhibitors of InhA from *M. Tb*. *J. Med. Chem.* **49**(21), 6308–6323 (2006)
4. A. Punkvang et al., Investigating the structural basis of arylamides to improve potency against *M. Tuberculosis* strain through molecular dynamics simulation. *Eur. J. Med. Chem.* **45**, 5585–5593 (2010)
5. Schroeder et al, Molecular dynamics simulation studies of the wild type I 21V and I 16T mutants of isoniazid resistant *M. Tb* InhA in complex with NADH, towards understanding of NADH–InhA different affinities. *Biophys. J.* **89**, 876–884 (2005)
6. X. He et al., Inhibition of the *MTb* enoyl acyl carrier protein reductase InhA by arylamides. *Bioorg. Med. Chem.* **15**(21), 6649–6658 (2007)
7. G. Subba Rao, R. Vijayakrishnan, M. Kumar, Structure based design of a novel class of potent inhibitors of InhA, the enoyl acyl carrier protein reductase from *Micobacterium tuberculosis*: A computer modeling approach. *Chem. Biol. Drug Des.* **72**, 444–449 (2008)
8. M. Kumar, R. Vijayakrishnan, G. Subba Rao, In silico structure-based design of a novel class of potent and selective small peptide inhibitor of *M. Tb*. Dihydrate reductase, a potential target for anti TB. drug discovery. *Mol. Divers.* **14**(3), 594–604 (2010)

9. A. F. Kouassi et al., Computer-aided design of orally bioavailable pyrrolidine carboxamide inhibitors of enoyl-acyl carrier protein reductase of *Mycobacterium tuberculosis* with favorable pharmacokinetic profiles. *Int. J. Mol. Sci.* **16**, 29744–29771 (2015)
10. J. Muralidharan, K. Suguna, N. Surolia, Exploring the interaction energies for the binding of hydroxydiphenyl ethers to enoyl acyl carrier protein reductases. *J. Biomol. Struct. Dyn.* **20**, 589–594 (2003)
11. S.G. Kini, A.K. Bhat, Synthesis, antitubercular activity and docking study of novel cyclic azole substituted diphenyl ether derivatives. *Eur J. Med. Chem.* **44**, 492–500 (2009)

# Physical Proof and Simulation of Ternary Logic Gate in Ternary Quantum Dot Cellular Automata



Puspak Pain, Arindam Sadhu, Kunal Das and Maitreyi Ray Kanjilal

**Abstract** Ternary quantum dot cellular automata (tQCA) is an emerging as well as an interesting field of research area after successful fabrication of binary QCA. Ternary logic is a critical choice for solving greater data storage, faster arithmetic operation on complex data, and so on. In this paper, tQCA basic logic gates like ternary AND, OR, NOT gates and buffers have been reported. tQCA layout for basic logic gates is simulated with tQCA simulation software (TQCA\_1.7.0.2). Involvement of coulombic interactive force is also explored as physical proof of NOT gate operation in eight-dot tQCA device model.

**Keywords** Ternary logic · Quantum dots · tQCA · Tunnel junction · Coulombic interaction · Physical proof

## 1 Introduction

According to ITRS reports in the era of ‘More than Moore’ technical trends, quantum dot cellular automata (QCA) is a most emerging post-CMOS technology in nanoscale device design [1, 2]. A paradigm shift from current CMOS technology to post-CMOS nanoscale device design becomes a prime research interest due to the limitation of CMOS technology [2, 3]. Technologies like nanowire (NW), carbon nanotube (CNT), single-electron transistors (SETs), and graphene-based devices are also promising for the alternative progression platform in the future. QCA is one

---

P. Pain (✉) · A. Sadhu · K. Das · M. R. Kanjilal  
Narula Institute of Technology, 81, Nilgunj Road, 700109 Agarpara, Kolkata, West Bengal, India  
e-mail: [puspak.pain@nit.ac.in](mailto:puspak.pain@nit.ac.in)

A. Sadhu  
e-mail: [arindam.hit11@gmail.com](mailto:arindam.hit11@gmail.com)

K. Das  
e-mail: [kunal.das@nit.ac.in](mailto:kunal.das@nit.ac.in)

M. R. Kanjilal  
e-mail: [maitreyi.kanjilal@nit.ac.in](mailto:maitreyi.kanjilal@nit.ac.in)

© Springer Nature Singapore Pte Ltd. 2020  
K. Maharatna et al. (eds.), *Computational Advancement in Communication Circuits and Systems*, Lecture Notes in Electrical Engineering 575,  
[https://doi.org/10.1007/978-981-13-8687-9\\_34](https://doi.org/10.1007/978-981-13-8687-9_34)

of the potential and promising technologies, which can overcome the limitations of CMOS technology such as charge quantization, power dissipation, and leakage of current [4]. A binary QCA cell comprises of four quantum dots (QDs) and two tunnel junctions, as shown in Fig. 1. Two extra electrons are confined in a four quantum dot system and can only tunnel through tunnel junction under the control of clock signal between adjacent dots. Due to quantum confinement, electrons cannot tunnel outside the cell. Information can only propagate from one cell to another cell due to coulombic interaction. The QCA technology is also known as post-CMOS zero current technology as the electron does not flow in QCA circuit although in micro module; i.e., QCA cell charge gets tunneled from one QD to another QD. In QCA, the passive component like wire can flow information only, whereas in the active component like majority voter computation takes place [4, 6]. The basic difference between tQCA and binary QCA (bQCA) cell is the number of QDs present in the cell and number of polarization states [7].

The rest of the paper comprises of the following sections. In Sect. 2, the description of the ternary logic system and tQCA cell is presented. Section 3 is dedicated to the design and implementation of the proposed work. The result and discussion are explored in Sect. 3. Finally, the conclusion is drawn in Sect. 4.

## 2 Basic Ternary Logic System and TQCA

Ternary logic is a specialization of multi-valued logic (MVL) family that demonstrate the use of three significant logic levels, true, false, and intermediate, having the capabilities of added data storage to solve complex arithmetic operations in numerical analysis and communication protocol for non-binary logic. The prime upgradation offered by MVL of reduced intricacy in the design is smaller on-chip area to improve firmness of fabrication. The high-bandwidth parallel and serial data transfer makes it a smart area of research. QCA platform is now utilized for ternary logic realization. Ternary QCA (tQCA) cell device design is in the infancy stage, and logic circuit realization is also in a very early stage. Hence, an exhaustive research work is required in this field. tQCA cell comprises of eight QDs that are arranged in a circular ring within a square-shaped cell. It is considered that there will be two extra electrons within a cell. Hence, the total number of electrons that can be occupied in this system is  $(8M + 2)$ , where each QD can have ' $M$ ' number of electrons [2, 5, 7].

Two different ternary logic systems such as balanced and unbalanced logic have been proposed by the research community. The balanced or symmetric system uses  $-V_{DD}$  for logic 0, 0 V for logic 1, and  $+V_{DD}$  for logic 2, whereas an unbalanced system uses 0 V for logic 0,  $V_{DD}/2$  for logic 1, and  $V_{DD}$  for logic 2. This tristate stable functionality of tQCA allows it to store a single ternary bit in a quantum state [3, 5, 6].

Ternary QD can be categorized as semiconductor-based, molecular or metal island cell, comprised of eight quantum dots confined in a circular arrangement with two extra electrons occupied within the cell. Electrons confined in a quantum dots with



### 3 Design and Implementation of tQCA Gates

The fundamental building blocks of any ternary circuits are ternary logic gates like ternary AND, ternary OR, and ternary inverter. In this section, different tQCA logic gates are described and the simulator TQCA\_1.7.0.2 [13] is used for the tQCA logic gate simulation, where ‘A’ state ( $p = -1.00$ ) is defined as A ( $-45^\circ$ ), ‘B’ state ( $+1.00$ ) is defined as B ( $+45^\circ$ ), and ‘C’ or ‘D’ are in two identical state of polarization ( $1/2$ ) as ( $0^\circ$ ) [8, 9, 11, 12].

#### 3.1 tQCA AND Gate

Two-input ternary AND gate is defined by the truth table in Table 1, where A1 and B1 are the two inputs and Y1 is the output. The K-map for ternary AND is given in Table 2. The output Y1 is undefined ( $U$ ) either  $A1 = +45^\circ$  or  $B1 = +45^\circ$  with a fixed polarization ( $-45^\circ$ ) tQCA cell.

The ternary circuit layout of AND gate in tQCA is shown in Fig. 2a.

**Table 1** Truth table of ternary AND gate

A1	B1	Y1
-1	-1	-1
0	-1	-1
+1	-1	-1
-1	0	-1
0	0	0
+1	0	0
-1	+1	-1
0	+1	0
+1	+1	+1

**Table 2** Ternary K-map of ternary AND gate using tQCA

	-45	0	+45
-45	-45	-45	-45
0	-45	0	$U$
+45	-45	$U$	+45

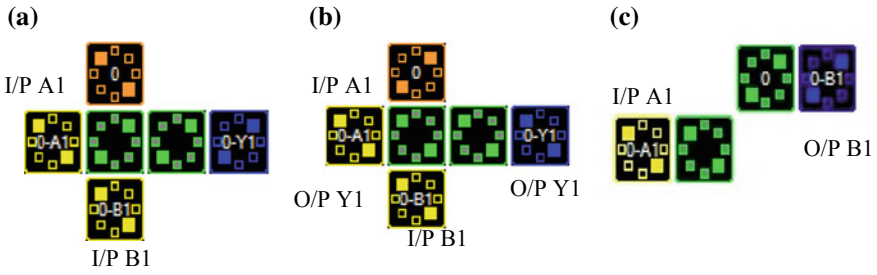


**Fig. 2** a tQCA layout of AND gate, b tQCA layout of OR gate, c tQCA layout of NOT gate (inverter)

### 3.2 tQCA OR Gate

Two-input ternary OR gate is described by the truth table in Table 3, where A1 and B1 are the two inputs and Y1 is the output. The K-map for ternary OR is shown in Table 4.

**Table 3** Truth table of ternary OR gate

A1	B1	Y1
+1	+1	+1
-1	-1	-1
-1	+1	+1
-1	0	0
0	-1	0
0	0	0
+1	0	+1
0	+1	+1
+1	-1	+1

**Table 4** Ternary K-map of OR gate in tQCA implementation

	-45	0	+45
-45	-45	<i>U</i>	+45
0	<i>U</i>	0	+45
+45	+45	+45	+45



### 3.3 tQCA NOT Gate

A NOT gate can be formed by inverting the position of electrons of two tQCA cells in a diagonal orientation, so that input logic ‘0’ will result as output ‘1’ and input logic ‘1’ will result as output ‘0’ [8, 9]. The same idea is incorporated in tQCA NOT gate realization. For this reason, tQCA cells arranged in a diagonal orientation lead to align in opposite polarization of input cell. In Fig. 2c, tQCA layout of an inverter is represented.

The truth table and K-map for ternary NOT gate are given in Tables 5 and 6.

### 3.4 Physical Proof

Physical proof for five inputs MV in tQCA has reported in [14]. Similarly, the tQCA NOT gate simulation output is shown in Fig. 3c.

The potential energy  $U$  between two electron charges is calculated using Eq. (1), where ‘ $k$ ’ is constant for a particular material and ‘ $r$ ’ is the distance between two electric charges  $q_1$  and  $q_2$ . By putting the values of ‘ $k$ ’ for Si and electric charges, we obtained inter-cell potential energy  $U_{mn^*}$  and intra-cell potential energy  $U_{mn}$  and  $U_{m^*n^*}$  as depicted in Fig. 4.

$$U = k\left(\frac{q_1q_2}{r}\right) = 7.69 * 10^8 * (1.6^2 * 10^{-38}) = 19.68 * 10^{-30}(\text{J}) \quad (1)$$

where  $k = \frac{1}{4\pi\epsilon_0\epsilon_r}$  and it can be calculated as  $k = \frac{1}{4*8.85*10^{-12}*11.68*3.14} = 7.69*10^8$  for ‘Si’, where  $\epsilon_0$  is permittivity of free space and  $\epsilon_r = 11.68$  is the relative permittivity of ‘Si’. Now for inter-cell coulombic interaction forces considering the radius of the tQCA cell ‘ $a$ ’ as 10 nm, now

$$U_{85^*} = 1.61 * 10^{-21}(\text{J})$$

$$U_{84^*} = 9.84 * 10^{-21}(\text{J})$$

$$U_{83^*} = 1.64 * 10^{-21}(\text{J})$$

**Table 5** Truth table of ternary OR gate

A1	Y1
-1	+1
0	0
+1	-1

**Table 6** Ternary K-map of OR gate in tQCA implementation

Input	A1	-45	0	+45
Output	Y1	+45	0	-45

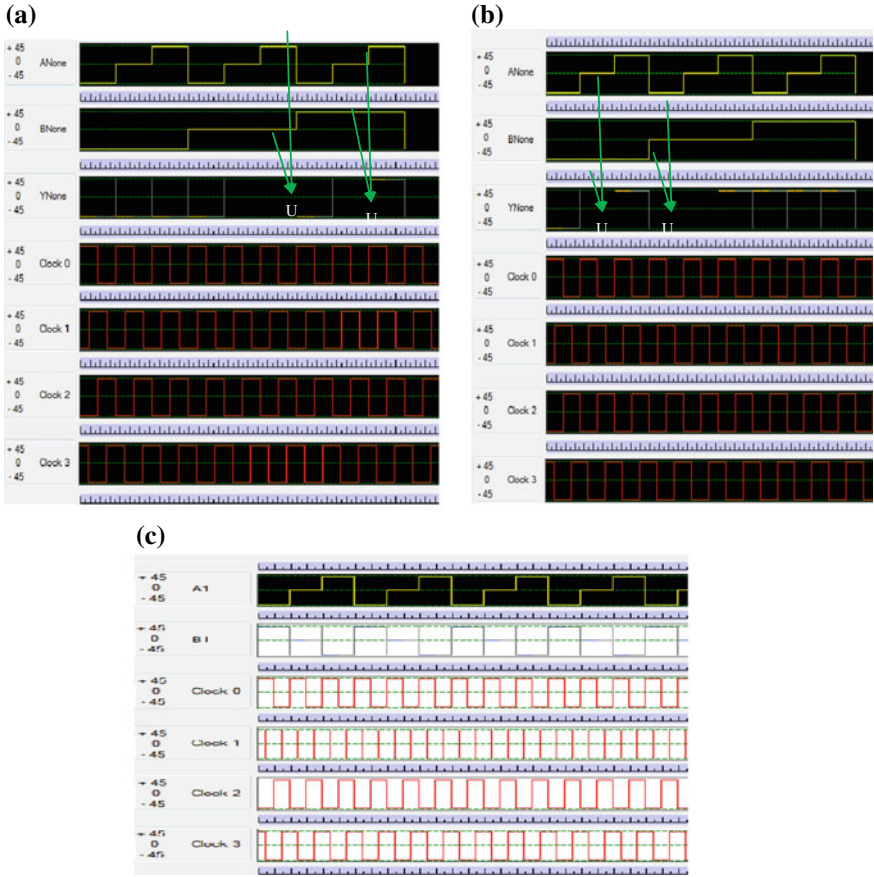


**Fig. 3** a tQCA AND gate simulation output, b tQCA OR gate simulation output, c tQCA NOT gate simulation output

$$U_{82^*} = 0.89 * 10^{-21} (J) \tag{2}$$

$$U_{44^*} = 0.695 * 10^{-21} (J)$$

$$U_{45^*} = 0.546 * 10^{-21} (J)$$

$$U_{43^*} = 0.546 * 10^{-21} (J)$$

$$U_{42^*} = 0.440 * 10^{-21} (J) \tag{3}$$

$$U_{87^*} = 0.88 * 10^{-21} (J)$$

$$U_{86^*} = 0.98 * 10^{-21} (J)$$

$$U_{81^*} = 0.88 * 10^{-21} (J)$$

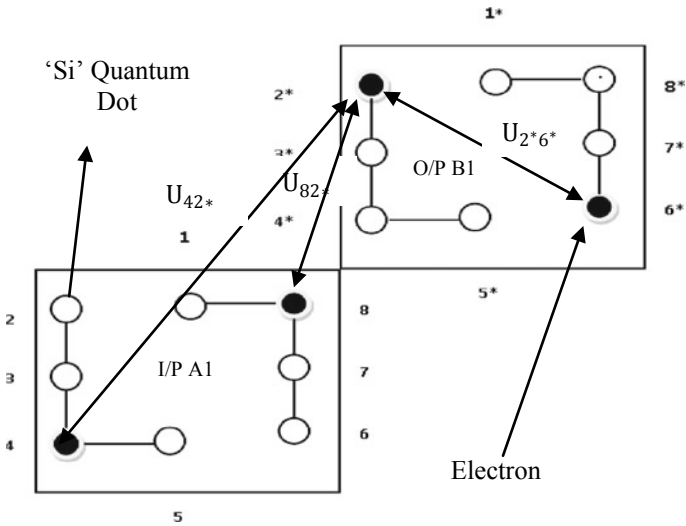


Fig. 4 Potential energy calculation for tQCA diagonal cells

$$U_{88^*} = 0.695 * 10^{-21}(\text{J}) \tag{4}$$

So,

$$\begin{aligned} U_{82^*} + U_{42^*} &= 1.33 * 10^{-21}(\text{J}) \\ U_{83^*} + U_{43^*} &= 2.186 * 10^{-21}(\text{J}) \\ U_{84^*} + U_{44^*} &= 10.53 * 10^{-21}(\text{J}) \\ U_{85^*} + U_{45^*} &= 2.156 * 10^{-21}(\text{J}) \end{aligned} \tag{5}$$

$$\begin{aligned} U_{88^*} + U_{48^*} &= 1.04 * 10^{-21}(\text{J}) \\ U_{87^*} + U_{47^*} &= 1.27 * 10^{-21}(\text{J}) \\ U_{86^*} + U_{46^*} &= 1.42 * 10^{-21}(\text{J}) \\ U_{81^*} + U_{41^*} &= 1.27 * 10^{-21}(\text{J}) \end{aligned} \tag{6}$$

Again for intra-dot coulombic interaction forces  $U_{2^*1^*}$ ,  $U_{2^*8^*}$ ,  $U_{2^*7^*}$ , and  $U_{2^*6^*}$  are calculated below.

$$\begin{aligned} U_{2^*8^*} &= 0.98 * 10^{-21}(\text{J}) \\ U_{2^*7^*} &= 0.88 * 10^{-21}(\text{J}) \\ U_{2^*1^*} &= 1.96 * 10^{-21}(\text{J}) \\ U_{2^*6^*} &= 0.69 * 10^{-21}(\text{J}) \end{aligned} \tag{7}$$

Since the value of coulombic interaction force  $U_{2*6*}$  in Eq. (7) is lower than the summation of potential energies ( $U_{88*} + U_{48*}$ ) in Eq. (6), i.e.,

$$U_{2*6*} < (U_{88*} + U_{48*}) \tag{8}$$

Which forces the extra electron to be confined and stabilized in an accurate state of the output cell (B1) in QD-6\* as shown in Fig. 4. It refers that the input cell (I/P A1) is in the potential energy of (+1) polarization and the output cell (O/P B1) having its opposite potential energy of (-1) polarization.

### 3.5 tQCA Buffers

Buffer performs no inversion logic operation. The truth table and layout of three types of ternary buffers such as standard ternary buffer (STB), positive ternary buffer (PTB), and negative ternary buffer (NTB) are presented in Fig. 5a, b, c and Table 7, respectively. Figure 6a shows that STB output state exactly follows to its input state, whereas in PTB and NTB, logic '0' appears in output as (+1) and (-1) are exposed in Fig. 6b, c, respectively. tQCA layout of PTB and NTB may have an important impact to generate positive and negative edge-triggered clocks in ternary QCA logic design in the future.

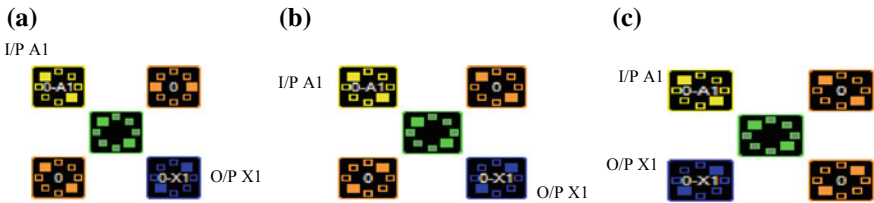


**Fig. 5** a tQCA layout of standard ternary buffer (STB), b tQCA layout of positive ternary buffer (PTB), c tQCA layout of negative ternary buffer (NTB)

**Table 7** Truth table of tQCA buffers

Input (A1)	Output (X1)		
	STB	PTB	NTB
0	0	+1	-1
+1	+1	+1	+1
-1	-1	-1	-1

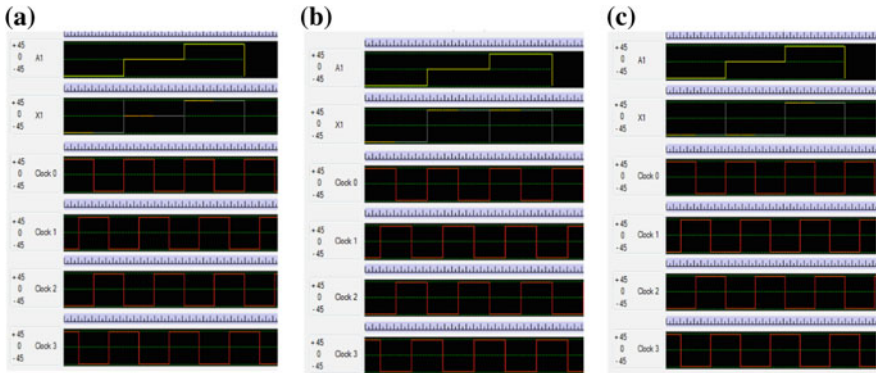


**Fig. 6** **a** tQCA STB simulation output, **b** tQCA PTB simulation output, **c** tQCA NTB simulation output

## 4 Conclusion

The effort is made to design ternary logic gate in ternary quantum dot cellular automata and also to provide a physical proof for the same. In this work, we have simulated ternary AND, OR, and NOT gates and buffers (STB, PTB, NTB) with tQCA simulator. The ternary AND, OR gate has been established in the simulation result of Fig. 3a, b, respectively. There are two undefined states that are noticed at output for given combination of inputs  $\{('+1', '0'), ('0', '+1')\}$  or  $\{(+45^\circ, 0), (-45^\circ, 0)\}$  and  $\{(' -1', '0'), ('0', '-1')\}$  or  $\{(-45^\circ, 0), (0, -45^\circ)\}$ , respectively. The physical proof of ternary NOT gate in ternary QCA is expressed in terms of coulombic interactive forces. The maximum possibility to occupy the particular QD by the extra electron to be stable is also calculated by neighboring QD coulombic interaction. Here, three different types of buffer in ternary QCA are also presented. Finally, it can be concluded that this research work will be a step toward the ternary QCA logic gate design.

**Acknowledgements** The authors are grateful to the Science and Engineering Research Board (DST-SERB), Government of India, for providing with the grant for the accomplishment of the project under the Project File No. ECR/2016/000613.

## References

1. International Technology Roadmap for Semiconductors (Semiconductor Industries Association, San Jose, CA, 2001), <http://public.itrs.net>
2. K. Das, D. De, M. De, Modified ternary Karnaugh map and logic synthesis in ternary quantum dot cellular automata. *IETE J. Res.* **62**(6), 774–785 (2016)
3. C.S. Lent, P.D. Taugaw, W. Porod, G.H. Bernstein, Quantum cellular automata. *Nanotechnology* **4**, 49–57 (1993)

4. P. Bhattacharjee, K. Das, M. De, D. De, SPICE modeling and analysis for metal island ternary QCA logic device, in *Information Systems Design and Intelligent Applications* (Springer, New Delhi, 2015), pp. 33–41
5. C.S. Nandurkar, K.N. Kasat, Design of low power low voltage circuit using CMOS ternary logic. *Int. Res. J. Eng. Technol.* **3**(6) (2016)
6. L. Bajec, N. Zimic, M. Mraz, The ternary quantum-dot cell and ternary logic. *IOP Nanotechnol.* **17**(8), 1937–1942 (2006)
7. K. Das, D. De, M. De, Realisation of semiconductor ternary quantum dot cellular automata. *Micro & Nano Lett.* **8**(5), 258–263 (2013)
8. C. Lent, P. Tougaw, A device architecture for computing with quantum dots, in *Proceeding of the IEEE*, vol. 85–4, pp. 541–557 (1997)
9. I. Amlani, A. Orlov, G. Snider, C. Lent, W. Porod, G. Bernstein, Experimental demonstration of electron switching in a quantum-dot cellular automata (QCA) cell. *Superlattices Microstruct.* **25**(1–2), 273–278 (1999)
10. P. Pecar, M. Mraz, N. Zimic, M. Janez, I.L. Bajec, Solving the ternary QCA logic gate problem by means of adiabatic switching. *Jpn. J. Appl. Phys.* **47**(6), 5000–5006 (2008)
11. P. Pecar, A. Ramsak, N. Zimic, M. Mraz, I. Lebar Bajec, Adiabatic pipelining: a key to ternary computing with quantum dots. *IOP Nanotechnol.* **19**(49), 495–501 (2008)
12. S.M. Mohaghegh, R. Sabbaghi-Nadooshan, M. Mohammadi, Innovative model for ternary QCA gate. *IET Circuits Devices Syst.* **12**(2), 189–195 (2018)
13. M. Khani, R. Sabbaghi-Nadooshan, Ternary Quantum-Dot Cellular Automata Simulator Software, <http://tqca.ir>. Accessed 2018
14. K. Navi, S. Sayedsalehi, R. Farazkish, M.R. Azghadi, Five-input majority gate, a new device for quantum-dot cellular automata. *J. Comput. Theor. Nanosci.* **7**(8), 1546–1553 (2010)

# Optical Properties of Fe-Doped ZnO Thin Film on p-Si by Spin Coating



Amalendu Bera and Sourav Chattopadhyay

**Abstract** The optical property of a semiconductor can be changed significantly by doping with magnetic materials like Fe. The structural and optical properties of Fe-doped ZnO thin films with different doping concentrations deposited on p-Si substrate by sol-gel spin coating method have been studied explicitly at room temperature. The X-ray diffraction (XRD) shows the polycrystalline nature of the ZnO film. With doping, the peak position of (002) plane shifts towards lower  $2\theta$ , indicating the substitution of  $Zn^{+2}$  by  $Fe^{+2}$ . A broad absorption peak from 2.8 to 3.2 eV for all the doping concentrations has been observed from UV spectroscopy, and the calculated band gap varies from 3.12 to 3.28 eV with increasing doping concentrations. Photoluminescence of pure ZnO shows excitonic peak near 400 nm with intense green emission from deep donor level. The excitonic peak shifts towards higher energies with increasing doping as well as a few deep defect-level peaks appear near blue and violet regions.

**Keywords** Fe-doped ZnO · Optical properties · Defects · Band structure

## 1 Introduction

The present era of electronics focuses not only on electrical conduction but also on spin of electron. Such spin-dependent electronics has a wide area of applications such as memory devices [1], optical and display devices [2], sensors [3]. The spin-dependent LED is one of the promising devices in the electronic industry because of its wide applications on display and medical instruments and attracts much attention of researchers in the present days. To fabricate spin-dependent LEDs, it is necessary to understand the band structure and optical properties in semiconductor properly. In the past few years, many researchers are working on ZnO because of its potential

---

A. Bera · S. Chattopadhyay (✉)  
Department of Electronics, Ramakrishna Mission Residential College (Autonomous),  
Narendrapur, Kolkata 700103, West Bengal, India  
e-mail: [nanophy.sourav@gmail.com](mailto:nanophy.sourav@gmail.com); [sceskin@outlook.com](mailto:sceskin@outlook.com)

application on many fields of science and technology ranging from UV light emitter [4], surface acoustic wave devices [5], varistors [6], piezoelectric device [7], transparent high-power electronics and chemical gas sensing [8], etc. Being wide band gap, transition metal-doped ZnO DMS film shows  $T_c$  above room temperature [9], attracts much attention of researchers and is trying to control its properties like electrical, chemical, optical and magnetic properties. Though there are lots of debates on the reason behind ferromagnetism in semiconductors, the Fe-doped ZnO shows potential applications in spintronics device field. It shows good junction magnetoresistive behaviour with different magnetic and non-magnetic metal junctions [10, 11], which make Fe-doped ZnO a potential member for fabricating spin-polarized light-emitting diodes. So a thorough study on optical properties of Fe-doped ZnO is required to understand the behaviour of light emitted from LEDs by estimating its optical band structures.

In the present work, Fe-doped ZnO thin film prepared by sol-gel spin coating technique on p-Si substrate has been studied explicitly to find out structural and optical properties at room temperature and effect of doping on these properties for future LED device applications. A band structure from optical properties has been proposed for these materials.

## 2 Experimental Procedures

Zinc acetate  $\text{Zn}(\text{COOCH}_3)_2 \cdot 2\text{H}_2\text{O}$  is taken as a source of zinc and iron nitrate  $(\text{FeNO}_3)_3$  as the precursor for iron (chemical from Sigma-Aldrich with 99.9% purity). Methanol ( $\text{CH}_3\text{OH}$ ) and ethanolamine (ETA) are chosen as a solvent and ligand, respectively. Si wafer has been cleaned first by acetone under ultrasonic cleaner, followed by sequential oxidation desorption process and complexing with  $\text{H}_2\text{O}_2\text{-NH}_4\text{OH-H}_2\text{O}$  and  $\text{H}_2\text{O}_2\text{-HCl-H}_2\text{O}$ . Finally, the  $\text{SiO}_2$  layer has been removed using 1:50 solution of HF.

Zinc acetate and iron nitrate were dissolved in methanol at room temperature and then stirred at 80 °C for an hour. When the solution was stirred, the ETA was put into it drop by drop. The molar ratio of ETA and zinc acetate was 1.0. At last, a clear and homogeneous ZnO solution was formed. The concentration of zinc acetate was 0.3 mol/L, and the atomic percentage of  $\text{Fe}^{3+}/\text{Zn}^{2+}$  in the ZnO sol was 0, 1, 3 and 5%. The solutions were aged for 24 h at room temperature. Then the coating solution was dropped onto pre-cleaned silicon substrate, which was rotated at 2500, 3000 and 3500 rpm for 30 s. After deposition by coating, the film was dried at 100 °C for 3–5 min in hot plate to evaporate the solvent and remove organic residuals. The procedures from coating to drying were repeated several times. The film was then heated on hot plate at 400 °C for 1 h.



The structural properties have been investigated using Cu-k $\alpha$  X-ray diffractometer in the  $2\theta$  range of  $20^\circ$ – $80^\circ$ . Optical properties were investigated by using PerkinElmer UV spectrometer. The photoluminescence properties of thin film are characterized by room-temperature photoluminescence spectrometer.

### 3 Results and Discussion

*Structural study:* Fig. 1 shows X-ray diffraction (XRD) pattern of Fe-doped ZnO. All peaks correspond to hexagonal wurtzite structure of Fe-doped ZnO with concentration up to 5%. No trace of iron metal, oxides or any binary zinc iron phases is

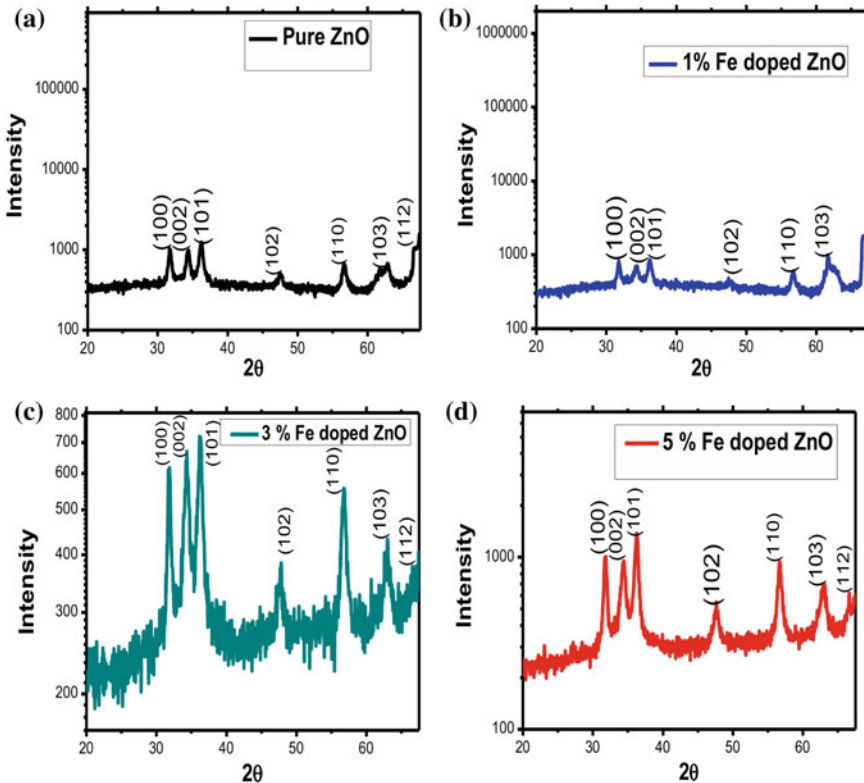


**Fig. 1** XRD pattern of **a** pure ZnO, **b** 1% Fe-doped ZnO thin film, **c** 3% Fe-doped ZnO thin film and **d** 5% of Fe-doped ZnO thin film on p-Si substrate

**Table 1** X-ray diffraction analysis of Fe-doped ZnO

Sample	Plane	2 $\theta$	FWHM	Average grain size (D) nm
Pure	(100)	31.82	0.38	44
	(002)	34.35	0.48	
	(101)	36.24	0.47	
1% Fe-doped ZnO	(100)	31.79	0.38	41.68
	(002)	34.33	0.51	
	(101)	36.21	0.48	
3% Fe-doped ZnO	(100)	31.78	0.52	36.73
	(002)	34.30	0.58	
	(101)	36.15	0.54	
5% Fe-doped ZnO	(100)	31.76	0.46	28.61
	(002)	34.29	0.60	
	(101)	36.14	0.55	

observed within the sensitivity of XRD, which implies that Fe doping did not change the hexagonal wurtzite structure of ZnO thin films with polycrystalline in nature. The main peaks [(100), (002) and (101)] are shifted to lower angle with doping. This indicates that the films suffer from high compressive stress along the interfaces [12]. The full width at half maximum (FWHM) becomes wider with the increasing Fe concentration, which implies that Fe<sup>+2</sup> replaces Zn<sup>+2</sup> inside the film (given in Table 1). The change of FWHM with Fe doping might be due to the change of internal stress factor. Lattice defect and disorder can play a significant role in this kind of behaviours.

By using the modified Scherer's formula [13], we calculated the average crystallite size of the films. Average crystallite sizes were 44, 41, 36 and 28 nm for pure, 1, 3 and 5% Fe doped samples as given in Table 1.

*Optical properties:* Fig. 2a shows the transmittance spectra of the ZnO which show a good optical transmittance in the UV–Visible range (380–780 nm). Optical transmittance gets reduced when doping concentration is high. The structural changes and formation of defects might be the reason behind it. Which also effects on optical conductivity. High-energy region (UV region) clearly shows that for a fixed wavelength, refractive index increases with doping concentrations. The change of optical density with doping might be the reason behind this kind of behaviour, and with respect to air, light velocity decreases within the material with higher doping. Optical conductivity dramatically increases in UV region which means that available free carriers absorb photon energy. Rapid decreases of optical conductivity in

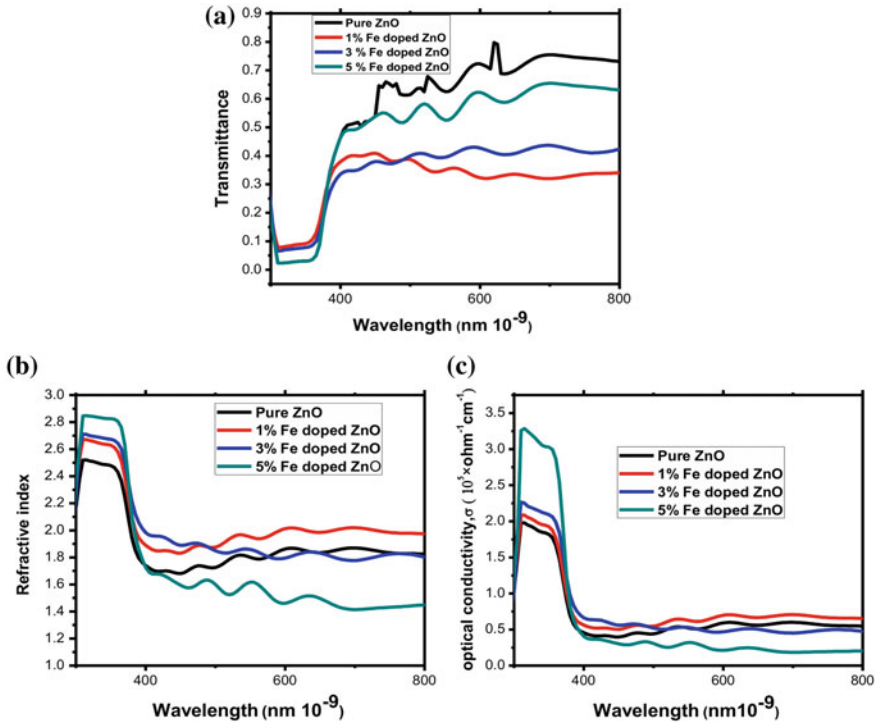


**Fig. 2** a Transmittance spectra of pure and Fe-doped ZnO, b Calculated refractive index and c Optical conductivity plot from transmittance spectra of pure and different Fe-doped ZnO thin films

the visible region imply that free carriers are trapped. Figure 2b, c shows calculated refractive index and optical conductivity plot with wavelength, respectively.

To find out optical band gap of thin film, the well-known Tauc plot [14] has been used. The plotting of  $(\alpha h\nu)^{1/2}$  versus the photon energy ( $h\nu$ ) gives a straight line in a certain region. The extrapolation of this straight line will intercept the ( $h\nu$ )-axis to give the value of the direct optical energy gap ( $E_g$ ) as shown in Fig. 3. It is found that the band gap of undoped and 1, 3 and 5% Fe-doped ZnO films is 3.12 (Fig. 3a), 3.26 (Fig. 3b), 3.24 (Fig. 3c) and 3.28 eV (Fig. 3d), respectively. The increase in band gap with doping may be due to the decrease of grain size with doping.

The room-temperature photoluminescence (PL) spectra for pure and different doped films are shown in Fig. 4. The effect of Fe concentration in ZnO clearly shows the excitation peak shift towards lower wavelength. This shift of the peak position indicates the variation in the excitonic band gap. UV emission in the PL spectra is an indication of good crystallinity of the film. In this study, along with excitonic peak,

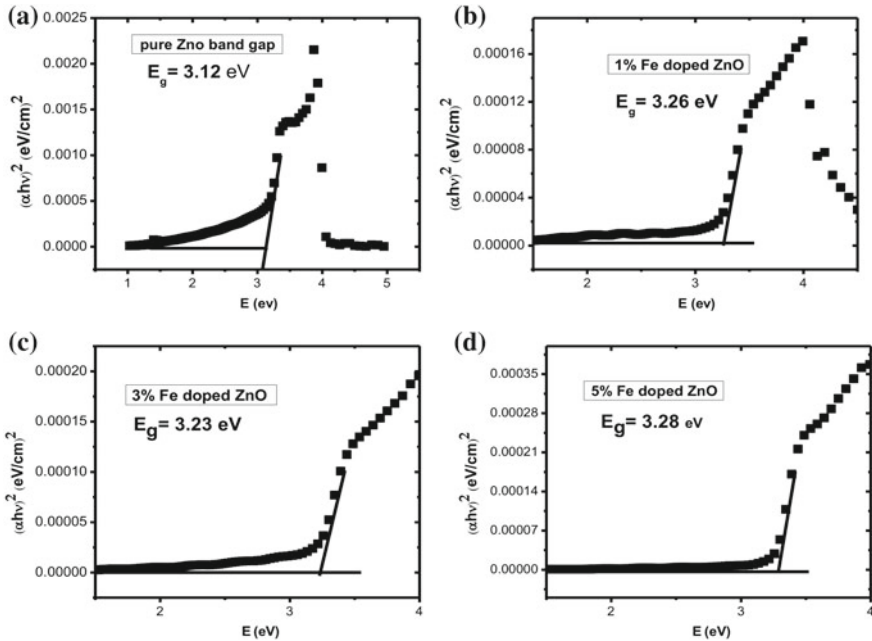


**Fig. 3** Band gap calculation of **a** pure ZnO, **b** 1% Fe-doped ZnO, **c** 3% Fe-doped ZnO and **d** 5% Fe-doped ZnO thin film

another wide peak has appeared in green emission region, which is more intense. This green emission in ZnO is mainly due to the formation of deep donor level, originated from oxygen vacancy ( $V_o$ ) or zinc interstitial [15]. More number of peaks appear in higher doped films as given in Table 2. Different levels of bonding, generally oxide-related bonding, incorporate extra peaks in PL spectra. The reason behind many peaks might be due to the formation of defect level with doping. According to PL spectra, a band structure of 5% Fe-doped ZnO at room temperature is proposed in Fig. 5. Aside with band edge emission we found four peaks at 402, 426, 473 and 512 nm in 5% Fe doped sample. Where peaks 402 and 426 nm correspond to violet emission and 473 nm correspond to blue emission. Chen et al. [16] have shown peak near 410 nm gets redshift with Fe doping which is like our results. One deep-level emission is shown at 512 nm, and it corresponds to green emission which is also present in other films except for 3% Fe-doped film. It gets shifted towards lower wavelength for 3% doping.

**Table 2** Photoluminescence analysis of Fe-doped ZnO

	First peak		Second peak		Third peak		Fourth peak		Fifth peak	
	$\lambda_c$	FWHM	$\lambda_c$	FWHM	$\lambda_c$	FWHM	$\lambda_c$	FWHM	$\lambda_c$	FWHM
Pure ZnO	399.20	62.72	562.09	57.78	577.12	139.03	-	-	-	-
1% Fe-doped ZnO	383.90	13.66	398.58	42.47	462.44	60.36	-	-	-	-
3% Fe-doped ZnO	383.70	17.37	401.16	44.57	425.76	16.72	468.23	16.30	499.00	51.75
5% Fe-doped ZnO	381.50	15.85	402.5	15.58	426.86	36.00	473.54	30.25	512.66	30.79

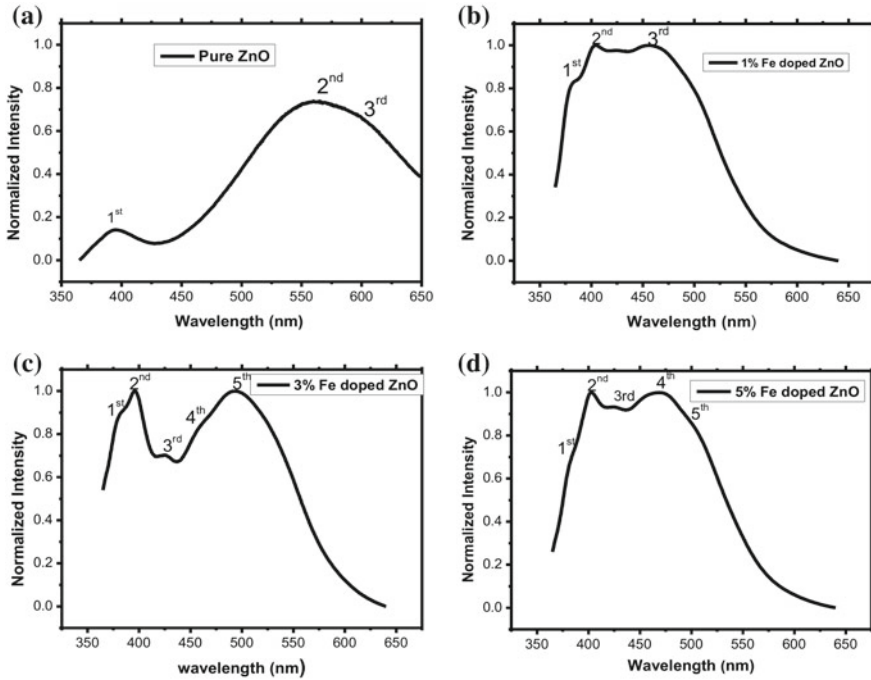
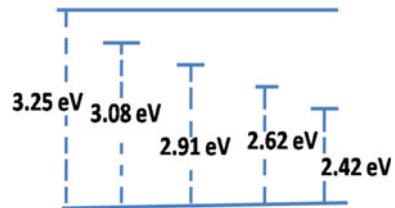


**Fig. 4** Photoluminescence spectra of **a** pure ZnO, **b** 1% Fe-doped ZnO, **c** 3% Fe-doped ZnO and **d** 5% Fe-doped ZnO thin film

**Fig. 5** Band structure of 5% Fe-doped ZnO thin film



### 4 Conclusion

The effect of Fe doping in ZnO on structural and optical properties has been investigated explicitly, and possible band structure has been proposed. The X-ray diffraction pattern shows the polycrystalline ZnO phase with wurtzite structure. The absence of another phase of Fe proves the efficient substitutional doping of Fe. The average grain size of all thin films up to 5% doping is in nanometre scale. UV–Visible spectroscopy results show that films are transparent in nature and have high optical conductivity in UV region. There is a change in optical band gap with doping which might be due to the decrease of grain size. Photoluminescence spectroscopy (PL) results show that with increasing doping, the first excitonic peak moves towards lower wavelength.

New peak appears with doping. The band structure with defects has been proposed to understand the behaviour of Fe-doped ZnO films for light-emitting devices.

**Acknowledgements** We would like to thank DST-SERB for financial support to carry out these works. Also, we would like to thank Prof. Debnarayan Jana (University of Calcutta) for providing PL spectroscopy, Department of Chemistry, Ramakrishna Mission Residential College, and Indian Association for the Cultivation of Science (IACS) for providing necessary facilities.

## References

1. W.Y. Chang, Y.C. Lai, T.B. Wu, S.F. Wang, F. Chen, M.J. Tsai, Unipolar resistive switching characteristics of ZnO thin films for non-volatile memory applications. *Appl. Phys. Lett.* **92**(022110), 1–3 (2008)
2. S. Tiwari, S. Tiwari, B.P. Chandra, Characteristics of a.c. electroluminescence in thin film ZnS:Mn display devices. *J. Mater. Sci.: Mat. Electron.* **15**, 569–574 (2004)
3. F. Schmaljohann, D. Hagedorn, F. Löffler, Thin film sensors for measuring small forces. *J. Sens. Sens. Syst.* **4**, 91–95 (2015)
4. M.H. Huang, S. Mao, H. Feick, H. Yan, Y. Wu, H. Kind, E. Weber, R. Russo, P. Yang, Room-temperature ultraviolet nanowire nanolasers. *Science* **292**, 1897–1899 (2001)
5. X.Y. Du, Y.Q. Fu, S.C. Tan, M. Sunglyul, ZnO film thickness effect on surface acoustic wave modes and acoustic streaming. *Appl. Phys. Lett.* **93**, 094105, 1–3 (2008)
6. Y. Wang, Z. Peng, Q. Wang, C. Wang, X. Fu, High-performance varistors simply by hot-dipping zinc oxide thin films in  $\text{Pr}_6\text{O}_{11}$ : Influence of temperature. *Sci. Rep.*, 41994 (2017)
7. D. Bhatia, H. Sharma, R.S. Meena, V.R. Palkar, A novel ZnO piezoelectric microcantilever energy scavenger: fabrication and characterization. *Sens. Bio-Sens. Res.* **9**, 45–52 (2016)
8. L. Wang, Y. Kang, X. Liu, S. Zhang, W. Huang, S. Wang, ZnO nanorod gas sensor for ethanol detection. *Sens. Actuators, B* **162**, 237–243 (2012)
9. T. Dietl, H. Ohno, F. Matsukura, J. Cibert, D. Ferrand, Zener model description of ferromagnetism in zinc-blende magnetic semiconductors. *Science* **287**, 1019 (2000)
10. S. Chattopadhyay, J. Panda, T.K. Nath, Enhanced temperature dependent junction magnetoresistance in  $\text{La}_{0.7}\text{Sr}_{0.3}\text{MnO}_3/\text{Zn}(\text{Fe}, \text{Al})\text{O}$  carrier induced dilute magnetic semiconductor junctions. *J. Appl. Phys.* **113**, 194501, 1–5 (2013)
11. S. Chattopadhyay, T.K. Nath, Room temperature enhanced positive magnetoresistance in Pt and carrier induced  $\text{Zn}(\text{Fe})\text{O}$  and  $\text{Zn}(\text{Fe}, \text{Al})\text{O}$  dilute magnetic semiconductor junction, *J. Appl. Phys.* **108**, 083904, 1–5 (2010)
12. G. Anil Kumar, M.V.R. Reddy, K.N. Reddy, Structural and Optical properties of ZnO thin films grown on various substrates by RF magnetron sputtering, in *IOP Conference Series: Materials Science and Engineering*, vol. 73 (2015), p. 012133, 1–4
13. A. Monshi, M.R. Foroughi, M.R. Monshi, Modified Scherrer equation to estimate more accurately nano-crystallite size using XRD. *World J. Nano Sci. Eng.* **2**, 154–160 (2012)
14. A. Das, S.K. Gautam, D.K. Shukla, F. Singh, Correlations of charge neutrality level with electronic structure and p-d hybridization. *Sci. Rep.* **7**, 40843 (2017)
15. S. Majumdar, P. Banerji, Effect of Li incorporation on the structural and optical properties of ZnO. *Superlattices Microstruct.* **45**, 583–589 (2009)
16. A.J. Chen, X.M. Wu, Z.D. Sha, L.J. Zhuge, Y.D. Meng, Structure and photoluminescence properties of Fe-doped ZnO thin films. *J. Phys. D Appl. Phys.* **39**, 4762 (2006)

**Part VII**  
**Reconfigurable Computing**



# AVR Microcontroller-Based Error-Free Public Addressing System



Suvamoy Bhattacharyya, Partha Sarkar, Arijit Sen, Ashesh Sinha and Sandip Chanda

**Abstract** In the field of electric traction, automatic public addressing system is required to manage the safe and error-free in public addressing, rail signals, and rail gate crossing controlling. This system plays a major role in the development of a traction system. In this conventional system, an operator has to monitor the different parameters of the traction system like train signaling, public addressing, rail gate crossing, etc., which are different for different locomotives. This work makes the whole system automated by using the sensor and microcontroller. With the help of sensors, we can collect the conditions of the parameters as input to the microcontroller and the output of the microcontroller is used to automate the system with the correct measures within a short time.

**Keywords** Automatic public addressing system · RFID sensor · AVR microcontroller · Arduino

---

S. Bhattacharyya · S. Chanda  
Department of EE, Narula Institute of Technology, Kolkata, India  
e-mail: [suvamoy.bhattacharyya@gmail.com](mailto:suvamoy.bhattacharyya@gmail.com)

S. Chanda  
e-mail: [sandipee1978@gmail.com](mailto:sandipee1978@gmail.com)

P. Sarkar (✉)  
Department of ECE, National Institute of Technology Durgapur, Durgapur, India  
e-mail: [parthasarkar.info@gmail.com](mailto:parthasarkar.info@gmail.com)

A. Sen · A. Sinha  
Department of EE, R. K. Mission Shilpapitha, Belgharia, Kolkata, India  
e-mail: [senari1998@gmail.com](mailto:senari1998@gmail.com)

A. Sinha  
e-mail: [asheshsinha2@gmail.com](mailto:asheshsinha2@gmail.com)

## 1 Introduction

In Indian Railway traction system, single-phase ac system is the most popular. During 2012–2013, on an average, on any given day, 12,617 trains were running on Indian Railway tracks and 1.9% of India's total population was on trains; the public addressing system, rail gate controlling, and automatic signaling make it secure to avoid collision not only between two trains but also between human and train. Advancement of technology can be used in a traction field to monitor and automate the system for a better outcome. The most important advantage is to reduce accidents due to public addressing failure, we have introduced technology to monitor the parameters which are related to that field and give the corresponding output can be automatically done by the microcontroller as per program inserted within it. The main advantage of a microcontroller using RFID sensors is 100% human error-free public addressing with gate and signal controlling system.

The microcontroller is the heart of the system. This system is useful as per the pre-programmed schedule along with the input taken by the sensors. The public addressing, rail gate, and rail signal can be managed by the output designed of Atmel ATmega8. RFID sensor's serial port output has meant that it is able to send data directly to the controller for processing. The data is displayed on the LCD screen in the system.

Hopefully, this system can be more useful for the regular passenger in the day-to-day life and due to 100% human error-free system is safer than manual operation.

## 2 Proposed Model

At first, the rail track which is adjacent to the rail gate and station also is taken as the zone of the RFID sensor. The LCD display is placed at the rail station, and then, two RFID readers are connected in parallel. The RFID1 which is nearer to the rail station is located adjacent to the nearer end of the rail gate, and the RFID2 which is quite far from the rail station than RFID1 is located a distance apart from the far end of the rail crossing gate and placed between two tracks at a safe position. The rail signal is placed as per the required position. Initially, the rail signal is green that means the locomotive can pass through the track safely and the rail line crossing gate is open. The specified RFID card is placed under the specified locomotive; remember that the hex code of the RFID cards is changeable. Whenever the locomotive is passed over the RFID2 reader, it sends a signal to the microcontroller, and according to the program in the microcontroller, it sends a data signal to the rail gate and the rail signal also. After getting the data signals, the rail gate remains closed, the rail signal becomes red, and also LCD display shows the rail announcement on the display. When the locomotive is passed over the RFID1, it resets all the operations except the announcement.

### **3 Hardware Description of Model**

#### ***3.1 Atmega328 Microcontroller Unit***

Atmel ATmega328 used in this CPT is a 28-pin narrow dual-input package (DIP) IC. AVR possesses a modified Harvard architecture with 8-bit RISC single-chip microcontroller. The low-power Atmel 8-bit AVR is chosen for this CPT because this RISC-based microcontroller consists of 8-KB programmable flash memory, 512 K E2PROM, 1 KB of SRAM, and a 10-bit A/D converter. This available memory is used to store total time and alarm time after each time they are saved or changed. This MCU operates between 2.7 and 5.5 V which is supplied by 7805 voltage regulator and supports a throughput of 16 MPS with operating frequency 16 MHz [1].

#### ***3.2 Advanced RISC Modified Harvard Architecture***

The basic advantages of Atmega328 microcontroller regarding its architecture are its vast 130 instructions,  $32 \times 8$  general-purpose registers, most instructions having one-clock-cycle execution, and an on-chip multiplier [1].

#### ***3.3 High Endurance Memory Segments***

On the other hand, regarding its high endurance nonvolatile memory, it possesses 8 Kbytes of self-programmable flash memory, 512 bytes of E2PROM, 1 Kbyte of internal static RAM, and data retention of 20 years at 85 °C and for 100 years at 25 °C [1].

#### ***3.4 RFID Sensor***

RC522/PN532 is a highly integrated read and write card chip applied to the 13.56 MHz contactless communication. Launched by the NXP Company, it is a low-voltage, low-cost, and small-sized non-contact card chip and is the best choice for intelligent instrument and portable handheld devices. MF RC522/PN532 uses advanced modulation and demodulation concept which is fully presented in all types of 13.56 MHz passive contactless communication methods and protocols. MFRC522 also supports MIFARE series of high-speed non-contact communication, with a two-way data transmission rate of up to 424 kbit/s. As a new member of the 13.56 MHz highly integrated reader card series, MF RC522 is much similar to the existing MF

RC500 and MF RC530 when there are also great differences. It communicates with the host machine via the serial manner which needs less wiring [2].

### **3.5 $16 \times 2$ LCD Unit**

The LCD is interfaced with the AVR microcontroller in 4-bit mode and is used to show total time, running time, and alarm time. The  $16 \times 2$  LCD device used can show 16 characters per column, and there are two such rows. In this LCD, each character is displayed in  $5 \times 7$ -pixel matrix. The LCDs are programmed with the help of two registers namely command and data registers. The command register stores the instructions that are given to the LCD such as initialization, clearing the screen, controlling display, and setting the cursor position. The data register stores the data that is to be displayed on the LCD [3].

## **4 System Modeling**

Here, we consider the main hardware components. Atmel ATmega328 microcontroller is used to regulate the operation, and the LCD display, battery, and servomotor are used to control the rail gate very precisely and complete the system operation. Traction parameters are taken as inputs for the microcontroller. The announcement of upcoming trains and other parameters are considered as the traction inputs which were detected by different sensors. The microcontroller is programmed with open-source software for embedded C. The schematic diagram of the proposed model is shown in Fig. 1.

## **5 Working Methodology and Discussion**

Automatic public addressing system with rail gate and signal control monitors 24 h in case of high-density traction system where various trains pass through the whole day and night. This is done for public safety and collision-free exiting of locomotive and other vehicles at rail crossings. The total system is operated by a specified microcontroller which is worked at proper DC supply along with battery backup. When the locomotive passes over the first sensor, the microcontroller starts its function, it operates the motor, rail gate remains closed, and the upcoming train name is shown on LCD display. At that moment, the train signal turns into green from red. After that, whenever the train passes over the second sensor, the microcontroller resets all the operation and every action comes to its previous position.

**Circuit Diagram:-**

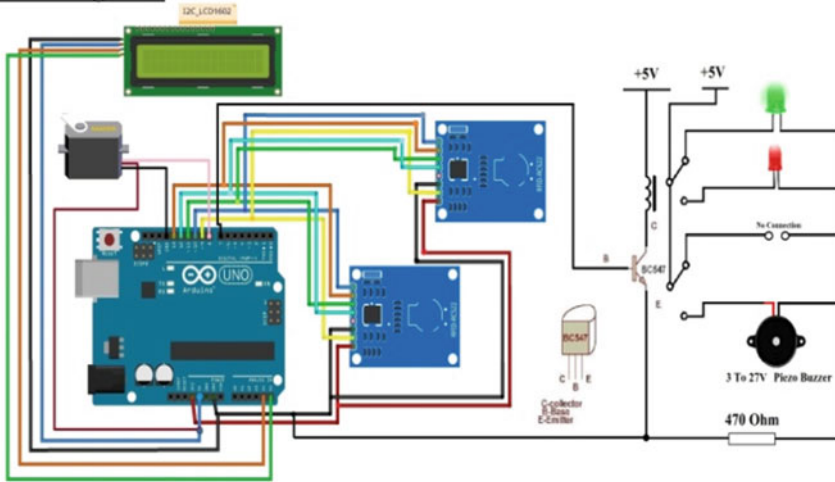


Fig. 1 Schematic diagram of RFID-based error-free public addressing system

## 6 Conclusion

In this modeling, the system is beneficial in terms of proper error-free addressing, reduced physical pressure on the station operator, proper signaling system, and collision-free operation. Here, the system can automatically run the public addressing system by using the RFID sensor. Simultaneously, the system can automatically approach the train signaling and rail gate crossing control. In future work, it can be extended as automatic rail track break detector with the help of impedance relay network which can be controlled and recorded through the microcontroller.

## References

1. O.J. Svendsli, Atmel's Self-Programming Flash Microcontrollers. Atmel White Paper, 2464 C-AVR-10/03
2. RFID RC522, Web: [www.naylampmechatronics.com/blog/22\\_Tutorial-Lector-RFID-RC522.html](http://www.naylampmechatronics.com/blog/22_Tutorial-Lector-RFID-RC522.html)
3. 16X2 LCD Datasheet

# Prototype Model for Controlling of Soil Moisture and pH in Smart Farming System



Suvamoy Bhattacharyya, Partha Sarkar, Sharthak Sarkar, Ashesh Sinha and Sandip Chanda

**Abstract** In this prototype model, soil moisture sensor and pH sensor are the main sensors used in an automated way. Here, the farming field has been divided into four numbers of zones according to moisture content and pH value. The optimum quantities and proportion of nitrogen, phosphorus, and potassium (NPK) values have been made based on balanced fertilization. For controlling, AVR microcontroller has been used with supporting modules like DS3231 RTC module, SD card module, servomotors, and GSM module. The desired requirement of water content in irrigation for different crops is measured, and accordingly, the frequency and quantity of water distribution in the irrigation system have been fixed up. A robotic hand-type mechanism has been made to supply water and fertilizer to different zones in the field whenever required. A message alert will automatically be sent to the phone of the farmer whenever the pump is turned ON for effective irrigation as well as balanced fertilization.

**Keywords** Automatic irrigation · Balanced fertilization · NPK values · Robotic hand

---

S. Bhattacharyya · S. Chanda  
Department of EE, Narula Institute of Technology, Kolkata, India  
e-mail: [suvamoy.bhattacharyya@gmail.com](mailto:suvamoy.bhattacharyya@gmail.com)

S. Chanda  
e-mail: [sandipee1978@gmail.com](mailto:sandipee1978@gmail.com)

P. Sarkar (✉)  
Department of ECE, National Institute of Technology Durgapur, Durgapur, India  
e-mail: [parthasarkar.info@gmail.com](mailto:parthasarkar.info@gmail.com)

S. Sarkar · A. Sinha  
Department of EE, R. K. Mission Shilpapitha, Belgharia, Kolkata, India  
e-mail: [sharthaksarkar01@gmail.com](mailto:sharthaksarkar01@gmail.com)

A. Sinha  
e-mail: [asheshsinha2@gmail.com](mailto:asheshsinha2@gmail.com)

## 1 Introduction

Agriculture plays an important role in any country specifically India where the population is a major concern which becomes a livelihood provider. In India, agriculture system is mostly manual based. With technological development in the agriculture sector, several problems have been arises like excessive use of groundwater and fertilizers. Here, a prototype model has been developed to control soil moisture and pH. This model is mainly helpful for the farmers as they can rely on automation to automatically supply water to the field on the basis of the moisture content of the soil. The moisture content of the soil is measured with the help of a soil moisture sensor. A robotic hand is used to supply water to the field from the water tank. The water tank can also be filled up automatically when the sensor senses the deficiency of water in the tank. A farmer can keep a record of the number of times the water is supplied to the field and simultaneously the number of times the pump is getting ON and at which time it is getting ON. This entire system has been recorded as data logging. The data is logged with the help of an SD card module, and the real time is noted down with the help of a real-time clock module (RTC) DS3231. Whenever the pump is turned ON, a message alert is sent to the phone of the farmer, and this is done with the help of a GSM module (SIM900A). The utility of this type of low-cost construction and usefulness of automation in agriculture have provided balanced fertilization, ensuring sustainable agriculture [1].

In a literature survey, we have studied to explore related works on implementation of the smart farming system and its related fields. A microcontroller based an automated irrigation controlling system using rain gun has been mentioned where irrigation will take place as per the requirement of water as in [2]. A GSM-based water and soil management irrigation system for efficient use of resources and crop planning has been proposed in [3]. A remote sensing and control of an irrigation system using a distributed wireless sensor network have proposed an efficient system for the development of field management using sensor communication as in [4]. An automatic system for agriculture and domestic plant watering using drip irrigation has been mentioned which can provide water to the farms according to their moisture and soil types as in [5].

## 2 Problem Statement

Rather than manual-based irrigation system, the zone-based automated irrigation system is more efficient on the basis of requirement of groundwater and electric power to run motor. The pH sensor measures the pH of the soil, and the pH measured corresponds to a particular percentage of macronutrients present in the soil using Table 1.

Using moisture sensor, the deficiency of nutrients in the soil is detected and also maintain soil fertility as well as the soil pH through a relationship between soil

**Table 1** pH values with percentage of NPK nutrients

pH value	N content (%)	P content (%)	K content (%)
4.5 (extremely acidic)	30	23	33
5 (very strong acid)	53	34	52
5.5 (strong acid)	77	48	77
6 (medium acid)	89	52	100
7 (neutral)	100	100	100

pH and the amount of nutrients present in the soil. So, automated controlling of soil moisture and pH increases crop yields, ensuring balanced fertilization as well as sustainable agriculture.

### 3 Design Methodology

Here, Atmel ATmega328P-PU microcontroller is used in this prototype model for smart controlling of soil moisture and pH. It is eight-bit RISC single-chip microcontroller with modified Harvard architecture and supports a throughput of 16 MPS with clock frequency at 16 MHz. Soil moisture sensor senses the moisture content of the soil. The soil is divided into several zones, and each zone contains one soil moisture sensor and they operates in parallel. Each soil moisture sensor senses the moisture content of the soil and compares it with the predefined value of moisture content. The alternative method has been taken to use pH sensors for detection of macronutrients deficiency in the soil to maintain soil fertility as well as maintain the soil pH through a relationship between soil pH and the amount of nutrients present in the soil. The design flow for controlling of soil moisture and pH control is shown in Fig. 1.

An SD card module for data logging and RTC module to note down the time of operation of the watering system have been used. A robotic hand made with the help of servomotors has been used. If the moisture content of the soil is less than the predefined moisture content, then the microcontroller operates the robotic hand which de-locates itself to that zone whose moisture content is low, and thereafter, the microcontroller operates the pump and a message alert is sent to the phone of the farmer and the time of operation along with the zone number is written on the SD card. In the first part, a detail investigation has been carried out and resulted in suitable statistics of data on the measure of the pH level in the soil. The heart of the automated fertilization unit is the pH sensor. The pH sensor measures the pH of the soil, and the pH measured corresponds to a particular percentage of macronutrients present in the soil. Now with an instance of time, the microcontroller compares the value of moisture content of the zone where water is supplied to the predefined value of the moisture content. Now if the microcontroller finds that the moisture of the soil is less than the predefined value, then it will operate the pump but as soon as



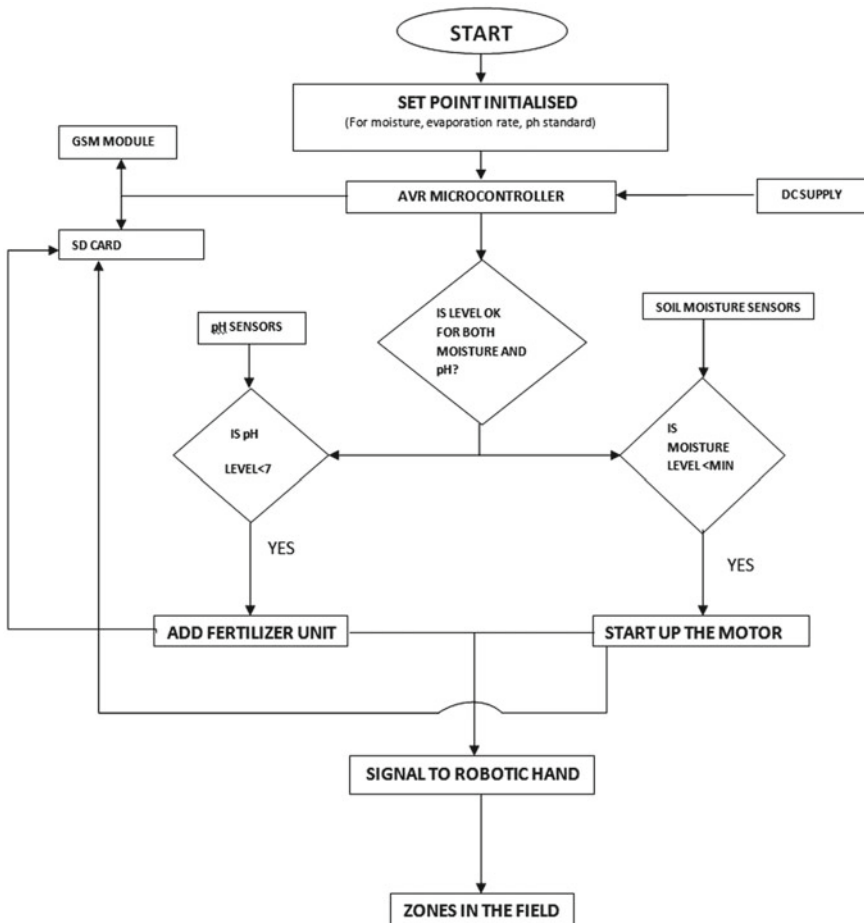


Fig. 1 Design flow of smart controlling of soil moisture and pH

it finds that the moisture content is equal or greater than the predefined value, it will switch OFF the pump and the robotic hand returns back to its original position. The process continues until we switch OFF the power supply. The microcontroller unit with various modules is programmed with embedded C. The flowchart of this program is shown in Fig. 2.

In the proposed model, the robotic arm-based system can be rotated horizontally and also move vertically with a flexible pipe which can extend to the crop field zone. The vertical movement is for negotiating of wind speed which can displace precise water and fertilizer in a particular zone. Several tanks are used for storing water and macronutrients like nitrogen, phosphorus, and potassium (NPK). The CAD-based proposed model with the adjustable robotic arm is shown in Fig. 3.

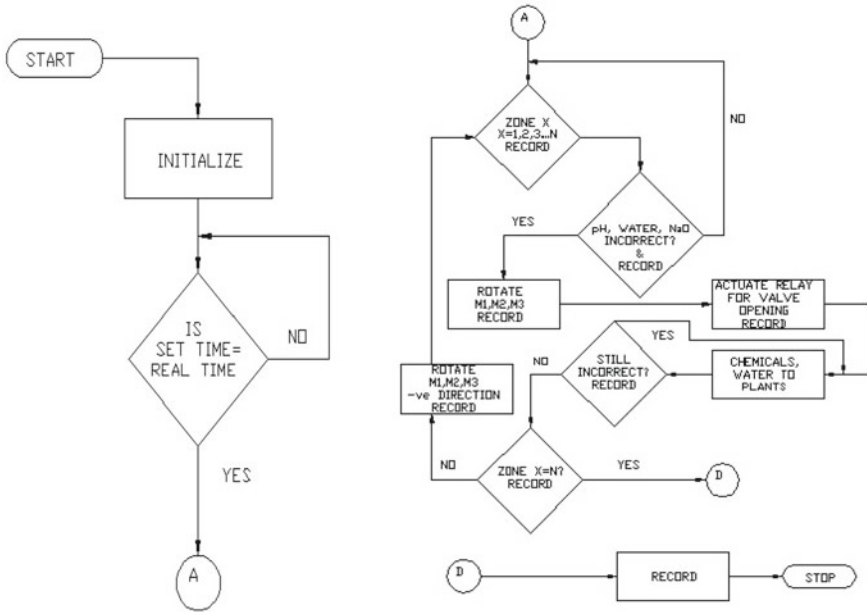


Fig. 2 Corresponding program flowchart

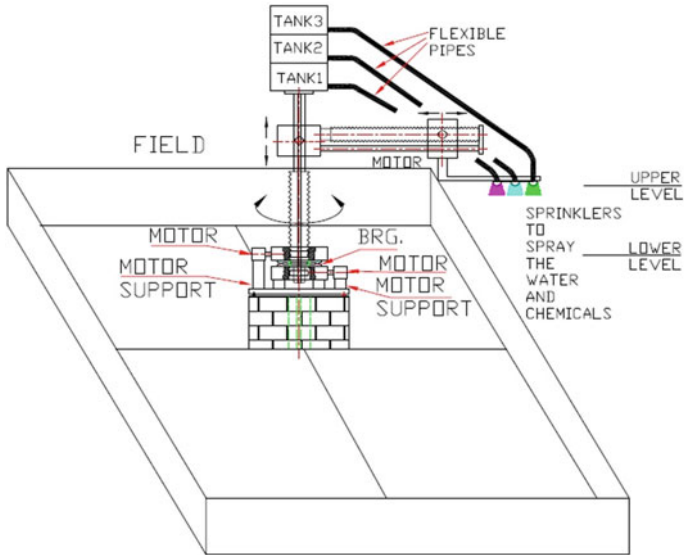
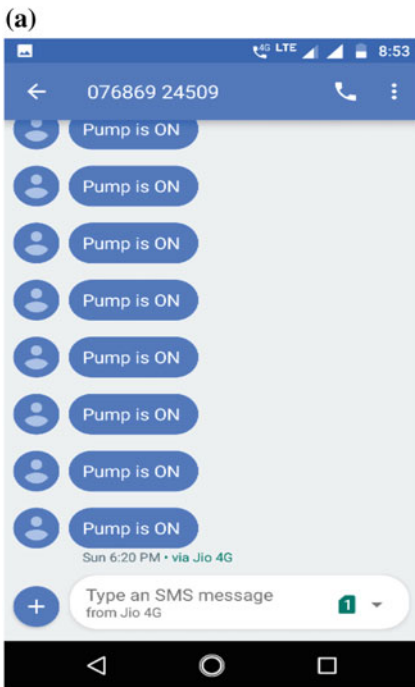


Fig. 3 CAD-based proposed model with a robotic arm

### 4 Result and Discussion

The GSM-based message for motor pump status and the corresponding data logger output for the future database are also shown in Fig. 4a, b, correspondingly.

The system is beneficial in terms of precise and proper utilization of water specifically in case of groundwater. It also reduces physical presence and pressure on the farmer. Due proper percentage of nitrogen, phosphorus, and potassium (NPK) content in the soil which yields for balanced fertilization. So the optimum quantities of soil moisture and NPK values are based on balanced fertilization and sensing data has been collected from a respective sensor, thus there is a definite improvement in controlling of soil moisture and pH as it is zone-based agriculture system. So, overall eco-friendly irrigation system is in terms of reduction of water wastage and toxicity by the fertilizer.



(b)

24.02.2018 -- 20:20:53	PUMP count 3	<u>Zone1</u>
Sunday		
25.02.2018 -- 17:09:45	PUMP count 1	<u>Zone1</u>
Sunday		
25.02.2018 -- 17:10:24	PUMP count 2	<u>Zone1</u>
Sunday		
25.02.2018 -- 17:23:14	PUMP count 1	<u>Zone1</u>
Sunday		
25.02.2018 -- 17:24:15	PUMP count 2	<u>Zone1</u>
Sunday		
25.02.2018 -- 17:26:58	PUMP count 1	<u>Zone1</u>
Sunday		
25.02.2018 -- 17:48:28	PUMP count 1	<u>Zone1</u>
Sunday		
25.02.2018 -- 17:51:40	PUMP count 1	<u>Zone1</u>
Sunday		
25.02.2018 -- 17:53:54	PUMP count 1	<u>Zone1</u>
Sunday		
25.02.2018 -- 17:56:56	PUMP count 1	<u>Zone1</u>
Sunday		
25.02.2018 -- 18:00:27	PUMP count 1	<u>Zone1</u>
Sunday		
25.02.2018 -- 18:01:56	PUMP count 2	<u>Zone1</u>
Sunday		
25.02.2018 -- 18:10:01	PUMP count 1	<u>Zone1</u>
Sunday		
25.02.2018 -- 18:16:09	PUMP count 1	<u>Zone1</u>
Sunday		
25.02.2018 -- 18:20:11	PUMP count 1	<u>Zone1</u>

Fig. 4 a Message alert in farmer mobile for pump status. b Corresponding real-time database of pump status and zone status

## 5 Conclusion

The overall profit margin for the farmer will increase with negligible error. In this paper, we have proposed agricultural zone-based automatic controlling of soil moisture and macronutrients, so the wastage of water and fertilizers are reduced becomes more environmentally friendly. The efficiency of farming is increased. The utility of this type of low-cost construction and usefulness of automation in agriculture have provided balanced fertilization, ensuring sustainable agriculture and increasing crop yields.

## References

1. G. Dev, Balanced fertiliser use increases crop yield and profit. *Better Crops Int.* **12**(2), 25–27 (1998)
2. R. Suresh, S. Gopinath, K. Govindaraju, T. Devika, N. Suthanthira Vanitha, GSM based Automated Irrigation Control using Raingun Irrigation System. *Int. J. Adv. Res. Comput. Commun. Eng.* **3**(2) (2014)
3. D.S. Pavithra, M.S. Srinath, GSM based automatic irrigation control system for efficient use of resources and crop planning by using an android mobile. *IOSR J. Mech. Civ. Eng.* **11**(1), 49–55 (2014)
4. Y. Kim, R.G. Evans, W.M. Iversen, Remote sensing and control of an irrigation system using a distributed wireless sensor network. *IEEE Trans. Instrum. Meas.* **57**(7) (2008)
5. B.R. Shiraz Pasha, B. Yogesha, Microcontroller based automated irrigation system. *Int. J. Eng. Sci.* **3**(7), 06–09 (2014)

# Author Index

## A

Anand, Mukul, 15

## B

Bag, Rajib, 269

Bandyopadhyay, Aritra, 269

Banerjee, Ananya, 205

Banerjee, Shubhendu, 269

Banik, Ankita Dutta, 313

Bera, Amalendu, 387

Bera, P. S., 49

Bhattacharjee, Pritam, 305

Bhattacharya, Soumyajit, 25

Bhattacharyya, Suvamoy, 399, 405

Biswas, P., 49

Biswal, Dibyajyoti, 157

Biswas, Priyankar, 25

Biswas, Shreya, 139

Bose, Ronojit, 103

## C

Chakrabarti, Chandrima, 205

Chakrabarty, Maitrayee, 59

Chakraborty, Avishek, 255

Chakraborty, Debashis, 191

Chakraborty, Gourav, 279

Chanda, Chandan Kumar, 3

Chanda, Sandip, 145, 399, 405

Chandra, Anindita, 175

Chandra, Aniruddha, 217, 227

Chatterjee, Shreya, 175

Chatterjee, Siddhartha, 255

Chattopadhyay, Sourav, 387

Chourasia, Jagriti, 205

Chowdhury, Anirban, 25

## D

Das, Anirban, 205

Das, Aritra, 103

Das, Arnima, 103

Das, Atanu, 269

Das, Kunal, 241, 375

Das, Moloy Kumar, 37

Das, P., 49

Das, Paromita, 217

Das, Promila, 145

Das (Roy), Srabani, 279

Das, Sahana, 129

Das, Sayan, 73, 81

Das, Susmita, 103

Das, Tanmay, 37

De, A., 145

De, Abhinandan, 59

Deb, Pratyusha Biswas, 103

De, Debashis, 241

Dev, Rahul, 15

Dey, Anilesh, 157, 165, 217, 227

Dey, Kaushik, 313

Dhar, Ankita, 129

Dutta, Pallav, 227

Dutta, Ritam, 345

Dutta, Rohan, 205

## F

Firojuddin, Sk., 331

## G

Ganguly, Biswarup, 139

Ganguly, Souradip, 205

Ghosh, Anupam, 113

Goswami, Sanjay, 59, 357, 367

**H**

Hait, Paresh, 37  
 Hazra, Pranab, 175

**J**

Jana, Poulami, 287

**K**

Kanjilal, Maitreyi Ray, 241, 375  
 Konar, Sukumar Chandra, 345  
 Kumar, Amit, 15  
 Kumar, Pradeep, 15

**M**

Majumder, Alak, 305  
 Majumder, Paushali, 357, 367  
 Mandal, Kamal Krishna, 25, 37  
 Mandal, Kunal Kumar, 255  
 Mandal, Surajit, 297  
 Mandal, Tarak Nath, 313  
 Mehera, Ranjan, 313  
 Mondal, Arkadeep, 73, 81  
 Mondal, Saptarshi, 255  
 Mondal, Soumaymoy, 37  
 Mondal, Souren, 37  
 Mukherjee, Himadri, 129  
 Mukherjee, Pronami, 89  
 Mukherjee, Somraj, 205

**N**

Nandy, Sayani, 25  
 Nayak, Suraj Kumar, 157, 165  
 Neogi, Biswarup, 217

**O**

Obaidullah, Sk. Md., 129

**P**

Pain, Puspak, 331, 375  
 Paitya, Nitai, 345  
 Pal, Jagadish, 3  
 Pal, Kunal, 157, 165

Pal, Rajat Kumar, 313  
 Pal, Soumen, 331  
 Panda, Saradindu, 279  
 Patel, Bikash, 73, 81  
 Pathak, Manish Kumar, 3  
 Paul, Bishaljit, 3  
 Paul, Suman, 175  
 Paul, Swatilekha, 165  
 Phadikar, Amit, 287  
 Phadikar, Santanu, 129

**R**

Rahul, 139  
 Ray Kanjilal, Maitreyi, 103  
 Roy, Kaushik, 129  
 Roy, Ranjit, 25, 37

**S**

Sadhu, Arindam, 241, 375  
 Samanta, Saikat, 255  
 Santosh, K. C., 129  
 Santra, Soumen, 297  
 Sanyal, Salil Kumar, 191  
 Sarkar, Dipu, 59  
 Sarkar, Indrani, 357, 367  
 Sarkar, Partha, 399, 405  
 Sarkar, Sharthak, 405  
 Sarkar, Sudhangshu, 227  
 Sen, Arijit, 399  
 Sengupta, Arjun, 113  
 Sengupta, Tapas Kumar, 89  
 Sinha, Ashesh, 399, 405

**T**

Talukdar, Prerana, 157

**V**

Vishwakarma, Priyanka, 139

**Y**

Yadu, Gitika, 165